

Lecture Notes in Civil Engineering

Kamal Jain

Vishal Mishra

Biswajeet Pradhan *Editors*

Proceedings of UASG 2021: Wings 4 Sustainability

Unmanned Aerial System in Geomatics

 Springer

Lecture Notes in Civil Engineering

Volume 304

Series Editors

Marco di Prisco, Politecnico di Milano, Milano, Italy

Sheng-Hong Chen, School of Water Resources and Hydropower Engineering,
Wuhan University, Wuhan, China

Ioannis Vayas, Institute of Steel Structures, National Technical University of
Athens, Athens, Greece

Sanjay Kumar Shukla, School of Engineering, Edith Cowan University, Joondalup,
WA, Australia

Anuj Sharma, Iowa State University, Ames, IA, USA

Nagesh Kumar, Department of Civil Engineering, Indian Institute of Science
Bangalore, Bengaluru, Karnataka, India

Chien Ming Wang, School of Civil Engineering, The University of Queensland,
Brisbane, QLD, Australia

Lecture Notes in Civil Engineering (LNCE) publishes the latest developments in Civil Engineering—quickly, informally and in top quality. Though original research reported in proceedings and post-proceedings represents the core of LNCE, edited volumes of exceptionally high quality and interest may also be considered for publication. Volumes published in LNCE embrace all aspects and subfields of, as well as new challenges in, Civil Engineering. Topics in the series include:

-Construction and Structural Mechanics-Building Materials-Concrete, Steel and Timber Structures-Geotechnical Engineering-Earthquake Engineering-Coastal Engineering-Ocean and Offshore Engineering; Ships and Floating Structures-Hydraulics, Hydrology and Water Resources Engineering-Environmental Engineering and Sustainability-Structural Health and Monitoring-Surveying and Geographical Information Systems-Indoor Environments-Transportation and Traffic-Risk Analysis-Safety and Security To submit a proposal or request further information, please contact the appropriate Springer Editor: Pierpaolo Riva at pierpaolo.riva@springer.com (Europe and Americas); Swati Meherishi at swati.meherishi@springer.com (Asia—except China, Australia, and New Zealand); Wayne Hu at wayne.hu@springer.com (China).

All books in the series now indexed by Scopus and EI Compendex database!

Kamal Jain · Vishal Mishra · Biswajeet Pradhan
Editors

Proceedings of UASG 2021: Wings 4 Sustainability


Unmanned Aerial System in Geomatics

 Springer

Editors

Kamal Jain
Department of Civil Engineering, Centre
of Excellence in Disaster Mitigation
and Management (CoEDMM)
Indian Institute of Technology Roorkee
Roorkee, Uttarakhand, India

Vishal Mishra
Department of Civil Engineering
Indian Institute of Technology Roorkee
Roorkee, Uttarakhand, India

Biswajeet Pradhan 
Centre for Advanced Modelling
and Geospatial Information Systems
(CAMGIS)
University of Technology Sydney
Ultimo, NSW, Australia

ISSN 2366-2557

ISSN 2366-2565 (electronic)

Lecture Notes in Civil Engineering

ISBN 978-3-031-19308-8

ISBN 978-3-031-19309-5 (eBook)

<https://doi.org/10.1007/978-3-031-19309-5>

© The Editor(s) (if applicable) and The Author(s), under exclusive license to Springer Nature Switzerland AG 2023

This work is subject to copyright. All rights are solely and exclusively licensed by the Publisher, whether the whole or part of the material is concerned, specifically the rights of translation, reprinting, reuse of illustrations, recitation, broadcasting, reproduction on microfilms or in any other physical way, and transmission or information storage and retrieval, electronic adaptation, computer software, or by similar or dissimilar methodology now known or hereafter developed.

The use of general descriptive names, registered names, trademarks, service marks, etc. in this publication does not imply, even in the absence of a specific statement, that such names are exempt from the relevant protective laws and regulations and therefore free for general use.

The publisher, the authors, and the editors are safe to assume that the advice and information in this book are believed to be true and accurate at the date of publication. Neither the publisher nor the authors or the editors give a warranty, expressed or implied, with respect to the material contained herein or for any errors or omissions that may have been made. The publisher remains neutral with regard to jurisdictional claims in published maps and institutional affiliations.

This Springer imprint is published by the registered company Springer Nature Switzerland AG
The registered company address is: Gewerbestrasse 11, 6330 Cham, Switzerland

Preface

Second International Conference on Unmanned Aerial Systems in Geomatics-2023 (UASG-2021) was organized by the Department of Civil Engineering, Indian Institute of Technology Roorkee (IIT Roorkee) Roorkee, India, during 02–04 April 2021. UASG-2021 was conducted in the midst of Covid-19 pandemic and it was completely online. UASG-2021 was a great experience for its users as attendees, speakers and presenters with a huge global audience of around 500 registered and 1000+ free users for whom we made the sessions live on an open portal. The inauguration ceremony itself had almost 300 attendees from all over the world with 800 views on the open portal. There were 25 sessions, in which 8 keynote speakers distinguished and eminent in their respective fields shared their ideas and experiences, 4 theme-based sessions with over 30 plenary speakers focussed on different aspects and considerations related to Unmanned Aerial Vehicles (UAVs) as well there were 3 special sessions covering specific details about various aspects and applications of UAVs.

The main theme of this conference was “Wings for Sustainability”. We all are aware of the word “Sustainable Development”. With the increase in human population, it is becoming very necessary to adopt such practices. The focus of the conference was how drones can be instrumental in achieving the Sustainable Development and the 17 Sustainable Development Goals envisioned by the United Nations for 2030. The Sustainable Development Goals (SDGs), otherwise known as the Global Goals, are a set of objectives within a universal agreement to protect all that makes the planet habitable and ensure that all people enjoy peace and prosperity, now and in the future.

UAVs are being used around the world as means of recreation as well as for inspection, surveys and for data collection. Thus, they are becoming tools of development. These UAVs can be used in a variety of creative ways to advance Sustainable Development Goals. From aiding citizens in Search and Rescue during a disaster, from infrastructure planning to monitoring peace and security they can be anywhere and everywhere. The papers were invited on the theme “Wings for Sustainability” but were not restricted to this only. The selected and revised papers are produced here

in this proceedings. We hope that these papers will directly or indirectly contribute to Sustainable Development.

Roorkee, India
Ultimo, Australia
Roorkee, India

Kamal Jain
Biswajeet Pradhan
Vishal Mishra

Acknowledgements

We are grateful to all those people who have supported us and had their contributions in this volume of Proceedings.

Efforts taken by peer reviewers contributed to improve the quality of papers and provided constructive critical comments; improvements and corrections to the authors are gratefully appreciated. We are very grateful to the members of Organizing committee, Technical Program Committee, Keynote Speakers, Plenary speakers, Session Chairs, student volunteers and Administrative assistants from institute management of IIT Roorkee who selflessly contributed to the success of this Conference. Also, we are thankful to all the authors who submitted their papers, because of which the conference became a story of success. It was the quality of their presentations and their passion to communicate with the other participants that really made this conference series a grand success.

We would like to specially mention the student volunteer Ms. Prathiba A.P. (Research Scholar, IIT Roorkee) who tirelessly worked along with Ms. Malika Aswal for the publication.

We appreciate the support of Dr. Adrish Mullick, Dr. Ganesh Khadanga, Akshay Pandey, Harshit, Srashti Singh, Eshta Ranyal, Chandrahas Singh, Abhishek Rai and Shubham Awasthi in the organization of this conference.

This conference was organized in association with the INTERNATIONAL SOCIETY FOR PHOTOGRAMMETRY & REMOTE SENSING (ISPRS) and Indian Society of Remote Sensing (ISRS) under the joint patronage of the UNESCO & the Indian National Commission for Cooperation with UNESCO (INCCU) with the support of the National e-Governance Division, Ministry of Electronics & Information Technology, Government of India (under Digital India Programme), Survey of India, Defence Research and Development Organization, SP Singla Constructions Pvt. Ltd., Kambill Systems and Raveneye Geospatial Private Limited.

Last but not least, we are thankful to each and every person, whom we could not name, for supporting us in every step of our journey towards success. Their support was not only the strength, but also an inspiration for organizers.

Edited by
Prof. Kamal Jain
Prof. Biswajeet Pradhan
Vishal Mishra

Contents

Comparison of DEM Generated from UAV Images and ICESat-1 Elevation Datasets with an Assessment of the Cartographic Potential of UAV-Based Sensor Datasets	1
Ashutosh Bhardwaj, Surendra Kumar Sharma, and Kshama Gupta	
UAV to Cadastral Parcel Boundary Translation and Synthetic UAV Image Generation Using Conditional-Generative Adversarial Network	11
Ganesh Khadanga and Kamal Jain	
UAV-Based Terrain-Following Mapping Using LiDAR in High Undulating Catastrophic Areas	21
Chandra Has Singh, Kamal Jain, and Vishal Mishra	
Forest Fire Detection from UAV Images Using Fusion of Pre-trained Mobile CNN Features	39
Bhuma Chandra Mohan	
Deep Learning-Based Improved Automatic Building Extraction from Open-Source High Resolution Unmanned Aerial Vehicle (UAV) Imagery	51
Chintan B. Maniyar and Minakshi Kumar	
Design and Development of Human Temperature Measuring System Using Drone Based Multispectral and Thermal Images	67
S. Meivel, S. Maheswari, and D. Faridha Banu	
Feature Extraction in Urban Areas Using UAV Data	87
Surendra Kumar Sharma, Minakshi Kumar, Sandeep Maithani, and Pramod Kumar	
The Role of ‘Unmanned Aerial Vehicles’ in Smart City Planning and Management	99
Rewati Raman and Ushnata Datta	

Elevation Data Acquisition Accuracy Assessment for ESRI Drone2Map, Agisoft Metashape, and Pix4Dmapper UAV Photogrammetry Software 121
 Deepak Tyagi, Vishal Mishra, and Harshit Verma

Characterization of Urban Vegetation from an Unmanned Aerial Vehicle (UAV) Image 133
 Minakshi Kumar and Shefali Agrawal

Environmental Gaseous Sensing Using Sniffer Drone for Urban Development Control 145
 Norzailawati Mohd Noor and Mazlan Hashim

Drone Technology in Waste Management: A Review 157
 Richa Choudhary and Susheela Dahiya

Solar Roof Panel Extraction from UAV Photogrammetric Point Cloud 173
 S. K. P. Kushwaha, Harshit, and Kamal Jain

Spacio-Statistical Model to Predict Crime Locations Based on Past Crime Events and UAV Based Monitoring of the Predicted Surveillance Route 187
 Hasmukh Chauhan, Pranav Pandya, and Chancy Shah

Automatic Ship Detection Using CFAR Algorithm for Quad-Pol UAV-SAR Imagery 199
 Harshal Mittal and Ashish Joshi

A Deep Learning Approach for Detection and Segmentation of Airplanes in Ultrahigh-Spatial-Resolution UAV Dataset 211
 Parul Dhingra, Hina Pande, Poonam S. Tiwari, and Shefali Agrawal

Influence of European UAS Regulations on Image Acquisition for 3D Building Modeling 229
 Grzegorz Gabara

Effects of Flight Plan Parameters on the Quality and Usability of Low-Cost UAS Photogrammetry Data Products for Tree Crown Delineation 243
 Jojene R. Santillan, Jun Love E. Gesta, and Marcia Coleen N. Marcial

The Segmentation of Drone Image derived 3D Point Cloud Using a Combination of RANSAC, DBSCAN and Clustering Methods 267
 Puyam S. Singh, Iainehborlang M. Nongsiej, and Valarie Marboh

An Automated Process to Filter UAS-Based Point Clouds 279
 Volkan Yilmaz

Some Enhancement of Aerial and Terrestrial Photo for 3D Modeling of Texture-Less Object Surface 289
 Catur Aries Rokhmana and Hanif Muhammad Fauzi

Role of Drone Technology in Sustainable Rural Development: Opportunities and Challenges 301
 Venkata Ravibabu Mandla, Nagaveni Chokkavarapu, and Veerendra Satya Sylesh Peddinti

Disaster Risk Mapping from Aerial Imagery Using Deep Learning Techniques 319
 Amit Kumar Jena, Sai Sudhamsa Potru, Deepak Raghavan Balaji, Abhinayana Madu, and Kuldeep Chaurasia

High-Resolution Mapping of Forest Canopy Cover Using UAV and Sentinel-2 331
 Charanjeet Singh Nijjar, Sachchidanand Singh, Tanisha Jaiswal, and Shivani Kalra

Design and Method of an Agricultural Drone System Using Biomass Vegetation Indices and Multispectral Images 343
 S. Meivel, S. Maheswari, and D. Faridha Banu

UAV-LiDAR and Terrestrial Laser Scanning for Automatic Extraction of Forest Inventory Parameters 375
 Khadija Meghraoui, Hamza Lfalah, Imane Sebari, Souhail Kellouch, Sanaa Fadil, Kenza Ait El Kadi, and Saloua Bensiali

A UAS-Based Approach for Orchard Geo-Information Management System 395
 Abhishek Adhikari, Minakshi Kumar, and Shefali Agrawal

High-Speed Wi-Fi Systems for Long Range FANETS: Real Problems, Experiments, and Lessons Learnt 411
 Utkarsh Ahuja

Algal Bloom Detection Using UAV Imagery: A Case Study on Waddepally Lake, Warangal 423
 Allu Ayyappa Reddy, M. Shashi, and Kumarapu Kumar

Ballistics Algorithm for Airborne Remote Sensor Position in Catastrophe Zones 435
 Vipinkumar R. Pawar, Sudhakar Mande, and Imdad Rizvi

Practical Applications for UAS Designed to Assist Climatologists in Studying Toxic Gas Emissions Relative to Climate Change 457
 Ian Godfrey and José Pablo Sibaja Brenes

Review of Uncrewed Aerial Vehicle Swarm System Coordination and Communication 485
Chandra Has Singh, Vishal Mishra, and Kamal Jain

Simulation of Clustering Protocol and Mobility Model for UAV Networks 501
Abhishek Joshi, Sarang Dhongdi, and K. R. Anupama

Obstacle Avoidance for Quadcopters in Formation Flying Based on A* Algorithm 517
Kumud Ranjan Roy

Coverage Estimation Using Probabilistic Line-of-Sight Model for Unmanned Aerial Vehicle Communication 533
Ankita K. Patel and Radhika D. Joshi

Blockchain Technology Based Security for UAV IoT Environment 545
Renu Mishra and Sandeep Saxena

Power Management of Drones 555
D. S. Vohra, P. K. Garg, and S. K. Ghosh

Technology for Power Supply to UAVs through Medium of Air 571
Devineni Pavan and Merugu Suresh

An Efficient Application of Machine Learning for Assessment of Terrain 3D Information Using Drone Data 579
Ankush Agarwal, Aradhya Saini, Sandeep Kumar, and Dharmendra Singh

Abbreviations

2D	Two Dimensions
3D	Three-dimensional
A	Ampere
A*	A star
AA	Autonomous aircraft
ABS	Aerial Base Station
AC	Alternating Current
AI	Artificial Intelligence
AIC	Agriculture insurance company
ALS	Aerial Laser Scanning
ALS	Airborne laser scanning
AM	Amplitude Modulation
ANN	Artificial neural network
APC	Armour Personnel Carriers
API	Application Programming Interface
APV	Automatically piloted vehicle
ArcGIS	Advanced Repair Guidance Information System
ASM	Angular Second Moment
ASTER	Advanced Spaceborne Thermal Emission and Reflection Radiometer
ATLAS	Advanced Topographic Laser Altimeter System
AVHRR	Advanced Very High-Resolution Radiometer
AWDI	Alternate Wet and Dry Irrigation index
BC	Blockchain
BCE	Binary Cross Entropy
BIM	Building information modeling
BLDC	Brushless Direct current
BNDVI	Blue-normalized difference vegetation index
BPF	Band Pass filter
BPNN	Back-propagation neural networks
BWDRVI	Blue-wide dynamic range vegetation index

C	Capacity
CAPAP	Public Administration Centre for Spatial Analysis
CBH	Crown Base Height
cc	Coherence
CC	Constant Current
CC	Crown Centroid
CCD	Charge Coupled Device
CFAR	Constant False Alarm Rate
cGAN	conditional Generative Adversarial Network
CH	Cluster-Head
CH	Crown Height
CHM	Canopy Height Model
Ci	Connectivity Value
CL	Crown Length
CLAHE	Contrast Limited Adaptive Histogram Equalization
CMOS	Complementary Metal-Oxide Semiconductor
CNN	Convolutional Neural Network
CO ₂	Carbon dioxide
CON	Contrast
COTS	Commercially off the shelf
COVID19	Corona Virus Disease 2019 caused by SARS-CoV-2
CPP	Canopy Positional Proximity
CSF	Cloth Simulation Filtering
CSRE	Compressive Strength of cement Stabilized Rammed Earth
CSTEP	Centre for Study of Science, Technology, and Policy
CTH	Crown Total Height
CV	Constant Voltage
CW	Crown Width
DB	Davies–Bouldwin Index
DBH	Diameter at Breast Height
DBSCAN	Density-Based Spatial Clustering of Applications with Noise
DC	Direct Current
DCM	Direction cosine matrix
DEM	Digital Elevation Module
DenseNet	Dense Convolution Network
DFT	Discrete Fourier Transform
DiCENET	Dimension-wise Convolutions for Efficient Networks
DJI	Da-Jiang Innovations
DLR	German Aerospace Center
DNN	Deep Neural Network
DOAS	Differential Optical Absorbance Spectroscopy
DoD	Department of Defense
DP	Digital Photography
DRAM	Dynamic random access memory

DS	Digital Signature
DSC	Dice Similarity Coefficient
DSM	Digital Surface Model
DSM	Digital soil mapping
DTL	Distributed Transaction Ledger
DTM	Digital Terrain Model
DV	Decision variable
EASA	European Union Aviation Safety Agency
EC	Electrical conductivity
ELM	Extreme learning machine
EM	Electro-Magnetic
EMC	Electromagnetic Compatibility
EMF	Electromagnetic field
EOD	End of day
ETM+	Enhanced Thematic Mapper Plus
EU	European Union
EVI	Enhanced Vegetation Index
ExGI	Excess Green Index
f0	Resonant Frequency
F1, F2, F3, F4	Thrusts
FAA	Federal Aviation Administration
FANET	Flying Area Network
FANET	Flying Ad-Hoc Network
FANETS	Flying Ad-Hoc NETWORKS
FAPAR	Fraction-Absorbed Photosynthetically Active Radiation
FBNET	Facebook-Berkeley Networks
fc	Carrier Signal
FCN	Fully Convolutional Networks
FCS	Flight control systems
FD	Fractal Dimension
FH	Flying Height
FLIR	Forward-looking infrared
FN	False Negative
FP	False Positive
FP	Flight Plan
fp	Low Frequency electrical signal
fs	Sampling Frequency
FWHM	Full width at half maximum
g	Earth's gravitational field
G(R)	Gain at receiver
G(T)	Gain at transmitter
GAN	Generative Adversarial Network
GBNDVI	Green-blue normalized difference vegetation index
GCC	Ground Control Center
GCP	Grown Plant Certification Program

GCP	Ground Control Point
GCS	Ground control station
GDP	Gross Domestic Product
GEOSAIL	A canopy two-layer model
GIS	Geographical Information System
GLAS	Geoscience Laser Altimeter System
GLCM	Gray level co-occurrence matrix
GNDVI	Green Difference Vegetation Index
GNDVI	Green Normalized Difference Vegetation Index
GNSS	Global Navigation Satellite System
GPIO	General-purpose input/output
GPS	Global Positioning System
GPS+IMU	Global Positioning System + Inertial Measuring Unit
GPU	Graphical Processing Unit
GRD	Ground Range Detected
GSD	Ground Sampling Distance
GSHHG	Global Self-consistent, Hierarchical, High-resolution Geography
GUI	Graphical user interface
GV	Green Vegetation
HAB	Harmful Algal Blooms
HCRF	Higher-order conditional random fields
HEED	Hybrid Energy-Efficient Distributed
Hr	Hour
IAIL	Inria Aerial Image Labelling Dataset
ICAO	International Civil Aviation Organization
ICESat-1	Ice, Clouds, and Land Elevation Satellite
ICT	Information and communication technology
IEEE	Institute of Electrical and Electronics Engineers
IFV	Infantry Fighting Vehicles
IIRS	Indian Institute of Remote Sensing
IMU	Inertial Measurement Unit
InSAR	Synthetic Aperture Radar Interferometry
IoCTs	Internet of Connected Things
IoD	Internet of Drones
IoT	Internet of Things
IoU	Intersection over Union
IR	Infrared radiation
ISO	International Organization for Standardization
ISRO	Indian Space Research Organization
IT	Information Technology
ITU	International Telecommunication Union
Ixx, Iyy, Izz	Moment of inertia
j	Quadcopter's body inertia matrix
JPG	Joint Photographic Expert Group

JPL	Jet Propulsion Laboratory
JSON	JavaScript Object Notation
KDC	Key Distribution Centre
KDE	Kernel Density Estimations
kHz	Kilo Hertz
Km	Kilometer
km	Torque factor
kn	Thrust factor
KV	Kilo Voltage
LAI	Leaf Area Index
LAZ	Compressed LiDAR file format
LCI	Leaf Chlorophyll Index
LEACH	Low-Energy Adaptive Clustering Hierarchy
Li-ion	Lithium Ion
LiDAR	Light Detection and Ranging
LiPo	Lithium Polymer
LoD	Levels of detail
LoS	Line of sight
LQR	Linear quadratic regulator
LRI	Landslide Risk Index
LSI	Landslide Slope Index
LSR	Least Square Regression
LST	Land surface temperature
LSTM	Long Short Term Memory
LSWI	Land Surface Water Index
LUAS	Light unmanned aeroplane systems
LURS	Light unmanned rotorcraft systems
m	Quadcopter's mass
mAh	Mili Ampere Hour
MANET	Mobile Ad-hoc Networks
MBI	Morphological Building Index
MFRN	Multiple Feature Reuse Network
MHz	Mega Hertz
MILP	Mixed integer linear programming
MJ/Kg	Mega Joules per Kilogram
ML	Machine Learning
MLPs	Multilayer Perceptron's
MNASNET	Mobile Neural Architectural Search
MNDWI	Modified Normalized Difference Water Index
MODIS	Moderate Resolution Imaging Spectroradiometer
MPC	Model predictive control
MRS	Multi resolution Segmentation
MS	Multispectral
MSRI	Modified Simple Ratio Index
MSR	Modified simple ratio

MTVI	Modified Triangular Vegetation Index 1&2
MVS	Multiview Stereopsis
n-DSM	Normalized digital surface model
NAS	Neural Architecture Search
NASA	National Aeronautics and Space Administration
NBR	Normalized Burn Ratio
NCC	Non coronary cusp
NDGV	Normalized Differential Green vegetation
NDMI	Normalized Difference Moisture Index
NDRE	Normalized Difference RedEdge
NDSM	Normalized Digital Surface Model
NDVI	Normalized Difference Vegetation Index
NDVI-Red edge index	Normalized Difference Vegetation Index Red Edge
NDWI	Normalized Difference Water Index
NGBDI	Normalized Green Blue Difference Index
NiCd	Nickel Cadmium
NIR	Near Infrared
NS-3	Network Simulator—3
NSTS	National standard scenarios
OB	Angular positions
OBIA	Object-Based Image Analysis
OCF	Orchard Compactness Factor
ODM	OpenDrone Maps
OGIS	Orchard Geo-Information System
OLI	Operational Land Imager
op-amp	Operational Amplifier
OpenCV	Open Source Computer Vision Library
OSM	Open Street Map
OTA	Over The Air
P	Parallel
P(R)	Power at receiver
P(T)	Power at transmitter
PAR	Photosynthetically Active Radiation
PD	Probability of Detection
PFA	Probability of false alarm
PIB	Press Information Bureau
PID	Proportional-Integral-Derivative
Pix4Dmapper	Professional photogrammetry software
PKI	Public key Infrastructure
PLS	Partial least squares
PLS-PM	PLS path modeling
PLSR	PLS regression
PNED	Linear positions
PoW	Proof of Work
PPK	Post-Processed Kinematic

PPP	Public-private partnership
PROSPECT	Leaf model
PTIN	Progressive TIN Densification
QGIS	Quantum Geographic Information System (software)
RADAR	Radio Detection and Ranging
RAM	Random Access Memory
RANSAC	Random Sample Consensus
RBSE	Research Based Science Education
RC	Remote Control
ReLU	Rectified Linear Unit
ResNet	Residual Network
RF	Random Forest
RF	Radio Frequency
RGB	Red-Green-Blue
RGB channel	Red, Green, and Blue channel
RHT	Random Hough Transform
Ri	Residual Energy Value
RL	Reinforcement learning
RLC	Resistor(R), Inductor(L), Capacitor(C)
RMSE	Root Mean Squared Error
ROC	Receiver Operating Characteristics
ROR	Record of Rights (ROR)
ROS	Robot Operating System
ROS	Remote Ocean Systems
ROVIO	Robust Visual-Inertial Odometry
RPA	Remotely Piloted Aircraft
RPAS	Remotely Piloted Aircraft Systems
RPD	Ratio of performance to deviation
RPM	Rounds Per Minute
RPV	Remotely piloted vehicle
Rs	Rupees (Indian Currency Ruppees)
RS	Remote Sensing
RS	Imagery: Remote Sensing Imagery
RTH	Return To Home
RTK	Real-time Kinematic
RVI	Ratio vegetation index
Rx	Receiver
S	Series
S-N-E-W	South north east west
S.O.D.A.	Sensefly Sensor Optimized for Drone Applications
SAIL	Scattering of Arbitrarily Inclined Leaves
SAR	Synthetic Aperture Radar
SAVI	Soil Adjusted Vegetation Index
SCADA	Supervisory Control and Data Acquisition
SCP	Semi Classification Plugin

SD	Secure Digital
SDCARD	Secure Digital card
SDG/ SDGs	Sustainable Development Goals
SE-ResNet	Squeeze-and-Excitation Residual Nets
SEM	Scanning Electron Microscope
SEM	Structural equation modeling
SfM	Structure from Motion
SI	Slope Index
SI	Shape Index
SIFT	Scale-invariant feature transform
SLC	Single Look Complex
SLIC	Simple Linear Iterative Clustering
SLICO	Simple linear iterative clustering zero
SMC	Sliding mode control
SMRF	Simple Morphology-based Method
SOC	System On Chip
SOC	Soil organic carbon
SOCC	System On Chip Computer
SORA	Specific Operations Risk Assessment
SQI	Soil quality index
SSD	Single Shot MultiBox Detector
SSH port	Secure Shell port
STA	Seasonal Trend Analysis
STR	Stepwise regression
STS	Standard scenarios
SVM	Support Vector Machine
SVMR	Support vector machine regression
SVR	Support vector regression
SWI	Soil Water Index
SWIR	Shortwave infrared
T-VWSI	Temperature Vegetation Water Stress Index
TanDEM-X	TerraSAR-X add-on for Digital Elevation Measurement
TCI	Temperature Condition Index
TLS	Terrestrial Laser Scanning
TMC	Thousand Million Cubic Feet
TN	True Negative
TNAU	Tamil Nadu Agricultural University
TOF	Trees outside forest
TOF	Time of flight
TOPEX-Poseidon	Topography Experiment-Positioning, Ocean, Solid Earth, Ice Dynamics, Orbital Navigator
TP	True Positive
TSAVI	Transformed Soil Adjusted Vegetation Index
TVI	Transformed Vegetation Index
Tx	Transmitter

UA	Unmanned Aircraft
UAN	Unmanned Aerial Network
UAS	Uncrewed Aerial System, Unmanned Aerial System, Unmanned Aircraft System
UAV	Unmanned/Unoccupied/Uncrewed Aerial Vehicle
UAV-LiDAR	Unmanned Aerial Vehicle-Light Detection And Ranging
UAVO	Unoccupied/Unmanned Aerial Vehicle Operator
UAVs	Unoccupied/Unmanned aerial vehicle system
UGV	Unoccupied/Unmanned Ground Vehicle
UHR	Ultra high-resolution
UHSR	Ultrahigh-Spatial-Resolution
ULB	Urban Local Bodies
UTM	Universal Transverse Mercator
UV drone	Ultra-Violet drone
UWB	Ultra Wide Band
V	Voltage
VANET	Vehicular Ad-Hoc Network
VCI	Vegetation Condition Index
VDVI	Visible-Band Difference Vegetation Index
VG	Virtual Ground
VHI	Vaginal Health Index
VHR	Very High-Resolution
VIIRS	Visible Infrared Imaging Radiometer Suite
VLOS	Visual Line of Sight
VNIR	Visible near infrared
VRA	Village revenue area
VRS	Virtual Reference Station
VSOP	Semi-Analytic Planetary Theory (French: Variations Séculaires des Orbites Planétaires)
VTOL	Vertical Take-off and Landing
VXL	Traxxas version XL (Version of Traxxas Remote Control (RC) Car)
W/Kg	Watts per Kilogram
WDVI	The weighted difference vegetation index
WEF	World economic forum
WGS84	World Geodetic System of 1984
WHO	World Health Organization
Wi-Fi	Wireless fidelity
Wireless LAN	Wireless Local Area Network
WOA	Whale Optimization Algorithm
WPC	Wireless Planning and coordination wing
WRI	Water Ration Index
WSNs	Wireless Sensor Networks
Xb, Yb, Zb	Body-fixed reference frame
XI, YI, ZI	Inertial frame

XML	Extensible Markup Language
YOLO	You Only Look Once
π	Pi
φ, θ, ψ	Roll, pitch, and yaw angles
ω	Omega

Comparison of DEM Generated from UAV Images and ICESat-1 Elevation Datasets with an Assessment of the Cartographic Potential of UAV-Based Sensor Datasets



Ashutosh Bhardwaj, Surendra Kumar Sharma, and Kshama Gupta

Abstract The availability of Very High-Resolution (VHR) remote sensing datasets from the Unmanned Aerial Vehicle (UAV) based sensors are changing the methods of cartographic mapping as well as visualization by taking advantage of both the high spatial resolution as well as high radiometric resolutions. A high-fidelity digital elevation model (DEM) can be prepared using these UAV datasets, which can produce high-quality orthoimages. In the present study, the space-borne lidar elevation datasets from the Ice, Clouds, and Land Elevation Satellite (ICESat-1) and TanDEM-X 90 m DEM from TerraSAR-X add-on for Digital Elevation Measurement (TanDEM-X) mission are utilized for the comparison of elevation values from DEM generated using UAV datasets for the experimental site in Switzerland. The experimental site is part of Yverdon-Les-Bains, which is a municipality in the district of Jura-Nord VuDOI, canton of Vaud, Switzerland. The openly accessible dataset from the Sensefly Sensor Optimized for Drone Applications (S.O.D.A.) includes 235 true-color RGB images acquired from a flight height of 106 m, at an average Ground Sampling Distance (GSD) of 2.64 cm. The datasets are processed in Pix4D software for the bundle block adjustment, followed by the generation of DEM and orthomosaic. The comparison of ICESat-1 elevation data with DEM depicts a difference of about 26 cm on plain ground, which is reasonably good considering the use of a Global Navigation Satellite System (GNSS) network in Real-Time Kinematic (RTK) mode. The quality report depicts the mean of geolocation accuracy in X, Y, and z as 2.73 cm, 2.73 cm, and 3.46 cm respectively, which is practically highly accurate. Root Mean Square Error (RMSE) in X, Y, and z is computed as 1.7 cm, 2.27 cm, and 2.31 cm respectively. The study depicts that practically the cartographic

A. Bhardwaj (✉)

Photogrammetry and Remote Sensing Department, Indian Institute of Remote Sensing, Dehradun, India

e-mail: ashutosh@iirs.gov.in

S. K. Sharma · K. Gupta

Urban and Regional Studies Department, Indian Institute of Remote Sensing, Dehradun, India

e-mail: surendra@iirs.gov.in

K. Gupta

e-mail: kshama@iirs.gov.in

© The Author(s), under exclusive license to Springer Nature Switzerland AG 2023

K. Jain et al. (eds.), *Proceedings of UASG 2021: Wings 4 Sustainability*,

Lecture Notes in Civil Engineering 304,

https://doi.org/10.1007/978-3-031-19309-5_1

potential for the UAV dataset is suitable for mapping at a scale range of 1:250 to 1:300 or better for such plain terrain conditions, meeting the engineering drawing requirements for facility management and utility mapping.

Keywords Scale · Cartographic potential · Accuracy · Orthomosaic

1 Introduction

Digital images acquired from aerial platforms such as aircraft or UAVs are providing VHR datasets having spatial resolutions of the order of a few centimeters. These datasets when processed under a quality-controlled environment yield accuracies of the order of better than a pixel. Similarly, the Light Detection and Ranging (LiDAR) technique is also providing vertical accuracy of the order of a few centimeters to decimeters depending on the ground feature. Whereas the digital images provide a continuous picture of the study area, the LiDAR datasets provide discrete information based on their footprints. VHR satellite-based sensors such as Cartosat-2 series, Cartosat-3, Quickbird, and Worldview series of satellites are approaching higher and higher spatial resolution suitable for orthoimages as photogrammetric products and large-scale mapping ranging from 1:2500 to 1:10,000 or better under stringent control conditions [1, 2]. However, the VHR UAV datasets can comply with mapping scale requirements of 1:250 to 1:300 with good ground control points or highly accurate position and attitude sensor parameters.

1.1 UAV

UAV or the Unmanned Aircraft System (UAS) which refers to an unmanned aircraft or an aircraft with no pilot, is currently providing the VHR datasets with immense potential in the service sector including disaster management. The UAVs are primarily categorized as nano (<250 g), micro (>250 g and <2 kg), small (>2 kg and <25 kg), medium (>25 kg and <150 kg), and large (>150 kg) depending on their weight inclusive of the payloads. The UAVs are also referred to as Remotely Piloted Aircraft (RPA) or drones in common language. UAVs have extensively been used for various applications such as forestry [3], agriculture [4], structural damages [5], image classification [6], geological structures [7], urban flood [8], DEM generation [9, 10], vehicle detection [11] and data fusion-based studies [12, 13].

1.2 ICESat Missions

The Ice, Clouds, and Land Elevation Satellite (ICESat) Missions include two spaceborne lidar-based payload-carrying satellites namely, ICESat-1 (launched on 13 January 2003) and ICESat-2 (launched on 15 September 2018). These missions provide highly accurate elevation datasets which are utilized for elevation accuracy assessments as well as data fusion [14–19]. Currently, the Openaltimetry portal is providing the ICESat/GLAS (Geoscience Laser Altimeter System) data including the GLAH06 (Level-1B) Global Elevation Data, Version/Release 34, which incorporates improvements over Release 33 data products (<https://openaltimetry.org/datainfo.html>) [20]. ICESat-1 used a diode-pumped Q-switched Nd:YAG laser operating in the near-infrared (1064 nm) for the measurement of surface topography besides the visible green light (532 nm) pulses to measure the vertical distribution of clouds and aerosols. The spots produced on the Earth's surface have a 70 m diameter and the spacing between spots is about 175 m, caused by the orbital motion of the spacecraft [21]. ICESat-2 carries the Advanced Topographic Laser Altimeter System (ATLAS), a laser altimeter that sends 10,000 pulses per second toward Earth and records the travel time of individual photons for measurements of the surface topography [22, 23].

The effects of LiDAR at various wavelengths, including the eye-safe 1064 nm Near-InfraRed (NIR) wavelength have been studied for penetration to human skin [24] and tree canopy. Ground surface and forest canopy characteristics are found to be uniquely represented at different LiDAR wavelengths. Canopy attenuation was greatest at 532 nm due to leaf tissue absorption [25]. The tree area has a higher penetration rate than buildings and therefore yields a higher number of multiple returns [26]. The UAV and spaceborne LiDAR technologies are considered in this study for the comparative study since both of them have the capabilities to provide elevation information and products with a high order of accuracy [7].

2 Study Area

The study area is part of Yverdon-les-Bains, which is a municipality in the district of Jura-Nord Vaud OI in Switzerland (Fig. 1). The study area primarily 0.46 sq. km consists of a technology park, agricultural fields, buildings, and parking areas. The area is on the south of Lake Neuchatel.



Fig. 1 Study area with boundary and ICESat-1 data points overlaid on the Google Earth platform

3 Material and Method

The openly accessible dataset downloaded from the senseFly portal includes 235 sensefly (S.O.D.A.) true-color RGB images acquired from a flight height of 106 m, at an average GSD of 2.64 cm. The method involves the standard photogrammetric procedures for the bundle block adjustment, DEM generation, and orthoimage generation using Pix4D software (Fig. 2). The ICESat-1 dataset is selected from Openaltimetry web-based platform and downloaded as an excel file. The preprocessing of the ICESat-1 data including shapefile generation from downloaded files and clipping is done in open-source QGIS software. The comparison of the elevation values for the DEM generated from the UAV dataset (H_{DEM}) is done with the elevation values from openly accessible ICESat-1 datasets ($H_{ICESat-1}$) from different campaigns (Table 1).

Additionally, the openly accessible TanDEM-X 90 m DEM elevation values (HTDM) available from the website platform provided by the German Aerospace Center, DLR (<https://download.geoservice.dlr.de/TDM90/>) were generated using Synthetic Aperture Radar Interferometry (InSAR) were utilized for comparative assessment considering its good performance for the plain regions [27].

The ellipsoid used by ICESat/GLAS is about 70 cm smaller than the World Geodetic System (WGS84) ellipsoid [28]. Thus Eq. 1 is used for the transformation of height values in meters from TOPEX/Poseidon (Topography Experiment—Positioning, Ocean, Solid Earth, Ice Dynamics, Orbital Navigator) to the WGS84 datum.

$$H_{WGS84} = H_{ICESat-1} - 0.7 \quad (1)$$

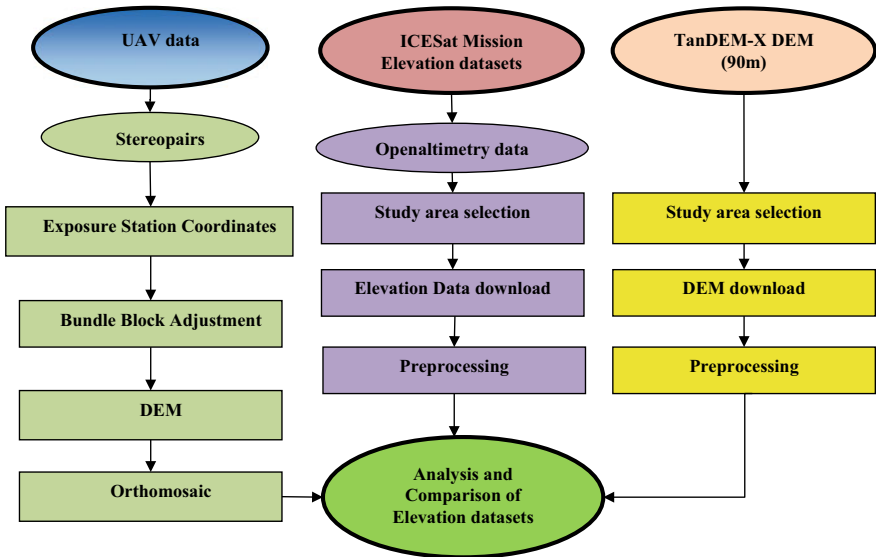


Fig. 2 Methodology for photogrammetric procedure for UAV dataset and its comparison with ICESat datasets

4 Results and Discussion

Table 1 depicts the comparison of elevation data from the ICESat-1 mission with the DEM generated from UAV images and shows a difference of about 26 cm on the plain ground with metallic road primarily, and 44 cm on the plain ground with the permeable surface (soil and vegetation) for complete footprint. The difference in elevation values, ΔH between ICESat-1 and UAV-DEM, are reasonably good considering the use of a Virtual Reference Station (VRS) and GNSS network in RTK mode for UAV missions. Similarly, the comparative results are highly satisfactory for points 3 and 7 with ΔH of 0.351 m and 0.194 m respectively in Table 1. Here, the footprint for point 3 is majorly on the ground with few trees and buildings at a distance near the boundary of footprints. Whereas the footprint for point 7 is majorly on the ground with metallised road and parking areas. Primarily the results show that the ICESat-1 and TanDEM-X 90 m, elevation values have an underestimation of height as compared to the elevation values of DEM generated from UAV data, which can be attributed to the capability of LiDAR as well as InSAR to penetrate the features. Points 1, 4 and 6 represent the regions with larger deviations as the center of the footprint lies on or near the buildings, from where the maximum energy has returned to the spaceborne LiDAR sensor. The comparison depicted that the difference between $H_{ICESat-1}$ and H_{TDM} is ranging from nearly -3.8 m to 0.3 m at different locations, depending on the uniformity of the terrain and feature. Similarly, the difference between H_{DEM} and H_{TDM} ranges from nearly -0.9 m to 11.8 m at different locations (Table 1) (Fig. 3).

Table 1 Describes the elevation values and differences in H_{DEM} , $H_{ICESat-1}$, and H_{HTDM}^*

S. no.	Track ID, campaign	Major feature	Longitude	Latitude	H_{DEM} (in m)	$H_{ICESat-1}$ (in m)	ΔH (in m)	H_{HTDM} (in m)	$H_{ICESat-1}-H_{HTDM}$ (in m)	$H_{DEM}-H_{HTDM}$ (in m)
1	298, Laser 3B	Building and ground	46° 45' 51.44"	6° 38' 31.25"	502.241	486.113	16.128	490.370	-3.557	11.871
2	298, Laser 3B	Ground (Open ground)	46° 45' 45.84"	6° 38' 32.46"	487.731	487.29	0.441	488.641	-0.651	-0.910
3	298, Laser 3B	Ground, trees, and buildings	46° 45' 48.18"	6° 38' 33.68"	487.636	487.285	0.351	490.477	-2.492	-2.841
4	298, Laser 3F	Building and ground	46° 45' 48.18"	6° 38' 47.07"	491.623	489.591	2.032	489.959	0.332	1.664
5	298, Laser 3A	Building and ground	46° 45' 49.25"	6° 38' 48.21"	486.770	486.507	0.263	489.959	-2.752	-3.189
6	298, Laser 3E	Building and ground	46° 45' 50.67"	6° 38' 50.27"	486.805	490.184	-3.379	489.271	1.613	-2.466
7	298, Laser 3F	Ground (road, parking area)	46° 45' 53.74"	6° 38' 45.86"	485.662	485.468	0.194	488.469	-2.301	-2.807
8	298, Laser 3A	Building and ground	46° 45' 54.8"	6° 38' 46.99"	485.771	484.888	0.883	489.385	-3.797	-3.614

* H_{DEM} —Elevation values obtained from the generated DEM from UAV, $H_{ICESat-1}$ —Elevation values obtained from ICESat-1 Mission, H_{HTDM} —DEM obtained from Tandem-X

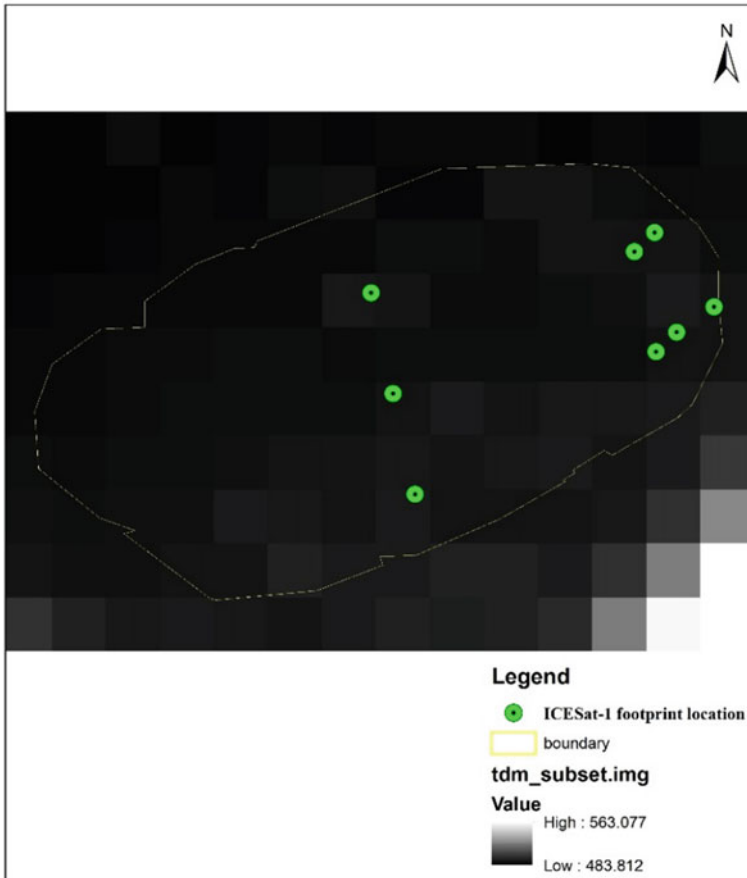


Fig. 3 TanDEM-X 90 m DEM overlaid with the boundary of the study site and ICESat-1 footprint locations

The bundle block adjustment results in the quality report illustrate the mean of geolocation accuracy within a pixel range, i.e. 2.73 cm, 2.73 cm, and 3.46 cm for X, Y, and Z respectively. The RMSE in X, Y, and Z is 1.7 cm, 2.27 cm, and 2.31 cm respectively within a pixel range. The mean of geolocation accuracy and RMSE thus has a practically high accuracy needed for many of the applications. The model accuracies achieved by the UAV datasets in the study depict that practically the cartographic potential for the UAV dataset is suitable for mapping at a scale range of 1:250 to 1:300 or even better for such plain sites, meeting the 2-Dimensional as well as 3-Dimensional mensuration requirements of engineering drawing needed for the facility management and utility mapping. However, as the optical DEMs are prone to the digging and hanging of mass points, DEM editing will be required for generating good mapping products at these large scales after inclusion or validation with ground control points (GCPs) [29, 30]. The use of GCPs in the study can

enhance the assessment of accuracy in more absolute terms [2]. Further, the quantitative comparison can be utilized for the generation of a framework and strategy for data or DEM fusion methods [19, 30, 31]. Aerial platform-based InSAR DEM availability is limited, however, may have the potential to provide equivalent DEMs, when compared to UAV-based DEMs.

5 Conclusion

The UAV datasets are providing very high accuracies of the order of pixel in both planimetry and vertical dimensions with VRS-RTK GNSS and attitude sensors. The spaceborne LiDAR (ICESat-1), which also has high accuracy, mostly has an underestimation for the elevation values concerning the estimations done through UAV-based sensors. This can be attributed to the fact that LiDAR is able to do penetration in the ground to some extent depending on the type of surface material. The study concludes that overall, the performance of UAV-based DEM or the elevation values from spaceborne LiDAR is better than currently available openly accessible TanDEM-X 90 m (InSAR-based DEM) from satellite platforms. The ICESat-2 data was also planned for the comparison since it has smaller footprints. ICESat-2 footprints were also searched on the portal, however, ICESat-2 currently does not have a footprint on the study site, and thus the study was limited to comparison with ICESat-1 datasets.

Acknowledgements The authors thank the National Aeronautics and Space Administration (NASA), German Aerospace Center (DLR), and senseFly Inc. for their web-based portals providing datasets for education and research. The authors are highly thankful to the Director, Indian Institute of Remote Sensing (IIRS) for his support and encouragement of the research activities. The authors are thankful for the creative research effort of the Open Source Geospatial Foundation for providing Quantum GIS to the research community.

References

1. Gupta K, Bhardwaj A, Kumar P, Pushpalata (2015) Procedural rule-based 3D city modeling and visualization using high-resolution satellite data. *Int J Adv Remote Sens Gis Geogr* 3(2), 16–25
2. Bhardwaj A, Joshi GH, Raghavendra S, Agrawal S (2011) Analysis of Spaceborne LiDAR (ICESat-1) data for retrieval of terrain elevation and its characteristics. In: *Regional conference on geomatics for good governance*, p 103
3. Saliu IS et al (2020) An accuracy analysis of mangrove tree height mensuration using forestry techniques, hypsometers and UAVs. *Estuar Coast Shelf Sci* 248:106971. <https://doi.org/10.1016/j.ecss.2020.106971>
4. Yu D et al (2020) Improvement of sugarcane yield estimation by assimilating UAV-derived plant height observations. *Eur J Agron* 121:126159. <https://doi.org/10.1016/j.eja.2020.126159>
5. Cavalagli N, Gioffrè M, Grassi S, Gusella V, Pepi C, Volpi GM (2020) On the accuracy of UAV photogrammetric survey for the evaluation of historic masonry structural damages. *Proc Struct Integr* 29:165–174. <https://doi.org/10.1016/j.prostr.2020.11.153>

6. Tiwari A, Sharma SK, Dixit A, Mishra V (2021) UAV remote sensing for campus monitoring: a comparative evaluation of nearest neighbor and rule-based classification. *J Indian Soc Remote Sens* 49(3):527–539. <https://doi.org/10.1007/S12524-020-01268-4/TABLES/3>
7. Cawood AJ, Bond CE, Howell JA, Butler RWH, Totake Y (2017) LiDAR, UAV or compass-clinometer? Accuracy, coverage and the effects on structural models. *J Struct Geol* 98:67–82. <https://doi.org/10.1016/j.jsg.2017.04.004>
8. Leitão JP, de Sousa LM (2018) Towards the optimal fusion of high-resolution digital elevation models for detailed urban flood assessment. *J Hydrol* 561:651–661. <https://doi.org/10.1016/j.jhydrol.2018.04.043>
9. Kršák B et al (2016) Use of low-cost UAV photogrammetry to analyze the accuracy of a digital elevation model in a case study. *Meas J Int Meas Confed* 91:276–287. <https://doi.org/10.1016/j.measurement.2016.05.028>
10. Akturk E, Altunel AO (2019) Accuracy assessment of a low-cost UAV derived digital elevation model (DEM) in a highly broken and vegetated terrain. *Meas J Int Meas Confed* 136:382–386. <https://doi.org/10.1016/j.measurement.2018.12.101>
11. Singh CH, Mishra V, Jain K, Shukla AK (2022) FRCNN-Based Reinforcement Learning for Real-Time Vehicle Detection Tracking and Geolocation from UAS. *Drones* 6(12):406. <https://doi.org/10.3390/drones6120406>
12. Castillo-García P, Muñoz Hernandez LE, García Gil P (2017) Chapter 5—Data fusion for UAV localization. In: Castillo-García P, Muñoz Hernandez LE, García Gil P (eds) *Indoor navigation strategies for aerial autonomous systems*. Butterworth-Heinemann, pp 109–129
13. Sankey JB et al (2021) Quantifying plant-soil-nutrient dynamics in rangelands: fusion of UAV hyperspectral-LiDAR, UAV multispectral-photogrammetry, and ground-based LiDAR-digital photography in a shrub-encroached desert grassland. *Remote Sens Environ* 253:112223. <https://doi.org/10.1016/j.rse.2020.112223>
14. Cook AJ, Murray T, Luckman A, Vaughan DG, Barrand NE (2012) Earth system science data a new 100-m digital elevation model of the Antarctic peninsula derived from ASTER Global DEM: methods and accuracy assessment. *Earth Syst Sci Data* 4:129–142. <https://doi.org/10.5194/essd-4-129-2012>
15. Satgé F et al (2015) Accuracy assessment of SRTM v4 and ASTER GDEM v2 over the Altiplano watershed using ICESat/GLAS data. *Int J Remote Sens*. <https://doi.org/10.1080/01431161.2014.999166>
16. Kramm T, Hoffmeister D (2019) A relief dependent evaluation of digital elevation models on different scales for Northern Chile. *ISPRS Int J Geo-Inf* 8(10):430. <https://doi.org/10.3390/ijg18100430>
17. Duncanson L et al (2020) Biomass estimation from simulated GEDI, ICESat-2 and NISAR across environmental gradients in Sonoma County, California. *Remote Sens Environ* 242:111779. <https://doi.org/10.1016/j.rse.2020.111779>
18. Vaka DS, Kumar V, Rao YS, Deo R (2019) Comparison of various DEMs for height accuracy assessment over different terrains of India. In: *International geoscience and remote sensing symposium (IGARSS)*, 2019, pp 1998–2001. <https://doi.org/10.1109/IGARSS.2019.8898492>
19. Bhardwaj A (2021) Quality assessment of merged NASADEM products for varied topographies in India using ground control points from GNSS. <https://mol2net-06.sciforum.net/#section1478>
20. Zwally HJ et al (2014) GLAS/ICESat L2 global land surface altimetry data, version 34. NASA national snow and ice data center distributed active archive center, Boulder, Colorado USA. <https://doi.org/10.5067/ICESAT/GLAS/DATA227>
21. Schuttz BE, Zwally HJ, Shuman CA, Hancock D, DiMarzio JP (2005) Overview of the ICESat mission. *Geophys Res Lett* 32(21):1–4. <https://doi.org/10.1029/2005GL024009>
22. Martino AJ, Neumann TA, Kurtz NT, McLennan D (2019) ICESat-2 mission overview and early performance. In: *Proceedings of SPIE 11151, sensors, systems, and next-generation satellites XXIII*, vol 11151, no 10, p 11. <https://doi.org/10.1117/12.2534938>
23. Khalsa SJS et al (2020) OpenAltimetry—rapid analysis and visualization of Spaceborne altimeter data. *Earth Sci Informatics*. <https://doi.org/10.1007/s12145-020-00520-2>

24. Ash C, Dubec M, Donne K, Bashford T (2017) Effect of wavelength and beam width on penetration in light-tissue interaction using computational methods. *Lasers Med Sci* 32(8):1909–1918. <https://doi.org/10.1007/s10103-017-2317-4>
25. Hopkinson C, Chasmer L, Gynan C, Mahoney C, Sitar M, Francis T (2016) Multisensor and multispectral LiDAR characterization and classification of a forest environment. *Can J Remote Sens* 42(5):501–520. <https://doi.org/10.1080/07038992.2016.1196584>
26. Teo TA, Wu HM (2017) Analysis of land cover classification using multi-wavelength LiDAR system. *Appl Sci* 7(7):1–20. <https://doi.org/10.3390/app7070663>
27. Bhardwaj A (2019) Assessment of vertical accuracy for TanDEM-X 90 m DEMs in plain, moderate, and rugged terrain. *Proceedings* 24(1):8. <https://doi.org/10.3390/iecg2019-06208>
28. NSIDC (2021) Frequently asked questions. NASA distributed active archive center (DAAC). <https://nsidc.org/data/icesat/faq.html#p9>. Accessed 16 Mar 2021
29. Tampubolon W, Reinhardt W (2014) UAV data processing for large scale topographical mapping. *Int Arch Photogramm Remote Sens Spat Inf Sci ISPRS Arch* 40(5):565–572. <https://doi.org/10.5194/isprsarchives-XL-5-565-2014>
30. Bhardwaj A, Jain K, Chatterjee RS (2019) Generation of high-quality digital elevation models by assimilation of remote sensing-based DEMs. *J Appl Remote Sens* 13(04):1. <https://doi.org/10.1117/1.JRS.13.4.044502>
31. Papasaika H, Kokiopoulou E, Baltasvias E, Schindler K, Kressner D (2011) Fusion of digital elevation models using sparse representations. *Photogramm Image Anal* 171–184. https://doi.org/10.1007/978-3-642-24393-6_15

UAV to Cadastral Parcel Boundary Translation and Synthetic UAV Image Generation Using Conditional-Generative Adversarial Network



Ganesh Khadanga and Kamal Jain

Abstract The precise boundaries of the cadastral parcels from the Unmanned Aerial Vehicle (UAV) data are essential for any eGovernance application. The pix2pix, image-to-image translation using the conditional Generative Adversarial Network (cGAN) models, has emerged as an alternative to the traditional machine learning and image processing algorithms. It has been used and demonstrated for productive purposes in different domains without any change in the pix2pix network model and loss functions. The pix2pix model is implemented in this research for extracting the cadastral parcel boundaries using the existing UAV data set, and the corresponding digitised data. The input data set is prepared using the python modules. The model is also used to predict the synthetic UAV data from the map data. The predicted boundary of the model is very useful. The proposed model can reduce the manual labour and human interventions in outlining the parcel boundary from UAV data.

Keywords Pix2Pix · Image-to-image translation · c-GAN · CNN · UAV · Deep learning · Parcel

1 Introduction

The record of rights (ROR) of a land parcel, along with the boundary maps, identifies the extent of an agriculture land parcel. The land records with accurate boundary information are essential for any sort of developmental programme initiated by the Government. Technological developments have been used for recording the boundary from remote sensing and UAV data for cadastral mapping. The approaches like image-to-image translation [1] have been used for identifying and modelling the regularities or patterns in the input data set. The Generative Adversarial Network

G. Khadanga (✉) · K. Jain
Indian Institute of Technology Roorkee, Roorkee, Uttarakhand, India
e-mail: ganesh@nic.in

K. Jain
e-mail: kjainfce@iitr.ac.in

(GAN) has been found to be used for image segmentation and boundary extraction tasks by many researchers.

GAN consists of the generator part and the discriminator part. The generator part generates the new images, and the discriminator part tries to classify the generated image as real or fake. Thus in GANs, the generator and discriminator model is trained together in such a way that the discriminator model is fooled most of the time and indicates that the generator generates the images that belong to the domain.

The authors [2, 3] in the pix2pix algorithm used a GAN conditioned on the source image and imposed an L1 (absolute deviations) loss between the generated image and its ground-truth map. This requires the existence of ground-truth paired images from each of the source and target domains. The quality of the generated images improves as the generator and discriminator compete to reach the nash equilibrium expressed by the minimax loss of the training procedure. The U-Net [1, 4, 5] architecture for the generator, is simply an encoder-decoder architecture with skip connections between them. For the discriminator, a PatchGAN is used. A PatchGAN [3] is similar to a common discriminator, except that it tries to classify each patch of $N \times N$ size whether it is real or fake.

In GAN models the generator is the main part, and the discriminator is an adaptive loss function that gets discarded once the generator has been trained [6]. The paper also describes a new training methodology for generative adversarial networks. The generator and discriminator are grown progressively with low resolution and then add a layer with increasing details. This has enabled GAN to produce high-quality output. The sliced Wasserstein distance indicates that the distribution of the patches is similar and is also proposed as a metric for evaluating GAN results. The relationship between the original images and the reconstructed was introduced by adding a controller to pix2pix [7]. A detailed analysis of quantitative and qualitative measures for evaluating the generative model is described in Ref. [8]. The authors Valencia-Rosado et al. used the Pix2Pix framework with the water map feature and generated the river deltas and coastal areas. However, the authors have not indicated any quantitative evaluation of the results [9]. Fetty et al. [10] have trained cGAN with four different generators (SE-ResNet, DenseNet, U-Net, and Embedded Net), and an ensemble model was created from the four network outputs. The author has also indicated that the cGAN architecture can be considered a useful model as it only needs a small sample size for the generator-discriminator cross-training. The authors [11] proposed additions of partial dense connections in the cGAN generator for linear segmentation. The network thus can learn the differences between object and background in a relatively short time. The authors Abdollahi and Pradhan proposed the SegNet model with Bi-directional Convolutional LSTM in cGAN generator part to generate the segmentation map from the existing building dataset [12]. Jafrasteh et al. [13] proposed the cGAN with mean squared error loss for fining the faults and fractures with limited inputs.

TuiGan model [14] as proposed is able to transfer the domain distribution of the input image to the target domain by progressively translating the image from coarse to fine. The progressive translation enables the model to extract the underlying relationship between two images by continuously varying the receptive fields at

different scales. TuiGAN model realises the image-to-image translation with only two unpaired images. Image-to-Image translation is also valuable for applications such as colourisation and super-resolution, edge-to-image formation, style transfer, data augmentation, and inpainting.

The primary contribution of this study is the preparation of the specialised data set and training of the model based on cGAN for boundary extraction and synthetic UAV image generation. UAV dataset, with its high resolution, are very suitable for extraction of geospatial information at a much larger scale [15, 16]. The data is prepared from the UAV images and the corresponding manually digitised cadastral map files using the python modules. The fitted model can be used to predict the parcel boundaries and synthetic UAV images for a new dataset. This work can also be treated as a practical field application of computer vision for the automation of cadastral boundary extraction.

2 Data Set

The UAV images and the corresponding vectors maps consisting of cadastral parcel boundary is cropped into patches of 256×256 pixels using python modules. The set of images pairs of 512×256 size is prepared from the UAV image and the corresponding cadastral map image. Total 595 images were prepared. The features are also color coded. Few samples of the dataset is shown in Fig. 1. The GAN network was applied to this data set (Fig. 2).



Fig. 1 Parcel data set (256×256) UAV data with corresponding plots with boundary

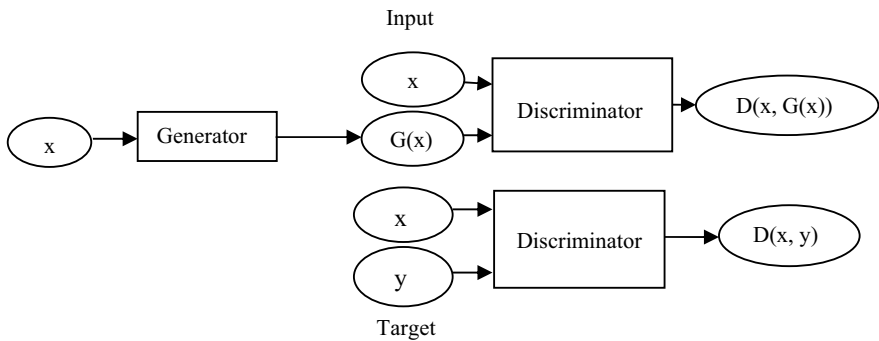


Fig.2 Description of the conditional GAN model [2]

3 Network Architecture

The conditional-GAN consists of the generator G and the discriminator D . The generator tries to produce an image like a real image and fool the discriminator [2]. The discriminator tries to differentiate between the real image and the fake image from the generator for a given reference input image. Figure 2 describes the conditional-GAN architecture.

The objective of a conditional-GAN consists of two parts: adversarial loss and L1 Loss (mean absolute error). The x is the observed image, z is the random noise and y is the output image, and the adversarial loss can be expressed as

$$L_{cGAN}(G, D) = E_{x,y}[\log D(x, y)] + E_{x,z}[\log(1 - D(x, G(x, z)))] \quad (1)$$

L1 distance is added to the generator loss to encourage the low-frequency correctness of the generated image. L1 distance is preferred over L2 distance as it produces images with less blurring. Thus the objective for the min-max game is:

$$(G^*, D^*) = \arg \min_G \max_D [L_{cGAN}(G, D) + \lambda L_{L1}(G)] \quad (2)$$

The model as proposed by Isola et al. [3] is taken up. The model takes an input image of size $3 \times 256 \times 256$ and generates an output image $G(x)$ of the same size.

U-Net generator is an encoder-decoder network with symmetrical long skip connections. The network consists of 8 encoding layers and 8 decoding layers, with skip connections from layer i to layer $n-i$, where n is the total number of layers. Each encoding and decoding block follows the form of the convolution/deconvolution-Batchnorm-Leaky Relu.

The convolutional PatchGAN classifier with architecture similar to the classifier in pix2pix is used as a discriminator. PatchGAN discriminator determines whether an image is real or fake by using local patches of size 70×70 , rather than the entire image. The discriminator takes in two images, the input image (x) and the unknown image ($G(x)$ or y), pass them through 5 down-sampling convolutional-BatchNorm-LeakyReLU layers, and outputs a matrix of 30×30 , in which each element corresponds to the classification of one patch. The model is trained for 100 epochs until the loss plateaus. The generator and discriminator loss are shown in Fig. 3 (Figs. 4 and 5).

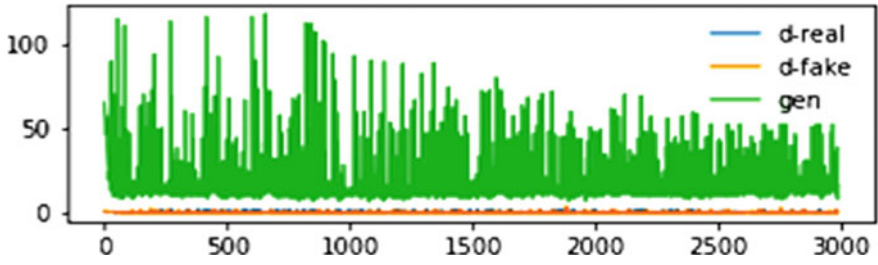


Fig. 3 The generated error plots for each iterations (loss vs iterations upto 3000 is shown)



Fig. 4 The generated output with the image-to-image translation model during training. The source UAV image (top), the ground truth (in the middle), and the predicted image during training (bottom)

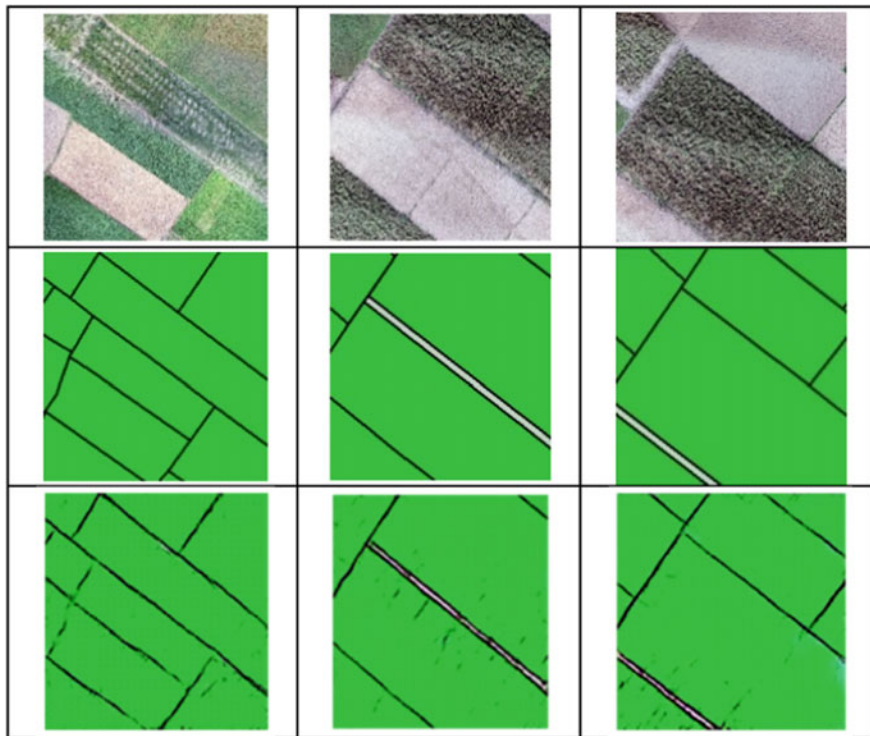


Fig. 5 Sample model prediction for the test data set (1st row: UAV data, 2nd row: ground truth, 3rd row: predicted boundary)

4 Translating Cadastral Parcel Maps to Synthetic UAV Images

The pix2pix network as described above is applied to translate the cadastral parcel images to possible UAV images. The predicted UAV data for the cadastral parcel maps are shown in Fig. 6. The generator and discriminator losses are shown in Fig. 7.

5 Results and Discussions

The model is trained with the test dataset consisting of 400 images. The model is executed for 100 epochs. The predicted boundaries of the UAV images are shown in Fig. 5. The UAV images are shown in the top row and the ground truth is shown in the 2nd row of Fig. 5. The 3rd row contains the predicted images out of the model with U-Net as generator. The error plot is shown in Fig. 3. The boundaries of the cadastral

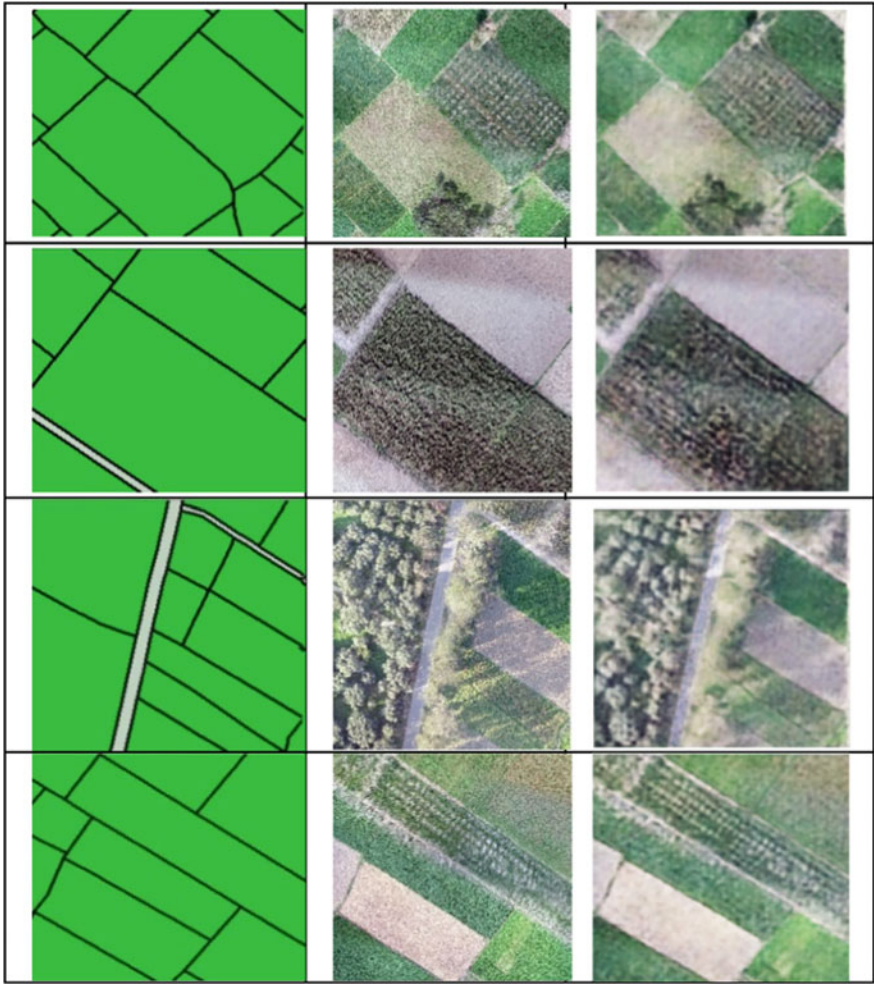


Fig. 6 Sample model prediction for the test data set (1st column: map data, 2nd row: UAV data-ground truth, 3rd column: synthetic UAV images predicted)

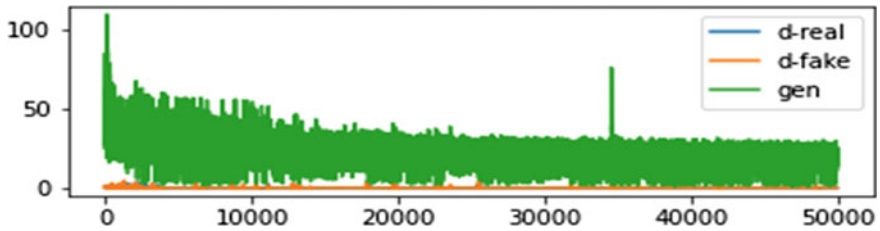


Fig. 7 Generator and discriminator losses for synthetic image generation for each iteration

parcels are extracted to a great extent. However, the boundaries of many fields are partially extracted. The same can be completed with little manual post-processing activity.

The texture of the synthetic images are visually very promising and it can be used as an alternative to the real UAV images. The generator and discriminator losses are shown in Fig. 7.

The subpixel methodology, colorimetry, and contextual information, as proposed by Suresh and Jain [17], can also be used for boundary extraction and classification. The boundaries of the plots are quite satisfactorily extracted.

Though the result is satisfactory, there is scope for enhancement of the results to match the ground truth. Further experiments can be done with a larger data set and techniques like data argumentation can also be taken up to enhance the result.

The automation of input data preparation and the use of data augmentation techniques, pre-processing and post-processing of data for fast and accurate results are the key challenges. The use of temporal data is also a promising field.

6 Conclusion

The investigations are done for extraction of the parcel boundaries from the UAV images using the cGAN modules. The synthetic UAV images are also generated using above network by reversing the inputs. The proposed approach contributes to the research area of the automatic generation of parcel boundaries from the specialised dataset as prepared from the UAV images. The extraction of the parcel boundaries using the proposed approach is quite satisfactory. This will enhance the ways to continuously update the cadastral boundaries by the revenue field functionaries. The synthetic UAV images generation approach can be used in difficult areas where the UAVs can not be deployed because of technical and administrative issues. There are still constraints in the approach like obstruction to visible boundaries because of trees and shadow. The modules are required for data augmentation and enhance the extraction process. Presently the methodology will complement the operators in automation of the parcel boundary generation.

References

1. Brownlee J (2019) Generative Adversarial Networks with Python
2. Hu J, Yu W, Yu Z (2018) Image-to-image translation with conditional-GAN. Stanford University, Deep Learning
3. Isola P, Zhu J, Zhou T, Efros A (2017) Image-to-image translation with conditional adversarial networks. In: CVPR
4. Kalin J (2019) Generative Adversarial Networks Cookbook. Packt Publishing
5. Ronneberger IO, Fischer P, Brox T (2015) U-net: convolutional networks for biomedical image segmentation. [arXiv:1505.04597.6](https://arxiv.org/abs/1505.04597)

6. Karras T, Aila T, Lehtinen LJ (2018) Progressive growing of GANs for improved quality, stability, and variation. In: ICLR 2018
7. Wang X, Yan H, Huoy C, Yuz J, Pany C (2018) Enhancing Pix2Pix for remote sensing image classification. In: 24th International conference on pattern recognition (ICPR), Beijing, China, August 20–24, 2018
8. Borji A (2018) Pros and cons of GAN evaluation measures. *J Comput Vis Image Understand*
9. Valencia-Rosado LO, Guzman-Zavaleta ZJ, Starostenko O (2021) Generation of synthetic elevation models and realistic surface images of river deltas and coastal terrains using cGANs. *IEEE Access* 9:2975–2985. <https://doi.org/10.1109/ACCESS.2020.3048083>
10. Fetty L, Löfstedt T, Heilemann G, Furtado H, Nesvacil N, Nyholm T, Georg D, Kuess P (2020) Investigating conditional GAN performance with different generator architectures, an ensemble model, and different MR scanners for MR-sCT conversion. *Phys Med Biol* 65:105004
11. Jiang H, Chen X, Shi F, Ma Y, Xiang D, Ye L, Su J, Li Z, Chen Q, Hua Y, Xu X, Zhu W, Fan Y (2019) Improved cGAN based linear lesion segmentation in high myopia ICGA images. *Biomed Opt Express* 10(5):2355–2366. <https://doi.org/10.1364/BOE.10.002355>
12. Abdollahi A, Pradhan B, Gite S, Alamri A (2020) Building footprint extraction from high resolution aerial images using generative adversarial network (GAN) architecture. *IEEE Access* 8:209517–209527. <https://doi.org/10.1109/ACCESS.2020.3038225>
13. Jafrasteh B, Manighetti I, Zerubia J (2020) Generative adversarial networks as a novel approach for tectonic fault and fracture extraction in high-resolution satellite and airborne optical images. *Int Arch Photogramm Remote Sens Spatial Inf Sci XLIII-B3-2020:1219–1227*. <https://doi.org/10.5194/isprs-archives-XLIII-B3-2020-1219-2020>
14. Lin J, Pang Y, Xia Y, Chen Z, Luo J (2020) TuiGAN: learning versatile image-to-image translation with two unpaired images
15. Singh C, Mishra V, Harshit H, Jain K, Mokros M (2022) Application of UAV swarm semi-autonomous system for the linear photogrammetric survey. *Int Arch Photogramm Remote Sens Spat Inf Sci* 43:407–413
16. Tiwari A, Sharma SK, Dixit A, Mishra V (2021) UAV remote sensing for campus monitoring: a comparative evaluation of nearest neighbor and rule-based classification. *J Indian Soc Remote Sens* 49(3):527–539
17. Suresh M, Jain K (2017) Egypt. *J Remote Sens Space Sci*. Subpixel level mapping of remotely sensed image using colorimetry

UAV-Based Terrain-Following Mapping Using LiDAR in High Undulating Catastrophic Areas



Chandra Has Singh, Kamal Jain, and Vishal Mishra

Abstract Expanding needs for using UAV (Uncrewed Aerial Vehicles) remote sensing approaches, such as terrain-following aerial mapping applications using LiDAR (light detection and ranging) in catastrophic applications. New extracts in UAV mapping still contain a limited number of studies for analyzing fine-scale mapping accuracy in UAV remote sensing methods—terrain-following aerial mapping for UAVs based on external airborne LiDAR integrated with the flight controller. We introduce the UAV system for the terrain after mapping the high-rise area by circumventing obstacles around it, expanding it so that UAVs flying at low altitudes can collect high-quality ground information while protecting them from all kinds of obstacles up and down. A more informative map is prepared to speed up the rescue and relief operations of the devastated area. Then on-destructive techniques have been surveyed and explored Solani riverbank sites of the high undulating area in Roorkee, Haridwar district in the Indian state of Utrakhnad. This work aims to critically analyze fine-scale remotely sensed data for mapping using LiDAR and UAV obtained the structure from motion photogrammetry. This work outlines the approaches applied to remote sensing data to reveal potential sensitivities, reflecting the close visual methods of the catastrophic region.

Keywords Terrain following · UAV · LiDAR · Aerial mapping · Structure from motion · Photogrammetry · Undulating

C. H. Singh · K. Jain · V. Mishra (✉)

Department of Civil Engineering, Indian Institute of Technology Roorkee, Roorkee 247667, India
e-mail: vmishra1@ce.iitr.ac.in

C. H. Singh

e-mail: chandrahas@ce.iitr.ac.in

K. Jain

e-mail: kjainfce@iitr.ac.in; kjainfceiitr@gmail.com

1 Introduction

UAVs are revolutionizing the domain of Remote Sensing and Photogrammetry. They are excellent tools for data collection under their adaptability, versatility, cheaper cost, and high resolution of sampling. As technology evolves, new methods and sensors are devised for different applications. UAV applications span from river bed mapping [1], Campus monitoring [2], Precision Agriculture [3], and UAVs being used for surveillance and reconnaissance in the tense war zone.

In cases of natural hazards, flying at extremely low altitudes is necessary and challenging. The mission's main task is to fly by following the fluctuations of the ground surface so that, as much as possible, the micro-sensory information on the ground can be captured in the UAV cameras, which will help the survivors prove to be more helpful in the search and rescue operations. In many areas, it is necessary to fly following the area's slope to see the emergency of a mudslide or landslide [4]. The principal mission goal of the UAV is to accurately map the area of interest or 3D mapping and generate geomatical models with a high level of resolution to make accurate geospatial measurements. Estimating the volume of a landslide or measuring the amount of lava ejected from a volcanic vent is an essential factor that helps the relevant authorities better understand the status and progress of the hazardous event [5]. The analysis of ground distortions at the micro-level allows surveillance and, in some cases, accurate prediction of hazards by nature. Terrian following flights near the ground surface were also explored as a solution for accurate estimation of yield and precise agricultural harvest. All the examples given prove the usefulness of hardware and software techniques to enable the UAV to follow a low-altitude trajectory considering the subtle geospatial geometry of the landscape [6]. The solution presented in this paper proposes a survey intervention to map the area of interest highly detailed with a multidisciplinary approach to terrain-following mapping missions. For this, various aspects were considered in Airborne LiDAR, ranging from integrating the LiDAR with the flight controller of the UAV to the effective execution of the mission [7]. The proposed methodology uses a single LiDAR system to obtain terrain information during flight. The mission implementation is fully compatible with low-cost hardware and open-source flight planning software [8].

All aspects of this research paper have been collected in several parts. Section 2 gives a critical overview of the techniques currently used in terrain-following flight planning. Our proposed solution is presented in Sect. 3, and the various aspects of the solution are explained. Section 4 describes the experimental setup used for the terrain-following mapping and highlights LiDAR integration with UAVs and communication of UAVs from GCS. Section 5 is mainly devoted to dataset and flight planning. The data processing and surface model generation to generate the map are described in Sect. 7, whereas the results obtained in actual test scenarios are reported and analyzed in Sect. 8. Finally, the findings and future enhancements are reported in Sect. 9.

2 Literature Review

Currently, terrain-following systems are provided on aerial vehicles such as UAVs to register images with all dimensions of precise geospatial coordinates relative to the area of interest by estimating the UAV position in a terrain map. Based on real-time LiDAR data during flight and after accurately forecasting vehicle position, Autopilot also provides alerts to avoid obstacles for impending action [9]. In a related literature review, an oft-repeated approach to the collection of ground data extensively of a truly uninhabited unknown area is to employ UAVs equipped with cameras. Such flight planning is usually referred to as post-terrain mapping because it considers the particular morphology of the region of interest and terrain to be observed [10]. A control strategy called the OptiPilot is introduced in [11] that allows a fixed-wing UAV to fly independently autonomously. It is a one-way customized optical flow terrain detector that performs the task of gathering information about the surface. The ground detection system occurs at the height of approximately 9 m above ground level (AGL) and reacts to the presence of fixed obstacles. This suggested method represents the first solution to the problem of flying at medium altitudes using a strategy complete with sensor-to-actuator control. The output of the optical flow algorithm contains essential information that is used to detect obstacles and orientation parameters mapped to roll and pitch control signals, which control its navigation, causing the vehicle to tilt and change its height up and down. Such an approach has a weakness as it requires a lot of dedicated and custom hardware, and it is very challenging to integrate it seamlessly with the UAVs and flight controllers being used extensively in the market in addition, this strategy, which is based on adopting optical flow, but on some surfaces such as ice fields, landslides, volcano lava fields, it is difficult to find visible points and then it is not only challenging to obtain results from the process adopted. A similar optical-flow-based solution [12] is presented, where the lowest altitude during testing reaches 15 m AGL. In this, the authors have focused on developing a mission planning solution that takes different heights as obstacles in the open terrain. The suggested resolution is based on the algorithmic fast marching square path planning method. The reported results are only based on software simulations; altitudes of 2, 5, and 10 m AGL were adopted to test the algorithm. A robust control strategy combining sensors and GPS for flights following terrain is presented in [13]. The authors developed a second-order hexacopter dynamics model in this work by adopting flight controller factors' localization and orientation feedback, including a barometer, GPS, and IMU. The authors could fly between 2 and 6 m AGL with the strategy developed. However, they cannot deal with the troubles encountered during post-terrestrial flights. Several techniques have been presented in [14] for guidance or navigation for the low-altitude path of uncrewed helicopters, including laser sensors integrated with the UAV mounted under the vehicle's front nose to scan the terrain.

Although this approach entails a costly micro-sensing system and control payload and is computationally intensive, it can diagnose the problem to a great extent as it will detect terrain fluctuations in advance. The UAV increases or decreases the height accordingly [15].

Additionally, several commercial and software solutions were proposed that allow for flying in the area of interest. In a case like this, a database of the area of interest and the terrain elevation already available must first be uploaded from the Ground Control Station (GCS) to the autopilot storage. During the initial flight, the Autopilot uses terrain data to maintain a constant altitude above the ground [16]. However, in high mountain areas like 80 m AGL or more, the first recommendation is to fly at altitudes of 80 m AGL or more. The data available in the GCS does not have the same accuracy as we need to work, so low-altitude ultrasonic sensors are facing while not working so effectively from that height.

3 Proposed Solution

Our proposed method was developed to perform terrain-following flight missions at lower altitudes (below 20 m AGL). The desired height for the mission's exit was provided to avoid an obstacle in the path of the task, thus allowing the flight to decrease or increase altitude, taking into account the vehicle's performance. Furthermore, unlike the strategies mentioned in Sect. 2, our approach is suitable for low-cost UAVs with limited onboard computing resources [17]. The result of our workflow is a sequence of integrating airborne LiDAR with Autopilot to obtain a terrain-following mapping.

The methodology of our suggested method is structured as follows:

- the desired Points of Interest are selected on the map;
- the desired height, speed, and overlapping for map generation is set;
- The Terrain enable has been set to 1 to run the system of terrain-following smoothly and the minimum and maximum limits of LiDAR have been programmed to Autopilot up to a suitable value;
- The altitude type was set to "Terrain", using a recent version of the Mission Planner (or other GCS supporting terrain-following) on the Flat Plan screen. All mission commands once included "alt" fields will be interpreted as altitudes above Terrain;
- The waypoint file is uploaded to the onboard autopilots, thus making the UAV flight controller ready to autonomously execute the entire mission as you usually do in auto mode [18].

During the design and development stages, the efficiency and robustness of the LiDAR-based terrain-following method and function after mapping was verified and tested behind the geomatics lab ground at IIT Roorkee. After that, the process was tested in a real-time environment. We conducted an initial on-field trial along the banks of the Solani River area, a high undulating area that was best suited for testing. Finally, we surveyed a bank of the Solani River.

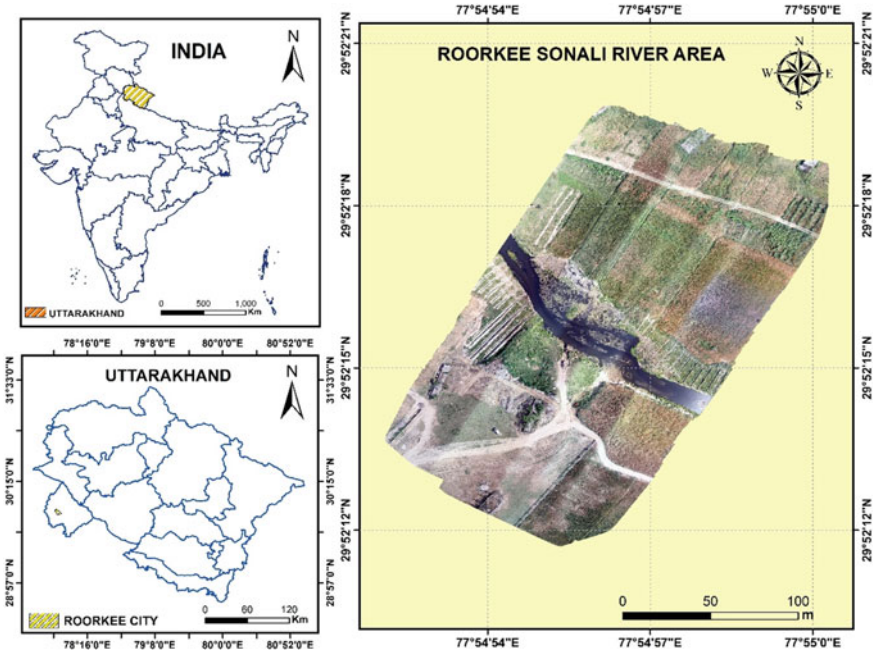


Fig. 1 Study area for Terrain-following mapping

4 Study Area

The selection of the area of interest is a critical and challenging task using complex experiments like terrain-following mapping, for this an area with fluctuations along the banks of the Solani river flowing in the eastern area of IIT Roorkee located in Roorkee city of Uttarakhand state in India was selected (Fig. 1).

This is a very favorable condition, according to the experiment. This area is very high undulating, with dunes of great height on both sides of the river through which the river flows. For this experiment, a total area mapping of 0.021 km² of Solani River was done, which was more bumpy. The lowest ground altitude is 204.3249969 m, while the peak height in that region is 208.0390015 m.

5 Experimental Setup

The solution presented was a 460 mm dimension quadcopter developed and tested using a material such as carbon fiber, equipped with a highly stable autopilot flight controller such as the Pixhawk imagery acquisition of aerial mapping in various

areas. It was decided to adopt the mission planner (<https://ardupilot.org/planner/docs/common-connect-mission-planner-autopilot.html>) last accessed on 2021/03/23) open-source software suite, which provides a complete and versatile control stack providing different flight planning facilities [19]. The RFD900+’s air unit radio communication was set to 56,700 baudrate on the Serial1 port of the Autopilot with the MAVLink (micro air vehicle communication) protocol, which was used for communication with the autopilot and ground control station (GCS) and position information of the UAV and was done to send the command of the mission.

It was possible to retrieve all telemetry data from global positioning system (GPS) and inertial measurement unit (IMU) parameters, as well as to send commands from the GCS to the Autopilot [20] (Fig. 3).

The setup developed for the on-field tests is outlined in Fig. 2. The 1D TF-03 Mini-LiDAR was used to detect the terrain surface, which is lighter in weight and provides significantly better quality data. It executes high-level navigation functions through terrain data that send appropriate commands to the Autopilot over the serial port. The Cube Black Flight Controller communicates with the GCS over the RFD900+ radio telemetry connection. The Mission Planner ground control interface allows us to set up and configure the Autopilot for the area of interest and plan and manage all phases of the mission [21].



Fig. 2 UAV with airborne LiDAR

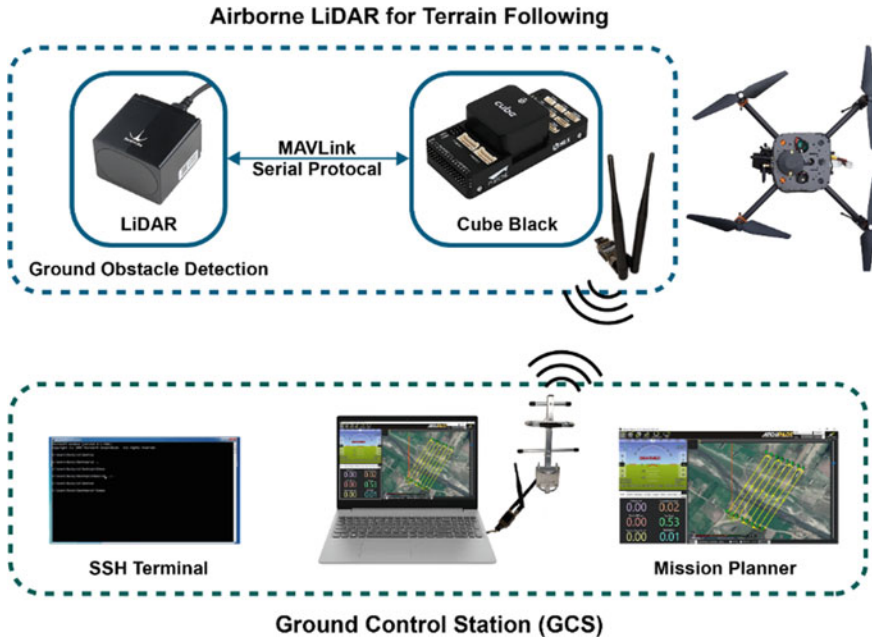


Fig. 3 Experimental setup for Terrain-following mapping

6 Dataset Used

The UAV data acquisition of the Solani riverbank was taken up with the help of any of the group members. The dataset was obtained with a 450 mm self-built UAV, using the GoPro Hero6 camera model with an optical sensor (Fig. 4).

A total of 302 images were acquired at the height of 20 m, which was also collected from 25 and 30 m, and side overlap and front overlap were kept optimal. We have used the mission planner for the flight of areas of interest. The steps acquired during the mission are processed. The parameters of data acquisition are tabulated in Table 1 [16].

7 Methodology

All sensors mounted on the UAV are checked before takeoff, and the GPS position is required to lock the position of the home so that the UAV can return safely to the launch position after the mission is completed. First, the area of interest is selected, and an appropriate altitude for the flight is set by feeding all the proper parameters of the flight plan in Autopilot. The complete details are given in Table 1 (Fig. 5).



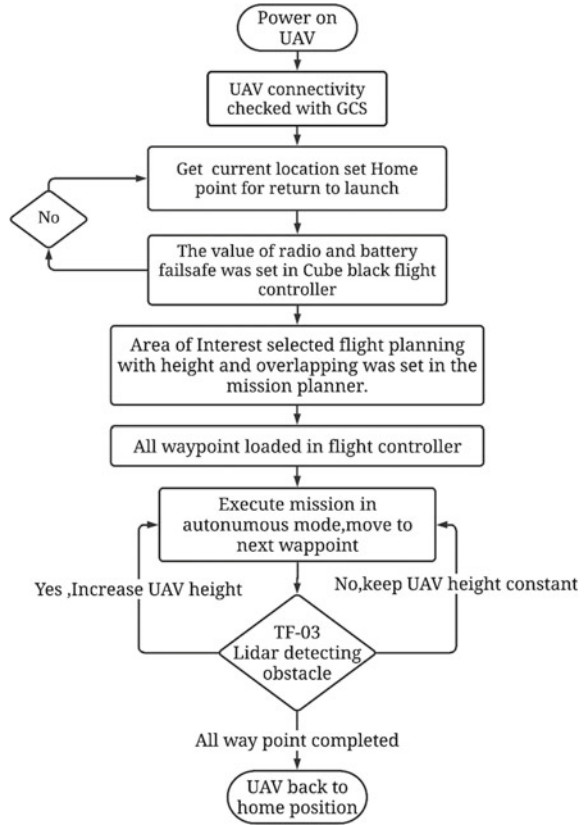
Fig. 4 Flight plan of the area in mission planner

Table 1 Flight and camera parameters

Parameter	Dataset
Flying height	20,25,30 m
Side overlap	70%
Front overlap	75%
Camera model	Hero 6 Black
Exposure time	1/846 s
ISO-speed	ISO-100
Focal length	3 mm
Dimensions	4000 × 3000
F-stop	f/2.8

Initially, flight planning was performed considering the data acquisition parameters and optimum flying height. So that there are multiple objects in the UAV’s line of sight of a flight plan. Data acquisition was made with the help of a UAV with an optical sensor mounted on it. With the help of LiDAR, we protect from all obstacles in the way of flight. Wherever the obstacle is encountered, LiDAR will detect it beforehand and increase its height from the height of the barrier and when there are no obstacles, it will increase its elevation to a fixed height. If the peak was increased earlier due to any obstruction, it reduces its height to the height previously fed in it. During this time, the camera fitted with the UAV keeps taking pictures continuously. Thus, this straightforward and robust solution has been suggested for terrain-following mapping [22].

Fig. 5 Complete methodology for Terrain-following mapping



8 Surface Model Construction

3D model reconstruction process Pix4Dmapper (<https://www.pix4d.com/product/pix4dmapper-photogrammetry-software>), a photogrammetry software for mapping from images captured by UAVs, was created by collecting information on camera position and orientation parameters which is estimated through the famous photogrammetric bundle block adjustment (BBA), which obtains the camera position directly from the image’s metadata. In essence, the map reconstruction process is based on automatic extraction and maximizing matching of visual key points between aerial images acquired by UAV, which are then used to obtain the camera’s pose (i.e., altitude and position) during flight [18].

The flight plan for image acquisition must be conducted to ensure that several key points can be matched, namely, that adequate overlap between captured images is provided. This is achieved by following a back-and-forth pattern considering the dimensions of all the mapping factors [23].

The accuracy of the reconstructed 3D model depends entirely on the Ground Sampling Distance (GSD), which is correlated to the real-world distance from the ground between two consecutive pixel centers in the acquired image. The decision of flight altitude above ground level is dependent on the aerial camera parameters (image dimension, focal length of camera, sensor width) with the UAV and related to the GSD of a single image by the following:

$$h(m) = \frac{\text{image width [pixel]} \times \text{GSD} \left[\frac{\text{cm}}{\text{pixel}} \right] \times \text{focal length [mm]}}{\text{sensor width [mm]} \cdot 100}$$

The Pix4D mapper requires some additional information to georeference the model. In particular, it must be known to locate the correct position of the images, scale appropriately, and orient the model correctly. This information is automatically imported from the photos if the onboard geotagging system is used to save the GPS coordinates and orientation parameters as metadata in the acquired image files, or we have to geotag the flight data and images from an autopilot [24]. Therefore, georeferenced models' accuracy is closely related to the absolute accuracy of onboard GPS receiver type (single-band or multi-band) used for geotagging images. Although the processing of data acquired by UAV in Pix4Dmapper averages the Image positions, inaccuracies in the coordinates can lead to significant errors in model positions that affect the accuracy of the entire model [25].

9 Results and Discussions

After successful initial testing, on-field testing was conducted on the banks of the Solani River. The data in Fig. 6 shows that the UAV follows the specified reference path with elevation variation between the two trends due to the time required to reach the specified route. The UAV has been flown on three desired elevations (i.e., at 20 m, 25 m, and 30 m height) from the ground. The altitudes trends have been shown in the figure and Table (Figs. 7, 8 and 9).

In Fig. 10, the executed trajectory and the proposed waypoints of flight projected on the longitude-latitude plane are superimposed to show the terrain-following feature.

The same trajectories in Fig. 11 are given above the point cloud generated by Pix4D. This final figure allows us to appreciate how UAVs follow the more complex morphology of Terrain when flying close to the ground (Fig. 12).

The data acquired in the Solani River area bank data description reconstructed by Pix4Dmapper using 346 images obtained during flights at low altitudes allows us to obtain a high-resolution 3D textured mesh for accurate measurements. The smallest information can be used to identify the object on any ground, thus supporting the benefit of the proposed method that we can use for a catastrophic area.



Fig. 6 Data processing in Pix4D

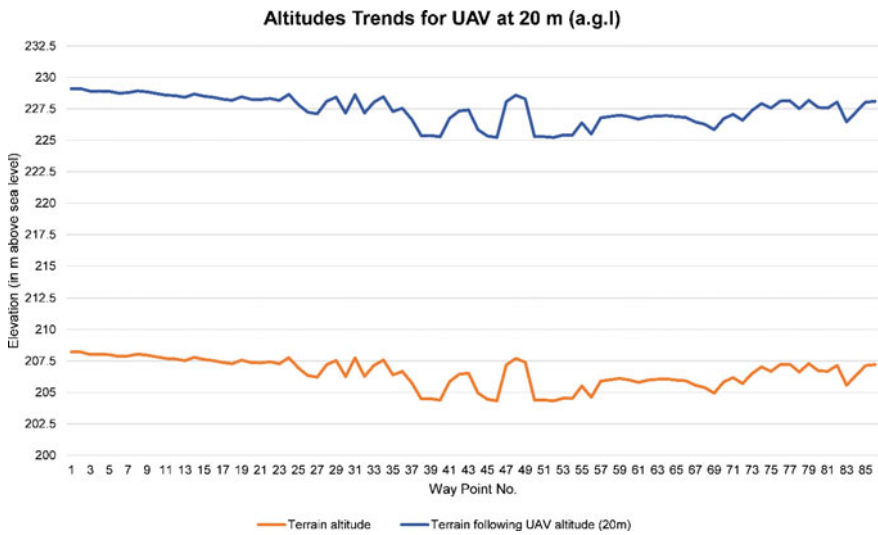


Fig. 7 On-field test-terrain-following mapping (20 m): altitudes of the ground terrain in meters (in blue) and the altitude of the executed trajectory by UAV in meters (in red)

In Fig. 13, we can see mixed results obtained with the help of Pix4D, in which orthomosaic, DSM, and contour were constructed at a distance of 0.5 m. Above all this, the proposed flight plan built in the mission planner is shown superimposed with the executed flight plan to show that the terrain following has been fully used in the sample of the suggested measures. As seen in the figure, altitude fluctuates a lot on both sides of the river and is actually a very fluctuating area.

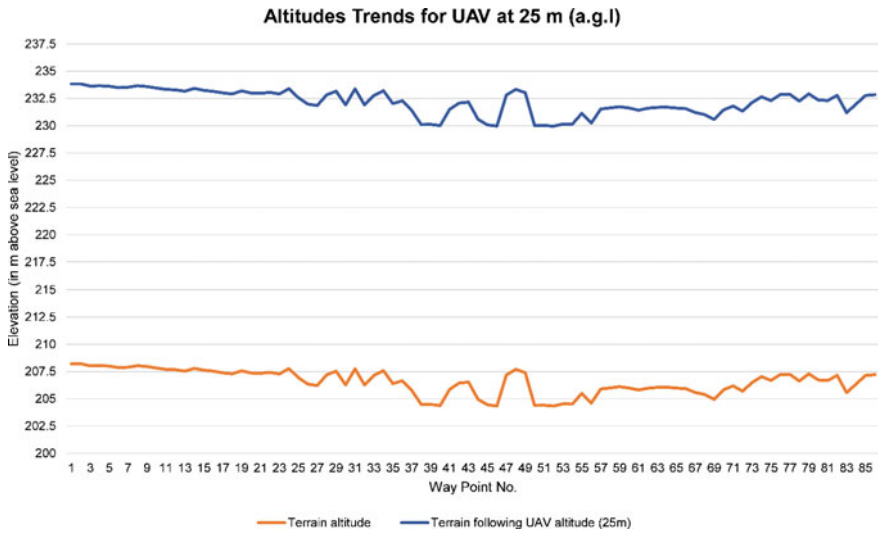


Fig. 8 On-field test-terrain-following mapping (25 m): altitudes of the ground terrain in meters (in blue) and the altitude of the executed trajectory by UAV in meters (in red)

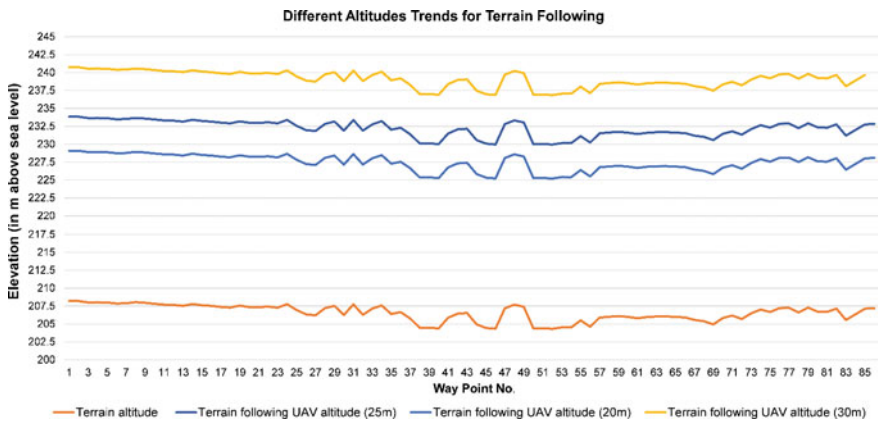


Fig. 9 On-field test-terrain-following mapping (20, 25, and 30 m): altitudes of the ground terrain in meters (in blue) and the altitude of the executed trajectory by UAV in meters (in red)

In this way, it was observed that the locality could successfully achieve the following with the help of LiDAR. So far, we have seen the following available terrain measurements, and we were already aware of all the dimensions of the locality. The solution suggested in this paper is a surprisingly simple and convenient way by which we can observe and survey an area surrounded by any disaster where no human activity is possible (Table 2).

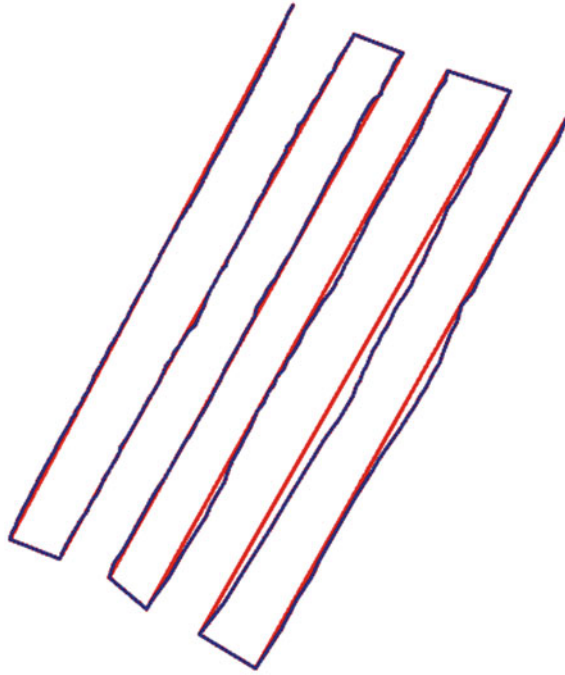


Fig. 10 On-field test—Solani river bank: reference path (in red) and performed trajectory (in blue), together with the assigned waypoints (in green) in the longitude-latitude plane

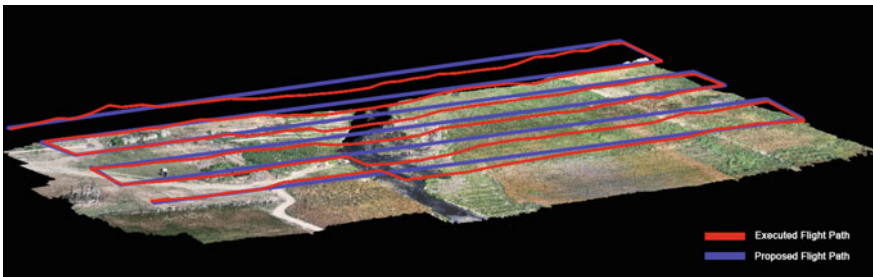


Fig. 11 On-field test—Solani river bank: the executed Flight path of Terrain follows in red and the proposed flight plan in the mission planner in blue

10 Conclusions and Future Work

This paper presents a method for UAV flights close to the ground following the terrain profile and considers all kinds of uncertainties of both the flight controller and the onboard GPS. As explained, these types of missions are beneficial for collecting

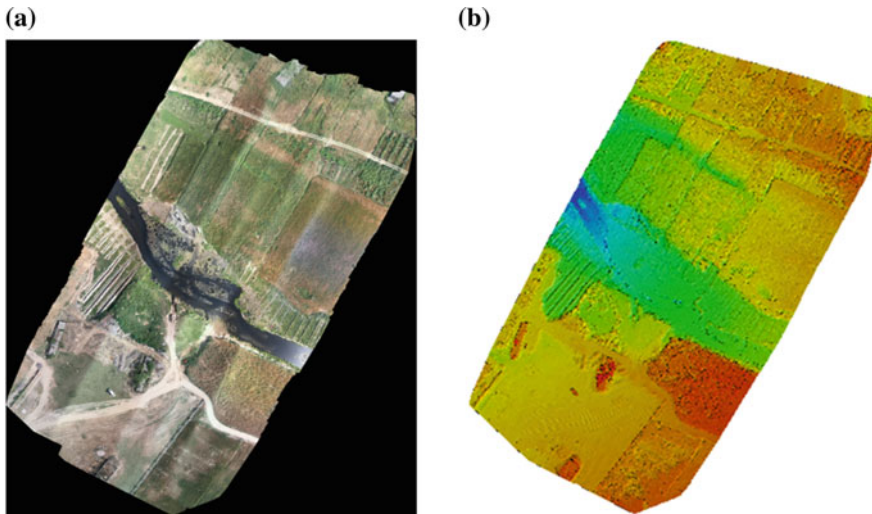


Fig. 12 **a** On-field test—Solani river bank: Orthomosaic generated by Pix4D Mapper using 346 Images. **b** On-field test—Solani river bank: DSM generated by Pix4D of the testing area

images needed to survey close to the ground, which has a broad spectrum of applications that contribute significantly to human life. The proposed solution is versatile, covering the assignment of the desired mission and all the items for the survey mission. The suggested solution, in a very balanced and accessible manner, involves all the technical aspects to produce results. The task can be used in many commercial and open-source ground control stations and integrated with almost all autopilots and multirotor.

Experimental missions correctly verified initial results obtained from stages during testing and development. The vehicle always kept a safe distance from difficult Terrain and all obstacles on the way, with all the dimensions of a standard GPS.

In short, one can summarize the main contributions of this work as follows:

- Generation of onboard real-time Terrain-following flights at lower altitudes than available solutions for low altitude autopilot in the market;
- Mission specificity, the desired altitude for the survey mission according to the disaster areas, and the desired performance of the vehicle were obtained with the help of LiDAR so that the final result can be obtained with greater accuracy;
- In the method adopted, in which the terrain-following has been obtained with the help of Lidar, we do not have an obligation to know the information about the Terrain of the area of interest; we accept it during the flight itself. All low-altitude Terrain following flight methods adopted earlier must require geospatial information of Terrain;
- Low-cost hardware adoption in the design and development of UAVs for Terrain-following.

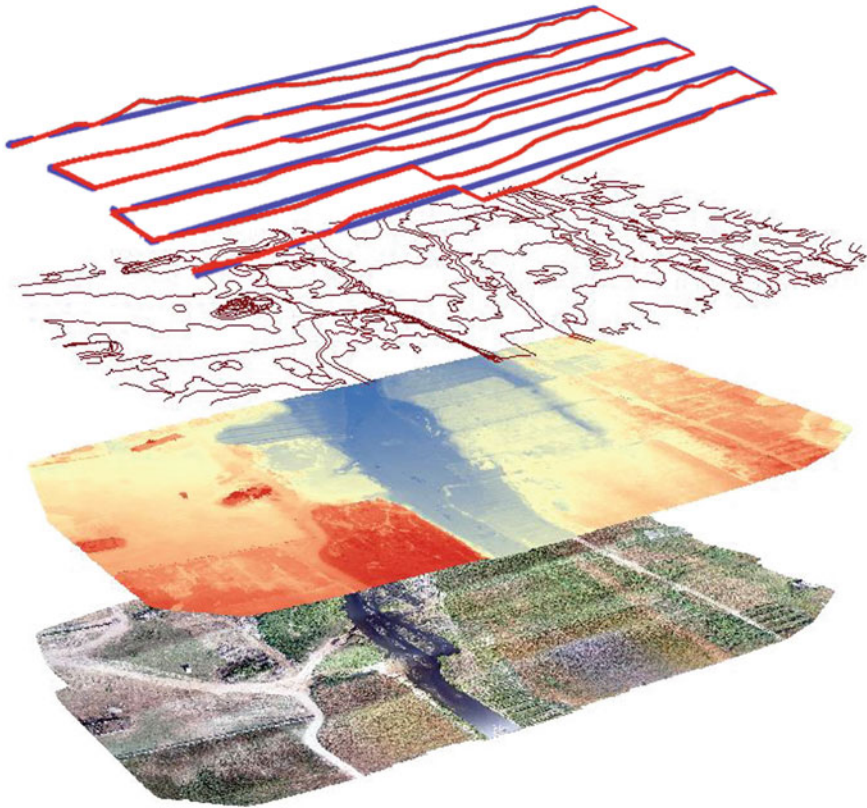


Fig. 13 On-field test—Solani river bank: all results related to mapping in which the Terrain following test was performed

Table 2 Error estimation for different altitude trends

Desired elevation (m)	Mean of the differences of actual elevation from the desired elevation at each waypoint (m)	Standard deviation of the differences of actual elevation from the desired elevation at each waypoint	Error percentage
20	1.090498	0.017535	4.4500
25	0.650573256	0.376728321	2.5258
30	2.549123256	0.376728321	8.4333

One of our solution’s main limitations is the very high surface terrain in which it is challenging to obtain LiDAR data, leaving little room to improve its position in a timely manner so that obstacles in the way are difficult to cross. This prevents our approach from being applied when accountability is the critical factor.

Another limiting aspect concerns the GPS and the lack of robustness against possible serious failures of LiDAR or dynamic changes in Terrain. However, this limitation can be overcome by providing the UAV with range sensors and 3D LiDAR, and reactive-based local barrier control.

For which it is required to deploy a high-speed calculating device with UAV that would generate an alert message by processing the data in time. In addition, the current solution was conceived and tested only for multirotor because only this type of vehicle is capable of surveying more generally, with less time, to hover above a specified time. Further investigation will be required as to whether this solution should be compatible with other aerial vehicles such as fixed-wing or VTOL (vertical takeoff landing). Finally, moving to solutions for low-altitude flight, using more sensors or LiDAR can integrate appropriate control strategies in which the Terrain-following mapping feature can be further enhanced.

References

1. Singh C, Mishra V, Harshit H, Jain K, Mokros M (2022) Application of UAV swarm semi-autonomous system for the linear photogrammetric survey. *Int Arch Photogram Remote Sens Spat Inf Sci* 43:407–413
2. Tiwari A, Sharma SK, Dixit A, Mishra V (2021) UAV remote sensing for campus monitoring: a comparative evaluation of nearest neighbor and rule-based classification. *J Indian Soc Remote Sens* 49(3):527–539
3. Jain K, Pandey A (2021) Calibration of satellite imagery with multispectral UAV imagery. *J Indian Soc Remote Sens* 49(3):479–490
4. Srinivasan MV, Thurrowgood S, Soccol D (2006) An optical system for guidance of Terrain following in UAVs. In: 2006 IEEE International conference on video and signal based surveillance, pp 51–51. IEEE
5. Kozmus K, Grigillo D, Petrovič D (2020) Optimization of UAV flight missions in steep Terrain. *Remote Sens* 12(8):1293
6. Nex F, Remondino F (2014) UAV for 3D mapping applications: a review. *Appl Geomat* 6(1):1–15
7. Stefanik KV, Gassaway JC, Kochersberger K, Abbott AL (2011) UAV-based stereo vision for rapid aerial terrain mapping. *GISci Remote Sens* 48(1):24–49
8. Yang Y, Huang Y, Yang H, Zhang T, Wang Z, Liu X (2021) Real-time terrain-following of an autonomous quadrotor by multi-sensor fusion and control. *Appl Sci* 11(3):1065
9. Chen C, Chang B, Li Y, Shi B (2021) Filtering airborne LiDAR point clouds based on a scale-irrelevant and terrain-adaptive approach. *Measurement* 171:108756
10. Zufferey JC, Beyeler A, Floreano D (2010) Autonomous flight at low altitude with vision-based collision avoidance and GPS-based path following. In: 2010 IEEE International conference on robotics and automation, pp 3329–3334. IEEE
11. Campos IS, Nascimento ER, Freitas GM, Chaimowicz L (2016) A height estimation approach for Terrain following flights from monocular vision. *Sensors* 16(12):2071
12. González V, Monje CA, Moreno L, Balaguer C (2017) UAVs mission planning with flight level constraint using fast marching square method. *Robot Auton Syst* 94:162–171
13. Chen Y, Zhang G, Zhuang Y, Hu H (2019) Autonomous flight control for multi-rotor UAVs flying at low altitude. *IEEE Access* 7:42614–42625
14. Johnson EN, Mooney JG (2014) A comparison of automatic nap-of-the-earth guidance strategies for helicopters. *J Field Robot* 31:637–653

15. Bhowmick J, Singh A, Gupta H, Nallanthighal R (2021) A novel approach to computationally lighter GNSS-denied UAV navigation using monocular camera. In: 2021 7th International conference on automation, robotics and applications (ICARA), pp 114–121. IEEE
16. Yasin JN, Mohamed SA, Haghbayan MH, Heikkonen J, Tenhunen H, Plosila J (2021) Low-cost ultrasonic based object detection and collision avoidance method for autonomous robots. *Int J Inf Technol* 13(1):97–107
17. Lyu Y, Cao M, Yuan S, Xie L (2021) Vision based autonomous UAV plane estimation and following for building inspection. [arXiv:2102.01423](https://arxiv.org/abs/2102.01423)
18. Raja M, Guven U (2021) Design of obstacle avoidance and waypoint navigation using global position sensor/ultrasonic sensor. *INCAS Bull* 13(1):149–158
19. Cardell M (2021) UAV navigation using local computational resources: keeping a target in sight
20. Jeong S, Park E, Seo KU, Do Yoo J, Kim HK (2021) MUVIDS: false MAVLink injection attack detection in communication for unmanned vehicles. In: Workshop on automotive and autonomous vehicle security (AutoSec), vol 2021, p 25
21. Flanagan C (2021) Multi-vehicle control and autonomy for swarming quadrotors. In: AIAA Scitech 2021 Forum, p 0001
22. Bi X (2021) Infrared sensors and ultrasonic sensors. in environmental perception technology for unmanned systems, pp 143–168. Springer, Singapore
23. Chaudhry MH, Ahmad A, Gulzar Q, Farid MS, Shahabi H, Al-Ansari N (2021) Assessment of DSM based on radiometric transformation of UAV data. *Sensors* 21(5):1649
24. Zhao J, Guan J, Li YJ, Du HW, Zhu ZM, Zhao Y, Ma TF (2021) Aerial triangulation study of unmanned aerial vehicles in forest area based on Pix4D. In: New developments of IT, IoT and ICT applied to agriculture, pp 241–248. Springer, Singapore
25. Perry BJ, Guo Y, Atadero R, van de Lindt JW (2021) Unmanned aerial vehicle (UAV)-enabled bridge inspection framework. In: Bridge maintenance, safety, management, life-cycle sustainability and innovations: proceedings of the tenth international conference on bridge maintenance, safety and management (IABMAS 2020), June 28-July 2, 2020, Sapporo, Japan, p 158. CRC Press

Forest Fire Detection from UAV Images Using Fusion of Pre-trained Mobile CNN Features



Bhuma Chandra Mohan

Abstract In this work, a Convolutional Neural Network based approach is presented for accurate classification of forest areas with fire from UAV images. In general, the deeper the CNN architecture, the classification of ‘fire’ versus ‘no fire’ is more accurate. However, deeper architectures consume lot of battery power and impose constraints on the processor used in UAV. It is time taking too. Hence, architectures like ResNet50 are not suitable as 23 million parameters are required to train a ResNet50 model. In this regard, mobile CNN architectures are quite handy and they require very few parameters of typical 1–7 millions. They are faster also and take very less time for inference. In this work, the features from selected pre-trained mobile CNN architectures i.e., Squeezenet, MobileNetv1, MobileNetv2, MnasNet, MobileNet v3, SqueezeNext, ShuffleNet, CondenseNet, DiCENet, FBNet, MixNet, and EfficientNet Lite-0, EfficientNet Lite-1 are used in the classification process. All the architectures are pre-trained on ‘imagenet’ dataset with 1000 classes and 14 millions of images. Features from the last pooling layer of each network are obtained. Feature fusion (concatenation) from the selected mobile CNN architectures is considered for classifying the images with ‘fire’ and ‘no fire’. SVM classifier is applied to the fused feature vector. In general, as the size of the fused feature vector increases, the classification accuracy increases. A wildfire image dataset with 2096 images is chosen with balanced classes of ‘fire’ and ‘no fire’. With a 80% train and test split, the mean classification accuracy obtained is in excess of 98%. Various other performance metrics are also given to emphasize the merit of the proposed approach.

Keywords Forest fire detection · Mobile CNN architectures · Feature fusion of pre-trained networks

B. C. Mohan (✉)
Bapatla Engineering College, Bapatla, India
e-mail: chandrabhuma@gmail.com

© The Author(s), under exclusive license to Springer Nature Switzerland AG 2023
K. Jain et al. (eds.), *Proceedings of UASG 2021: Wings 4 Sustainability*,
Lecture Notes in Civil Engineering 304,
https://doi.org/10.1007/978-3-031-19309-5_4

39

1 Introduction

Every year more than millions of people are evacuated due to wildfires globally. Wildfire is quite common in the forests. In 2020, 52,113 wildfire cases have been reported globally, and 8,889,297 acres of land got burned. Compared to 2019, it is double in terms of acres burned. In India, in 2019, over 30,000 forest fires were reported. Death rate is also alarming due to forest fires. If detected at an early stage, it can be confined and life-saving measures can be taken effectively. Monitoring the forest areas for wildfire identification using UAVs [1, 2] is an inexpensive and accurate method. Classical machine learning algorithms depend on the texture, color, and smoke features [3] for classifying the images with ‘fire’ [4]. An exhaustive survey of various fire monitoring systems, classification algorithms, detection algorithms and various modalities is given in [5]. In recent past, deep learning architectures are gaining popularity and are able to offer higher classification accuracies not achievable with machine learning algorithms. But, deep learning algorithms, CNNs in particular require large training data and computational resources. To overcome these difficulties, mobile CNN architectures were proposed targeting mobile and portable devices. A brief review of the existing works in the classification of ‘fire’ and ‘no fire’ images is given next. The paper is organized as follows. A review of recent works is given in Sect. 2. Various mobile CNN architectures and their parameter sizes are given in Sect. 3. Proposed algorithms is briefed in Sect. 4. Experimental simulations are presented in Sect. 5. Conclusions are given in Sect. 6.

2 Review of Recent Works

Detecting flame and smoke from the fire is easy in a ground-based imaging system. Cameras can be mounted on the towers in the forests. But their purview is limited and hence imaging of deeper areas is not possible with these fixed cameras. In this regard, unmanned aerial vehicles i.e., drones can cover broader and deeper areas with more closer view of the fireplace than fixed cameras. Dangerous areas and in accessible areas can be covered with UAVs. In general, UAVs utilize optical or infrared charge-coupled device (CCD) for capturing the images in addition to other sensors. Traditional methods include the texture features from the fire and smoke areas from the images and applying the classifiers on the features. Barmpoutis et al. [6] used a flame dynamic texture analysis for classification of fire images. Color, motion and spatial-temporal features are used in this. Using 2D wavelet decomposition, 3D wavelet decomposition both spatial and temporal texture analysis of the flame is done in [7]. Sudhakar et al. [8] used a motion-based algorithm for detecting the fire in the forest through UAVs. Additional information from landscape data and meteorological information is used in this work. Accurate detection and classification of fire images in the forests are done by using a fixed-wing drone and a rotary-wing drone [9]. Both optical cameras and thermal cameras were used. Once, the fixed-wing drone

detects a fire, a closer view is obtained by a rotary wing drone. Chen et al. [10] used a traditional multi-layer CNN architecture with an image size of 64×64 as input. The dataset comprised 950 images. In [11], fire front shape and the way it propagates was analyzed using an onboard visual and infrared camera. Multiple views were obtained with multiple vehicles for improved monitoring. Compared to traditional features and classifiers, deep learning approaches are gaining popularity and utilizing deep CNN architectures in the fire detection systems is becoming common in UAVs. By localizing and segmenting the fire area Zhao et al. [12] used a saliency detection algorithm for fire classification and detection algorithm. Tang et al. [13] and Jiao et al. [14, 15] used YOLOv3 (You Only Look Once) architecture for detecting the fire. The captured images were of high-resolution 4K images in [13].

Integration of fog computing and CNN architecture was proposed by Srinivas and Dua [16]. They used AlexNet as the CNN architecture. For detecting both flame and smoke, Barmpoutis, et al. [17, 18] have proposed a setup using UAVs. By employing 360-degree sensor cameras, number of sensors and can be reduced. The burden of data acquisition and computational costs is also reduced. Smoke and flame area is segmented using DeepLab V3+ networks. In addition, the authors have also proposed a “Fire detection 360-degree dataset”, They obtained an F-score detection rate of 94.6% with fewer sensors. In this work, a dataset [19] available in kaggle is utilized and was prepared by them using public images from google and other resources. It comprises 2096 images having equal number of ‘fire’ and ‘no fire’ images. Sample images from each class are depicted in Fig. 1.



(a) Fire Images



(b) No Fire Images

Fig. 1 Sample images from the UAV forest fire dataset

3 Mobile CNN Architectures

In general, CNN architectures that are deeper and wider are able to capture complex features of an image. However, deeper architectures consume lot of memory and consume and battery power when deployed on mobile platforms. As computational resources on a mobile platform i.e., drones, are minimal, deeper architectures cannot be used. Mobile CNN architectures are lightweight and consume less memory and inferencing is very fast. Hence, suitable for real-time processing of image or video data. In 2016, a small model known as SqueezeNet [20] was proposed. It consists of a fire module. With less number of parameters, it was able to perform similar to Alexnet on ‘imagenet’ dataset. In a squeeze layer, data is compressed. There are eight fir modules in SqueezeNet. At the end of the net, a convolution layer exists. SqueezeNetv1.1 has 1.25 million parameter.rs and has top-1 57.5% accuracy on ‘imagenet’ dataset. Model size is less than 0.5MB. A simple CNN was developed for mobile vision applications in 2017 known as MobileNetv1 [21]. In MobileNetv1, depthwise separable convolution was used instead of convolution layers. Hence, required learned parameters are less. No max pooling is used to reduce the spatial dimensions, but there is a global average pooling layer at the end. With a depth multiplier of 1, it has 4.24 million parameters and has shown 70.9% top-1 accuracy on ‘imagenet’.

In MobileNetv2 [22], same depthwise convolution used in MobileNetv1 is used, but in the middle. One expansion layer before the depthwise convolution and one bottleneck layer after the depthwise convolution is employed. Further, a residual connection is there in the block. This is between the bottleneck layers, hence known as an inverted residual connection. MobileNetv2 has 3.47 million parameters and has shown an accuracy of 71.8% on top-1 category of ‘imagenet’. The performance varies with a hyper parameter called depth multiplier. An architecture targeted for mobile devices known as Mobile Neural Architectural Search (MNASNet) [23] was developed in 2018. Similar to MobileNetv2, MNASNet has an expansion layer, depthwise convolution, and bottleneck layer, residual connection. Both 3×3 and 5×5 convolutions are used and in the MBConv block, the expansion layer uses a factor of 3. A new module known as the squeeze and excitation module is introduced in order to reduce the feature map spatial dimensions to 1×1 . The importance of features is learned by the squeeze and excitation module. MNASNET-A1 has 3.9 million parameters, 75.2% accuracy and MNASNET-A3 has 5.2 million parameters and 76.7% accuracy on ‘imagenet’.

An improvement over MNASNet was MobileNetv3 [24] and was proposed in 2019. Usage of Swish activation layer, squeeze and excitation module redesign, and redesign of expensive layers are the modifications to MNASNet and led to MobileNetv3. This architecture is developed with a focus on Android devices. MobileNetv3 has two versions i.e., MobileNetv3 (small), and MobileNetv3 (large) having 2.9 millions and 5.4 millions parameters and 67.5% and 75.2% classification accuracies on ‘imagenet’. SqueezeNext [25] is a modification of SqueezeNet. Two bottleneck layers are used in a row. Instead of using sing 3×3 convolution, two single

1x3 and 3x1 convolution is used. An expansive layer and residual connection exist. Depthwise separable convolutions are not used in SqueezeNext. With just 0.7 million parameters, 1.0-SqNxt-23 has an accuracy of 59.05%. Point convolutions or dense convolutions are computationally expensive. Group convolution is a remedy to this. However, there is not information shared between the groups. Residual connection is also present in the process. A shuffle operation was employed on these results in ShuffleNet [26]. There are 5 variants of ShuffleNets. ShuffleNet v1 1.0x (8 groups) needs only 2.4 million parameters and has shown 68% accuracy and ShuffleNet v2+ (large) has 6.7 million parameters and 77.1% accuracy was reported. The architecture of CondenseNet [27] is similar to DenseNet initially. Reuse of features is employed to achieve higher accuracy. But using all the features may not be helpful. Groupwise splitting of filters per layer is employed. Usually, 4 or 8 groups per layer are used. As training progresses, features that are not prominent are pruned from the model on per-group basis. An index layer acts as a look-up table and is helpful in the inference process. CondenseNet-74 (8 groups) and CondenseNet-74 (4 groups) require 2.9 and 4.8 millions parameters and have shown 71% and 73.8% accuracy.

The concept of dimension-wise convolution and fusion was employed in DiCENet [28]. Width-wise and height-wise convolution on the input image is known as dimension-wise convolution. For a tensor $D \times H \times W$, (D stands for depth, H stands for Height, and W for width), in dimension-wise convolution, the input tensor is sliced along either W or H axis but not D axis. The filter window works on either $D \times W$ or $D \times H$. In an interleaved manner, the outputs of the convolutions (depth, width, and height) are concatenated. Both local fusion and global fusion are used in DiCENet. DiCENet 1.0, DiCENet 1.5 and DiCENet 2.0 are three variants and 1.81, 2.65, and 3.98 million parameters are required respectively. Top-1 accuracies reported were 66.5%, 69.5%, and 71.0%. In FBNet [29], a 1x1 convolution for expansion, RELU activation function, depthwise convolution, a bottleneck layer with no activation and a residual connection are basic blocks. There are nine configurations one can search for in this FBNet. Over all structure is fixed, however, choosing specific 9 blocks for the 22 layers makes this FBNet flexible. FBNet-A, FBNet-B and FBNet-C require 4.3, 4.5 and 5.5 million parameters and reported accuracies were 73.3%, 74.5% and 75.2%.

In depthwise convolution, the size of the kernel plays an important role. Putting multiple kernel sizes in a layer known as MixConv is used in MixNet [30]. Kernel sizes of 3×3 are common, and in some networks, 5×5 and 7×7 kernels are used with the notion that the accuracies are improved as kernel size increases. This is true to some extent, it is observed that with a size of 9×9 kernel, the classification accuracy drops. Channels are split into groups. Depthwise convolution is applied for each group with different kernel sizes. At the end, concatenation is applied. MixNet-S, MixNet-M, and MixNet-L are proposed in this category and 4.1, 5.0 and 7.3 million parameters are required for each one respectively. A top-1 accuracy of 78.9% was reported for MixNet-L. A recent architecture is EfficientNet [31] proposed in 2020. Scaling of network width, depth, and input resolution is implemented using compound scaling. Various scaling parameters are used for width, depth and input resolution. These scaled architectures are based on a basic network known

under EfficientNet B0. EfficientNet-Lite is targeted for mobile devices. Relu6 is used as an activation function. EfficientNet-Lite0, EfficientNet-Lite1, EfficientNet-Lite2, EfficientNet-Lite3, and EfficientNet-Lite4 models are lightweight models having 4.7, 5.4, 6.1, 8.2 and 13.0 million parameters. EfficientNet-Lite4 has demonstrated an accuracy of 81% top-1 class.

4 Proposed Algorithm

Initially, the dataset is split into training and test set with a split ratio of 80% train and 20% test data. For a selected mobile CNN architecture, the sizes of the images in the dataset are resized as per the selected architecture. Features can be extracted from any layer of the CNN architecture. However, the features extracted from the last pooling layers are more discriminating in general. Feature vectors from the last pooling layer of a pre-trained mobile CNN architecture is computed for both train and test image data. Feature vectors of the selected mobile CNN architectures are concatenated and given to an SVM (Support Vector Machine) classifier. A concatenated test feature vector is given to the trained SVM classifier. Classification accuracy is computed for the test image data. The images in the train and test set are shuffled and the experiment is repeated for ten times. Mean classification accuracy is computed for the ten iterations. This is to ensure that the model is more generalized and not overfitting. The feature vector size increases due to concatenation. However, the resulting feature is more discriminating than the individual feature vector from a mobile CNN. It is summarized in Fig. 2 as a flow chart.

5 Experimental Simulations

All the pre-trained models features are extracted using the repository given in [32, 33] using Pytorch framework in google colab environment. All the selected mobile CNN architectures are pre-trained on ‘imagenet’ dataset. Imagenet dataset consists of 1000 classes and more than 14 million images. Features are extracted from the last pooling layer of a pre-trained network. Various models and the size of the feature vector is given in Table 1. All the images in the dataset are pre-processed as per the input size of the chosen pre-trained model. The train and test split chosen is 80%–20%. Hence, there are 1676 images in the train set and 420 images in the test set totaling to 2096 images. The classification problem is a binary classification problem. Support Vector Machine (SVM) classifier with linear kernel is chosen for classification. To ensure generalizability of the model train and test images are shuffled at random and the experiment is repeated ten times. The mean classification accuracy of various mobile CNN architectures is given in Table 1. To have a comparison, Resnet50 [34] is also included in Table 1 even though it is not a mobile CNN architecture. There

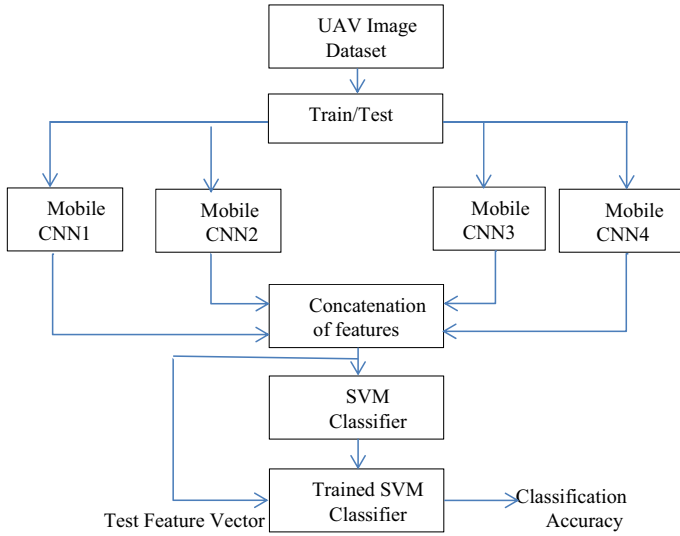


Fig. 2 Flow chart of the proposed algorithm

are 23 million parameters in Resnet50, much higher than most of the mobile CNN architectures.

MixNet-L is able to classify with an accuracy of 97.14%. The performance of Dicenetwd5 is very poor. Except this case, most of the mobile CNN architectures are able to classify the images with ‘Fire’ and with ‘No Fire’ demonstrating a classification accuracy of higher than 93%. To improve the classification accuracy further, the features from the Dicenet_w1, Mixnet_1, Fbnetc_100 and Mobilenetv3_large_100 are concatenated. Size of the resulting feature vector is 5264. After fusing (concatenating), the peak classification accuracy obtained is 98.8% and the mean classification accuracy obtained is 98.21%. Iteration-wise classification accuracies are given in Table 2a for 80% train –20% test split. For 10% train –90% test split, accuracies are given in Table 2b. Without fusing, the performance of the selected four networks is shown in Fig. 2 As shown in Fig. 3, the fused feature vector is able to classify with higher accuracy compared to an individual feature vector. In 4th and 8th iterations, a peak classification accuracy of 98.8% is obtained and the resulting confusion matrix is shown in Fig. 4. The simulation is run for 10 iterations and various performance metrics calculated over ten iterations is given in Table 3.

6 Conclusions

In this work, an algorithm for classifying the images with ‘fire’ and ‘no fire’ is proposed. Pooled features from the selected pre-trained mobile CNN architectures are concatenated. The concatenated feature vector is given to the binary SVM classifier

Table 1 Pre-trained mobile CNN architectures and classification accuracies

Architecture	Feature vector size	Mean classification accuracy
Condensenet74_c4_g4	2064	96.7619
Condensenet74_c8_g8	2064	96.0476
Dicenet_w1	464	96.4286
Dicenet_w2	976	96.5238
Dicenet_w3d2	704	96.2619
Dicenet_w3d4	344	94.5952
Dicenet_w5d4	576	96.3333
Dicenet_w7d8	840	96.6190
Dicenet_wd2	192	93.5714
Dicenet_wd5	128	62.1190
Fbnetc_100	1984	96.6905
Mixnet_l	1536	97.1429
Mixnet_m	1536	96.8333
Mixnet_s	1536	96.5476
Mnasnet_100	1280	96.5000
Mobilenetv2_100	1280	95.8333
Mobilenetv2_110d	1280	96.2619
Mobilenetv2_120d	1280	96.7619
Mobilenetv2_140	1792	96.5000
Mobilenetv3large_100	1280	96.7143
Resnet50	2048	96.9524
Shufflenet_g1_wd4	144	93.5476
Shufflenetv2_wd2	1024	95.4286
Sqnx23_w1	128	93.3571
Efficientnet_lite0	1280	95.5000
Efficientnet_lite1	1280	94.5000
Efficientnet_lite2	1280	94.6667
Efficientnet_lite3	1280	95.4286

with a linear kernel. Even at 10% train and 90% test split, a mean classification accuracy of 97.1% is achieved after fusing the features from four pre-trained mobile CNN architectures. It is in excess of 98% for an 80% train and 20% test case. Each experiment is repeated 10 times after shuffling the training and test image data to ensure the generalizability of the proposed algorithm. This ensures that there is no overfitting problem. Various performance measures, i.e., classification accuracy, F-measure, sensitivity, specificity, and precision are computed. Since the selected architectures are lightweight in terms of trainable parameters and inference speed, they can be easily deployed in any mobile platform like drones. It may be concluded

Table 2 a Fused mobile CNN architectures and classification accuracies (80%train and 20%test).
b Fused mobile CNN architectures and classification accuracies(10%train and 90%test)

Fused architectures	Iteration	Classification accuracy per iteration
	1	98.5714
	2	96.9048
	3	98.3333
Dicenet_w1	4	98.8095
Mixnet_l	5	97.8571
Fbnetc_100	6	98.5714
Mobilenetv3large_100	7	97.6190
Feature Vector Size:	8	98.8095
5264	9	98.0952
	10	98.5714
	Mean classification accuracy	98.2100
	1	97.8791
	2	96.9777
	3	96.2354
Dicenet_w1	4	97.1898
Mixnet_l	5	96.3945
Fbnetc_100	6	97.2428
Mobilenetv3large_100	7	97.5610
Feature Vector Size:	8	96.9777
5264	9	97.6670
	10	97.5080
	Mean classification accuracy	97.1600

that by properly fusing selected mobile CNN architectures features, it is possible to achieve higher classification accuracies of more than 98% even with less number of images and with limited computational resources paving the way for deployment in drones and other UAVs. This is justified in this work with exhaustive simulations.

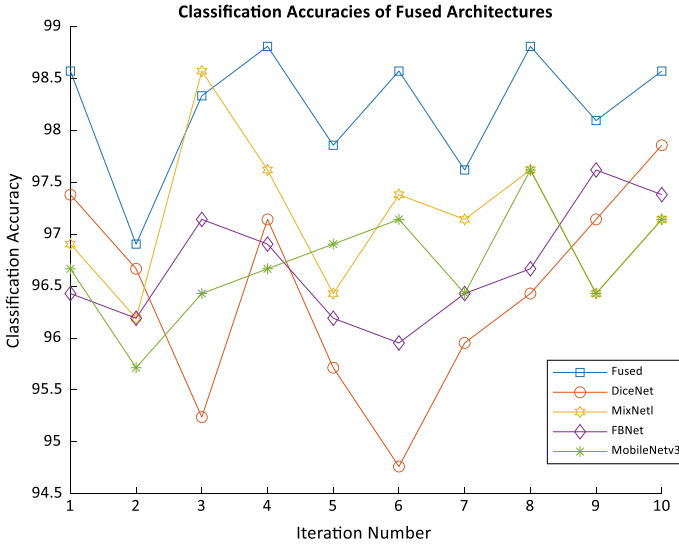


Fig. 3 Classification accuracy of fused features compared to individual features

Output Class ↑	Fire	206 49.0%	1 0.2%	99.5% 0.5%
	No Fire	4 1%	209 49.8%	98.1% 1.9%
		98.1% 1.8%	99.5% 0.5%	98.8% 1.2%
	Fire	No Fire		
Target Class →				

Fig. 4 Confusion matrix for peak classification accuracy

Table 3 Various performance metrics over 10 iterations

Performance metric	Fire class	No fire class
True positive	2051	2074
False positive	49	26
False negative	26	49
True negative	2074	2051
Precision	0.976	0.987
Sensitivity	0.987	0.976
Specificity	0.976	0.987
Accuracy	98.21%	98.21%
F-measure	0.982	0.982

References

1. Gaur A, Singh A, Kumar A, Kumar A, Kapoor K (2020) Video flame and smoke based fire detection algorithms: a literature review. *Fire Technol* 56:1943–1980
2. Kaabi R, Frizzi S, Bouchouicha M, Fnaiech F, Moreau E (2017) Video smoke detection review: state of the art of smoke detection in visible and IR range. In: Proceedings of the 2017 International conference on smart, monitored and controlled cities (SM2C), Kerkennah-Sfax, Tunisia, 17 February 2017, pp 81–86
3. Yuan C, Zhang Y, Liu Z (2015) A survey on technologies for automatic forest fire monitoring, detection, and fighting using unmanned aerial vehicles and remote sensing techniques. *Can J For Res* 45:783–792
4. Allison RS, Johnston JM, Craig G, Jennings S (2016) Airborne optical and thermal remote sensing for wildfire detection and monitoring. *Sensors* 16:1310
5. Barmpoutis P, Papaioannou P, Dimitropoulos K, Grammalidis N (2020) A review on early forest fire detection systems using optical remote sensing. *Sensors* 20:6442. <https://doi.org/10.3390/s20226442>
6. Barmpoutis P, Dimitropoulos K, Grammalidis N (2014) Smoke detection using spatio-temporal analysis, motion modeling and dynamic texture recognition. In: Proceedings of the 22nd European signal processing conference, Lisbon, Portugal, 1–5 September 2014; pp 1078–1082
7. Prema CE, Vinsley SS, Suresh S (2018) Efficient flame detection based on static and dynamic texture analysis in forest fire detection. *Fire Technol* 54:255–288
8. Sudhakar S, Vijayakumar V, Kumar CS, Priya V, Ravi L, Subramaniaswamy V (2020) Unmanned aerial vehicle (UAV) based Forest Fire Detection and monitoring for reducing false alarms in forest-fires. *Comput Commun* 149:1–16
9. Kinaneva D, Hristov G, Raychev J, Zahariev P (2019) Early forest fire detection using drones and artificial intelligence. In: Proceedings of the 2019 42nd international convention on information and communication technology, electronics and microelectronics (MIPRO), Opatija, Croatia, 20–24 May 2019, pp 1060–1065
10. Chen Y, Zhang Y, Xin J, Yi Y, Liu D, Liu H (2018) A UAV-based forest fire detection algorithm using convolutional neural network. In: Proceedings of the IEEE 37th Chinese control conference, Wuhan, China, 25–27 July 2018, pp 10305–10310
11. Merino L, Caballero F, Martínez-De-Dios JR, Maza I, Ollero A (2012) An unmanned aircraft system for automatic forest fire monitoring and measurement. *J Intell Robot Syst* 65:533–548
12. Zhao Y, Ma J, Li X, Zhang J (2018) Saliency detection and deep learning-based wildfire identification in UAV imagery. *Sensors* 18:712
13. Tang Z, Liu X, Chen H, Hupy J, Yang B (2020) Deep learning based wildfire event object detection from 4K aerial images acquired by UAS. *AI* 2020 1:166–179
14. Jiao Z, Zhang Y, Mu L, Xin J, Jiao S, Liu H, Liu D (2020) A YOLOv3-based learning strategy for real-time UAV-based forest fire detection. In: Proceedings of the 2020 Chinese control and decision conference (CCDC), Hefei, China, 22–24 August 2020, pp 4963–4967
15. Jiao Z, Zhang Y, Xin J, Mu L, Yi Y, Liu H, Liu D (2019) A deep learning based forest fire detection approach using UAV and YOLOv3. In: Proceedings of the 2019 1st International conference on industrial artificial intelligence (IAI), Shenyang, China, 23–27 July 2019, pp 1–5
16. Srinivas K, Dua M (2020) Fog , Computing and deep CNN based efficient approach to early forest fire detection with unmanned aerial vehicles. In: Proceedings of the international conference on inventive computation technologies, Coimbatore, India, 29–30 August 2019. Springer, Cham, Switzerland, pp 646–652
17. Barmpoutis P, Stathaki T (2020) A novel framework for early fire detection using terrestrial and aerial 360-degree images. In: Proceedings of the international conference on advanced concepts for intelligent vision systems, Auckland, New Zealand, 10–14 February 2020. Springer, Cham, Switzerland, pp 63–74

18. Barmpoutis P, Stathaki T, Dimitropoulos K, Grammalidis N (2020) Early fire detection based on aerial 360-degree sensors, deep convolution neural networks and exploitation of fire dynamic textures. *Remote Sens* 12:3177
19. Chugh P, Mathews ET, Bharat Kumar G. Forest fire detection through UAV imagery using CNNs. <https://www.kaggle.com/jovian/jvn-forest-fire-detection-uav-images>
20. Iandola FN, Han S, Moskewicz MW, Ashraf K, Dally WJ, Keutzer K (2016) AlexNet-level accuracy with 50x fewer parameters and <0.5MB model size. [arXiv:1602.07360](https://arxiv.org/abs/1602.07360)
21. Howard AG, Zhu M, Chen B, Kalenichenko D, Wang W, Weyand T, Andreetto M, Adam H (2017) MobileNets: efficient convolutional neural networks for mobile vision applications. [arXiv:1704.04861](https://arxiv.org/abs/1704.04861)
22. Sandler M, Howard A, Zhu M, Zhmoginov A, Chen L-C (2019) MobileNetV2: inverted residuals and linear bottlenecks. [arXiv:1801.04381](https://arxiv.org/abs/1801.04381)
23. Tan M, Chen B, Pang R, Vasudevan V, Sandler M, Howard A, Le QV (2019) MnasNet: platform-aware neural architecture search for mobile. [arXiv:1807.11626](https://arxiv.org/abs/1807.11626)
24. Howard A, Sandler M, Chu G, Chen L-C, Chen B, Tan M, Wang W, Zhu Y, Pang R, Vasudevan V, Le QV, Adam H (2019) Searching for MobileNetV3. [arXiv:1905.02244](https://arxiv.org/abs/1905.02244)
25. Gholami A, Kwon K, Wu B, Tai Z, Yue X, Jin P, Zhao S, Keutzer K (2018) SqueezeNext: hardware-aware neural network design. [arXiv:1803.10615](https://arxiv.org/abs/1803.10615)
26. Zhang X, Zhou X, Lin M, Sun J (2017) ShuffleNet: an extremely efficient convolutional neural network for mobile devices. [arXiv:1707.01083](https://arxiv.org/abs/1707.01083)
27. Huang G, Liu S, van der Maaten L, Weinberger KQ (2018) CondenseNet: an efficient densenet using learned group convolutions. [arXiv:1711.09224](https://arxiv.org/abs/1711.09224)
28. Mehta S, Hajishirzi H, Rastegari M (2020) DiCENet: dimension-wise convolutions for efficient networks. [arXiv:1906.03516](https://arxiv.org/abs/1906.03516)
29. Wu B, Dai X, Zhang P, Wang Y, Sun F, Wu Y, Tian Y, Vajda P, Jia Y, Keutzer K (2019) FBNet: hardware-aware efficient ConvNet design via differentiable neural architecture search. [arXiv:1812.03443](https://arxiv.org/abs/1812.03443)
30. Tan M, Le QV (2019) MixConv: mixed depthwise convolutional kernels. [arXiv:1907.09595](https://arxiv.org/abs/1907.09595)
31. Tan M, Le QV (2020) EfficientNet: rethinking model scaling for convolutional neural networks. [arXiv:1905.11946](https://arxiv.org/abs/1905.11946)
32. Wightman R (2019) PyTorch image models, GitHub repository. <https://doi.org/10.5281/zenodo.4414861>
33. <https://github.com/rwightman/pytorch-image-models>
34. He K, Zhang X, Ren S, Sun J (2015) Deep residual learning for image recognition. [arXiv:1512.03385](https://arxiv.org/abs/1512.03385)

Deep Learning-Based Improved Automatic Building Extraction from Open-Source High Resolution Unmanned Aerial Vehicle (UAV) Imagery



Chintan B. Maniyar and Minakshi Kumar

Abstract Automatically extracting buildings from remotely sensed imagery has always been a challenging task, given the spectral homogeneity of buildings with non-building features as well as the complex structural diversity within the image. Traditional machine learning (ML) based methods deeply rely on a huge number of samples and are best suited for medium-resolution images. Unmanned aerial vehicle (UAV) imagery offers the distinct advantage of very high spatial resolution, which is helpful in improving building extraction by characterizing patterns and structures. However, with increased finer details, the number of images also increases many folds in a UAV dataset, which require robust processing algorithms. Deep learning algorithms, specifically Fully Convolutional Networks (FCNs) have greatly improved the results of building extraction from such high resolution remotely sensed imagery, as compared to traditional methods. This study proposes a deep learning-based segmentation approach to extract buildings by transferring the learning of a deep Residual Network (ResNet) to the segmentation-based FCN U-Net. This combined dense architecture of ResNet and U-Net (Res-U-Net) is trained and tested for building extraction on the open source Inria Aerial Image Labelling (IAIL) dataset. This dataset contains 360 orthorectified images with a tile size of 1500 m² each, at 30 cm spatial resolution with red, green and blue bands; while covering total area of 805 km² in select US and Austrian cities. Quantitative assessments show that the proposed methodology outperforms the current deep learning-based building extraction methods. When compared with a singular U-Net model for building extraction for the IAIL dataset, the proposed Res-U-Net model improves the overall accuracy from 92.85% to 96.5%, the mean F1-score from 0.83 to 0.88 and the mean IoU metric from 0.71 to 0.80. Results show that such a combination of two deep learning architectures greatly improves the building extraction accuracy as compared to a singular architecture.

C. B. Maniyar (✉) · M. Kumar

Photogrammetry and Remote Sensing Department, Indian Institute of Remote Sensing, Dehradun UK 248001, India

e-mail: chintanmaniyar@gmail.com

© The Author(s), under exclusive license to Springer Nature Switzerland AG 2023

51

K. Jain et al. (eds.), *Proceedings of UASG 2021: Wings 4 Sustainability*,

Lecture Notes in Civil Engineering 304,

https://doi.org/10.1007/978-3-031-19309-5_5

Keywords Transfer learning · Fully convolutional networks · Image segmentation · Building extraction

1 Introduction

1.1 Background

Remote sensing imagery, both satellite and aerial, contains a lot of terrain-feature-specific information such as land-cover spread, building footprints, waterbody extent, vegetation and forest boundaries etc. Extracting this feature information without losing relative context within the image is a very important remote sensing image processing milieu [1, 2]. Feature extraction is usually done by identifying a common pattern among pixels and grouping them together, that group of pixels then being a feature [3]. One of the most crucial aspects for accurate image feature extraction is finer spatial details such as edges and corners. Primitive feature extraction methods were time-consuming and required a lot of expensive human intervention [4]. This was mostly because of the unavailability of higher spatial resolution data in conjunction with the technical infrastructure at the time. However, with advancements in digital systems for image processing and also the increased availability and accessibility of high spatial resolution data from both satellites and Unmanned Aerial Vehicles (UAVs), image feature extraction has consistently been one of the hottest research topics in remote sensing image processing [5].

1.2 Previous Works

In remote sensing feature extraction, building extraction is one of the most vital aspects of research. With its applications spread in various pipelines of urban mapping and management, disaster management, change detection, maintaining and updating geodatabases etc., building extraction has caught the attention of researchers worldwide for developing robust and accurate algorithms to automate the process [6]. Primitive methods of building extraction were based on applying statistical and morphological operations on individual pixels to group them together [7], hence automating the task up to some extent. One of the most prevalent issues in building extraction that has propagated from early methods to the recent methods is the differentiation of foreground and background as well as building and non-building objects [8]. To be able to differentiate between these, spectral and geometrical cues such as color, shape and line have been used to extract buildings from very high-resolution imagery [9]. Another study combined distinctive corners while estimating building outlines to extract buildings [10], but was unable to extract irregular-shaped buildings. In the beginning of the decade, a generic index called Morphological Building Index (MBI) was introduced to extract buildings from high-resolution satellite imagery, based on

spectral information [11]. While this method was able to successfully extract buildings with an irregular shape, it failed in shadowy regions and also could not extract buildings located close by (instance extraction). A consequent study to MBI proposed a Morphological Building/Shadow Index which defined a building index as well as a shadow index, and was specifically aimed at bridging the shortcomings of the MBI method [12].

With the recent availability of strong computing systems as well as finer resolution data, artificial intelligence-based deep learning algorithms such as Convolutional Neural Networks (CNNs) are being aggressively used for building extraction given their advantage of hierarchical feature extraction without losing any contextual information [13, 14, 15]. In general, a deep learning architecture consists of a network structure with many hidden layers leading to hierarchical feature extraction thus, eliminating the problem of inadequate representation of learning features [16]. Building-A-Nets is an adversarial network to for robust extraction of building rooftops. Multiple Feature Reuse Network (MERN) is a resource-efficient rich CNN to detect building edges from high spatial resolution satellite imagery [17]. A special type of pre-trained CNN, called a Fully Convolutional Network (FCN) is also being widely used for transfer learning-based building extraction. A few such popular FCNs are VGG-16 [18], ResNet [19], Deeplab [20], DenseNet [21], SegNet [22] and U-Net [23]. Studies specifically on building extraction from UAV images have also increased of late. SegNet and U-Net have been used in an ensemble manner to improve building footprint extraction from high-resolution UAV imagery [24]. Techniques such as dilated spatial pyramid pooling [25], multi-stage multi-task learning [26], and channel attention mechanisms [27] have been used to improve the building segmentation accuracy from UAV data. Variants of U-Net architecture have also been tested for building extraction and studies indicate that the U-Net is the most suitable for dense image building extraction [15, 28, 29].

1.3 Objective and Summary

Sometimes, the FCN based segmentation is visually degraded in case of blurred building boundaries [30]. Moreover, high spatial resolution data is generally restricted to three or four spectral channels, which makes it difficult to differentiate buildings and other spatially similar features [24]. To address these issues, this study proposes a deep learning-based segmentation approach that combines a pre-trained FCN with a U-Net being trained for building extraction, to extract buildings from high-resolution RGB UAV imagery. The learning of a deep Residual Network (ResNet) trained on the ImageNet dataset is transferred to the segmentation-based FCN U-Net, hence forming a combined Res-U-Net architecture. In this Res-U-Net, the pre-trained ResNet helps capture more context in case of features spatially similar to buildings while the U-Net learns building segmentation based on a unique loss function (discussed in Sect. 2.3) that simultaneously accounts for crispness as well as the region of a segmented building, hence preventing prediction leakage

outside of feature in case of blurred boundaries. Consequent sections of the paper discuss the dataset details, data preparation and training methodology, results and their inferences, and conclude the study.

2 Dataset Details

This study uses the Inria Aerial Image Labelling (IAIL) dataset. This dataset contains a total of 360 orthorectified images (180 for training and 180 for testing) with a tile size of 1500 m² each, at 30 cm spatial resolution with red, green and blue bands. Each image is of size 5000 × 5000 pixels. While covering an area of 81 km²/city in select 3 US cities of Austin, Chicago, Kitsap County and select Austrian cities of Vienna and West Tyrol, this dataset contains 36 images from each city having high variance in terms of urban density and building spacing. Moreover, numerous instances of shadowy features and shadowy backgrounds are present, especially in the images from Chicago, US. The ground truth of the training set is provided as a binary feature image with only two classes namely building and non-building. Since ground truth is provided only for the training set of 180 images, we use only those 180 images to train and validate our model. Figure 1 shows the UAV image and its corresponding ground truth as available from the IAIL training set, for each of the five cities.

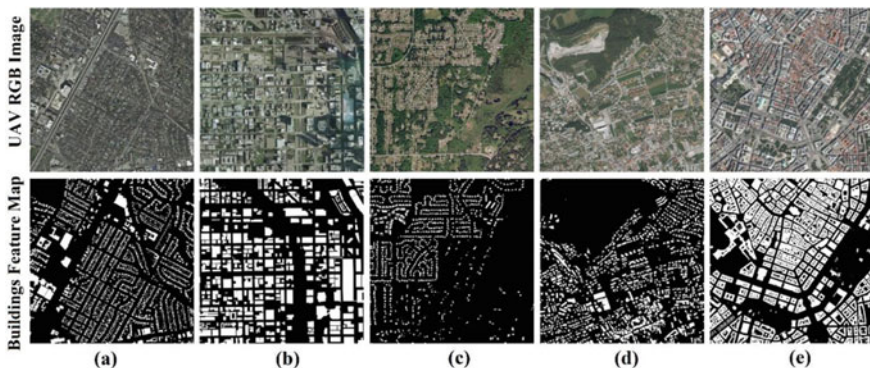


Fig. 1 Data samples from the IAIL dataset, one from each city **a** Austin, USA, **b** Chicago, USA, **c** Kitsap County, USA, **d** West Tyrol, Austria, **e** Vienna, Austria



Fig. 2 Data preparation methodology for a single image

3 Methodology

3.1 Data Preparation Methodology

A single image is of size 5000×5000 pixels. We further split it into small data chips of size 224×224 pixels in accordance to the proposed network architecture. This results into 484 such tiles from a single image. However, certain number of chips contain no buildings or hardly any buildings at all, creating a bias in the type of data which could result in model misfit. To ensure uniformity of 224×224 chips in terms of buildings, we further filter the 484 chips using a High Label Filter (Eq. 1). This is basically a ratio of the number of labelled pixels to the total number of pixels in a 224×224 chip. We use a threshold of 0.3 in the High Label Filter to further filter these 484 chips. This excludes the chips having label density less than 30% and hence the earlier bias in the data is now removed. Figure 2 shows the data preparation methodology for a single image. This process is performed for all 180 images as well as labels. Passing the 87,120 224×224 chips obtained from 5000×5000 180 images (180×484) through the High Label Filter, we get 27,164 224×224 chips. The proposed model is trained and validated on these 27,164 chips and entire images of size 5000×5000 are used for testing.

$$HLF = \frac{\sum_{i=0}^{224 \times 224} building_pixel_i}{\sum_{i=0}^{224 \times 224} image_pixel_i} \quad (1)$$

3.2 Network Architecture

In this study, the U-Net architecture is implemented with a dynamic decoder to learn building extraction as a fully convolutional network (FCN). The whole architecture essentially consists of two major operations—image contraction performed by the encoder and image expansion performed by the decoder (Fig. 3). The encoder is responsible for pooling out the necessary information from within the convolution kernel which is done by max pooling operations. The decoder helps preserve precise local information such as building edges in case of blurred images which is done by upsampling and convoluting over transposed kernels. Each step of encoder is

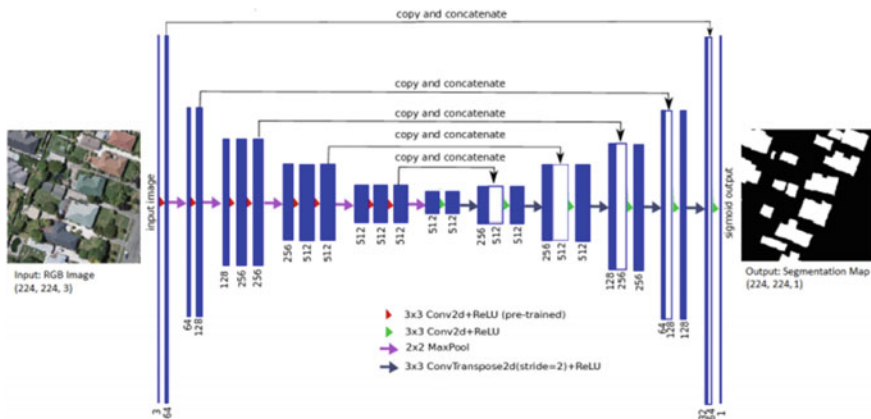


Fig. 3 Proposed Res-U-Net architecture described in terms of U-Net encoders and decoders, along with the pre-trained ResNet34 layers

connected with the corresponding inverse step of the decoder using successive skip connections. The advantage of using a dynamic network is the automatic creation of the decoder based on how the encoder is initialized [31] as well as working with almost any patch-size [32].

U-Net being an end-to-end FCN can easily be initialized with the weights of a deeper CNN. We further initialize the proposed dynamic U-Net architecture with the weights of ResNet34 trained on ImageNet, forming a Res-U-Net. The proposed Res-U-Net comprises of multiple sequential blocks as well as dynamic U-Net blocks initialized with ResNet34. Each encoder-decoder block of the architecture consists of a series of 2D batch normalization and ReLU activations which extract the trainable features from the data. Table 1 shows the specific network architecture of the proposed Res-U-Net architecture. The input to the network is an RGB image of shape $(224, 5 \ 224, 3)$ to which the network segments buildings and outputs segmented maps of shape $(224, 224, 2)$. Here, the prediction contains two channels, one of which is a boolean array having discrete prediction for every pixel being a building or not and the other is a float32 array which contains the logit probability score for every pixel being a building. This is helpful in refining the results by further pooling the probability scores with bounded functions such as sigmoid.

3.3 Training the Network

After weight initialization of the proposed Res-U-Net, transfer learning methodology was used to train for building extraction. Figure 4 shows the step-by-step training methodology. Out of 27,164 image-label pairs, the network was trained on 23,089 pairs (85%) and was validated on the remaining 4075 (15%) pairs of images and their

Table 1 Specific proposed network architecture with individual layer parameters

Layer			Kernel size	Output shape	Stride
Conv2d			7×7	$64 \times 112 \times 112$	2
Sequential block 1	Conv2d		3×3	$64 \times 56 \times 56$	1
	Conv2d		3×3	$64 \times 56 \times 56$	1
	Conv2d		3×3	$64 \times 56 \times 56$	1
Sequential block 2		Down block 1	1×1	$128 \times 28 \times 28$	2
	Conv2d		3×3	$128 \times 28 \times 28$	1
	Conv2d		3×3	$128 \times 28 \times 28$	1
	Conv2d		3×3	$128 \times 28 \times 28$	1
	Conv2d		3×3	$128 \times 28 \times 28$	1
Sequential block 3		Down block 2	1×1	$256 \times 14 \times 14$	2
	Conv2d		3×3	$256 \times 14 \times 14$	1
	Conv2d		3×3	$256 \times 14 \times 14$	1
	Conv2d		3×3	$256 \times 14 \times 14$	1
	Conv2d		3×3	$256 \times 14 \times 14$	1
	Conv2d		3×3	$256 \times 14 \times 14$	1
Sequential block 4		Down block 3	1×1	$512 \times 7 \times 7$	2
	Conv2d		3×3	$512 \times 7 \times 7$	1
	Conv2d		3×3	$512 \times 7 \times 7$	1
Conv2d			3×3	$1024 \times 7 \times 7$	1
Conv2d			3×3	$512 \times 7 \times 7$	1
	Conv2d		3×3	$1024 \times 7 \times 7$	
U-Net block 1		Pixelshuffle		$256 \times 14 \times 14$	1
	Conv2d		3×3	$512 \times 14 \times 14$	1
	Conv2d		3×3	$512 \times 14 \times 14$	1
	Conv2d		3×3	$1024 \times 14 \times 14$	
U-Net block 2		Pixelshuffle		$265 \times 28 \times 28$	1
	Conv2d		3×3	$384 \times 28 \times 28$	1
	Conv2d		3×3	$384 \times 28 \times 28$	1
	Conv2d		3×3	$768 \times 28 \times 28$	
U-Net block 3		Pixelshuffle		$192 \times 56 \times 56$	1
	Conv2d		3×3	$256 \times 56 \times 56$	1
	Conv2d		3×3	$256 \times 56 \times 56$	1
	Conv2d		3×3	$512 \times 56 \times 56$	
U-Net block 4		Pixelshuffle		$128 \times 112 \times 112$	1
	Conv2d		3×3	$96 \times 112 \times 112$	1
	Conv2d		3×3	$96 \times 112 \times 112$	1

(continued)

Table 1 (continued)

Layer			Kernel size	Output shape	Stride
PixelShuffle_ICNR	Conv2d		1×1	$384 \times 112 \times 112$	1
		Pixelshuffle		$96 \times 224 \times 224$	
Sequential extension	Conv2d		3×3	$99 \times 224 \times 224$	1
	Conv2d		3×3	$99 \times 224 \times 224$	1
Conv2d			1×1	$222 \times 224 \times 224$	1

corresponding labels. The network was trained with a batch size of 6 and a patch size of 224×224 for 30 epochs, with roughly 1200 batches being processed per epoch. The training was cut-off based on loss convergence (Fig. 5a). The learning was carried out on nearly 20 million parameters extracted at different layers of the network. The network was optimized with ADAM optimizer at a learning rate of 0.0001 and a decay rate of 0.9.

A unique combination of Binary Cross Entropy (BCE) loss (Eq. 2) and dice loss (Eq. 3) was used to train the network. BCE is a probability distribution-based loss [33] and hence was used to minimize the entropy between the prediction and the ground truth in terms of buildings as features. It was also helpful in preserving the crispness near the boundary regions. Dice loss is a region-based Intersection-over-Union like metric [34] and it was used to maximize the overlap and similarity between the

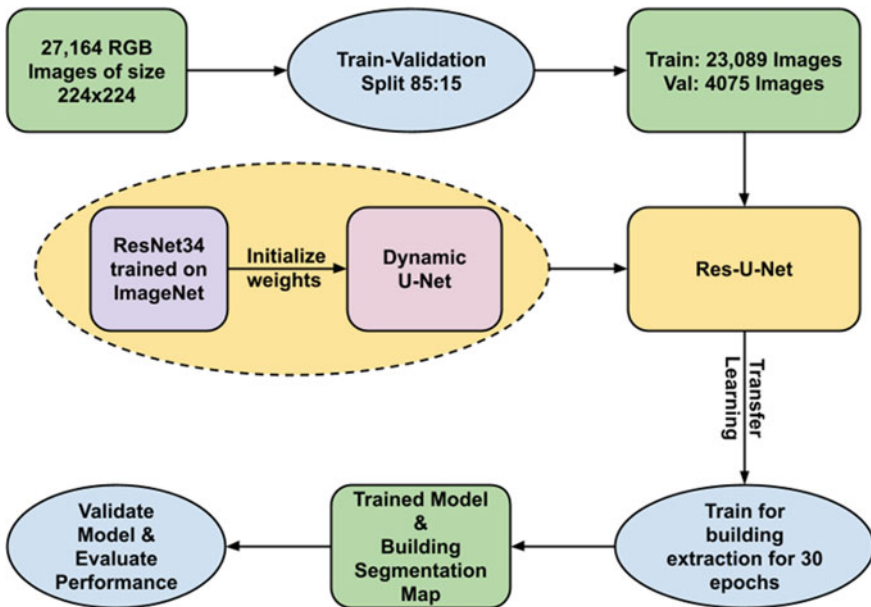


Fig. 4 Network training methodology for building extraction using transfer learning

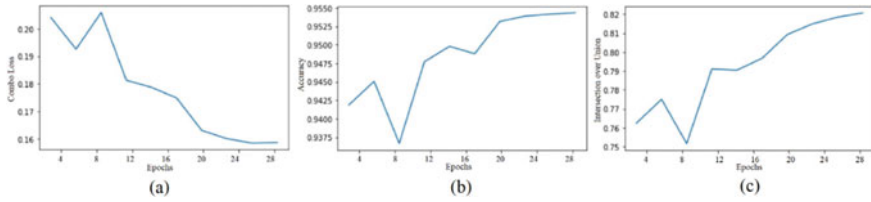


Fig. 5 a Combo loss variation, b accuracy variation and c IoU variation in 30 epochs of training

predicted region and the ground truth of the feature region. Hence, a combo loss was defined (Eq. 4) which focused on both boundary and region preservation. Figure 5a shows the loss-based convergence of the model after 30 epochs of training. After training for 30 epochs and processing 36,000 batches the model began to converge and was saved at the end of 30 epochs with an overall accuracy of 95.7% and mean Intersection over Union (IoU) of 0.83.

$$BCE_{Loss} = -\frac{1}{patchsize} \sum_{i=1}^{patchsize} g_i \times \log p_i + (1 - g_i) \times \log(1 - p_i) \quad (2)$$

$$Dice\ Loss = \frac{2 \times \sum_{i=0}^{patchsize} p_i g_i}{\sum_{i=0}^{patchsize} p_i^2 + \sum_{i=0}^{patchsize} g_i^2} \quad (3)$$

$$Combo\ Loss = BCE_{Loss} + DiceLoss \quad (4)$$

where g = ground truth image, p = predicted building mask

4 Results and Discussion

Figure 6 shows the results for building extraction for select RGB images from each city of the IAIL dataset. The first column is the input to the model, the second column is the ground truth, the third column is the segmented building map as predicted by the model and the fourth column shows the evaluation of the prediction with True Positives (TP) in white, True Negatives (TN) in black, False Positives (FP) in red and False Negatives (FN) in yellow. These are original images of size 5000×5000 from the IAIL dataset. The predictions are obtained by clipping to chips of 224×224 , segmenting buildings and then again merging to the original size of 5000×5000 . In Fig. 6 we try to show all the different conditions for building extraction such as the surrounding land-cover classes, urban density, shadows etc. from each city. Figure 6a, c, f show successful building extraction in case of high urban density with closely spaced buildings, with rare instance segmentation challenges. Figure 6b shows effective building extraction even in shadowy regions. It can be noted that the shadows are not falsely classified as buildings, which has been a

very popular challenge in building extraction [12]. Figure 6a, b, f show successful building extraction in presence of spectrally similar features such as cemented roads and parking lots as well as spatially similar features such as roads, open grounds and vegetation patches having shape similar to buildings. The model is also able to segment buildings even when the dominant land cover in the image is not urban— Fig. 6d, e contain a large cover of vegetation, Fig. 6b, e contain a large area of water.

To quantify the prediction made by the model in terms of binary segmentation, the metrics of accuracy (4), precision (5), recall (6) and F1-score (7) were used. To further perform a feature-based evaluation, object-based metrics such as branching factor (8), miss factor (9), detection percentage (10) and IoU or quality percentage (11) (otherwise also popularly known as jaccard index) were used. Table 2 shows the metrics of the individual images in Fig. 6.

$$accuracy = \frac{tp + tn}{tp + tn + fp + fn} \quad (5)$$

$$precision = \frac{tp}{tp + fp} \quad (6)$$

$$recall = \frac{tp}{tp + fn} \quad (7)$$

$$f1 = 2 \times \frac{precision * recall}{precision + recall} \quad (8)$$

$$branchingFactor = \frac{fp}{tp} \quad (9)$$

$$missFactor = \frac{fn}{tp} \quad (10)$$

$$detectionPercentage = 100 \times \frac{tp}{tp + fn} \quad (11)$$

$$qualityPercentage/IoU = 100 \times \frac{tp}{tp + fn + fp} \quad (12)$$

where tp = True Positive, fp = False Positive, tn = True Negative and fn = False Negative.

Figure 7 shows the city-wise metrics of model validation. Tyrol West and Vienna from the IAIL dataset exhibit highly favourable conditions for building extraction. Extracting buildings from Chicago and Kitsap has been the most challenging. This is due to shadowy regions, typically the shadows being cast on other buildings. Though the proposed model successfully discriminates between shadowy regions and buildings and avoids shadows as false positives, it faces significant challenges

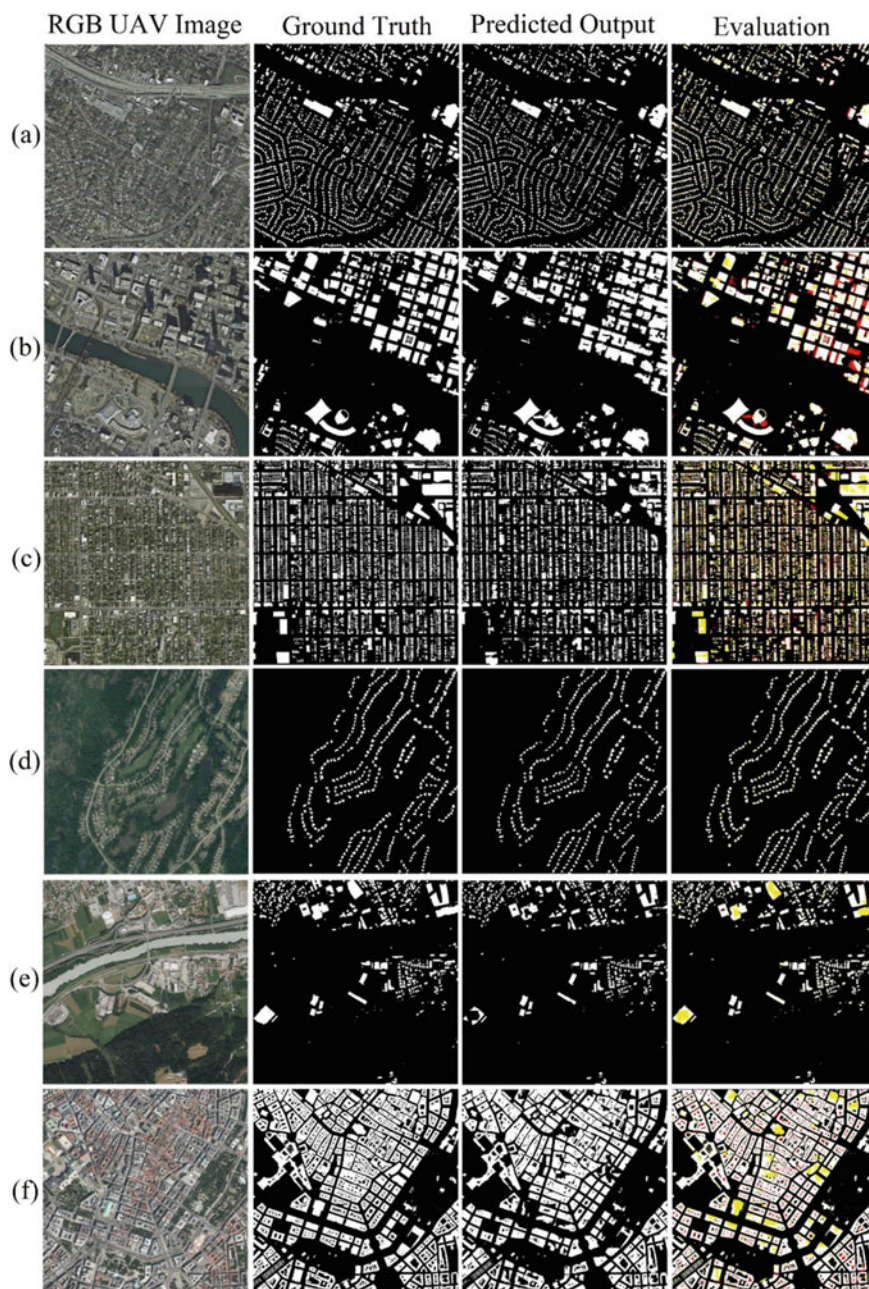


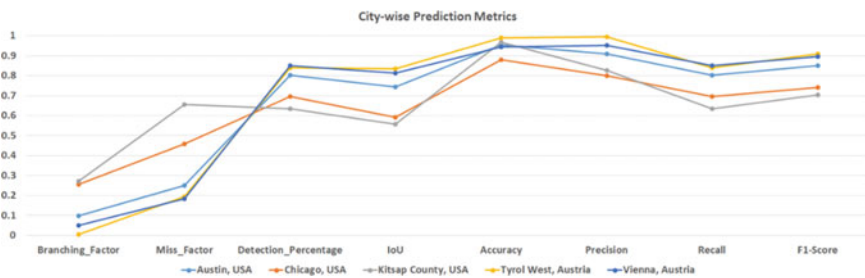
Fig. 6 Select instances of building extraction results from each city of the IAIL dataset. First column is RGB input to the model, the second column is model prediction for building segmentation, third column is ground truth and the fourth column is the evaluation image showing TP (white), TN (black), FP (red) and FN (yellow). **a, b** From Austin, USA, **c** from Chicago, USA, **d** from Kitsap County, USA, **e** from Tyrol West, Austria, **f** from Vienna Austria

Table 2 Metrics for individual images of Fig. 6

	Accuracy	Precision	Recall	f1-score	Branching factor	Miss factor	Detection percentage	IoU
Figure 6a	0.961	0.943	0.802	0.867	0.060	0.246	0.802	0.765
Figure 6b	0.942	0.850	0.764	0.859	0.177	0.152	0.868	0.752
Figure 6c	0.870	0.833	0.666	0.745	0.200	0.500	0.666	0.589
Figure 6d	0.991	0.997	0.851	0.920	0.001	0.176	0.851	0.845
Figure 6e	0.982	0.994	0.796	0.889	0.006	0.257	0.796	0.801
Figure 6f	0.927	0.938	0.893	0.915	0.006	0.120	0.893	0.843

in extracting the buildings which are under shadows. This drastically increases the rate of false negatives, as the model excludes the buildings under shadows as only shadowy regions (Fig. 8a, b). A potential reason for this could be loss of spectral variance as well as the spatial distinction of a building that is under shadow. Moreover, another isolated issue encountered in a Kitsap image is a patch of waterbody being falsely segmented as building, resulting into a high number of false positives (Fig. 8c). This could be due to multiple reasons such as spectral similarity of the waterbody area due to turbidity, or saturation of DN values in those areas due to direct glint on sensor. Such instances of shadowed buildings and typical water areas are prominent in the images from Chicago and Kitsap and hence the extraction results are lowest for these two cities from the IAIL dataset. Figure 8 shows select instances buildings under shadows which result in a high number of false negatives.

Despite these specific challenges and rare instance segmentation issues, the overall performance of the model when evaluated on the validation set of 4075 images is highly favourable. The high values of the evaluation metrics, especially IoU, also indicate that the proposed model can segment buildings well within the feature edges and there is no region loss except for when the building itself is under a shadow. When compared with other deep learning-based approaches, the proposed model increases the average IoU to 0.80 and average F1 score to 0.86. Table 3 shows the overall evaluation metrics of the model for the validation set as well as a comparison of those metrics with other studies on the same IAIL dataset.

**Fig. 7** City-wise prediction metrics from the IAIL dataset validation part

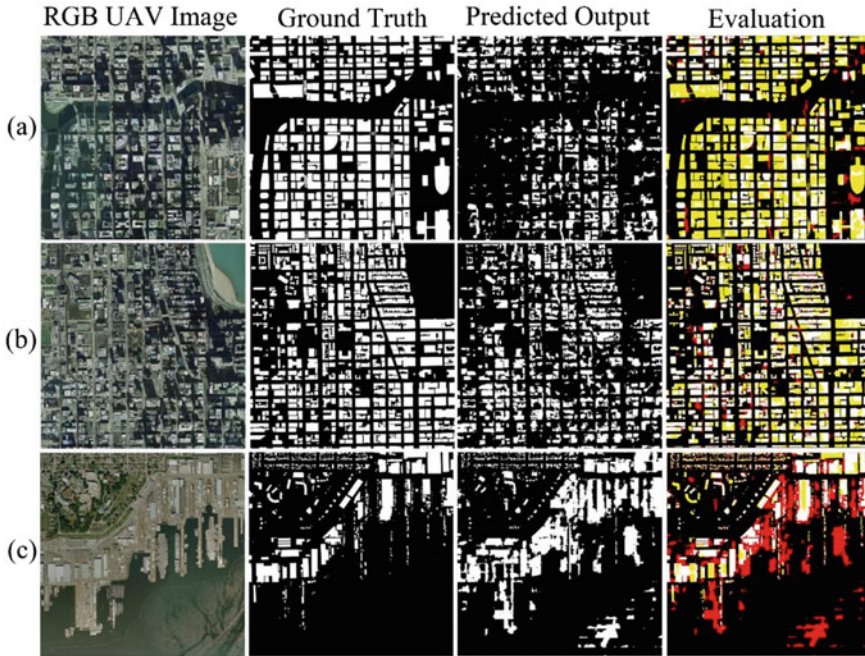


Fig. 8 Select instances where buildings are covered under shadows, leading to high false negative rate. First column is RGB input to the model, second column is model prediction for building segmentation, third column is ground truth and fourth column is evaluation image showing TP (white), TN (black), FP (red) and FN (yellow). **a, b** From Chicago, USA, **c** from Kitsap County

Table 3 Overall metrics of the proposed approach and their comparison with existing approaches

Method	Proposed Res-U-Net	Dilated spatial pyramid pooling [25]	GAN-SCA [27]	MSMT-Stage-1 [26]	AMLL [28]	Dilated CNN [29]
	0.965	0.894	0.966	0.961	0.959	0.928
	0.883	–	–	–	–	–
	0.861	–	–	–	–	–
	0.88	–	–	–	–	0.83
	0.193	–	–	–	–	–
	0.230	–	–	–	–	–
	93.42	–	–	–	–	–
	0.80	–	0.777	0.733	0.725	0.710

5 Conclusion

In this research work, building extraction from UAV imagery was explored using deep learning and transfer learning methodology. A Res-U-Net architecture consisting of U-Net blocks initialized with pre-trained ResNet34 weights and was used to learn building extraction from the IAIL dataset. The combination of ResNet and U-Net was used in an attempt to overcome the problems of blurred building boundaries and limited spectral resolution in building extraction. Moreover, a combined loss function that accounts both for the building region, as well as building boundaries, was used to train the proposed Res-U-Net. The model was trained and validated on 180 images from across five different cities of US and Austria. These images depicted high variance in terms of urban density and dominant land cover of the image. The proposed model was successfully able to segment buildings in all cases with rare instance segmentation issues. Model performance was measured using quantitative metrics of confusion matrix as well as object-based metrics such as branching factor, miss factor and IoU. When comparing these metrics with those of existing deep learning-based methods, highly favorable results were noted. Specific challenges such as extracting buildings lying under shadow and excluding turbid/active waterbody as a building were also identified and are open for research.

References

1. Momm H, Easso G (2011) Feature extraction from high-resolution remotely sensed imagery using evolutionary computation. *Evol Algorithms*. <https://doi.org/10.5772/15915>
2. Gomez-Chova L, Camps-Valls G, Munoz-Mari J, Calpe J (2008) Semi-supervised image classification with huberized Laplacian support vector machines. *IEEE Geosci Remote Sens Lett* 5(3):336–340. <https://doi.org/10.1109/ICET.2013.6743545>
3. Benediktsson JA, Pesaresi M, Arnason K (2003) Classification and feature extraction for remote sensing images from urban areas based on morphological transformations. *IEEE Trans Geosci Remote Sens* 41(9) PART I:1940–1949. <https://doi.org/10.1109/TGRS.2003.814625>
4. Sowmya A, Trinder J (2000) Modelling and representation issues in automated feature extraction from aerial and satellite images. *ISPRS J Photogramm Remote Sens* 55(1):34–47. [https://doi.org/10.1016/S0924-2716\(99\)00040-4](https://doi.org/10.1016/S0924-2716(99)00040-4)
5. Zou Q, Ni L, Zhang T, Wang Q (2015) Deep learning based feature selection for remote sensing scene classification. *IEEE Geosci Remote Sens Lett* 12(11):2321–2325. <https://doi.org/10.1109/LGRS.2015.2475299>
6. Huang Z, Cheng G, Wang H, Li H, Shi L, Pan C (2016) Building extraction from multisource remote sensing images via deep deconvolution neural networks. Huang Z, Cheng G, Wang H, Li H, Shi L, Pan C (2016) National laboratory of pattern recognition (NLPR) Institute of Au. In: 2016 IEEE International geoscience remote sensing symposium, pp 1835–1838
7. Karathanassi V, Iossifidis C, Rokos D (2000) A texture-based classification method for classifying built areas according to their density. *Int J Remote Sens* 21(9):1807–1823. <https://doi.org/10.1080/014311600209751>
8. Eskandarpour R, Khodaei A (2018) Leveraging accuracy-uncertainty tradeoff in SVM to achieve highly accurate outage predictions. *IEEE Trans Power Syst* 33(1):1139–1141. <https://doi.org/10.1109/TPWRS.2017.2759061>

9. Li W, He C, Fang J, Fu H (2018) Semantic segmentation based building extraction method using multisource GIS map datasets and satellite imagery. In: IEEE Computer society conference on computer vision and pattern recognition workshops, December 2018, vol 2018-June, pp 233–236. <https://doi.org/10.1109/CVPRW.2018.00043>
10. Cote M, Saeedi P (2013) Automatic rooftop extraction in nadir aerial imagery of suburban regions using corners and variational level set evolution. *IEEE Trans Geosci Remote Sens* 51(1):313–328. <https://doi.org/10.1109/TGRS.2012.2200689>
11. Huang X, Zhang L (2011) A multidirectional and multiscale morphological index for automatic building extraction from multispectral geospatial imagery. *Photogramm Eng Remote Sens* 77(7):721–732. <https://doi.org/10.14358/PERS.77.7.721>
12. Huang X, Zhang L (2012) Morphological building/shadow index for building extraction from high-resolution imagery over urban areas. *IEEE J Sel Top Appl Earth Obs Remote Sens* 5(1):161–172. <https://doi.org/10.1109/JSTARS.2011.2168195>
13. Zhu XX et al (2017) Deep learning in remote sensing: a review. <https://doi.org/10.1109/MGRS.2017.2762307>
14. Zhang L, Xia GS, Wu T, Lin L, Tai XC (2016) Deep learning for remote sensing image understanding. *J Sensors* 2016. <https://doi.org/10.1155/2016/7954154>
15. Erdem F, Avdan U (2020) Comparison of different U-net models for building extraction from high-resolution aerial imagery. *Int J Environ Geoinformatics* 7(3):221–227. <https://doi.org/10.30897/ijegeo.684951>
16. Chollet F (2018) Deep learning mit python und keras: das praxis-handbuch vom Entwickler der KerasBibliothek. MITP-Verlags GmbH & Co, KG
17. Li L, Liang J, Weng M, Zhu H (2018) A multiple-feature reuse network to extract buildings from remote sensing imagery. *Remote Sens* 10:1350, 10(9):1350. <https://doi.org/10.3390/RS10091350>
18. Simonyan K, Zisserman A (2015) Very deep convolutional networks for large-scale image recognition. <http://www.robots.ox.ac.uk/>. Accessed 11 Jan 2021
19. He K, Zhang X, Ren S, Sun J (2016) Deep residual learning for image recognition. In: Proceedings of the IEEE computer society conference on computer vision and pattern recognition, December 2016, vol 2016–December, pp 770–778. <https://doi.org/10.1109/CVPR.2016.90>
20. Chen LC, Zhu Y, Papandreou G, Schroff F, Adam H (2018) Encoder-decoder with Atrous separable convolution for semantic image segmentation. In: Lecture notes in computer science (including subseries Lecture Notes in Artificial Intelligence and Lecture Notes in Bioinformatics), February 2018, vol 11211 LNCS, pp 833–851. https://doi.org/10.1007/978-3-030-01234-2_49
21. Yang H, Wu P, Yao X, Wu Y, Wang B, Xu Y (2018) Building extraction in very high resolution imagery by dense-attention networks. *Remote Sens* 10(11):1768. <https://doi.org/10.3390/rs10111768>
22. Badrinarayanan V, Kendall A, Cipolla R (2017) SegNet: a deep convolutional encoder-decoder architecture for image segmentation. *IEEE Trans Pattern Anal Mach Intell* 39(12):2481–2495. <https://doi.org/10.1109/TPAMI.2016.2644615>
23. Ronneberger O, Fischer P, Brox T (2015) U-net: Convolutional networks for biomedical image segmentation. LNCS (Including Subseries Lect Notes Artif Intell Lect Notes Bioinformatics) 9351:234–241. https://doi.org/10.1007/978-3-319-24574-4_28
24. Abdollahi A, Pradhan B, Alamri AM (2020) An ensemble architecture of deep convolutional Segnet and Unet networks for building semantic segmentation from high-resolution aerial images. *Geocarto Int*. <https://doi.org/10.1080/10106049.2020.1856199>
25. Morocho-cayamcela ME (2020) Increasing the segmentation accuracy of aerial images with dilated spatial pyramid pooling. *ELCVIA Electron Lett Comput Vis Image Anal* 19(2):17–21
26. Marcu A, Costea D, Slusanschi E, Leordeanu M (2018) A multi-stage multi-task neural network for aerial scene interpretation and geolocalization
27. Pan X et al (2019) Building extraction from high-resolution aerial imagery using a generative adversarial network with spatial and channel attention mechanisms. *Remote Sens* 11(8):917. <https://doi.org/10.3390/rs11080917>

28. Huang B et al (2018) Large-scale semantic classification: outcome of the first year of inria aerial image labeling benchmark. In: International Geoscience Remote Sensing Symposium, vol 2018 July, pp 6947–6950. <https://doi.org/10.1109/IGARSS.2018.8518525>
29. Khoshboresh-Masouleh M, Alidoost F, Arefi H (2020) Multiscale building segmentation based on deep learning for remote sensing RGB images from different sensors. *J Appl Remote Sens* 14(03):1. <https://doi.org/10.1117/1.jrs.14.034503>
30. Maggiori E, Tarabalka Y, Charpiat G, Alliez P (2017) High-resolution aerial image labeling with convolutional neural networks. *IEEE Trans Geosci Remote Sens* 55(12):7092–7103. <https://doi.org/10.1109/TGRS.2017.2740362>
31. Iglovikov V, Shvets A (2021) TeraNet: U-Net with VGG11 encoder pre-trained on imagenet for image segmentation. <http://arxiv.org/abs/1801.05746>. Accessed 01 Mar 2021
32. Lamba H (2019) Understanding semantic segmentation with UNET. *Towards Data Science*. <https://towardsdatascience.com/understanding-semantic-segmentation-with-unet-6be4f42d4b47>. Accessed 21 Jan 2021
33. Zhang Z, Sabuncu MR (2018) Generalized cross entropy loss for training deep neural networks with noisy labels
34. Sudre CH, Li W, Vercauteren T, Ourselin S, Cardoso MJ (2017) Generalised dice overlap as a deep learning loss function for highly unbalanced segmentations. *Lect Notes Comput Sci (Including Subser Lect Notes Artif Intell Lect Notes Bioinformatics)*, vol 10553 LNCS, pp 240–248. https://doi.org/10.1007/978-3-319-67558-9_28

Design and Development of Human Temperature Measuring System Using Drone Based Multispectral and Thermal Images



S. Meivel , S. Maheswari , and D. Faridha Banu 

Abstract People's failure to maintain a social distance is causing the COVID19 virus to spread. We have used the drone thermal images for a maximum of 10 km of coverage to detect temperature and reduce virus spread areas. The part of the work is based on utilizing disinfectant spraying drones, disinfectant testing with the guidance of doctors, setting the path planning of drones for surveying the temperature of people, and monitoring the infected place using GPS. When the thermal camera of the drone detects the temperature values using remote sensing images, the drone covers crowded places like hospitals, cinemas, and temples using remote sensing images. One drone model is designed to provide present results using thermal images. The Proposed drone can cover an affected area of up to 16,000 square meters per hour for capturing remote sensing images. It predicts affected areas using faster CNN algorithms with 2100 thermal images. Thermal mapping is used to monitor the social distance between people, alert people that a virus is spreading, and reduce the risk factor of people's movement. In this paper, remote sensing images are analysed and detect higher temperature areas using thermal mapping (Messina and Modica in Remote Sensing 12:1491, 2020).

Keywords Thermal image · IoT drone · Remote sensing · Bio-mass prediction theorems · Pix4D mapper

S. Meivel (✉)

Department of Electronics and Communication Engineering, M. Kumarasamy College of Engineering, Thalavapalayam, Karur 639113, Tamil Nadu, India
e-mail: meivels.ece@mkce.ac.in

S. Maheswari

Department of Electrical and Electronics Engineering, Kongu Engineering College, Thoppupalayam, Perundurai 638060, Tamilnadu, India

D. F. Banu

Department of Electronics and Communication Engineering, Sri Eshwar College of Engineering, Coimbatore 641202, Tamilnadu, India

1 Introduction

Remote sensing analysis is described when using drones to target at 6 km/h to spray only affected areas to avoid wastage of sanitizing liquid. Under the Essential Commodities Act, alcohols utilized in assembling hand sanitizers have been topped under the Essential Commodities Act during the coronavirus episode [6]. Direct costs, production, sale, circulation, transport, development, stockpiling, and data of alcohol used in the manufacture of hand sanitizers, which are used as a preventive measure to avoid disease caused by COVID-19. Fabricate liquor-based hand sanitizer splashes with ethyl alcohol as a primary substance on a mass scale in a similar plant, which may make this liquor-based sanitizer exceptionally easy and make it accessible on the market soonest. Sprayer module The sprayer is used to saturate the Sanitizer Sprayer in the tallest building nearest the tank. The Sanitizer Sprayer controller is separate from the actuator. The RF receiver and transmitter are important for the spray system. The tank is used for storing sanitize materials for the spray system. The tank has a storage level of 2,000 gm. It sprays the full level of the Sanitizers Sprayer of the system. The nozzle is also important for the sprayer module. The nozzle is controlled by the transmitter and receiver of the tank and sprayer of the module. Drone navigation depends on IoT board GPS and satellite GPS. A thermal camera's remote sensing image focused on the Drone navigation system when the gyroscope is running to measure gear angles, air stress, magnet direction, S-N-E-W, and acceleration of BLDC motors [1] using canopy. At the ground station, the drone flight defined the flight path, height, trigger, and velocity force. Automated flight paths can be set for detection of the image using thermal sensors, and the flight plan can be changed using Drone IoT programs [16].

1.1 Environmental Impacts

Use the remote sensing of spraying drones using GIS software and the Biomass Prediction Algorithm Sprayer Module (Aluminum Type). The IoT board and Python programme were found to help the module implementations [22]. Gray scale and RGB scale photographs were created from images captured by an IR camera using the S360 module. Rovio performs in the inter-navigation system when using drone image estimation. Multistage image pre-processing is tracked when performing filters [8]. The Extended Kalman filter is used to estimate the image data from readings of the ROVIO+Drone+odometer. DJI cameras interfaced ROS to the drone's autopilot. The PID controller controls the nonlinear version of predictive data, odometer data, and commands to the drone's autopilot.

1.2 Impacts of Drone Spraying

The security system of the Agricultural department uses a particular drone for spraying infected areas in a city or village. The drone image is used in the Covid19 thermal value and surrounding virus flow. Individual drones capture thermal video at 20000 m²/h. An army drone can spray and surround villages and cities to hit the virus. When the drone automated, it already stored all the sprayed data and mapping to avoid repeat spraying. Now In coastal areas, the drone captures videos and sprays to infect particular places, but it is a limited spray. Sprayed footage can be captured by drone cameras within 3–100 m. The mapping survey found the killing virus spreading due to a reduction in the death rate. The UAV system proved to use a faster method for delivering spray content when critical situations [21]. Tamil Nadu agriculture and security Drones have proven to release infected areas like roofs, trees, gardens, restaurants, skyscrapers, and crowded areas. Drones are covered, and the thermal camera—OpenCV library files provide 90% accuracy of infected results [25]. It also prevents people via the alert system or signals through the IoT board from speaking.

2 Literature Survey

- A large amount of sanitizer is carried by heavy drones for high-speed spray. The USA was affected by the COVID19 virus in 2020. The country handles heavy drones with a big container up to 30 kg or 40 kg in volume to spray. The country will follow in 24 h to control the virus's spreading area through a heavy drone vehicle, as planned. Therefore, in such cases, detect the virus where it is spreading high and where it is spreading low while implementing a drone IoT system. They invest in simple and smart data delivery, publishing it to people or publishing it to the US government. Public awareness of drone technology is low because of its inflexible and limited capability. The US government spends dollars and employed non-profit social workers to simplify all tasks. They implemented Disinfection of villages and cities while reducing the COVID19 virus. Therefore, they mostly used crop-spraying drones to disinfect streets in the cities and villages. The DJI drones covered 20000sq.m/hour to complete the spraying in affected areas only. However, they were left unaffected in each place. The other countries did not use a particular drone to spray the sanitizer content. They use all types of drones, like those that are used as crop-spraying drones, police drones, and consumer drones, because the drones are fitted with tanks to disinfect villages and cities. Villagers and city people are interested in spraying sanitizer content through drones to disinfect streets in the city or village when they save neighbors from COVID 19.
- In India, police security officers and healthcare departments are finding results for the most affected areas [17]. They reported on every day using drones with IR or thermal cameras. A high-powered spraying system is used for spreading

seeds. The drone and UV robots focus on and secure COVID19 patients when programmed and planned. This drone and robots kill or remove viruses using a thermal camera. UV drones have been implemented in the healthcare industry to detect COVID19 people and disinfect villages and cities [16]. In EOD, the WHO recommends monitoring social distance coverage and coughing area detection in order to disinfect villages and cities and dispose of medical tissues in a secure location after use [5]. Optimization and simplification of disinfecting villages and cities will be applied to drones in the future, like mask detection and thermal detection. [7] Covid19 detects people, detects humidity, and cough areas detection through heavy drones. Army and Navy people trained as pilots, licensed people to disinfect villages and cities. UV robots are too much more expensive than heavy drones, and they are used in low traffic usage. Power consumption is reduced in drones due to battery cover and low usage. The drone covered infection places only and sprayed infection places only. But, robots use high power to spray and it takes a long time to complete. Spraying drones are more flexible and stable to complete the schedule speed process. All types of drone converted to the Covid19 Drone from other applications. They followed the disinfected village and city, optimized these programs, sped up operations, instructed damaged parts, maintained surveillance, and detected Covid19 people [14].

3 Research Analysis of Drone Spraying

The normal body temperature is 33–37 °C. The Drone NIR Camera scanned >37 °C using a thermal camera. When detecting body temperature from virus places, the IoT section commands the drone to spray sanitizer. We have calculated real-time temperature data using GIS software. GIS Software is managed by an administrator or an IoT controller for the automation of Drone Spray. No, you need to spray all places where there is a chemical reaction due to the chemical reaction or firing of the Sanitizer. Timing and power management of sanitizer sprinklers in the virus-infected area when the temperature is >37 °C or >99 °F, the IoT controller, or Admin, give the command to the drone sprayer up to cover 5 km/h. The sanitizing sprayer's weight and battery weight should be less to carry a payload for timing and power management of the sprayer. Chemical sanitizer is better than organic sanitizer when you need quick results in an emergency case. Organic sanitizer is better than chemical sanitizer when it comes to reducing viruses, but the slow result is still worth it. Automated spraying may reduce the virus infection in affected areas. Organic sanitizers do not affect human skin [11]. Maybe suggest organic sanitizer spraying. Drone sanitizer spraying covered 10 m/min in normal mode. This speed depends on the spraying speed of the pump motor.

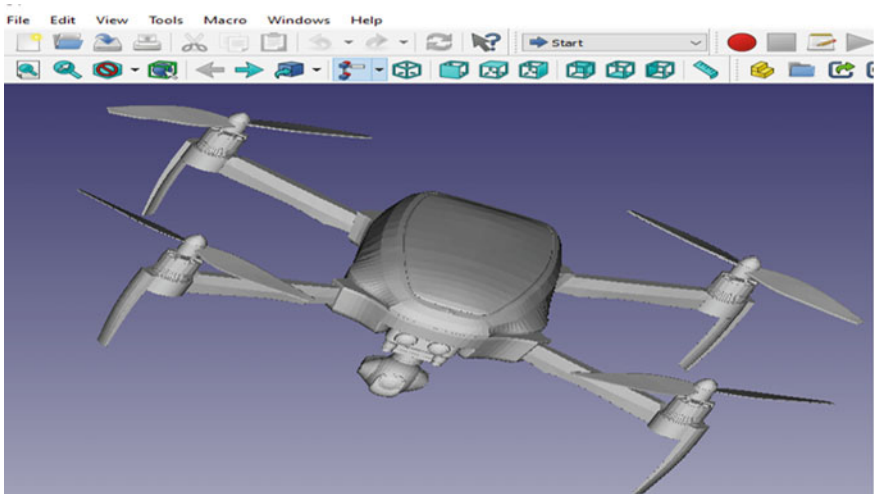


Fig. 1 Isometric 3D view

4 Design of a Drone with Forward Looking InfraRed (FLIR) Camera

The innovative Drone was created using 3D software such as Solid-Works and then printed for use. The drone product includes frames, four BLDC motors, IoT controller, GPS receiver, an Inbuilt Arduino Pilot Board, and FLIR camera. This paper describes FLIR camera image processing for the detection of thermal value. The Faster CNN algorithm solves the detection problems of people's activation with temperature using FLIR real-time images. Figure 1 depicts an isometric 3D view, Fig. 2 depicts the drone's right side 3D view, and Fig. 3 depicts the drone's rear side 3D view. The FLIR camera supports the biomass induction algorithm and IoT sensor driver functions for the detection of temperature values. Figure 4 shows the top side view of the drone design. The entire mechanism is very lightweight, and the camera view is controlled by wifi. This paper mainly describes image processing for detecting the temperature range of objects and tracking the objects. A sanitizer spraying mechanism can be attached to the bottom of this drone setup.

5 Methodology

The methodology is based on remote sensing of spraying drones using drone mapping [24]. It includes three steps. These are processed 1, process 2 and human temperature detection. In process 1, we identified sensing temperature data from remote sensing images. Controlled drone path line for detecting human activities and face detection

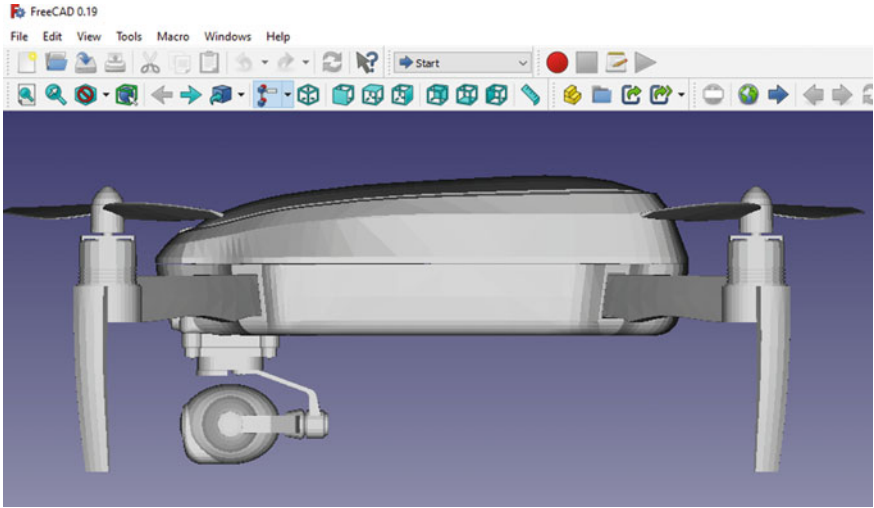


Fig. 2 Right side 3D view

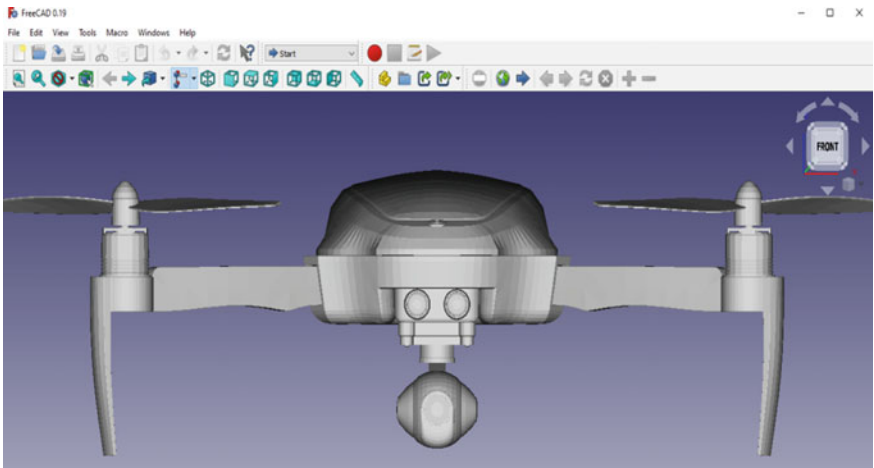


Fig. 3 Rear side 3D view

in process 2. In the human temperature detection stage, collected temperature data can be stored in a database. Figure 5 depicts the processes of temperature detection stages and explains all of the stage's steps.

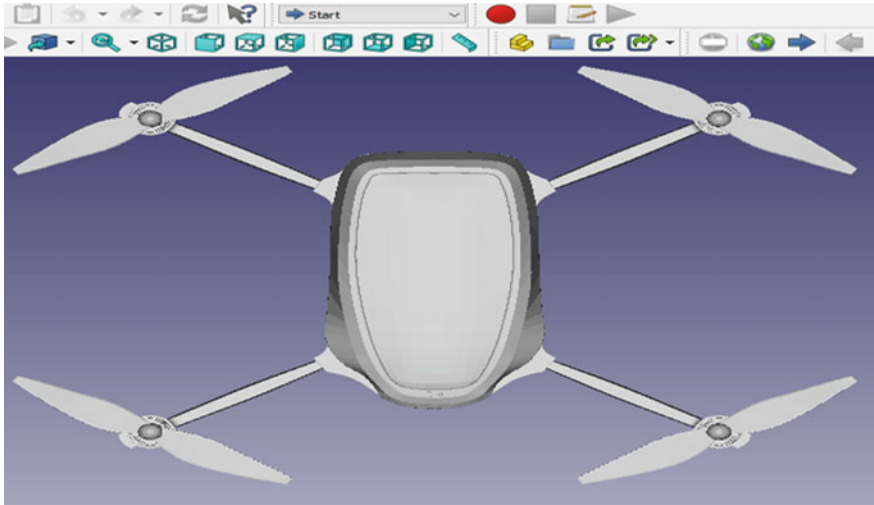


Fig. 4 Top side 3D view

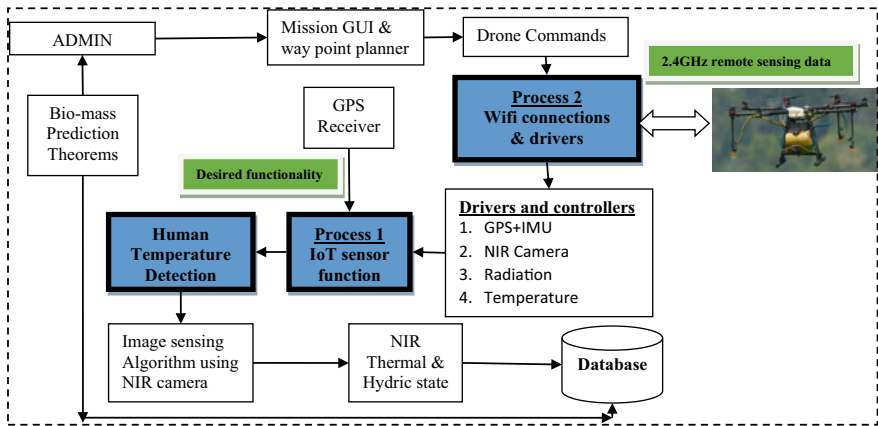


Fig. 5 Remote sensing of spraying drone using GIS software

5.1 Biomass Prediction Algorithm

The biomass prediction algorithm is mentioned in Fig. 6. It detected camera movement and temperature range between objects.

This programme follows the steps in Fig. 6.

- Step 1 Connect the SSH port.
- Step 2 Execute the Remote Trigger Algorithm for Detecting Viruses.

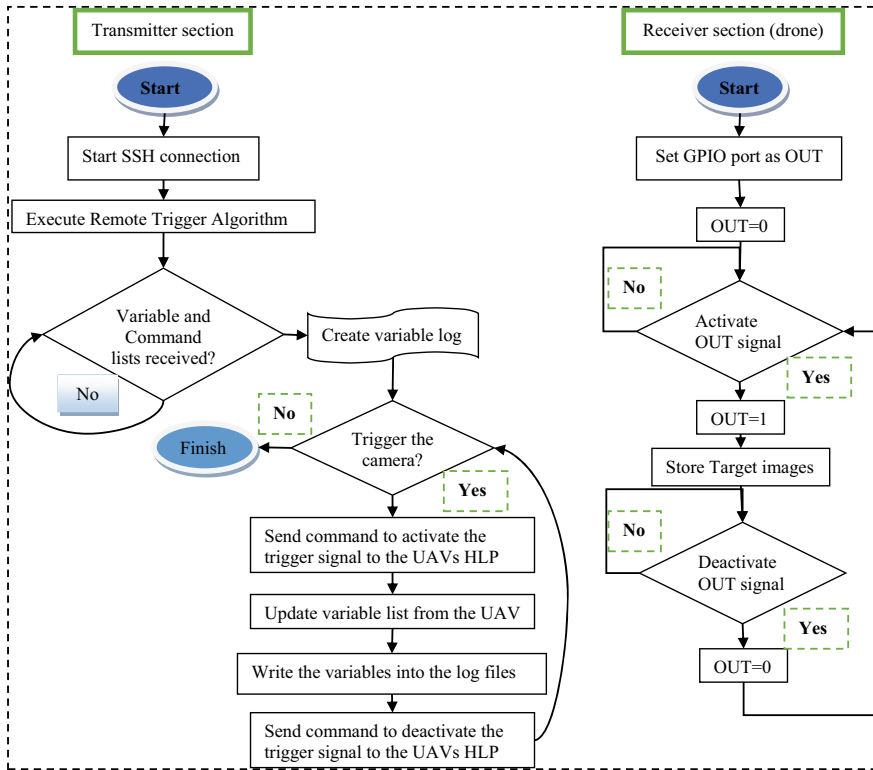


Fig. 6 Algorithm of biomass prediction algorithm

- Step 3 If a command is received from the IoT controller, create variable logs. If a command is received from the IoT controller, rotate step 3.
- Step 4 If you trigger the NIR camera, activate the UAV to find the location. If you did not trigger the NIR camera, repeat step 4. Updated variable list from the UAV.
- Step 5 Spray the Sanitizer content onto the affected places using the Admin command.
- Step 6 After spraying, send commands to deactivate the trigger signal.

5.2 Admin

The biomass prediction algorithm was reprogrammed and uploaded to this IoT controller. The Admin server secures and connects the GPS planning.

5.3 Mission GUI and Waypoint Planner

The planning mission was executed and mapped using Pix4D mapper software. The Mission GUI drivers give commands when they reach targets.

5.4 Drone Commands

During an emergency lockdown period for the detection of human body temperature, the Drone commands are received. The commands controlled drone activities for automated spraying.

5.5 Process 2

Wi-Fi Connection Used in the RF Transmitter: The wireless protocol IEEE 802.11 g is used for real-time data transmission [20]. When detecting the Coronavirus using GIS analysis, the admin gives the command to spray the Sanitizer content. All real-time data is stored in a database using NIR analysis.

5.6 Drivers and Controllers

GPS+IMU drivers are used for GPS mappings. NIR Camera drivers control the camera rotation and zooming. Radiation drivers helped to find the location of target places. Temperature sensor drivers are used for temperature detection in a crowd or a person.

5.7 GPS Receiver

The GPS receiver provided tracking of the target's GPS location. It also displays the latitude and longitude of target places to spray sanitizer.

5.8 Process 1

All sensors are connected in Process1 for sensing of images and the number of camera sensors connected using GIS to survey the Coronavirus. Drone commands

are accepted by the IoT sensor controller. The drone's NIR camera sends GPS value, NIR image, radiation value, and thermal value of location. It is easily connected to all device drivers using a wireless interface.

5.9 Human Temperature Detection

The Region of Interest (RoI) finds the face edge and detects facial detection. When the radiometric mode is activated, 14-bit values of images are scanned and the temperature range is calculated. The output signal of the scene temperature is measured. Here, R is the camera's responsivity. Tk is absolute temperature in units of Kelvin, and F is the number of frames per bit. Scene Temperature $S = \frac{R}{\{e^{\frac{R}{T_k}} - F\}}$ and Absolute Temperature $T_k = \frac{B}{\ln(\frac{R}{S-O} + F)}$

5.10 Image Sensing Algorithm Using NIR Camera

The Image sensing algorithm using NIR images is used for temperature measurement and object tracking in Fig. 7. Infrared images are captured by the FLIR sensors [25]. These NIR images are given image modification (Threshold values). Using higher pixels, it is possible to detect the selection of the objects and their matching with the template in Fig. 8. The temperature of the objects and their detection are measured after they have matched with the template. We can track the objects using the template in GPS coordination of the targeted place.

The faster CNN programme detects face mask detection, temperature measurement, and social distance measurement when using real-time images taken in affected areas. This temperature measurement is based on the following steps. Threshold value detection, filling the holes, selection of the objects, and template tracking.

5.10.1 NIR Thermal and Hydric State

The NIR thermal and Hydric State detected and displayed the results. It stores all the results in a database. We can compare the present data with previous data to research the temperature results and variation results in different ranges.

5.10.2 Database

The database data is displayed on common official websites for the updating of people's temperature. All results are stored in the same location of DRAM memory on the server side.

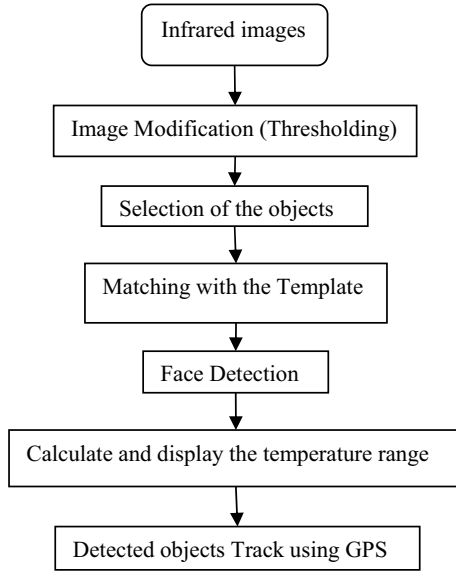


Fig. 7 Flow chart of the temperature detection algorithm

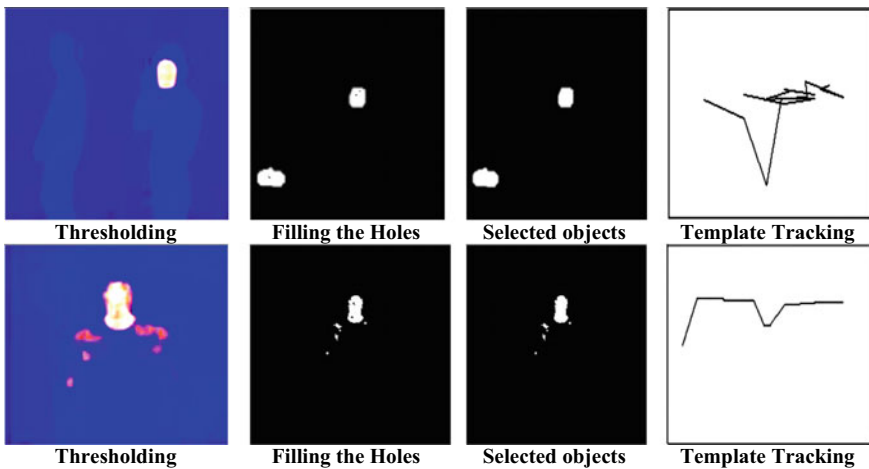


Fig. 8 Image sensing algorithm using NIR images for objects 1 and 2

6 Temperature Scanning Using Thermal Images

The machine vision and image analysis methods compared with effective results in finding the COVID19 virus. Some technologies diagnosed sick people and checked them on manually. It reduced the COVID19 via airborne. Machine vision focused

Inspection, Identification, and Gauges instrumentation [3]. However, these instrumentations are the same as ventilators, respirators, and gears. This Instrumentation helped to COVID19 patients and protecting the doctors when they serviced the patient. In Fig. 6, a Thermal camera Installed and scanned in all airports to the detecting of all Thermal views [26]. It showed elevated body temperature. It detected the Temperature range of each people. When the COVID19 virus affected the immune system, internal body temperature increased. This temperature range is similar to face Temperature. A thermal camera detected only the thermal view of people and did not detect any virus. The thermal image has shown a high-resolution image and temperature range of the body or face [7].

The 3D camera was fixed and deployed in the drone or any of the 360° rotational parts like the servomotor on the wall. A drone camera setup is utilized for sanitizer spraying and food delivery using drone image vision [4]. It is detected by positive and negative COVID19 patients in Fig. 9. The thermal image of the drone was updated at the spraying location to reduce the COVID19 virus. The chest radiography images help in the detection of COVID19 virus cases.

They predicted three Categories

- (a) normal cases,
- (b) virus-infected cases,
- (c) COVID19 virus cases and Non-COVID19 virus cases.

In Fig. 10, temperature scanning was accurate and stable when set to high resolution. In less than 2 m, this scan measured body temperature ranging from 37.0 °C to 40.0 °C. The DJI drone measured the temperature of objects and the temperature of a group or separate. It also measured heart rate, respiratory rates, blood pressure and skin tone [2]. Color changes or movements of the skin, nose, and eyes have been used to calculate heart rate. It observed the coughing and sneezing of people. Long distance monitoring and detection, illumination variations, and multi camera

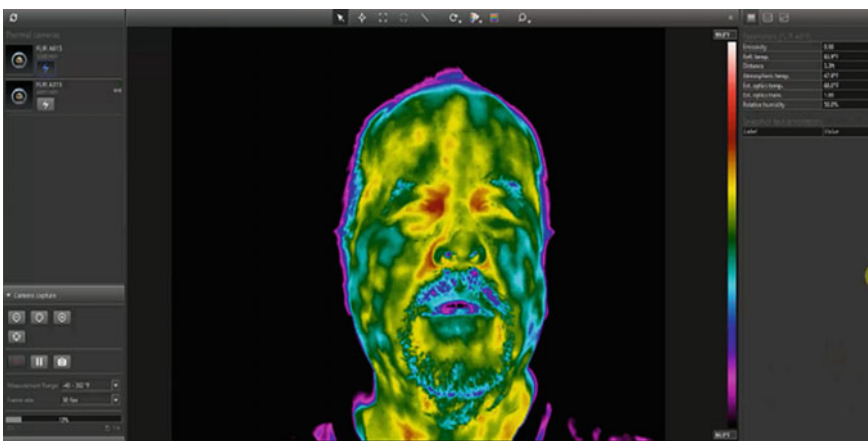


Fig. 9 Machine vision and image analysis

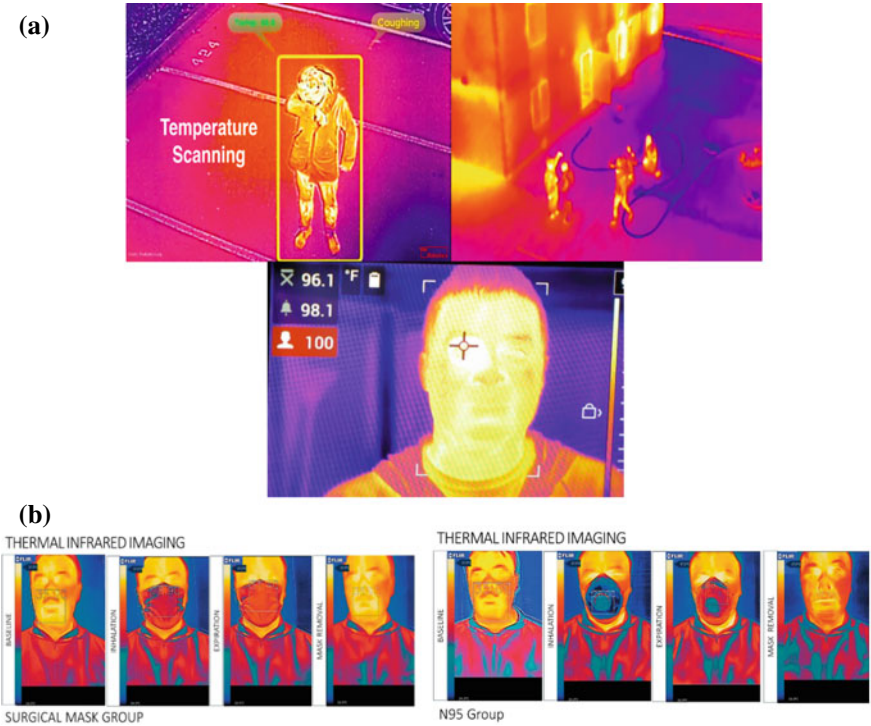


Fig. 10 a Temperature scanning per person. b Temperature Scanning of person's activity

fusion were possible to determine. The temperature was reduced by 37° when using different directions and different speeds of driving the drone.

Now Covid19 infections are spreading and people are losing their sense of taste. Using the IoT-Raspberry pi3 development board, drone multispectral cameras and thermal cameras detect temperature, temperature image, and mask detection. It aids in the detection of taste loss by detecting image changes. The Drone is capable of recording at 100db (or) 1 m distance for recording and delivering an unmatched level of versatility for detecting infections and viruses. DJI drones carried 10 L of disinfectants, covering an area of 25 km per day. It helps to clear the crowd and control it. The crowd was using thermal cameras. Calibration and testing of the thermal camera and drone are required to find an accurate temperature value [12, 13]. Autonomous drones are used for the detection of viruses and to avoid human beings, increasing the monitoring of temperature measurements [19].

7 Mask Detection and Thermal Detection Using Thermal Mapping

The high-resolution camera detects body temperatures with an accuracy of one degree or Fahrenheit. When your body temperature rises above normal, look for signs of COVID-19 infection. The thermal image identified those who have a high body temperature and are positive for Covid19 infection. The thermal camera is used by energy companies to connect pipelines using low-cost drones with a 30 g payload [9]. This camera detected body temperature elevation [10]. It can detect the body temperature of 20 people in a second. Medical equipment detects viruses slowly because it takes a long time and provides only 65% accuracy.

This camera detects the route of a virus spreading area. For example, when some people carry a virus to all places, this camera detects the virus spreading throughout the whole conference hall. When wearing glasses, this NoIR or FLIR camera detects accurate reading and shows a clear view of a subject's eyes. This camera screening showed coughing, difficulty breathing, and CO₂ percentage value. QGIS and ArcGIS-pro software can be used to analyse thermal images of the coughing area and predict virus lines. This prediction showed a 90% accurate result and prioritized it. PCR testing was used to find COVID19 virus confirmation cases. The treatment strategy is based on the different cases of infection and plans for remedies. The Classification Algorithm was performed and showed accurate results. CNN based classification performs feature extraction and combines different results with architectures. Drone technology provides engineering, servicing, integration, and distribution for the fastest deployment. This technology can easily detect virus infections and coughing areas, body temperature, respiratory rate, pulse rate, and blood pressure. The drone technology is mainly used for quick results and providing 100 tests/hour in different places.

7.1 Thermal Mapping Using Pix4D Mapper

In Figs. 11 and 12, Pix4D Mapping is one technique for detecting physical distance and finding population density. This is a COVID19 spreading feature. It needs high resolution mapping with a population density image. It displays people's social distancing, rod view, social boundaries, management of society's gates, delivery vehicles, and security work.

The mapping was created to show where virus spread is high and where virus spread is low. Patients [18], cluster analysis of the spread, location tracking records, and prediction analysis for various parameters.

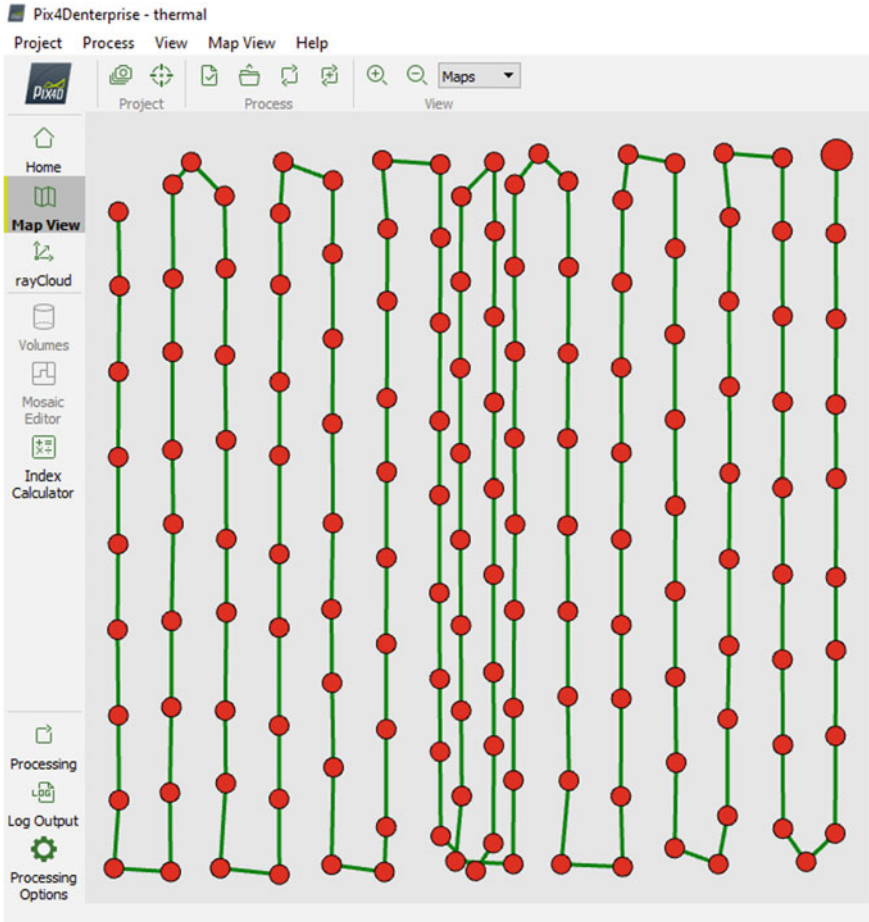


Fig. 11 Map view of drone mission path planning

8 Classification

The thermal images are detected in a minimum of 2000 remote sensing images with texture information files [23]. In Table 1, it is classified as Hypothermia-x, Normal-x, Temperature-x, and Hyperpyrexia-x. Hypothermia-x mentioned Ice Fever and the potential for normal conditions. Normal x readings are mentioned as normal conditions of the people or individual people. Temperatur—x stage is above normal and is stated as >380 °C for higher fevers. These readings may be taken at the initial stage of virus spreading. Hyperpyrexia –x mentioned >42 °C for virus severe fever confirmation. These readings may be taken at higher stages of virus spread.

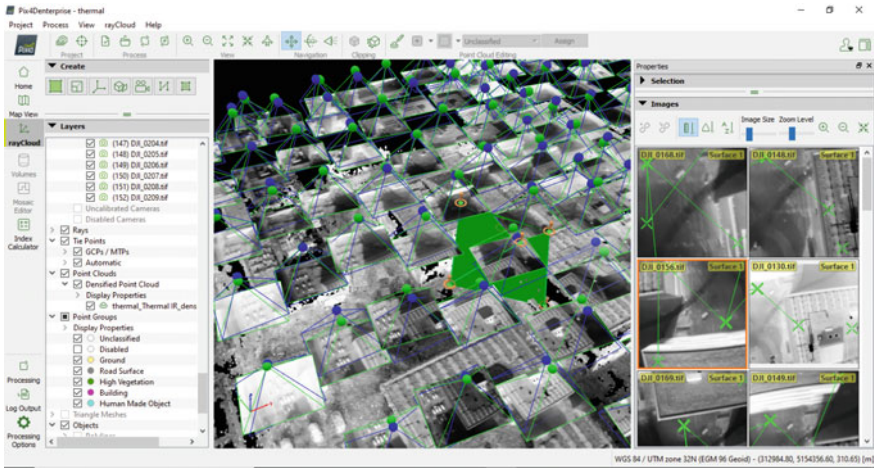


Fig. 12 Ray cloud—selected surface to finding temperature of a street area

Table 1 Classifications of thermal images

Classed as	Temperature (°C)	Temperature (°F)
Hypothermia-x	<35.0	95.0
Normal-x	36–38	98–100°F
Temperature-x	>38 or 38	100 or 101
Hyperpyrexia-x	>40 or 42	104 or 107

9 Outcome Results of Thermal Mapping

The drone mapping results are plotted as temperature versus reflectance. These readings are taken from the dataset on the websites of Kaggle and FLIR. In Figs. 13 and 14, the dataset of FLIR images are extracted using the Biomass Prediction Algorithm and image sensing algorithms. These extracted results provide temperature readings and reflectance readings of the people in a targeted place. This chapter, Chaps. 7–9 explained these particular steps. Temperature readings are gradually decreasing from 40.75 °C to 30.1 °C in this graph. It mentioned the temperature of the body in different places. All the readings are plotted in Fig. 15.

10 Conclusion

The designed drone can cover 16,000 m² in 1 h for the detection of infected and disinfected areas. This process helps and secures COVID 19 and other people. When using a biomass prediction algorithm, thermal scanning processes have detected

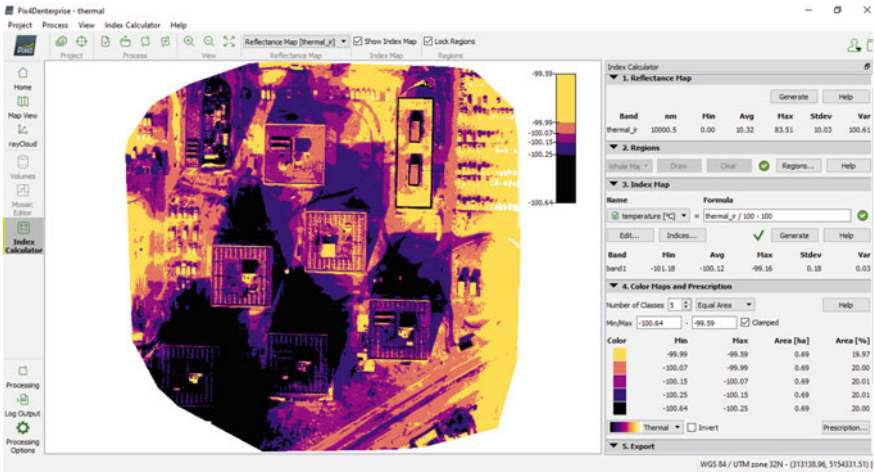


Fig. 13 Feature extraction of thermal mapping images

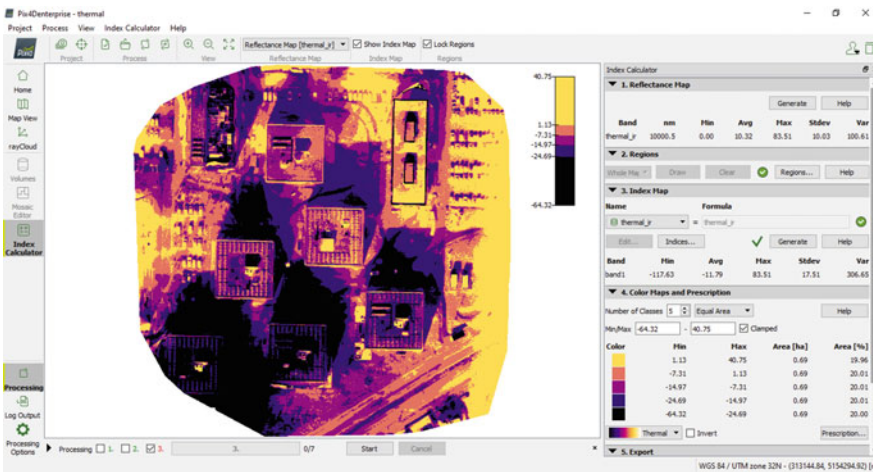


Fig. 14 Feature extraction using one street area

affected areas in streets or cities. In this paper, remote image sensing values are analyzed and detected in infection areas. The detected thermal image shows the virus-affected area, the virus-spreading places, body thermal values, humidity values, social distance in meters, and the nearest COVID19 people using Tensor Flow and OpenCV dataset packages on Raspberrypi3 IoT devices. This concept represents a method that can automatically detect human faces with high temperatures among other objects. Compared to methods that are used now, this method is faster and more accurate and doesn't require human labor. Methods, which are currently used for

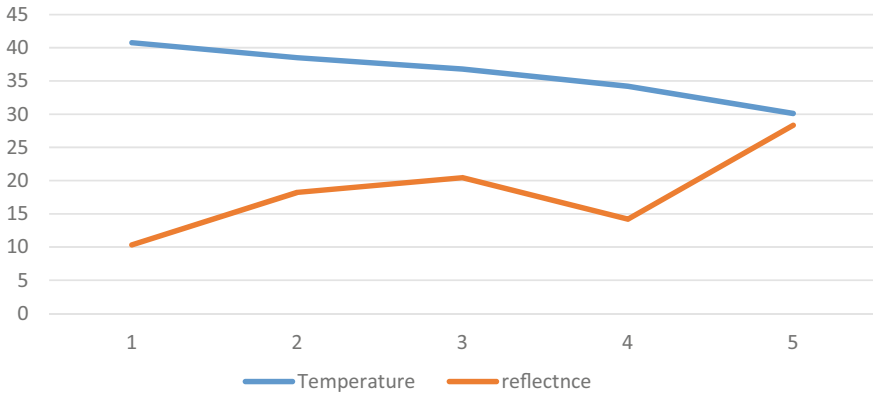


Fig. 15 Temperature versus reflectance

temperature detection, need a lot of time. The method presented in the concept is able to do automatic temperature detection in a very short time. In addition, the presented algorithm is able to track objects of interest (human faces with temperature) and draw their movement paths. The proposed methods are tested on the 2100 temperature images and display the temperature of a street person when applying the Faster CNN algorithm and Thermal Mapping.

References

1. Chang A, Jung J, Maeda MM, Landivar JA, Carvalho HDR, Yoem J (2020) Measurement of cotton canopy temperature using radiometric thermal sensor mounted on the unmanned aerial vehicle (UAV). *J Sens* 2020:1–7. <https://doi.org/10.1155/2020/8899325>
2. Heikkinen T, Marttila J, Salmi AA, Ruuskanen O (2002) Nasal swab versus nasopharyngeal aspirate for isolation of respiratory viruses. *J Clin Microbiol* 40(11):4337–4339
3. Ekins S, Freundlich JS, Clark AM, Anantpadma M, Davey RA, Madrid P (2015) Machine learning models identify molecules active against the Ebola virus in vitro. *F1000Research* 4
4. Zhang L, Ai H-X, Li S-M, Qi M-Y, Zhao J, Zhao Q, Liu H-S (2017) Virtual screening approach to identifying influenza virus neuraminidase inhibitors using molecular docking combined with machine-learning based scoring function. *Oncotarget* 8(47):83142
5. Eng CL, Tong JC, Tan TW (2014) Predicting host tropism of influenza a virus proteins using random forest. *BMC Med Genomics* 7(S3):S1
6. Babayan SA, Orton RJ, Streicker DG (2018) Predicting reservoir hosts and arthropod vectors from evolutionary signatures in RNA virus genomes. *Science* 362(6414):577–580. <https://doi.org/10.1126/science.aap9072>
7. Harvey MC, Rowland JV, Luketina KM (2016) Drone with thermal infrared camera provides high resolution geo referenced imagery of the Waikite geothermal area, New Zealand. *J Volcanol Geoth Res* 325:61–69. <https://doi.org/10.1016/j.jvolgeores.2016.06>
8. Maes W, Huete A, Steppe K (2017) Optimizing the processing of UAV-based thermal imagery. *Remote Sens* 9(5):476. <https://doi.org/10.3390/rs9050476>
9. Valente J, Roldán J, Garzón M, Barrientos A (2019) Towards airborne thermography via low-cost thermopile infrared sensors. *Drones* 3(1):30. <https://doi.org/10.3390/drones3010030>

10. Marques G, Pitarma R (2019) Non-contact infrared temperature acquisition system based on internet of things for laboratory activities monitoring. *Proc Comput Sci* 155:487–494. <https://doi.org/10.1016/j.procs.2019.08.068>
11. Jain VM, Karibasappa GN, Dodamani AS, Prashanth VK, Vasant G (2016) Comparative assessment of antimicrobial efficacy of different hand sanitizers: an in vitro. *Mali Dental Res J* 13(5):424–431
12. Virtue J, Turner D, Williams G, Zeliadt S, McCabe M, Lucieer A (2021) Thermal sensor calibration for unmanned aerial systems using an external heated shutter. *Drones* 5(119). <https://doi.org/10.3390/drones5040119>
13. Aragon B, Johansen K, Parkes S, Malbeteau Y, Al-Mashharawi S, Al-Amoudi T, McCabe MF (2020) A calibration procedure for field and UAV-based uncooled thermal infrared instruments. *Sensors* 20(11):3316. <https://doi.org/10.3390/s20113316>
14. Kayan H, Eslampanah R, Yeganli F, Askar M (2018) Heat leakage detection and surveillance using aerial thermography drone. In: 2018 26th signal processing and communications applications conference (SIU). <https://doi.org/10.1109/siu.2018.8404366>
15. Messina G, Modica G (2020) Applications of UAV thermal imagery in precision agriculture: state of the art and future research outlook. *Remote Sens* 12(9):1491. <https://doi.org/10.3390/rs12091491>
16. Islam A, Young SS (2020) A block chain based secure healthcare scheme with the assistance of unmanned aerial vehicle in Internet of Things. *Comput Electr Eng* 84:106627
17. Sethuraman SC, Vijayakumar V, Walczak S (2020) Cyber attacks on healthcare devices using unmanned aerial vehicles. *J Med Syst* 44(1)
18. Tuli S, Tuli S, Tuli R, Gill SS (2020) Predicting the growth and trend of COVID-19 pandemic using machine learning and cloud computing internet of things, vol 11
19. Palossi D, Loquercio A, Conti F, Flamand E, Scaramuzza D, Benini L (2019) A 64-mW DNN-based visual navigation engine for autonomous nano-drones. *IEEE Internet Things J* 6(5):8357–8371
20. Whaiduzzaman M, Hossain M, Shovon AR, Roy S, Laszka A, Buyya R, Barros A (2020) A privacy-preserving mobile and fog computing framework to trace and prevent COVID-19 community transmission
21. Wickramasinghe NFT, Bodendorf R (2020) Delivering superior health and wellness management with IoT and analytics. Springer
22. Islam A, Young SS (2020) A blockchain-based secure healthcare scheme with the assistance of unmanned aerial vehicle in Internet of Things. *Comput Electr Eng* 84:10662
23. Li L, Zhang Q, Wang X, Zhang J, Wang T, Gao TL, Duan W, Fai Tsoi KK, Wang FY (2020) Characterizing the propagation of situational information in social media during COVID-19 epidemic: a case study on Weibo. *IEEE Trans Comput Soc Syst* 7(2):556–562
24. Mastrodimos N, Lentzou D, Templalexis C, Tsitsigiannis DI, Xanthopoulos G (2019) Development of thermography methodology for early diagnosis of fungal infection in table grapes: the case of *Aspergillus carbonarius*. *Comput Electron Agric* 165:104972
25. Belfiore N, Vinti R, Lovat L, Chitarra W, Tomasi D, De Bei R, Meggio F, Gaiotti F (2019) Infrared thermography to estimate vine water status: optimizing canopy measurements and thermal indices for the varieties merlot and moscato in northern Italy. *Agronomy* 9:821
26. Crusiol LGT, Nanni MR, Furlanetto RH, Sibaldelli RNR, Cezar E, Mertz-Henning LM, Nepomuceno AL, Neumaier N, Farias JRB (2020) UAV-based thermal imaging in the assessment of water status of soybean plants. *Int J Remote Sens* 41:3243–3265

Feature Extraction in Urban Areas Using UAV Data



Surendra Kumar Sharma, Minakshi Kumar, Sandeep Maithani,
and Pramod Kumar

Abstract As the rapid development is being focused in the urban area, there is a need for the utilisation of a system for updating this profile immediately. The usage of Uncrewed Aerial Vehicle (UAV) for mapping purposes is one of the current technologies being used in recent years. UAVs are widely used in a variety of domains due to their low price, ability to deliver very high resolution data, and ability to fly at low altitudes without being constrained by overcast weather. Typically, data extraction methods for UAVs are still quite limited, and traditional approaches are still used. For mapping applications, orthoimage features are often manually recognised and digitised using visual interpretation skills. Unfortunately, these approaches are time-consuming, costly, and repetitive. Pixel-based classification approach is frequently utilised to help extract low-level features, in which the image is categorised only based on spectral characteristics. The drawback of this approach is that the pixels in the overlapping region are misclassified as a result of class confusion. Moreover, pixel based classification performs very poorly in high resolution images. The Object-Based Image Analysis (OBIA) classification technique has large potential for automatic data extraction from Very High Resolution (VHR) images. OBIA techniques start with segmentation of image followed by classification and feature extraction using contextual information and rule base. In this study, an attempt is made to assess the capability of OBIA for detailed classification of highly dense urban areas mapped by UAV with a VHR imagery of the order better than 5 cm. The image is segmented using multiresolution image segmentation with a suitable scale, compactness and smoothness to form homogeneous image objects. Various parameters (spectral, texture, context and elevation) are computed for the VHR UAV Images. Rules are formulated to extract and categorise urban features specifically for roads and buildings. The segmented roads are classified into categories based on width and connectivity. Buildings extracted are categorised based on their elevation and

S. K. Sharma (✉) · S. Maithani · P. Kumar
Urban and Regional Studies Department, Indian Institute of Remote Sensing, Dehradun, India
e-mail: ssharma3@ce.iitr.ac.in

M. Kumar
Photogrammetry and Remote Sensing Department, Indian Institute of Remote Sensing, Dehradun, India

size. The study efficiently demonstrates the potential of VHR orthoimage and Digital Surface Model (DSM) for urban classification using the OBIA techniques. The finest of details captured by UAV can be effectively classified using the segmentation and classification approach.

Keywords Unmanned aerial vehicle · Feature extraction · Object-based image analysis · Multiresolution segmentation

1 Introduction

Imaging systems based on UAVs have been proven to be beneficial in a variety of remote sensing applications, including environmental, urban/land use, image classification [1], and agricultural studies [2, 3]. UAVs provide a number of benefits over traditional remote sensing platforms, including greater flexibility and reduced costs in data collection, as well as increased speed and safety. More importantly, UAVs may fly quite near to the target, resulting in images with extremely high resolution (cm to dm pixel size). The high-resolution images provide enough detail for object identification and parameter extraction.

UAVs can also provide real-time photography of regions that are challenging to reach by conventional processes. The UAV data is used to create a high-resolution Digital Terrain Model (DTM), DSM, and orthomosaic, which can be utilised further for different applications [3, 4]. UAV-based remote sensing data offers a lot of potential for building classification and extraction because it may unveil the smallest features in urban areas [5, 6]. It makes it easier to distinguish between imperious surfaces such as buildings, roads, parking lots, and urban land. It can also estimate acquisition points and maybe do direct georeferencing [7]. The classification using pixel-based techniques is relatively restricted since it has significant issues coping with the rich information content of high-resolution data such as high-resolution satellite data and UAV images [8]. It yields inconsistent results and misses expectations in extracting the objects of interest.

Currently, the OBIA approach is particularly relevant in the context of image classifications for high spatial resolution and UAV images. OBIA techniques start with the segmentation of images followed by classification and feature extraction using contextual information and rule base comprising of spectral, textural, neighbourhood, and object-specific shape parameters [9]. Segmentation is described as the division of a complete image into a number of segments or sets of pixels with the purpose of transforming the image's current pixels into more meaningful objects [10]. The resolution and scale of the intended objects should be used to determine segmentation and topology creation. For high and extremely high resolutions, the OBIA approach outperforms the pixel-based technique [8, 11–13].

In this work, an attempt is made to evaluate the capabilities of OBIA for detailed classification of very dense urban areas captured by UAV with VHR data of the order of 5 cm. The main objective of the current study is to establish a methodology for

extracting detailed land use with the sub-objectives of finding suitable segmentation algorithms for such VHR imagery. Various parameters (spectral, texture, context and elevation) were evaluated, and rules were formulated to extract and categorise urban features specifically for roads and buildings. The study aims to demonstrate the extraction of the finest of details captured by UAV can be effectively classified using the segmentation and classification approach.

2 Test Area and Dataset

This study uses highly dense urban area situated in the nearby Roorkee city of Uttarakhand, India. The geographical extent of the study area spans from $77^{\circ} 54' 19.49''$ E longitude to $77^{\circ} 54' 21.34''$ E longitude and from $29^{\circ} 52' 0.273''$ N latitude to $29^{\circ} 51' 56.86''$ N latitude. It comprises of densely packed buildings of varying heights and aerial coverage (Fig. 1). The study area consists of both manmade features (buildings, roads, pavements and parking lots etc.) and natural features (bare soil, grasslands, shrubs and trees).

The imagery was obtained using the UAV DJI Phantom-4 pro (Fig. 2), which includes a non-metric camera with visible colour bands (red, green, and blue) having 12 megapixel resolution.

For the current study, a set of 102 images recorded with a ground sampling distance of 1.79 cm from a height of 150 m.

3 Methodology

The methodology adopted composes of four components. (i) Photogrammetric Processing of UAV images. (ii) Segmentation of Orthoimage. (iii) Rules formation for detailed classification and feature extraction (iv) Accuracy evaluation. The complete methodology flow is illustrated in Fig. 3.

3.1 Photogrammetric Processing

Collected UAV images were processed in Pix4Dmapper Pro and the orthomosaic image with the DSM and DTM were generated. The orthomosaic image had a very high spatial resolution of 20 cm, and DSM and DTM were obtained at a resolution of 20 cm and 90 cm, respectively. Figures 4 and 5 shows orthomosaic and DSM of the study area.

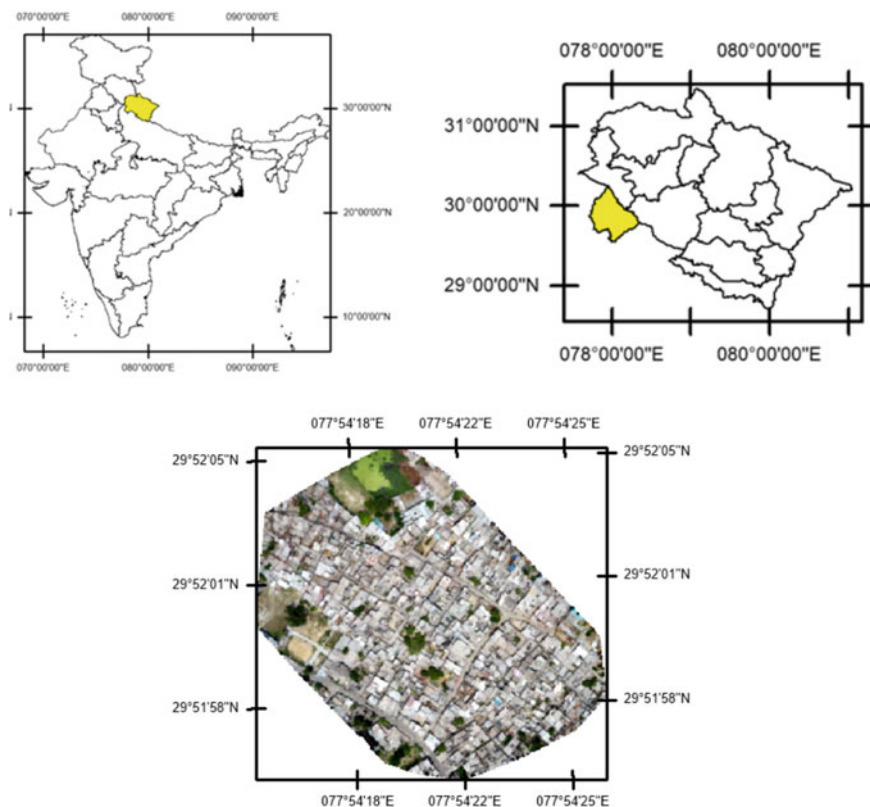


Fig. 1 Location map and study area

Fig. 2 DJI phantom 4 pro UAV used in the current study



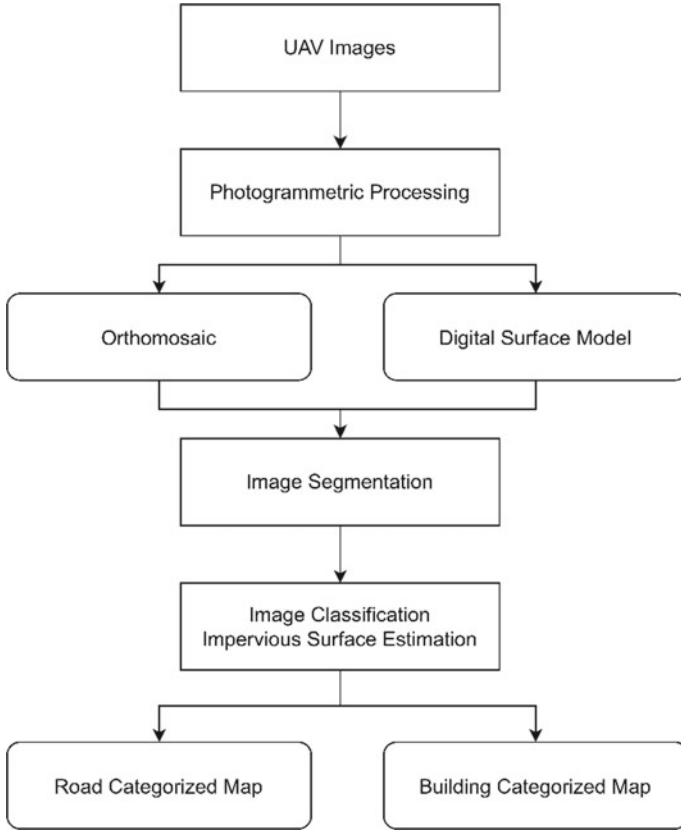


Fig. 3 Workflow adopted for urban feature extraction

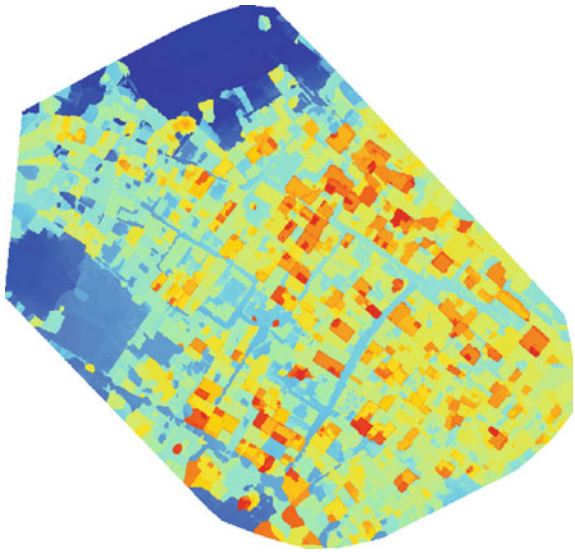
3.2 Image Segmentation

An integrated dataset comprising of orthomosaic image are then segmented using a multiresolution segmentation technique. Multi resolution Segmentation (MRS) is a well-known technique to segment image objects into homogeneous patterns. Object dimension such as size, shape and texture etc. can be measured. These simple image objects provide image data and act as building blocks and information carriers for further classification. Beyond merely spectral information, image objects include plenty of other characteristics that may be utilised for classification, including shape, texture, and relational/contextual data. Multiresolution segmentation distinguishes contiguous areas in an image if they are highly contrasted, even if the areas themselves include a texture or noise. It's a bottom-up region merging approach that starts with a single pixel object and works its way up to multiple objects and pixels. A clustering strategy is used to combine small image objects into larger ones. The weighted



Fig. 4 Generated orthomosaic of the study area

Fig. 5 Generated DSM of the study area



heterogeneity of the generated image objects is minimised by the underlying optimisation technique. Each phase merges a pair of nearby image objects, resulting in the minimal increase in the defined heterogeneity. If the smallest increase crosses the scale parameter's threshold, the procedure is terminated. The object primitives such as scale parameter, shape, DSM were used for segmentation. These parameters should be tuned such that the procedure yields homogenous areas with clearly defined boundaries for the object of interest. Multi-resolution segmentation was performed at various scales. The size of the objects created during segmentation is determined by the scale parameters. The entire image is segmented during image segmentation, and image objects are created based on numerous customisable shape heterogeneity criteria. Change the size of the resultant image objects by using the scale parameter. A large scale parameter produces large objects, and vice versa.

3.3 Image Classification and Impervious Surface Estimation

Following the segmentation of the image with MRS, OBIA is used to classify the generated image objects. OBIA contains two phases. The image segmentation makes for the first phase, and the second is the image object classification. Object metrics were utilised to create rulesets prior to the classification of image objects. To quantify the parameters for object identification, object metrics are estimated. Hence after being segmented, area, length, breadth, compactness, density, asymmetry, roundness, elliptic fit, rectangular fit, main direction, border index, and shape index were determined from the segmented objects. The spectral features included the mean of each layer, index features included the blue by green layer index and n-DSM was used for classification and estimation of impervious surface.

3.4 Quantitative Assessment

The accuracy of classification and feature extraction was evaluated using features extracted by manual digitisation. True Positive (TP), True Negative (TN), False Positive (FP), and False Negative (FN) were derived by comparing extracted and reference features. TP refers to features that are classified in the same category in both the reference and extracted data. The term TN denotes the features that are not classified as the same feature in the reference. FP represents features extracted in the classified results but not existing in the reference image, whereas FN specifies features not classified but available in the reference image. The accuracy of the retrieved objects is assessed using these metrics. The correctness, completeness and quality was evaluated for accuracy assessment.

4 Results and Discussions

Figures 4 and 5 show the obtained Orthomosaic and DSM, respectively, using the photogrammetric processing of UAV images.

The test area (Fig. 6a) was extracted from the orthomosaic. The MRS image segmentation technique is used to perform object-based image analysis on the test region. The orthomosaic picture's red, green, and blue layers, together with DSM derivatives, were utilised as input for image segmentation. Numerous iterations of MRS were executed with different object primitives of scale parameter, shape factor and compactness are adjusted through the trial and error method and the suitable scale, shape, and compactness parameters were set as 150, 0.6 and 0.5 for Level 2 and 200, 0.6 and 0.5 for Level 1 Classification. The results of MRS are presented in Fig. 6b-d.



Fig. 6 MRS segmentation using different object primitives and resulting image objects

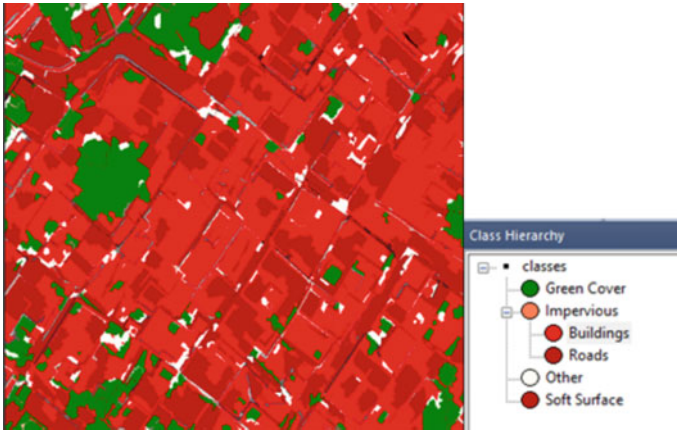


Fig. 7 Classified image

After segmentation, the resulting image objects were queried for different object primitives. Geometrical shape features and spectral features are obtained from the segmented objects. Border Index, compactness, area, length, width, roundness, shape index, main direction and mean brightness were useful in the classification and estimation of the impervious surfaces using the standard nearest neighbour approach. Results of classification are presented in Fig. 7. Rules were formulated for detailed categorisation and extraction of targeted objects using object parametric rectangular fit, radius of smallest enclosing ellipse, elliptic fit, asymmetry, blue by green spectral indices and nDSM. Figure 8 illustrates the level II classification for the buildings in the test area. Figure 9 presents the extracted green cover and roads, and Fig. 10 depicts different objects extracted from the image. The accuracy of the extracted objects was assessed on the completeness, correctness, and quality for different objects. High completeness and correctness values are observed for buildings, green cover and soft surface as compared to roads. This could be attributed to the fact that owing to the extremely high spatial resolution of UAV there was a difference in the manual estimation and actual extraction of road boundaries. The object-based accuracy measure acquires a high overall accuracy along with 94.14% of completeness, 89.61% of correctness and 82.07% of overall quality.

5 Conclusions

Urban planners require quick access to building data, which may be gathered through remote sensing techniques. Due to the spectral complexity of the environment, automatic building extraction utilising remotely sensed data has several limitations, particularly in urban regions. The goal of the research was to create an efficient method for extracting urban areas from UAV images with very high spatial resolution.

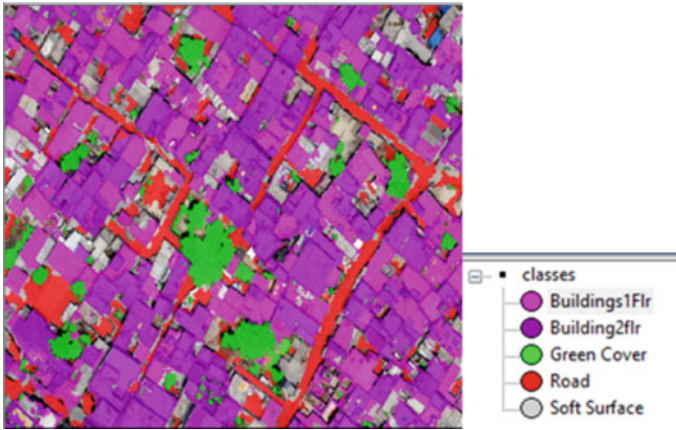


Fig. 8 Level-2 classified image

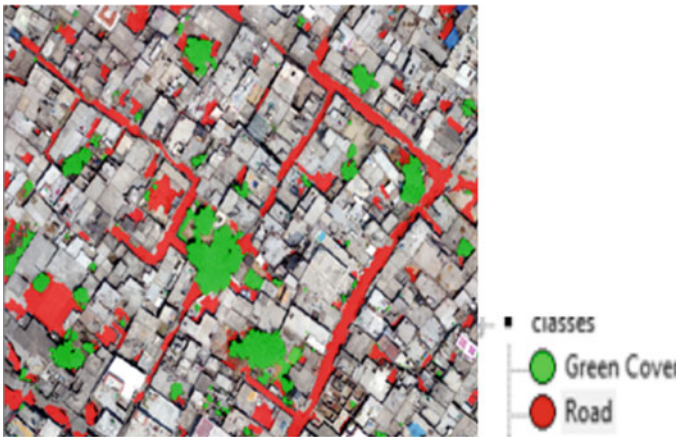


Fig. 9 Extracted green cover and roads

OBIA analysis allows for the detection and extraction of numerous urban objects such as buildings, roads, and trees. The segmented roads are classified into categories based on width and connectivity. Buildings extracted are categorised based on their elevation and size. The study efficiently demonstrates the potential of VHR orthoimage and DSM for urban classification using the OBIA techniques. The presented approach extracts features with great accuracy while requiring less human interaction. The improved segmentation parameters, such as scale, shape, and size, are discovered to be best for extracting urban regions.

The combination of UAV with OBIA can provide a quick and effective method of updating maps, particularly in frequently changing urban areas. As a result, the

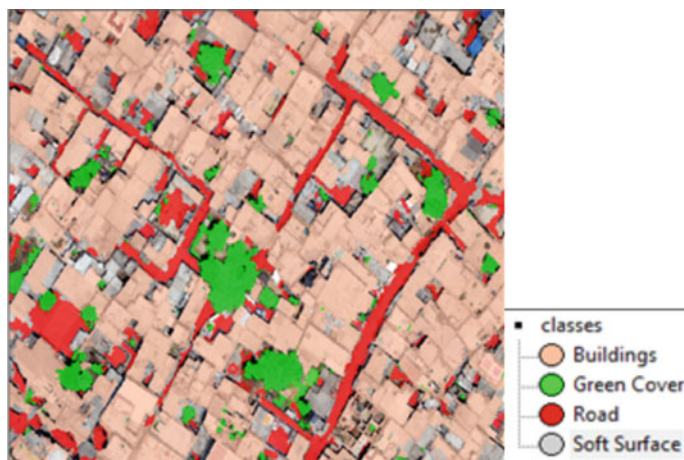


Fig. 10 Extracted objects

study's findings provide new insight into the use of OBIA in information extraction from UAV data.

References

1. Merugu S, Tiwari A, Sharma SK (2021) Spatial-spectral image classification with edge preserving method. *J Indian Soc Remote Sens* 49(3):703–711. <https://doi.org/10.1007/s12524-020-01265-7>
2. Lahoti S, Lahoti A, Saito O (2020) Application of unmanned aerial vehicle (UAV) for urban green space mapping in urbanizing indian cities. *Unmanned Aerial Veh Appl Agricult Environ* 177–188. https://doi.org/10.1007/978-3-030-27157-2_13
3. Shakhathreh H, Sawalmeh AH, Al-Fuqaha A, Dou Z, Almaita E, Khalil I, Othman NS, Khreishah A, Guizani M (2019) Unmanned aerial vehicles (UAVs): a survey on civil applications and key research challenges. *IEEE Access* 7:48572–48634. <https://doi.org/10.1109/ACCESS.2019.2909530>
4. Karantzas K, Koutsourakis P, Kalisperakis I, Grammatikopoulos L (2015) Model-based building detection from low-cost optical sensors onboard unmanned aerial vehicles. *Int Arch Photogram Remote Sens Spat Inf Sci ISPRS Arch* 40(1W4):293–297. <https://doi.org/10.5194/ISPRSARCHIVES-XL-1-W4-293-2015>
5. He H, Zhou J, Chen M, Chen T, Li D, Cheng P (2019) Building extraction from UAV images jointly using 6D-SLIC and multiscale siamese convolutional networks. *Remote Sens* 11(9):1040. <https://doi.org/10.3390/RS11091040>
6. Wu H, Nie G, Fan X (2020) Classification of building structure types using UAV optical images. *Int Geosci Remote Sens Symp (IGARSS)* 1193–1196. <https://doi.org/10.1109/IGARSS39084.2020.9323613>
7. Nex F, Remondino F (2014) UAV for 3D mapping applications: a review. *Appl Geomatics* 6(1):1–15. <https://doi.org/10.1007/S12518-013-0120-X/FIGURES/11>
8. Marangoz AM, Oruç M, Karakis S, Sahin H (2004) Comparison of pixel-based and object-oriented classification using Ikonos imagery for automatic building extraction-Safranbolu Testfield. In: *Proceedings of the XXth ISPRS Congress*

9. Tiwari A, Sharma SK, Dixit A, Mishra V (2021) UAV remote sensing for campus monitoring: a comparative evaluation of nearest neighbor and rule-based classification. *J Indian Soc Remote Sens* 49(3):527–539. <https://doi.org/10.1007/s12524-020-01268-4>
10. Khatriker S, Kumar M (2018) Building footprint extraction from high resolution satellite imagery using segmentation. *Int Arch Photogram Remote Sens Spat Inf Sci ISPRS Arch* 42(5):123–128. <https://doi.org/10.5194/ISPRS-ARCHIVES-XLII-5-123-2018>
11. Kumar M, Bhardwaj A (2020) Building Extraction from Very High Resolution Stereo Satellite Images Using OBIA and Topographic Information. *Environ Sci Proc* 5(1):1. <https://doi.org/10.3390/IECG2020-08908>
12. Laliberte AS, Rango A, Havstad KM, Paris JF, Beck RF, McNeely R, Gonzalez AL (2004) Object-oriented image analysis for mapping shrub encroachment from 1937 to 2003 in southern New Mexico. *Remote Sens Environ* 93(1–2):198–210. <https://doi.org/10.1016/J.RSE.2004.07.011>
13. Yu Q, Gong P, Clinton N, Biging G, Kelly M, Schirokauer D (2006). Object-based detailed vegetation classification with airborne high spatial resolution remote sensing imagery. *Photogram Eng Remote Sens* 72(7):799–811. <https://doi.org/10.14358/PERS.72.7.799>

The Role of ‘Unmanned Aerial Vehicles’ in Smart City Planning and Management



Rewati Raman and Ushnata Datta

Abstract A massive wave of urbanisation has grasped both developed and developing nations in the last decade. Various studies showcase the rising trend of rapid urbanisation growth due to demographic shifts, catalysed by numerous global and local parameters. India is professed to house 50 percent of its population in urban areas by 2030. The urban citizen’s rising expectations regarding infrastructure, amenities and safety will dovetail with this phenomenon. To cater to the demands of increased urbanisation, the concept of Smart cities is being advocated as an apt solution. Even so, there is widespread ambiguity about the challenges associated with adopting smart solutions into the existing urban social form. Though there have been many tentative explanations regarding the basic framework of a smart city, there are no known validated definitions. The main notable feature is the use of information and communication technologies (ICTs) within the cyclic dynamics of a city to facilitate the smooth and cost-effective working of urban areas. This ICT infrastructure enables real-time data collection, analysis, response, and storage. This has been deemed beneficial due to the increase in efficiency of operation and management services involved with the day-to-day functioning of any urban area. Smart cities advocate using information and communication technologies (ICTs) within the dynamics of a city to enable the real-time collection, analysis, and storage of big data. This is beneficial due to the increased efficiency of operation and management services involved with an urban area’s daily functioning. One such technological intervention is the ‘drone’ or the ‘unmanned aerial vehicles (UAVs)’. UAVs have a wide variety of uses in a smart urban fabric, from geospatial integration to traffic management, surveillance, disaster response, etc. In the current nascent stage of research and development of UAVs as one of the innovative solutions for smart cities in India, questions arise regarding privacy, cost of production, technical knowledge,

R. Raman (✉)

Department of Architecture, Planning and Design, Indian Institute of Technology (BHU)
Varanasi, Varanasi, India
e-mail: rraman.apd@iitbhu.ac.in; rraman@ar.iitr.ac.in

U. Datta

Department of Architecture and Planning, Indian Institute of Technology Roorkee, Roorkee, India
e-mail: udatta@ar.iitr.ac.in

safety and security with their large-scale use. This paper aims to assess the applicability of UAVs in overall smart city planning and management. The feasibility analysis method is adopted to analyse the felicitousness of UAVs in a smart city's planning and design phases. The results of the study undertaken in this paper highlight the challenges and opportunities in the planning and management of smart cities by integrating UAVs. The paper enumerates the relevance and appropriate benefits of using UAVs to plan, design, and perpetuate Indian smart cities.

Keywords Information and communication technologies · Smart city management · Smart city planning · Unmanned aerial vehicles

1 Introduction

Drones or Unmanned Aerial Vehicles (UAVs) are autonomous and aerodynamic devices that carry a certain payload and vary in size, design, and function over a wide plethora of utilisation. The UAVs can be distantly piloted manually by humans or independently by preinstalled computer programming [1]. Initially developed for defence activities, they have now been marketed for diverse civil solicitations (See Fig. 1) [2]. Extensive research has been undertaken to enumerate and expand UAV applicability's possible amalgamation in the urban planning paradigm, among other injunctions. UAVs are now being developed to facilitate the marriage between physical infrastructure and the internet of things (IOTs) through 'cloud robotics' [3].

In this context, using UAVs as an integral part of the information and communication technology (ICT) layer of an urban area undergoing the smart city planning process can be hypothesised as beneficial. It will primarily be useful in managing and monitoring a smart city. Other applications of UAVs include real-time collection, processing, and storage of big data, visual monitoring, vehicle detection [4], traffic management, surveillance, disaster response, environmental management, security,



Fig. 1 An unmanned aerial vehicle

etc., through various layers of the smart city [5]. Subsequently, questions also arise regarding the methods of integration, policy regulation and privacy preservation in the wake of pervasive UAV usage [6].

Therefore, this paper aims to present a coherent account of the aspects of the smart city and its planning process in the wake of the 'Smart City Mission 2015' launched in India in 100 chosen cities. A discussion is then supervised regarding a smart city's information and communication technologies (ICTs) layer, followed by deliberation on UAVs and the Internet of Things (IoTs). In the next section of the paper, UAVs' feasible application in the smart city planning process and its consequent monitoring and maintenance are reflected upon and analysed to identify the best practices, opportunities, and challenges. In the end, a final dialogue is provided to enumerate the future research and application pathways for the germaneness of UAVs in the smart city planning process.

2 Literature Review

UAV research concerning the urban planning paradigm has yielded many positive directions within the last two decades. The couched versatility of UAVs in informing the majority of the facets of planning, operation and maintenance of a city makes it an invaluable technological asset for smart city planners [5]. The essentiality of UAVs in smart city planning and management has been highlighted in many research works in the last 20 years. The research has primarily focused on individual components, technologies or applications. Seldom have more holistic investigations been carried out towards disseminating the role of UAVs in smart city planning and management. To understand the application mechanism of UAVs in various facets of smart cities as a whole, it is a prerogative first to examine the research's distinct constituents in parts. Though UAVs primarily began with military applications [7], their dexterity in data collection soon popularised them as an effective tool in smart cities of the future [5, 8, 9]. Initial research concentrated on developing algorithms, cloud architectures and IoT platforms for increasing the efficiency of UAV flights [10–16] along with the concerns of cybersecurity and privacy concern of citizens [17, 18, 16]. While solutions to the mitigation of cybersecurity threats are being developed [19–22], the privacy debate remains ubiquitous.

Subsequently, extensive research was done towards understanding the unique application potential of UAVs smart city components such as surveillance [23–28], infrastructure construction [29, 30], traffic management [31–34], aerial imagery [32, 29, 36, 37, 34, 38], disaster management [39, 40, 36, 41, 42, 43], medical assistance [44, 43], environment monitoring [34, 45, 46], product or merchandise delivery [47, 48, 34, 49, 50], campus monitoring [51], etc.

Researchers have also undertaken numerous investigations towards the technological aspect of drones to inform and improve the enhanced applicability of UAVs in smart cities. Inquiries involving the advancement of technical elements of UAVs include machine learning and algorithm optimisation [52, 53], edge computing [54,

55, 56, 57, 45, 49, 58], sensors [59–61], internet of things [19, 62, 63, 56, 26, 61, 64, 43, 50, 37, 58, 65], cloud architecture and robotics [66, 67, 43], etc. among others. The specifications and technologies are continuously evolving to strengthen and streamline the benefits that UAVs can contribute concerning the day-to-day control and functioning of a smart city, making it even more efficient. The sections following this brief delineation of literature evidence on the function of UAVs in smart city planning and management will thus enumerate in detail the concept and procedural information about smart cities and UAVs, culminating in a consolidated evidence tabulation regarding the widespread application of drones in planning, operation and management stages of a smart city.

3 Background

A United Nations study of 2014 states that by the year 2050, 70% of the world's population will be living in cities, compared to 30% in rural zones [68]. Similarly, it is predicted that by the year 2030, nearly 40 to 50% of India's population will live in urban areas, contributing to 70% of the country's GDP [69]. This phenomenon requires dexterous action from the government and urban development authorities to facilitate the seamless incorporation of the growing urban population while improving the efficiency of all the urban systems [70]. Technological intervention is thus inevitable along with socio-economic, physical and environmental reforms in urban areas in India and worldwide. The Smart City concept has developed as a result, and it advocates the amalgamation of ICT solutions as an additional layer in the city dynamics for improving the functionality and efficiency of urban services [70].

3.1 *Smart City*

The Smart City concept is relatively new in origin, as it has been researched and developed since the 1990s, when several attempts have been made to define it [68]. Due to the subjective nature of the word 'smart', a single conclusive definition has not yet been formulated for the term 'Smart City', even though it encompasses facets of governance, ICT, surveillance, infrastructure, sustainability, quality of life, etc. A 2015 study by the Centre for Study of Science, Technology, and Policy (CSTEP) of 100 smart city definitions from several sources shows that the ICT framework emerges as the crux of the smart city concept (See Fig. 2) [71].

Many cities worldwide are now upgrading to be technologically enabled, and governance supported smarter energy management, waste management, water management, urban mobility, citizen services, building systems, surveillance, healthcare, education, and communication. Amsterdam and Barcelona are two of the most popular smart cities, which have adopted smart interventions in the form of smart

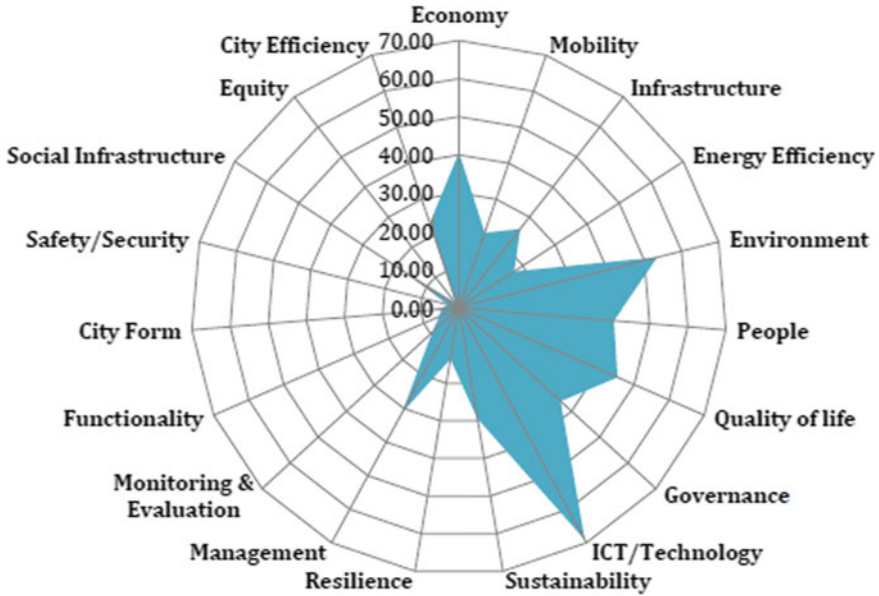


Fig. 2 Graphical web diagram of different facets of smart city planning as derived from 100 definitions by CSTEP

grids, smart metering, vehicle-2-grid systems, SCADA, smart parking, data portal, smart homes, etc. Hence, smart cities encourage collaboration, network integration and service connectivity to improve administrative bodies’ decision-making abilities. It also promotes citizen participation and access to information for the masses to establish a more transparent governance framework.

The Government of India also launched the ‘Smart City Mission’ in 2015 to facilitate 100 cities to become smart cities and become flag bearers of urban development for the entire country. A total of 5 stages of challenges were held, namely, lighthouse cities, fast track cities and rounds seconds, third and fourth. The chosen 100 cities had to give proposals for their respective smart city planning process during each round. The best proposals from a fixed number of cities were selected and awarded funds to move on to the next implementation stage. According to the Smart city mission statement and guidelines, the core infrastructure elements that the Indian smart cities should possess are adequate water supply, assured electric supply, sanitation, solid waste management, efficient urban mobility, public transport, affordable housing, robust IT connectivity, digitalisation, good governance, e-governance, citizen participation, sustainable environment, safety and security of citizens, education provision and health reforms [69]. Even though physical urban reforms are a part of the smart city mission, there is marked stress on incorporating ICT solutions in the form of UAVs, smart parking, smart meters, video monitoring, telemedicine, tele-education, electronic service delivery, etc.

3.2 Smart City Planning Process

The smart city planning process is dictated to be sustainable and technologically cohesive. Decentralisation of existing megacities gives impetus to tier 2 and tier 3 cities as well as satellite cities. Optimisation of infrastructure to conform to a set systemic approach streamlines smart cities' operation and maintenance while leaving room for planning upgradation concerning future urbanisation needs. One of the beneficial aspects of smart city planning is its participatory approach through citizen feedback, making the whole process more transparent. Energy reforms, mixed land use planning, walkability, public open spaces, inclusivity, and compactness have also been given impetus in the smart city planning process. The strategies for smart city planning are divided into area-based development and pan-city initiatives. Pan-city initiatives are essentially the ICT interventions strategically planned around the city with the help of sensors, big data, IoT, UAVs, etc. Area-based development reckons the type of planning process. The three strategies for area-based development that each smart city can choose from are as follows: (a) 'Retrofitting' for city improvement, (b) 'Redevelopment' for city renewal, and (c) 'Greenfield development' for city extension. Table 1 gives a detailed account of each strategy's distinctions depending on the planning process's variations, area extent, and infrastructure development type.

The smart city planning process individual to each city was chosen according to the final proposal presented by each city in the 'city challenges'. In each challenge, other than the winning cities, all other cities were given feedback to make changes to their proposals and present again to compete for approval and funding in the next challenge. Therefore, according to various factors pertaining to the need, location, population, urban form typology, and potential, the intrinsic smart city planning process was chosen for all hundred cities selected for the 'Smart City Mission' to be developed into smart cities by the year 2022. This thus shows the vision of the mission is inclusive and multi-pronged to provide the most profoundly distinctive solutions in the form of three different smart city planning strategies to each of the hundred cities for maximising the probability of positive results.

3.3 ICT Technologies

Information and communication technologies (ICTs) are an additional layer of infrastructure in the city, which functions based on orchestration intelligence, empowerment intelligence, and instrumentation intelligence. The underlying concept behind the ICT intelligence platform is based on problem-solving, open platform, cluster innovation, real-time data collection, and faster data analysis, processing, and response. They are essentially intelligent collaborative networks with a multi-pronged approach to data collection and creating a knowledge ecosystem for decision-making and innovation through ICT integration in a smart city. Smart grids

Table 1 Details of the three strategies of the smart planning process for the Smart City Mission India, 2015

Type of Area-based development	Planning process	Area extent	Infrastructure development focus
Retrofitting	Planning within an existing municipal ward with the help of citizen participation	Minimum 500 acres	Mostly ICT applications on building and area-level along with minor urban design and planning solutions
Redevelopment	Replacement of existing physical infrastructure with a completely new and improved planning solution by incorporating mixed land use planning	Minimum 50 acres	Compact, walkable and environmentally responsible planning with smart interventions towards improving energy efficiency
Greenfield development	Planning an entirely new smart city in a vacant area using innovative planning and ICT interventions	Minimum 250 acres	Development of new physical, social and environmental infrastructure along with smart ICT interventions while making the city compact and energy efficient

and open data systems take advantage of big data and the internet of things with sensors, UAVs, actuation technology, and networks to form a loop of information flow within a smart city environment to fast-track response time for operation and maintenance of a smart city. The main components of an ICT framework include the city's physical infrastructure connected to a portal or device or services for data collection, like—citizen portals, sensors, actuators, smart meters or UAVs. These, in turn, relay the information collected to the hubs or a central command centre where the data is intercepted, analysed, responded to and stored for future use. The command centres or data management centres act as controls, while the technology platforms act as ICT infrastructure (See Fig. 3).

ICT solutions are adroit for resource optimising, especially in Indian cities, with already strained resources. For example, the smart meter will be immediately notified if there is a leak in the pipes of the water supply system. Real-time mutually beneficial data of the different urban dynamics helps in precise decision making towards running smooth operation and maintenance of the city or even during times of crisis or disaster. Collection, analysis, storage, and use of information flowing through the dynamic fabric of an urban area is the key to meeting citizens' aspirations and providing a good quality of life through ICT integration in a smart city.

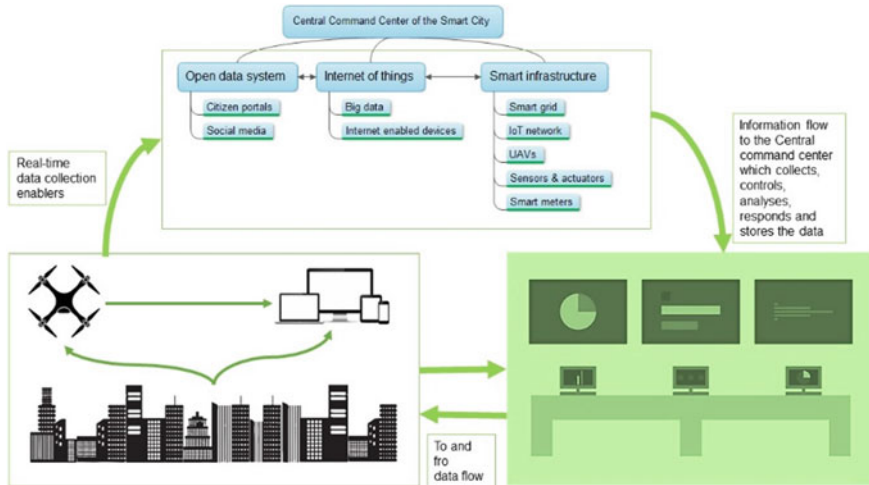


Fig. 3 Working design of smart city infrastructure

3.4 Unmanned Aerial Vehicles (UAVs)

The UAV or drone, as it is popularly known, is a device capable of flying or being flown on its own, without a human pilot on board, through prior computer programming or autonomous manoeuvring [18]. Even though it began with military applications, extensive research and development have made many advancements with respect to size, cost, typology, functionality, etc., so much so that now UAVs have a large-scale commercial reach [7]. UAVs can be classified based on usage and an aerial platform. According to use, the drone is classified on the basis of its intrinsic function, for example, drones for aerial photography, drones for traffic surveillance, drones for 3D mapping of an urban area, drones for facial detection, etc. On the other hand, based on the aerial platform used, drones can be classified as single rotor helicopter type, multi-rotor type, fixed-wing type, and fixed-wing hybrid VTOL type.

Single rotor drones look like miniature helicopters with one big rotor overhead and a small rotor on its tail end. It is one of the most stable varieties of drones due to the reduced number of rotors and has a higher-flying time, but it is not cost-effective due to its complicated design and is accident prone due to its large-sized overhead rotor. Multi-rotor drones are the most commonly used type of UAV, which is also commercially available for anyone from civilians to professionals. Multi-rotor UAVs are also the most commonly used for urban applications toward city-level data absorption. These are the cheapest and simplest drones with a wide variety of applications and flexibility. The multi-rotor drones can further be classified as tricopters, quadcopters, hexacopters, and octocopters, depending upon the number of rotors on them (See Fig. 4). The disadvantages of multi-motor UAVs are their short time of flying due to limited battery life, relatively slower speed, and reduced durability factor. Fixed wing drones are akin to commercial airplanes as they have

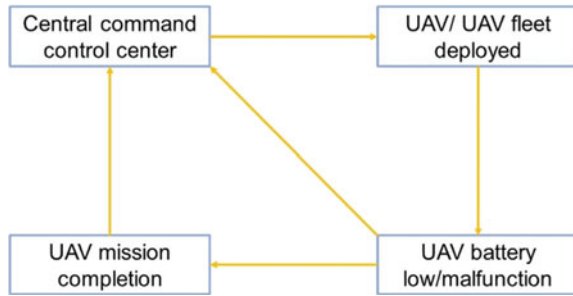


Fig. 4 Different types of UAV

wings and fly as per their pre-programmed flight paths for more extended periods of time. They are used for mapping, surveillance, 3D capture applications, etc. Although fixed-wing drones are fuel-efficient, they are not as cost-effective as multi-rotor drones. Lastly, the fixed wing hybrid VTOL type of drone is a cross between rotor type and fixed wing type of drones. It is controlled via remote control to take flight on the course required and may also carry sensors for surveillance and other activities. The hybrid type of UAV is still in its nascent research and development state.

It is readily available in the market, accessible to the general population, and used for applications like georeferencing, spatial planning, 3D visualisation of cities, buildings and topography, visual surveillance, video recording, etc. It is also being used to deliver packages autonomously at a faster speed. For instance, Amazon launched ‘Prime Air’, wherein orders from the clients are delivered by drones that are pre-programmed to deliver the particular item at the exact address. UAVs enabled with solar power can also fly for long periods without the need for refuelling. Hence, they can be used to provide broadband connectivity or emergency services as required in a smart city environment [18]. The GPS, Wi-Fi, Bluetooth, and camera-enabled drones are being researched for urban surveillance applications as well as to form a fleet of compact size aerial layers of real-time data collection over the city for transmission to the command centres using IoT for immediate response or for improving city operation and maintenance [72]. The data collected by the UAVs is in the form of videos, photos, 3D point clouds, environmental data, positioning data coordinates and third-party device data [11]. UAVs are being researched and considered for widespread use because they are small in size, flexible in design, and versatile

Fig. 5 Smart City UAV work cycle



data collection and relaying while being cost-effective. Some prolific examples of far-reaching positive impacts of UAVs can be seen in drones delivering medicine in rural Africa, disaster mitigation and response in Haiti, tackling wildfire mishaps at Yosemite National Park, etc. [72]. In smart cities, drones can be used for urban agriculture, traffic management, environmental management, round-the-clock surveillance, disaster response, telecommunication, weather monitoring, mapping, resource estimation, etc. [11]. For example, in the Smart City Mission of India, all cities will have a central command centre which will have the required IoT-enabled platform for data analysis, reaction, and storage, which will function as the control centre for assigning functions to a drone or fleets of drones regarding their flight path, and mission assignment (See Fig. 5).

3.5 Internet of Things (IoTs)

Internet of Things (IoTs) or Internet of Connected Things (IoCTs) facilitates the concept of ‘Connectivity for All’ [73]. Therefore, it supports networking and congruence between all the different urban amenities and services through the internet, wherein data is collected from them to understand their innate behaviour and functioning. IoT functions are based on a network connectivity framework and ‘big data’ driven algorithms over the ‘World Wide Web’ or the internet. IoT has global relevance through ICT-enabled devices and other computing devices. IoT and cloud computing can be called the brain of the ideal smart city by providing control over all its components, namely, smart grids, smart environmental management, smart mobility, smart economy, smart governance, smart people, smart living, building automation systems, smart vehicles, UAVs, etc. (Fig. 6) [21]. Electronics, sensors, actuators, software, a network for connectivity over the internet for cost-effective, and compact devices like UAVs to collect and exchange real-time dynamic urban information [74].

IoT platforms can thus be used for real-time regulation over UAVs, unified access to central command centres, transfer of large amounts of data from drone to cloud, conduct urban surveillance missions with fleets of UAVs, to establish a cooperative

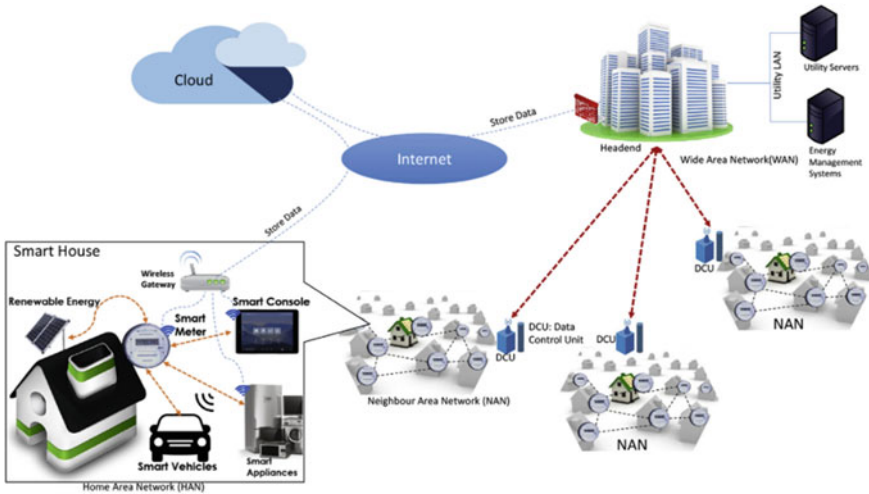


Fig. 6 A standard smart grid architecture connected and supported by IoT and cloud computing [21]

network framework for all the UAVs in service in a particular location, and to provide cloud-based programming of UAVs through APIs [75]. Commercialisation and price reduction have rendered UAVs or drones useful candidates for IoT applications in smart cities [76]. The IoT architecture used for manoeuvring UAVs is known as the Internet of Drones (IoDs), which helps in securing connectivity between the UAV user and the drone for controlling them, accessing the data collected by them and programming them for any desired reaction if needed [75]. Autonomous control of UAVs is accomplished through computer algorithms to establish IoT use for accurate real-time response through intelligence and network integration [76]. The IoT network for cloud services for UAVs essentially consists of an interface component, a computation component and a storage component for data assimilation, scrutiny, prompt response and storage [75].

4 UAV Application in Smart City Planning Process, Maintenance, and Operation

In the Smart City planning process, planners consider the city as a dynamic system whose subsystems are concatenated and interdependent. The complexity of interconnectedness and interdependency of the city as a system is appreciated in the smart city planning process. The crux of smart city planning and management is to understand and manage the intricacy of urban systems by application of ICT and its trends. A smart city, as a development tool, is being portrayed as a key component of sustainable development for the world. With the rapid technological advancement

in the field of UAVs, drones are going to play a vital role in smart city planning and development. The application of UAVs in a smart city will depend on the type of payload assigned to the UAV. The functional characteristic of UAVs will differ with respect to the use of varying types of payload. The different types of payloads for UAVs can be categorised as follows; a) Camera and Sensors, b) Communication Devices, and c) Other Payloads. A range of plausible uses of UAVs in smart city planning and development, having these types of payloads are listed in Table 2.

Urban planning exercises comprise multiple interlinking steps that manifest into a holistic design for a particular city. Similarly, the smart city planning process also

Table 2 Types of UAV payloads and their feasible applications in Smart City

Types of UAV Payload	Feasible applications	Authors
Camera and Sensors	Survey, Inspection and detection, Disaster Monitoring and Management, Surveying and Mapping, Traffic monitoring and management, Crowd management, Wildlife monitoring and management, 3d modelling, Aerial Photography, Environmental Monitoring, Detection, Infrastructure Inspection, Surveillance, Smart resource and asset management, Smart tracking assets, Navigation etc	[77, 78, 46, 79, 80, 19, 47, 81, 40, 82, 42, 34, 43, 41, 36, 39, 34, 51, 83, 84, 85, 31, 48, 32, 33, 34, 86, 87, 29, 67, 88, 89, 34, 36, 45, 67, 30, 23, 24, 32, 25, 26, 27, 28, 42, 38]
Communication Devices	Broadband connectivity on demand, Cellular networks, Dedicated radio networks, Dedicated closed networks, Ham radio, Medical assistance etc	[90, 44, 43, 53, 91, 85, 59, 50, 87, 51, 92, 54]
Other Payloads	Product Delivery, Taxi, Disaster Relief, Medical Assistance, Firefighting, Gaming, Urban Farming and Agriculture, Construction, Last-mile deliveries in congested areas, pandemic management, etc	[44, 40, 93, 42, 34, 43, 41, 36, 39, 94, 9, 5, 95, 18, 96, 97, 24, 98]

consists of several phases that cater to the initial development stage and the subsequent operation and management phase of a smart city. The phases of a smart city planning process consist of the preparatory planning phase, master planning phase, zoning phase, design and implementation phase, and operational phase. The induction of UAVs into the plethora of smart city planning processes will take advantage of all the stages of city operation and management daily. The viable uses of UAVs in the smart city planning process are listed in Table 3.

4.1 Challenges

UAVs are still a growing phenomenon undergoing extensive research, development, and commercialisation. Since their inception, drones have shown many benefits in a short period, which will only improve with time through skilful research efforts. Still, simultaneously, some challenges and issues have also been identified, which have been discussed below.

(1) Privacy and ethical use—there is an omnipresent concern regarding the invasion of privacy and probable unethical use of drones, especially in the absence of a cohesive policy framework to regulate the use of drones which are now also easily available in stores open to public access and use. (2) Cost—The developed UAVs are exorbitant in manufacturing, operation and maintenance. (3) Regulatory framework—there is a lack of policies, regulations and sensitisation regarding the use of UAVs, whether by civilians or urban local bodies, which is giving rise to concerns of safety, security and privacy when used for recreational purposes as government surveillance. (4) Hacking and hijacking threats—these range from information leakage from the IoT cloud to malicious codes and viruses to third-party hacking to introduction of malware by nefarious parties to de-authentication attacks to GPS spoofing to hijacking drone remotely to use as cyber-attack manifestations. (5) Technical difficulties—building a seamless platform of integration of the UAVs with the smart city and designing a network for the mobility of the fleet of drones in the aerial domain for various purposes are the main technical issues, along with the development of algorithms, wireless sensors, and fail-safe systems to mitigate the risk of crashing. (6) Potential of commercial use—though companies like Amazon, Facebook, etc. have now started researching, developing and investing in the integration of UAVs towards the expansion of their businesses into the smart domain, there is still a long way to go in this respect due to the high additional financial investment needed for this purpose.

Table 3 Potential uses of UAVs in the Smart City planning process

Phase of smart city planning process	Fields of activity in which UAVs can be used	Authors
Preparatory planning phase	Surveying, Aerial photography	[77, 78, 67, 29, 88, 34, 36]
Master planning phase	Surveying, Monitoring, 3d Modelling, Aerial Photography	[77, 78, 67, 29, 88, 34, 36, 33, 53, 46]
Zoning phase	Surveying, Monitoring, 3d Modelling, Aerial Photography	[77, 78, 67, 29, 88, 34, 36, 53, 33, 46]
Design and Implementation phase	Monitoring and management, 3d modelling, Product Delivery, Mapping, Infrastructure Inspection, Smart resource and asset management, Aerial Photography	[49, 46, 67, 29, 88, 34, 36, 99, 47, 34, 49, 42]
Operation and management phase	Monitoring and management, Inspection and Detection, Traffic Monitoring and Management, Crowd Management, Product Delivery, Taxi, Object Tracking, Medical Assistance, Firefighting, Urban Farming, Environmental Monitoring, Navigation, On-demand Broadband Connectivity, Radio Networking, Security and safety	[46, 20, 99, 47, 55, 34, 49, 42, 100, 90, 44, 43, 53, 91]

5 Discussion and Way Forward

The new paradigm of smart cities, especially in the current Indian planning scenario, would benefit profusely from the induction of UAVs into the ICT layer of the city. The compact and flexible design of UAVs and the advantage of autonomous aerial manoeuvring makes them proficient candidates for the deployment of a large arena of services and function for the seamless planning, operation and maintenance of smart cities with the added advantage of resource optimisation, real-time unhindered data collection, prompt response and storage of dynamic urban data for future requirements of the city. Typologies of UAVs and their respective uses are varied and can provide a large network of applications, even in locations or situations where human access is difficult. UAVs can be incorporated into phases of the urban planning process to achieve the formulation of an efficient smart city. UAVs are useful in the preparatory planning phase owing to their competent data collection applications. The data collected can be used in the master planning phase for discrete design innate to the individual character of the city or region, which is parallel to the concept of the Smart City Mission in India, where the individualistic approach has been lauded to preserve the omnipresent organic character of each city. UAVs are also beneficial in the zoning development and implementation phases of planning. Still, they will be the most effective in the operation and maintenance phase when the day-to-day activity monitoring and reciprocation of the smart city will be in focus. Having said so, due to the deficiency of a regulatory framework, challenges and issues also abound in the utilisation factor of UAVs, in terms of privacy, safety, security and technical mishaps, wherein the chinks have to be filled up with research and development to assure better and smooth application of the UAVs in the smart city planning process, operation and management for agile data collection, real-time response and the prerequisite of a better quality of life.

References

1. Tipton CW, Hoffman RC, Robertson DN, Godfrey RP, Friessnegg T, Ramesh R, Engineering G (2001) Unmanned aerial vehicle roadmap 2000–2025
2. Mohammed F, Idries A, Mohamed N, Al-Jaroodi J, Jawhar I (2014). Opportunities and challenges of using UAVs for Dubai Smart City. In: 2014 6th international conference on new technologies, mobility and security - proceedings of NTMS 2014 conference and workshops, pp 1–4. <https://doi.org/10.1109/NTMS.2014.6814041>
3. Santagata E, Baglieri O, Dalmazzo D, Tsantilis L (2013) A cloud robotics architecture for an emergency management and monitoring service in a smart city environment. *Mater Struct* 46(10):1673–1682. <https://doi.org/10.1617/s11527-012-0006-0>
4. Singh CH, Mishra V, Jain K, Shukla AK (2022) FRCNN-Based Reinforcement Learning for Real-Time Vehicle Detection Tracking and Geolocation from UAS. *Drones* 6(12):406. <https://doi.org/10.3390/drones6120406>
5. Mohammed F, Idries A, Mohamed N, Al-Jaroodi J, Jawhar I (2014). UAVs for smart cities: opportunities and challenges. In: 2014 international conference on unmanned aircraft systems,

- ICUAS 2014 - conference proceedings, pp 267–273. <https://doi.org/10.1109/ICUAS.2014.6842265>
6. Gallacher D (2016) Drones to manage the urban environment: risks, rewards, alternatives. *J Unmanned Veh Syst* 4(2):115–124. <https://doi.org/10.1139/juvs-2015-0040>
 7. Rash C, LeDuc P, Manning S (2006) Human factors in U.S. military unmanned aerial vehicle accidents. In: *Human factors of remotely operated vehicles*. Elsevier, pp 117–131. [https://doi.org/10.1016/S1479-3601\(05\)07009-8](https://doi.org/10.1016/S1479-3601(05)07009-8)
 8. Marris E (2013) Drones in science: fly, and bring me data. *Nature* 498(7453):156–158. <https://doi.org/10.1038/498156a>
 9. Morrison A, Tronstad R, Martinussen ES (2013) Design notes on a lonely drone. *Digit Creat* 24(1):46–59. <https://doi.org/10.1080/14626268.2013.768534>
 10. Foina AG, Sengupta R, Lerchi P, Liu Z, Krainer C (2015) Drones in smart cities: Overcoming barriers through air traffic control research. In: *2015 workshop on research, education and development of unmanned aerial systems (RED-UAS)*. IEEE, pp 351–359. <https://doi.org/10.1109/RED-UAS.2015.7441027>
 11. Giyenko A, Cho YI (2016) Intelligent unmanned aerial vehicle platform for smart cities. In: *Proceedings - 2016 joint 8th international conference on soft computing and intelligent systems and 2016 17th international symposium on advanced intelligent systems, SCIS-ISIS 2016*, pp 729–733. <https://doi.org/10.1109/SCIS-ISIS.2016.0159>
 12. Jensen OB (2016) Drone city - power, design and aerial mobility in the age of “smart cities.” *Geogr Helv* 71(2):67–75. <https://doi.org/10.5194/gh-71-67-2016>
 13. Shariat A, Tizghadam A, Leon-Garcia A (2016) An ICN-based publish-subscribe platform to deliver UAV service in smart cities. In: *Proceedings - IEEE INFOCOM, 2016-Sept*, pp 698–703. <https://doi.org/10.1109/INFCOMW.2016.7562167>
 14. Stevenson JD, O’Young S, Rolland L (2015) Estimated levels of safety for small unmanned aerial vehicles and risk mitigation strategies. *J Unmanned Veh Syst* 3(4):205–221. <https://doi.org/10.1139/juvs-2014-0016>
 15. Sundar K, Rathinam S (2014) Algorithms for routing an unmanned aerial vehicle in the presence of refueling depots. *IEEE Trans Autom Sci Eng* 11(1):287–294. <https://doi.org/10.1109/TASE.2013.2279544>
 16. Winter SR, Rice S, Tamilselvan G, Tokarski R (2016) Mission-based citizen views on UAV usage and privacy: an affective perspective. *J Unmanned Veh Syst* 4(2):125–135. <https://doi.org/10.1139/juvs-2015-0031>
 17. Sterbenz JPG (2016) Drones in the smart city and IoT: protocols, resilience, benefits, and risks. In: *Proceedings of the 2nd workshop on micro aerial vehicle networks, systems, and applications for civilian use - DroNet ’16*. : ACM Press, New York, USA, pp. 3–3. <https://doi.org/10.1145/2935620.2949659>
 18. Vattapparamban E, Guvenc I, Yurekli AI, Akkaya K, Uluagac S (2016) Drones for smart cities: issues in cybersecurity, privacy, and public safety. *Int Wirel Commun Mob Comput Conf (IWCMC) 2016*:216–221. <https://doi.org/10.1109/IWCMC.2016.7577060>
 19. Aldaej A, Ahanger TA, Atiquzzaman M, Ullah I, Yousufudin M (2022) Smart cybersecurity framework for IoT-empowered drones: machine learning perspective. *Sensors* 22(7). <https://www.scopus.com/inward/record.uri?eid=2-s2.0-85127120421&doi=10.3390%2Fs22072630&partnerID=40&md5=9bac316c9d0b840377b490de1bc9bfb2>
 20. Baig Z, Syed N, Mohammad N (2022) Securing the smart city airspace: drone cyber attack detection through machine learning. *Future Internet* 14(7). <https://www.scopus.com/inward/record.uri?eid=2-s2.0-85133522893&doi=10.3390%2Ffi14070205&partnerID=40&md5=ef36d03bd9cddb6220269bce9d7e8c7a>
 21. Baig, ZA, Szewczyk P, Valli C, Rabadia P, Hannay P, Chernyshev M, Peacock M (2017) Future challenges for smart cities: Cyber-security and digital forensics. *Digit Investig* 22:3–13. <https://www.scopus.com/inward/record.uri?eid=2-s2.0-85027456918&doi=10.1016%2Fj.diin.2017.06.015&partnerID=40&md5=f7de9669ecaf8157d15d0b5602acce85>
 22. Baig ZA, Szewczyk P, Valli C, Rabadia P, Hannay P, Chernyshev M, Peacock M (2017) Future challenges for smart cities: cyber-security and digital forensics. *Digit Investig* 22:3–13. <https://doi.org/10.1016/J.DIIN.2017.06.015>

23. Akram MW, Bashir AK, Shamshad S, Saleem MA, AlZubi AA, Chaudhry SA, Zikria YB (2021) A secure and lightweight drones-access protocol for smart city surveillance. *IEEE Trans Intell Transp Syst.* <https://www.scopus.com/inward/record.uri?eid=2-s2.0-85121397641&doi=10.1109%2FTITS.2021.3129913&partnerID=40&md5=e82e6cc6f023492302cb42c3be5ea438>
24. Gohari A, Ahmad AB, Rahim RBA, Supa'at ASM, Razak SA, Gismalla MSM (2022) Involvement of surveillance drones in smart cities: a systematic review. *IEEE Access* 10:56611–56628. <https://www.scopus.com/inward/record.uri?eid=2-s2.0-85130784183&doi=10.1109%2FACCESS.2022.3177904&partnerID=40&md5=cf528fb347a5e3fd3c8ef4faa6799910>
25. Jin Y, Qian Z, Yang W (2020) UAV cluster-based video surveillance system optimisation in heterogeneous communication of smart cities. *IEEE Access* 8:55654–55664. <https://www.scopus.com/inward/record.uri?eid=2-s2.0-85082598151&doi=10.1109%2FACCESS.2020.2981647&partnerID=40&md5=fe107241b8e3d3118bbdc184e9a27051>
26. Kim H, Ben-Othman J (2018) A collision-free surveillance system using smart UAVs in multi domain IoT. *IEEE Commun Lett* 22(12):2587–2590. <https://www.scopus.com/inward/record.uri?eid=2-s2.0-85054621440&doi=10.1109%2FLCOMM.2018.2875477&partnerID=40&md5=ab514d6e42be3c92e6235e2f10da8e1b>
27. Kim H, Mokdad L, Ben-Othman J (2018) Designing UAV surveillance frameworks for smart city and extensive ocean with differential perspectives. *IEEE Commun Mag* 56(4):98–104. <https://www.scopus.com/inward/record.uri?eid=2-s2.0-85045921660&doi=10.1109%2FMCOM.2018.1700444&partnerID=40&md5=91f6a796739259ff049bca8b7ebed622>
28. Nikooghadam M, Amintoosi H, Islam SH, Moghadam MF (2021) A provably secure and lightweight authentication scheme for Internet of Drones for smart city surveillance. *J Syst Arch* 115. <https://www.scopus.com/inward/record.uri?eid=2-s2.0-85097800036&doi=10.1016%2Fj.sysarc.2020.101955&partnerID=40&md5=cbc0a00bbbaaa89502edf19f84438393>
29. Li J, Yao YX, Duan P, Chen Y, Li S, Zhang C (2018) Studies on three-dimensional (3D) modeling of UAV oblique imagery with the aid of loop-shooting. *ISPRS Int J Geo-Inf* 7(9).
30. Shirowzhan S, Tan W, Sepasgozar SME (2020) Digital twin and CyberGIS for improving connectivity and measuring the impact of infrastructure construction planning in smart cities. *ISPRS Int J Geo-Inf* 9(4). <https://www.scopus.com/inward/record.uri?eid=2-s2.0-85083321923&doi=10.3390%2Fijgi9040240&partnerID=40&md5=ef3d9bdc2455373d422e38881a5d13b4>
31. Beg A, Qureshi AR, Sheltami T, Yasar A (2021) UAV-enabled intelligent traffic policing and emergency response handling system for the smart city. *Pers Ubiquitous Comput* 25(1):33–50. <https://www.scopus.com/inward/record.uri?eid=2-s2.0-85080857116&doi=10.1007%2Fs00779-019-01297-y&partnerID=40&md5=59cdc91296802515e0997c44e07ecfdd>
32. Jain A, Ramaprasad R, Narang P, Mandal M, Chamola V, Yu FR, Guizan M (2021) AI-enabled object detection in UAVs: challenges, design choices, and research directions. *IEEE Netw* 35(4):129–135
33. Khan NA, Jhanjhi NZ, Brohi SN, Usmani RSA, Nayyar A (2020) Smart traffic monitoring system using Unmanned Aerial Vehicles (UAVs). *Comput Commun* 157:434–443. <https://www.scopus.com/inward/record.uri?eid=2-s2.0-85083820120&doi=10.1016%2Fj.comcom.2020.04.049&partnerID=40&md5=9ade9565dc7c289ebc704ef93a7ee5c6>
34. Mohamed N, Al-Jaroodi J, Jawhar I, Idries A, Mohammed F (2020) Unmanned aerial vehicles applications in future smart cities. *Technol Forecast Soc Chang* 153.
35. Su JH, Liao JJ, Gu DJ, Wang ZY, Cai GR (2021) Object detection in aerial images using a multiscale keypoint detection network. *IEEE J Sel Top Appl Earth Obs Remote Sens* 14:1389–1398
36. Munawar HS, Ullah F, Qayyum S, Khan SI, Mojtahedi M (2021) UAVs in disaster management: application of integrated aerial imagery and convolutional neural network for flood detection. *Sustainability* 13(14).

37. Sharma A, Singh PK, Kumar Y (2020) An integrated fire detection system using IoT and image processing technique for smart cities. *Sustain Cities Soc* 61. <https://www.scopus.com/inward/record.uri?eid=2-s2.0-85086804177&doi=10.1016%2Fj.scs.2020.102332&partnerID=40&md5=686ecd3bcfd4c089f01e5392174c400d>
38. Xiao J, Zhu R, Hu RM, Wang M, Zhu Y, Chen D, Li DR (2018) Towards real-time service from remote sensing: compression of earth observatory video data via long-term background referencing. *Remote Sens* 10(6).
39. Bourbakis N, Ktistakis IP, Seleem T (2020) Smart cities-detecting humans in regions of disasters: synergy of drones, micro-robots in underground tunnels. *Int J Artif Intell Tools* 29(5). <https://www.scopus.com/inward/record.uri?eid=2-s2.0-85092435805&doi=10.1142%2F50218213020500062&partnerID=40&md5=f63bdac942cccaa737429a543efd389b>
40. Huynh DV, Do-Duy T, Nguyen LD, Le MT, Vo NS, Duong TQ (2022) Real-time optimized path planning and energy consumption for data collection in unmanned ariel vehicles-aided intelligent wireless sensing. *IEEE Trans Ind Inform* 18(4):2753–2761
41. Qadir Z, Ullah F, Munawar HS, Al-Turjman F (2021) Addressing disasters in smart cities through UAVs path planning and 5G communications: a systematic review. *Comput Commun* 168:114–135. <https://www.scopus.com/inward/record.uri?eid=2-s2.0-85099627653&doi=10.1016%2Fj.comcom.2021.01.003&partnerID=40&md5=f9eacf96073df0591f3487dfca9bca>
42. Saha S, Vasegaard AE, Nielsen I, Hapka A, Budzisz H (2021) UAVs path planning under a Bi-objective optimisation framework for smart cities. *Electronics* 10(10).
43. Sood SK (2020) Fog-Cloud centric IoT-based cyber physical framework for panic oriented disaster evacuation in smart cities. *Earth Sci Inform*.
44. Doraswamy B, Krishna KL, Giriprasad MN (2022) A secure unmanned aerial vehicle service for medical system to improve smart city facilities. *Int J Adv Comput Sci Appl* 13(2):495–504. <https://www.scopus.com/inward/record.uri?eid=2-s2.0-85126135187&doi=10.14569%2FIJACSA.2022.0130258&partnerID=40&md5=19dd0d412f4b3832faefe1bb7c40ee4e>
45. Khosravi MR, Samadi S (2021) BL-ALM: A blind scalable edge-guided reconstruction filter for smart environmental monitoring through green IoMT-UAV networks. *IEEE Trans Green Commun Netw* 5(2):727–736. <https://www.scopus.com/inward/record.uri?eid=2-s2.0-85103298646&doi=10.1109%2FTGCN.2021.3067555&partnerID=40&md5=171acd8e1fd16f36067006748bbc0776>
46. Sharma R, Arya R (2022) UAV based long range environment monitoring system with Industry 5.0 perspectives for smart city infrastructure. *Comput Ind Eng* 168. <https://www.scopus.com/inward/record.uri?eid=2-s2.0-85126070588&doi=10.1016%2Fj.cie.2022.108066&partnerID=40&md5=c3a339a0a79235e35219061a5f6c19d9>
47. Asaamoning G, Mendes P, Magaia N (2021) A Dynamic clustering mechanism with load-balancing for flying Ad Hoc networks. *IEEE ACCESS* 9:158574–158586
48. Bouassida S, Neji N, Nouveliere L, Neji J (2021) Evaluating the impact of drone signaling in crosswalk scenario. *Appl Sci-Basel* 11(1).
49. Ren X, Vashisht S, Aujla GS, Zhang P (2022) Drone-edge coalesce for energy-aware and sustainable service delivery for smart city applications. *Sustain Cities Soc* 77. <https://www.scopus.com/inward/record.uri?eid=2-s2.0-85119918251&doi=10.1016%2Fj.scs.2021.103505&partnerID=40&md5=ba382df9392ae0bc1db6a5c0c838d3b3>
50. Shao B, Leeson MS (2021) PaFiR: Particle Filter Routing - a predictive relaying scheme for UAV-assisted IoT communications in future innovated networks. *Internet Things* 14.
51. Tiwari A, Sharma SK, Dixit A, Mishra V (2021) UAV remote sensing for campus monitoring: a comparative evaluation of nearest neighbor and rule-based classification. *J Indian Soc Remote Sens* 49(3):527–539
52. Alqurashi FA, Alsolami F, Abdel-Khalek S, Sayed Ali E, Saeed RA (2022) Machine learning techniques in internet of UAVs for smart cities applications. *Journal of Intelligent and Fuzzy Systems*, 42(4), 3203–3226. <https://www.scopus.com/inward/record.uri?eid=2-s2.0-85127451313&doi=10.3233%2FJIFS-211009&partnerID=40&md5=9b3151d4c91fe7fa277148dbec338c722>

53. Malekloo A, Ozer E, AlHamaydeh M, Girolami M (2022) Machine learning and structural health monitoring overview with emerging technology and high-dimensional data source highlights. *Struct Health Monit-An Int J* 21(4):1906–1955
54. Alsamhi SH, Almalki FA, AL-Dois H, Shvetsov A V, Ansari MS, Hawbani A, ... Lee B (2021) Multi-Drone Edge Intelligence and SAR Smart Wearable Devices for Emergency Communication. *Wireless Communications and Mobile Computing*, 2021. <https://www.scopus.com/inward/record.uri?eid=2-s2.0-85122984823&doi=10.1155%2F2021%2F6710074&partnerID=40&md5=28bd732ee665e4b76005ea80b1cbaf55>
55. Garg S, Singh A, Batra S, Kumar N, Yang LT (2018) UAV-empowered edge computing environment for cyber-threat detection in smart vehicles. *IEEE Netw* 32(3):42–51. <https://www.scopus.com/inward/record.uri?eid=2-s2.0-85048335823&doi=10.1109%2FMNET.2018.1700286&partnerID=40&md5=ac7585fdceaa29e9ae06b26c0362cd8b>
56. Hu L, Liu A, Xie M, Wang T (2019) UAVs joint vehicles as data mules for fast codes dissemination for edge networking in Smart City. *Peer-To-Peer Netw Appl* 12(6):1550–1574. <https://www.scopus.com/inward/record.uri?eid=2-s2.0-85066617886&doi=10.1007%2F912083-019-00752-0&partnerID=40&md5=2c7c45e9d24b81667bce942164608c74>
57. Hu Z, Bai Z, Yang Y, Zheng Z, Bian K, Song L (2019) UAV aided aerial-ground IoT for air quality sensing in smart city: architecture, technologies, and implementation. *IEEE Netw* 33(2):14–22. <https://www.scopus.com/inward/record.uri?eid=2-s2.0-85063768947&doi=10.1109%2FMNET.2019.1800214&partnerID=40&md5=bd613b22c3d239d7f47d4fd27251337a>
58. Tan Z, Qu H, Zhao J, Zhou S, Wang W (2020) UAV-aided edge/fog computing in smart IoT community for social augmented reality. *IEEE Internet Things J* 7(6):4872–4884. <https://www.scopus.com/inward/record.uri?eid=2-s2.0-85086584724&doi=10.1109%2FJIOT.2020.2971325&partnerID=40&md5=7c41ab954554666331b2bf8baa6154a8>
59. Darsena D, Gelli G, Iudice I, Verde F (2021) Detection and blind channel estimation for UAV-aided wireless sensor networks in smart cities under mobile jamming attack. *IEEE Internet Things J*. <https://www.scopus.com/inward/record.uri?eid=2-s2.0-85120899774&doi=10.1109%2FJIOT.2021.3132381&partnerID=40&md5=35280edc6928588cec10c0b3c057663c>
60. Khalifeh A, Darabkh KA, Khasawneh AM, Alqaisieh I, Salameh M, Alabdala A, Rajendiran K (2021) Wireless sensor networks for smart cities: network design, implementation and performance evaluation. *Electronics (Switzerland)* 10(2):1–28. <https://www.scopus.com/inward/record.uri?eid=2-s2.0-85100109661&doi=10.3390%2Felectronics10020218&partnerID=40&md5=afe7e7350b9255538a3e31e4fb0d1b2c>
61. Liu J, Liu Z, Zhang H, Yuan H, Manokaran KB, Maheshwari M (2021) Multi-sensor information fusion for IoT in automated guided vehicle in smart city. *Soft Comput* 25(18), 12017–12029. <https://www.scopus.com/inward/record.uri?eid=2-s2.0-85102235589&doi=10.1007%2Fs00500-021-05696-3&partnerID=40&md5=a688b61e78a9f39de867cde9d4eca51f>
62. Deebak BD, Al-Turjman F (2020) A smart lightweight privacy preservation scheme for IoT-based UAV communication systems. *Comput Commun* 162:102–117. <https://www.scopus.com/inward/record.uri?eid=2-s2.0-85090056135&doi=10.1016%2Fj.comcom.2020.08.016&partnerID=40&md5=8e0e7873df03d2d3e99cf351086e8cbe>
63. Hoque MA, Hossain M, Noor S, Islam SMR, Hasan R (2021) IoTaaS: drone based internet of things as a service framework for smart cities. *IEEE Internet Things J*. <https://www.scopus.com/inward/record.uri?eid=2-s2.0-85122576054&doi=10.1109%2FJIOT.2021.3137362&partnerID=40&md5=3f1aa21fcc7ebd04f6160e50ca3030cf>
64. Qi F, Zhu X, Mang G, Kadoch M, Li W (2019) UAV network and IoT in the sky for future smart cities. *IEEE Netw* 33(2):96–101. <https://www.scopus.com/inward/record.uri?eid=2-s2.0-85063769486&doi=10.1109%2FMNET.2019.1800250&partnerID=40&md5=36422722ddc9036c8c2b61828117c239>
65. Zahmatkesh H, Al-Turjman F (2020) Fog computing for sustainable smart cities in the IoT era: caching techniques and enabling technologies - an overview. *Sustain Cities Soc*, 59.

- <https://www.scopus.com/inward/record.uri?eid=2-s2.0-85084182624&doi=10.1016%2Fj.scs.2020.102139&partnerID=40&md5=8041a8e993b33b4aa3f18f859f82ee36>
66. Ermacora G, Rosa S, Toma A (2016) Fly4SmartCity: a cloud robotics service for smart city applications. *J Ambient Intell Smart Environ* 8(3):347–358. <https://www.scopus.com/inward/record.uri?eid=2-s2.0-84968779361&doi=10.3233%2FAIS-160374&partnerID=40&md5=4e7a6dee1043d83d5e28ff3ee4a813d6>
 67. Mehranfar M, Arefi H, Alidoost F (2021) Knowledge-based 3D reconstruction of bridge structures using UAV-based photogrammetric point cloud. *J Appl Remote Sens* 15(4).
 68. Ramaprasad A, Aurora Sánchez-Ortiz TS (2007) A Unified Definition of a Smart City. *Encyclopedia of Digital Government* 1:634–642. <https://doi.org/10.1007/978-3-540-74444-3>
 69. Ministry of Urban Development Government of India (2015) Smart city mission statement & guidelines. Routledge. <https://doi.org/10.4324/9780203076224>
 70. Kumar H, Singh MK, Gupta MP, Madaan J (2018) Moving towards smart cities: solutions that lead to the smart city transformation framework. In: *Technological forecasting and social change*, (April), pp 1–16. <https://doi.org/10.1016/j.techfore.2018.04.024>
 71. Bhattacharya S, Rathi S (2015) Reconceptualising smart cities: a reference framework for India
 72. Jensen OB (2016) New ‘foucauldian boomerangs’: drones and urban surveillance. *Surveill Soc* 14(1):20–33
 73. Sharma V, You I, Pau G, Collotta M, Lim JD, Kim JN (2018) LoRaWAN-based energy-efficient surveillance by drones for intelligent transportation systems. *Energies* 11(3). <https://doi.org/10.3390/en11030573>
 74. Renwick JD, Klein LJ, Hamann HF (2017) Drone-based reconstruction for 3D geospatial data processing. In: *2016 IEEE 3rd world forum on internet of things. WF-IoT 2016*, pp 729–734. <https://doi.org/10.1109/WF-IoT.2016.7845501>
 75. Koubaa A, Qureshi B, Sriti MF, Javed Y, Tovar E (2017) A service-oriented Cloud-based management system for the Internet-of-Drones. In: *2017 IEEE international conference on autonomous robot systems and competitions, ICARSC 2017, (Section 3)*, pp 329–335. <https://doi.org/10.1109/ICARSC.2017.7964096>
 76. Fotouhi A, Ding M, Hassan M (2017) Understanding autonomous drone maneuverability for Internet of Things applications. In: *18th IEEE international symposium on a world of wireless, mobile and multimedia networks, WoWMoM 2017 - conference*, pp 1–6. <https://doi.org/10.1109/WoWMoM.2017.7974336>
 77. Du R, Santi P, Xiao M, Vasilakos A V, Fischione C (2019) The sensible city: a survey on the deployment and management for smart city monitoring. *IEEE Commun Surv Tutor* 21(2):1533–1560. <https://www.scopus.com/inward/record.uri?eid=2-s2.0-85056584676&doi=10.1109%2FCOMST.2018.2881008&partnerID=40&md5=d118dacc0e60339c1c39958c803fdd74>
 78. Alsamhi SH, Ma O, Ansari MS, Almalki FA (2019) Survey on collaborative smart drones and internet of things for improving smartness of smart cities. *IEEE Access*, 7, 128125–128152. <https://www.scopus.com/inward/record.uri?eid=2-s2.0-85075391498&doi=10.1109%2FAccess.2019.2934998&partnerID=40&md5=b924be44c58864e9758231a1c7bf3ae5>
 79. Zakaria NA, Zainal Z, Harun N, Chen L, Saleh N, Azni F (2018) Wireless internet of things-based air quality device for smart pollution monitoring. *Int J Adv Comput Sci Appl*, 9(11), 65–69. <https://doi.org/10.14569/IJACSA.2018.091110>
 80. Nasution TH, Muchtar MA, Simon A (2019) Designing an IoT-based air quality monitoring system. In: *IOP conference series: materials science and engineering*, vol 648, p 012037. Institute of Physics Publishing. <https://doi.org/10.1088/1757-899X/648/1/012037>
 81. Hernández-Vega JI, Varela ER, Romero NH, Hernández-Santos C, Cuevas JLS, Gorham DGP (2018) Internet of things (IoT) for monitoring air pollutants with an unmanned aerial vehicle (UAV) in a smart city. In: *Lecture notes of the institute for computer sciences, social-informatics and telecommunications engineering, LNICST. Springer*, vol 213, pp 108–120. https://doi.org/10.1007/978-3-319-73323-4_11

82. Rohi G, Ejofodomi O, Ofualagba G (2020) Autonomous monitoring, analysis, and countering of air pollution using environmental drones. *Heliyon* 6(1):e03252. <https://doi.org/10.1016/j.heliyon.2020.e03252>
83. Nguyen DD, Rohacs J, Rohacs D (2021) Autonomous flight trajectory control system for drones in smart city traffic management. *ISPRS Int J Geo-Inf* 10(5). <https://www.scopus.com/inward/record.uri?eid=2-s2.0-85107233327&doi=10.3390%2Fijgi10050338&partnerID=40&md5=31e8db4e6fb0491932458f6ee3c3a240>
84. El-Sayed H, Chaqfa M, Zeadally S, Puthal D (2019) A traffic-aware approach for enabling Unmanned Aerial Vehicles (UAVs) in smart city scenarios. *IEEE Access* 7:86297–86305. <https://www.scopus.com/inward/record.uri?eid=2-s2.0-85068979645&doi=10.1109%2FAccess.2019.2922213&partnerID=40&md5=47556b70453cad34910206ea0af5f37b>
85. Akter S, Dao TN, Yoon S (2021) Time-constrained task allocation and worker routing in mobile crowd-sensing using a decomposition technique and deep Q-learning. *IEEE Access* 9:95808–95822
86. Roldán-Gómez JJ, Garcia-Aunon P, Mazariegos P, Barrientos A (2020) SwarmCity project: monitoring traffic, pedestrians, climate, and pollution with an aerial robotic swarm: Data collection and fusion in a smart city, and its representation using virtual reality. *Pers Ubiquitous Comput*. <https://www.scopus.com/inward/record.uri?eid=2-s2.0-85081906360&doi=10.1007%2Fs00779-020-01379-2&partnerID=40&md5=35d46673924bb038fc3f20008fa1d8e4>
87. Liu CH, Chen ZY, Zhan YF (2019) Energy-efficient distributed mobile crowd sensing: a deep learning approach. *IEEE J Sel Areas Commun* 37(6):1262–1276
88. Roberts R, Inzerillo L, Di Mino G (2020) Using UAV based 3d modelling to provide smart monitoring of road pavement conditions. *Information (Switzerland)* 11(12):1–24. <https://www.scopus.com/inward/record.uri?eid=2-s2.0-85097521577&doi=10.3390%2Finfo11120568&partnerID=40&md5=a1b02552799170e8174e3e17e2b9b4c2>
89. Sharma A, Singh PK (2021) UAV-based framework for effective data analysis of forest fire detection using 5G networks: an effective approach towards smart cities solutions. *Int J Commun Syst*. <https://www.scopus.com/inward/record.uri?eid=2-s2.0-85104642779&doi=10.1002%2Fdac.4826&partnerID=40&md5=ea4b0e4ced9414917bd8f366a3891979>
90. Dai MH, Su Z, Xu QC, Zhang N (2021) Vehicle assisted computing offloading for unmanned aerial vehicles in smart city. *IEEE Trans Intell Transp Syst* 22(3):1932–1944
91. Postolache O, Dobre OA (2020) TC-13-wireless and telecommunications in measurements - in action. *IEEE Instrum Meas Mag* 23(8):14–17
92. Xu HY, Xu XL, Xiao F (2021) Dubhe: a deep-learning-based B5G coverage analysis method. *Eurasip J Adv Signal Process* 2021(1).
93. Ilic D, Milosevic I, Ilic-Kosanovic T (2022) Application of unmanned aircraft systems for smart city transformation: case study Belgrade. *Technol Forecast Soc Chang* 176.
94. Moguel E, Conejero JM, Sánchez-Figueroa F, Hernández J, Preciado JC, Rodríguez-Echeverría R (2018) Towards the use of unmanned aerial systems for providing sustainable services in smart cities. *Sensors (Switzerland)* 18(1). <https://doi.org/10.3390/s18010064>
95. Talcott CL, Wu D, McCann JA, Kim M, Arkhipov DI, Venkatasubramanian N, Regan AC (2016) ADDSEN: adaptive data processing and dissemination for drone swarms in urban sensing. *IEEE Trans Comput* 66(2):1–1. <https://doi.org/10.1109/tc.2016.2584061>
96. Tripicchio P, Satler M, Dabisias G, Ruffaldi E, Avizzano CA (2015) Towards smart farming and sustainable agriculture with drones. In: *Proceedings - 2015 international conference on intelligent environments, IE 2015*, pp 140–143. <https://doi.org/10.1109/IE.2015.29>
97. Gallacher D (2017) Drone applications for environmental management in urban spaces: a review. *Int J Sustain Land Use Urban Plan* 3(4). <https://doi.org/10.24102/ijslup.v3i4.738>
98. Menouar H, Guvenc I, Akkaya K, Uluagac AS, Kadri A, Tuncer A (2017) UAV-enabled intelligent transportation systems for the smart city: applications and challenges. *IEEE Commun Mag* 55(3):22–28. <https://doi.org/10.1109/MCOM.2017.1600238CM>

99. Ortiz S, Calafate CT, Cano J-C., Manzoni P, Toh CK (2019) A UAV-Based Content Delivery Architecture for Rural Areas and Future Smart Cities. *IEEE Internet Computing*, 23(1), 29–36. <https://www.scopus.com/inward/record.uri?eid=2-s2.0-85058099072&doi=10.1109%2FIMC.2018.2884277&partnerID=40&md5=1e5cc4f8dc514840b776b76183bc3427>
100. Teng H, Dong M, Liu Y, Tian W, Liu X (2021) A low-cost physical location discovery scheme for large-scale Internet of Things in smart city through joint use of vehicles and UAVs. *Futur Gener Comput Syst* 118:310–326. <https://www.scopus.com/inward/record.uri?eid=2-s2.0-85099786711&doi=10.1016%2Fj.future.2021.01.032&partnerID=40&md5=5ba9d38b3f582b93c2098c40c6b7728f>

Elevation Data Acquisition Accuracy Assessment for ESRI Drone2Map, Agisoft Metashape, and Pix4Dmapper UAV Photogrammetry Software



Deepak Tyagi, Vishal Mishra, and Harshit Verma

Abstract Whether planning urban development, conducting a hydrological construction in different terrain conditions, or analyzing terrain features for oil and gas exploration: accurate elevation information is vital. Digital Terrain Model (DTM) and Digital Surface Model (DSM) is the elevation model that provides elevation information of terrain and earth features (object), respectively. This study aims to assess the elevation accuracy of some of the most preferred Uncrewed Aerial Vehicle (UAV) data processing software from ESRI, Pix4D, and Agisoft Photoscan. In this study, DJI Phantom 4 is used to collect 147 very high-resolution overlapped images in the selected study area (Department of Civil Engineering, IIT-Roorkee, India) at the defined height. Collected images are processed using all the selected platform elevation datasets, i.e. Digital Surface Model (DSM) is generated. Vertical elevation error is estimated by elevation profile and statistical comparisons of UAV-derived elevation in the DSM datasets. This study helps to select the best UAV data processing software for the project that requires high elevation accuracy in topographical mapping or urban object utilization.

Keywords Drone2Map · UAV · Pix4D · Agisoft photoscan

1 Introduction

The recent advancement and expansion of UAVs as remote sensing devices, as well as improvements in the miniaturization of equipment and data acquisition procedures, have resulted in a rising trend in this domain of photogrammetry and remote sensing [1]. Although UAV data acquisition technology is still in its beginning days of

D. Tyagi · V. Mishra (✉)
Esri India, Chennai, India
e-mail: vmishra1@ce.iitr.ac.in

H. Verma
Indian Institute of Technology Roorkee, Roorkee, India

research where it is not only struggling to become the matured photogrammetry technologically but also looking forwards to different governments for legal permissions. Despite this also utilization of UAV technology in precision farming, ecosystem studies, atmospheric investigation, disaster management and mitigation planning, the terrain in monitoring, geological and geophysical research, [2–5] utilities monitoring and management and many more continue to increase.

As the introduction of the UAV systems has also increased the acquisition speed in the field of 3D mapping [6], the current study specifically focuses on the elevation data acquisition, processing, and accuracy assessment. 3D information using UAVs is reconstructed using high-resolution overlapping images are used, which involves both the photogrammetric and computer algorithms based on the dense image matching technique. These algorithms find the matching points or features from the overlapping images and then calculate the 3D information pixel by pixel for the whole image. Nowadays, with the advancement in photogrammetric software, the complexity of handling this high-resolution dataset has decreased for the user. The advanced photogrammetry software is capable of handling various steps of images based 3D model by generating tie points [7–9], point cloud [10], DTMs, DSMs [11], Orthophotos, mesh models and so on. This development in this field has led to the development of new software platforms which are trying to make processing for the user to be simpler and automatic. The new methods for post-processing the data obtained are continuously under development with backing up the traditional approaches [12, 13 7]. The developed algorithms need to be tested and developed accordingly in order to provide the most accurate output. In the case of aerial images, using the traditional method to determine the accuracy is tested on two parameters firstly, on the high accuracy of point coordinate determination, and secondly, on the basis of 3D models generated by it. In the present study, experiments are performed to check the optimization of the Digital Surface Model developed by using different software platforms [14, 15]. The study involves the comparison between three well-known commercial software Agisoft Metashape, Drone2Map, and Pix4D [16]. This software is used to process the dataset of urban built-up areas. Based on the result generated, the accuracies of different software to identify different features was justified.

2 Study Area

Roorkee is a city in the Haridwar district of Uttarakhand, which lies on the banks of the Ganga canal. It has almost flat terrain situated at the Shivalik Hill range of The Himalayas with an average elevation of 268 m. Roorkee enjoys all the seasons, from summer to winter and monsoon, with an average rainfall of 1170 mm. Roorkee is also known for the Indian Institute of Technology Roorkee (IIT-R), which is one of the oldest Engineering College in India (Fig. 1). This institute has 21 academic departments which provide excellence in the field of engineering, humanities, applied sciences, social sciences, and humanities. The present study is focused on the Civil

Engineering Block of IIT-Roorkee. The study area is situated between $29^{\circ} 51.722'N$, $29^{\circ} 51.827'N$ to $77^{\circ} 54.084'E$, $77^{\circ} 53.843'E$, which covers a total area of 0.062 km^2 .

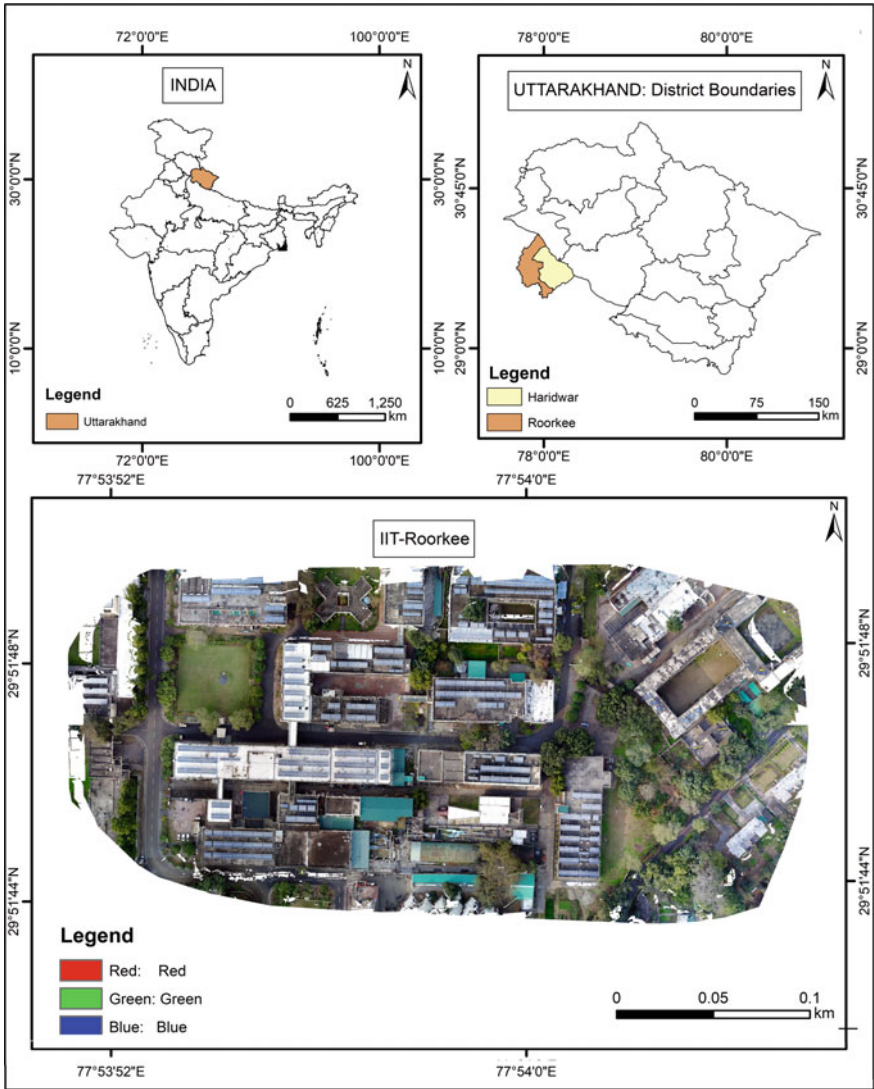


Fig. 1 Study Area

3 Devices Used, Data Acquisition and Software Used

For aerial data collection of images DJI Phantom 4 Pro was used. DJI Phantom 4 Pro is a Quadcopter that is one of the most advanced UAVs of DJI (Fig. 2a). The model of the camera embedded on the UAV was FCS310 with a 1" CMOS sensor with an effective pixel of 20MP, which provides images in three sizes i.e.: 5472 X 3648, 4864 X 3648, and 5472 X 3078. It can provide the images in three formats JPEG, DNG (RAW), and JPEG+DNG. These images can be captured using single as well as burst mode. To capture the image with less distortion, it has the camera attached to the gimbal that provides stabilization (pitch, roll, and yaw) with an angular vibration of $\pm 0.02^\circ$.

The flight plan was designed in Pix4D capture, which was provided to the UAV system. The flight was operated in fully automated mode to capture the images. To capture the data, a flight height of 100m was fixed. A set of a total of 147 images was captured, which were covered in a block of 11 strips, as shown in Fig. 2b. To get the maximum stereoscopy image, the flight planning was executed with 80% longitudinal and 70% lateral overlap. As per these overlaps, the flight took eleven strips to cover the whole area under study.

3.1 Commercial Photogrammetry Software Used

a. AgiSoft (Metashape) :

This is a standalone software that can perform photogrammetric processing of the digital images and can help to generate the 3D spatial data which can be used for GIS purposes. Agisoft is widely accepted worldwide among researchers and even with the little knowledge of stereo-photogrammetry process the data. Being commercial software algorithms used to process spatial data are not public but still many steps of the processing can be controlled and easily configured. Since

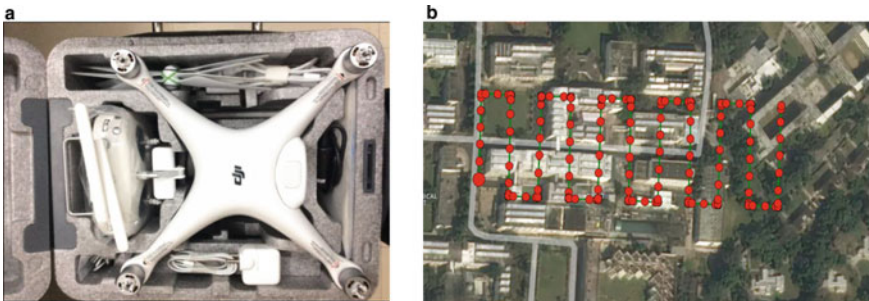


Fig. 2 a DJI Phantom 4Pro. b Flight Path

2010 this had been included in various studies where it had produced accurate and quality results.

b. Drone2Map:

This product is launched by ESRI 2016 which has simplified the drone image processing.

Drone2Map helps to convert raw drone imagery into the 3D spatial GIS data. This is one of the easiest to use software, which automated almost all the image processing work. One can create produce 2D and 3D products just in few clicks which can be used for analysis and visualization.

c. Pix4Dmapper:

This is an advanced photogrammetry software which can be used to produce 3D maps and 3D models using different types of raw images. This can produce 3D models using computer vision and photogrammetry algorithm from fisheye lens, DSLR, thermal, multispectral and RGB images.

4 Methodology

The workflow of the study is explained below in Fig. 3, which is elaborated in the following text. The initial part of the study is flight planning and data acquisition using the Uncrewed Aerial System. The collection of data was completed with the help of DJI Phantom 4 Pro this data.

These obtained data were processed using Agisoft, Drone2map and Pix4D to generate the DSM model. The initial step for image processing is the alignment of the images in their respective positions using the EXIF data embedded in images, which contains information regarding location and orientation parameters.

Then the tie points were analyzed from the overlapping images. These tie points collective from the whole image were termed as points cloud. The points cloud generated is classified on the basis of the difference in the elevation values and creates the DSM model. The user interface varies in terms of different software as well as in the method of creating; as in the case of Agisoft, manually classes need to be defined but the classes are automatically defined in the case of Pix4D and Drone2Map. The generated DSM from the three software were resampled at 2 cm so a comparative study between them can be conducted. DSM was compared on two bases, first based on the elevation profile and secondly based on statistical analysis.

5 Results and Discussion

UAV-derived UAV map using Agisoft Metashape. The elevation range varies from 250.84 m to 281.722 m. As shown in Fig. 4a. UAV derived UAV map using Drone2Map. The elevation value varies from 251.974 m to 276.889 m. As shown in

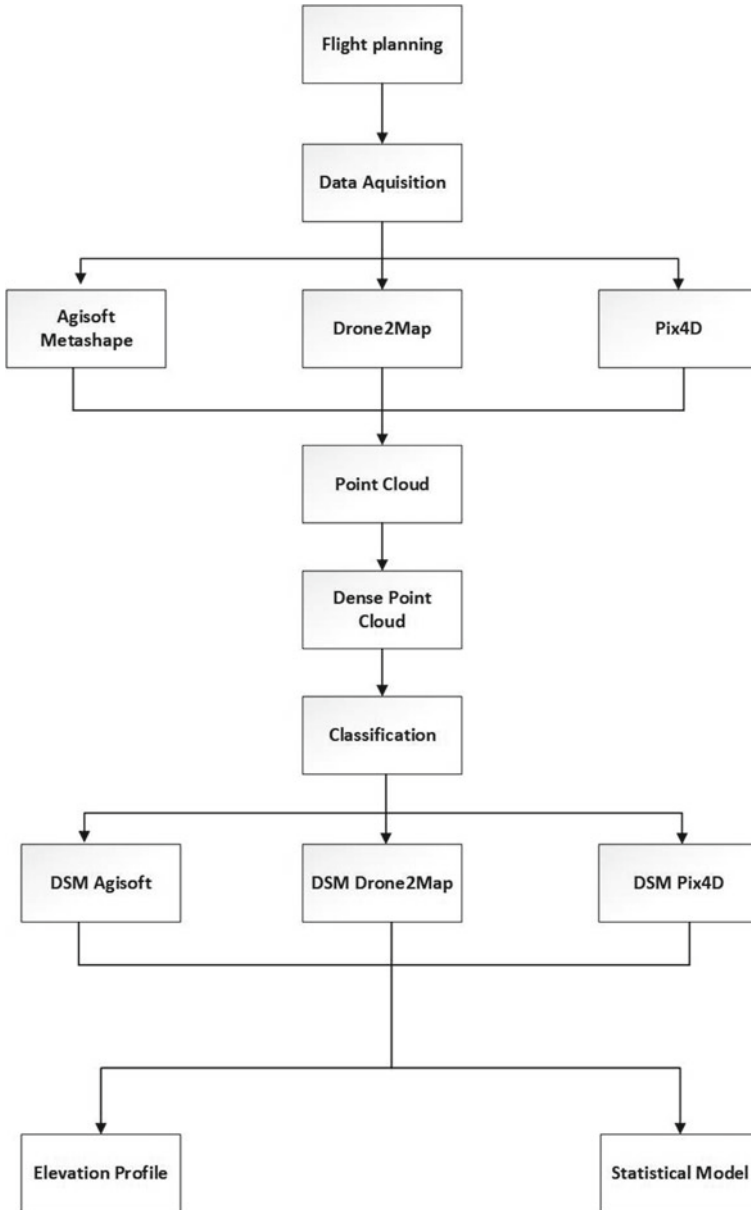


Fig. 3 Methodology of the study

Fig. 4b. UAV derived map using Pix4D. The elevation value varies from 251.984m to 279.026m. As shown in Fig. 4c.

DSM generated using these three software (Agisoft Photoscan, Pix4D mapper and Drone2map) were assessed on the basis of relative accuracy. Two ways are established for depicting the evaluation of results from these DSMs. First, elevation profiles are created for the different feature elements such as roads, buildings and trees over three surface models to visualize the variation. The basic statistical analysis is done on the subtracted DSM for evaluation. Basic comparison parameters for assessment are the mean error and standard deviation of those subtracted DSMs.

In order to analyze the elevation information generated by different software, the DSM model created by them was taken into consideration. For this purpose relative study of the DSM was conducted. An automatic procedure was adopted to create the DSM from Pix4D and Drone2Map. While in the case of Agisoft Photoscan, initially, classification of the point cloud was done to differentiate the points of the varying objects, and then DSM was generated from the classified points cloud.

5.1 Relative Elevation Profile Assessment

The first visual interpretation of the DSMs generated depicts that this software was not able to create DSM for the whole area at once. It had some gaps left, which maybe be due to the less number of overlapping images and poor texture at the corner of the images. Now the output of the DSM model generated was compared by extracting elevation profiles over different land cover types such as trees, buildings, and roads.

1. As per the graph shown below in Fig. 5a, Agisoft gives a proper building feature edge rather than Drone2Map and pix4d Mapper, which has two dips in between the data that is due to a lack of points extracted for surface modeling on the surface of the building feature.
2. In comparing road features from DSM generated from these three software, it can be deduced as there is a vertical shift in the elevation of road surface generated from Agisoft and Drone2Map or Pix4d mapper, which might be possible due to different algorithms used for extracting elevation data from the image. Being at the same level, only Pix4D had some abrupt elevation points near the ending points, while Drone2Map was able to properly delineate the elevation profile. As shown in Fig. 5b.
3. In vegetated areas, it is accepted to have a small height difference at the crown. From the graph shown below in Fig. 5c, both Agisoft and Pix4D Mapper shows large elevation dips over the canopy regions, which proves Drone2Map's DSM better.

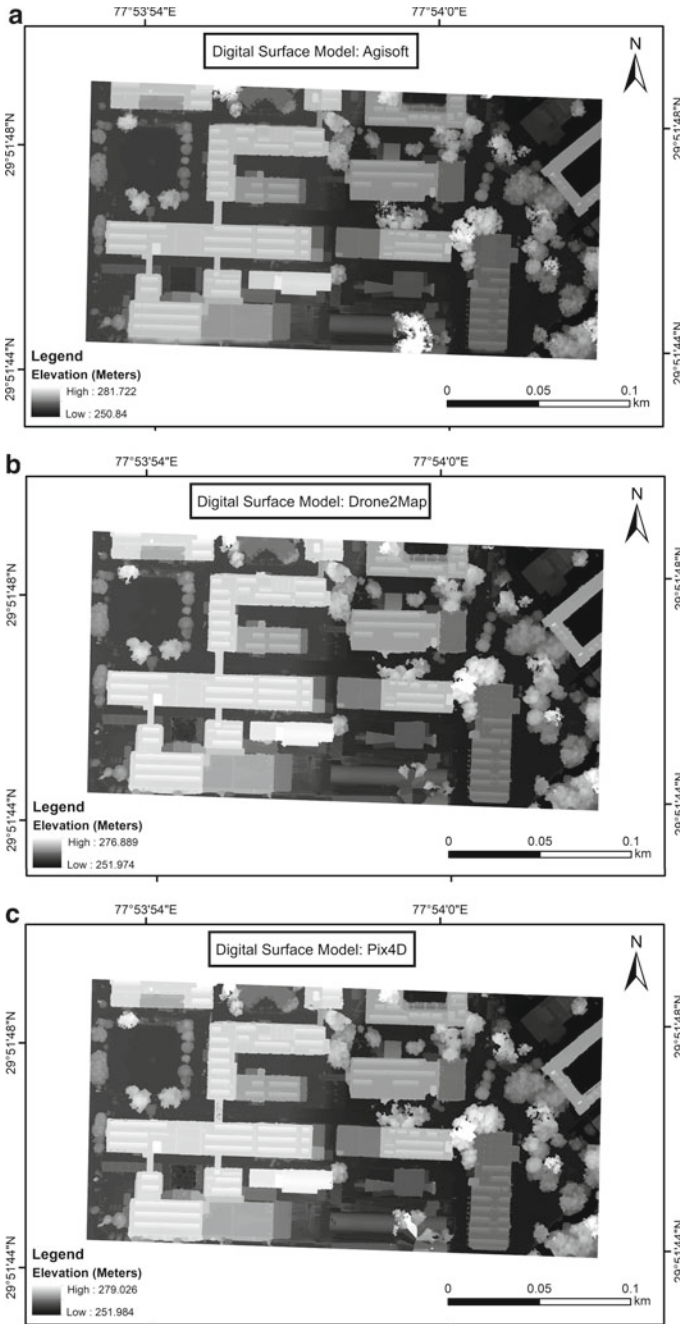


Fig. 4 a DSM Agisoft. b DSM Drone2Map. c DSM Model Pix4D

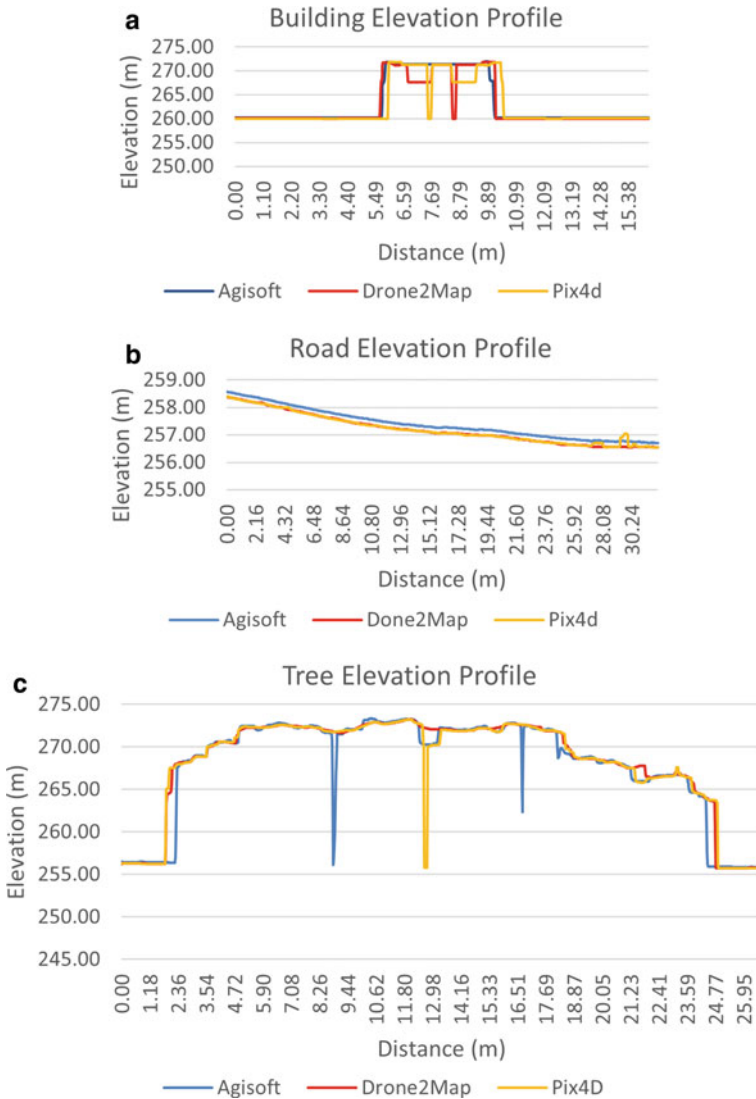


Fig. 5 a Building elevation profile. b Road elevation profile. c Tree elevation profile

5.2 Relative DSM Comparison

The next relative comparison was performed based on the statistical analysis of the DSM model. It involves the comparison of the mean error of DSMs and standard deviation. The lowest values of the mean error were obtained near Agisoft and Pix4D, as shown in Table 1. The values of the mean error are near 0, which indicates that there is no bias associated with the mean error of the DSM generated. At the same time,

Table 1 Statistics of DSM difference in the flat region

Software	Min	Max	Mean Error	SD
D2M-Agisoft	-22.9533	23.2715	-0.0543	2.0289
D2M-Pix4D	-19.9310	20.1488	-0.06405	1.3320
Pix4D-Agisoft	-22.4667	23.4980	0.0097	1.9102

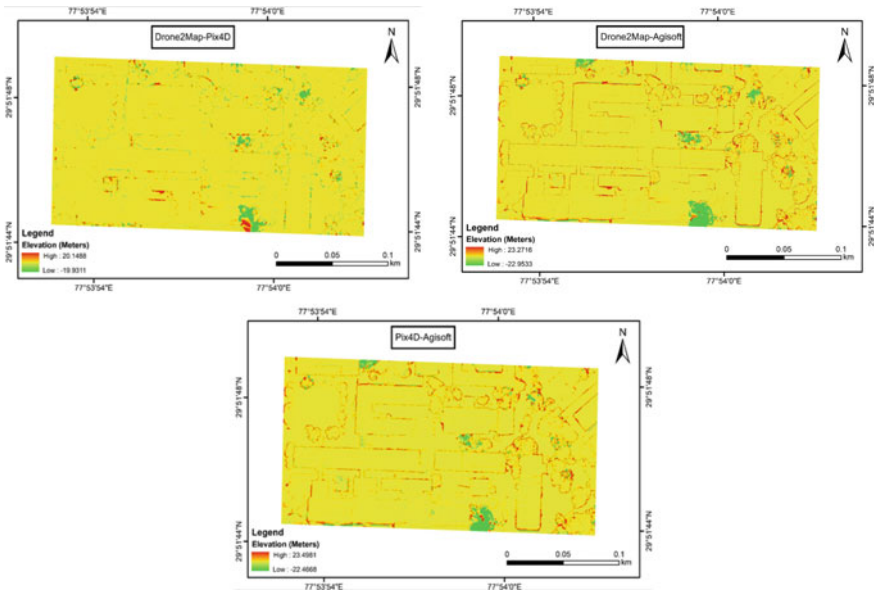


Fig. 6 a Drone2Map—Pix4D. b Drone2Map—Agisoft. c Pix4D—Agisoft

there is a considerable difference between Drone2Map and Pix4D points towards the slight difference in the point cloud densities or towards the level of smoothing applied by Drone2Map. Comparison between the standard deviation of subtracted DSM shows that the results of Agisoft and Drone2Map are pretty similar as far as the elevation range of most of the data is concerned (Fig. 6).

6 Conclusion

The study was conducted to find the processing capability of different commercial photogrammetric software platforms using High-Resolution Images. This processing involves the capability of UAV photogrammetry and computer vision to identify the featurere constructing 3D geometry. The assessment of the output generated was done in terms of various visual and statistical metrics. While comparing in

terms of visual data, a vertical profile was calculated over different features in which Done2Map was able to create a more accurate DSM over the tree canopy while the other two software at the same time had dips which can be denoted as the lack in point cloud generation. Even in terms of the elevated road, Drone2Map was able to provide the proper elevation profile. Other than in-built parameters, there are several other factors such as hardware configuration, terrain conditions, and many others that also affect the quality of DSM generated using this photogrammetric software. The quality of output generated by each software can be enhanced by changing the parameters to get better results as per the need of the project.

References

1. Anuj Tiwari KJ (2018) No Title. *Int J Sci Res Publ* 442–446. <http://citeseerx.ist.psu.edu/viewdoc/download?doi=10.1.1.657.1278&rep=rep1&type=pdf#page=443>
2. Colomina I, Molina P (2014) *ISPRS journal of photogrammetry and remote sensing unmanned aerial systems for photogrammetry and remote sensing: a review*. *ISPRS J Photogramm Remote Sens* 92:79–97. <https://doi.org/10.1016/j.isprsjprs.2014.02.013>
3. Metrology V, Eisenbeiss H, Zhang L, Sensing R (n.d.) Comparison of DSMs generated from mini UAV imagery and terrestrial laser scanner in a cultural heritage application, pp 90–96
4. Remondino F, Barazzetti L, Nex F, Scaioni M, Sarazzi D (2011) UAV photogrammetry for mapping and 3d modeling – current status and future perspectives XXXVIII(September) 14–16
5. Tiwari A, Sharma S, Jain K (2017) Emerging opportunities and challenges in UAV enabled Earth observations and remote sensing technology (December)
6. Tiwari A, Dixit A (2015) Unmanned aerial vehicle and geospatial technology pushing the limits of development. *Am J Eng Res (AJER)* 4(01):16–21. www.ajer.org
7. Barazzetti L, Remondino F, Scaioni M, Brumana R, Adjustment B, Vehicles UA (2010) Fully automatic uav image-based sensor orientation
8. Leuven KU, Wetenschappen FT, Esat D, Psi A (1999) Self-calibration and metric 3D reconstruction from uncalibrated self-calibration and metric 3D reconstruction from uncalibrated
9. Strecha C, Fua P (2010) Dynamic and scalable large scale image reconstruction. *IEEE Comput Soc Conf Comput Vis Pattern Recognit* 2010:406–413. <https://doi.org/10.1109/CVPR.2010.5540184>
10. Ye N, Leeuwen L. Van, Nyktas P (2019) Analysing the potential of UAV point cloud as input in quantitative structure modeling for assessment of woody biomass of single trees. *Int J Appl Earth Obs Geoinformation* 81(April):47–57. <https://doi.org/10.1016/j.jag.2019.05.010>
11. Wu Z, Ni M, Hu Z, Wang J, Li Q, Wu G (2019) Mapping invasive plant with UAV-derived 3D mesh model in mountain area — a case study in Shenzhen Coast, China. *Int J Appl Earth Obs Geoinformation* 77(January):129–139. <https://doi.org/10.1016/j.jag.2018.12.001>
12. Agency ES (2006) Helicopter UAV for photogrammetry and rapid response, pp 2–5
13. Engel A, Teichert B (n.d.) The photogrammetric potential of low-cost uavs in forestry and agriculture
14. Alidoost F, Arefi H (2017) Comparison of UAS-based photogrammetry software for 3d point cloud generation : a survey over a historical site, IV(October), 14–15
15. Sona G, Pinto L, Pagliari D (2014) Experimental analysis of different software packages for orientation and digital surface modelling from UAV images (2011). <https://doi.org/10.1007/s12145-013-0142-2>
16. Lindstaedt M, Kersten TP (2019) Investigations into the quality of image-based point clouds from UAV imagery investigations into the quality of image-based point clouds from UAV imagery (June). <https://doi.org/10.5194/isprs-archives-XLII-2-W13-539-2019>

Characterization of Urban Vegetation from an Unmanned Aerial Vehicle (UAV) Image



Minakshi Kumar and Shefali Agrawal

Abstract Advances in UAV technology and processing made it feasible to obtain ultra high-resolution (UHR) imagery and three-dimensional (3D) data, which can be efficiently used for urban forestry, green space mapping, green infrastructure planning and monitoring with high accuracy and at a cost-effective manner. The conventional feature extraction image analysis techniques fail on UHR UAV Images as the geometry of features is very well defined and characterized by a very heterogeneous texture. The approach required for such ultra-high-resolution images should support the cognitive analysis that we use in visual image interpretation, which is a form of knowledge-driven analysis incorporating shape, texture, pattern and contextual information. The present study aims at delineating and extract vegetation types and height estimation using UHR UAV images in parts of urban slums and dense urban environments. The methodology involved utilizes a multiresolution image segmentation to create basic image objects at a scale that allows for homogenous object extraction while maintaining variability. Normalized Differential Green Vegetation (NDGV) and Visible-Band Difference Vegetation Index (VDVI) band ratios are computed by combining the red, green and blue (RGB) spectrum of the UHR image. Digital Surface Model (DSM) and Digital Terrain Model (DTM) were input to the canopy height model (CHM) for height estimation and refinement of different vegetation categories. Crown shape parameters and texture parameters are tested and compared for vegetation characterization and categorization. Results show the 3D data set derived from UAV UHR imagery's potential in detection of treetops, delineation of vegetation and its categorization.

Keywords Multiresolution segmentation · Texture parameters · Ultra high-resolution images · Canopy height model

M. Kumar (✉) · S. Agrawal
Indian Institute of Remote Sensing (IIRS), Indian Space Research Organisation (ISRO),
Dehradun, India
e-mail: minakshi@iirs.gov.in

S. Agrawal
e-mail: shefali_a@iirs.gov.in

1 Introduction

The potential of using satellite image data for forest inventory, mapping trees outside the forest (TOF), and individual tree crown delineation is a well-established methodology. The accurate characterisation of vegetation type distribution in the forest, as well as non-forested areas, is an important task for forest management and vegetation research. In recent times, UAVs have been used experimentally in a large number of forestry applications. UAVs are an easy-to-use, low-cost tool for remote sensing as compared to manned aircraft. Since UAVs can fly near canopies and acquire ultra-high-resolution images with a spatial resolution of a few centimetres, very detailed features, for example, the tree features at the leaf level can be seen. Hence it is possible to map various features like vegetation with the use of simple RGB digital images facilitating cost-effective monitoring and mapping with broad application potential [1]. Identifying individual trees, mapping, discriminating between species and quantifying individual plants requires specific acquisition parameters and processing approaches [2–4] using remote sensing. Very high-spectral resolution satellite data have been successful in the identification of tree species, however, ultra-high spatial resolution data from UAVs has more potential to be a feasible tool for individual feature extraction and species determination. In forest inventories, individual tree detection and identification is a desirable product [5]. A 3-D data set derived from UAV imagery representing the altitude, the difference between the ground level and the top of the vegetation referred to as CHM has gained much attention in recent years (Fujimoto et al., 2019). The difference between DSM and DTM known as a normalized digital surface model (n-DSM) is the widely used method in height estimations [6] that have utilized DEM and n-DSM for refining the segmentation results. In addition, its potential has been demonstrated in the detection of tree tops, estimation of parameters and delineation of tree crowns. Reference [7] used CHM for the separation of ground pixels from vine rows but concluded that their elevations were not quite following the actual height of the vines due to a smoothing effect of the reconstructed CHM. However, further comparison between CHM and a vigour map obtained from normalized difference vegetation index (NDVI) values showed a good correlation.

Even though more fine details in a UHR UAV Image, obtaining meaningful information remains challenging and relies mainly on visual interpretation. This manual extraction is time-consuming and becomes unfeasible in larger areas. Additionally, pixel-based image analysis techniques have limitations in processing such UHR datasets. The conventional techniques also fail on UHR UAV Images as the geometry of features is very well defined, and characterized by a very heterogeneous texture. As the information content of the imagery increases with spatial resolution, the classification accuracy seems to decrease. This can be attributed to the fact of increasing within-class variability inherent in more detailed, higher spatial resolution data. In such images, grouping pixels to form image objects or segments is a way to analyse such high-resolution data. Additional spectral, structural and textural information

contained in an object can also be taken into account [8]. Object-based image analysis (OBIA) techniques have demonstrated great potential to automatically extract information from very high-resolution images [9, 10] including those captured by UAVs [11, 1] extracted several tree crowns from the three-dimensional model and segmentation of RGB Images obtained by the UAV. [11] used simple Linear Iterative Clustering (SLIC) segmentation and random forest classification method for tree canopy extraction from the ultra-high resolution ortho-image derived from UAV platforms. [12] developed a methodology for individual tree species identification based on crown shape parameters using spaceborne high-resolution imagery. However, crown measurements in satellite imagery are more difficult than on UAV images since trees show more structural detail at higher resolutions and hence it would be more viable in a UHR UAV image.

An attempt has been made in this present study to delineate and extract vegetation types and height estimation using UHR UAV images in parts of an urban slum environment. The methodology utilizes an OBIA approach where multiresolution image segmentation is performed to create basic image objects. Different Visible band ratios computed from the RGB UHR image and CHM are evaluated for height estimation and refinement of different vegetation categories. Crown shape parameters and texture parameters are tested and compared for vegetation characterization and categorization.

2 Materials and Methods

2.1 Study Area Description

The methodology was tested on two datasets. The dataset used was the urban slum area of Chingrajpara, Bilaspur, and Chhattisgarh, India (Fig. 1). The ortho mosaic, Digital Surface Model and Digital Terrain model were generated from a set of 85 images captured at a ground sampling distance of 2.19 cm from a height of 150 m covering a total area of 0.13 km² with DJI Phantom 4pro and DJI Inspire 2 (Fig. 2a–c). The images were processed using Pix4Dmapper Pro version 4.3.31. The ortho mosaic and DSM were provided at 2 cm resolution and DTM at 22 cm.

2.2 Vegetation Crown Delineation

Firstly, the pixels in the image are converted into Image objects by a multiresolution segmentation algorithm. Various scale parameters are tested to create the basic image objects at a scale that allows for objects to be relatively homogeneous whilst capturing the full scene variability. The next processing step required the first level classification for vegetation. A band ratio can best discriminate green vegetation

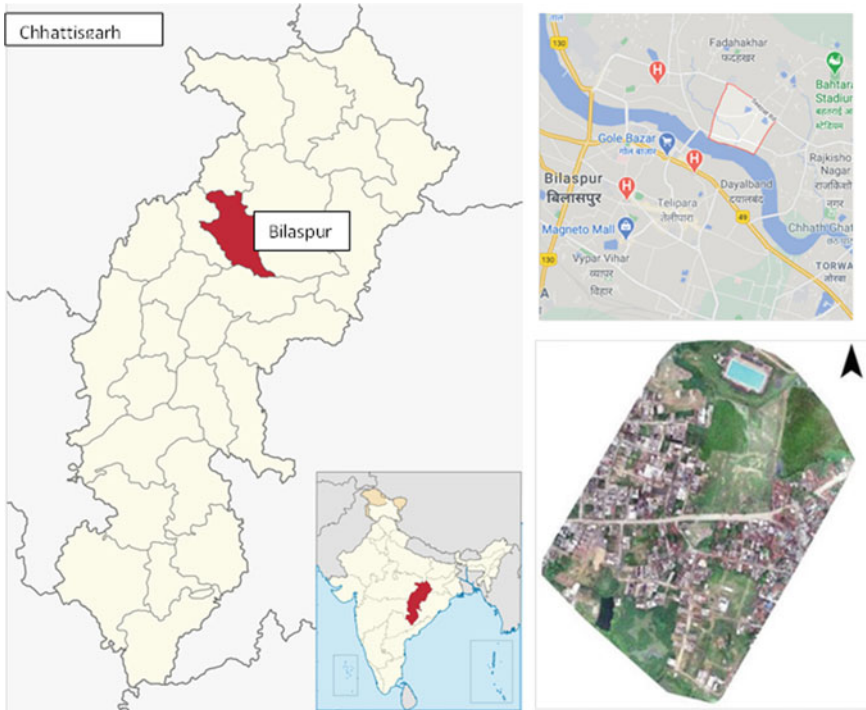


Fig. 1 Location map of study area

using deviation from the normalised vegetation index. Several vegetation indices in the Visible Spectra Region developed by [13] were computed. This can be attributed to the fact that data acquisition through UAV is mainly in the visible (RGB) bands due to the easy availability of high-resolution lightweight cameras at a low price.

The indices evaluated were

$$\text{Green Vegetation (GV)} = G/R. \quad (1)$$

$$\text{Normalized Green Differential vegetation (NGDV)} = \frac{\text{Green} - \text{Red}}{(\text{Green} + \text{Red})}. \quad (2)$$

$$\begin{aligned} &\text{Visible Band Difference Vegetation Index (VDVI)} \\ &= \frac{(2 * \text{Green} - \text{Red} - \text{Blue})}{(2 * \text{Green} + \text{red} + \text{blue})}. \end{aligned} \quad (3)$$

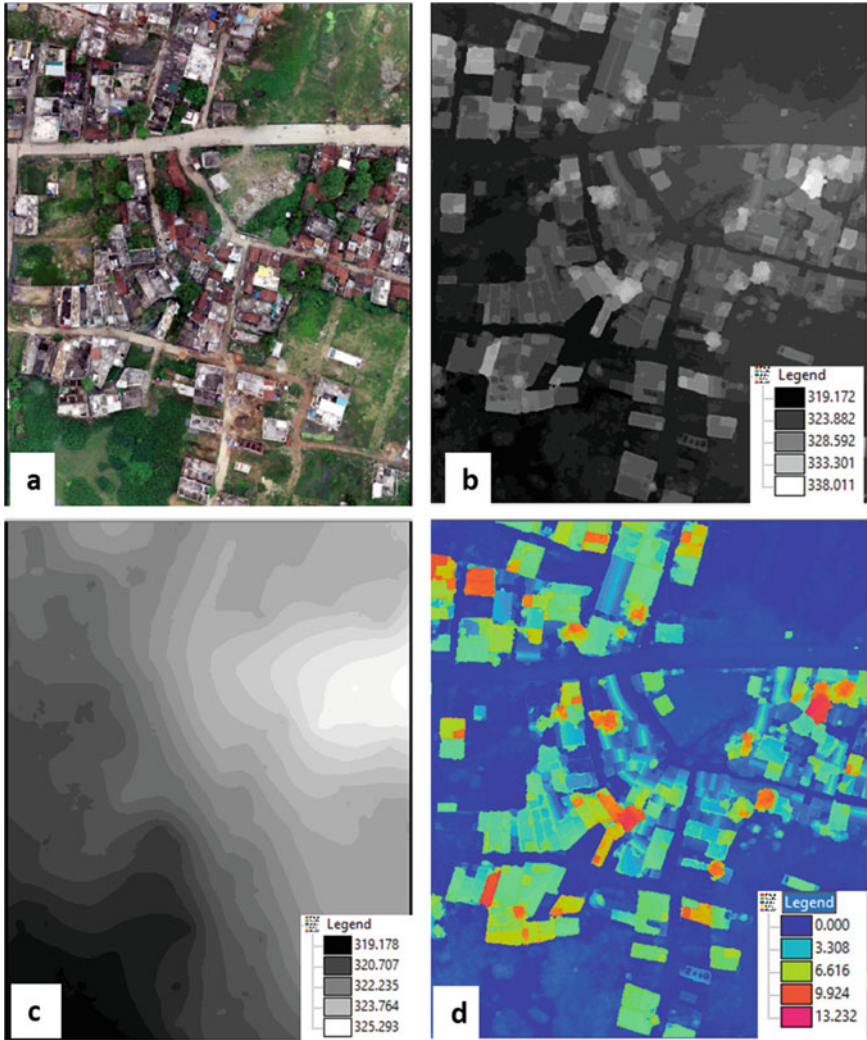


Fig. 2 a RGB Ortho Image, b Digital Surface Model (DSM), c Digital Terrain Model and d Normalised Surface Model(nDSM) for the study Area

2.3 *nDSM or Canopy Height Model (CHM) Creation*

The topmost crown part of a tree inside the forest is known as the canopy. The tree height above the ground may be called CHM [5]. The UAV images are processed to generate the DSM and DTM for the study which can be used in the estimation of CHM. A DSM is a representation of the earth’s surface along with the features on top of it, such as buildings and trees while a DTM represents the bare earth surface with

all protruding objects removed. A CHM then is the depiction of the highest point in a tree from the base ground landscape. A normalized DSM (nDSM) or a CHM can be then obtained by subtracting DTM from the DSM. The nDSM for the study is presented in Fig. 2d.

$$\text{CHM} = \text{DSM} - \text{DTM}. \quad (4)$$

3 Texture Parameters

Texture analysis was developed as an image analysis method for medical images [14]. The texture is a description of the spatial distribution of tonal intensities, making it a useful parameter in the segmentation and classification of similar regions. Haralick texture features proposed by [15] are calculated from a grey level dependency matrix called Gray level co-occurrence matrix (GLCM), which is a common method to represent image texture. The matrix is constructed by counting the co-occurrence of a pair of neighbouring grey levels in the image. It is a square matrix of size $N \times N$ where N represents the number of grey levels in the window. The diagonal elements in the GLCM represent pixel pairs which occur together in combination. The GLCM is converted to a normalized GLCM which represents the frequency or probability of each pair. It is also common to add GLCMs from opposite neighbours (all directions) before normalization. The texture description Contrast (CON), Angular Second Moment (ASM), Entropy, Homogeneity, Correlation etc. are then derived from the normalised GLCM. The texture feature “contrast” has a low value for elements with similar gray level values and elements with dissimilar gray levels are given a high weight. Computation of ASM use each element of GLCM as a weight for itself. High values of ASM indicate that the window when the window is very orderly that is when co-occurrence frequency is concentrated in a few places in the GLCM (the main diagonal direction). The measure CON also known as the sum of squares variance has a higher weight for the GLCM element that is far from the main diagonal and hence contrast increases with the increase in the difference between neighbouring pairs. Entropy is a measure of the randomness of pixel pair association. It has different values for edges with different characteristics [16]. Though the above GLCM textures were developed for pixel-based analysis, it is very useful in OBIA for remote sensing data [17–19].

4 Geometrical Parameters

For individual vegetation discrimination, distinctive geometrical shape parameters are used to measure the outlines of the identified canopy. They are form factor that varies with surface irregularities, compactness, aspect ratio (also called eccentricity),

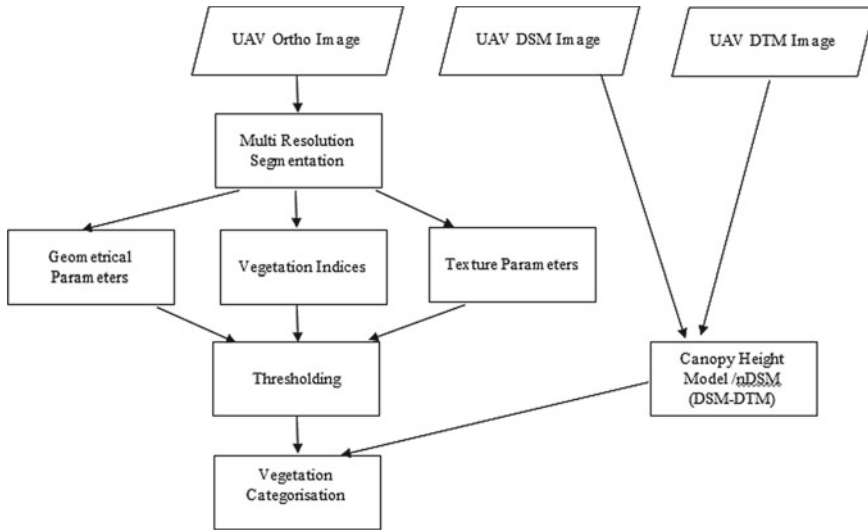


Fig. 3 Methodology flow diagram

and fractal dimension (FD) for a delineated crown boundary is calculated by using the crown perimeter/area rate, The Asymmetry feature compares an image object with an approximated ellipse around the given image object. The calculation is based on the variance in x-direction and y-direction, which results in a feature value, which increases with an increasing image object asymmetry. The Shape index is a measure of overall shape complexity. The feature value is 1 for compact objects (i.e. square or almost square) and increases without limit for more irregular shapes. The overall methodology of the study is illustrated in Fig. 3.

5 Results and Discussion

Figure 4a presents the subset of the image used to develop discrimination rules. The first step involved Multi Resolution Segmentation. The RGB Image is segmented at different scale parameters ranging from 70 to 100 to obtain optimum segments of homogenous vegetation features yet separate them from other features. An experiment is done by adding the DSM and the DTM layer for segmentation, which greatly improved the segmented features then segmenting the RGB alone.

Three vegetation indices GV, NGDV and VDVI (Fig. 4b and c) using the visible bands of the RGB ortho image are computed. The range of VDVI for Vegetation features ranged from 0.18 to 0.345. The NGDV ranged between 0.15 to 0.64 and the GV ranged between 1.36 to 4.62. The CHM values varied between 0.03 and 12.47 m for the vegetation features. There are two categories of heightened trees, one above 8m others between 2.5 m to 8 m. The shrubs had a height between 1 to 2.5 m and the

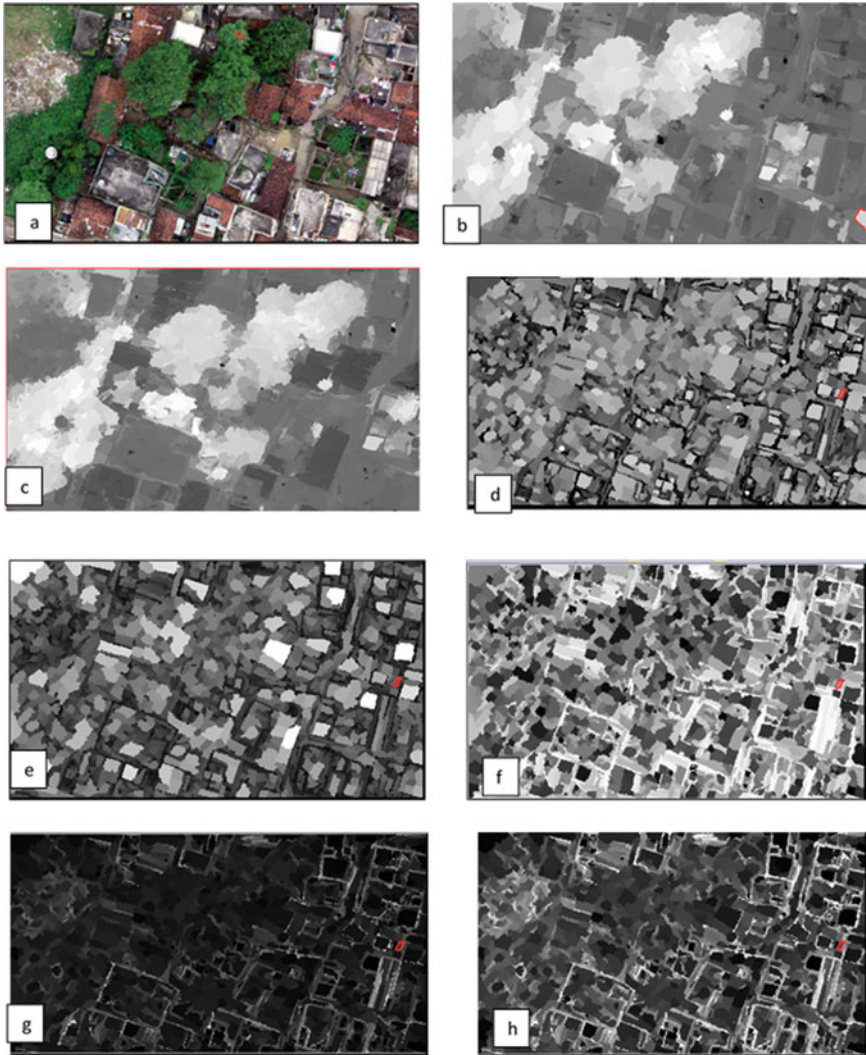


Fig. 4 a RGB Ortho, b NGDV, c VDVI, d Aspect, e Form Factor, f Asymmetry, g Shape Index and h Fractal Dimension

scrub vegetation was mainly less than 1 m. The Geometrical features Aspect, Form factor, Asymmetry, Shape-index and Fractal dimension are illustrated in Fig. 4d–h. All the three Vegetation indices were useful in discrimination and anyone can be used alternatively (Fig. 5a). Out of the geometrical parameters: Formfactor, Aspect, Asymmetry and Fractal Dimension were useful in discrimination largely (Fig. 5c). Out of the four texture parameters, GLCM Angular Second Moment was the most useful (Fig. 5b).

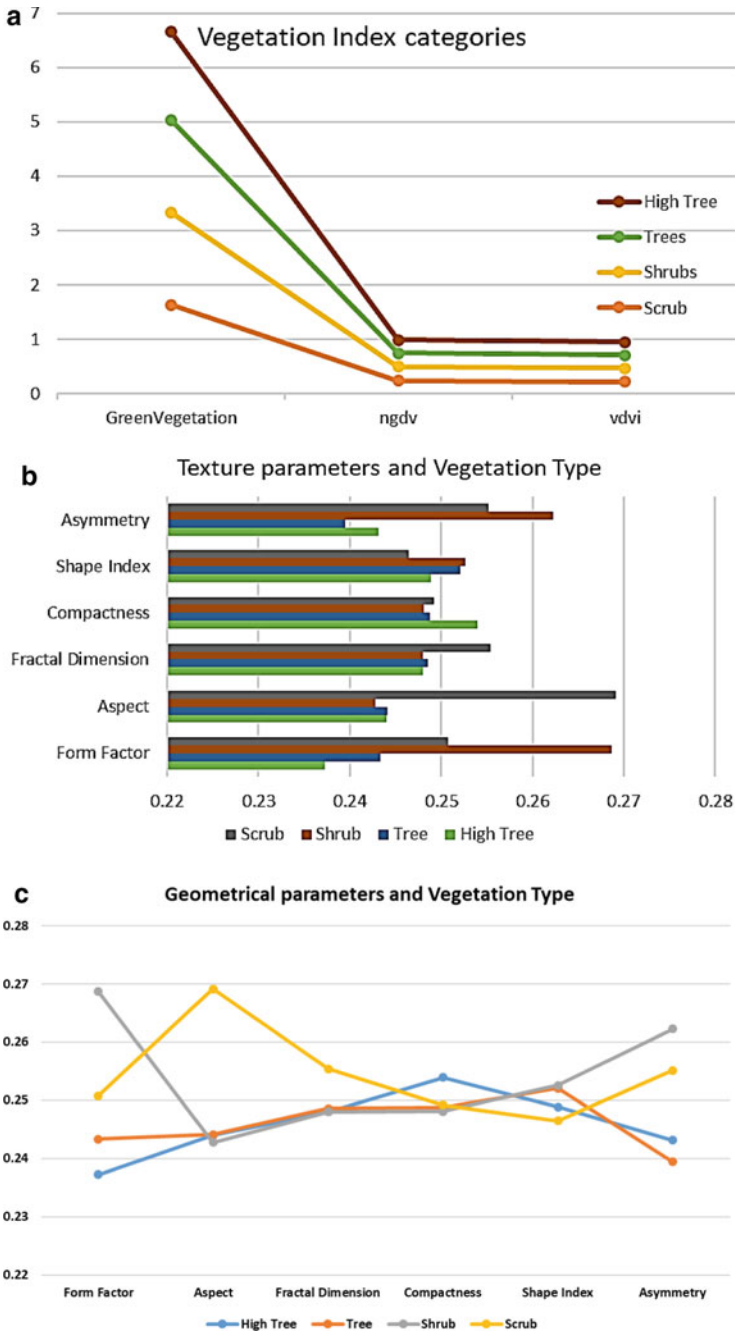


Fig. 5 a Vegetation indices. b Texture parameters and c Geometrical parameters in discriminating Vegetation type

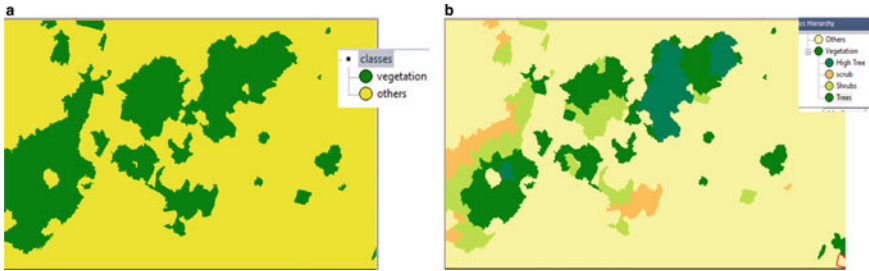


Fig. 6 a Level 1 classified image. b Vegetation type classification results

There were some creepers or vine plants in the study area over the slum house's sloping roofs. The vegetation indices value for such vine plants were high and due to the height, they have been classified into shrubs or trees. The level 1 classified results are presented in Fig. 6a and vegetation type classification in Fig. 6b

6 Conclusions

The capability to delineate individual tree crowns and vegetation types automatically would be a major step for applications of remote sensing in ecology, forestry and land management. Our work demonstrated vegetation delineation techniques that integrate both structural, textural and spectral characteristics to effectively delineate mixed vegetation classes. In this article, we presented an Object-based image analysis approach which integrated visual band indices along with geometrical and Textural features to categorise vegetation in slum areas using a UAV UHR Imagery. The detection and discrimination of individual vegetation types in ultra and very high-resolution images still represent a challenge for the remote sensing community. This study can contribute to developing a methodology for more detailed inventories of these environments by providing valuable data on trees to facilitate their management and monitoring.

References

1. Onishi M, Ise T (2021) Explainable identification and mapping of trees using UAV RGB image and deep learning. *Sci Rep* 11(1):1–15. <https://doi.org/10.1038/s41598-020-79653-9>
2. Baena S, Moat J, Whaley O, Boyd DS (2017) Identifying species from the air: UAVs and the very high-resolution challenge for plant conservation. *PLoS ONE* 12(11):1–21. <https://doi.org/10.1371/journal.pone.0188714>
3. Khadanga G, Jain K (2020) Agriculture parcel boundary detection from remotely sensed images. In: *Proceedings of 3rd international conference on computer vision and image processing*. Springer, Singapore, pp 307–312

4. Kumar M, Roy PS (2013) Utilizing the potential of world view -2 for discriminating urban and vegetation features using object-based classification techniques. *J Indian Soc Remote Sens* 41(3). <https://doi.org/10.1007/s12524-012-0257-9>
5. Miraki M, Sohrabi H, Fatehi P, Kneubuehler M (2021) Individual tree crown delineation from high-resolution UAV images in a broadleaf forest. *Eco Inform* 61(March):101207. <https://doi.org/10.1016/j.ecoinf.2020.101207>
6. Shukla A, Jain K (2020) Automatic extraction of urban land information from unmanned aerial vehicle (UAV) data. *Earth Sci Inf* 13(4):1225–1236
7. Matese A, Di Gennaro SF, Berton A (2017) Assessment of a canopy height model (CHM) in a vineyard using UAV-based multispectral imaging. *Int J Remote Sens* 38(8–10):2150–2160. <https://doi.org/10.1080/01431161.2016.1226002>
8. Tiwari PS (2009) Potential of IRS P-6 LISS IV for agriculture field boundary delineation. *J Appl Remote Sens* 3(1):033528. <https://doi.org/10.1117/1.3133306>
9. Khatriker S, Kumar M (2018) Building footprint extraction from high-resolution satellite imagery using segmentation. *Int Arch Photogramm Remote Sens Spat Inf Sci-ISPRS Arch* 42(5):123–128. <https://doi.org/10.5194/isprs-archives-XLII-5-123-2018>
10. Kumar M, & Bhardwaj A (2020) Building extraction from very high-resolution stereo satellite images using OBIA and topographic Information. In: The 3rd international electronic conference on geosciences, December, 1–6. <https://sciforum.net/manuscripts/8908/manuscript.pdf>
11. Adhikari A, Kumar M, Agrawal S, Raghavendra S (2020) An integrated object and machine learning approach for tree canopy extraction from UAV datasets. *J Indian Soc Remote Sens* 2. <https://doi.org/10.1007/s12524-020-01240-2>
12. Kim C, Hong S-H (2008) Identification of tree species from high-resolution satellite imagery by using crown parameters. *Remote Sens Agric Ecosyst Hydrol* X 7104:71040N. <https://doi.org/10.1117/12.800074>
13. Xue J, Su B (2017) Significant remote sensing vegetation indices: a review of developments and applications. *J Sens*. <https://doi.org/10.1155/2017/1353691>
14. Brynolfsson P, Nilsson D, Torheim T, Asklund T, Karlsson CT, Trygg J, Nyholm T, Garpebring A (2017) Haralick texture features from apparent diffusion coefficient (ADC) MRI images depend on imaging and pre-processing parameters. *Sci Rep* 7(1):1–11. <https://doi.org/10.1038/s41598-017-04151-4>
15. Haralick RM, Dinstein I, Shanmugam K (1973) Textural features for image classification. *IEEE Trans Syst Man Cybern* SMC-3(6):610–621. <https://doi.org/10.1109/TSMC.1973.4309314>
16. Hall-Beyer M (2017) Practical guidelines for choosing GLCM textures to use in landscape classification tasks over a range of moderate spatial scales. *Int J Remote Sens* 38(5):1312–1338. <https://doi.org/10.1080/01431161.2016.1278314>
17. Kumar M, Srivastav SK, Garg PK (2017) A support vector machine approach to object-based image analysis for feature extraction from high-resolution images. In: 38th Asian conference on remote sensing - space applications: touching human lives, ACRS 2017
18. Tabib Mahmoudi F, Samadzadegan F, Reinartz P (2013) Object-oriented image analysis based on a multi-agent recognition system. *Comput Geosci* 54:219–230. <https://doi.org/10.1016/j.cageo.2012.12.007>
19. Tiwari PS, Pande H, Kumar M, Dadhwal VK (2009) Potential of IRS P-6 LISS IV for agriculture field boundary delineation. *J Appl Remote Sens* 3(1). <https://doi.org/10.1117/1.3133306>

Environmental Gaseous Sensing Using Sniffer Drone for Urban Development Control



Norzailawati Mohd Noor and Mazlan Hashim

Abstract This study aims to present an environmental gaseous sensing analysis using drones in urban development control for the industrial area. The data collection method is based on the possibility of gas dispersion in a heavy industrial area in Klang, Malaysia, to the neighbouring land uses. The sniffer has carried five types of gaseous sensors and is mounted in DJI Matrice 100 quadcopter UAV. However, for this study, we analysed two significant gases related to an industrial area consisting *Carbon dioxide* (CO_2) and *Hydrocarbon* (C_xH_y). The information has been collected in two modes of time which are in the early morning and afternoon. The data were mapped and analysed with a vector layer to identify whether it breaches concentration limits for gases collected. The finding stated that the morning concentration reading is denser compared to the afternoon. Results show that CO_2 and C_xH_y are still under control and minimise the risk for the local population. However, the safety precaution should be undertaken since gas dispersion's future potential would go beyond and affect the surrounding activities. In conclusion, this study shows the UAV's potential as one of the best mechanisms to monitor the environmental effect. Simultaneously, there is a need to review existing urban development control since climate change and sustainability are linked through their interaction in industries, and their surrounding land uses.

Keywords Environmental aseous · Sniffer drone · Industrial · Land use and urban planning

N. Mohd Noor (✉)

Urban and Regional Planning Department, Kulliyah of Architecture and Environmental Design, International Islamic University of Malaysia, Kuala Lumpur, Malaysia

e-mail: norzailawati@iium.edu.my

M. Hashim

Research Institute for Sustainable Environment (RISE), Bangunan Canselori Sultan Ibrahim, Universiti Teknologi Malaysia, Aras 2, Kuala Lumpur, Malaysia

e-mail: mazlanhashim@utm.my

© The Author(s), under exclusive license to Springer Nature Switzerland AG 2023

145

K. Jain et al. (eds.), *Proceedings of UASG 2021: Wings 4 Sustainability*,

Lecture Notes in Civil Engineering 304,

https://doi.org/10.1007/978-3-031-19309-5_11

1 Introduction

The development control function seeks to manage and regulate property development to ensure that all development takes place at an appropriate time and place and in such a manner that it conforms to a pre-determined set of policies or standards [1, 2]. The development control imposed on the industrial area consists of development guidance for industrial development including the buffer zone implementation. The buffer zone's main aim is to preserve the quality of life by adopting the sustainable development concept. It also ensures that appropriate consideration is given when selecting a site to avoid or minimize environmental conflicts arising from land use incompatibility (DOE, 2012). Public concern about air pollution appears to have increased over the past decades. As humans that are exposed to air pollution, water pollution and soil pollution among others, we also face an increased risk of falling victim to illness and disease. Industries may be significant contributors to air pollution experienced by local populations [3, 4]. Many studies have investigated the possible contribution to poor air quality accounting for 4.5 million premature death worldwide and 5% of those diagnosed with lung cancer will be due to extended exposure to pollution. A small percentage of chest infections, lung diseases, asthma and heart diseases can also be attributed to pollution [5, 6, 7].

The International Energy Agency (IEA) reported Malaysia's carbon emission was a total of 194 million tons in 2011, which has seen an increase of 290.7% from 1990 levels. Research using a long-range energy alternative planning system (LEAP) projected that without any mitigation measures, Malaysia's carbon dioxide (CO₂) emission in 2020 will amount to 285.73 million tons; a 68.86% increase compared to the year 2000. About these facts, the cities are becoming hotter and societies might highly have exposed to health problems. Malaysia's industrial activities, also affect the GHG emission resulting from industrial. The highest percentage of gaseous emission from industry is CO₂ as of 2014, CO₂ emissions from the manufacturing and construction sectors were 12.97 per cent of total fuel combustion in Malaysia. The highest in the last 43 years was 48.40 in 1971, while its lowest in 2014 was 12.97 (IEA, 2014) [8]. CO₂ emissions from manufacturing and construction industries also include emissions from industrial automotive producers generating electricity and/or heat from the combustion of fuels in industry. Carbon dioxide is a colourless gas with a density about 60% higher than that of dry air. It occurs naturally in Earth's atmosphere as a trace gas. The current concentration is about 0.04% (410 ppm) by volume, having risen from pre-industrial levels of 280 ppm. The scale below shows that if the ppm value is above 1,000 ppm the environment is not safe for the people. While a hydrocarbon is an organic chemical compound composed exclusively of hydrogen and carbon atoms. Hydrocarbons occur naturally and form the basis of crude oil, natural gas, coal, and other important energy sources. Hydrocarbons are highly combustible, producing carbon dioxide, water, and heat when burnt. Therefore, they are highly effective and sought after as a source of fuel. The highest percentage of hydrocarbon for the industrial category is subjected to 2.2% based on areas in the United States. Methane leaking from hydrocarbon wells and pipelines is

not just wasted energy and money, but a potent source of environmentally damaging greenhouse gas emissions. As regulations tighten and sensor technology improves both satellites and drones are helping detect such leaks.

Assessment of air quality has been traditionally conducted by ground-based monitoring, and more recently by manned aircraft and satellites. Small drones equipped with environmental sensing payloads are emerging as a valuable tool in different meteorology disciplines such as atmospheric chemistry, industrial emission monitoring and urban development control [9–11]. An environmental sensing payload gives drones a unique set of abilities such producing 3D air quality maps with high spatial resolution, monitoring toxic gases in dangerous or hard to reach locations or analysing the chemical composition of the lower atmosphere [12, 13]. The increase in the commercial drone manufacturing sector, which now offers a broad selection of small drones that are affordable for most research group. The availability of low-cost lightweight gaseous sensing instruments, as well as increasing social concern and tightening regulations on air pollution and global warming. The growing interest in drones for gas sensing applications is also evident from the recent market appearance of gas detectors specifically designed for drone applications and drones with integrated gas sensors. Aerial drones can be classified into two different categories according to their design: fixed wing mainly used for sampling over long distances and; rotary wing and used in localized studies [14–17]. The use of multiple rotors at the periphery, equidistant around a central core, allows the allocation of sensors and sampling systems on the centre of the craft, far away from potential turbulences and interference [18] UAV/drones equipped with gas sensors to measure carbon dioxide, ozone, hydrocarbon and other pollutants have been used for air quality monitoring in land use activities in cities, greenhouses, mines and other dangerous or difficult to access location. This paper investigates the use of a UAV sniffer drone for environmental analyses in urban development control for the industrial area. Being one of the first attempts to apply drone technology to the heavy industrial area with dangerous chambers, our objective was not only to map the environmental gaseous but also to identify the potential of drone technology for development control in an industrial area in Malaysia.

2 Study Area

The study area of Klang Industrial Area is located between 02°52N to 02°59N latitudes and 101°16E to 101°23E longitudes. Klang Industrial Area is surrounded by massive development in Klang City. The total area of the Klang Industrial Area is 3748.03 hectares which consists based on the type of industry activities. The type of industrial activities are heavy industries which consist of 488.05 hectares, light industries comprise 413.24 hectares, medium industries within the area of 2039.858 hectares and service industries allocate an area of 20.2 hectares. The area comprises



Fig. 1 Location of study in Heavy Industrial Area of Klang, Malaysia

66.64 acres of heavy industry. This area involved in manufacture, electrical substations and industrial gas supplier. The company that includes in the case study area are three main companies which contribute to manufacturing industries. These industries are focusing on palm oil processing, provision of industrial gas and manufacturing and distribution of industrial, specialty and medical gases respectively (Fig. 1).

3 Material and Methods

3.1 Drone Data and Ancillary Information

The data has been collected from the drone and ancillary data sources. The main data collected from the primary sources consist of gaseous data from sniffer drones that are mounted to DJI Matrice Quadcopter (Table 1). The ancillary information collected from secondary sources includes road network, drainage patterns, cadastral maps of alienated land parcels, urban maps and records of industrial development at the site.

Table 1 Drone and sensor specifications used in this study

Element	Description
Drone Features	DJI Matrice 100. QuadCopter, 5 km control range, HD video downlink, 1 kg payload capacity, 20 min flight time with Sniffer4D installed
Sensor	CO ₂ module, 0–5,000 ppm High-resolution O ₃ + NO ₂ module; Wide-range CxHx (CH ₄) module; High-res CO module; High-res SO ₂ module;
Processing Software	Sniffer4D Mapper

3.2 Methods

The fieldwork was carried out in September 2020 under the permit of the International Islamic University as an authority which managed research in Klang Industrial areas. For the drone mission, a sniffer4D sensor as a mobile sensor on an air pollutant mapping system carried 5 types of gaseous. It was mounted in a Quadcopter drone of DJI matrice 100. Flight tracks at 100 m were planned in Drone Deploy software and uploaded through its datalink (Fig. 2a). The time was set up early in the morning to get the accurate reading for gaseous that emitted from industrial activities.

The georeferenced images from the drone were further mosaic in Sniffer4D mapper Version 1.3.10.23 and Pix4D Mapper. The mosaic image was exported as a regular image with RGB values and a Digital Elevation Model (DEM) (Fig. 2b). The produced RGB and DEM images were further rectified using the Quantum Geographic Information system (Q-GIS3.16-Havannah software) were

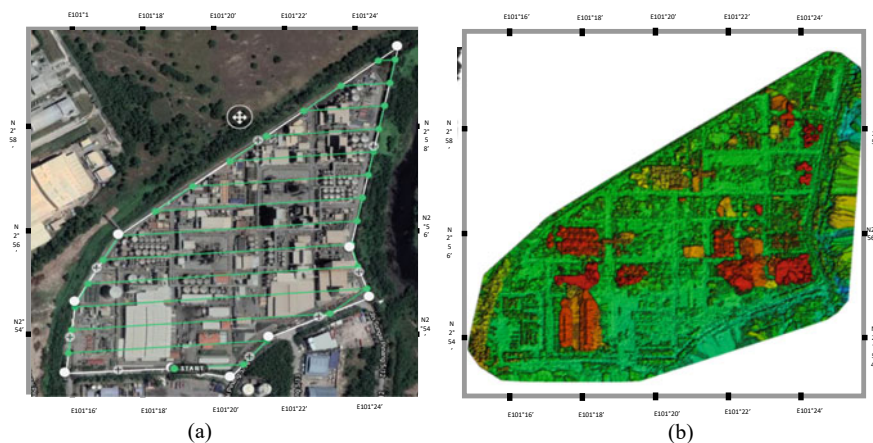


Fig. 2 a The flight path assigned to the study area; b Digital Elevation Model

further rectified with the coordinate reference system was assigned to EPSG:3380 (Selangor)/UTMWGS.

4 Result and Discussion

4.1 Industrial on Carbon Dioxide

The case study area is in a normal range of outdoor CO₂ but the concentration value maybe in future will reach the hazardous level. The case study area in which we take the reading of CO₂ represents many types of heavy to medium industrial activities. Based on the Minnesota Department of Health, which used the same hazardous scale as mentioned above have set the average concentration should not exceed 10,000 ppm over 8 h, and the average concentration should not exceed 30,000 ppm over 15 min (Fig. 3).

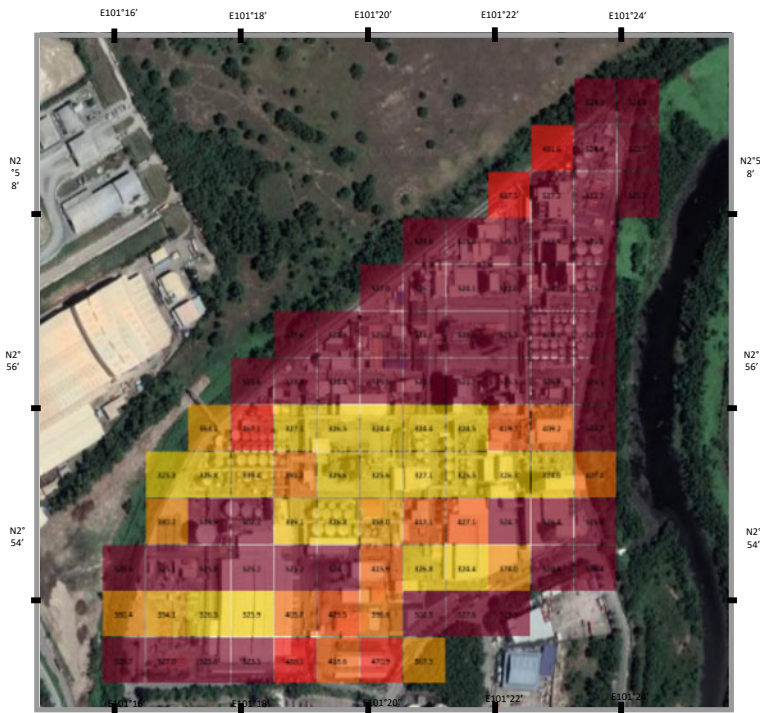


Fig. 3 Reading path for Carbon dioxide (CO₂) by Sniffer4D drone at Pulau Indah at 100 m altitude (Mission Time 2020/09/03 07:20:32 to 2020/09/03 07:36:11)

These standards have been developed for healthy working adults and might not be suitable for sensitive populations such as children and the elderly. As stated above, the range of CO₂ in the case study area for 100 m is 267.018 ppm respectively, which is below 1,000 ppm. The scale shows that if the ppm value is above 1,000 ppm the environment is not safe for the people. This situation shows that the value may be increased, thus the government must have a mitigation measure to avoid any disaster or pollution happened which results from the high concentration of CO₂ (Fig. 4 and Table 2).

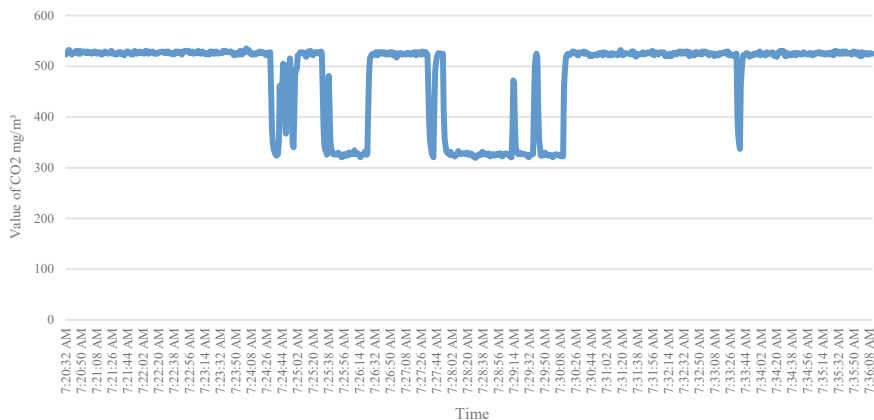


Fig. 4 The concentration values for carbon dioxide (CO₂) captured in the study area

Table 2 Details of CO₂ data captured by sniffer drone

Details of data capturing	Units
The total detected area (m ²)	256,431.844
CO ₂ Average Concentration	480.632 mg/m ³
CO ₂ Maximum Grid Concentration	527.348 mg/m ³
CO ₂ Minimum Grid Concentration	324.284 mg/m ³
CO ₂ Maximum Point Concentration	535.143 mg/m ³ 2020/09/03 07:24:02
CO ₂ Minimum Point Concentration	319.287 mg/m ³ 2020/09/03 07:28:29

4.2 Industrial on Hydrocarbon

There are many gas limits for industrial activities and one of them is the gas emission limit for hydrocarbon. At concentrations hundreds to thousands of times above the levels present in the atmosphere, these compounds are only very reactive. At levels below 500 ppm, no effects have been identified. The aromatic hydrocarbons are biochemically and biologically active. The vapours are much more irritating to environmental factors such as higher temperatures, weather inversions, and low wind speed. Inhalation of vapours of aromatic compounds and haematological compounds may result in systemic injury. As stated for the industrial gas category the limit is subjected to a 2.2% maximum for a certain area. In addition, it is stated that the percentage of 1% = 10000 ppm. Therefore, the limit hazardous gas of hydrocarbon from industry has stated that below 500 ppm (U.S. Department of Health, Education, and Welfare). Hence, to relate with the industry site shows that the average hydrocarbon is 0.078% which is equivalent to 780 ppm. It shows the hazardous level for hydrocarbon. The reading is high and reaches the hazardous level because hydrocarbon gas is mostly emitted from the industry stated in the area. Liquids, gases, and vapours can be hydrocarbons. Oil and gas extraction sites will release dissolved hydrocarbon gases such as methane, ethane, propane, and butane from production liquids and even evaporate. At atmospheric temperature and pressure, hydrocarbon gases found in crude oil are readily released into the air. The hydrocarbon is usually are compacted and released from a pressurized tank that usually found in the liquid manufacturing industries (Figs. 5 and 6 and Table 3).

The overall result shows that the value of CO₂ is between an average of 291.928 ppm – 290.890 ppm and it is still below the hazardous level for CO₂. The value of the hydrocarbon is 650 ppm – 700 ppm which has the highest value of the three sessions. The value has reached a hazardous level for the hydrocarbon gaseous. In the case of high concentration, it shows the range of medium to high concentration levels of carbon. Even though the concentration level did not reach a hazardous scale, local authorities and responsible parties must take precautionary steps to control the carbon emission in an industrial area. Hence, the Municipal Council must take into consideration carbon emissions in future development and a significant step for local authorities in collaboration with regional and national authorities would be to define and fund appropriate institutions/s to collect and report this data in a standardized format, which offers a comparative analysis of headline indicators at local, national and international level.

The recommendation for zoning of industrial areas based on gaseous emission is important because based on findings medium and high concentration levels are closely located to each other. For this reason, local and regional areas of the industry will be an important analytical unit to ensure that the emission of gaseous takes place at the lowest concentration and to avoid dangerous climate change in good time. Local authorities also play an important and powerful role as green economy regulators, asset owners and potential customers. Therefore, local government should encourage green skills by encouraging sustainability and triple bottom line reporting,

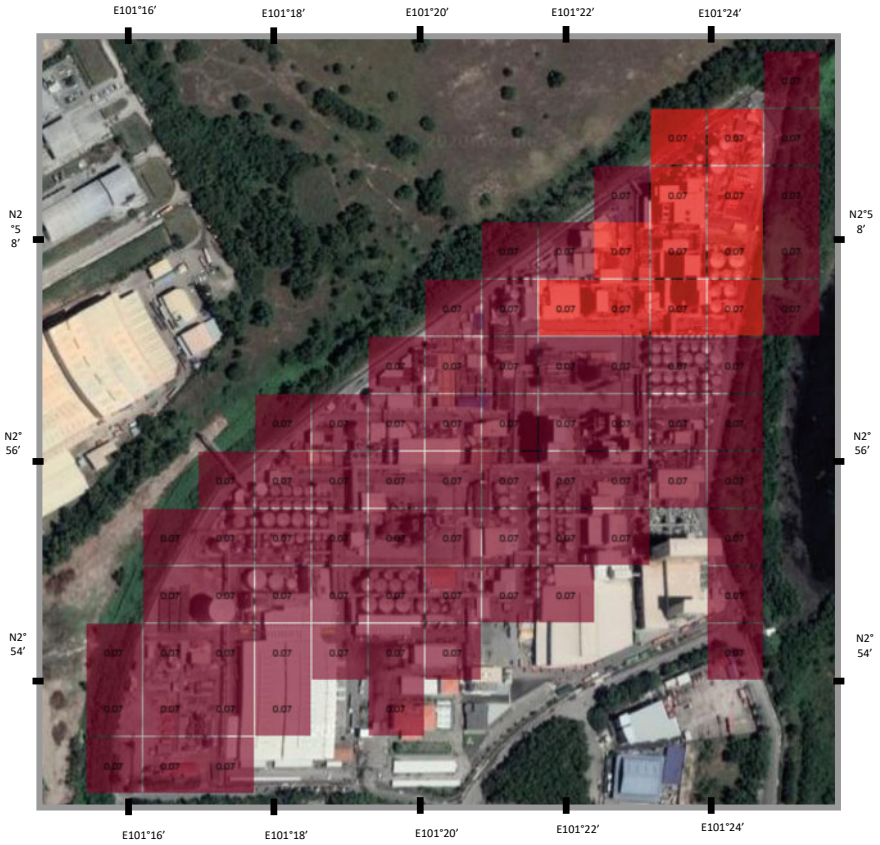


Fig. 5 Reading path of Hydrocarbon by SnifferA4 drone at Pulau Indah at 100 m Altitude (Mission Time 2020/09/03 07:20:32 to 2020/09/03 07:36:11)

and sustainable practices in the building and design industries in zoning future industry development. The study in Klang Industrial area, Malaysia to carbon emission that contributes to GHG emission, has unfortunately attempted to match several other gaseous that contribute to GHG emission such as nitrogen and ozone due to financial and time constraints. So the analysis focused solely on carbon dioxide and carbon monoxide emissions in the Industrial area. It is recommended that other industrial areas should be carried out for future research on the other gaseous emissions that lead to GHG emissions. Taking into account GHG emissions in Malaysia as the city is threatened by rapid urbanization, this continuous study has to be done to develop any future industrial area requirements to control the development.

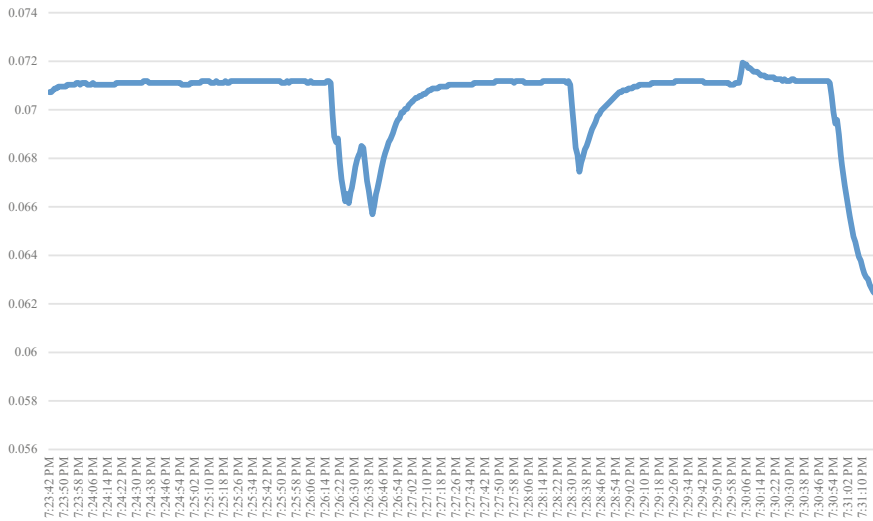


Fig. 6 The concentration values for carbon dioxide (CxHy) captured in the study area

Table 3 Details of CxHy data captured by sniffer drone

Reading	Unit
The total detected area (m ²)	204,447.406
CxHy Average Concentration	0.070%
CxHy Maximum Grid Concentration	0.071%
CxHy Minimum Grid Concentration	0.066%
CxHy Maximum Point Concentration	0.072%
	2020/09/03 19:30:04
CxHy Minimum Point Concentration	0.062%
	2020/09/03 19:31:17

5 Conclusion

Overall, this research has used a UAV-based system to capture the environmental sensing gaseous for development control purposes. The UAV/drone system includes the DJI Matrice 100 carrying a SnifferA4 sensor. Through this demonstration, the system proved to be a safe, effective and economical tool for assessing development control in a heavy industrial area. Ultimately, the pollutant control measure can be derived by the system simultaneously assessing development control for the industrial area. This research on using UAV/drone to capture environmental sensing gaseous is important in supporting SDG number 11 which is “inclusive, safe and resilient communities”. But this ambition is multifaceted and covers incongruous policy priorities and industries. One critical area of tension is evident between the goals of compact city (CC) growth (resource and land use, etc.) and urban green

space (UGS) goals (important in, for example, living ability, biodiversity, and climate regulation) as GHG emission also related to climate change.

Acknowledgements Thanks to the International Islamic University of Malaysia, Universiti Teknologi Malaysia and the Ministry of Higher Education (MOHE) for funding a research grant of Malaysia Research University Network (MRUN) Translational grant. Thanks are also owing to the anonymous reviewers for their valuable comments that helped to considerably improve the manuscript.

References

1. Booth P (1983) Development control and design quality: part 1: conditions: a useful way of controlling design?, vol 54, Issue 3. <https://www.jstor.org/stable/40112001>
2. Miller CE (1990) Development control as an instrument of environmental management: a review, vol 61, Issue 3
3. Mohd Noor N, Abdullah A, Hashim M (2018) Remote sensing UAV/drones and its applications for urban areas: a review. IOP Conf Ser: Earth Environ Sci 169(1). <https://doi.org/10.1088/1755-1315/169/1/012003>
4. Petrovic J, Lecic D, Pavlovic D (2016) Sustainable urban development and industrial pollution. *Industrija* 44(1):167–185. <https://doi.org/10.5937/industrija1-10466>
5. Buteau S, Shekarrizfard M, Hatzopoulou M, Gamache P, Liu L, Smargiassi A (2020) Air pollution from industries and asthma onset in childhood: a population-based birth cohort study using dispersion modelling. *Environ Res* 185. <https://doi.org/10.1016/j.envres.2020.109180>
6. Lyu R, Clarke KC, Zhang J, Jia X, Feng J, Li J (2019) The impact of urbanization and climate change on ecosystem services: a case study of the city belt along the Yellow River in Ningxia, China. *Comput Environ Urban Syst* 77. <https://doi.org/10.1016/j.compenvurbysys.2019.101351>
7. Roy R, Braathen NA (n.d.) The rising cost of ambient air pollution thus far in the 21st century results from The BRIICS and the OECD countries. <https://doi.org/10.1787/d1b2b844-en>
8. IEA (2014) Key World Energy Statistics 2014, OECD Publishing, Paris, https://doi.org/10.1787/key_energ_stat-2014-en
9. Alvear O, Zema NR, Natalizio E, Calafate CT (2017) Using UAV-based systems to monitor air pollution in areas with poor accessibility. *J Adv Transp*. <https://doi.org/10.1155/2017/8204353>
10. Burgués J, Marco S (2020) Environmental chemical sensing using small drones: a review. In: *Science of the total environment*, vol 748. Elsevier B.V. <https://doi.org/10.1016/j.scitotenv.2020.141172>
11. Hedworth HA, Sayahi T, Kelly KE, Saad T (2021) The effectiveness of drones in measuring particulate matter. *J Aerosol Sci* 152. <https://doi.org/10.1016/j.jaerosci.2020.105702>
12. Anweiler S, Piwowarski D, Ulbrich R (2017) Unmanned aerial vehicles for environmental monitoring with special reference to heat loss. In: *E3S web of conferences*, vol 19. <https://doi.org/10.1051/e3sconf/20171902005>
13. Ruiz-Jimenez J, Zanca N, Lan H, Jussila M, Hartonen K, Riekkola ML (2019) Aerial drone as a carrier for miniaturized air sampling systems. *J Chromatogr A* 1597:202–208. <https://doi.org/10.1016/j.chroma.2019.04.009>
14. Chang CC, Wang JL, Chang CY, Liang MC, Lin MR (2016) Development of a multicopter-carried whole air sampling apparatus and its applications in environmental studies. *Chemosphere* 144:484–492. <https://doi.org/10.1016/j.chemosphere.2015.08.028>
15. Corrigan CE, Roberts GC, Ramana MV, Kim D, Ramanathan V (2008) Capturing vertical profiles of aerosols and black carbon over the Indian Ocean using autonomous unmanned aerial vehicles. *Atmos Chem Phys* 8. www.atmos-chem-phys.net/8/737/2008/

16. Noor NM, Afiq A, Abdullah A, Abdullah A, Ibrahim I, Sabeek S (2019) 3D city modeling using MULTIROTOR drone for city heritage conservation. *MALAYSIA J Malays Inst Plans* 17
17. Noor NM, Ibrahim I, Abdullah A, Aiman Abdullah AA (2020) Information fusion for cultural heritage three-dimensional modelling of Malay cities. *ISPRS Int J Geo-Inf* 9(3). <https://doi.org/10.3390/ijgi9030177>
18. Zhang J, Ji Y, Zhao J, Zhao J (2017) Optimal location of a particulate matter sampling head outside an unmanned aerial vehicle. *Particuology* 32:153–159. <https://doi.org/10.1016/j.partic.2016.09.012>

Drone Technology in Waste Management: A Review



Richa Choudhary and Susheela Dahiya

Abstract A clean Environment is the basic right of every human being. For the last two decades, India is dealing with huge environmental issues and one of the major issues is waste management. There is a huge gap between the generation and processing of waste in India. Some of the current methods of dealing with waste disposal are causing more harm than benefit to the environment and public health. Huge advancement in technologies such as Artificial Intelligence, Machine learning, smart sensors, IoT, UAVs or Drones, automation, etc. has improved human life in every domain such as healthcare, Agriculture, Consumer Services, and Manufacturing. There is huge scope in harnessing the potential of these technologies in the field of Waste Management. Due to the advancement in sensors and availability of cost-effective commercial Drones, Drones have shown significant improvement and huge application scope in different domains. There is a huge prospect of using drones in waste management. It is one of the popular tools and technology, whose use can be explored in different areas of Waste Management. Government and Waste Management organizations can utilize smart UAVs or Drones to efficiently manage waste disposal at Landfills and dumping zones. In this paper, an attempt has been made to review and identify the different areas of waste management where Drones can be utilized efficiently in India. This article also reviews the various challenges and requirements of using Drone technology in waste management.

Keywords UAVs · Drone · Smart sensors · Waste management

1 Introduction

One of the major challenges the world is currently facing is waste management. In India, the amount of waste generated is huge as compared to waste processing. According to the report published by PIB (Press Information Bureau), Delhi (2020), the volume of waste will increase from 62 million tons to 150 million tons by the year

R. Choudhary (✉) · S. Dahiya
School of Computer Science, University of Petroleum & Energy Studies, Dehradun, India
e-mail: richachoudhary.86@gmail.com

© The Author(s), under exclusive license to Springer Nature Switzerland AG 2023
K. Jain et al. (eds.), *Proceedings of UASG 2021: Wings 4 Sustainability*,
Lecture Notes in Civil Engineering 304,
https://doi.org/10.1007/978-3-031-19309-5_12

157

2030 [1]. Another report published in a leading newspaper in March 2021, states that 40% of plastic waste remains uncollected in India every day which further harms the environment and public health.

Waste management is a term used for the process of collection, transportation, segregation, processing, and disposal of waste. This process is managed by the Urban Local Bodies (ULB), Gram Panchayat, and few waste management organizations. In India, currently, there is a huge gap between waste generation and waste processing. The rapid increase in population and socio-economic growth led to urbanization and industrialization in the country [2]. This fast pace of development has led to the growth of waste generation as well which in turn led to pressure on the government to start taking bold steps in the direction of waste management. In the past decade, the world has witnessed a huge advancement in the technologies like Artificial Intelligence, Machine Learning, Internet of Things, smart devices, advancements in sensors, Unmanned Aerial Vehicles (UAV), and automation has changed the face of the earth in many domains. There is a critical need as well as a huge scope for using these new technologies to effectively manage waste and fill up the gap between waste generation & waste processing.

In the past decade, UAVs or Drones have shown significant contributions in a variety of applications such as aerial photography, surveillance [3], crowd monitoring, agriculture, mapping of land use, data collection for analytics etc. Drones enables researchers to study regions which are not safe or unreachable from a safer distance with better accuracy than traditional methods [4, 5]. The prospects of Drones in waste management are also huge [6]. Current methods of waste management are not effective to deal with this increasing volume of waste [7].

This paper provides the use of drones in waste management. In Sect. 2 of the paper, we provide the generic usage and capabilities of drones in different areas. In the next section, the in-depth use of drones in waste management has been discussed. In the last section, we discussed the various requirements and challenges of using drone technology in waste management.

2 Status of Landfills and Solid Waste in India

Waste management refers to the efficient processing of the waste for sustainable development. The process of waste management starts from the collection of waste and ends at the disposal of this waste at landfills or dumping zones. The major issue in India is the illegal dumping of solid waste. According to Sunil Kumar et. al [8] 90% of the waste in India is dumped illegally. There are serious health hazards of dumping waste in open areas. People living near the open dumping sites are already facing health issues like nose and throat infections, problems in breathing and several other.

The legal sites of dumping the waste are the areas which are kept away from the residential areas and are known as landfills. The waste should be dumped either at Landfills or should be sent to waste processing plants. But the current Landfill sites

are piled up with the huge volume of untreated waste. Also, a maximum number of states are having very few landfill sites as compared to the waste generated, which demands effective use of landfill sites. Figure 1 shows the statewide number of landfill sites in India and Fig. 2 shows the comparison between statewide waste generation and waste processing.

Maximum number of states are having very few landfill sites as compare to the waste generated, so effective use of landfill sites is required to fit the garbage. The current methods are not effective to process the tons of mixed solid waste. The government spends most of the amount on collection of waste and rest on the transportation & processing of waste. The biggest challenge in the processing of waste is the segregation of different types of waste material. The solid waste collected by the municipality can be segregated in different categories like organic waste, paper, glass, plastic, metal, inert, and rubber [2]. Figure 3 shows the composition of waste collected by the municipality in India.

In India, due to the lack of proper regulation, infrastructure and awareness among people, huge amount of mixed solid waste is being generated which needs segregation before further processing into recycling and reuse. The current methods of treating mixed solid waste are burning and gasification, which poses several health hazards to the people working in the plant or living near the landfill areas. In landfills, the natural way of decomposition of waste is done by an anaerobic reaction between the organic matter (such as food, vegetable, dry grass, etc.) which emits harmful gases like methane. In rainy days, landfills are the contamination zones of various harmful

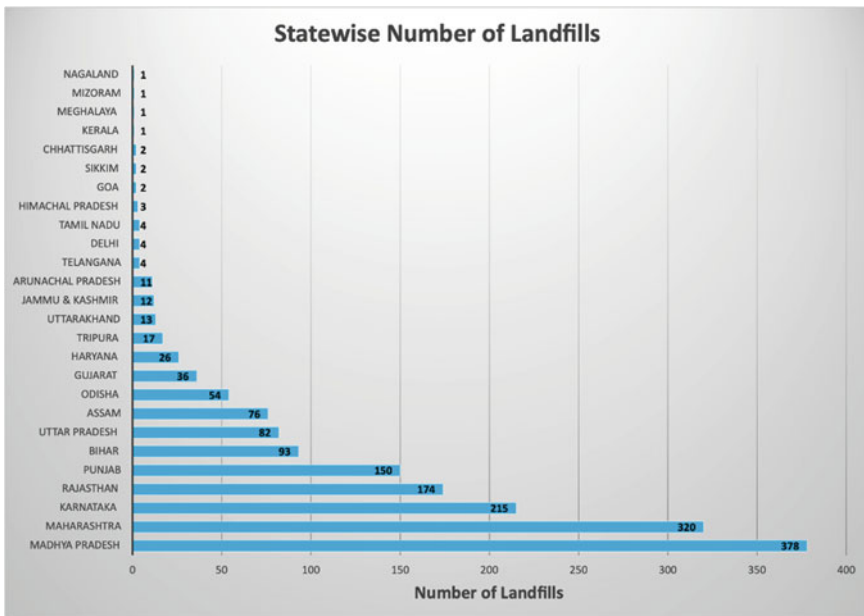


Fig. 1 Statewise number of landfill sites in India

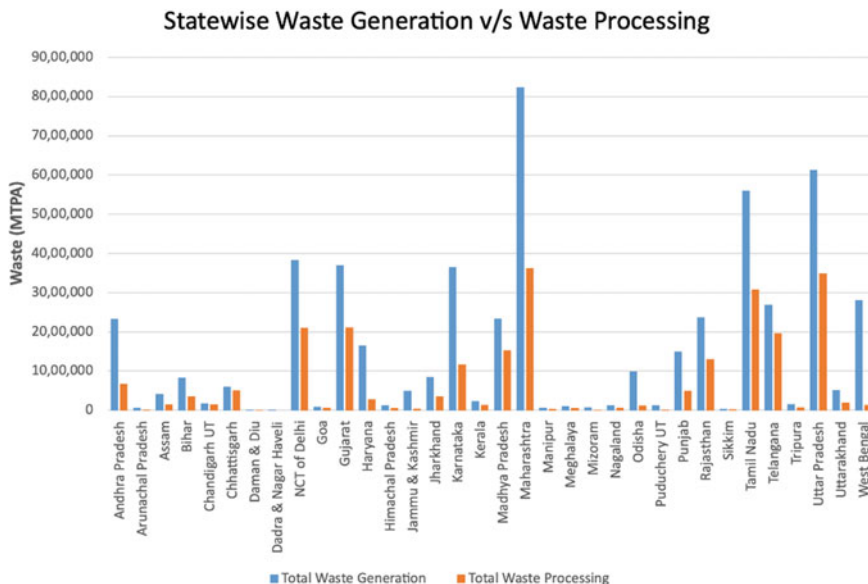


Fig. 2 State/UT-wise status of solid waste generated (Millions tones per Annum) and Processed (Millions tones per Annum) (Source <http://swachhbharaturban.gov.in/>)

Waste Composition of Municipal Solid waste in India

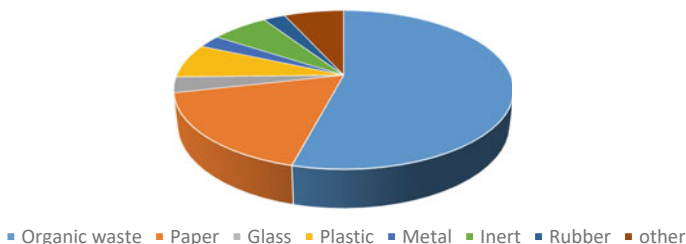


Fig. 3 Composition of municipal solid waste in India

bacteria, mosquitoes and pathogens. The release of toxins gases, leaking of harmful liquid, and mountains of garbage are the major issues with the current landfills in India. The new technologies such as drones can help us in a very efficient manner to improve the conditions of landfills as well as the inefficient waste treatment.

3 UAVs or Drones

UAVs or Drones is an unmanned aerial device which is controlled by a ground base controller and the communication is established between the two using Wi-Fi, Bluetooth or ZigBee network [4]. Initially, drones were only used in the military but in past few years, the usage of drones have been discovered in almost all areas such as agriculture, aerial photography, wildlife conservation, data collection, disaster management to name a few [9].

There is a wide variety of drones available in market ranging from task specific to commercial UAVs. With advancement in sensors and automation, the performance and application areas of drones have improved remarkably. Due to their smaller size, ease in use and latest sensors technology, drones can be used in wide range of applications (Table 1). The major application areas of Drones are listed in Table 2.

3.1 Types of Drones

The basic design of drone is divided into two parts: the actual drone and the payload. Payload in a drone is nothing but the extra weight it carries apart from the drone weight. As a payload almost anything can be attached to the drone like a thermal camera, weather sensors, the package for shipment, emergency medicines, etc. [9, 15] Drones can be differentiated on the basis of their wings, size, weight, storage capacity, source of energy, type of take-off/landing. Table 2 lists the difference among drones on the basis of these parameters. Drones are also divided into two major application areas: surveying and data collection. Drones used in surveying will have different specifications as compared to drones used for data collection.

Table 1 Application areas of Drones

Area	Application	References
Smart Agriculture	Helps in monitoring crops, soil and land mapping, and surveying of the agricultural area	[4]
Aerial Photography	Takes high-resolution pictures/video which have wide range of application area. For ex: crowd monitoring, collection of data, geographical survey etc	[10, 11, 12]
Wild-life conservation	Drones can have thermal cameras which can help to monitor wild species in day and night	[13]
E-commerce	Drones can be used to ship the lightweight packages in near location to its controller. Amazon has already started using the drones for delivering packages	[11, 12]
Geographic mapping	This feature makes drones attractive in many fields. Drones helps us in getting imagery of difficult locations which are not safe for human to reach	[4, 14]

Table 2 Various features of drones along with their usage in different domains

Difference Parameter	Types	Explanation
Wings	<ul style="list-style-type: none"> • Fixed wings drone • Multicopter drone • Hybrid drone 	<ul style="list-style-type: none"> • Mainly used for data collection • Multicopter drones are mainly used for recreational purposes • Hybrid means taking best of both is used in specific tasks or operations
Size/weight	<ul style="list-style-type: none"> • Large size drones • Medium size drones • Mini drones 	Size and weight decide the power and capacity Large size drones are usually used in Military or geographical surveying
Storage capacity	<ul style="list-style-type: none"> • Usually, drones come with 4 to 8 GB of storage 	This storage capacity is very less compared to images collected in one flight time. Cloud based solutions are used in drones to store the data
Source of Energy	<ul style="list-style-type: none"> • Battery operated • Solar panel operated • Fuel operated 	Maximum no of drones are battery operated, very few are created with fuel /kerosene option
Take off/landing	<ul style="list-style-type: none"> • Vertical takeoff & landing • Requires little runway 	Usually, drones are VOTL –vertical takeoff and landing e.g. DJI Mavic Air2. Very few drones require a little runway for takeoff
Autonomy	<ul style="list-style-type: none"> • Fully autonomous • Human operated 	Fully autonomous, Requires controller/mobile app for navigation

3.2 Working of Drones

A standard drone consists of unmanned aircraft, ground station. Communication between drones is established by using either Wi-Fi or Bluetooth network. Drones are launched from the specific area of application to the target area for data collection or for surveying [15]. The path to the target area could be autonomous or navigated by the pilot on ground through some controller or computer or using mobile app (as shown in the Fig. 3). Drones surveys the targeted area by clicking images, videos or collects the data using sensors. The usual flight time for drones is 30–35 min. The area to survey and flight time requirement decides the type of drone required [13].

Data collected by the drones in form of images /pictures, then this data is stored either in internal storage of drones or data stream is transmitted to the base station, or the live feed can be directly stored at cloud-based storage to process later. This data is then processed by the specific software to present the visualization or results of the collected data [16, 17].

The analysis of data collected by drones can be done in real-time or can be processed later. Waste management industry can harness the potential of data collection and surveying to effectively process or monitor the dumping zones (Fig. 4).

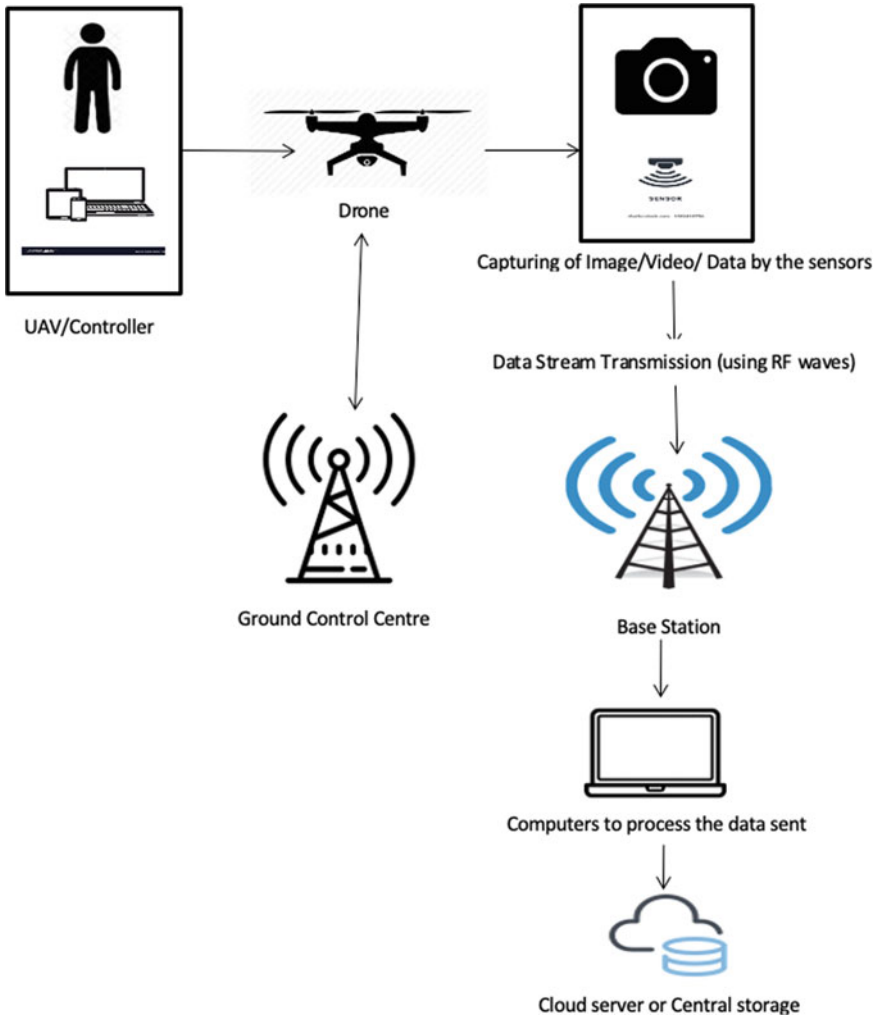


Fig. 4 Schematic illustration of the working of drone for data transmission to base station

4 Use of Drones in Waste Management

Waste management consists of various steps such as collection, segregation, transportation, processing and disposal of waste at the landfills or dumping area. Drones can play a major role in this process of waste management [6]. Drones can help in managing illegal dumping, identifying open dump areas, landfill site selection, landfill monitoring, calculating airspace of landfill, collecting waste from coastlines etc. The major areas of waste management where drones can be used for effective and fast results are as follows.

4.1 Waste Collection

Drones can be used to keep check on littering at public areas. They can be used to monitor the industries waste disposal. They can notify the concerned agency on illegal dumping of the industrial waste by the industries [11, 18]. Keeping this check on the industries will force them to treat the industrial waste properly which in turn cause less harm to the environment.

4.2 Landfill Site Selection

Landfills are hazardous areas for the human beings who work or live around it. Managing the landfills to accommodate the huge volumes of garbage is very essential for the effective waste management. To create a landfill, lots of manual work and surveying is needed. According to the new municipal waste management act 2016, the landfills should not be constructed around 500 m of residential area and It should be at least 200 m away from highway. Also, no Landfill should be constructed around wildlife Habitat. It should be constructed in near proximity of agricultural land, park, and water body like pond or river [19]. Drones can be deployed for the site selection, they can survey the land from all directions and this data can be analyzed later to decide upon usage of land as a Landfill site [20, 21]. Drones can help in finding an appropriate landfill site and also help in checking whether the existing landfill sites are as per the act or not.

4.3 Landfill Monitoring

Landfills have severe issues which creates air, water and soil pollution. Landfills contains huge amount of garbage, one of the examples is Delhi Landfill which looks

like mountain of garbage. Landfill emits harmful gases due to the anaerobic reaction of organic waste. It also results in contamination of ground water and surface water due to leachate. Landfills are also a home to several harmful pathogens and mosquitoes, bad odor etc. [19].

Drones can effectively help in manage these issues as it is not feasible for the Government to monitor all the Landfill sites on regular basis. In such scenario, drones come handy as they are easy to operate, lightweight machine which can fly autonomous or using a controller. Drones can be used for landfill monitoring in following manner.

To monitor the gas emissions using the specific sensors as payload: Drones can be used to monitor gas emissions any no of times depending on the size and conditions of the landfill site.

To survey the Landfill area: Drones provides the visual data of any geographic location of landfill with high precision. This high-quality data can be utilized to understand the impact of Landfill on the environment. This data can also be analyzed using appropriate software to plan for the waste treatment [11].

4.4 Calculating the Airspace of Landfill

Landfill site is created away from residential area, wildlife habitat, water bodies, agriculture land and highways. This type of area is not easily available in a country like India wherever increasing population always demands land consumption. Due to this, very effective use of existing landfill sites like fitting high volume of garbage in smaller area is required. Drones can particularly help in calculating the airspace of any site along with the usage of high-end software.

GPS enabled drones can perform the land survey and can transmit the collected data of landfill sites [22]. With the help of high-end software, this data can be used to create 3-D model of the site which will help in estimating 3-D model of remaining air space of a landfill [11]. This estimation can be used to compact the garbage without overfilling of the space. This estimation is very hard to achieve by using traditional methods, which usually takes weeks to survey the area and calculate the airspace [2]. This estimation takes only few hours with the help of drones.

4.5 Collecting Waste from Coastlines

At few places in countries outside India, drones are also used to collect the garbage at coastlines [11]. The drone swims in the water to catch the floating garbage and keeps the bay area clean.

4.6 Decision Making for Waste Management Organizations

Surveying of the site and data analysis using drones helps the managers or policy makers in waste management to keep track of things for better decision making like when to create a new cell at landfill, where to install the machines at garbage site, and can also help in quick response to any emergency situation [18, 22] (Table 3).

5 Requirements for Using Drone Technology

Before using drone technology in waste management, it is necessary to first understand the laws and regulations of the country along with the requirement and availability of required hardware and software. The different requirements of using drone technology are discussed below.

Table 3 Uses of Drones in waste management—use case studies

References	Use case study	Conclusion
[23]	Monitoring of 12 dumps and 1 Landfill is done using UAVs at the Perm region and Sverdlovsk Region of Russia from 2017 to 2021	UAVs provided data is rich and can effectively help in timely decision making. It is helpful for Landfill operators as well as other stake holders
[24]	SFEI (San Francisco Estuary Institute) team created Machine learning-based Trash detection system and used Drones Aerial Imagery to collect the data	It concluded more can be done using less i.e. drones are very time efficient in aerial imagery
[25]	Landfill of Borgo Montello of Italy is using UAVs to design the 3D model of the site from 153 Images captured using UAV	3D modelling of Landfill created using UAV is effective in carrying out the periodical survey. The use of UAV in photogrammetric can be further improved and standardized
[26]	Oslo, Fjord Norway has approved the use of UAV in managing the trash spots underwater	The use of drones underwater to clean the seabed has shown that UAVs saves time and are cost effective
[27]	UAVs are used to collect the floating waste from Mithi river at Mumbai India before it enters the sea	Mapping of river course where plastic enters into river is done using UAV and is effective in laying out the guidelines to reduce the plastic in river

5.1 Understand the Aviation Laws or Regulations of the Country

Drones are machines which fly to capture the data with powerful technology and their unregulated use can have serious consequences. Before using the drones, it is required to understand the norms and regulations for a particular country. Currently, in India, there is no proper guidelines formulated for use of drones [12]. But there are no fly zones where drones are not allowed which needs to be considered while using drones in waste management by private organizations.

5.2 Check for Permissions of Allowed Sensors

Drones comes with wide variety of sensors such as heat sensors, weather related sensors, thermal cameras and a lot more. There are few types of sensors which may not be allowed in a particular area. So, this needs to be clarified before using any type of sensor in drones.

5.3 Availability of the Software to Process Collected Data by Drones

Drones can collect the data and transmit it to the receiver or base station. This collected data needs analysis to generate information from it. Different type of data is collected by drones such as- images, videos, data collected by different sensors, geo spatial data etc. All these different types of data need high-end software to process them and provide visualization for the end users [5]. In waste management industry, it is important to select the proper software according to the data the organization is collecting or analyzing.

5.4 Availability of the Network

Drones are of two types—autonomous drones and pilot operated drones where pilot controls the drone from ground only. Autonomous drones do not require network for navigation, but network availability is required to transmit the collected data. For drones, which can be controlled by the controller from ground needs network for navigation as well as for data transmission. If the data transmission is live feed, then it becomes more crucial to have continuous availability of the network [4, 17].

5.5 Ethical Issues of Using Drones

Drones are very powerful tool to collect data, but it is also very crucial to handle such technology with utmost sense of responsibility. Drones can access the data from sky and have high resolution cameras with powerful zoom capability. The data collection can be accessed by unauthorized people. Drones can be used for unauthorized data collection such as taking pictures of the nearby restricted areas or people which results in breaching the privacy [4]. There is need to address these issues and government needs to formulate clear instruction and guidelines regarding the use of drones. Unethical use of such technology can have very serious consequences which can deprive us from the benefits of the technology.

5.6 Requirement of Selecting Optimal Hardware

Drones' deployment requires certain setup to harness the full potential of its capabilities. To set up the drone's usage in waste management, it is required to answer two questions: what type of data collection is required, what are the available sensors in market to fulfill that data collection? Also, to deploy drones in surveying a particular area, it should be known the exact area to be covered, demography of the area. All these questions will help to select the optimal drone hardware to suit the requirement of the research activity.

5.7 Availability and Ease of Maintenance

Drones are light weighted machine that can access the area otherwise unsafe or dangerous for humans to reach. Their ease in use and maintenance is making them popular day by day in most of the domains. Drones can easily replace heavy helicopters and planes traditionally used for surveying of the area. They can cover the area from high altitudes to closer to ground levels as compared with traditional methods. This gives them the advantage of the ease in use and maintenance.

6 Challenges of Drone Technology

6.1 Privacy and Security

Privacy and security are the major concern in using drones. Drones have powerful technology and comes with wide variety of sensors. Most of the drones can transmit high resolution data in real time which can make the intended breaching of privacy

and invasion in the private property or trespassing quite easy. In India, current laws for use of drones are vaguely worded and does not provide clear instructions, which makes it more difficult to assure the privacy while using drones in any industry.

6.2 Requirement of Specific Software to Gather Data

Before deploying drones in waste management industry, it is required to understand the type of data collection required, the area to be surveyed and the area for which monitoring needs to be done. All these different areas will give different set of data. All sets of collected need proper storage, processing and visualization of the information. Also, there is a need of the skilled professionals who can fully utilize the potential of drone technology.

6.3 Legislature Uncertainty

Without clear regulation and laws, it is difficult for the stakeholders to invest in drones use for waste management. Urban local bodies (ULB) and concerning government sector should formulate clear instruction for usage of drones in waste management. This will give the boost to investment of drones in waste management industry.

6.4 Safety

Usage of drones is there in almost all the domains. There are few areas where use of needs can jeopardize the safety for e.g., in wildlife conservation, it increases the risk and decreases the safety for the wild animals. Drones are otherwise safer to use, but sometimes the weather conditions or usage of heavy drones can pose safety issues. These issues need to be addressed by training the controller to respond effectively, if something goes wrong. In waste management options for safe use of drones needs to be explored more.

6.5 Weather Conditions

Drones' functionality can be influenced by the weather conditions such as rain, winds, low visibility. All these factors can affect the flight of drone and can hamper the data collection from a landfill site.

6.6 Requirement of Specific Skills

Drones can be efficient and fast in providing the data, but the data processing needs specific skills and software to understand or process the collected data. Transmission of data broadly depends on network availability. Real time data collection and transmission by drones can be slow and can also impact the real time analyses of data. It also depends on the user skills to make most out of the data transmitted in real time for analysis or decision making.

7 Conclusion

Drones have enhanced the speed and quality of research in all application areas. Recent studies have shown that drones are fast and more reliable than the traditional methods for survey or data collection. Waste management is a multifaceted industry comprising of tasks like garbage collection, landfilling, and recycling. These diverse tasks of waste management industry need different types of technology to work at different fronts. Waste management data collection is typically difficult due to its hazardous and dangerous conditions to humans. Until recently, surveying and monitoring landfill sites was a time-consuming, costly and dangerous affair but aerial surveys and monitoring through drones can revolutionize the waste management industry. To successfully deploy the drones in waste management research, specific requirements and conditions needs to be fulfilled, once the setup is ready drones can be cost-effective, fast, reliable and can provide real-time data visualization for better decision making for the stakeholders. Drones provides the option of promising results and can handle waste treatment effectively, but before using drones it is important to address the questions concerning ethics, regulation and implementation of drones. Waste management sector needs proper infrastructure, guidelines and funding laid by ULB to include stakeholders. Also, there is need of proper training and awareness to handle the real time issues while monitoring using drones.

References

1. <https://pib.gov.in/PressReleaseDetailm.aspx?PRID=1667099>
2. Somayaji SRK, Kaliyaperumal S, Velayutham V (2020) Managing and monitoring E-waste using augmented reality in India. In: Karrupusamy P, Chen J, Shi Y (eds) Sustainable communication networks and application. ICSCN 2019. Lecture notes on data engineering and communications technologies, vol 39. Springer, Cham. https://doi.org/10.1007/978-3-030-34515-0_4
3. Singh CH, Mishra V, Jain K, Shukla AK (2022) FRCNN-Based Reinforcement Learning for Real-Time Vehicle Detection Tracking and Geolocation from UAS. Drones 6(12):406. <https://doi.org/10.3390/drones6120406>

4. Maddikunta PKR, Hakak S, Alazab M, Bhattacharya S, Gadekallu TR, Khan WZ, Pham Q-V (2021) Unmanned aerial vehicles in smart agriculture: applications, requirements, and challenges. *IEEE*. <https://doi.org/10.1109/JSEN.2021.3049471>
5. Caillouet C, Giroire F, Razafindralambo T (2019) Efficient data collection and tracking with flying drones. *Ad Hoc Netw Elsevier* 89(C):35–46. <https://doi.org/10.1016/j.adhoc.2019.01.011>
6. Merkert R, Bushell J (2020) Managing the drone revolution: A systematic literature review into the current use of airborne drones and future strategic directions for their effective control. *J Air Transp Manag* 89:101929. ISSN 0969-6997. <https://doi.org/10.1016/j.jairtraman.2020.101929>
7. Gevaert CM, Sliuzas R, Persello C, Vosselman G (2018) Evaluating the societal impact of using drones to support urban upgrading projects. *ISPRS Int J Geo-Inf* 7:91. <https://doi.org/10.3390/ijgi7030091>
8. Kumar S, Smith SR, Fowler G, Velis C, Kumar SJ, Arya S, Rena, Kumar R, Cheeseman C (2017) Challenges and opportunities associated with waste management in India. *R Soc Open Sci* 4160764160764
9. Zeng Y, Wu Q, Zhang R (2019) Accessing from the sky: a tutorial on UAV communications for 5G and beyond. *Proc IEEE* 107(12):2327–2375
10. <https://www.allerin.com/blog/10-stunning-applications-of-drone-technology>. Accessed 10th March 2021
11. <https://www.propelleraero.com/blog/using-drones-for-waste-management-the-beginners-guide/>. Accessed 11 March 2021
12. <https://www.latestlaws.com/articles/regulation-of-drones-in-india/>. Accessed 11 March 2021
13. Butcher PA, Colefax AP, Gorkin RA, Kajiura SM, López NA, Mourier J, Purcell CR, Skomal GB, Tucker JP, Walsh AJ, Williamson JE, Raoult V (2021) The drone revolution of shark science: a review. *Drones* 5:8. <https://doi.org/10.3390/drones5010008>
14. Vergouw B, Nagel H, Bondt G, Custers B (2016) Drone technology: types, payloads, applications, frequency spectrum issues and future developments. In: Custers B (ed) *The future of drone use. Information technology and law series, vol 27*. T.M.C. Asser Press, The Hague. https://doi.org/10.1007/978-94-6265-132-6_2
15. Casagrande G, Khaddar MA, Parisi S (2020) Technology and the local community: uses of drones in #NoDAPL movement and Dandora dumpsite storytelling. *Am Behav Sci* 64(13):1906–1920. <https://doi.org/10.1177/0002764220952133>
16. Huuskonen J, Oksanen T (2018) Soil sampling with drones and augmented reality in precision agriculture. *Comput Electron Agric* 154:25–35. ISSN 0168-1699. <https://doi.org/10.1016/j.compag.2018.08.039>. <https://www.sciencedirect.com/science/article/pii/S0168169918301650>
17. <https://www.wastetodaymagazine.com/article/landfill-monitoring-drones/>. Accessed 10 March 2021
18. *Municipal Solid Waste Landfills, Chapter XVII*
19. <https://www.droneblog.com/2020/05/12/10-ways-drones-are-being-used-for-waste-management/>. Accessed 11 March 2021
20. Marturano F, Ciparisse J-F, Chierici A, d'Errico F, Di Giovanni D, Fumian F, Rossi R, Martellucci L, Gaudio P, Malizia A (2020) Enhancing radiation detection by drones through numerical fluid dynamics simulations. *Sensors* 20:1770. <https://doi.org/10.3390/s20061770>
21. Leizer K, Károly G (2018) Possible areas of application of drones in waste management during rail accidents and disasters. Óbuda University, Doctoral School on Safety and Security Sciences Budapest, Hungary. <https://doi.org/10.7906/indecs.16.3.8>. Accessed 31 Aug 2018
22. Meka S (2014) Municipal solid waste management in India: a review and some new results. *Int J Civ Eng Technol* 5:1–8
23. Filkin T, Sliusar N, Ritzkowski M, Huber-Humer M (2021) Unmanned aerial vehicles for operational monitoring of landfills. *Drones* 5(4):125. <https://doi.org/10.3390/drones5040125>
24. <https://www.esri.com/about/newsroom/arcnews/improving-trash-monitoring-with-drone-imagery-artificial-intelligence-mapping/>. Accessed 21 Dec 2021

25. Baiocchi V, Quintilio N, Martina T, Giampaolo S, Maria A, Domenica C (2019) UAV for monitoring the settlement of a landfill. *Eur J Remote Sens.* <https://doi.org/10.1080/22797254.2019.1683471>
26. <https://www.nytimes.com/2018/03/04/world/europe/norway-fjords-litter-drones.html>. Accessed 26 Dec 2021
27. Sharma HB, Vanapalli KR, Cheela VRS, Ranjan VP, Jaglan AK, Dubey B, Goel S, Bhattacharya J (2020) Challenges, opportunities, and innovations for effective solid waste management during and post COVID-19 pandemic. *Resources, conservation and recycling*, vol 162, p 105052. ISSN 0921-3449. <https://doi.org/10.1016/j.resconrec.2020.105052>

Solar Roof Panel Extraction from UAV Photogrammetric Point Cloud



S. K. P. Kushwaha, Harshit, and Kamal Jain

Abstract Many buildings are using solar panels as an additional source of electricity. As solar energy is renewable energy and the maintenance cost of solar panels is cheap. This research uses a statistical approach of analyzing point clouds generated from UAV-based photogrammetric processing. An algorithm has been developed to extract solar panels on the building rooftops. The data acquisition is done using an Unmanned Aerial Vehicle (UAV) platform mounted with an optical sensor. The RGB images acquired are further used to generate a photogrammetric point cloud dataset. Geomatics engineering building of Indian Institute of Technology Roorkee, India is considered as the study area, on which solar panels were already installed on its roof. Normal vectors are computed for each points in the building point cloud dataset. The normal vector has its components in the x-axis, y-axis, and z-axis correspondingly. Based on the contribution of the z-component of normal vectors, the points are classified into roof, facade, and solar panel points respectively. The results obtained are evaluated by comparing classified points with respect to manually classified solar panel points. This comparison suggests that the developed algorithm is effective in extracting the solar roof panels efficiently. This research can be used to calculate the effective area of solar panels.

Keywords UAV · Solar roof panels · Photogrammetric point cloud · Normal vectors · Classification

S. K. P. Kushwaha (✉) · Harshit · K. Jain
Geomatics Group, Department of Civil Engineering, Indian Institute of Technology Roorkee,
Roorkee, India
e-mail: s.k.p.kushwaha92@gmail.com

Harshit
e-mail: harshit@ce.iitr.ac.in

K. Jain
e-mail: kjainfce@iitr.ac.in

1 Introduction

As urbanization is expanding at an exponential rate in major parts of the globe, the limitation of resources are seen quite often. Electricity is one of such resources in which we have seen power shortages many times. Many cities have been turning towards solar energy usage as an additional energy source to the growing demands. Solar roof panels have been installed on the building rooftops or in open spaces with direct sun illumination. Unmanned Aerial Vehicle (UAV) has many advantages like faster data acquisition, very high-resolution, multi-temporal data, etc. Due to its advantages UAV's play a vital role in many domains like forest degradation mapping [1], damage assessment of cultural heritage monuments [2], landslide monitoring [3], Tree canopy mapping [4], etc. UAV's can also play a crucial role in analyzing solar panels which are already installed on any building. One can assess the damages as well as the efficiency of the solar panels with the help of advanced processing of high-resolution UAV datasets. Extracting solar panels could help us derive the solar potential utilized of the existing system over a roof and give us an idea of its efficiency.

Point cloud data from various techniques have enriched us with various information about our surroundings. They have improved our perception and provided a better way of analyzing and understanding our natural and built environment's behavior. Classifying the point cloud efficiently is a critical challenge considering its complex 3D geometry, noise, error-prone, varying point density, and often contains a gap. Many studies have been conducted to classify urban scene point clouds [5–7].

A gradient-based building extraction using LiDAR and photogrammetry imagery is performed as the building roof planes have a constant elevation variation along the roof's slope [8, 9]. Another method, using the parameterization approach for segmenting ALS point clouds in order to extract building roofs with their geometric features, is shown in [10] for the determination of the solar potential. Furthermore, a shading analysis utilizing the usable area of those roofs with the most suitable orientation for the installation of solar panels is computed for any given date and time of the day. The building's individual sub-elements can be recognized through sub-segmentation using geometric and radiometric characteristics jointly obtained from photogrammetric point cloud [11].

With the development of richness in datasets and software-intensive workflows, some machine learning methods have also been used for roof detection. Roof plane extraction from a point cloud is a complex task. Since point cloud data has no connection information and does not provide any semantic characteristics of the surface [12]. Research has been carried out to extract and classify the rooftop from airborne LiDAR based on slope criteria by a model builder in ArcMap [13]. Using GIS tools, a case study is also done to identify roof surfaces from LiDAR point clouds [14].

Voxel-based region growing has also been used to segment out building roofs from an airborne LiDAR point cloud. Building planar surfaces consist of distinctive geometric features like smoothness, continuity, and convexity [15]. Planer surfaces

are also segmented from the unstructured point cloud based on the 2D Hough transform and octree [16]. A deep learning approach has also been used to detect building roofs and facades from Aerial LiDAR data [17].

1.1 Normal Vector

A vector perpendicular to the plane consisting of the points that makes the plane is called a normal vector to that plane (Fig. 1).

Normal vector computation,

Let us consider three points P, Q, and R in a 3D space, then the equation of a plane passing through the three points is;

$$f(\Phi) = ax + by + cz = d \quad (1)$$

where P, Q, and R satisfy the equations.

The normal vector to the plane $f(\phi)$ is $n = (a, b, c)$ and is given by;

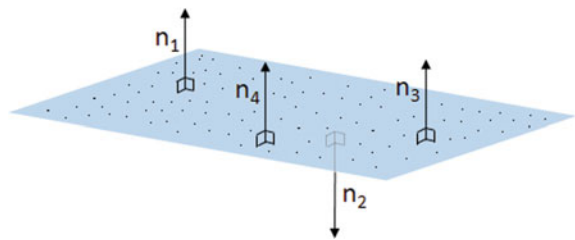
$$\vec{n} = a\vec{i} + b\vec{j} + c\vec{k} \quad (2)$$

The unit normal vector at the given point T (X_t, Y_t, Z_t) is given by;

$$\hat{n} = \frac{a\hat{i} + b\hat{j} + c\hat{k}}{\sqrt{a^2 + b^2 + c^2}} | T(X_t, Y_t, Z_t) \quad (3)$$

The normal vector at each point is an excellent parameter to segregate the point cloud into its corresponding feature orientation. From the literature review, it was observed that the normal vector of each laser point has shown as an excellent feature in decomposing the point cloud into segments describing planar patches. This gave us the idea that utilizing the same normal components for photogrammetric point cloud could provide more information beyond roof extraction. In this research, normal vectors were computed using an open-source python package—Open3D [18], and pandas with a Jupyter notebook were used to implement the approach.

Fig. 1 Normal vectors to the plane consisting of few points in a 3D space



The utilization of the normal components has proven to be the best statistical approach for planar-based segmentation and classification. By constructing an octree-based hierarchical representation, normal estimations can be done at different point cloud scales. Usually, in an urban environment, the normal vectors are in a particular direction as there are many planar surfaces. That makes it easier to segregate buildings [19]. A research has been done to extract facade, roof, and slant roofs using semi-manual filtering of normal vector components [20].

City scale level roof type classification for solar energy productivity using machine learning was also attempted [21]. Mohajeri presented a study using the machine-learning technique for classifying roof shapes for city scale. The SVM classifier's effectiveness in identifying the six types of roof shapes, that is, flat, gable, hip, gambrel and mansard, cross/corner gable and hip, and complex roofs in a European city, was presented. His research derived that the ratio between the useful roof area and the building footprint is close to one. The Photo Voltaic (PV) installation's potential depends on the shape, size, and orientation of the available space or roof. A similar type of research has been carried out at a regional level to determine the solar potential using LiDAR [22]. The accurate solar potential of the points can be calculated when parameters like the shadowing effect, the horizon of each points, effect of cloud cover are considered [23]. Jochem also presented a method that uses the full 3D information for feature extraction and solar potential analysis. A relative height threshold is defined to separate possible roof points from the point cloud, followed by segmenting these points into homogeneous areas fulfilling the limited constraints of roof planes.

Our research provides a statistical approach to analyze point clouds generated from UAV-based photogrammetric processing to classify and extract solar panels. This research focuses on developing an algorithm that extracts all the corresponding solar panel points into a separate file.

2 Study Area and Dataset Used

2.1 Study Area

This research required a building on which solar panels were already installed. The study area chosen is the Geomatics engineering building of the Indian Institute of Technology Roorkee, Uttarakhand, India. The location of the study area is shown in Fig. 2.

The building under consideration is an isolated building of all departmental complex. So, we have chosen this building to check our hypothesis and the efficiency of our algorithm. Solar panels were already installed on the roof of the building.

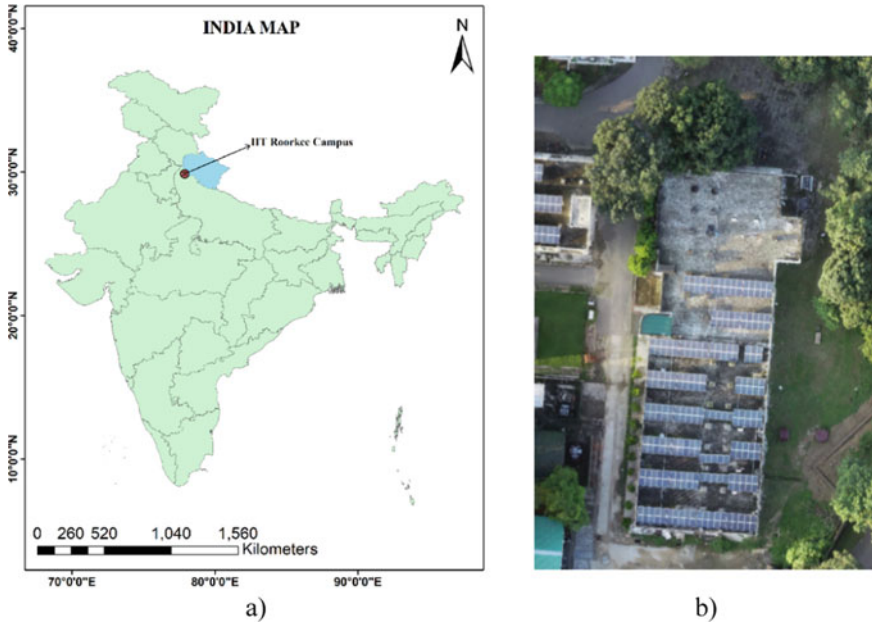


Fig. 2 a Study area map with its location, b An RGB image of the study area for visualization

2.2 Dataset Used

The UAV data acquisition of the Geomatics building was done within the Indian Institute of Technology Roorkee campus. The dataset was acquired with the DJI Phantom 4 Pro model with an optical sensor. Total 38 images were acquired at a flying altitude of 80 m. We have used the point cloud dataset generated through photogrammetric processing of the UAV images. The parameters of the data acquisition are tabulated in Table 1.

Table 1 Data Acquisition parameter details

Parameter	Dataset
UAV - Model	DJI Phantom 4 Pro
Optical Sensor	FC6310 (8.8 mm)
Flying Height	80 m
Side Overlap	50%
Front Overlap	70%
Spatial Resolution	2.34 μm

3 Methodology

Initially, flight planning was done considering the data acquisition parameters and optimum flying height. So that there are no objects in the UAV's line of flight. Data acquisition was made using a UAV with an optical sensor. The RGB images acquired were preprocessed in the Agisoft Metashape Professional Software using Structure from Motion (SfM) to produce a dense point cloud dataset of the study area. Further, a building point cloud is manually segmented out using CloudCompare, from the point cloud dataset for our research purpose on which our algorithm can be tested (Fig. 3).

The building point cloud dataset is used as an input to the algorithm developed. Normal vectors are computed for all the points in the photogrammetric point cloud. As discussed in Sect. 1.1, each normal vector has its corresponding vector components in the (N_x) x-axis, (N_y) y-axis, and (N_z) z-axis, respectively (Fig. 4).

An algorithm was based on open-source python libraries such as Open3D, Pandas, and NumPy for basic analysis over dense point cloud in the Jupyter notebook. After normal computation, a statistical approach was acquired to apprehend the behavior of various components of normal vectors for different areas of the dataset.

After analysis, the difference in vector components was found for roof, facade, and solar panels, which were used to compute the classification parameters. Finally, these parameters were coded as a primary function to be implemented over the original point cloud. Based on the N_z values, the points are classified into Roof, Facade, and Solar panels. Once the solar roof points are extracted, the algorithm's efficiency is evaluated compared to the manually segmented point cloud.

The methodology followed in this research is also represented in a flowchart in Fig. 5.

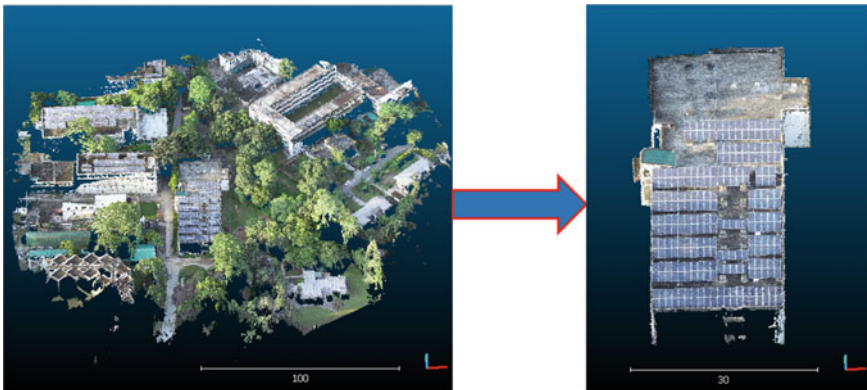


Fig. 3 Photogrammetric dense point cloud of UAV data acquired and study area building segmented out

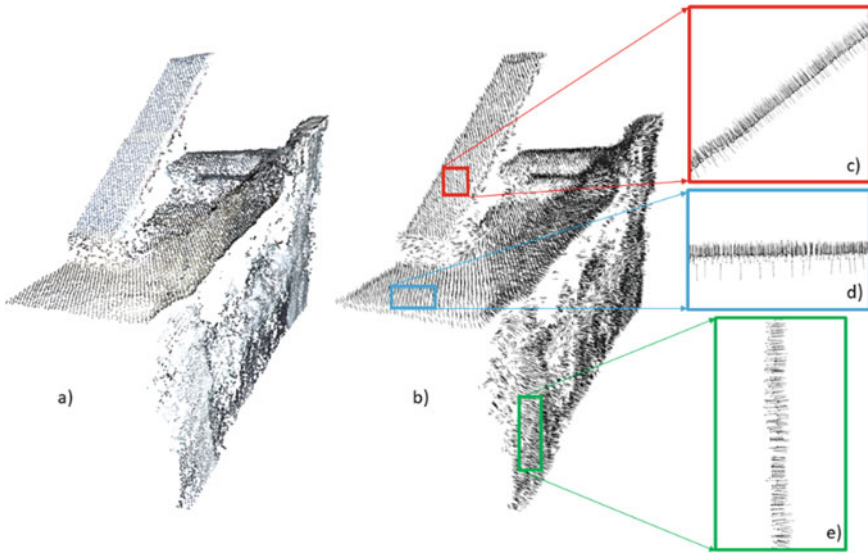


Fig. 4 **a** A subset of the RGB photogrammetric point cloud, **b** Normal vectors of the point cloud, **c** Solar panel normals orientation, **d** Roof normals orientation, and **e** Facade normals orientation

4 Results and Discussions

The developed algorithm has produced efficient results in extracting the solar panels, facade, and roof points from the building photogrammetric point cloud. The roof points are shown in red, facade points in yellow, and rooftop solar panel points in green colour in Fig. 6a, b, and c, respectively.

The effective surface area of the solar panels are clearly distinguished from the overall point cloud.

4.1 Evaluation of the Results

The photogrammetric point cloud of the building is shown in Fig. 7a, and the classified point cloud results obtained from the algorithm are shown in Fig. 7b.

The results obtained from the algorithm are analyzed at various locations of the classified point cloud, and some of the few subsets are depicted in Fig. 8.

Figure 8a1 represents a portion of a protruded structure constructed on the extension of the building's vertical piers. Figure 8b1 represents a portion of the tin roof. Figure 8c1 represents the flat surface at the entrance of the building. Figure 8d1 represents the point cloud's portion at the interface of the windows and the facade of the building. Figure 8e1 represents the portion of the solar panel points on the roof of the building.

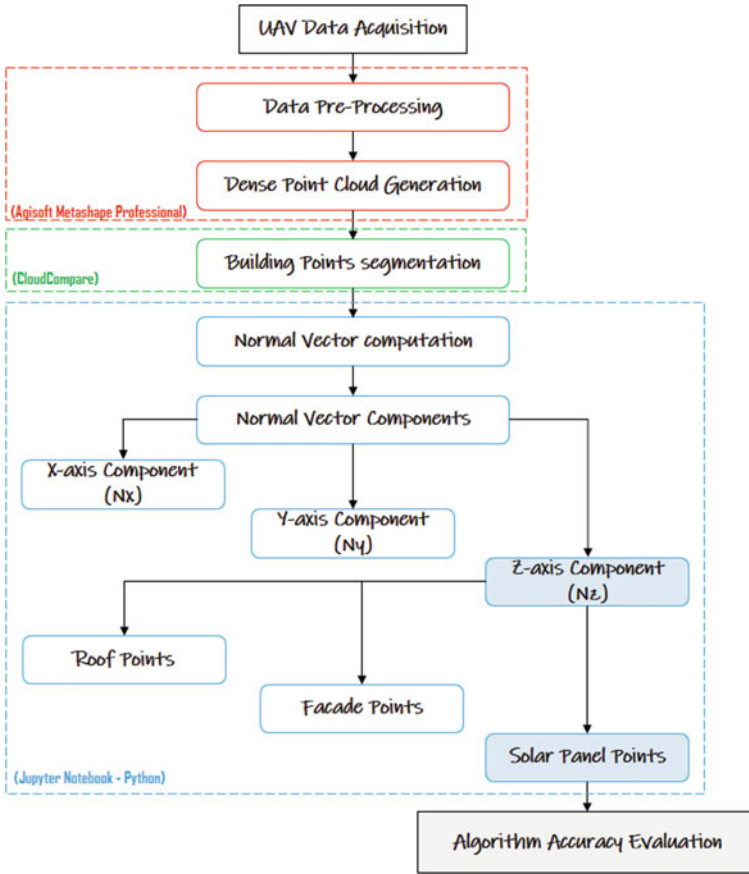


Fig. 5 Research workflow

Figure 8a3, b3, c3, d3 and e3 represents the corresponding classified points of the portions shown in Fig. 8a2, 8b2, 8c2, 8d2 and 8e2 respectively.

We can see some points are misclassified at the interface between vertical and horizontal surfaces as these interfaces are not exactly perpendicular to each other. The interface surfaces are smooth with a curve that has induced a misclassification error as the solar panels' normal vectors (Fig. 8a3 and 8b3). There is also noise at the interface between the facade and window structure which has also produced errors (Fig. 8d3). Due to the low density of the facade points, normal vector computation was quite challenging in classification.

The parameters considered in this research for evaluation [24] are given below (Tables 2 and 3).

$$\text{Type I error} = \frac{FN}{TP + FN} = 0.174 \tag{4}$$

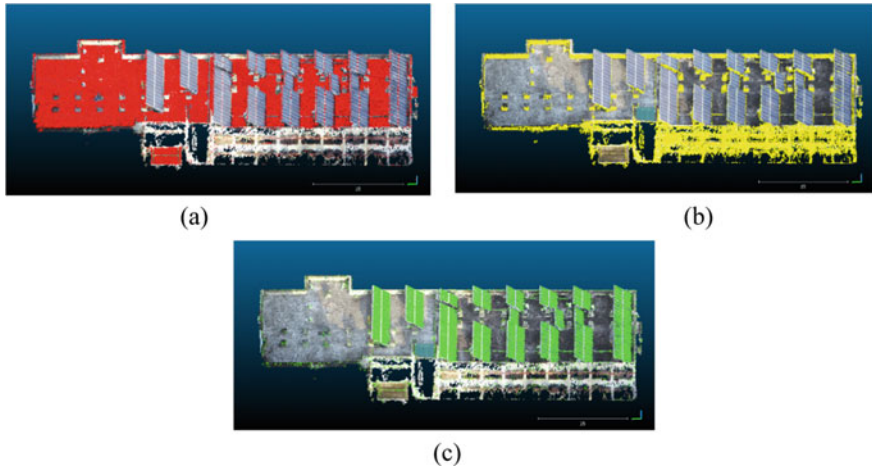


Fig. 6 Point cloud extraction of **a** Roof, **b** Facade, and **c** Solar panel points

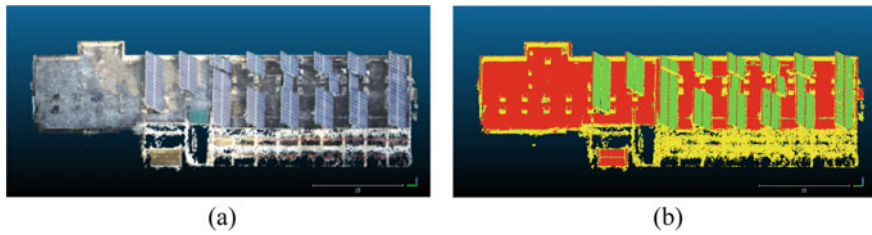


Fig. 7 **a** Photogrammetric point cloud of the building, **b** classified point cloud based on the developed algorithm

$$\text{Type II error} = \frac{FP}{FP + TN} = 0.051 \quad (5)$$

$$\text{Total error} = \frac{FN + FP}{TP + FN + FP + TN} = 0.072 \quad (6)$$

$$Po = \frac{TP + TN}{TP + FN + FP + TN} = 0.927 \quad (7)$$

$$Pe = \frac{(TP + FN)X(TP + FP) + (FP + TN)X(FN + TN)}{(TP + TN + FP + FN)^2} = 0.711 \quad (8)$$

$$\text{Kappa} = \frac{Po - Pe}{1 - Pe} = 0.747 \quad (9)$$

$$\text{Completeness} = \frac{TP}{TP + FN} = 0.825 \quad (10)$$

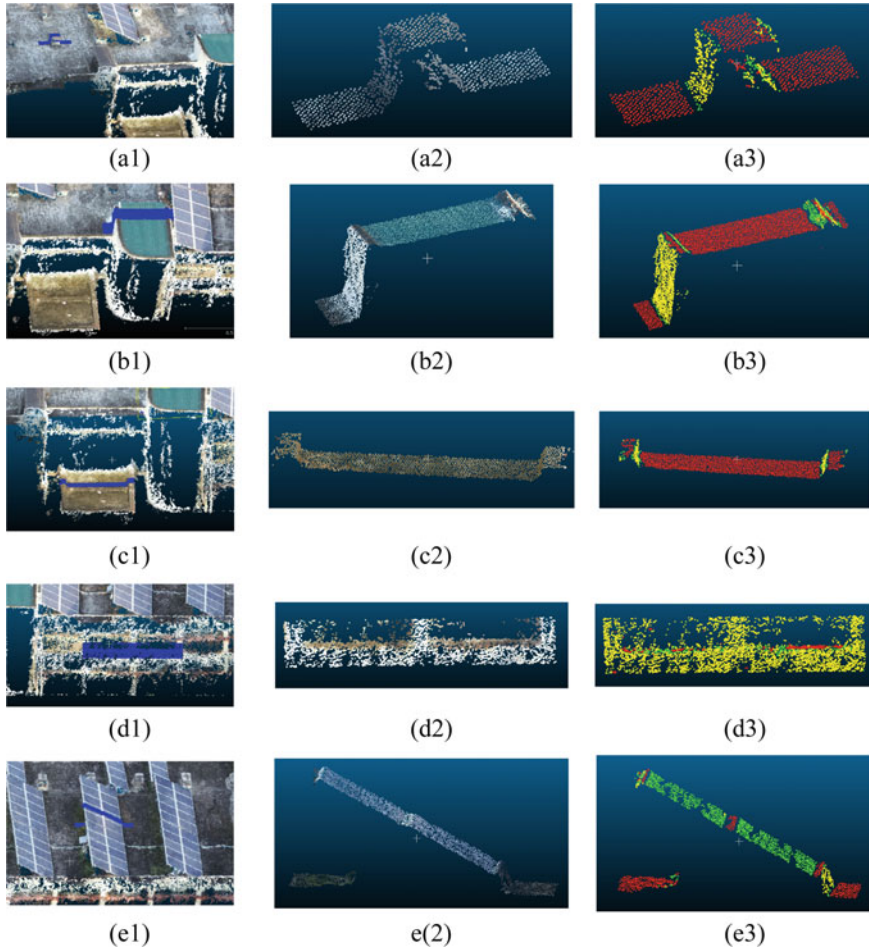


Fig. 8 Different subsets of the point cloud are shown corresponding to its RGB point cloud and classified point cloud

$$\text{Correctness} = \frac{TP}{TP + FP} = 0.764 \quad (11)$$

$$\text{Quality} = \frac{TP}{TP + FN + FP} = 0.657 \quad (12)$$

where, **Type I error** is the percentage of solar roof panel points rejected as non-solar panel points, and **Type II error** is the percentage of non-solar panel points accepted as solar roof panel points. **Total error** is the percentage of incorrectly classified points. **Completeness** is the percentage of reference data being detected. **Correctness** is the percentage of correct detection. **Quality** is the overall success

Table 2 Total number of points corresponding to each class of point cloud

Geomatics building points	Solar panel points			
	Actual points	Correctly detected points	Wrongly detected points	Undetected points
1,813,155	304,972	251,638	77,468	53,334

Table 3 Total number of points corresponding to False Positive (FP), False Negative (FN), True Positive (TP), and True Negative (TN)

FP	77,468
FN	53,334
TP	251,638
TN	1,430,715

rate. The **Kappa coefficient** is a statistical measure of the inter-ratio agreement, which is believed to be a more robust measurement than a simple percentage, **TP (True Positive)** is the number of solar roof panel points classified by both manual as well as algorithm, **TN (True Negative)** is the number of non-solar panel points classified by both datasets, **FP (False Positive)** is the number of solar panel points classified only by the proposed algorithm, **FN (False Negative)** is the number of solar panel points classified only by the reference dataset.

5 Conclusions

The proposed algorithm, has proved to be efficient in obtaining solar panel points from the building's overall point cloud dataset. The algorithm has also extracted points corresponding to the roof and facade efficiently. The interface points between the roof and solar panels, roof, and facade can contribute to an error in the normal vectors computed. So, the number of nearby points required to compute the normal vectors has to be appropriately chosen, keeping the point density and data structure into consideration.

One of the main limitations of this approach was that the classification is done solely based on normals computed over the point cloud. The algorithm can also be further improvised to extract points belonging to slant roofs and slant solar panels based on RGB values of each points in the photogrammetric point cloud.

The accuracies obtained for extraction of building solar panels, roofs, and facades were efficient considering **Completeness as 0.825** and **Correctness as 0.764**. This research is focused on testing the efficiency of the proposed algorithm to extract solar panels installed on the building roof. This research can further be used to calculate the effective area of solar panels, which can be used to calculate the solar panels' productivity.

The developed algorithm has produced efficient results in extracting solar panel points.

References

1. Singh A, Kushwaha SKP (2020) Forest degradation assessment using UAV optical photogrammetry and SAR data. *J Indian Soc Remote Sens* 2. <https://doi.org/10.1007/s12524-020-01232-2>
2. Baranwal E, Seth P, Pande H, Raghavendra S, Kushwaha SKP (2020) Application of unmanned aerial vehicle (UAV) for damage assessment of a cultural heritage monument. *Lect Notes Civ Eng* 51:123–131. https://doi.org/10.1007/978-3-030-37393-1_13
3. Sestras P, Bilaşco Ş, Roşca S, Dudic B, Hysa A, Spalević V (2021) Geodetic and UAV monitoring in the sustainable management of shallow landslides and erosion of a susceptible urban environment. *Remote Sens* 13(3):1–29. <https://doi.org/10.3390/rs13030385>
4. Adhikari A, Kumar M, Agrawal S, Raghavendra S (2020) An integrated object and machine learning approach for tree canopy extraction from UAV Datasets. *J Indian Soc Remote Sens* 2. <https://doi.org/10.1007/s12524-020-01240-2>
5. Ozdemir E, Remondino F (2018) Segmentation Of 3D photogrammetric point cloud for 3D building modelling *XLII(October)*:135–142. <https://doi.org/10.5194/isprs-archives-XLII-4-W10-135-2018>
6. Ozdemir E, Remondino F, Golkar A (2019) Aerial point cloud classification with deep learning and machine learning algorithms *XLII(October)*:843–849. <https://doi.org/10.5194/isprs-archives-XLII-4-W18-843-2019>
7. Vosselman G (2013) Point cloud segmentation for urban scene classification. *Int Arch Photogramm Remote Sens Spat Inf Sci-ISPRS Arch* 40(7W2):257–262. <https://doi.org/10.5194/isprsarchives-XL-7-W2-257-2013>
8. Siddiqui FU, Teng SW, Awrangjeb M, Lu G (2016) A robust gradient based method for building extraction from LiDAR and photogrammetric imagery. *Sensors (Switzerland)* 16(7). <https://doi.org/10.3390/s16071110>
9. Hujebri B, Ebrahimikia M, Enayati H (2019) Automatic building extraction from lidar point cloud data in the fusion of orthoimage. *Int Arch Photogramm Remote Sens Spat Inf Sci-ISPRS Arch* 42(4/W18):541–546. <https://doi.org/10.5194/isprs-archives-XLII-4-W18-541-2019>
10. Soilán M, Riveiro B, Linares P, Padín-Beltrán M (2018) Automatic parametrization and shadow analysis of roofs in urban areas from ALS point clouds with solar energy purposes. *ISPRS Int J Geo Inf* 7(8):1–14. <https://doi.org/10.3390/ijgi7080301>
11. Vetrivel A, Gerke M, Kerle N, Vosselman G (2015) Segmentation of UAV-based images incorporating 3D point cloud information. *Int Arch Photogramm Remote Sens Spat Inf Sci-ISPRS Arch* 40(3W2):261–268. <https://doi.org/10.5194/isprsarchives-XL-3-W2-261-2015>
12. Gilani SAN, Awrangjeb M, Lu G (2018) Segmentation of airborne point cloud data for automatic building roof extraction. *GIScience Remote Sens* 55(1):63–89. <https://doi.org/10.1080/15481603.2017.1361509>
13. Kushwaha SKP, Yogender, Raghavendra S (2019) A semi-automatic approach for rooftop extraction and classification from airborne lidar. In: *Proceedings volume 11174, seventh international conference on remote sensing and geoinformation of the environment (RSCy2019)*; 111740K. <https://doi.org/10.1117/12.2532044>
14. Gergelova MB, Labant S, Kuzevic S, Kuzevicova Z, Pavolova H (2020) Identification of roof surfaces from LiDAR cloud points by GIS tools: a case study of Lučenec, Slovakia. *Sustainability (Switzerland)* 12(17). <https://doi.org/10.3390/SU12176847>
15. Xu Y, Yao W, Hoegner L, Stilla U (2017) Segmentation of building roofs from airborne LiDAR point clouds using robust voxel-based region growing. *Remote Sens Lett* 8(11):1062–1071. <https://doi.org/10.1080/2150704X.2017.1349961>
16. Tian P, Hua X, Yu K, Tao W (2020) Robust segmentation of building planar features from unorganized point cloud. *IEEE Access* 8:30873–30884. <https://doi.org/10.1109/ACCESS.2020.2973580>
17. Pirotti F, Zanchetta C, Previtali M, Della Torre S (2019) Detection of building roofs and facades from aerial laser scanning data using deep learning. *ISPRS Ann Photogramm, Remote Sens Spat Inf Sci* 42(2/W11):975–980. <https://doi.org/10.5194/isprs-Archives-XLII-2-W11-975-2019>

18. Zhou QY, Park J, Koltun V (2018) Open3D: a modern library for 3D data processing. 1801.09847v1
19. Zhao R, Pang M, Liu C, Zhang Y (2019) Robust normal estimation for 3D LiDAR point clouds in urban environments. *Sensors (Switzerland)* 19(5):1–17. <https://doi.org/10.3390/s19051248>
20. Kushwaha SKP, Dayal KR, Singh A, Jain K (2019) Building facade and rooftop segmentation by normal estimation. In: 6th international workshop lowcost 3D – sensors, algorithms, applications, XLII-2/W17(December), pp 173–177. <https://doi.org/10.5194/isprs-archives-XLII-2-W17-173-2019>
21. Mohajeri N, Assouline D, Guiboud B, Bill A, Gudmundsson A, Scartezzini JL (2018) A city-scale roof shape classification using machine learning for solar energy applications. *Renew Energy* 121:81–93. <https://doi.org/10.1016/j.renene.2017.12.096>
22. Nguyen HT, Pearce JM, Harrap R, Barber G (2012) The application of LiDAR to assessment of rooftop solar photovoltaic deployment potential in a municipal district unit. *Sensors* 12(4):4534–4558. <https://doi.org/10.3390/s120404534>
23. Jochem A, Höfle B, Rutzinger M, Pfeifer N (2009) Automatic roof plane detection and analysis in airborne lidar point clouds for solar potential assessment. *Sensors* 9(7):5241–5262. <https://doi.org/10.3390/s90705241>
24. Wang L, Xu Y, Li Y, Zhao Y (2018) Voxel segmentation-based 3D building detection algorithm for airborne LIDAR data. *PLoS ONE* 13(12):1–26. <https://doi.org/10.1371/journal.pone.0208996>

Spacio-Statistical Model to Predict Crime Locations Based on Past Crime Events and UAV Based Monitoring of the Predicted Surveillance Route



Hasmukh Chauhan, Pranav Pandya, and Chancy Shah

Abstract Crime is heterogeneously distributed and occurs at the most vulnerable places. Crime occurs under poor surveillance and safety, due to lack of public protection and results in damage to public property or human life, and creates a public discrepancy in that particular location. Crime is disastrous because of its unpredictability and unpreparedness for enforcement officers. Finding the probability of occurrence of crimes within such vulnerabilities will help us to deploy certain countermeasures to reduce crime. Crime is limited to location and place. Geographically crime can be considered as a function of lack of surveillance, delay in mobility and control, and probably hidden escape paths utilized by criminals. In this research, a Spatio-Statistical Model was developed for probability-based Crime Prediction using past data and location intelligence technology. Neighborhood Analysis was performed to evaluate the clustering distance between individual crime occurrences within Vadodara city and individual police stations in the neighborhood. The spatial distance is converted into Geographical Coordinate System to calculate latitudinal and longitudinal extents of crime zones in each taluka of the city, which is then utilized to create the Interpolated probability raster for each crime zone with a pixel value equivalent to the probability of occurrence of crime in that location. The Inverse distance weighted (IDW) interpolation technique generated an interpolated surface which was then represented spatially with quantile divisions to form probability zones with the adjoining nearest police jurisdiction. This will enable law enforcement officers to make probability-based surveillance decisions while incorporating the past data intelligence, time of occurrence of crime, and make efficient serviceable patrolling routes and improve crime control with minimal resources. Using this

H. Chauhan (✉)

Birla Vishvakarma Mahavidyalaya, Autonomous Engineering Institution, V.V. Nagar, Anand, Gujarat, India

e-mail: hjchauhan@bvmengineering.ac.in

P. Pandya

Symbiosis International University, Pune, Maharashtra, India

C. Shah

Institute of Science & Technology for Advanced Studies & Research (ISTAR), V.V. Nagar, Anand, Gujarat, India

© The Author(s), under exclusive license to Springer Nature Switzerland AG 2023

K. Jain et al. (eds.), *Proceedings of UASG 2021: Wings 4 Sustainability*,

Lecture Notes in Civil Engineering 304,

https://doi.org/10.1007/978-3-031-19309-5_14

model, the police officers will be able to create patrol routes based on time and zone of highest probability of crime, to ensure safety. The time-based probability of crime is also calculated using the Bayesian probability formula to get the peak crime hours so that surveillance need to be increased at the appropriate time. UAVs mounted with thermal vision can be deployed in the generated high probability zones at the highest probable time of the crime, to monitor the situation aerially without alarming the criminals. In this research it is created an open-source pixel-based route selection algorithm that could identify hotspot locations of crime so that law enforcement officers can watch human movements and follow them silently using UAV's thermal camera in nighttime also to obtain their hideouts and catch criminals.

Keywords Crime data · UAV · Location intelligence · Surveillance

1 Introduction

Crime is a man-made disaster, but it originates when the criminal finds a social vulnerability such as human carelessness, inadequacy in taking precautions, walking in dark alleys alone at night i.e. lack of personal safety, carrying valuables in unsafe areas, parking vehicles in unregulated regions, etc. All these factors that contribute to crime are geographically identifiable and discrete in nature [1]. Crime occurs under poor surveillance and safety, due to lack of public protection and results in damage to public property and/or human life, creating chaos in that particular area. This ultimately damages the public image of law enforcement and government. Crime is dangerous because of its unpredictability aspect, which leaves law enforcement officers unprepared when they face crime. Finding the probability of occurrence of crimes within such vulnerabilities will help authorities to deploy certain counter-measures to reduce crime. Predicting crime locations could help law enforcement agencies to counter it with appropriate approaches while utilizing the same number of police personnel. Thus the efficiency and effectiveness of police could be increased. Crime is limited to location and place. Geographically crime can be considered as a function of lack of surveillance, delay in mobility and control, and probably hidden escape paths utilized by criminals. In the following research, a Spatio-Statistical Model was developed for probability-based crime prediction using past data and location intelligence technology.

The utilization of Location Intelligence for crime mapping encourages delineation, and investigation of crime problem areas, alongside different patterns and examples. It is a key segment of crime investigation and the policing system. GIS uses geography and computer-generated maps as an interface for integrating and accessing massive amounts of location-based information. GIS permits police work force to design adequately for crisis reaction, decide relief needs, examine verifiable occasions, and foresee future occasions. It can likewise be utilized to get basic data to crisis responders upon dispatch or while in transit to an occurrence to aid strategic arranging and reaction. GIS helps crime officers decide potential crime

locales by analyzing complex apparently disconnected criteria and showing them all in a graphical, layered, spatial interface or guide [2].

Every single law implementation office and law authorization officer's extreme objective is to prevent crime. Using crime maps the police divisions can recognize where the crime is increasingly noticeable, and furthermore where the exploited people are found. This data would demonstrate which neighborhoods are the most hotspots. Using this data, the Police can follow criminals' movements from area to area. This is finished by separating the crime by the time of day and by day of week and by day of the month. For instance, in deciding the criminal mentality for thefts, one could take the times of the month and reason that the offenders are progressively dynamic in the start of the month. This, and data on the victims, could reveal to us that the criminals are concentrating on unfortunate casualties that get their help at the start of the month.

Finding the probability of occurrence of crimes within such vulnerabilities will help the authorities to deploy certain countermeasures to reduce crime. Predicting crime locations could help law enforcement agencies to counter it with appropriate approaches while utilizing the same number of police personnel. Thus the efficiency and effectiveness of police could be increased.

2 Literature Review

Crime analysis is a function of law enforcement which includes systematic analysis of crime data and identifying and analyzing patterns and trends in crime. Crime mapping is integral to all types of crime investigation in that it has a significant impact in every analysis. Crime mapping does not remain solitary; rather, it is a procedure that happens inside the bigger procedure of crime investigation [3, 4].

There has been a great deal of work done on the subject of crimes. To assist individuals in following law enforcement, large datasets have been evaluated, and information such as location and kind of crime has been retrieved. These datasets have been used in the past to identify crime hotspots based on location along with numerous mapping applications that display the specific location of crimes as well as the types of crimes in each particular city. Despite the fact that crime scenes have been located, there is no information on the crime's date and time of occurrence [5].

In modern criminology, understanding how social and environmental variables influence the spatiotemporal distribution of criminal activity is a critical topic. Previous research done in this domain provides feasible solution to analyze exactly the crime impact of environmental characteristics to a specific place because of the advent of statistical approaches such as Risk Terrain Modeling (RTM) [5]. However, the function of social information in determining the distribution of criminal actions, on the other hand, has received little attention in the criminological study literature [6].

Research Gap: Despite the fact that there has been previous research, none of it considers the three components (place, time, and crime type) together. Furthermore, there is virtually little research that can reliably forecast where future crimes will occur [4, 7, 8]. This research provide a data-mining methodology for predicting crime based on crime categories and employing geographical and temporal hotspots for crime in research.

3 Study Area

Vadodara is the third-largest city of Gujarat state (Fig. 1). It is the administrative headquarters of Vadodara District and is situated on the banks of the Vishwamitri River. In 2011, Vadodara had a population of 2.065 million people. City is well known for the Lakshmi Vilas Palace, the residence of Baroda State's Maratha royal family, the Gaikwads. It also has Maharaja Sayajirao University of Baroda, the largest university in Gujarat. An important industrial, cultural and educational hub of western India, the city has various institutions of national and regional importance and various small to large scale industries (Table 1).

Vadodara is gearing towards becoming a smart city, and yet it has observed continual growth in crime rate. With increasing crime events, the stability and safety of citizens [4]. Previous similar studies and approaches, on the other hand, primarily identify crime hotspots based on the area of high crime density, without taking into account crime type or crime occurrence date and time [9, 10].

Table 1 Details of study area

Coordinates	22.30°N 73.19°E
Altitude	35.5 Mts. above mean sea level
Area	159.95 km ²
Population	2,065,771
Population Density	10,335/km ²
Literacy Rate	94.5%
Railway	Vadodara is towards the Western Railway Mumbai Delhi and Mumbai Ahmedabad line
Roadway	Vadodara has road connectivity with National Highway No. 8
Bus Transport	The Gujarat State Transport Corporation has appointed its buses between Vadodara and Ahmedabad and also on main towns and tourist centres of Gujarat
Airport	The city has an international airport connected with Mumbai and Delhi

Source Wikipedia <https://en.wikipedia.org/wiki/Vadodara>



Fig. 1 Location of the study area—Vadodara City (Source <http://www.maphill.com/india/gujarat/location-maps/physical-map/highlighted-country/>, <https://www.google.com/maps/place/Vadodara,+Gujarat/@22.3220425,73.0330003,11>)

4 Crime Data Collection and Analysis

Crime is dependent on geographical factors, so location-based crime data were collected. Data collection included the origin place of the crime, date, time, number of people involved, and the type of crime according to the Indian Penal Code (IPC 1860). These datasets were Geotagged and point features (Crime Spots) were generated for each crime incident [11] (Table 2).

Neighborhood analysis was performed to evaluate such geographical factors to count and classify Neighborhood regions within the city to be vulnerable to crime [12, 13]. These regions were clustered and the distance between individual crime occurrences within Vadodara city and individual police stations in the neighborhood was correlated and evaluated. Later, the spatial distances between zonal geographical centers and crime spots were converted into geographical coordinate system to

Table 2 Spatial and attribute data collected

Crime data	Date of crime	Time	Type	Place	No. of people involved
Police station	Name	Location	Police station number		
Vadodara City	Boundary shapefile	OSM road network	Buildings and facilities		

calculate latitudinal and longitudinal extents of crime zones in each taluka of the city. This was helpful in making crime zone maps for Vadodara city [13]. Also, using the crime spot, an interpolated probability raster was prepared using the Inverse Distance Weighted (IDW) interpolation technique which was then represented spatially to form probability zones with the adjoining nearest police jurisdiction for each crime zone with pixel value equivalent to the probability of occurrence of crime in that location [2].

5 Results and Discussion

5.1 Crime Occurrence Statistics

In the collected crime data, the date of occurrence of crime was recorded which helped us prepare a date-time crime database, using which crime was organized per week (Fig. 2a), monthly (Fig. 2b) and seasonal (Fig. 2c) as shown below.

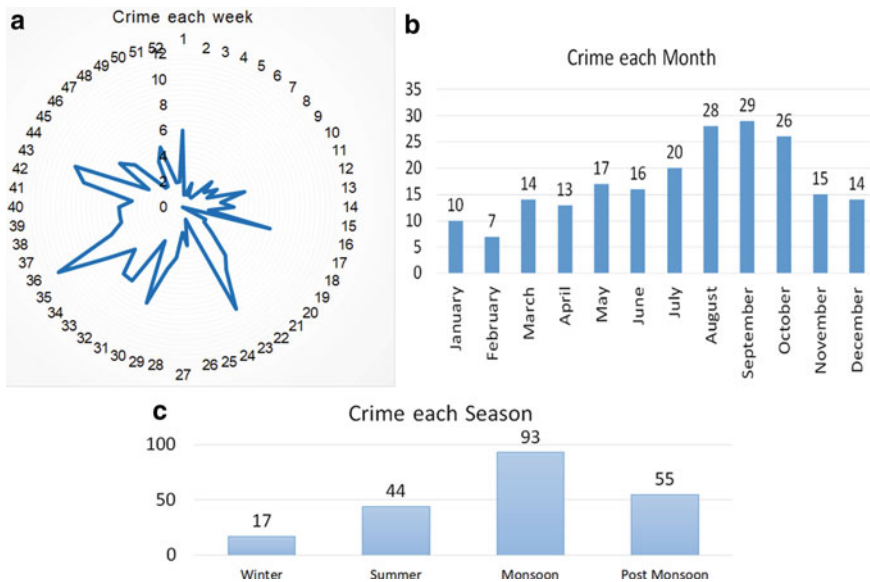
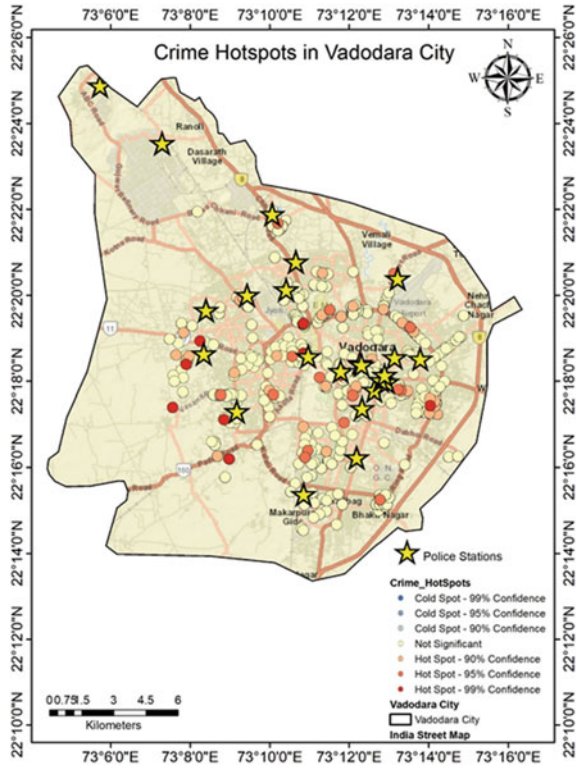


Fig. 2 a Crime Occurrences per week for 1 year. b Crime count for whole year with crime occurring in each month. c Crime occurrence in each season

Fig. 3 Distribution of police station and visualization of crime occurrences in Vadodara City



5.2 Intelligence in Crime Handling

Some regions of Vadodara city are more populated than others, in those areas more crime rate than other regions is observed, e.g., Alkapuri area. Police station's influence in a city is limited by the regional area a patrolling vehicle can cover as quickly as possible [2, 3].

The Fig. 3 represents the crime occurrences in green with the police station in the star. The map expresses the excess amounts of crime occurrences with respect to police stations.

5.3 Time Based Crime Prediction

A sophisticated body of evidence exists from previous research works which suggests the utility of clinical versus statistical-prediction of criminal behavior [7]. In terms of the spatial distribution of crime, little is known about the predictive validity of both clinical and statistical prediction models [14, 15]. Therefore, how well do experts

(i.e., front-line officers) predict which geographic regions should be targeted for preventative measures is always under question [4]. Crime and location research reveals that crime occurrences cluster spatially within their local hotspots. Statistical forecasts based on the geographic persistence characteristic of hot spots can be used as a benchmark for professional judgment-based prediction capabilities [7].

Crime Hotspot Analysis was done to identify the spatial locations of such hotspot within different wards of Vadodara City. Police have been able to more effectively target criminogenic areas thanks to hotspot mapping [16], whereby the location of a position with active crime occurrences is identified by clustering them together, which helps us to observe any hidden trend for vulnerabilities present in different regions. To make clusters of the crime occurrences table, first crime events are segregated into various categories based on IPC crime rules.

According to IPC there are 7 types of crime [11, 17]:

- Crimes against body
- Crimes under sexual offences
- Crimes relating to property offences
- Crimes relating to public order
- Crimes relating to economic crimes
- Human trafficking
- Crime against women

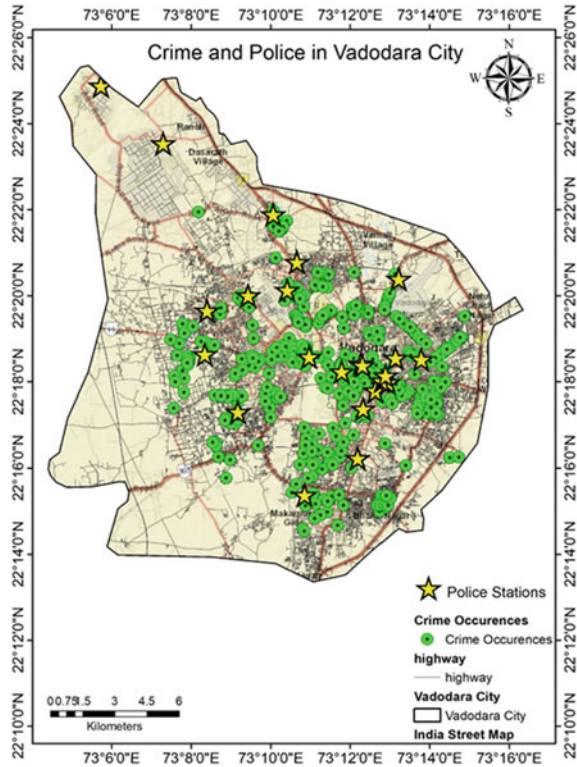
Clustering the crime occurrences, we observed that, there are more than one type of crime (marked in red). Location with persistence in occurrence of different types of crime are critical to overall safety of society because it indicates that certain regions have multitude vulnerabilities, and aren't related to random occurrences or mistakes [18]. For example, certain incidents of robbery can occur randomly, and certain planned crimes can take place at a certain location. But if some location has different types of crime occurring in that place, it indicates that the given location is vulnerable to many different contexts of crime, and addressing this must be at a higher priority [9]. Also these clustered locations indicate that a variety of populations are prone to be affected, and such regions are not safe for residence as well as economic activities (Fig. 4).

5.4 Crime Category Prediction

After categorizing the crime data and visualizing it, an interpolated raster was generated using an inverse distance weighted method [19]. This allowed for utilizing crime data and generating a predictive map of different regions where multiple types of crime can occur [10]. This map will help authorities and police personnel to allocate resources to be able to handle predicted categories of crime accordingly.

As people grow older and more familiar with the neighborhood, chances of occurrence of crime keep increasing. Different types of crime can occur in a specific place when certain vulnerabilities are existing, and the predictive map generated using

Fig. 4 Crime and police in Vadodara City



IDW method forecasts the regions where the probability of occurrence of different types of crime is highest [16].

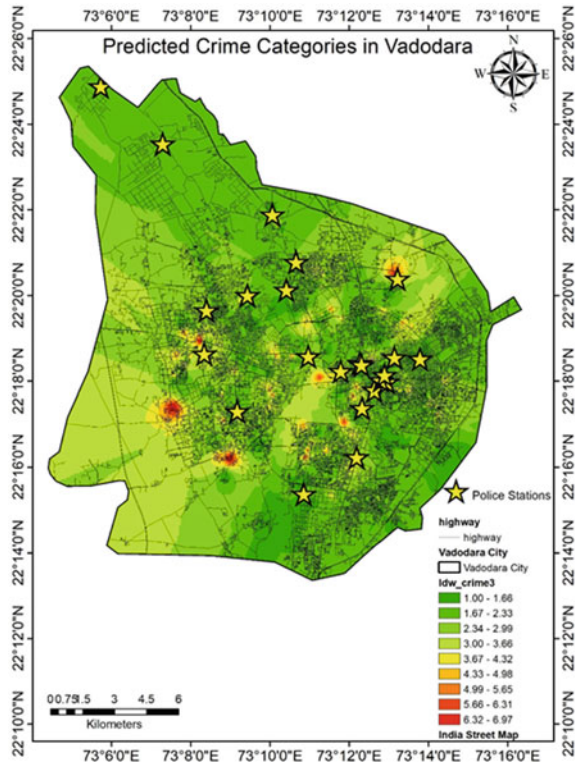
The thematic layer in Fig. 5 indicate the possibility of occurrence of crime of specified category in the specified region. Hence, police can allocate resources within the original bounds which should be competent to handle the different types of crime.

5.5 UAV Utilization in Fighting Crime

UAVs mounted with thermal vision can be deployed in the calculated high probability crime zones at the highest probable time of the crime, to monitor the situation aerially without alarming the criminals. Police officers can then spot the criminals using thermal vision cameras mounted on UAVs, and follow them to their hideout [2]. After confirming the criminals aerially using a drone, police can call for backup and can surround the hideout and catch all the criminals before resulting in casualties.

To make this all possible, in this research, we have created an open-source pixel-based selection algorithm that could identify human bodies thermally and law

Fig. 5 Prediction of different crime categories and their occurrences in Vadodara City



enforcement officers can watch human movements and follow them silently using UAVs to obtain their hideouts and catch criminal gangs altogether [16].

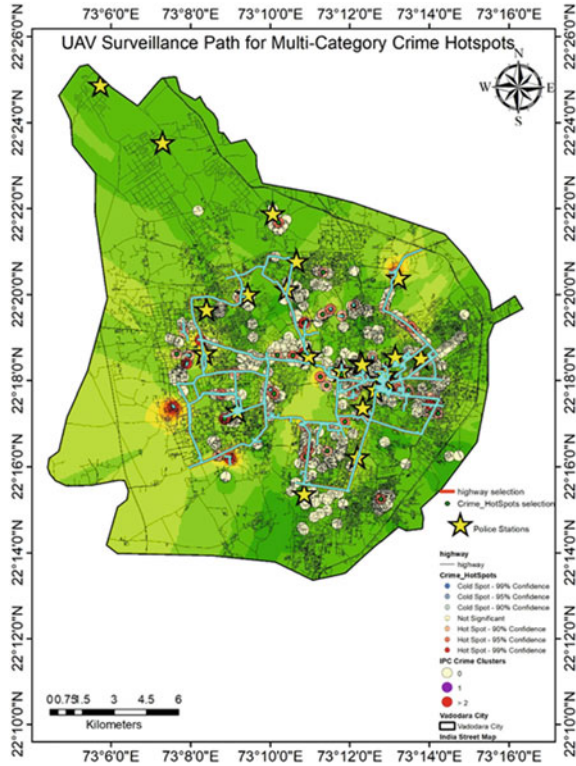
The chosen UAV path will cover all hotspots and multi-category zones, to help monitor and take necessary steps easily and efficiently (Fig. 6).

6 Conclusion

This will enable law enforcement officers to make probability-based surveillance decisions while incorporating (1) The past data intelligence, (2) the Time of occurrence of crime, and make efficient serviceable patrolling routes and improve crime control with minimal resources. Using this model, the police officers will be able to create patrol routes based on time and zone of highest probability of crime, to ensure safety. Furthermore, in order to get the peak crime hours when surveillance must be increased, the time-based probability of crime was calculated using the Bayesian probability formula.

UAVs mounted with thermal vision can be deployed in the calculated high probability crime zones at the highest probable time of the crime, to monitor the situation

Fig. 6 UAV surveillance path prepared from hotspot and category cluster map of Vadodara City



aerially without alarming the criminals. Police officers can then spot the criminals using thermal vision cameras mounted on UAVs, and follow them to their hideout. After confirming the criminals aerially using a drone, police can call for backup and can surround the hideout and catch all the criminals before resulting in casualties.

To make this all possible, in this research, we have created an open-source pixel-based selection algorithm that could identify human bodies thermally and law enforcement officers can watch human movements and follow them silently using UAVs to obtain their hideouts and catch criminal gangs altogether.

Acknowledgements We acknowledge grant received from AICTE under Research Promotion Scheme (RPS) to carry out research in this area.

References

1. Application of GIS in crime analysis: a gateway to safe city gupta, R1, Rajitha K, Basu S, Mittal SK 1 professor, civil engineering group, BITS- Pilani, Rajasthan-333031 Ph. (O)01596-42139, (R): 01596-44340 email: rajiv@bits-pilani.ac.in
2. A statistical study of increasing crime rate against women in India, Gujarat and Major Cities of Gujarat DR, Radadiya AJ. Rajyaguru2 IICDS department, women & child development, Navsari. 2 Professor, department of statistics, Veer Narmad South Gujarat University, Surat 2nd international conference on multidisciplinary research & practice Page 312 Volume III Issue I IJRSI ISSN 2321-2705
3. Crime data mining for indian police information system Manish Gupta*, B. Chandra and M. P. Gupta Indian Institute of Technology Delhi, Hauz Khas, New Delhi. India 110 016
4. Mapping crime: principle and practice by Keith Harries, Ph.D. December 1999 NCJ 178919U.S. Department of Justice Office of Justice Programs 810 Seventh Street N.W. Washington, DC 20531
5. Crime mapping and analysis using GIS by Pranav Kedia, Student, international institute of information technology, Bangalore, July 2016. <https://doi.org/10.13140/RG.2.2.11064.14081>
6. Mapping crime: understanding hot spots, Report U.S. Department of justice office of justice programs national institute of Justice. www.ojp.usdoj.gov/nij
7. GIS technologies in crime analysis and crime mapping M Vijaya Kumar, C Chandrasekar. International Journal of Soft Computing and Engineering (IJSC) ISSN: 2231-2307, Volume-1, Issue-5, November 2011
8. Crime mapping and analysis using GIS C.P. Johnson geomatics group, C-DAC, Pune University Campus, Pune 411007 johnson@cdac.ernet.in
9. Role of geospatial technology in crime mapping: a case study of Jharkhand state of India. American Journal of Geographical Research and Reviews (ISSN:2577-4433) Research Article AJGRR (2018) 1:5 Firoz Ahmad 1*, Md Meraj Uddin2, Laxmi Goparaju 1Vindhyan ecology and natural history foundation, Mirzapur, Uttar Pradesh, India. 2 University department of mathematics, MCA, Ranchi University, Ranchi, Jharkhand, India
10. McKinley J, Ruffell A Harrison M, Meier W, Kemp H, Graham C, Barry L (2008) Spatial thinking in search methodology: a case study of the “Nobody murder enquiry”. West of Ireland. In: Ritz K, Dawson L, Miller D (eds) Criminal and environmental soil forensics. Springer. New York, pp 285–302
11. Introduction to crime mapping 04-Boba-4723.qxd 6/9/2005 12:29 PM Page 37
12. Pros and cons of crime mapping, Benjamin Matias American public university instructor: Dr. Robert Mathis CMRJ512 police administration research paper: crime mapping
13. Crime mapping and spatial analysis By Mostafa Ahmadi ITC primary supervisor: Y. Sun.MSc ITC secondary supervisor: Dr. A. Sharifi Iranian supervisor: Dr. M. J. Valadan, international institute for geo-information science and earth observation, February 2003
14. Ghawana T (2014) Crime mapping using geospatial technologies: a case study of NCT Delhi. <https://doi.org/10.13140/2.1.3185.5681>
15. Carcach C (2016) The spatial analysis of crime statistics and crime mapping. 08 July 2016
16. Farrell G, Pease K (1993) In: Goldstein H (ed) Once bitten, twice bitten: repeat victimization and its implications for crime prevention, vol 46. Her Majesty’s Stationery Office, London; (1990) Problem-oriented policing.: McGraw-Hill, New York
17. Menard S (2000) The ‘normality’ of repeat victimization from adolescence through early adulthood. Justice Q 17(3):543–574
18. Eck JE, Chainey S, Cameron JG, Leitner M, Wilson RE (2005) Mapping crime: understanding HotSpots, NIJ
19. Carneiro T, Medeiros Da Nóbrega RV, Nepomuceno T, Bian G, De Albuquerque VHC, Filho PPR (2018) Performance analysis of google colab as a tool for accelerating deep learning applications. IEEE Access 6:61677–61685. <https://doi.org/10.1109/ACCESS.2018.2874767>

Automatic Ship Detection Using CFAR Algorithm for Quad-Pol UAV-SAR Imagery



Harshal Mittal and Ashish Joshi

Abstract Remote Sensing data, either airborne or satellites, are very much useful for incorporating the Geographical Information System (GIS) technology. SAR sensors are good as compared to optical sensors for monitoring maritime activity due to their capability of penetrating clouds and can work without depending upon any weather condition. SAR sensors can work day and night while optical sensors need a source to illuminate the surface hence can only work in the daytime. Many studies have been done on UAV SAR sensors for different applications like oil spills, ship detection, etc. Moreover, the polarimetric technique helps in understanding the feature much more in detail by using phase information like orientation and shape of the object using scattering behavior. In this paper, the main focus of the study is the Automatic ship detection using the Adaptive Threshold Algorithm popularly known as Constant False Alarm Rate (CFAR) for polarimetric UAV SAR data. Coherency Matrix (T_3) is computed from quad-pol covariance SAR data C_3 and CFAR algorithm is applied to each element of the coherency matrix to detect ships. The sea surface follows the surface scattering and this can be highly helpful to distinguish the ships from the sea background. Moreover, due to the homogeneous background of imagery, the CFAR algorithm works more precisely as it can compute the adaptive threshold for each pixel using the background area by assuming it to the Gaussian in nature. Moreover, the Global Self-consistent, Hierarchical, High-resolution Geography Database (GSHHG) vector coastline layer and Digital Elevation Model (DEM) are used for masking out the land area to enhance the area of interest. In this study, T_{22} element of the scattering matrix shows better results in the detection of the ships and in determining the shape of the ships. Finally, the efficiency of the algorithm is measured using the Receiver Operating Characteristics (ROC) curve.

Keywords UAV-SAR · CFAR · Ship-Detection · GSHHG · Quad-Polarimetry

H. Mittal · A. Joshi (✉)

Photogrammetry and Remote Sensing Department, Indian Institute of Remote Sensing, ISRO, Dehradun 248001, India

e-mail: ashish@iirs.gov.in

1 Introduction

Synthetic Aperture Radar (SAR) is always a prominent data source for all maritime activities like oil spill detection, ship detection, wind direction estimation, etc. Moreover, it is also proved to be an advanced remote sensing technique [5] that is sensitive to the structural properties of the objects on the surface. Also, SAR polarimetry (PolSAR) is one of the advancements of the SAR that helps in understanding the feature properties more precisely. The SAR majorly transmits and receives Electromagnetic waves for the detection of any object. The interaction of these waves with the object helps us in understanding the structural property [1]. Using this technique, feature extraction and object detection can be done with the help of SAR imagery. As maritime Ship detection is considered, due to the homogeneous background [7] in the SAR imagery, the adaptive threshold CFAR Technique is the most widely used algorithm for the detection. However, some of the ambiguities and sea clutter are more often detected as false alarms. Also, to enhance the area of interest, land masking is one of the major tasks to precisely mask the land area. Although, vector based approach [6] shows a good result in order to mask the area due to the precise geometrical accuracy [2] of the dataset however it fails to mask out some artificial settlements near the coastline. Thus, to mask these settlements, Digital Elevation Model (DEM) is also used for the land water segmentation. In this paper, UAV Quad-Pol SAR data is used and the coherency matrix T_3 has been generated from the covariance matrix C_3 to decompose the imagery into single, double, and volume scattering [8]. The Southern California coast, CA area has been chosen and the CFAR algorithm is applied in each element of the scattering matrix. Also, to obtain the precise land mask, ASTER 30 m DEM is used along with GSHHG vector layer and a methodology has been described to remove land areas that are not removed by the vector-based approach. The efficiency of the algorithm is obtained using Receiver Operating Characteristics (ROC) curves.

2 Dataset and Study Area

In this paper, UAVSAR data of Southern California Coast, CA, acquired on April 16, 2011, has been used for the study. The Data is acquired by the UAV instrument (L-band) by the Jet Propulsion Laboratory (JPL), NASA (Fig. 1). The flight ID is 12105 and the mode of acquisition is PolSAR. In this study, orthorectified single look complex (SLC) data is used with 6 elements of a covariance matrix. The pulse rate used is 40 microsecond having 24,362 samples and 14,318 lines. The dataset is provided in the form of a covariance matrix. Six elements of the covariance matrix have been received that are $S_{hh}S_{hh}^*$, $S_{hv}S_{hv}^*$, $S_{hh}S_{hv}^*$, $S_{hh}S_{vv}^*$, $S_{hv}S_{vv}^*$ where $*$ denotes the complex conjugate of the respective channel. The obtained T_{22} backscatter imagery is shown in Fig. 2. Also, for the precise land masking, the Vector coastline layer (GSHHG) and ASTER DEM have been used and shown in Figs. 3

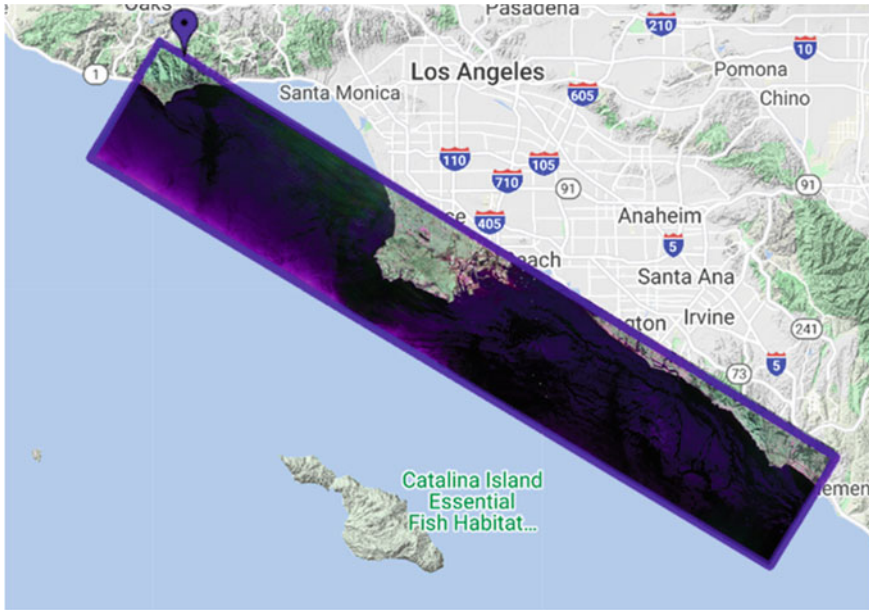


Fig. 1 Actual tile of southern California Coast, CA. https://uavsar.jpl.nasa.gov/cgi-bin/product.plj?obName=SCalBt_12105_11013_005_110416_L090_XX_01#data

and 4 respectively. Using the fusion of both the results, an effective land mask has been generated that helps in precise extraction of the area of interest.

The above DEM is extracted using the extent of the UAV SAR data and this acts as an input for the algorithm to generate the land mask.

3 Methodology

PolSAR datasets perform exceptionally well in the analysis of any maritime activities. For Ship detection, due to the homogeneous background, the CFAR algorithm is mostly used in order to extract the ship from the background pixels.

3.1 Land Masking

The land water mask is generated using the vector-based approach layer and DEM-based approach to generate the precise land mask. The results from both approaches have been discussed in the results and analysis section. In the vector-based approach, the GSHHG vector coastline layer is used and with the help of the extent of the raster

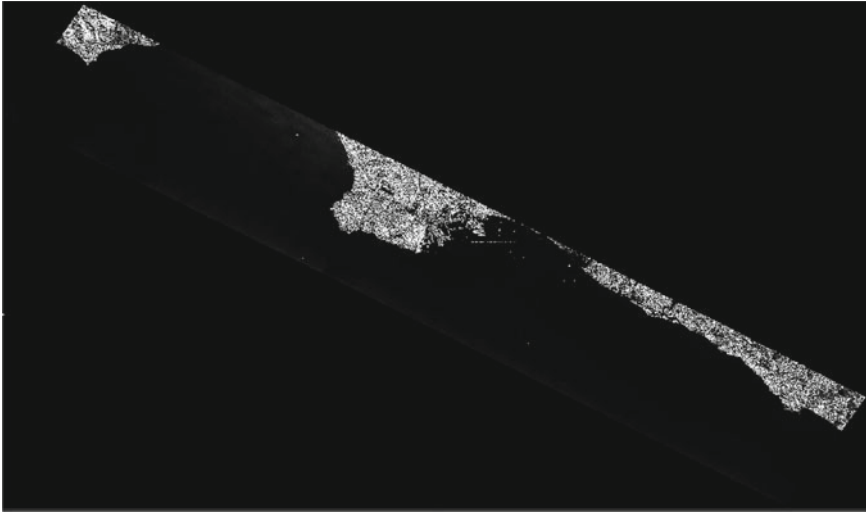


Fig. 2 UAV SAR imagery T_{22} generated scattering data



Fig. 3 GSHHG vector coastline layer

file, the buffer has computed that help in segmenting the land mask. Using the DEM, the sea area is masked by creating the mask of land as 0 and water to be 1 where binary 0 is given when the DEM pixel value is greater than 0 otherwise assuming it to be the sea area, 1 will be given to the rest of the pixel. The final mask is applied to the input raster and land water segmentation is performed (Fig. 5).



Fig. 4 ASTER 30 m DEM extracted for southern California Coast, CA

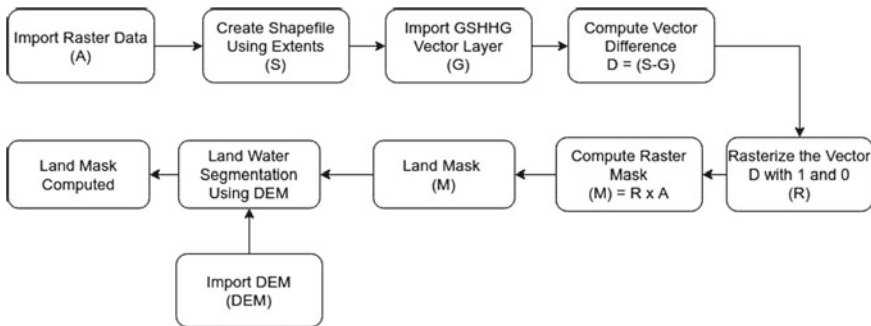


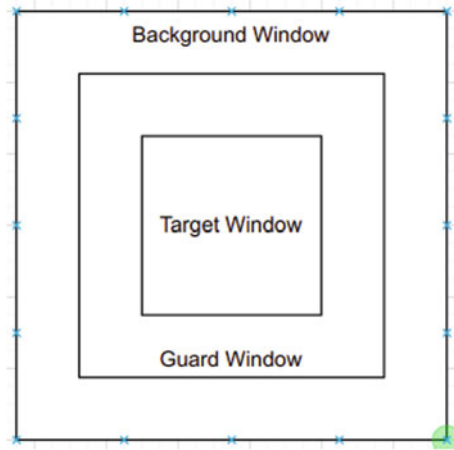
Fig. 5 Land water masking methodology using vector layer and ASTER 30 m DEM

3.2 Standard CFAR

In the Standard CFAR Algorithm, there are 3 windows, a target window that majorly contains the target ship, a background window is used to compute the adaptive threshold in order to compare the statistics from the target window and a guard window is created in between the target and the background. The main focus of the guard window is to ensure that no target window pixel [4] should lie common in the background window. The sample configuration of the window is shown in the Fig. 6.

The first two moments of the statistics of the background window are computed for each window iterating over the image. Also, the adaptive threshold is computed from the background using the probability of a false alarm [3] using Eq. 2.

Fig. 6 Basic configuration of the CFAR window



$$DV_i = \frac{x_i - \mu_i}{\sigma_i} \quad (1)$$

$$PFA = \int_T^{\infty} f_{pdf}(x) dx \quad (2)$$

By computing solving Eq. (2), the threshold can be computed for each sliding window. This respective threshold is compared with the Decision variable (DV_i) and the binary image is generated that contains values higher than that threshold.

3.3 Polarimetric Coherency Matrix Generation

The CFAR is applied over the decomposed T_3 matrix computed from the covariance matrix. As the instrument is mono-static hence, T_3 can be computed from C_3 using the following Eq. 3.

$$T_3 = U_{3(L \rightarrow P)} C_3 U_{3(L \rightarrow P)}^{-1} \quad (3)$$

where, $U_{3(L \rightarrow P)}$ is the special unitary transformation matrix given below. Here transformation $L \rightarrow P$ is from the Lexicographic target vector to the Pauli Target Vector [2].

$$U_{3(L \rightarrow P)} = \frac{1}{\sqrt{2}} \begin{bmatrix} 1 & 0 & 1 \\ 1 & 0 & -1 \\ 0 & \sqrt{2} & 0 \end{bmatrix} \quad (4)$$

After solving Eq. 3 we get the coherency matrix which is described below.

$$T_3 = \frac{1}{2} \begin{bmatrix} \langle (S_{hh} + S_{vv})^2 \rangle & \langle (S_{hh} + S_{vv})(S_{hh} - S_{vv})^* \rangle & 2\langle (S_{hh} + S_{vv})S_{hv}^* \rangle \\ \langle (S_{hh} - S_{vv})(S_{hh} + S_{vv})^* \rangle & \langle (S_{hh} - S_{vv})^2 \rangle & 2\langle (S_{hh} - S_{vv})S_{hv}^* \rangle \\ 2\langle (S_{hv})(S_{hh} + S_{vv})^* \rangle & 2\langle S_{hv}(S_{hh} - S_{vv})^* \rangle & 4\langle (S_{hv})^2 \rangle \end{bmatrix} \quad (5)$$

Here, T_{11} shows the Single/ odd bounce scattering, T_{22} shows the double bounce scattering and T_{33} shows the volume scattering. In this, CFAR is applied to each of the elements, and results are obtained. For the experiment purpose and depending upon the resolution of the dataset the target window is fixed at 50, the guard window is fixed at 60 and the background window is taken as 80. The probability of a False alarm is taken as 0.0001. The results are analyzed using ROC curves.

4 Results and Analysis

4.1 Land Masking Results

Using the methodology from Sect. 3.1, the results are obtained as shown in Fig. 7. In this, it can be observed that the area marked in the red circle is not masked due to some of the artificial settlements. When this masked raster image is applied to the methodology that uses DEM, the results are as shown in Fig. 8.

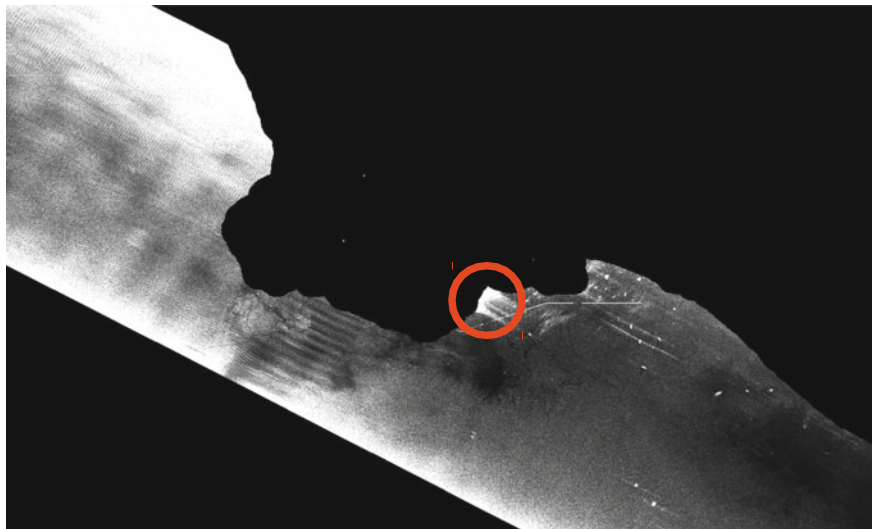


Fig. 7 Land water segmentation using GSHHG vector layer

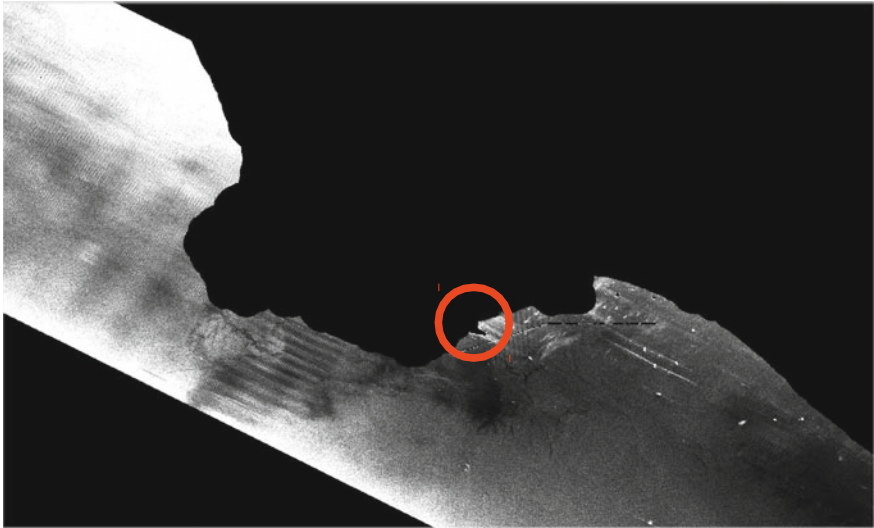


Fig. 8 Land water segmentation using vector layer and DEM

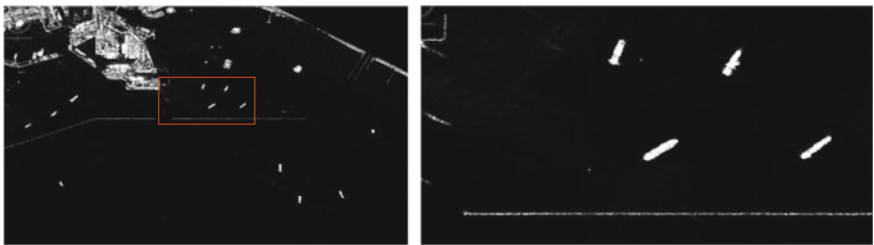


Fig. 9 Input images are shown where **a** represent the area near the coastline and **b** represents the zoomed area for the ships

In Fig. 8, it can be observed that DEM has shown better results in masking the area. This output masked data is now processed with the CFAR along with the parameters described in the methodology section (Figs. 9, 10 and 11).

4.2 CFAR Results

The CFAR algorithm is applied to T_{11} , T_{22} and T_{33} and it can be observed that T_{22} shows the best result as compared with the T_{11} and T_{33} (Fig. 12).

It can be observed that, T_{11} and T_{22} has worked far better than T_{33} . Moreover by comparing T_{22} and T_{11} by the shape of the ships detected, it can be concluded that, T_{22} shows better results. Hence, double bounce scattering shows the precise result

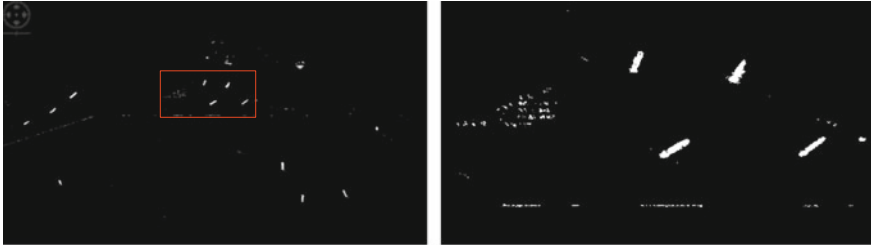


Fig. 10 CFAR results is shown for T_{33} where **a** represents the area near the coastline and **b** represents the zoomed portion of that area



Fig. 11 CFAR results are shown for T_{11} where **a** represents the area near coastline and **b** represents the zoomed area in the red box



Fig. 12 CFAR results are shown for T_{22} where **a** represents the area near coastline and **b** represents the zoomed portion of the area

in the automatic detection of ships. Looking closely at the ships, the double bounce scattering matrix detects the shape of the ships more precisely compared to the other scattering images. Also, the number of false alarms detected is highest in the T_{33} which exhibits the volume scattering. It can also be observed that image containing volume scattering suffers a lot of false alarm due to the depolarization of the EM waves. While in double bounce scattering, ships are better detected and background helps in normalizing the adaptive threshold to automatically detect the ships (Figs. 13 and 14).

At a certain window size and PFA, the threshold is automatically computed by the algorithm in each scattering image as shown in Table 1.

Fig. 13 Ship shape detected in T_{11}



Fig. 14 Ship shape detected in T_{22}



Table 1 Adaptive threshold value for each scattering matrix

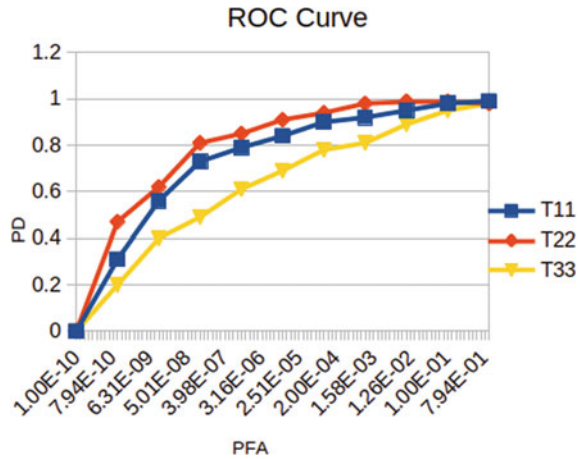
Image	Threshold
T_{11}	2.8×10^{-4}
T_{22}	3×10^{-5}
T_{33}	0.0003

For obtaining the efficiency of the algorithm, the ROC curve is plotted between the PFA and the Probability of Detection. The Probability of detection is basically the ratio of the number of the target pixel to the total number of the target pixel.

$$p_d = \frac{N_{target\ detected}}{N_{total\ target}} \tag{6}$$

The ROC is plotted between PFA and the Probability of Detection (PD) is shown in Fig. 15. Analyzing the ROC curve, it can be said that T_{22} worked efficiently for the CFAR algorithm.

Fig. 15 ROC curve obtained



5 Conclusion

In ship detection using polarimetric SAR data, there is two major concern that should be considered while implementing any algorithm. Firstly, is the land water segmentation, which is the most essential part in order to get the precise area of interest. Secondly, the utilization of the polarimetric information in the SAR data, that also plays a vital role in the automatic detection of ships. In this paper, T_3 coherency matrix has been computed from the covariance matrix of the UAV SAR imagery. In result, it is found that fusion of the vector layer with the DEM is the most suitable way to obtain precise land water segmentation. Upon the analysis, it can be concluded that, in the coherency matrix, T_{11} and T_{22} shows better results than T_{33} while among T_{11} and T_{22} , the shape of the ships are more precisely found in T_{22} . Hence, T_{22} shows the best results among all other elements of the scattering matrix in terms of false alarm and shape of the ships. The ROC curve also suggests that T_{22} shows the optimum results on the certain parameter of the CFAR algorithm.

Acknowledgements Authors provide their special thanks of gratitude to the Indian Institute of Remote Sensing, ISRO for providing the exceptionally best infrastructure and research facilities in this pandemic era too. Moreover, the authors thank all the scientists and seniors for guiding the research work.

References

1. Bhanu Prakash ME, Kumar S (2020) PolInSAR based polarimetric decomposition using cosine square distribution. In: 2020 7th international conference on signal processing and integrated networks, SPIN 2020, no. 3, pp 465–70. <https://doi.org/10.1109/SPIN48934.2020.9071416>

2. Çelik A, Yaman H, Turan S, Kara A, Kara F, Zhu B, Qu X et al (2018) POL RADAR image. *J Mater Process Technol* 1(1):1–8. <https://doi.org/10.1016/j.cirp.2016.06.001%0A>, <https://doi.org/10.1016/j.powtec.2016.12.055%0A>, <https://doi.org/10.1016/j.ijfatigue.2019.02.006%0A>, <https://doi.org/10.1016/j.matlet.2019.04.024%0A>, <https://doi.org/10.1016/j.matlet.2019.127252%0A>
3. Hajduch G, Leilde P, Kerbaol V (2006) Ship detection on ENVISAT ASAR data: results, limitations and perspectives. European Space Agency, (Special Publication) ESA SP, no. 613:23–26
4. Leng X, Ji K, Yang K, Zou H (2015) A bilateral CFAR algorithm for ship detection in SAR images. *IEEE Geosci Remote Sens Lett* 12(7):1536–1540. <https://doi.org/10.1109/LGRS.2015.2412174>
5. Liu Y, Hui Zhang M, Xu P, Wei Guo Z (2017) SAR ship detection using sea-land segmentation-based convolutional neural network. In: RSIP 2017—International workshop on remote sensing with intelligent processing, proceedings, pp 4–7. <https://doi.org/10.1109/RSIP.2017.7958806>
6. Manohara Pai MM, Mehrotra V, Aiyar S, Verma U, Pai RM (2019) automatic segmentation of river and land in SAR images: a deep learning approach. In: Proceedings—IEEE 2nd international conference on artificial intelligence and knowledge engineering, AIKE 2019, pp 15–20. <https://doi.org/10.1109/AIKE.2019.00011>
7. Meyer F, Hinz S (2009) Automatic ship detection in space-borne SAR imagery. *Int Arch Photogramm Remote Sens Spat Inf Sci* 38(1):1–6
8. Theoharatos C, Makedonas A, Fragoulis N, Tsagaris V, Costicoglou S (2015) Detection of ship targets in polarimetric SAR data using 2D-PCA data fusion. *Int Archiv Photogramm, Remote Sens Spat Inf Sci—ISPRS Archiv* 40(7W3):1017–1024. <https://doi.org/10.5194/isprsarchives-XL-7-W3-1017-2015>

A Deep Learning Approach for Detection and Segmentation of Airplanes in Ultrahigh-Spatial-Resolution UAV Dataset



Parul Dhingra, Hina Pande, Poonam S. Tiwari, and Shefali Agrawal

Abstract Advancements in unmanned aerial vehicle (UAV) technology have enabled the acquisition of images of a geographical area with higher spatial resolutions as compared to images acquired by satellites. Detection and segmentation of objects in such ultrahigh-spatial-resolution (UHSR) images possess the potential to effectively facilitate several applications of remote sensing such as airport surveillance, urban studies, road traffic monitoring crop monitoring, etc. Investigating these images for target extraction tasks turns out to be quite challenging, in the terms of the involved computation complexities, owing to their high spatial resolutions and information content. Due to the development of several deep learning algorithms and advanced computing tools, there exists a possibility of harnessing this information for computer vision tasks. Manual surveillance of airports or similar areas and manual annotation of images are cost-intensive and prone to human-induced errors. Therefore, there exists a substantial requirement of automating the task of keeping track of the airplanes parked on the premises of airports for civil and military services. With this paper, we propose a framework for detecting and segmenting such airplanes in UHSR images with supervised machine learning algorithms. To detect the target i.e., airplanes, MobileNets-deep neural network is trained, whereas to segment the target, U-Net-convolutional neural network is trained with our dataset. Further, the performance analysis of the trained deep neural networks is presented. The UHSR image dataset utilized in this research work is an airport dataset provided by SenseFly. Data is acquired by eBee classic drones, flying at a height of 393.7 ft., which provide 2D-RGB images with a ground resolution of 3.14 cm/px.

P. Dhingra (✉) · H. Pande · P. S. Tiwari · S. Agrawal
Indian Institute of Remote Sensing, ISRO, Dehradun, India
e-mail: parul.dhingra2709@gmail.com

H. Pande
e-mail: hina@iirs.gov.in

P. S. Tiwari
e-mail: poonam@iirs.gov.in

S. Agrawal
e-mail: shefali_a@iirs.gov.in

Keywords Airplanes · Deep learning · Object detection · Semantic segmentation · UAV dataset

1 Introduction

Unmanned aerial vehicles (UAVs) [1] are utilized in civil and military arenas for several purposes such as surveillance, security, recreational, educational, rescuing, and monitoring. Due to their low maintenance cost, undemanding installations, and ability to maneuver over a geographical region with high mobility and reliability, they are better suited for such purposes as compared to satellites. However, weather plays a crucial role in their functionality, as bad weather conditions can adversely affect their maneuvering capabilities. UAVs equipped with advanced high-resolution cameras readily provide images and videos of a geographical area with continuity, reliability, and fine details. These images or videos can be further analyzed and processed to extract meaningful information from them for various applications. Over the past few years, UAVs are employed to conduct search and rescue operations in the sea [2], sense the temperature of streams by using thermal sensors [3], monitor crops and droughts, transport goods, inspect construction sites, and various other active and passive remote sensing applications [4].

Images acquired by aerial missions are subjected to various image processing steps [1] to increase their readability and quality. Firstly, initial estimates of the orientation and position of each image are acquired by the log files. To reestablish the true orientation and position of the images acquired by UAVs, aerial triangulation is implemented. With this step, many automated tie points are generated for conjugate points corresponding to multiple images. The automated tie points are used to optimize the image orientation and position with bundle block adjustment. Further, a digital surface model is created with oriented images. The features in multiple image pairs are matched which generates a dense point cloud. Subsequently, a digital terrain model is generated, and to remove distortion in images, the orthorectification process is implemented. The images are then combined into a mosaic to produce seamless images of the geographical area of interest.

The high-resolution images can accommodate abundant and finer information about terrains, and therefore, possess the capability of discerning objects distinctly. This has led to research proliferation towards object detection in the field of remote sensing. The traditional object detection techniques [5] include selecting a desired area in the image, extracting the features in the desired area, and lastly, for classification using the training classifier. A few examples [6] of traditional object detection are feature descriptors like SURF, BRIEF, SIFT, etc. for object detection, and machine learning algorithms like SVM, K-Nearest Neighbor, etc. for predictions. However, these techniques lack robustness and adaptability, and thus, require rigorous tuning of thresholds and parameters for different environments. Deep learning paves the way for increasing the robustness of detection algorithms, as they can perform better in environments where brightness, SNR, and backgrounds in an image differ and

detect a wider range of objects in an image. Various deep learning algorithms like R-CNN, Fast R-CNN, YOLO, Faster R-CNN, SSD, R-FCN, etc. have been developed for various object detection tasks.

Traditionally, convolutional networks were used for classification tasks [7]. However, several segmentation applications require the assignment of class labels to each pixel. Ciresan et al. [8] proposed a network for such requirements, where the local region around the pixel was used to predict the class label. This algorithm was quite slow as it had to run separately for each local region/patch, and there was a trade-off between the use of context in terms of the size of patches and the accuracy of localization. To overcome these limitations, networks were developed where features from multiple layers were taken into account for classifier output. Further, Olaf Ronneberger et al. [7] developed a more advanced architecture where even with few training images precise segmentations could be achieved.

The main contributions of this paper include: (1) Developing a supervised learning framework for detecting airplanes in UHSR images using MoblieNet-deep neural network acquired by UAVs. (2) Manually labeling airport images, and successfully implementing U-Net architecture for segmentation of airplanes in images acquired by UAVs. (3) Presenting objective performance analysis of the trained deep neural networks.

The paper is organized as follows. Section 2 discusses the basic technical concepts underlying our research work. The method for the detection and segmentation of airplanes in UHSR images is presented in Sect. 3. Section 4 discusses the training and testing process, limitations, and objective analysis of the trained models. Section 5 states conclusions.

2 Background

The section explains about constituents of digital images and their spatial resolution, and further, provides the background of neural networks and convolutional neural networks (CNNs).

2.1 Digital Images and Spatial Resolution

Digital image analysis and processing enables formulating techniques to remove noise from images, increase their interpretability, extract the desired object, and compress them for storage or transmission purposes. Images can be either in digital or analog format. 2D-Digital images are signals, say $I^m(x,y)$, where x and y are two independent variables (spatial coordinates). The basic constituent of a digital image is a pixel. Pixels are picture elements that are square in shape. Digital images are a rectangular array of pixels [9]. For remote sensing applications, the sensors mounted on a platform capture the energy emitted or reflected by objects present in

a geographical area. The sensors can be mounted on satellites, airplanes, or UAVs according to the desired application. The value of each pixel is directly proportional to the intensity of the light captured and recorded by the optical sensors at a given point. A grayscale image, where each pixel can attain a value in the range of 0–255, can be represented by a single 2D array, whereas an RGB image with three channels is represented by a collection of three 2D arrays, each for the red, green and blue channels. Pixels are the physical points containing a digitized value recorded by optical sensors. Digital images can be referenced with rows and columns. Digital images are stored in various image file formats [10] such as bitmap (BMP), tagged image file format (TIFF), joint photographic expert graphic (JPEG), portable network graphics (PNG), etc. Four types of resolutions define the characteristics of a digital image, namely, spectral, spatial, radiometric, and temporal. The spatial resolution [10] of an image corresponds to the actual area in the scene represented by a single pixel in an image when a sensor performs imaging with the instantaneous field of view (IFOV). It is a measure of the smallest object in a scene that can be discerned by the optical sensor sensing over a geographical area. The high resolution of images allows us to differentiate objects that are closer to each other. In our work, we deal with 2D-digital images that are acquired by capturing the reflected sunlight energy in the visible region of the electromagnetic spectrum. These images have an ultrahigh-spatial resolution of 3.14 cm/px and are stored in Joint Photographic Expert Group (JPG) format.

2.2 Neural Networks

The brain is a highly non-linear data processing system, where complex computations are performed extremely fast. An artificial neural network tries to mathematically model the functioning of a brain for performing such non-linear computational tasks. The fundamental constituent of an artificial neural network is the artificial neuron [11]. A neural network is developed by interconnecting these neurons. The three basic elements of an artificial neuron are as follows. Firstly, the connecting links between the inputs and the neuron. With each link, there is a synaptic weight associated with it. Synaptic weights of artificial neurons can obtain negative as well as positive values. The input to a neuron is the summation of weighted inputs, with a bias added to it. Secondly, an adder to add weighted inputs and bias. The mathematical operation carried out at adder yields output v_k :

$$v_k = \sum_{j=1}^m w_{kj}x_j + b_k \quad (1)$$

At the k th neuron, x_j is input signal at j th synapse which is multiplied by the synaptic weight w_{kj} , and b_k is bias.

Thirdly, an activation function limits the value of the output from the neuron. They are also called squashing functions, as they squash the values of outputs to permissible finite values. The mathematical notation for an activation function $\varphi(\cdot)$ yielding output y_k is:

$$y_k = \varphi(v_k) \tag{2}$$

The neural network consists of one or more layers comprising neurons. A single-layered neural network is a network where inputs are fed directly to the output layer. In multi-layer networks, each neuron of a layer is connected with all the nodes of the input layer. The neurons within a layer are not connected. The feed-forward networks are the networks in which the signals are forwarded from one layer to the next without any feedback loop. There can be several layers between the source layer and the output layer. The layers in between the input layer and output layers are called hidden layers. The hidden layers enable the extraction of high-order statistics from input signals. The recurrent neural networks are the networks that contain at least one feedback loop. The recurrent networks are designed such that the output from every neuron in a layer is fed back to the network as input to all the neurons. The artificial neural network can be trained with supervised, unsupervised, or semi-supervised learning algorithms. In supervised learning, both the input signals and their corresponding desired outputs are utilized for training the network, thus we require labeled data. The input signal is fed to the network, and the loss is calculated by taking into account the predicted outcome and the ideal expected outcome. The unsupervised learning algorithms train the neural networks with unlabeled input signals. The semi-supervised way of learning takes into account both labeled and unlabeled training input signals. The applications of artificial neural networks for automating various tasks are automated driver assisting systems, speech recognition, handwriting recognition, etc. In our project, we have trained the neural network with supervised learning algorithms for automatic detection and segmentation of the target, i.e., airplanes.

2.3 Convolutional Neural Networks

Convolutional neural networks (CNNs) are widely used neural networks for extracting information from 2D-image data, where inputs are grid-structured, and there are spatial dependencies within the local regions [12]. The pixels in the neighborhood of an individual pixel often have similar values; hence, image data exhibits strong spatial dependencies, which makes it highly suitable for CNNs. The CNNs can be used for spatial, temporal, and spatiotemporal input data. The image data exhibits translation invariance, where an object has the same interpretation irrespective of its location in the image. In CNN, similar feature values are created from local regions that have a similar pattern. The basic operation executed in CNNs is mathematical convolution. A convolution operation is a sliding dot-product carried

out between the convolution filters and grid-structured inputs. The operation is beneficial for data that exhibits a high level of spatial locality. CNN's are neural networks in which at least one layer is the convolution layer. There can be one or multiple convolution layers in a neural network. As every feature value in the current layer is dependent on the small local region in the previous layer, the spatial relationships get inherited from one layer to the next layer. A three-dimensional grid structure with height, width, and depth define each convolution layer of a CNN. The depth refers to the number of feature maps in a convolutional layer. The primary building blocks of a typical feed-forward convolutional neural network are the convolution layer, pooling layer, rectified linear unit (ReLU) layer, fully connected layer, and loss layer. The convolution layer overlaps the kernel at every location in an image and performs a sliding dot product. The pooling layer performs the downsampling of the feature maps in a non-linear manner. Max pooling is one most commonly used non-linear functions in the pooling layers. A new feature map is produced as the pooling layer acts independently on every depth slice of the feature map. The input image is partitioned into non-overlapping regions in a feature map, and the pooling function obtains the maximum value in the particular region to generate a new feature map. The pooling layer reduces the size of the feature map and the parameters required to train the network, hence, the computational complexities within the convolutional neural network are reduced. The commonly used activation function in CNNs is ReLU activation function. The ReLU function squashes the negative values to zero, and therefore, does not permit negative values to propagate in the network. The dimensions of a layer remain the same when an activation function is applied, as it only maps the values in the feature map corresponding to the activation function. After the implementation of convolution and max-pooling layers, lastly, the outputs are generated by implementing a fully connected neural layer. The loss layer which is the final layer of the convolutional neural network determines the deviation between the expected ideal outcome and the predicted outcome. Softmax loss and sigmoid cross-entropy loss are examples of such loss functions in the loss layer. The CNNs are used to perform object detection, classification, and segmentation tasks in computer vision. We have implemented CNNs to automate the task of target extraction from UHSR images.

3 Methodology

This section introduces the method for extracting airplanes from the UHSR images in an automated way. Figure 1 depicts the framework implemented for automated target extraction. The framework is explained in detail in subsections to follow.

Dataset

The UHSR image dataset utilized in the project is captured by two eBee classic drones [13], flying at a height of 393.7 ft. The ground resolution of images is 3.14 cm/px. The images are taken over the geographical region of Le Bourget airport in Paris. The

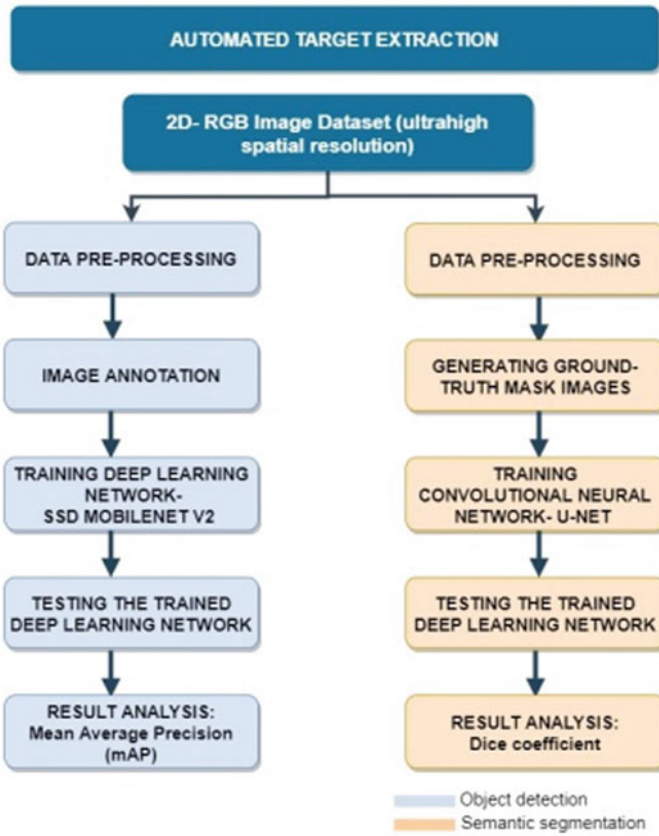


Fig. 1 Methodology for automated target extraction

dimension of the images is 4608×3456 pixels, and they are stored in JPG format. The 2D images possess red, green, and blue (RGB) channels, and thus, have a depth of three. The images contain one or multiple parked airplanes, along with several other objects like buildings, runways, automobiles, etc. Figure 2 introduces images from the airport dataset.

3.1 Object Detection

Object detection implies that we aim toward enclosing the target object i.e., an airplane with rectangular bounding boxes. The deep neural frameworks perform better for this category of application than shallow networks [14, 15]. Our training set consists of thirteen RGB images. The images are annotated with LabelImg where



Fig. 2 Images of the airport from the training dataset

annotations are stored in PASCAL VOC format. The trained network is tested with nine test images.

Data Pre-processing

The dimension of images is reduced to 800×600 pixels from 4608×3456 pixels to reduce the computational complexities and time required for training the deep neural network.

Image Annotation using Labeling

These processed images are manually annotated with LabelImg [16], version 1.8.0, open-source software for graphical image annotations. It generates the annotation files in XML (Extensible Markup Language) .xml format. The XML file saves the name of the image, size (800,600) and depth (3) of the image, name of the object annotated (airplane), and location of the manually annotated bounding boxes in the image. To train the neural network thirteen images are annotated manually (Fig. 3) which generates thirteen .xml files.

Fig. 3 Image annotation with LabelImg



Further, these thirteen individual .xml annotation files are combined and converted to CSV (Comma Separated Values) .csv file. The .csv file and image data are converted and stored in TFRecord (TensorFlow Record) format. The TFRecord format stores the data in binary format and significantly reduces the training time and occupies less space in the storage disk. The training data in the TFRecord file format is fed to the neural network.

Network Architecture: SSD MobileNet-v2

The SSD- MobileNet-v2 [17] deep learning architecture is implemented to classify and locate airplanes in digital images. The output of the network generates the bounding boxes around the desired feature and gives the confidence score for the class encapsulated by the box. In this architecture, the MobileNet-v2 model is used to classify features and subsequently, a single shot multi box detector model (SSD) is used to locate the feature with bounding boxes. MobileNet models [18] are lightweight neural network models that are based on depth-wise separable convolutions, which facilitates the reduction in the size of the model. There is a significantly lesser number of parameters required in this model, as compared to other advanced deep learning frameworks like GoogleNet and VGG16 [18] for object detection. The convolutional blocks in Mobilenet-v1 consist of two layers, namely, the depth-wise convolution layer, and the pointwise convolution layer. The depth-wise convolution means that to each channel, a single convolutional filter is applied. Further, pointwise convolution is applied to merge the outputs from the depth-wise layer. The main difference between standard convolution and depth-wise separable convolution is that, the former filters and combines the inputs to generate the output in a single step, whereas the latter divides it into two layers, the first to filter and the second to combine. This division helps in reducing the size of the model, and hence, associated computations. The MobileNet-v2 [17] consists of an inverted residual structure as its backbone, where the thin bottleneck layer possesses the short connections between them. The inverted residual with a linear bottleneck layer is given the input which is a low-dimensional representation. It expands it to a high dimension and further, depth-wise convolution filtering is performed. Finally, with the help of linear convolution, there is a backward projection to the lower dimension. These layers commendably enable the reduction in the memory footprint required during inference. The mobile net-v2 model comprises two types of blocks, the residual block (stride=1) and the downsizing block (stride=2). The ReLU6 in each block is the rectified linear unit activation function with maximum output limited to 6. The MobileNet-v2 architecture comprises, firstly, a fully convolutional layer having 32 filters, and subsequently 19 residual bottleneck layers. The SSD network [19] incorporates a feed-forward convolutional network. The SSD network is appended as the auxiliary network to the base network MobileNet-v2 architecture. The base network works as a feature extractor. The SSD network performs an object-detection task, where its outputs are bounding boxes and the corresponding confidence scores of the particular class. It implements non-max suppression as the last step for the detection of the object. The SSD MobileNet-v2 deep learning architecture is one of the most advanced and lightweight deep neural networks.

3.2 Semantic Segmentation

Semantic segmentation [20] intends to classify each pixel in an image to its corresponding class/label. In semantic segmentation, pixels of multiple objects belonging to the same class are considered as a single entity. We intend to implement semantic segmentation of the image, where, all airplanes will belong to the same class-‘airplane’. Let, there be m pre-defined labels, such that, $\text{label} = \{\text{label}_1, \text{label}_2, \dots, \text{label}_m\}$, where $j = 1$ to m . Let, the image consists of k number of pixels, such that, $\text{pixel} = \{\text{pixel}_1, \text{pixel}_2, \dots, \text{pixel}_k\}$, where $i = 1$ to k , then we intend to implement an architecture ‘S’ for semantic segmentation such that for each pixel: pixel, there is a class: label_s assigned to it [20]. We train the U-Net network with thirteen RGB images. The trained network is tested with nine images.

Data Pre-processing

To reduce the computational complexities while training the neural network, images are resized to a dimension of 256×256 and are converted to the grayscale format.

Image Annotations

The U-Net architecture is a supervised machine learning technique. For every training image, we create its corresponding ground-truth mask image. The mask images are such that the pixels belonging to the target possess a value of ‘255’, and the value of background pixels is ‘0’. The ground truth mask is generated using Microsoft Paint3D. The dimension of ground truth images is $256 \times 256 \times 1$. Figure 4 shows the examples of raw images from the dataset. Figure 5 presents their respective ground truth masks. Figure 6 shows the corresponding histogram for the ground truth masks, where the x-axis denotes the pixel values (0–255) and the y-axis denotes the count of pixels. The histogram indicates that the pixels of ground truth images have values of either 0 (background pixels) or 255 (pixels belonging to the target (airplane)).

Network Architecture: U-Net

The implementation of U-Net architecture for semantic segmentation requires less training data as compared to several other CNNs and provides good segmentation results [7]. The U-Net model comprises two paths, namely, contraction and expansion



Fig. 4 Raw images from the training dataset

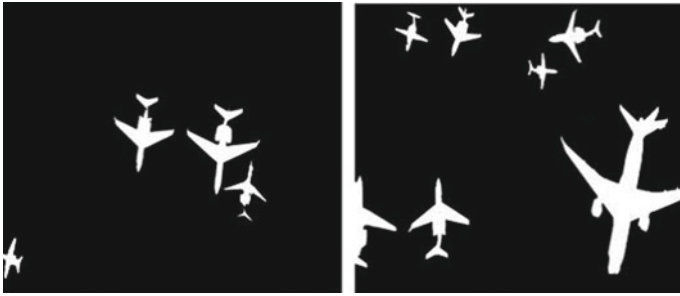


Fig. 5 Ground truth mask images

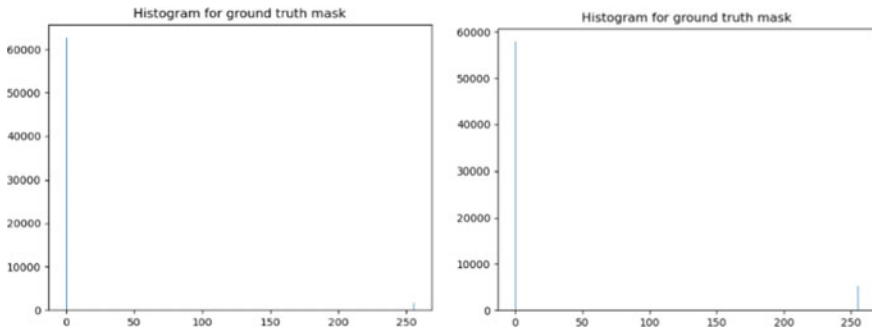


Fig. 6 Histograms of corresponding ground truth mask images respectively

paths. There are a total of 23 convolutional layers in the architecture. To harness the context information of each pixel, the contracting path extracts the features [21] at various levels. It is performed by sequential implementations of convolutions, activation functions, and max pooling. Subsequently, to increase the resolution of the segmented features, the expanding path, which is symmetric to the contraction path, is implemented. It consists of sequential implementations of up-convolutions and ReLU activation functions. Due to the contraction and expansion nature of the architecture, it is called a U-Net architecture. To capacitate propagating context information to higher resolution layers, the upsampling network consists of a large number of feature channels. There are no fully connected layers in the entire U-Net architecture. The final output from the expansion path consists of an image where the value of each pixel gives its class. The steps for the contracting path [7] are as follows. Firstly, it performs two 3×3 convolutions with 64 filters. After each convolution, the outputs are subjected to the ReLU activation function and are downsampled by using a 2×2 max-pooling operation with stride 2. With each downsampling step, the number of feature channels is doubled. The architecture for the expansion path is as follows. Firstly, the expansion path upsamples the feature map. Subsequently, to reduce the number of feature channels to half, a 2×2 up-convolution is implemented, followed by a concatenation step. Further, two 3×3

convolutions are implemented. The outputs from both the convolutions are subjected to the ReLU activation function. The final layer implements 1×1 convolutions, which relate a feature vector consisting of 64 components to the required number of labels.

4 Model Training and Results

The section presents the procedure implemented for training the deep neural networks, outputs predicted from the trained network, and additionally, the limitations of the network. The networks are implemented on the cloud-computing platform by utilizing the data storage and computational capabilities provided by Microsoft Azure and Google Colaboratory.

4.1 Object Detection

Training

To train the network [22], instructions are implemented in the Python programming language. The transfer learning technique is used for training the model. A pre-trained model where the base model is trained with Microsoft's Common Objects in Context-dataset [23] is utilized for transfer learning. This reduces the training time and the required computations and provides initial weights/checkpoints of the model. Further, we train the model to tune and update the weights/checkpoints of the model for our dataset consisting of thirteen images and their corresponding annotation files. The number of training steps and evaluation steps implemented are 4500 and 100 respectively. The value for batch size is 12. The model uses a sigmoid cross-entropy loss function for classification purposes and a smooth L1 loss function for localization purposes. The model is trained in a TensorFlow version 1.15 environment.

Test Results

The trained SSD MobileNet-v2 deep neural network model is tested with nine RGB images. The detected object is saved using the following parameters: x and y coordinates of the center of the bounding box, height and width of the bounding box, and confidence score. Figure 7 presents four test cases A, B, C, and D. Figure 8 presents predicted outputs from the trained network for the test cases.

Evaluation Metrics: Mean Average Precision

The confidence score (CS) [24] indicates the probability of the presence of an airplane in a bounding box and the accuracy of the box itself. The mathematical equation for calculating confidence score (CS) is:

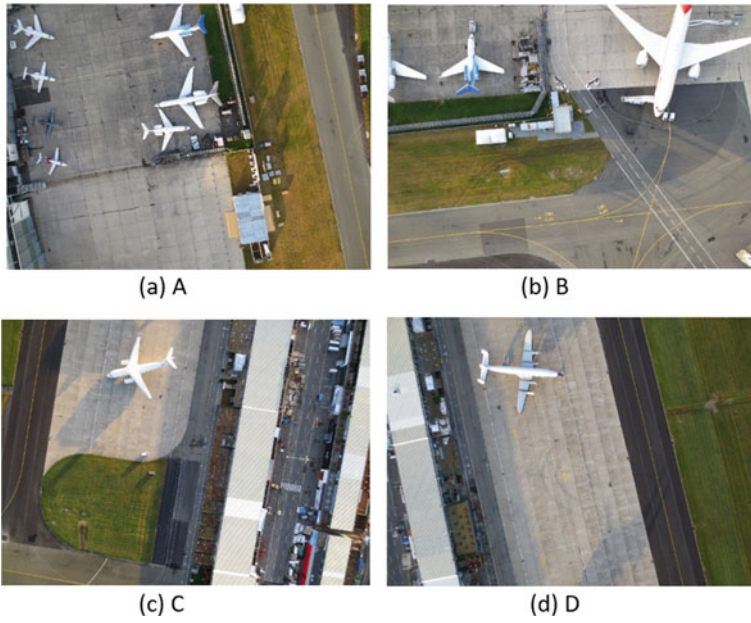


Fig. 7 Test cases: RGB images A, B, C, and D

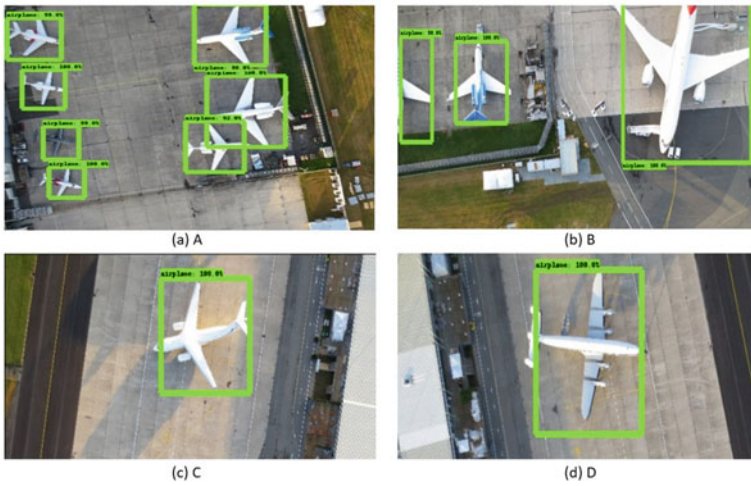


Fig. 8 Detection results from the trained model

$$CS = \text{Probability (object)} \times \text{IoU} \quad (3)$$

The Intersection Over Union (IoU) is the ratio of the area of overlap between the ground-truth bounding box and predicted bounding box and the total area encompassed by both. It calculates the similarity between the predicted bounding box and its respective ground-truth box. Average precision (AP) [25] is the weighted sum of precisions, where the weight is the increase in recall, at each threshold, and m is the number of thresholds.

$$AP = \sum_{m=0}^{m=n-1} [\text{Recalls}(m) - \text{Recalls}(m + 1)] * \text{Precision}(m) \quad (4)$$

Concerning COCO challenge accuracy metrics [25], we set ten different IoU thresholds from 0.5 to 0.95 in the steps of 0.05. The accuracy metrics mAP, is calculated by averaging over all the APs of the classes detected by the object detection model. Our model is trained to detect a single class i.e., airplanes. The mAP = AP value achieved for our trained detection model is 95.9%.

Limitations

SSD- MobileNet v2 is trained to enclose the airplane feature in rectangular bounding boxes. When the trained network is tested with nine images, it is observed that if an image consists of an object whose spatial features are similar to that of an airplane, then it captures that object too as the target. Figure 9 shows the two limitation cases A and B, where the objects other than airplanes are enclosed in rectangular bounding boxes.

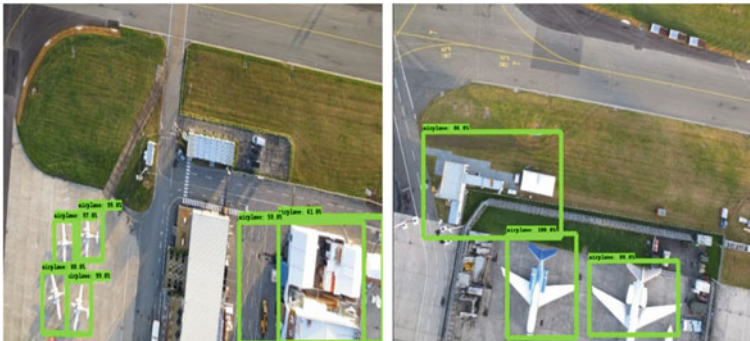


Fig. 9 Limitation cases for object detection

4.2 Semantic Segmentation

To train the network we perform all the computations on the Microsoft Azure cloud-computing platform. The instructions to train the model are written in Python programming language.

Training

The network [7] is trained by utilizing neural-network libraries provided by Keras API. The training data is stored in PNG (Portable Network Graphics) format. Before initiating the training process, the data augmentation step is carried out, as we are aiming to train the network with a lesser number of images. The data augmentation process helps in minimizing the risk of overfitting while training the neural network. To execute the data augmentation, a few of the operations executed are flipping, zooming, shearing, etc. The initial weights of the network are set up using transfer learning. Further, we train the U-Net with our training data to update the weights with several epochs. The model's weights get updated after every epoch if the loss reduces. The Adam-optimizer is used to update the model's weights after each iteration. The loss function implemented while training the network is binary cross-entropy loss [26]:

$$\text{Loss} = -\frac{1}{s} \sum_{i=1}^s a_i \log \hat{a}_i + (1 - a_i) \log (1 - \hat{a}_i) \quad (5)$$

where, \hat{a}_i is the i th value in the model output, s is the output size, and a_i is the target value.

Test Results

The neural network trained is trained with 150 epochs. The loss reduced from 1.5627 to 0.01195 after 150 epochs. Figure 10 presents several examples of outputs from the trained U-Net neural network with 150 epochs. The first row consists of original RGB images used for testing the network, the second row presents the corresponding grayscale images which are fed to test the trained neural network, and the third row presents the outputs from the trained U-Net neural network.

Evaluation Metrics: Dice Coefficient

Dice similarity coefficient (DSC) [27] evaluates the spatial overlap between the ground truth ('M') and the result obtained from the trained U-Net ('N') when tested with the test images. The mathematical equation for calculating the Dice similarity coefficient is:

$$\text{DSC} = 2(M \cap N)/(M + N) \quad (6)$$

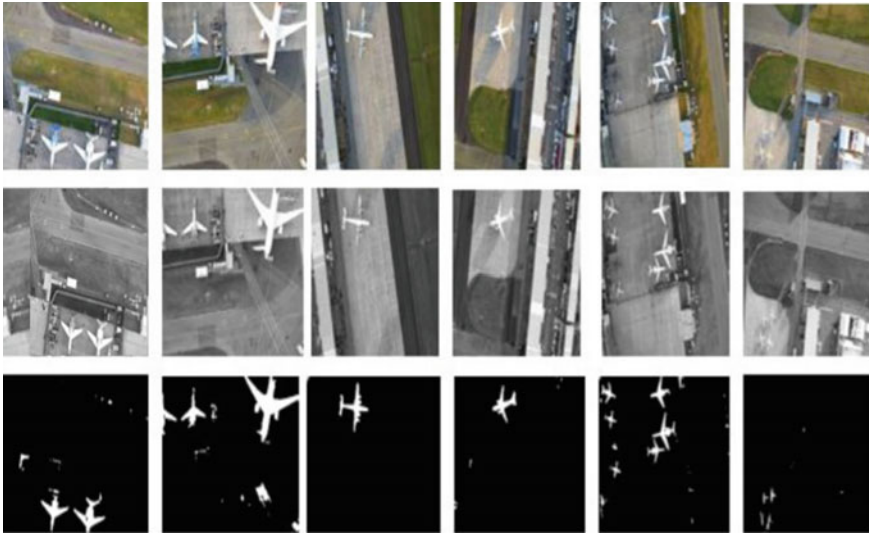


Fig. 10 Outputs from trained U-Net neural network. First row: Original RGB images for testing. Second row: Corresponding grayscale images fed to network for testing. Third row: Outputs from the trained U-Net

The values of the dice coefficient range from 0 to 1. The higher value implies higher segmentation accuracy and high similarity in terms of spatial overlap between ground truth image and output image from the U-Net network. The value of Dice similarity coefficients obtained for the test set is 0.72.

Limitations

The training process of the U-Net deep neural network includes learning the features of the target object with each iteration. When the U-Net model is implemented for our dataset, it is observed that along with the target object, occasionally, it also segments the objects which have a similar shape as that of the target object in the same category. Hence, the limitation cases are the instances where the test image contains an object (not an airplane) that has similar spatial features as an airplane in the spatial domain, and when tested with the trained U-Net it segments it as the target object.

5 Conclusions

We have presented a framework for automatic detection and segmentation of airplanes in UHSR images captured by eBee classic drones. To accomplish this task with supervised machine learning algorithms, we have implemented state-of-the-art SSD MobileNet-v2 for object detection, and U-Net for semantic segmentation. The proposed approach gives arguably good accuracy metrics results for detection and

segmentation tasks in the terms of mAP and dice coefficient respectively. The implemented architectures possess a limitation that objects that are similar in shape to the target i.e., airplanes, are detected or segmented as targets too. The architecture for the segmentation of images performs hard classification for each pixel, where each pixel belongs to a class with either 0 or 100% probability. There can be impure pixels in the image, especially at the boundaries of the target, where they might contain both, a background object and a target object in an image. Research work can be carried out towards developing such neural network architectures that can distinctively specify those pixels as well.

References

1. Shakhathreh H et al (2019) Unmanned Aerial Vehicles (UAVs): a survey on civil applications and key research challenges. *IEEE Access* 7:48572–48634
2. Wang S, Han Y, Chen J, Zhang Z, Wang G, Du N (2018) A deep-learning-based sea search and rescue algorithm by UAV remote sensing. In: *IEEE CSAA guidance, navigation, and control conference (CGNCC)*, pp 1–5
3. Jensen AM, Neilson BT, McKee M, Chen Y (2012) Thermal remote sensing with an autonomous unmanned aerial remote sensing platform for surface stream temperatures. In: *IEEE international geoscience and remote sensing symposium*, pp 5049–5052
4. Shakhathreh H, Sawalmeh AH, Al-Fuqaha A, Dou Z, Almait E, Khalil I et al (2019) Unmanned aerial vehicles (UAVs): a survey on civil applications and key research challenges. *IEEE Access* 7:48572–48634
5. Hwang S, Lee J, Shin H, Cho S, Hyunchul Shim D (2018) Aircraft detection using deep convolutional neural network for small unmanned aircraft systems. *AIAA Information Systems-AIAA Infotech @ Aerospace*
6. Lee A (2016) Comparing deep neural networks and traditional vision algorithms in mobile robotics
7. Ronneberger O, Fischer P, Brox T (2015) U-net: Convolutional networks for biomedical image segmentation. In: *Medical image computing and computer-assisted intervention—MICCAI*, Springer International Publishing, pp 234–241
8. Ciresan DC, Gambardella LM, Giusti A, Schmidhuber J (2012) Deep neural networks segment neuronal membranes in electron microscopy images. *NIPS*, pp 2852–2860
9. Parkin A (2018) *Computing color image processing*. Springer, Cham
10. Ghosh SK (2012) *Digital image processing*
11. Haykin SS (2009) *Neural networks and learning machines*, 3rd edn. Pearson Education, Upper Saddle River, NJ
12. Aggarwal CC (2018) *Neural networks and deep learning*. Springer International Publishing AG
13. Airport Dataset, SenseFly parrot group
14. Pathak AR, Pandey M, Rautaray S (2018) Application of deep learning for object detection. In: *International conference on computational intelligence and data science*. *Procedia Comput Sci* 132:1706–1717
15. Alganci U, Soydas M, Sertel E (2020) Comparative research on deep learning approaches for airplane detection from very high-resolution satellite images. *Remote Sens* 12(3):458
16. Labeling: graphical image annotation tool, MIT License
17. Sandler M, Howard A, Zhu M, Zhmoginov A, Chen L (2018) Mobilenetv2: inverted residuals and linear bottlenecks. In: *IEEE/CVF conference on computer vision and pattern recognition*, pp 4510–4520

18. Howard AG, Zhu M, Chen B, Kalenichenko D, Wang W, Weyand T et al (2017) Mobilenets. CoRR. abs/1704.04861
19. Liu W, Anguelov D, Erhan D, Szegedy C, Reed S, Fu C-Y et al (2016) SSD: single shot multibox detector. *Computer Vision—ECCV*, Springer International Publishing, pp 21–37
20. Bassiouny A, El-Saban M (2014) Semantic segmentation as image representation for scene recognition. In: *IEEE international conference on image processing (ICIP)*, pp 981–985
21. Chhor G, Bartolome Aramburu C (2017) Satellite image segmentation for building detection using -U-net- report. Stanford University
22. Chengwei (2019) How to train an object detection model
23. Lin T-Y, Maire M, Belongie S, Hays J, Perona P, Ramanan D, et al (2014) Pi. Microsoft coco: common objects in context. *Computer Vision—ECCV*, Springer International Publishing, pp 740–755
24. Erhan D, Szegedy C, Toshev A, Anguelov D (2014) Scalable object detection using deep neural networks. In: *IEEE conference on computer vision and pattern recognition*, pp 2155–2162
25. Padilla R, Passos WL, Dias TLB, Netto SL, da Silva EAB (2021) A comparative analysis of object detection metrics with a companion open-source toolkit. *Electronics* 10:279
26. Ho Y, Wookey S (2020) The real-world-weight cross-entropy loss function: modeling the costs of mislabeling. *IEEE Access* 8:4806–4813
27. Bharatha A, Zou KH, Warfield SK et al (2004) Statistical validation of image segmentation quality based on a spatial overlap index. *Acad Radiol* 11(2):178–189

Influence of European UAS Regulations on Image Acquisition for 3D Building Modeling



Grzegorz Gabara 

Abstract The dynamic development of 3D building reconstruction using digital images obtained with unmanned aerial systems (UAS) has been observed in recent years. The popularity of UAS is due to its wide technological availability at a low price, compared to geodetic measurement equipment, laser scanners, or manned flight missions. In practice, the usage of UAS for 3D building reconstruction and modelling allows the acceleration of the production process (image acquisition, processing, computation) while maintaining a high quality of the final product. With the increasing number of new flying objects in airspace and because of differences in UAS regulation in each EU country, it was necessary to adapt the rules for the operation of unmanned aircraft to standardize regulations, make operations easier, and assure aviation safety. Due to this fact, from 31 December 2020, the new European Union (EU) Commission Implementing Regulation 2019/947 on the rules and procedures for the operation of unmanned aircraft entered into force across the continent. The new regulations replaced each EU national's existing laws and applied to all UAS pilots. They have adopted a risk-based approach and do not distinguish between leisure or commercial activities like previous regulations. To assess the operational risk and to determine the category of flight mission, the weight and specifications of the UAS, the operation, and UAS pilot qualification are taken into account. Because of that, new categories of operations have been established. In this study, the review of 3D reconstruction using UAS was performed and the new EU UAS regulations in the context of the image acquisition of buildings in different levels of detail (LoD) were studied. For this purpose, the practical 3D reconstructions of buildings were analyzed. Furthermore, taking Poland as an example, new unified EU rules were compared with the previous ones.

Keywords Buildings · 3D reconstruction · Level of detail · Regulations · Unmanned aerial system

G. Gabara (✉)

Faculty of Geodesy and Cartography, Department of Photogrammetry, Remote Sensing and Spatial Information Systems, Warsaw University of Technology, Warsaw, Poland
e-mail: grzegorz.gabara.sci@gmail.com

1 Introduction

The interest in creating 3D models is inspired by a wide range of applications, such as urban design [57], urban analysis [4], emissions analysis [37], solar potential estimation [56], real-time disaster management [2, 45, 52], property visualization [55] and real estate valuations [8], historic building documentation [38, 41, 43], reconstruction of damaged buildings [34], virtual tourism [3], building information modelling (BIM) [9, 54], campus monitoring [10] and the augmented reality [7].

Since the development of 3D building presentation [15] for the geometric and semantic representation differentiation [8] and 3D model visual quality and completeness assessment, the level of detail (LoD) concept [6–8] is used. The 3D building models are inseparably related to the CityGML standard. Version 2.0 defines 5 LOD levels in its structure. These levels and differences between them were described by Biljecki et al. [6]. Initially, the LoD concept was used in graphic applications as faces number reduction with attempting to maintain visual fidelity [11, 12, 36], while GIS is used as a form of 3D models generalization [6, 25]. Biljecki et al. [8] have described this difference based on two buildings, one in LoD1 and the second in LoD2, where the first one has more faces than the second one, even though its LoD is lower. In the recent decade, due to the lack in the characterization of the LoD's for different building classes, which were pointed out by Döllner [5–8, 18, 28, 29, 48, 49], the description of the concept was modified and expanded [8].

Over the last decades, the 3D building model generation has evolved, initially, 3D models were prepared using stereophotogrammetry [1, 27] or direct geodetic measurement documentation. The easiest way to produce simple 3D models was to use high-scale geodetic maps and based on the number and height of the floors, add a third dimension (Z). Additionally, in the late 1990s, due to the development in the video game industry, the 3D models of the building were created to fulfil the narrative and artistic requirements of a particular scenario [51] (i.e., Tomb Raider) without taking into account the real dimensions and locations of objects [50]. In the 2000s the integration of spatial information about building from different databases was observed. This stage allows for obtaining 3D building models of high quality. Due to the progress in measuring tools, computing powers, disk storage capacity, and greater availability, the number of companies and research centres that deal with 3D buildings rose. The next stage in 3D building modelling was the usage of point clouds obtained using airborne laser scanning (ALS) and terrestrial laser scanning (TLS) [53]. Since around 2010, the structure from the motion approach which provides fully automated 3D reconstruction has become a very popular trend [37]. It allows the reconstruction of existing urban spaces using arbitrary imagery without any on-site measurements, significantly reducing the costs of 3D building modelling. Common usage of advanced computing algorithms with wide and easy access to technology, a low price of sensors, and their minimization result in fast data acquisition. Furthermore, due to this fact it is possible to load those sensors onto unmanned flying platforms. They enable avoiding some limitations and disadvantages of manned flight missions, terrestrial imagery, and laser scanning.

To describe the collection of remotely-piloted objects many terms had been introduced. The most popular was a drone, unmanned aerial vehicle (UAV), Unmanned Aircraft Systems (UAS), Remotely Piloted Aircraft (RPA), Remotely Piloted Aircraft Systems (RPAS), Unmanned Aircraft (UA), light unmanned aeroplane systems (LUAS), light unmanned rotorcraft systems (LURS), Autonomous aircraft (AA). All of these terms have been taking part in name evolution for years and all of them were used by Aviation Authorities (i.e., National Aviation Authorities, International Civil Aviation Organization, Federal Aviation Administration) in official documents or rules. An interesting introduction to this terminology is presented by Granshaw [26].

According to the Department of Defense (DoD) [39], four terms were used: drone as a land, sea, air vehicle that is remotely controlled, remotely piloted vehicle (RPV), which was defined as an air vehicle controlled by a person through a communication link, automatically piloted vehicle (APV), which was aerial vehicle controlled by instruction saved on-board the vehicle and UAV that includes RPV and APV. In 2005 International Civil Aviation Organization [31] and Federal Aviation Administration (USA) [32] for the Unmanned Aerial Vehicle (UAV), a ground control station (GCS), and a communication system between GCS and UAV defined a new term UAS. Furthermore, firstly in 2007 ICAO recommended using only this term, and in 2011 [30] informed that UAV is an obsolete term. In 2015 ICAO decided that terms like UAV or UAS were dropped and replaced with RPAS [33]. But, according to the recent definition section EU (EASA) [13] and U.S. (FAA) [17] regulation, the following terms are used: UAS small UAS and UA. Because of multiple terms and some discrepancies between regulations, in this study, the recent definitions will be used [19].

So far, many publications about UAS operation rules [16, 40, 44, 47] and 3D building modelling using UAS have been written [20, 21, 35, 38, 46], however, according to the author knowledge, the study, which deals with new UAS operation rules in the context of 3D building modelling does not exist at present.

In this study, the review of 3D building reconstruction was performed and the new EU UAS regulations in the context of the image acquisition of buildings in different levels of detail (LoD) were studied. For this purpose, the practical 3D reconstructions of buildings were analyzed. Furthermore, taking Poland as an example, new unified EU rules were compared with the previous ones.

2 3D Building Modeling

As mentioned before to describe the visual quality and completeness of 3D building models, the LoD concept of CityGML 2.0 is used. The five types of LoD are presented in Fig. 1 using a building located on Gabara and Sawicki [22, 23] test field.

The LoD0 is the contour of the building (footprint), LoD1 is extruded LoD0, LoD2 includes roof shape changes, LoD3 additionally provides information about architectural details of façades, while LoD4 contains LoD3 details with indoor features [8].

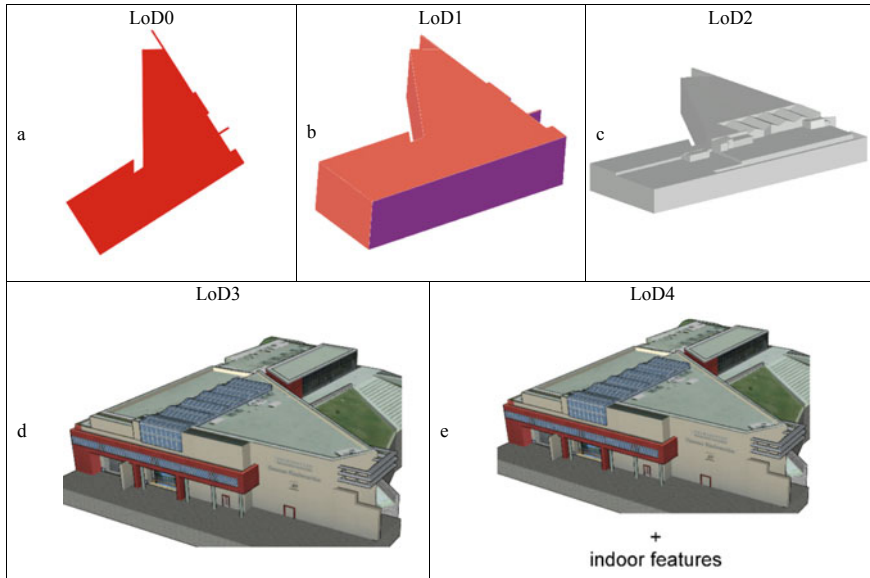


Fig. 1 Visualization of different LoD used for building representation. **a** The 2D visualization—LoD0, **b** The basic 3D visualization—LoD1, **c** The basic 3D visualization, which can be used for planning and spatial analysis—LoD2, **d** The 3D visualization of building used for a more advanced task, i.e., historic building documentation or reconstruction of damaged buildings—LoD3, **e** The most advanced 3D visualization, which can be used in BIM

The data for 3D building modelling in different LoDs uses TLS, terrestrial imagery (normal and convergent images), manned and unmanned airborne imagery (nadir and oblique images), and ALS. The usage of all of these techniques carries a load of advantages and disadvantages, which are described in Table 1.

Since buildings described in [24] were measured using both ALS (two independent measurements with different point cloud density: one acquired in national mapping campaign, second using RIEGL LMS-Q680i laser scanner) and airborne imagery (Phase One iXU-RS 1000) for modelling purposes, they will be used as a reference for presentation and comparison of different measuring techniques. Furthermore, as an addition, the unmanned flight mission using Yuneec H520 UAS with E90 camera was performed to describe some measurement issues solutions. Figure 3 presents the densification and quality of point clouds acquired with described techniques. Furthermore, it shows how multiple stripes of images could minimize the density of tie points only in parts of images. Additional images with different tilt angles give more areas of interest, and the dense point cloud covers even the homogenous structure of the façade.

Because of the wide application range, 3D building reconstruction has become a common trend. For this reason, it has been a focus of attention for city authorities, which are usually involved in campaigns for data acquisition for 3D building modelling purposes. In Poland, it is realized by the institutional way for the whole

country (in LoD1 and LoD2) by performing particular CAPAP project tasks, as described by Ostrowski et al. [42] or individually by hobbyists and enthusiasts, which create 3D models of recognizable or fame buildings.

3 Rules and Procedures for UAS Operations

Because of the high potential of UAS usage in data acquisition for 3D building modelling in this section the limitations of both old and new aviation rules in Poland are characterized. First of all, some of the UAS flight limitations are shared by both regulations. They are caused by special zones (i.e., Aerodrome Traffic Zones and

Table 1 Pros and cons of different data acquisition techniques

Acquisition technique	Advantages	Disadvantages
TLS	<ul style="list-style-type: none"> Reconstruction accuracy Data collection efficiency and capability High-level detail High geometric fidelity Allow generating LoD3 and LoD4 Easy change of project parameters (i.e., the distance between points in a point cloud) Possibility to obtain dense point cloud Fast data processing Easy to obtain additional epochs of data (i.e., for object monitoring)—even several times per year 	<ul style="list-style-type: none"> Laser scanner costs Data noise Data inconsistency (windows) Measurements with high details are time-consuming Usage only for low-rise buildings Beam reflection off the building roof plane Designed for small area Lack of details on roofs and noise (Fig. 2a) A stable control network is required for time series
Terrestrial Imagery	<ul style="list-style-type: none"> Reduced risk of accidents High accuracy high-level detail (ornamental details) High visual and geometric fidelity Allow generating LoD3 and LoD4 Dense point cloud Fast data acquisition Wide technological availability Easy change of project parameters (i.e., GSD) Easy to obtain additional epochs of data (i.e., for object monitoring)—even several times per year 	<ul style="list-style-type: none"> Problem with high-rise building reconstruction (different GSD and accuracy) Lack of details on roofs and noise (Fig. 2a) A photogrammetric network is necessary for high geometric accuracy reconstruction Used for only single building reconstruction Long data processing The issue related to tie point localization on building façades with homogenous structures (Fig. 2b) A stable control network is required for time series
ALS (manned flight missions)	<ul style="list-style-type: none"> Used for big areas Allow for high-building data acquisition The issue with vegetation that masks buildings do not exist Fast data acquisition Fast data processing No additional measurements are needed for time series (flight path is tied to GNSS reference stations) 	<ul style="list-style-type: none"> Low point cloud density (searching for building edges—measuring error) High costs of equipment High operational costs Additional epochs are realized once a year or less often Limitations related to aviation rules Allow obtaining only LoD2

(continued)

Table 1 (continued)

Acquisition technique	Advantages	Disadvantages
ALS (unmanned flight missions)	<p>Fast data acquisition</p> <p>Fast data processing</p> <p>Allow high-rise building data acquisition</p> <p>Easy change of project parameters (i.e., number of points per sq m)</p> <p>Low operational costs</p> <p>Possibility to obtain high point cloud density</p> <p>High geometric fidelity</p> <p>Allow obtaining LoD3</p> <p>The issue with vegetation that masks buildings do not exist</p> <p>Easy to obtain additional epochs of data (i.e., for object monitoring)—even several times per year</p> <p>When high accuracy GNSS + IMU receivers are used, there is no need for additional measurements for time series (flight path is tied to GNSS reference stations)</p>	<p>The capacity of acquiring data in small areas</p> <p>Additional limitations related to aviation rules</p> <p>A high-grade GNSS + IMU receiver is needed for high-accuracy measurements</p> <p>High costs of equipment</p> <p>Data noise</p> <p>Data inconsistency (windows)</p> <p>Measurements with high details are time-consuming</p>
Airborne imagery (manned flight missions)	<p>Allow high-rise building data acquisition</p> <p>Used for big areas</p> <p>High-level detail</p> <p>High geometric fidelity</p> <p>Dense point cloud</p> <p>Fast data acquisition</p> <p>Allow generating LoD3</p>	<p>High costs of equipment</p> <p>High operational costs</p> <p>Limitations related to aviation rules</p> <p>Long data processing</p> <p>The issue with vegetation that masks buildings (Fig. 2d)</p> <p>Additional direct measurement is needed for high-accuracy measurements</p> <p>Additional epochs are realized once a year or less often</p> <p>A stable control network is required for time series</p> <p>The lack of façades consistency when using only nadir images (Fig. 2c)</p>
Airborne imagery (unmanned flight missions)	<p>Allow high-rise building data acquisition</p> <p>Easy change of project parameters (i.e., GSD)</p> <p>Wide technological availability</p> <p>Low-cost technology</p> <p>Low operation costs</p> <p>High-level detail</p> <p>High geometric fidelity</p> <p>Dense point cloud</p> <p>Fast data acquisition</p> <p>Allow generating LoD3</p> <p>In the case of using a multicopter, it is possible to acquire a building shape masked by vegetation (in manual flight)</p> <p>Easy to obtain additional epochs of data (i.e., for object monitoring)—even several times per year</p>	<p>The capacity of acquiring data in small areas</p> <p>Additional limitations related to aviation rules</p> <p>Long data processing</p> <p>The partial issue with vegetation that masks buildings</p> <p>Additional direct measurement is needed for high-accuracy measurements</p> <p>A stable control network is required for time series</p> <p>The lack of façades consistency or reconstruction errors when using only nadir images (Fig. 2c)</p>



Fig. 2 Visualization of issues related to different measuring techniques. **a** Lack of details on roofs and noise using TLS or terrestrial imagery, **b** The issue related to tie point localization on building façade with homogenous structure, **c** The lack of façades consistency or reconstruction errors when using only nadir images, **d** The issue related to buildings partially occluded by vegetation—mainly occur in airborne imagery

Restricted Areas and other National Zones) and controlled traffic regions around airports.

The main difference between those aviation rules is the approach used to assure aviation safety. Most of the old rules related to UAS operations were stated by the Regulation of the Minister of Infrastructure (2019) and they are distinguishing commercial and non-commercial flight missions, while new rules [13] are founded on Specific Operations Risk Assessment (SORA) for UAS. The division in old rules

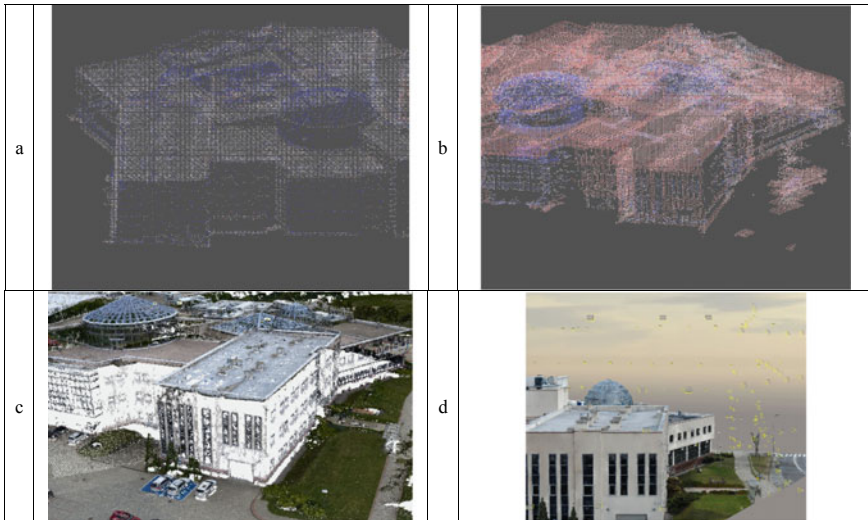


Fig. 3 Visualization of point clouds quality acquired with different measuring techniques. **a** LiDAR point cloud with the minimal density of 12 pts/m², **b** LiDAR point cloud with the minimal density of 25 pts/m², **c** point cloud acquired processing nadir images **d**) point cloud acquired processing oblique, nadir, and convergent images

is related to the type of flight and used UAS. Most commercial flights are done using heavier equipment and more often flight route is complicated, so the UAS pilot must be more careful and experienced. In the case of non-commercial operations, flights are performed using light UAS mostly by hobbyists and enthusiasts. Because of that, the possibility of doing some damage is lower.

3.1 Old UAS Operation Rules

The main limitation related to data acquisition for 3D building modelling are the following:

1. In the case of Visual Line of Sight (VLOS) and non-commercial operation using UAS heavier than 600 g, the distance to the dense settlement must be more than 100 m and more than 30 m to people and buildings.
2. In the case of VLOS and non-commercial operation using UAS lighter than 600 g, UAS pilot should assure safe distance to buildings and people, but the specific value is not defined. It depends on the UAS pilot.
3. In the case of VLOS and commercial operations, UAS pilots have to assure safe distance to people, cars, and other aviation space users.

There is no limitation on distance and UAS weight, however for commercial flight missions, UAS pilot needs Unmanned Aerial Vehicle Operator (UAVO) certificate,

which defines the UAS type and weight range. To get the certificate a person has to complete training performed by a competent authority and pass theoretical and practical exams. Taking into account data acquisition for high accuracy 3D building modelling for non-commercial purposes (e.g. enthusiasts do charity flights, or gather data for self-training in 3D modelling), the flight could be done using DJI Mavic 2 Air (570 g). The flight mission could be done using heavier UAS like DJI Phantom 4 Pro or Yuneec H520 with E90 camera, but in that case, the ground sample distance (GSD) is about 0.027 m.

3.2 *New UAS Operation Rules*

The new aviation rules conditioned UAS flights by the risk, distance to people, and UAS weight. Due to this, the new division into flight categories is related to the risk to people on the ground and other airspace users. The new thing is that all UAS heavier than 250 g have to be registered. Three flight categories are specified: open, which includes VLOS operations without any authorization but is limited by maximum flight height (120 m above ground). Furthermore, it is divided into 3 subcategories related to the distance to people:

1. A1 means flight over people but using UAS with a limited weight to 250 g and a maximum operating speed of 19 m/s. Also, in this subcategory, UAS has to meet C1 class conditions (additional annex with UAS requirements), and UAS pilot must complete an online training course and pass an online theoretical knowledge examination.
2. A2 means close to people, but UAS weight is limited to 2 kg and the horizontal safety distance to uninvolved people is more than 30 m (5 m to uninvolved persons when UAS has an active low-speed mode function). Furthermore, a person who wants to perform missions in that subcategory must complete self-practical training, do an online training course, and pass the online theoretical knowledge examination.
3. A3 means flights away from people and is limited by weight below 25 kg and the horizontal safety distance to residential, commercial, industrial, or recreational areas (more than 150 m). Also, UAS has to meet the conditions of class C2-C4, and UAS pilots must complete an online training course and pass an online theoretical knowledge examination.

For existing UAS that does not comply with the requirements of C1-C4 UAS categories, the transitional period (30 months) is established, which starts one year after the date of entry into force of EU Commission Delegated Regulation [13]. The UAS with a take-off mass lower than 500 g could be used in the A1 subcategory. In the case of UAS with a weight limitation of 2 kg, the minimum horizontal safety distance from people is 50 m.

The specified category includes VLOS and BVLOS operation, which requires approval from the competent authority due to the higher risk to third parties (operations that exceed the limits of the open category). The flight missions are realized based on standard scenarios (STS and national NSTS), which contain a set of procedures used for a specific type of operation. For such types of flights and to obtain confirmation of qualifications, the training, theoretical knowledge, and practical skills are examined. The last category in new aviation regulation is certified, and flight missions are classified in this category only when UAS and pilot are certified. Also, the operation is realized over assemblies of people or is used for people transportation or transportation of dangerous goods.

To analyze the limitations of each category and subcategories, popular UAS were matched to each of them. In A1, it is possible to use DJI Mavic Mini 2 (249 g) equipped with a 12MPix camera (1/2.3" CMOS sensor). It is not a high-grade tool for image acquisition but enthusiasts could be fine. In A2, the DJI Phantom 4 Pro or Mavic 2 Pro could be used. Considering the transitional period, the minimal GSD value of about 0.014 m could be obtained. In the A3 subcategory, all UAS mentioned before can be used, but the acquisition of images is useless because of the horizontal safe distance (150 m) to people. The obtained GSD will be about 0.05 m, so comparable to GSD obtained in manned airborne missions. The specified category should be compared with commercial flight missions (old UAS operation rules). For both special training is needed and to obtain the certificate, the theoretical and practical exams must be passed. Also, the price for the old weight category training is comparable to one standard scenario training. In the case of image acquisition for 3D building modelling, the UAS pilot had more comfort, fewer limitations, and fewer formalities (e.g., operator, pilot, and UAS registration) using previous aviation rules.

4 Conclusions

Undoubtedly, using UAS for image acquisition of buildings has contributed to 3D building modelling. The algorithms for 3D reconstruction were modified and, by extension, the 3D models' accuracy and completeness were enhanced. In this paper, the image processing issues were presented. The attention was drawn to computation without nadir and oblique images acquired from proper height and distance to the object, i.e., the lack of surface consistency, and higher point position errors. Also, the homogenous structure of the building façade scenario, including tie point placement on images, were analyzed. The results showed that in this case of terrestrial images, tie points are localized only in a part of the image while using images acquired by UAS, the issue is irrelevant because more structured objects are registered on photos. Furthermore, the scenarios with some ALS problems and airborne nadir imagery in the case of 3D building reconstruction were presented. These issues can be solved using a multicopter to acquire different image configurations (nadir, oblique, convergent).

Nevertheless, image acquisition using UAS should be performed according to aviation rules, which in the European Union have been changed [13]. Because of that, taking Poland as an example, the old and new UAS operation regulations in the context of the image acquisition of buildings in different levels of detail (LoD) were studied. Until new EU regulation entered into force, every person in Poland could use UAS for non-commercial operations [14] and, by extension, every person using a UAS camera could contribute to expanding repositories and databases with building images and 3D models. However, with the implementation of new rules, some new UAS limitations were introduced, but a legislator did not analyze their consequences in the context of 3D building modelling. Considering the requirements for the UAS pilot, the comparable conditions of flight are for the open category, in subcategories A1 and A3 (A2 requires passing an additional theoretical knowledge examination provided by the competent authority). In A1 the UAS is limited to Maximum takeoff mass (MTOM), including payload, of less than 250 g, which makes it impossible to use UAS (i.e., DJI Phantom) that enables image acquisition. In subcategory A3, the limitation is related to a horizontal distance of at least 150 m from residential, commercial, industrial, or recreational areas, which means that the ground sample distance of images acquired by popular DJI Phantom 3 Pro or DJI Phantom 4 Pro is big (approx. 0.065 m and 0.041 m, respectively) and final 3D building model is useless for many applications. Other categories and the A2 subcategory are related to meeting some costs and spending additional time by UAS pilots, but it enables good conditions for image acquisition of buildings. It should be pointed out that this will cause the commercialization of 3D building modelling and cut off hobbyists and enthusiasts. On the other hand, the risk-based approach was adopted to make aviation safer and avoid any accidents in every possible way. In the case of Poland, where previous aviation rules described in detail the usage of UAS and ensured safety, the new limitation seems to be prepared a bit in advance.

References

1. Albertz J, Wiedemann A (1995) Acquisition of CAD data from existing buildings by photogrammetry In: Pahl PJ, Werner H (eds), *Computing in Civil and Building Engineering*, A.A. Balkema, Rotterdam, Brookfield, pp 859–866
2. Baba T, Takahashi N, Kaneda Y, Inazawa Y, Kikkoin M (2014) Tsunami inundation modeling of the 2011 Tohoku earthquake using three-dimensional building data for Sendai, Miyagi Prefecture, Japan. In: Kontar YA et al (eds) *Tsunami events and lessons learned: environmental and societal significance, advances in natural and technological hazards research*. Springer, Dordrecht 35, pp 89–98. https://doi.org/10.1007/978-94-007-7269-4_3
3. Banfi F (2020) HBIM, 3D drawing and virtual reality for archaeological sites and ancient ruins. *Virtual Archaeol Rev* 11(23):16–33. <https://doi.org/10.4995/var.2020.12416>
4. Batty M, Chapman D, Evans S, Haklay M, Kueppers S, Shiode N, Smith A, Torrens PM (2000) *Visualizing the city: communicating urban design to planners and decision-makers*. Esri Press
5. van Berlo LAHM, Bomhof F (2014) Creating the Dutch national BIM levels of development. In: *2014 international conference on computing in civil and building engineering*. American Society of Civil Engineers, Orlando, FL, USA, pp 129–136

6. Biljecki F, Ledoux H, Stoter J, Zhao J (2014) Formalisation of the level of detail in 3D city modelling. *Comput Environ Urban Syst* 48:1–15. <https://doi.org/10.1016/j.compenvurbsys.2014.05.004>
7. Biljecki F, Stoter J, Ledoux H, Zlatanova S, Çöltekin A (2015) Applications of 3D city models: state of the art review. *ISPRS Int J Geo-Inf* 4(4):2842–2889. <https://doi.org/10.3390/ijgi4042842>
8. Biljecki F, Ledoux H, Stoter J (2016) An improved LOD specification for 3D building models. *Comput Environ Urban Syst* 59:25–37. <https://doi.org/10.1016/j.compenvurbsys.2016.04.005>
9. Borrmann A, König M, Koch C, Beetz J (2018) Building information modeling: why? What? How? In: Borrmann A, König M, Koch C, Beetz J (eds) *Building information modeling*. Springer, Cham. https://doi.org/10.1007/978-3-319-92862-3_1
10. Tiwari A, Sharma SK, Dixit A, Mishra V (2021) UAV remote sensing for campus monitoring: a comparative evaluation of nearest neighbor and rule-based classification. *J Indian Soc Remote Sens* 49(3):527–539. <https://doi.org/10.1007/s12524-020-01268-4>
11. Clark JH (1976) Hierarchical geometric models for visible surface algorithms. *Commun ACM* 19(10):547–554. <https://doi.org/10.1145/965143.563323>
12. Cohen JD, Aliaga DG, Zhang W (2001) Hybrid simplification: combining multiresolution polygon and point rendering. In: *Proceedings visualization. VIS '01*. IEEE, San Diego, CA, USA, pp 37–44. <https://doi.org/10.1109/VISUAL.2001.964491>
13. Commission Delegated Regulation (EU) 2019/945 of 12 March 2019 on unmanned aircraft systems and third-country operators of unmanned aircraft systems
14. Commission Regulation (EU) No 965/2012 of 5 October 2012: laying down technical requirements and administrative procedures related to air operations pursuant to Regulation (EC) No 216/2008 of the European Parliament and the Council
15. Coors V, Flick S (1998) Integrating levels of detail in a web-based 3D-GIS. In: Laurini R, Makki K, Pissinou N (eds) *Proceedings of the 6th ACM international symposium on advances in geographic information systems*. ACM, Washington, DC, USA, pp 40–45
16. Cramer M, Bovet S, Gültlinger M, Honkavaara E, McGill A, Rijdsdijk M, Tabor M, Tournadre V (2013) On the Use of RPAS in national mapping—The EuroSDR point of view. *ISPRS Int Arch Photogramm Remote Sens Spat Inf Sci XL-1/W2*:93–99
17. Department of Transportation (DOT) (2021) 14 CFR parts 11, 21, 43, and 107. Docket No.: FAA–2018–1087; Amdt. Nos. 11–64, 21–105, 43–51, 107–8
18. Döllner J (2005) Continuous level-of-detail modelling of buildings in 3D city models. In: Shahabi C, Boucelma O (eds) *GIS '05 proceedings of the 13th annual ACM international workshop on geographic information systems*. ACM, Bremen, Germany, pp 173–181
19. EASA (2021) Easy access rules for unmanned aircraft systems. Last Accessed 20 March 2021
20. Esposito S, Fallavollita P, Wahbeh W, Nardinocchi C, Balsi M (2014) Performance evaluation of UAV photogrammetric 3D reconstruction. In: *Geoscience and remote sensing symposium (IGARSS)*. IEEE, Quebec City, QC, pp 4788–4791. <https://doi.org/10.1109/IGARSS.2014.6947565>
21. Gabara G, Sawicki P (2018) Application of UAV imagery for inventory mapping—A case of industrial estate. In *Proceedings of the 2018 baltic geodetic congress (BGC Geomatics)*, IEEE, Olsztyn, Poland
22. Gabara G, Sawicki P (2019a) Kortowo test field for testing photogrammetric products accuracy—Design and first evaluation. *Int Arch Photogramm Remote Sens Spat Inf Sci XLII-1/W2*:23–29. <https://doi.org/10.5194/isprs-archives-XLII-1-W2-23-2019>
23. Gabara G, Sawicki P (2019) Multi-variant accuracy evaluation of UAV imaging surveys: a case study on investment area. *Sensors* 19:5229. <https://doi.org/10.3390/s19235229>
24. Gabara G, Sawicki P (2021) The quality evaluation of 3D building models based on the low-altitude imagery and airborne laser scanning point clouds
25. Glander T, Döllner J (2008) Automated cell-based generalization of virtual 3D city models with dynamic landmark highlighting. In: *Proceedings of the 12th ICA workshop on generalization and multiple representation*. Montpellier, France, pp 1–14

26. Granshaw SI (2018) RPV, UAV, UAS, RPAS ... or just drone? *Photogramm Rec* 33:160–170. <https://doi.org/10.1111/phor.12244>
27. Grussenmeyer P, Hanke K, Streilein A (2002) Architectural photogrammetry. In: Kasser M, Egels Y (eds) *Digital photogrammetry*. Taylor & Francis, pp 300–339
28. He S, Besuievsky G, Tourre V, Patow G, Moreau G (2012) All range and heterogeneous multi-scale 3D city models. In: Leduc T, Moreau G, Billen R (eds) *Usage, usability, and utility of 3D city models—European COST action TU0801*, EDP Sciences Nantes, France
29. He S, Moreau G, Martin JY (2013) Footprint-based generalization of 3D building groups at a medium level of detail for multi-scale urban visualization. *Int J Adv Softw* 5:378–388
30. ICAO (2011) *Unmanned Aircraft Systems (UAS)*. International Civil Aviation Organization, Circular 328-AN/190. Montreal, Quebec, Canada
31. ICAO (2005) *Global Air Traffic Management Concept*. International Civil Aviation Organization, Document 9854-AN/458. Montreal, Quebec, Canada
32. FAA (2005) *Unmanned Aircraft Systems Operations in the U.S. National Airspace System—Interim Operational Approval Guidance*, AFS-400 UAS Policy 05-01
33. ICAO (2015) *Manual on remotely piloted aircraft systems RPAS*. International Civil Aviation Organization, Document 10019-AN/507. Montreal, Quebec, Canada
34. Ioannidis C, Potsiou C, Badekas J (1996) 3D detailed reconstruction of a demolished building by using old photographs. *Int Archiv Photogramm Remote Sens XXXI(Part B5)*, Vienna 1996:16–21
35. Li M, Nan L, Smith N, Wonka P (2016) Reconstructing building mass models from UAV images. *Comput Graph* 54 C:84–93. <https://doi.org/10.1016/j.cag.2015.07.004>
36. Luebke D, Reddy M, Cohen JD, Varshney A, Watson B, Huebner R (2003) *Level of detail for 3D graphics*. Elsevier, San Francisco
37. Luhmann T, Robson S, Kyle S, Boehm J (2013) *Close range photogrammetry and 3D imaging*, 2nd edn. Berlin, Germany, De Gruyter
38. Markiewicz J, Tobiasz A, Kot P, Muradov M, Shaw A, Al-Shamma'a A (2019) Review of surveying devices for structural health monitoring of cultural heritage buildings. In: 12th international conference on developments in eSystems engineering (DeSE). IEEE, Kazan, Russia, pp 597–601. <https://doi.org/10.1109/DeSE.2019.00113>
39. Mosier RL (1988) DoD joint unmanned aerial vehicle (UAV) program master plan. Department of Defense Tactical Intelligence Systems Directorate, Washington, DC, USA
40. Nikodem F, Bierig A, Dittrich JS (2018) The new specific operations risk assessment approach for UAS regulation compared to common civil aviation risk assessment. DLRK, Friedrichshafen, Deutschland
41. Núñez AA, Buill PF, Regot MJ, de Mesa GA (2012) Generation of virtual models of cultural heritage. *J Cult Herit* 13:103–106. <https://doi.org/10.1016/j.culher.2011.06.004>
42. Ostrowski W, Pilarska M, Charlton J, Bakula K (2018) Analysis of 3D building models accuracy based on the airborne laser scanning point clouds. *Int Arch Photogramm Remote Sens Spat Inf Sci XLII-2*:797–804. <https://doi.org/10.5194/isprs-archives-XLII-2-797-2018>
43. Pieraccini M, Guidi G, Atzeni C (2001) 3D digitizing of cultural heritage. *J Cult Herit* 2(1):63–70. [https://doi.org/10.1016/S1296-2074\(01\)01108-6](https://doi.org/10.1016/S1296-2074(01)01108-6)
44. Rango A, Laliberte A (2010) Impact of flight regulations on effective use of unmanned aircraft systems for natural resources applications. *J Appl Remote Sens* 4(1):043539. <https://doi.org/10.1117/1.3474649>
45. Rezaeian M, Gruen A (2011) Automatic 3D building extraction from aerial and space images for earthquake risk management. *Georisk: Assess Manag Risk Eng Syst Geohazards* 5(1): 77–96. <https://doi.org/10.1080/17499511003679998>
46. Salach A, Bakula K, Pilarska M, Ostrowski W, Górski K, Kurczyński Z (2018) Accuracy assessment of point clouds from LiDAR and dense image matching acquired using the UAV platform for DTM creation. *ISPRS Int J Geo-Inf* 7:342. <https://doi.org/10.3390/ijgi7090342>
47. Srivastava S, Gupta S, Dikshit O, Nair S (2020) A review of UAV regulations and policies in India. In: Jain K, Khoshelham K, Zhu X, Tiwari A (eds) *Proceedings of UASG 2019*. UASG 2019. Lecture Notes in Civil Engineering, vol 51. Springer, Cham. https://doi.org/10.1007/978-3-030-37393-1_27

48. Stadler A, Kolbe TH (2007) Spatio-semantic coherence in the integration of 3D city models. *Int Arch Photogramm, Remote Sens Spat Inf Sci XXXVI-2(C43)*:8
49. Stoter J, Vosselman G, Goos J, Zlatanova S, Verbree E, Klooster R, Reuvers M (2011) Towards a national 3D spatial data infrastructure: case of The Netherlands. *Photogrammetrie - Fernerkundung - Geoinformation 2011*:405–420
50. Toker C, Erhan H (2014) An architectural modelling method for game environments and visualization. In: Gu N, Watanabe S, Erhan H, Hank Haeusler M, Huang W, Sosa R (eds) *Rethinking comprehensive design: speculative counterculture, proceedings of the 19th international conference on computeraided architectural design research in Asia CAADRIA 2014*, The Association for Computer-Aided Architectural Design Research in Asia (CAADRIA), Hong Kong, pp 605–614
51. Vanegas CA, Aliaga DG, Wonka P, Müller P, Waddell P, Watson B (2010) Modelling the appearance and behaviour of urban spaces. *Comput Graph Forum 29*:25–42. <https://doi.org/10.1111/j.1467-8659.2009.01535.x>
52. Verykokou S, Doulamis A, Athanasiou G, Ioannidis C, Amditis A (2016) UAV-based 3D modelling of disaster scenes for urban search and rescue. In: *IEEE international conference on imaging systems and techniques (IST)*. IEEE, Chania, Greece, pp 106–111. <https://doi.org/10.1109/IST.2016.7738206>
53. Wang R (2013) 3D building modelling using images and LiDAR: a review. *Int J Image Data Fusion 4*(4):273–292. <https://doi.org/10.1080/19479832.2013.811124>
54. Wang X, Love P, Kim M, Park C, Sing C, Hou L (2013) A conceptual framework for integrating building information modelling with augmented reality. *Autom Constr 34*(1):37–44. <https://doi.org/10.1016/j.autcon.2012.10.012>
55. Yao Z, Nagel C, Kunde F et al (2018) 3DCityDB—a 3D geodatabase solution for the management, analysis, and visualization of semantic 3D city models based on CityGML. *Open Geospat Data, Softw Stand. 3*:5. <https://doi.org/10.1186/s40965-018-0046-7>
56. Zhang X, Lv Y, Tian J, Pan Y (2015) An integrative approach for solar energy potential estimation through 3D modeling of buildings and trees. *Can J Remote Sens 41*(2):126–134. <https://doi.org/10.1080/07038992.2015.1043004>
57. Zhang X, Zhu Q (2004) Applications of 3D city models based spatial analysis to urban design. *Int Arch Photogramm Remote Sens Spat Inf Sci XXXV/B2*:325–329

Effects of Flight Plan Parameters on the Quality and Usability of Low-Cost UAS Photogrammetry Data Products for Tree Crown Delineation



Jojene R. Santillan, Jun Love E. Gesta, and Marcia Coleen N. Marcial

Abstract The continued understanding of the influence of flight planning characteristics on data quality is crucial in the demand for minimizing costs and maximizing the output potential of Uncrewed Aerial Systems (UAS) for forestry applications. This study was conducted to ascertain the effects of various combinations of flying height and percentage overlaps on the quality of photogrammetry data products generated from images acquired by a low-cost UAS (Mavic 2 Pro), with emphasis on tree crown delineation in a Mangium plantation forest in the Philippines. The quality of the products is evaluated based on their completeness and the accuracy of tree crown delineations. Results suggest that the percentage completeness increases as the flying height and percentage overlap increase. More than 90% completeness was achieved for 90% overlap regardless of the flying height. Tree crown delineations using multiresolution segmentation of Digital Surface Models (DSMs) generated from images with a flying height of 120 m and percentage overlap of 80% and 90%, achieved the highest overall accuracy of 43.35%. This study showed that a minimum of 80% overlap must be aimed when acquiring images to ensure higher completeness of the data products and that flying at 120 m above ground with at least 80% overlaps can provide more accurate tree crown delineations.

J. R. Santillan (✉) · J. L. E. Gesta · M. C. N. Marcial
Caraga Center for Geo-Informatics, Caraga State University, 8600 Butuan City, Philippines
e-mail: jrsantillan@carsu.edu.ph

J. L. E. Gesta
e-mail: jlegesta@carsu.edu.ph

M. C. N. Marcial
e-mail: mcnmarcial@carsu.edu.ph

Industrial Tree Plantation Research and Innovation Center, Caraga State University, 8600 Butuan City, Philippines

J. R. Santillan · J. L. E. Gesta
Department of Geodetic Engineering, College of Engineering and Geosciences, Caraga State University, 8600 Butuan City, Philippines

Keywords UAS · Flight plan · Digital surface model · Orthomosaic · Tree crown delineation

1 Introduction

There have been rapid advancements in the last decade in remote sensing-based mapping and monitoring of the environment and natural resources. One of these is the emergence of Uncrewed Aerial Systems (UAS). Images acquired by high-resolution digital aerial cameras installed in these so-called “drone” remote sensing platforms have provided users up to a centimetre level of detail and accuracy, prompting its applications in forestry, among many other fields. One importance of UAS is its potential to fill data gaps and supplement the capabilities of crewed aircraft and satellite remote sensing systems. UAS technology is also advantageous because of its low material and operational costs, flexible spatial and temporal resolution control, high-intensity data collection, and the absence of risk to crews [1].

Among the data products derived from overlapping UAS collected images and utilized for forestry applications are three-dimensional (3D) point clouds, Digital Surface Models (DSMs), Digital Terrain Models (DTMs), and orthomosaics. Popular applications of these products include tree detection and counting, individual tree crown delineations, generation of canopy height models, estimation of tree heights, and biomass predictions [2–6]. The potential of UAS technology in this application area is enormous. Even low-cost commercial off-the-shelf UAS are already being utilized to complement, if not replace, field-based forest inventories [7]. Low-cost UASs are often characterized by an uncrewed aerial vehicle (UAV) component that is lightweight and comprised only of a Red–Green–Blue (RGB) camera and built-in Global Navigation Satellite System (GNSS) and Inertial Measurement Unit (IMU). Compared to high-end UASs with multispectral (e.g., RGB + NIR) imaging capabilities and survey-grade positioning and inertial navigation systems, low-cost UASs have positioning accuracies ranging from ± 0.5 m to ± 1.5 m [8] which may already be sufficient for general plantation mapping applications.

Whether a UAS used in image acquisition is high-end or low-cost, products generated from images acquired by these UAS are generated through photogrammetric processing. Modern processing techniques and software involve the application of the Structure-from-Motion (SfM) and dense matching algorithms such as the Multiview Stereopsis (MVS), commonly referred to as the SfM-MVS approach [9].

Several studies have found that the success of the SfM-MVS approach in generating the data products is dependent on several factors that include flight planning characteristics (e.g., Ground Sample Distance (GSD), camera type, image overlap, and flying height), software package choice, and processing parameter settings [2, 5, 6, 10]. In a study conducted to evaluate the effects of flying height of a fixed-wing UAS on SfM processing capability for complex forest environments [10], superior performance in terms of image alignment success, the average number of tie points

per image, and planimetric model ground sampling distance, was found for the 100-m flying height above the forest canopy compared to flying heights of 50 and 120 m, with 85% front overlap and 70% sidelap set for all flying heights. In another study on individual tree detection in structurally complex conifer forests, the accuracy of the resulting tree maps was generally maximized by collecting UAS imagery at a high altitude (120 m) with at least 90% image-to-image overlap [11]. On the other hand, a study conducted by [6] showed that no statistically significant differences exist between image resolution, camera types, side overlap, and terrain slope in the accuracy of estimating biomass using UAS-derived point clouds. Model accuracy was also found to increase when using the RGB camera and finer image resolution while NIR camera and coarser resolution decreased model accuracy. Moreover, the authors suggested a reduction of side overlap from 80 to 70%, while keeping a fixed forward overlap of 90% or reducing flight time and cost of acquisitions [6]. The study of [5] that examined the effects of differences in SfM software on image processing of UAS images for tree height estimation revealed differences in the accuracy of the estimated tree heights by Pix4Dmapper, Terra Mapper, and Agisoft Photoscan, with the estimates by Pix4D in many flight conditions having smaller Root Mean Square Error (RMSE) values than those of the other software. In [10], Agisoft Photoscan generated higher quality SfM-MVS outputs, i.e., 11.8% greater image alignment and 9.9% finer resolution than Pix4Dmapper.

From these cited studies, there is no consensus on the specific flight planning characteristics, software, and processing parameter settings that must be adopted when conducting UAS image acquisitions and applying the SfM-MVS approach for forestry applications. Fraser and Congalton [10] noted that successful SfM modelling and generation of data products from UAS collected imagery requires diligent consideration of fundamental flight planning characteristics. Since unifying the flight parameters when capturing UAS images is difficult [5], there is a need to evaluate the influence of the flight and camera configurations when estimating forest attributes from UAS products [6]. This continued understanding of the influence of flight planning and processing characteristics on the quality and usability of UAS data products is crucial for minimizing costs and maximizing the output potential of UAS for forestry applications [10]. More so in the case of low-cost commercial off-the-shelf UAS that has penetrated the UAS market, offering forest plantation managers affordable access to UAS technology for plantation monitoring and inventorying activities. Several studies have established the utility of low-cost UAS in this application area, e.g., [7, 11–13]. However, most of these studies are species- and location-specific, utilized different UAS brands/models, and applied different photogrammetric processing and information extraction procedures. Therefore, the flight plans, image acquisition configurations, and processing steps that have been proven effective by these studies may differ when applied under different settings and field conditions. In the Philippines, particularly in the Caraga Region, where industrial tree plantations support more than 50% of the country's total log production [14], low-cost UAS is attractive to support plantation management activities, particularly tree inventorying. To our knowledge, there is a lack of studies that can

support the use of low-cost UAS for such purposes. Determining the best flight planning parameters for image acquisition and how these parameters could affect the quality and usability of data products generated from the low-cost UAS images are some research problems that need investigation.

Hence, this study was conducted to evaluate the use of a low-cost UAS, specifically Mavic 2 Pro (DJI, China), in acquiring images for the generation of data products useful for mapping and inventorying a tree plantation forest in the Philippines. Specifically, we analyzed the effects of various combinations of two flight planning parameters, namely flying above terrain (altitude) and percentage overlaps, on the quality of UAS photogrammetry data products and their degree of usability for tree crown delineation in plantation forests. We aimed to quantify the effects of four (4) flying heights (60, 80, 100, and 120 m above ground) and four forward (front) overlap and sidelap percentages (60, 70, 80, and 90% set for each flying height) to the completeness of DSM and orthomosaics generated using the SfM-MVS approach. We focused on evaluating the completeness of DSM and orthomosaic, and not the 3D point cloud, for the main reason that both the DSM and orthomosaic are commonly used inputs for tree crown delineations. We also aimed to quantify how the degree of completeness affects the accuracy of a tree crown delineation algorithm applied to the various DSMs generated. We also considered the effects of other factors on tree crown delineation accuracy.

2 Materials and Methods

2.1 Study Area

The study area is within the Caraga State University campus in Butuan City, Agusan del Norte, Philippines. It has a dimension of 364×175 m, with an area of 6.37 hectares (Fig. 1). The terrain is generally flat and planted with Mangium (*Acacia mangium Willd.*) and Mahogany (*Swietenia macrophylla King spp.*) trees, which are approximately 10–12 years old. These tree species are common in plantation forests in the Philippines. In the study area, rice fields surround the tree plantations.

2.2 UAS Flight Planning and Image Acquisitions

We used a Mavic 2 Pro (DJI China) UAS equipped with a Hasselblad L1D-20c RGB camera, a 1-inch CMOS sensor, and a remote controller. The camera lens' focal length is 10.26 mm, and the images acquired have dimensions of 5472×3648 pixels. A mobile phone camera with the Android operating system was connected to the remote controller for flight planning and acquisition.

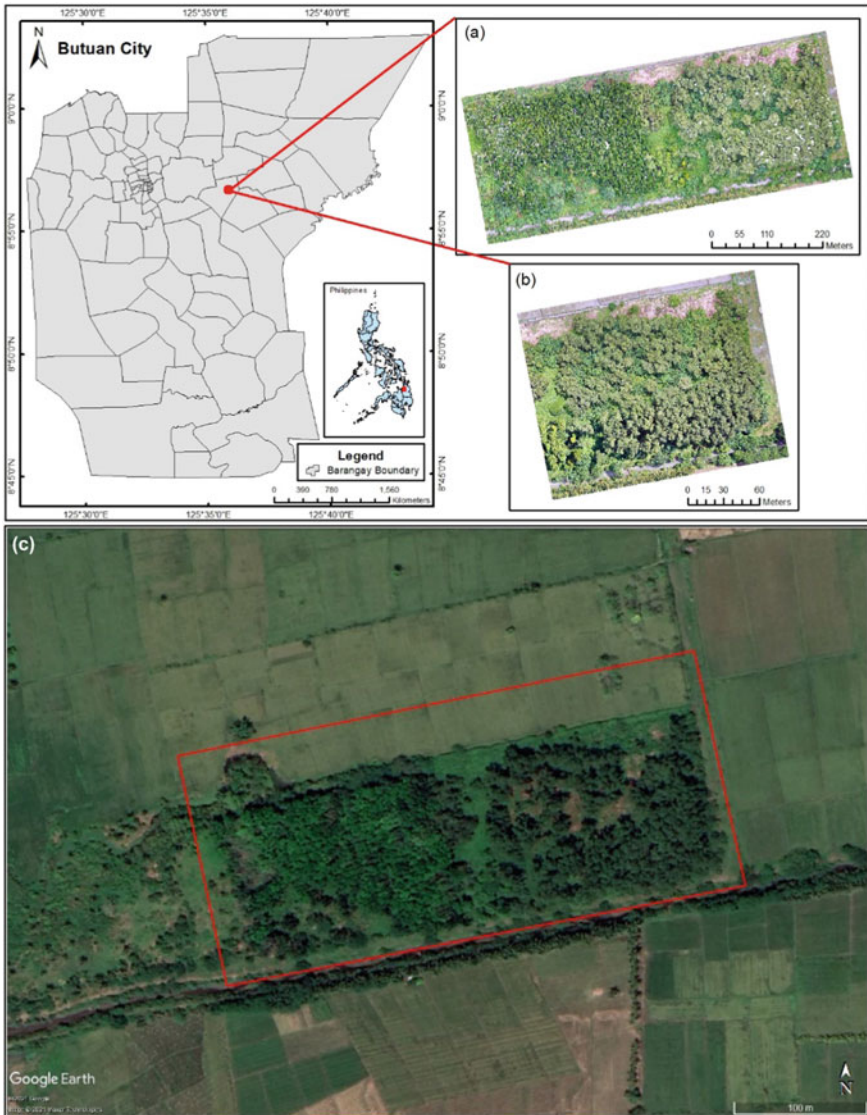


Fig. 1 a Location of the study area; b a portion of the study area containing Mangium trees that were considered for tree crown delineation; c a Google Earth image of the study area (in red rectangle) with the rice fields surrounding it

The free edition of DroneDeploy (<https://www.dronedeploy.com/>) was used to prepare a total of 16 standard (single grid-type) flight plans, each plan having a specific combination of flying height and percentage overlaps (Table 1). Since DroneDeploy already included the Mavic 2 Pro camera in its list of planning cameras, it was selected accordingly and no other parameters were changed except for the flying heights, overlap percentages, and flight direction. The flying heights considered are 60, 80, 100, and 120 m above ground. Forward overlap and side lap percentages were set the same, with values of 60%, 70%, 80% and 90%. These values were chosen so that the acquired images will have varying characteristics in scale, GSD, and ground coverage. We limit the flying height to 120 m to comply with the flying height limitations for non-commercial UAS flights imposed by the Civil Aviation Authority of the Philippines. Also, flight plans were prepared such that vertical images will be acquired.

The flight direction was set to 169° in all flight plans, which is the same direction as the longer dimension of the study site. This minimized the number of flight lines. Image acquisitions were done repetitively based on the prepared flight plans. The images were acquired on sunny days from July 15 to July 24, 2020, between 10 am to 2 pm to minimize the effect of shadows.

2.3 Processing of UAS Images

Images acquired for each flight plan were processed using Agisoft Metashape Professional Version 1.5 (Agisoft LLC, Russia) in a Windows 10 virtual machine configured using VMWare ESXi with the following technical specifications and components: Intel Xeon, 2.10 GHz, 64 cores; 75 GB RAM; and NVIDIA Tesla V100 graphical processing unit (GPU) with 32 GB memory.

The SfM-MVS steps implemented in Agisoft Metashape consist of (i) alignment of photos (images) to generate a sparse point cloud composed of tie points, (ii) building a dense point cloud, and (iii) building a DEM, wherein a DSM is generated using the dense point cloud, and (iv) building an orthomosaic. These steps comprise the general workflow for image processing in Agisoft Metashape. The settings used in each step are summarized in Table 2. More details about each step can be found in the user manual [15].

The “Build DEM” and “Build Orthomosaic” procedures were run twice. In the first run, interpolation and hole filling were initially disabled, respectively, to generate a DSM and orthomosaic that will be used for quantitative analysis of data completeness. This will ensure that the DSM and orthomosaic will not include interpolated data. It means that the output DSM and orthomosaic will only contain valid pixel values in portions with sparse and dense point clouds, i.e., in portions where the SfM-MVS procedure succeeded.

A second run was performed, this time enabling DSM interpolation and orthomosaic hole filling. The output DSMs from the second run for each flight plan were

Table 1 Summary of image acquisition parameters per flight plan

Flight plan No	Flying height above ground (m)	Side and front overlaps (%)	Estimated number of images	Estimated total flying time	Mapping flight speed (m/s)
FP1	60	60	140	7 min 06 s	8
FP2	60	70	240	12 min 49 s	6
FP3	60	80	520	25 min 25 s	4
FP4	60	90	2002	89 min 53 s	3
FP5	80	60	75	5 min 28 s	11
FP6	80	70	140	8 min 34 s	8
FP7	80	80	300	16 min 48 s	5
FP8	80	90	1141	53 min 02 s	3
FP9	100	60	47	4 min 32 s	13
FP10	100	70	79	6 min 04 s	10
FP11	100	80	190	11 min 16 s	7
FP12	100	90	712	38 min 03 s	3
FP13	120	60	40	4 min 33 s	15
FP14	120	70	66	5 min 46 s	12
FP15	120	80	138	9 min 14 s	8
FP16	120	90	514	26 min 16 s	3

then used for tree crown delineations. For both runs, the GSD of the orthomosaic was set to that of the DSM.

2.4 Quantitative Analysis of Data Completeness

The completeness of each of the 16 sets of DSMs and orthomosaic generated during the 1st run was analyzed by determining the proportion of the pixels with data and pixels with “no data” within the boundary of the study area (Fig. 2). The “no data” pixels are those portions of the DSM that have no equivalent data points in the dense point cloud, i.e., where tie point generation (during photo alignment) and dense matching failed. These “no data” portions will have interpolated values in the 2nd run, i.e., when DSM interpolation and orthomosaics hole-filling were enabled.

To perform the analysis, the raster files were clipped in ArcGIS 10.8 software (Esri, USA) with a common polygon shapefile of the study area boundary. The number of “with data” and “no data pixels” within the study area were determined through map algebra using ArcGIS Spatial Analyst extension. The completeness of each product was calculated by getting the percentage of the “with data” pixels to all pixels within the study area (“with data” pixels + “no data” pixels).

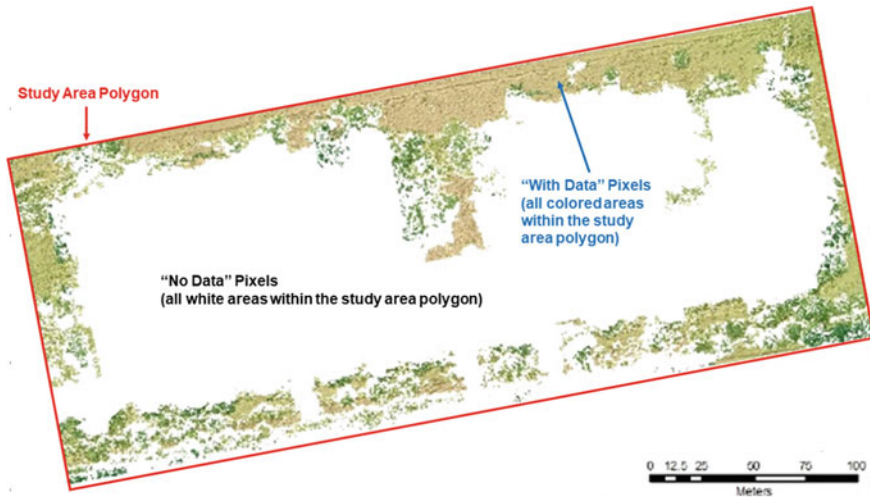


Fig. 2 Illustration of “with data” and “no data” pixels for the quantitative analysis of DSM completeness

2.5 *Tree Crown Delineation*

A portion of the study area containing 263 Mangium trees (Fig. 1b) was chosen for tree crown delineation. The output DSMs from the second run for this portion were subjected to tree crown delineation using a multiresolution segmentation algorithm in eCognition Version 9 software (Trimble Inc., USA). This algorithm performs a bottom-up segmentation (i.e., assembling objects to create larger objects) by consecutively merging pixels or existing image objects using a homogeneity criterion [16]. Moreover, it involves a combination of spectral and spatial heterogeneity of tree crowns for hierarchical region merging [17]. This algorithm utilizes a scale parameter and composites of homogeneity criterion (i.e., shape and compactness). The scale parameter is for determining the segment size; shape calculates a relative weighing against colour; compactness defines whether the smoothness affects the segmentation [18]. The optimum values and combination of the parameters were determined through a trial-and-error process using the Flight Plan 16 DSM 2nd run output. After trial and error, it was decided that the data products will be segmented with scale parameters, shape, and compactness of 90, 0.35, and 0.8, respectively.

To assess the accuracy of the delineation, individual tree crowns were manually delineated through visual interpretation of the FP 16 DSM and orthomosaic outputs. Before the delineation, a field survey was conducted to map the location of each tree within the study area. A Garmin Oregon 550 handheld GNSS receiver with positional accuracy of ± 5 m was used to get the average UTM 51 WGS 84 grid coordinates of each tree. For each tree, 2–3 min of observation time was devoted to getting the average coordinates. The tree location data (263 trees) was downloaded from the

GNSS receiver and exported as a GIS point shapefile. It was then overlaid to the DSM and orthomosaic in ArcGIS to guide the visual interpretation and on-screen digitizing of the tree crowns. Due to the differences in positional accuracy of the tree location data and the UAS data products, some of the tree points will not fall in the middle of the tree crowns. However, most of them are within their corresponding tree crowns, making the manual delineation relatively easier.

The delineated tree crowns, in GIS shapefile format, were used for comparison with the multiresolution segmentation results (Fig. 3). Five categories (Table 3) were used in assessing the accuracy of the tree crown delineations, with each category indicated by the spatial relationship of the manually delineated crowns with the automatically delineated crowns [19]. Matched and nearly matched were taken as correctly delineated tree crowns. Missed and merged corresponds to the omission errors and the split represents the commission errors. Below are the equations used in calculating these accuracy measures:

$$\text{Tree Crown Delineation Accuracy} = \frac{\text{Matched} + \text{Nearly Matched}}{\text{Total Number of Actual Tree Crowns}}$$

$$\text{Commission Error} = \frac{\text{Split}}{\text{Total Number of Actual Tree Crowns}}$$

$$\text{Omission Error} = \frac{\text{Missed} + \text{Merged}}{\text{Total Number of Actual Tree Crowns}}$$

Pearson's correlation coefficients were also used to explain and measure the strength and direction of the relationship between flight plan parameters, GSD, camera location errors, and data completeness to the tree crown delineation accuracy.

3 Results and Discussion

3.1 Characteristics of Acquired and Processed Images

The characteristics of the acquired and processed images are presented in Table 4. The FP4, with 60 m flying height (FH) and 90% overlaps, has the highest number of acquired images at 1,836; the FP13 (120 m FH and 60% overlaps) has the least number of images at 45. At any given percentage of the image overlaps, increasing flying heights leads to a lesser number of images; while a 10% increase in percentage overlaps at any given flying height almost doubles or triples the number of images acquired (Fig. 4a). While these results are expected for any UAS image acquisition activity, it can provide us with a clear understanding of the relationship between flying height and percentage overlaps. In large tree plantations, flying higher would be cost efficient because fewer images will need to be acquired to cover the whole

Table 2 Agisoft metashape settings

Step	Parameters/Settings	
Align photos	Accuracy	High
	Generic preselection	Checked
	Reference preselection	Checked
	Reset current alignment	Unchecked
	Key point limit	40,000
	Tie point limit	5,000
	Apply masks to	None
	Adoptive camera modelling fitting	Unchecked
Build dense cloud	Quality	High
	Depth filtering	Mild
	Reuse depth maps	Unchecked
	Calculate point colours	Checked
	Calculate point confidence	Unchecked
Build DEM	Projection	WGS 84/UTM Zone 51 N (EPSG:32,651)
	Source data	Dense cloud
	Interpolation	<i>Disabled (for 1st run); Enabled (for 2nd run)</i>
	Setup boundaries	Unchecked
Build orthomosaic	Surface	DEM
	Building mode	Mosaic (default)
	Refine seamlines	Unchecked
	Enable hole-filling	<i>Unchecked (for 1st run); Checked (for 2nd run)</i>
	GSD (Pixel size, m.)	(same as used in Build DEM)

plantation area compared to flying lower. Flying higher with lesser percentage overlaps will further decrease the number of images to be acquired (and hence, the flying time), resulting in a decrease in image acquisition and processing costs. However, flying higher or lower without the appropriate percentage overlaps can lead to image alignment problems when the images are subjected to the SfM-MVS processing.

In terms of the percentage of the acquired images that were successfully aligned during the first step of the SfM-MVS process, it was found that images acquired with at least 80 m of flying height and at least 80% image overlaps have more than 90% alignment success rate (Fig. 4b). This means that more than 90% of the acquired images were successfully tied (matched) with each other using keypoints that were identified in those images. With a sufficient number of images and keypoint matches, the SfM algorithm can perform bundle adjustments to simultaneously compute the 3D location of the camera stations and generate a sparse 3D point cloud [9]. This

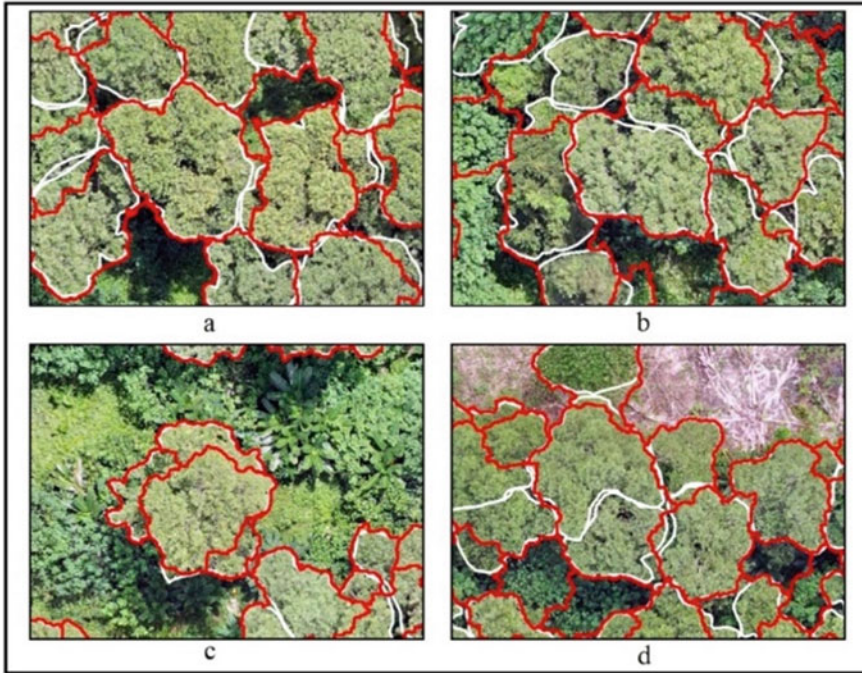


Fig. 3 Illustration of the categories used in accuracy assessment of tree crown delineations. The manually delineated crowns (white outline) are overlaid with the automatically delineated crowns (red outline): **a** matched; **b** nearly matched; **c** split; **d** merged

Table 3 Categories and its description used in the accuracy assessment of tree crown delineations (adopted from [19])

Category	Description
Matched	If the manually delineated crown and automatically delineated crown has more than 50% overlaps
Nearly matched	If the manually delineated crown and automatically delineated crown has more than 50% overlaps of only one segment
Merged	If there were multiple manually delineated crowns in an automatically-delineated crown
Split	If there were multiple automatically delineated crowns in the manually delineated crown
Missed	If 50% of the manually delineated crown has no overlaps with automatically delineated crowns

Table 4 Characteristics of acquired and processed UAS images

Flight plan No.	Flying height above ground (m)	Side and front overlaps (%)	Actual Number of Acquired Images	Number of aligned images	Image alignment percentage (%)	Camera location X error (m)	Camera location Y error (m)	Camera location Z error (m)	Camera location XY error (m)	Camera location total error (m)
FP1	60	60	148	90	60	1.88	0.69	2.00	2.00	2.83
FP2	60	70	252	201	80	1.53	0.70	1.53	1.68	2.27
FP3	60	80	509	478	94	0.99	0.41	0.73	1.07	1.29
FP4	60	90	1836	1972	100	0.80	0.81	1.53	1.13	1.90
FP5	80	60	80	56	70	2.86	0.52	1.65	2.91	3.35
FP6	80	70	148	138	93	2.07	0.43	1.19	2.11	2.42
FP7	80	80	312	312	100	1.26	0.43	0.72	1.33	1.51
FP8	80	90	942	942	100	0.63	0.53	1.65	0.82	1.84
FP9	100	60	54	43	83	3.23	1.22	1.26	3.45	3.67
FP10	100	70	86	84	99	2.50	0.76	3.19	2.61	4.12
FP11	100	80	201	200	100	1.42	0.60	1.13	1.54	1.91
FP12	100	90	735	729	100	1.32	0.72	0.82	1.51	1.71
FP13	120	60	45	45	100	3.61	1.23	1.02	3.81	3.95
FP14	120	70	73	72	100	2.97	1.04	0.76	3.15	3.24
FP15	120	80	148	147	100	1.81	0.57	1.17	1.89	2.23
FP16	120	90	533	533	100	0.78	0.45	1.13	0.90	1.44

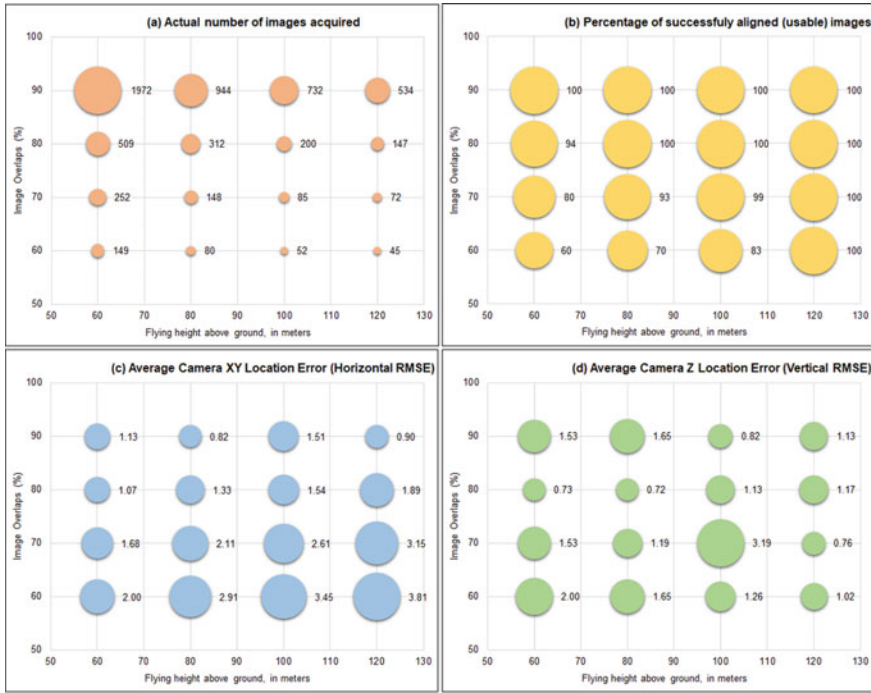


Fig. 4 Bubble graphs for the visualization of characteristics of acquired and processed UAS images concerning flying height above ground and image overlaps. The labels correspond to the parameter indicated in each graph

result suggests that image acquisition with these minimum flight configurations is cost-effective because it can acquire a higher number of usable images for UAS data product generation. Images obtained with 60% overlaps, particularly those acquired from 60 to 100 m flying heights, are the most prone to lower alignment percentages and must be avoided. Images acquired with 90% overlaps regardless of the flying height have 100% alignment. The same can be stated for images acquired at 120 m flying height, irrespective of the percentage overlaps.

On the other hand, the bundle adjustments resulted in average camera location error ranging from 1.07 m to 3.81 m along the horizontal (XY), and from 0.73 m to 3.19 m along the vertical (Z) (Fig. 4c, d). The camera XY location errors depend on the flying height and percentage overlaps. XY location errors are the least for images acquired with 90% overlaps. In general, an increase in flying height combined with a decrease in percentage overlaps resulted in a rise in the XY location errors. However, the same cannot be said for the Z location errors. The largest error is 3.19 m for images acquired at 100 m flying height and 70% overlaps. These camera location errors can be said to have been affected by the quality of the image alignment process, as well as the quantity and distribution of the generated key points. It can be recalled that the SfM algorithm relies on the generated key points to perform bundle adjustments for

estimating the camera locations. It should also be noted that the UAS used in the image acquisition is equipped with a built-in GNSS receiver that is not survey-grade and did not benefit from Post-processed Kinematic (PPK) or Real-time Kinematic (RTK) positioning. This resulted in less precise and less accurate coordinates of the camera locations recorded during the image acquisitions, which were complementarily used and optimized during the bundle adjustments [9].

3.2 *GSD and Completeness of the DSMs and Orthomosaics*

Images acquired at lower altitudes resulted in DSM and orthomosaics with smaller GSD values (Table 5, Fig. 9a). Hence, they are of higher spatial resolution. The smallest GSD of 2.65 cm was found for images acquired at a flying height of 60 m and 90% overlaps; the largest GSD was for images acquired at 120 m, and 60% overlaps. The average GSDs were computed as 2.86, 3.78, 4.90, and 5.85 cm/pixel, respectively, for flying heights of 60 m, 80 m, 100 m, and 120 m. It also shows that images acquired at 60 m and 80 m flying heights can produce data products with relatively small differences in GSD. The same can be observed for images acquired at 100 m and 120 m flying heights.

Shown in Figs. 5, 6, 7, and 8 are example outputs of the first run of DSM and orthomosaic generation procedures. By disabling DSM interpolation and orthomosaic hole-filling, the outputs clearly show where and how much the information can be provided by the data products and can be useable for tree crown delineation and other purposes. The location of missing data/information is also obvious in the resulting DSM maps which can inform the user of the limitations of the data products.

The DSM and orthomosaics derived using images acquired at percentage overlap greater than or equal to 80% have a higher percentage of completeness (Fig. 9b). The completeness ranges from 69.96% (60 m FH, 80% overlap) to 98.89% (120 m FH, 90% overlap). Images acquired at 60 m flying height and 60% overlap has the least percentage completeness at 23.76%. It can also be observed that there is a considerable increase in percentage completeness of products as the flying height increases (e.g., specifically for those images acquired at 60% and 70% image overlaps). However, the same cannot be stated for images acquired at 90% image overlaps. As far as the flight plan parameters considered in this study are concerned, it appears that a higher percentage of completeness was guaranteed with 90% image overlap regardless of the flying height. Nonetheless, 100% completeness was not achieved.

These results imply that the UAS data products generated through the SfM-MVS workflow will have missing data which needs to be interpolated or hole-filled to generate seamless DSMs and orthomosaics. Images acquired at 60% overlaps are the most prone to produce data products with the most missing data (i.e., less than 50%, especially if the flying height is set from 60 to 100 m above ground. The most practical configuration is to choose at least 100 m flying height with at least 80% overlap to ensure more than 90% data completeness.

Table 5 Summary of GSD and data completeness

Flight plan No.	Flying height above ground (m)	Side and front overlaps (%)	DSM and orthomosaic ground sample distance, cm/pixel	Total number of pixels within the study area	Number of pixels with data only	Data completeness (%)
FP1	60	60	2.97	71,792,673	17,061,197	23.76
FP2	60	70	2.92	74,199,747	29,902,491	40.30
FP3	60	80	2.90	75,416,957	52,762,278	69.96
FP4	60	90	2.65	90,429,036	85,790,169	94.87
FP5	80	60	3.96	40,411,847	12,143,596	30.05
FP6	80	70	3.87	42,409,467	28,151,289	66.38
FP7	80	80	3.74	45,516,418	40,896,168	89.85
FP8	80	90	3.53	50,850,023	49,287,430	96.93
FP9	100	60	5.00	25,402,882	8,799,226	34.64
FP10	100	70	5.16	23,863,651	15,252,614	63.92
FP11	100	80	4.87	18,905,354	18,001,667	95.22
FP12	100	90	4.56	30,540,923	30,119,157	98.62
FP13	120	60	6.04	17,406,415	9,518,051	54.68
FP14	120	70	5.97	17,820,712	14,749,939	82.77
FP15	120	80	5.79	18,905,353	18,000,177	95.21
FP16	120	90	5.60	20,237,898	20,013,634	98.89

3.3 Delineated Tree Crowns

Figures 10, 11, and 12 show some of the results of the tree crown delineations using multiresolution segmentation. Tree crowns delineations in DSMs generated using UAS images acquired at the highest-flying height (120 m), and image overlaps of 80% and 90% gained the highest overall accuracy of 43.35% (Table 6). A 31.18% accuracy was obtained for delineations performed in a DSM generated using images acquired at 100 m flying height and 90% image overlaps. On the other hand, accuracies were lowest for delineations in DSMs generated using images acquired at 60 m flying height and irrespective of percentage image overlaps, with omission errors ranging from 60.46% to as high as 97.34%. It is also evident that missed crowns are most dominant for this flight plan configuration, which would suggest that such configuration shall be avoided as far as the generation of DSM for crown delineation purposes is concerned. Low accuracies were obtained for 60 and 80 m altitudes regardless of the percentage overlap, primarily due to missed and merged tree crowns. Moreover, no missed tree crowns in DSMs generated using images acquired at 100 m and 120 m flying height with at least 80% overlap. This would indicate that these DSMs are useful for tree crown delineation—it is only that the

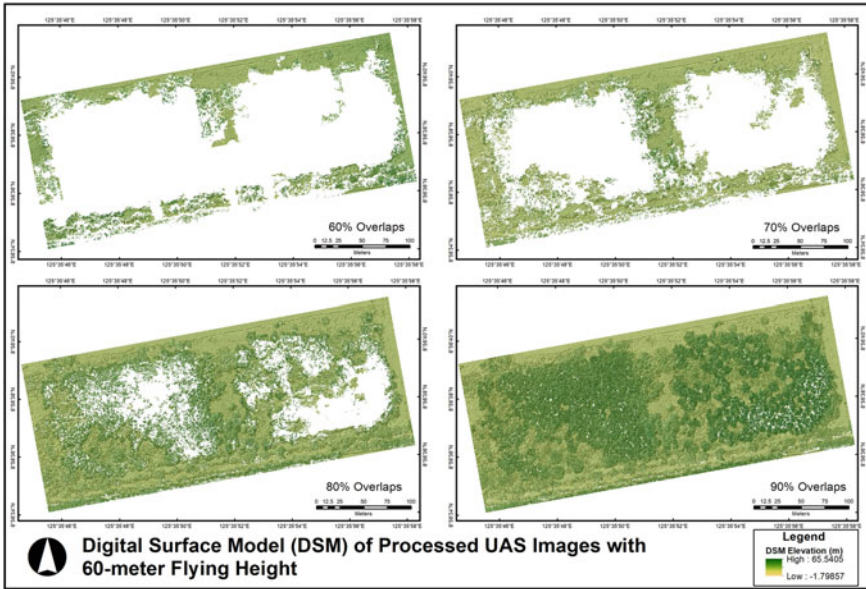


Fig. 5 Digital Surface Models (DSMs) generated from UAS images acquired at a flying height of 60 m above ground (interpolation disabled). White areas indicate missing data

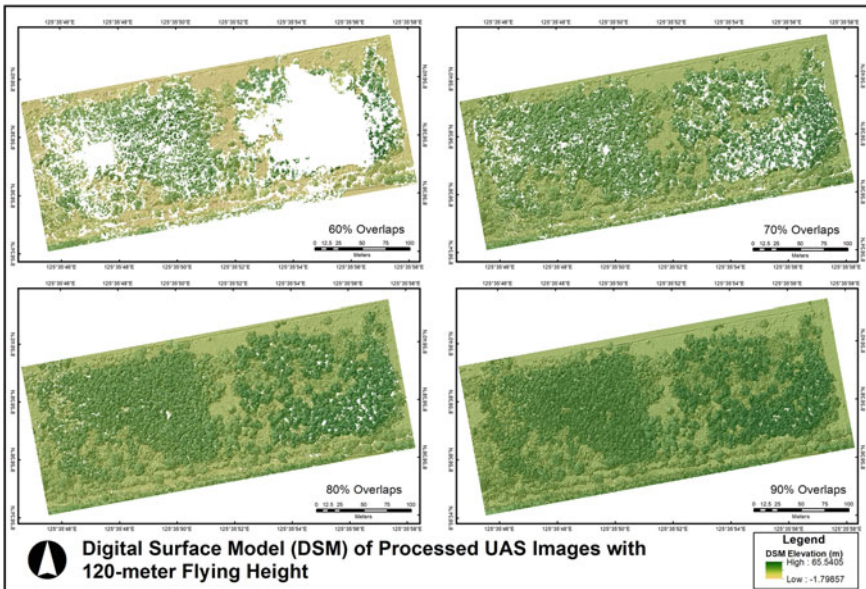


Fig. 6 Digital Surface Models (DSMs) generated from UAS images acquired at a flying height of 120 m above ground (interpolation disabled). White areas indicate missing data

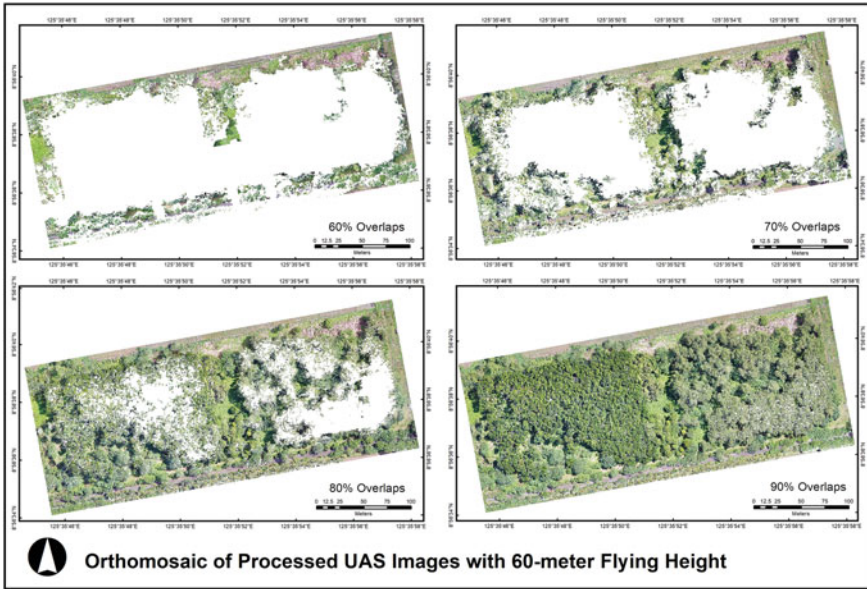


Fig. 7 Orthomosaics generated from UAS images acquired at a flying height of 60 m above ground (hole-filling disabled). White areas indicate missing data

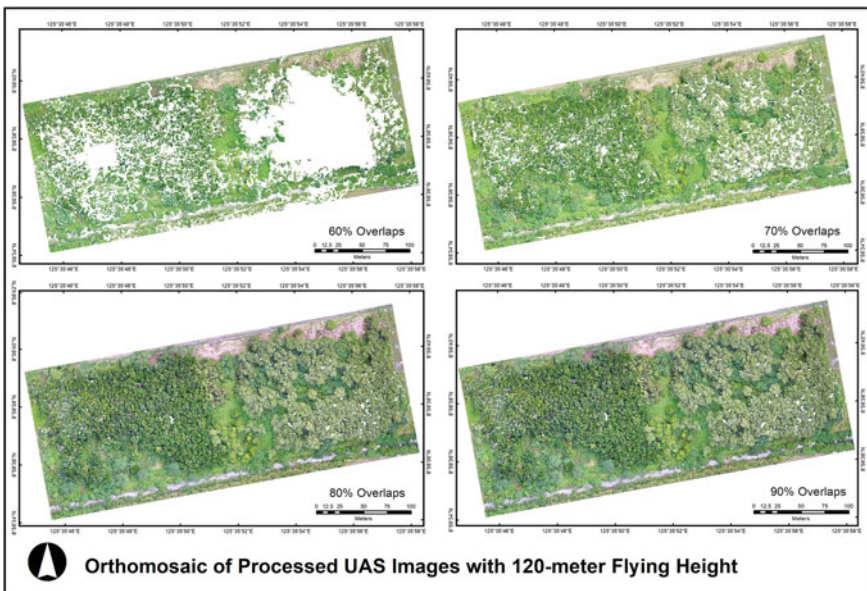


Fig. 8 Orthomosaics generated from UAS images acquired at a flying height of 120 m above ground (hole-filling disabled). White areas indicate missing data

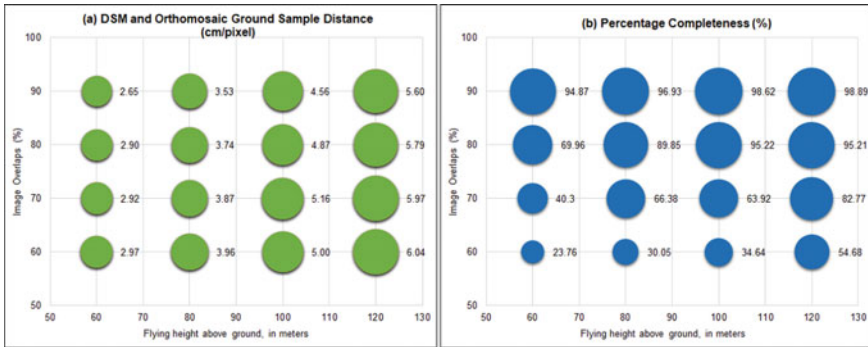


Fig. 9 GSD and completeness of the generated UAS data products

selected multiresolution segmentation parameters may not be optimal for accurate delineations. Tree crown delineations using DSMs generated at 120 m flying heights performed better in matched and nearly matched tree crowns. The accuracy values increased as percentage overlaps rose from 70 to 90%. This result conforms to that of [11] where they were able to generally maximize the accuracy of tree detection and the resulting treemaps by collecting images at higher flying height (120 m) with at least 90% overlaps.

Several factors may have contributed to the low accuracies of the tree crown delineation. A significant contributor would be the completeness of the DSM used in the delineations. It was obvious that DSMs with lower percentage completeness obtained the lowest accuracies. Increasing the percentage completeness tends to increase the accuracy, as supported by a positive Pearson’s correlation coefficient (r) of 0.66 (Table 7). However, the flying height above ground and DSM GSD have the more direct linear relationships with tree crown delineation accuracy, with r values of 0.76 and 0.68, respectively. This would indicate that generating a DSM using images acquired at higher flying height (higher GSD) would provide better accuracy.

The relationship between accuracy and image overlaps is not as strong as the previously mentioned variables. Camera location errors are inversely proportional to crown delineation accuracy, but the relationship between the two is weak. From these results, the most suitable configuration is to choose at least 120 m flying height with at least 80% overlap to ensure better accuracy in tree crown delineations.

On the methodology side, the crown delineation approach adopted in the study may have also impacted the accuracy of the delineations. Optimization of the multiresolution segmentation parameters would significantly improve the accuracy of the delineations, particularly for DSMs generated using images acquired at flying heights of 100 m or higher with at least 90% overlap.

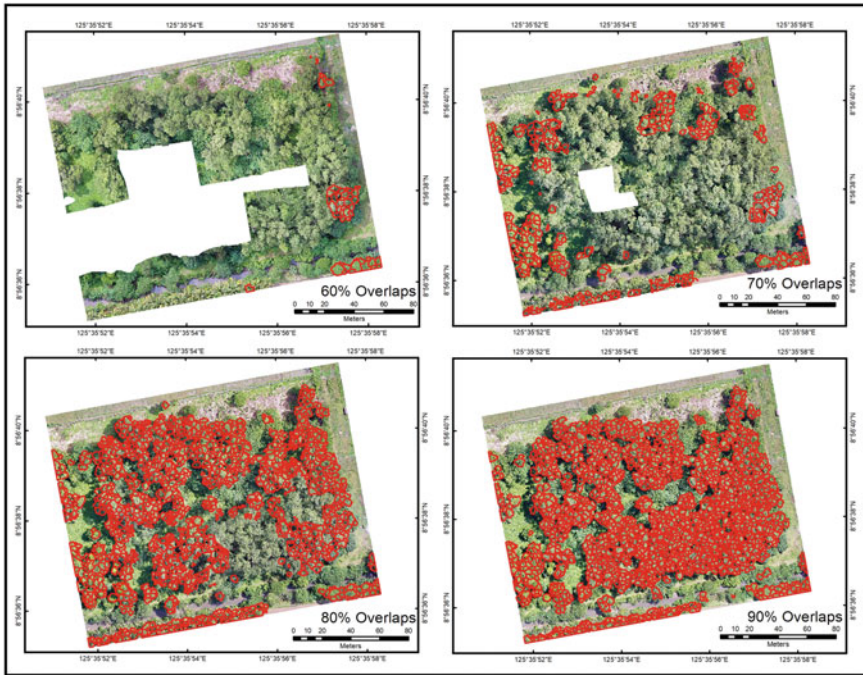


Fig. 10 Tree crowns delineated through multiresolution segmentation of a DSM derived using UAS images acquired at a flying height of 60 m above ground (hole-filling enabled). White areas indicate missing data

4 Summary and Conclusions

In this study, the effects of various combinations of two flight planning parameters, namely flying height above ground and percentage overlaps, on the quality of low-cost UAS photogrammetry data products, and their degree of usability for tree crown delineation in a Mangium plantation forest in the Philippines, were analyzed. UAS images were acquired using a Mavic 2 Pro UAS at four flying heights (60, 80, 100, and 120 m above ground) and four forward overlap and sidelap percentages (60, 70, 80 and 90% set for each flying height) were subjected to SfM-MVS processing to generate DSMs and orthomosaics. The quality of the products was evaluated based on their completeness and the accuracy of tree crown delineations. Significant results showed that the percentage of completeness of the DSM and orthomosaic increases as the altitude and percentage overlap both increases. More than 90% completeness was achieved for 90% overlap regardless of the flying height, with minor differences between them. A slightly similar value was achieved for 100 and 120 m altitude with 80% overlap. In terms of tree crown delineation, the highest overall accuracy of 43.35% was achieved for delineations performed in DSMs generated from images acquired at a flying height of 120 m and percentage overlaps of 80 and 90%.

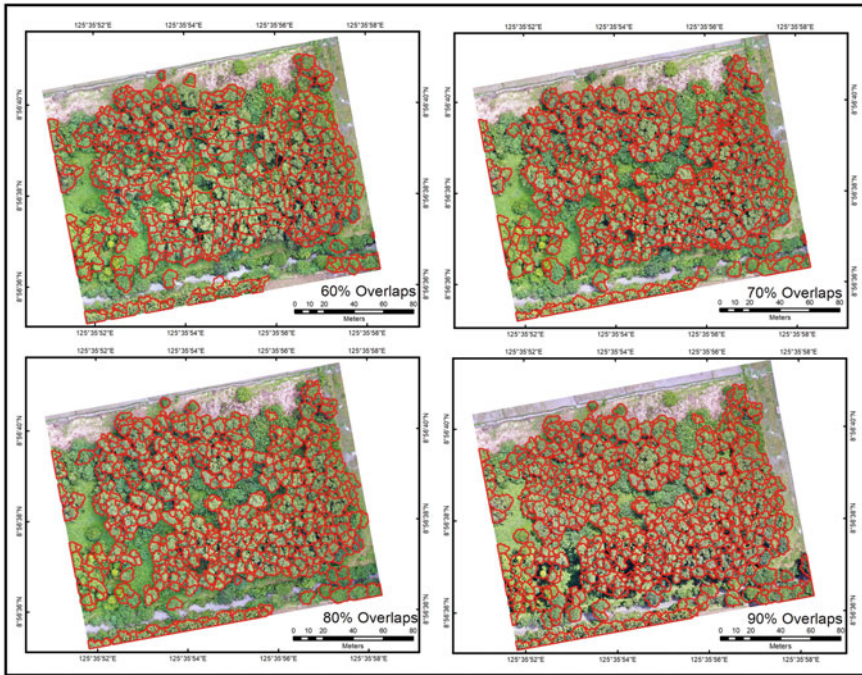


Fig. 11 Tree crowns delineated through multiresolution segmentation of DSM-derived UAS images acquired at a flying height of 120 m above ground (hole-filling enabled)

While obtaining a 43.35% highest overall accuracy in tree crown delineation is not impressive, the results reveal that better accuracy can be obtained from DSMs with higher percentage completeness. Specifically, those that were generated using images acquired at 120 m with a minimum percentage overlap of 80%.

The study's main conclusion is that at least 120 m flying height and at least 80% overlap must be aimed when acquiring images. It will ensure higher completeness of the UAS data products and help obtain more accurate tree crown delineations for Mangium plantation forests. While the study area is small and the tree crown delineation approach and analysis are simplistic, this study has attempted to provide a means to unify flight parameters when acquiring UAS images to generate products to estimate Mangium plantation forest attributes. It also contributed to the continued understanding of the influence of flight planning on UAS data quality which is essential to consider when minimizing costs and maximizing the potential of UAS for forestry applications. With the study results, it is hoped that low-cost UAS will become more attractive to support plantation management activities, particularly tree inventories, in the Philippines.

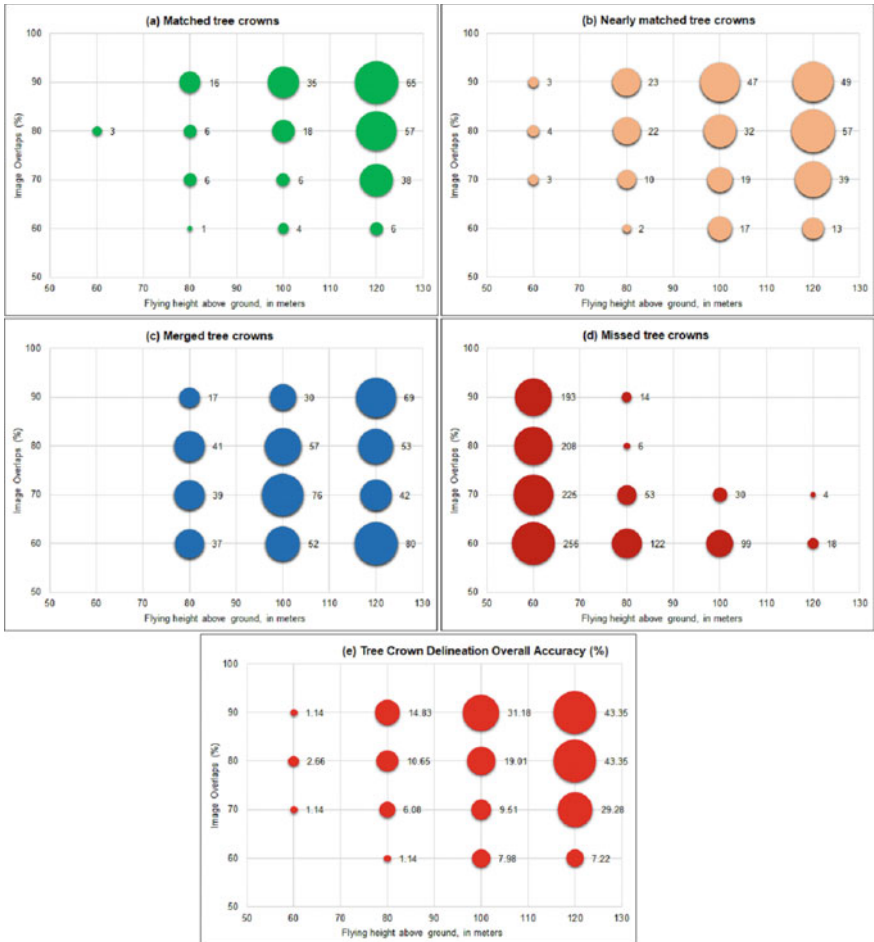


Fig. 12 Comparison of manually delineated and multiresolution segmentation-delineated tree crowns from DSMs generated at varying flying heights above ground and percentage overlaps

Table 6 Accuracy assessment results of tree crown delineations performed in DSMs generated using UAS images acquired at varying flying heights and percentage overlaps

Flight plan No.	Flying height above ground (m)	Side and front overlaps (%)	Matched	Nearly matched	Merged	Missed	Split	Total	Accuracy (%)	Omission error (%)	Commission error (%)
FP1	60	60	0	0	0	256	7	263	0.00	97.34	2.66
FP2	60	70	0	3	0	225	35	263	1.14	85.55	13.31
FP3	60	80	3	4	0	208	48	263	2.66	79.09	18.25
FP4	60	90	0	3	0	193	67	263	1.14	73.38	25.48
FP5	80	60	1	2	37	122	101	263	1.14	60.46	38.40
FP6	80	70	6	10	39	53	155	263	6.08	34.98	58.94
FP7	80	80	6	22	41	6	188	263	10.65	17.87	71.48
FP8	80	90	16	23	17	14	193	263	14.83	11.79	73.38
FP9	100	60	4	17	52	99	91	263	7.98	57.41	34.60
FP10	100	70	6	19	76	30	132	263	9.51	40.30	50.19
FP11	100	80	18	32	57	0	156	263	19.01	21.67	59.32
FP12	100	90	35	47	30	0	151	263	31.18	11.41	57.41
FP13	120	60	6	13	80	18	146	263	7.22	37.26	55.51
FP14	120	70	38	39	42	4	140	263	29.28	17.49	53.23
FP15	120	80	57	57	53	0	96	263	43.35	20.91	35.74
FP16	120	90	65	49	69	0	80	263	43.35	26.24	30.42

Table 7 Pearson's correlation coefficients (r) between tree crown delineation accuracy, flight plan parameters, and image processing results

Variable	Pearson's r		
	Accuracy	Omission error	Commission error
Flying height above ground (m)	0.76	-0.71	0.42
Side and front overlaps (%)	0.49	-0.44	0.24
Camera location X error (m)	-0.18	0.04	0.06
Camera location Y error (m)	-0.10	0.07	-0.02
Camera location Z error (m)	-0.32	0.30	-0.19
Camera location XY error (m)	-0.18	0.05	0.06
Camera location Total error (m)	-0.27	0.14	0.01
DSM GSD (cm/pixel)	0.68	-0.63	0.38
DSM completeness (%)	0.66	-0.72	0.51

Acknowledgements This work is an output of “Project 1. Development of a Geodatabase of Industrial Tree Plantations (ITP) in Caraga Region Using Remote Sensing and GIS” under the Accelerated R&D Program for Capacity Building of Research and Development Institutions and Industrial Competitiveness: Niche Centers in the Regions for R&D (NICER) Program: Industrial Tree Plantations Research and Innovation Center (ITPS) for Upgrading the Wood-Based Industry, funded and supported by the Department of Science and Technology (DOST)—Philippines and the Philippine Council for Agriculture, Aquatic and Natural Resources Research and Development (PCAARRD). We also acknowledge the CCGeo Batch 2020 On-the-Job Trainees from the BS Geodetic Engineering Program of Caraga State University for their assistance during the field surveys.

References

1. Tang L, Shao G (2015) Drone remote sensing for forestry research and practices. *J For Res* 26:791–797
2. Tinkham WT, Swayze NC (2021) Influence of Agisoft metashape parameters on UAS structure from motion individual tree detection from canopy height models. *Forests* 12(2):250
3. Salami E, Gallardo A, Skorobogatov G, Barrado C (2019) On-the-fly olive tree counting using a UAS and cloud services. *Remote Sens* 11(3):316
4. Gu J, Grybas H, Congalton RG (2020) Individual tree crown delineation from UAS imagery based on region growing and growth space considerations. *Remote Sens* 12(15):2363

5. Kameyama S, Sugiura K (2021) Effects of differences in structure from motion software on image processing of unmanned aerial vehicle photography and estimation of crown area and tree height in forests. *Remote Sens* 13(4):626
6. Domingo D, Ørka HO, Næsset E, Kachamba D, Gobakken T (2019) Effects of UAV image resolution, camera type, and image overlap on the accuracy of biomass predictions in a tropical woodland. *Remote Sens* 11(8):948
7. Lamping JE, Zald HS, Madurapperuma BD, Graham J (2021) Comparison of low-cost commercial unpiloted digital aerial photogrammetry to airborne laser scanning across multiple forest types in California, USA. *Remote Sens* 13(4292)
8. DJI (2022) Mavic 2, DJI. <https://www.dji.com/mavic-2/info>. Accessed 6 June 2020.
9. Iglhaut J, Cabo C, Puliti S, Piermattei L, Rosette J (2019) Structure from motion photogrammetry in forestry: a review. *Curr For Reports* 5(3):155–168
10. Fraser BT, Congalton RG (2018) Issues in unmanned aerial systems (UAS) data collection of complex forest environments. *Remote Sens* 10(6):908
11. Young DJ, Koontz MJ, Weeks J (2022) Optimizing aerial imagery collection and processing parameters for drone-based individual tree mapping in structurally complex conifer forests. *Methods Ecol Evol* 13(7):1447–1463
12. Bossoukpe M, Faye E, Ndiaye O, Diatta S, Diatta O, Diouf AA, Dendoncker M, Assouma MH, Taugourdeau S (2021) Low-cost drones help measure tree characteristics in the Sahelian savanna. *J Arid Environ* 187:104449
13. Harris RC, Kennedy LM, Pingel TJ, Thomas VA (2022) Assessment of canopy health with drone-based orthoimagery in a southern appalachian red spruce forest. *Remote Sens* 14(6):1341
14. Balanay RM, Reyes SG, Bongolan RL, Cutao JM, Casinginan RC, Omboy AV (2022) Assessing timber trade middlemen for development policy actions: a case study in the Caraga region, Philippines. *Human Soc Sci Commun* 9(185)
15. Agisoft LLC (2019) Agisoft Metashape User Manual: Professional Edition, Version 1.5. Agisoft LLC. https://www.agisoft.com/pdf/metashape-pro_1_5_en.pdf. Accessed 3 June 2020
16. Trimble Inc. (2019) Trimble eCognition suite user guide eCognition developer: basic rule set editing. https://docs.ecognition.com/v9.5.0/eCognition_documentation/User%20Guide%20Developer/4%20Basic%20Rule%20Set%20Editing.htm. Accessed 7 Dec 2020
17. Singh M, Evans D, Tan BS, Nin CS (2015) Mapping and characterizing selected canopy tree species at the Angkor world heritage site in Cambodia using aerial data. *PLoS ONE* 10(4):e0121558
18. Yilmaz V, Serifoglu Yilmaz C, Tasci L, Gungor O (2017) Determination of tree crown diameters with the segmentation of a UAS-based canopy height model. *Trans Internet Res* 13(2): 63–67
19. Jing L, Hu B, Noland T, Li J (2012) An individual tree crown delineation method based on multi-scale segmentation of imagery. *ISPRS J Photogramm Remote Sens* 70:88–98

The Segmentation of Drone Image derived 3D Point Cloud Using a Combination of RANSAC, DBSCAN and Clustering Methods



Puyam S. Singh, Iainehborlang M. Nongsiej, and Valarie Marboh

Abstract The 3D Point cloud derived especially from drone-derived images is highly unstructured, redundant and has varied density. These point clouds need to be segmented and classified into different groups representing similar characteristics in the scene presented which is a challenging task especially when the 3D scene contains a mix of varied man-made or unstructured natural scenes such as vegetation etc. Successful operation of such technology will lead to a wide variety of remote sensing, computer vision and robotics applications. In this paper, we have used a hybrid approach for effective segmentation of the point cloud. The combination of RANSAC, DBSCAN and Euclidean method of Cluster Extraction proved to be useful for precise segmentation and classification of the point cloud.

Keywords 3D point cloud · Segmentation · Clustering, DBSCAN, RANSAC

1 Introduction

Point clouds represent our world objects in a three-dimensional space. Each of these points has X, Y and Z coordinates. The drone imaging system could be deployed to rapidly collect the images and use them to generate the point clouds by the process of feature detection and matching the images. The processes such as Structure-from-Motion, Multi-View-Stereo and dense matching can use these highly overlapped images and generate a high-quality dense 3D point cloud. We used these techniques to get dense point clouds from the drone images collected by us. As compared to 3D point clouds captured by laser-based scanners such as LiDAR, the image-based derived point clouds such as this, have point clouds which are highly unstructured with no fixed scan positions as these images are taken from different locations and

P. S. Singh (✉)

Department of Space, Government of India, North Eastern Space Applications Centre,
Umiam 793 103, India

e-mail: ss.puyam@nesac.gov.in

I. M. Nongsiej · V. Marboh

Department of Computer Science, St. Anthony's College, Shillong 793 001, India

© The Author(s), under exclusive license to Springer Nature Switzerland AG 2023

K. Jain et al. (eds.), *Proceedings of UASG 2021: Wings 4 Sustainability*,

Lecture Notes in Civil Engineering 304,

https://doi.org/10.1007/978-3-031-19309-5_19

viewpoints. The 3D point clouds captured have lots of redundant points which need to be decimated for better analysis of speed and with less memory consumption. Further, every 3D point has limited attributes with no classification information making segmentation a challenging task.

Accurate segmentation and classification of these point clouds will benefit many applications from general geospatial analysis to sophisticated vision-based applications such as robotics. There are many segmentation techniques for point cloud segmentation but the majority of the methods focus on laser scanned derived point clouds. The limited available methods work on the common basis of grouping the point clouds with similar structures representing the objects in the scene. These types of segmentation lack semantic information as no prior knowledge is applied in the process. On the other hand, the newer methods with deep learning based require huge 3D point datasets and are compute intensive. The hybrid approach by leveraging a combination of known methods of RANSAC, DBSCAN and Euclidean-based cluster extraction in an inter-dependent way does give good results. These model fitting methods work well to accurately detect shapes and segment the point clouds although the output does suffer when the 3D points are noisy with outliers, oclusions and more complex scenes with mixed objects.

2 Materials and Methods

The Zenmuse X3-FC350 camera with a focal length of 4 mm having an effective resolution of 12.4 megapixels fitted on T600 DJI inspire series drone was used to capture about 120 images giving a maximum image size of 4000×3000 . We ensured at least 75% image overlapping. This helped us in getting repeated robust feature points in each image pair and matching these feature key points to generate a denser point cloud (Figs. 1 and 2).

For our experimentation, we took a subset of data stored in a LAZ file format having 7,38,583 points with X, Y, Z and R, G, and B attributes. The derived point cloud data having a mix of both the artificial building structure and vegetation structure is noisy, sparse, and unorganized. The sampling density of points is also uneven due to the varying nature of linear and angular rates of the scanner during data

Fig. 1 Dense point cloud generated

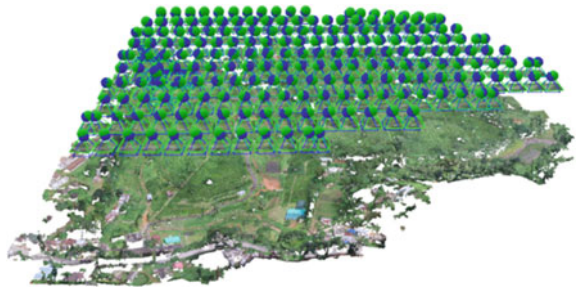


Fig. 2 Point cloud with different surface features



acquisition. In addition, the surface shape is arbitrary with sharp features with no statistical distribution pattern in the data. These problems present a difficult challenge when designing a segmentation algorithm. The use of deep learning methods such as semantic segmentation involves the usage of highly sized datasets. To overcome all these, a classical hybrid method of segmentation is used for our image-derived point cloud to obtain a more precise output for all the object instances present in the point cloud. The combination of model-based fitting algorithms such as RANSAC and clustering was adopted for the hierarchical grouping of these points and labels. This technique is robust to outliers and noise present in the data [1]. RANSAC is good for picking up a group of points having geometric primitives such as lines and circles present in the scene but fails to group other unstructured point clouds representing the trees and irregular structure [2–5]. Therefore, combining these two approaches can effectively segment all kinds of surface structures present within the point cloud.

The process of segmentation starts by initially applying the RANSAC algorithm with a planar model and segmenting all the points that lie on the homogenous plane. We then subtract the first output of RANSAC and the rest of the dataset is fed to a separate DBSCAN clustering algorithm. DBSCAN is good for clustering and grouping point with variable point cloud density [6]. This method proved to be more effective for 3D points with a higher altitude (Z) value relative to all other remaining points in the cloud but within each cluster of similar density. The DBSCAN-based segmented point clouds are further fine-tuned by applying the Euclidean Cluster Extraction algorithm in the third and final step. A brief diagram of the methodology is shown in Fig. 3.

3 Results and Discussions

3.1 Segmentation Using RANSAC

To obtain a planar model of our point cloud, we used RANSAC [7] which is a plane fitting method, that detects planes in point cloud data robustly. This method was considered in our approach because of its capability to segment all planar points present in the input 3D point cloud. All such segmented cloud is labelled as ‘ground’

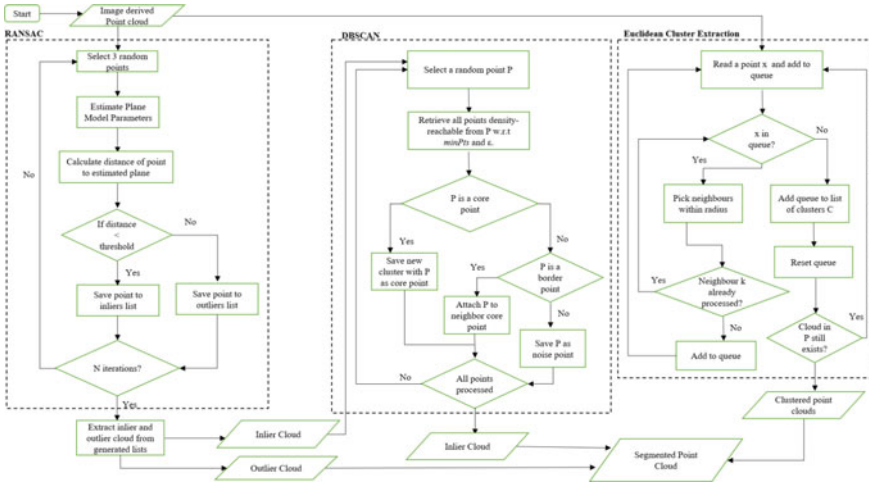


Fig. 3 A multi-hierarchical 3D point cloud segmentation

since only points with a relatively lower altitude (Z) value are considered as points representing the ground. Further, it filters out all non-ground points which can then be used as input into DBSCAN. Therefore, the outliers that RANSAC detects become the input points for DBSCAN. This way, the RANSAC method finds the largest set of points that fit a plane. RANSAC randomly selects three points from the data and calculates the parameters of the corresponding plane, after that tries to enlarge the plane according to a given distance threshold [8]. Any deviation in the point cloud from the defined threshold distance is treated as outliers. The plane is having a maximum number of inliers stored and segmented from the rest of the cloud. The process is repeated many times. The plane equation for our point cloud data can be defined as:

$$-0.02x + -0.00y + 1.00z + -816.03 = 0, \text{ (the distance threshold} = 1.1) \quad (1)$$

The resultant segmentation produces a point cloud of 402,563 points, containing the inliers i.e., those points that lie on the same ground plane. As evident from Fig. 4, we observed the efficacy of RANSAC, where all the planar points present in our point cloud, that are lying on the same plane are being segmented. This process proves to be effective when segmenting the grounded points which may or may not contain vegetation. However other structures such as buildings and bridges are not included in the segment. Further, the output depicts the efficiency of RANSAC whereby non-ground points such as rivers or water streams, trees and buildings are segmented out. Additionally, some patches of vegetation, whereby points do not lie on the same plane are also segmented out. An advantage of RANSAC is its ability to do a robust estimation of the model parameters, i.e., it can estimate the parameters with a high



Fig. 4 Planar ground points segmentation (right) from source point cloud (left) using RANSAC

degree of accuracy even when a significant number of outliers are present in the point cloud.

The building structures and water stream are segmented out with good precision. The RANSAC in conjunction with the planar model considers only neighbouring points which have a similar Z value in the X, Y, and Z coordinates of the point cloud. In other words, it leaves out all those points which have a relatively higher value for the Z coordinate.

3.2 Segmentation Using DBSCAN

For points that had a higher Z-value compared to other points on the plane in our point cloud data, the next step would be to segment them and obtain clusters, while keeping the planar points intact. For this process, we incorporated the Density-Based Spatial Clustering of Applications with noise (DBSCAN) algorithm [9]. The DBSCAN method needs at least two parameters: The minimum number of points *minPts*, and the searching radius ϵ . For our point cloud, we set $\epsilon = 1.9$ and *minPts* = 500 to get a more favourable output of clusters. This implies that only those points which are within a 1.9 unit distance in the cloud are considered. Also, for points to be considered as a cluster, there must be at least 500 points in that cluster. Most patches of vegetation and trees were accurately clustered in our result, although building and roof structures were not in different clusters. The overall number of clusters that were generated was 30 and most of them clustered with relatively fewer points than some clusters.

As depicted in Fig. 5, the noise points include most points that exhibit the object characteristics of trees, shrubs and some patches of vegetation. Also detected as noise, is a roof building structure and some cultivation area present in our point cloud. Therefore, segmenting these clusters is necessary and is undertaken by the next method presented in our approach, i.e., the Euclidean Cluster Extraction. The DBSCAN method proved to be a satisfactory approach to the segmentation of our point cloud data. With this algorithm, it is easy to detect clusters surrounded by different clusters. It is also robust towards outlier detection. However, it is sensitive to the clustering parameters, being ϵ and *minPts*. For our image-derived point cloud, the results of using DBSCAN are more accurate since the point cloud is dense since

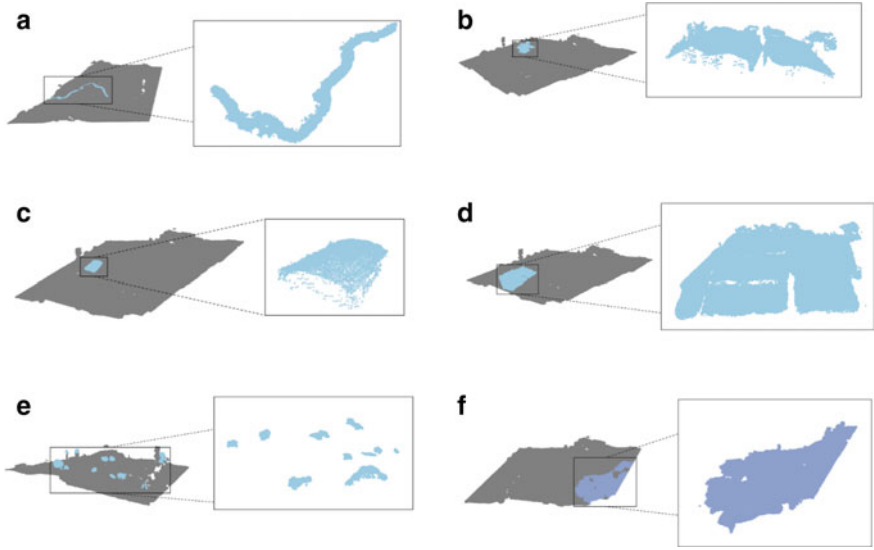


Fig. 5 Detected clusters. **a** Water stream cluster (23,153 points), **b** Building structures cluster (17,955 points), **c** Roof structure cluster (6,667 points), **d** Cultivated area cluster (46,725 points), **e** Trees/other vegetation clusters (13,925 points), **f** High slope cluster (117,651 points)

DBSCAN does not work well with sparse datasets. Additionally, since DBSCAN is more applied to satellite and UAV imagery, it is reasonable and more suitable to apply the algorithm on our point cloud derived from UAV images.

3.3 *Euclidean Cluster Extraction*

The final step in our approach aims to find clusters which were not already detected by DBSCAN as different clusters themselves. With the Euclidean Cluster Extraction method, we can detect and segment individual object point clusters by finding the nearest neighbours of a point in our data [10, 11]. To get more numbers as well as meaningful clusters, we set the distance threshold = 0.02 i.e., 2 cm and we obtained more than 20 clusters. However, only two clusters were finally considered to be included in our segmentation. These are depicted in Fig. 6a, b.



Fig. 6 **a** Roof structure cluster, **b** Roof structure cluster

These sets of clusters were earlier detected as noise by the DBSCAN method. However, by using Euclidean Cluster Extraction, the segmentation process is further accurate in segmenting the points that represent these object characteristics that are present in our point cloud. The cluster depicted in Fig. 6a consists of 5,507 points which represent a roof structure. However, some points exhibiting tree characteristics were also included along with the structure. The cluster depicted in Fig. 6b consists of 1,799 points representing a roof structure. When we incorporated all the detected clusters, we obtained our final segmented point cloud which is depicted in Fig. 7. The method yielded satisfying results of clustering roof building structures which were not earlier detected by previous methods. However, it generates other clusters which may not prove to be useful, thus the resulting clusters must be manually selected for usage and segmentation. This method is very fast to build and is useful for situations where either a volumetric representation of the occupied space is needed. Although Euclidean Cluster Extraction is more widely used for processing point clouds obtained using LiDAR scanners, it still proves to be as useful for our image-derived point cloud because our point cloud is just as dense as a LiDAR point cloud (Table 1).

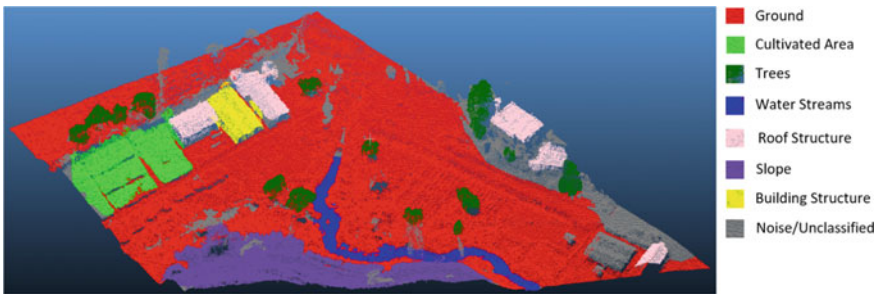


Fig. 7 Segmented point cloud

Table 1 Table captions should be placed above the tables

Segment	Number of 3D points
Ground	402,563
Building structure	17,955
Cultivated area	46,725
Trees	13,925
Slope	117,651
Roof structure	13,973
Water streams	23,153
Noise/Unclassified	85,178

3.4 Clustering Measure Assessment

To further analyse the generated clusters, evaluation of how well the clustering has performed can be quantified. Ideal clustering is characterised by minimal intra-cluster distance and maximal inter-cluster distance. There are majorly two types of measures to assess the clustering performance:

- (i) *Extrinsic Measures*: These require ground truth labels. Examples are Fowlkes-Mallows scores, Homogeneity, Completeness and V-measure.
- (ii) *Intrinsic Measures*: These do not require ground truth labels. Some of the clustering performance measures are Silhouette Coefficient, Calinski-Harabasz Index, Davies-Bouldin Index etc.

Since no ground truth labels are available for our point cloud data, the Davies Bouldwin (DB) Index serves as a good measure as it does not require ground truth labels and can be used to evaluate the efficacy of the clusters [12]. This index signifies the average similarity between clusters, where the similarity is a measure that compares the distance between clusters with the size of the clusters themselves. Zero is the lowest possible score. Values closer to zero indicate a better partition.

The index is defined as the average similarity between each cluster C_i for $i = 1, \dots, k$ and its most similar one C_j . In the context of this index, the similarity is defined as a measure R_{ij} that trades off:

- s_i , the average distance between each point of cluster i and the centroid of that cluster—also known as cluster diameter.
- d_{ij} , the distance between cluster centroids i and j .

A simple choice to construct R_{ij} so that it is nonnegative and symmetric is:

$$R_{ij} = \frac{s_i + s_j}{d_{ij}} \quad (2)$$

Then the Davies-Bouldin index is defined as:

$$DB = \frac{1}{k} \sum_{i=1}^k \max_{i \neq j} R_{ij} \quad (3)$$

DB Index values were calculated to primarily determine the optimal value of the eps (ϵ) of DBSCAN. First, the entire point cloud was processed using DBSCAN along with eps values ranging from 1.2 to 2.2. Any lower values resulted in 0 number of clusters and higher values resulted in higher DB Index values, both of which, are not ideal. This is depicted in Table 2.

Although the minimal value of the DB Index calculated is 1.14 however, the number of clusters generated is not sufficient. With a 1.9 eps value, however, the optimal number of clusters is achieved with a relatively minimal score for the DB Index. Table 2 is further represented as a graph in Fig. 8.

Table 2 DBSCAN on the entire point cloud

eps	DB index	Number of clusters
1.2	1.14	2
1.3	1.85	27
1.4	1.89	73
1.5	1.99	59
1.6	2.2	42
1.7	2.18	40
1.8	2.32	40
1.9	1.83	33
2.0	1.92	26
2.1	2.57	24
2.2	3.71	21

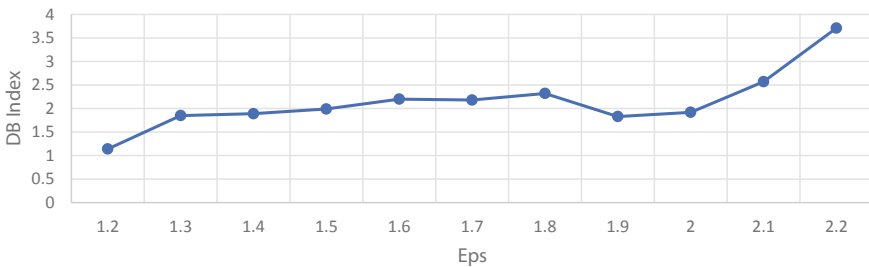


Fig. 8 Davies Bouldwin index for eps values of DBSCAN on entire point cloud

Second, the DB Index score was calculated to precisely determine the optimal eps value and number of clusters generated by DBSCAN on the outlier point cloud of RANSAC. In other words, only those points that were not segmented by RANSAC as the ground points were considered as input to DBSCAN. Table 3 presents a listing of the eps values and their corresponding DB indexes that were calculated.

In both cases, we observed that the eps value is identical since both produce an optimal number of clusters and a relatively lower DB Index. However, the difference lies in their DB indices whereby, DBSCAN applied only on the point cloud that RANSAC detected as outliers, has a lower DB Index than that of DBSCAN on the entire cloud. This indicates a better performance of the former in terms of efficient clustering than the latter. The table is further represented as a graph in Fig. 9.

Finally, the performance of the entire process of RANSAC, DBSCAN and Euclidean Cluster Evaluation was evaluated in terms of the DB Index, several clusters and its execution time and is compared with DBSCAN(only) used on the entire point cloud, which is depicted in Table 4. Our approach offers better performance in terms of unsupervised clustering and processing of the point cloud data than DBSCAN alone.

Table 3 DBSCAN on outlier point cloud of RANSAC

eps	DB index	Number of clusters
1.2	1.07	2
1.3	2.69	12
1.4	1.9	36
1.5	1.81	43
1.6	1.84	36
1.7	1.76	38
1.8	1.86	34
1.9	1.47	30
2.0	1.61	29
2.1	1.72	28
2.2	3.31	27

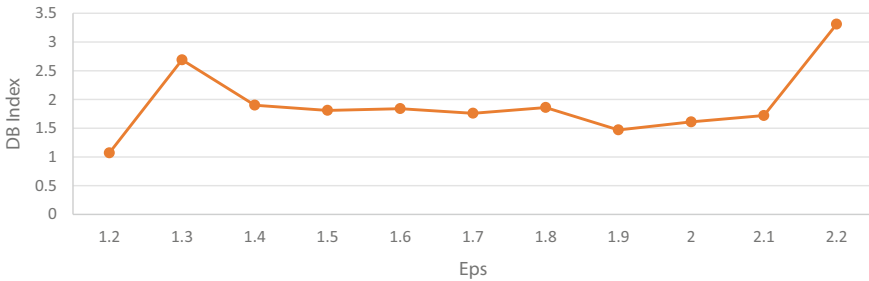


Fig. 9 Davies Bouldwin index for eps values of DBSCAN on outlier point cloud of RANSAC

Table 4 Comparison table of DBSCAN and our approach

Detail	DBSCAN (only)	RANSAC + DBSCAN + Euclidean cluster extraction
Davies bouldwin index	1.83	1.76
Execution time (s)	189.210074	34.245472
Number of clusters	33	32

The smaller the Davies-Bouldwin Index value, the better the clustering as it implies that the clusters are well separated, i.e., the distance between the cluster means is large. However, one drawback is that a good value reported by this method does not always imply the best information retrieval. But with no ground truth labels for unsupervised clustering, it is a powerful metric and is still widely used for measuring the accuracy of the clustering process.

4 Conclusions

The clustering algorithm such as DBSCAN is still widely used for finding meaningful clusters from satellite imagery. Our approach uses a purely mathematical model and geometric reasoning techniques such as RANSAC and DBSCAN, to segment our point cloud data. This approach allows fast running time and achieves good results in a simple scenario. The limitations of this approach are while determining which segment represents which object, sensitive to noise, and not working well in complex scenes with highly unstructured features. The reason is due to noise, uneven density, and occlusions in point cloud data leading to difficulty in finding and fitting complicated geometric primitives to objects. Although machine learning techniques give better results, they are usually slow and rely on the result of the feature extraction process.

This study, therefore, presents a segmentation task for point clouds using a combination of a geometric-based method and clustering to obtain more specific segments present in the point cloud. Our approach to segmentation of point clouds is simple yet effective and the combination of different methods yields different segments that are present in our point cloud. Although some methods such as the DBSCAN produces small clusters that are just blobs of vegetation, the overall segmentation procedure is still applicable and useful. Euclidean Cluster Extraction yielded satisfying results of clustering grassy terrains and roof building structures which were not earlier detected by previous algorithms.

References

1. Han X, Jin JS, Wang M, Jiang W, Gao L, Xiao L (2017) A review of algorithms for filtering the 3D point cloud. *Signal Process Image Commun* 57:103–112
2. Xie Y, Tian J, Zhu XX (2019) A review of point cloud semantic segmentation. *ArXiv*, abs/1908.08854
3. Nguyen A, Le HB (2013) 3D point cloud segmentation: a survey. In: 2013 6th IEEE conference on robotics, automation and mechatronics (RAM), pp 225–230
4. Besl PJ, Jain RC (1988) Segmentation through variable-order surface fitting. *IEEE Trans Pattern Anal Mach Intell* 10:167–192
5. Fischler MA, Bolles RC (1981) Random sample consensus: a paradigm for model fitting with applications to image analysis and automated cartography. *Commun ACM* 24:381–395
6. Filin S (2002) Surface clustering from airborne laser scanning data. *Int Arch Photogramm Remote Sens Spatial Inf Sci* 34:119–124
7. Kurban R, Skuka F, Bozpolat H (2015) Plane segmentation of kinect point clouds using RANSAC. *ICIT*
8. Tarsha-Kurdi F, Landes T, Grussenmeyer P (2008) Extended RANSAC algorithm for automatic detection of building roof planes from lidar data
9. Ester M, Kriegel H, Sander J, Xu X (1996) A density-based algorithm for discovering clusters in large spatial databases with noise. *KDD*
10. Rusu RB (2010) Semantic 3D object maps for everyday manipulation in human living environments. *KI - KünstlicheIntelligenz* 24:345–348

11. Schnabel R, Wahl R, Klein R. Efficient ransac for point-cloud shape detection. *Comput Graph Forum* 26:214–226
12. Davies DL, Bouldin DW (1979) A cluster separation measure. *IEEE Trans Pattern Anal Mach Intell.* PAMI-1 (2):224–227

An Automated Process to Filter UAS-Based Point Clouds



Volkan Yilmaz

Abstract Digital Terrain Models (DTMs), which represent the topography of the bare Earth surface, are widely used in many geomatics applications. In parallel to the emergence of sophisticated Unmanned Aerial Systems (UASs) in recent years, they are produced from point clouds generated through aerial images taken from digital imaging systems mounted on UASs. The first and most important step of DTM production is to remove the points of the above-ground objects such as trees, buildings, bridges, etc. A great variety of point cloud filtering strategies have been developed so far. However, due to the irregularities in the topography of the Earth's surface, all proposed approaches employ several user-defined parameters, which makes point cloud filtering dependent on the parameter values defined. Since complex topographies make it very hard to define some protocols to estimate the best parameter values, users usually have to try a large number of parameter values for optimal filtering performance, which is neither practical nor time-efficient. Hence, this study proposed to use the metaheuristic Whale Optimization Algorithm (WOA) to estimate the parameters of a simple morphology-based (SMRF) point cloud filtering algorithm to improve its performance, automating the filtering process. The performance of the proposed filtering methodology was compared not only against that of the standard SMRF algorithm but also against those of popular filtering algorithms Cloth Simulation Filtering (CSF) and Progressive TIN Densification (PTIN). The results showed that the proposed filtering methodology outperformed the PTIN and standard SMRF algorithms and presented a comparable performance with the CSF algorithm, which is one of the most robust point cloud filtering algorithms proposed to date. It can also be concluded that metaheuristic optimization algorithms can be used to automate the point cloud filtering process, minimizing the filtering errors caused by user intervention.

Keywords Digital terrain modelling · Point cloud filtering · Metaheuristic optimization

V. Yilmaz (✉)

Department of Geomatics Engineering, Karadeniz Technical University, 61080 Trabzon, Turkey
e-mail: volkanyilmaz.jdz@gmail.com

1 Introduction

The International Organization for Standardization (ISO) defines geomatics as the “discipline concerned with the collection, distribution, storage, analysis, processing, presentation of geographic data or geographic information” [1]. Geomatics experts survey certain parts (s) of the Earth and the obtained spatial data is used to produce maps or plans that are used in various engineering applications. Conventional surveying techniques have been used to gather accurate spatial data for decades. However, these techniques require a sufficient amount of budget and manpower, especially for large-scale terrains. Another means of surveying the surface of the Earth is by using aerial photos taken from digital cameras mounted on Unmanned Aerial Systems (UASs). The advanced UASs developed in recent years provide spatial data with 3D position accuracy comparable to terrestrial measurements. Using such systems in geomatics applications also saves time, cost, and manpower in many cases.

Producing 3D elevation models representing the topography of the surface of the Earth is one of the most common activities of geomatics experts. Two types of elevation models can be considered important in this regard, namely the Digital Surface Model (DSM) and Digital Terrain Model (DTM). A DSM comprises the elevation information of the ground surface together with the objects on it, whereas a DTM contains the elevation information of only the ground surface. Both of these elevation models can be produced through terrestrial measurement techniques. However, using UAS images for such a purpose enables the production of DSMs or DTMs with less cost in a shorter period.

DTMs can be used for a wide range of purposes, including the estimation of tree heights [2], disaster monitoring [3], archaeological interpretation of terrain anomalies [4], landslide monitoring [5], biomass estimation [6], individual tree detection [7], 3D highway modeling [8], crown diameter estimation in urban forests [9], 3D modeling of historical remains [10] and so on. The most important step of DTM production from UAS-based point clouds is point cloud filtering, which refers to the removal of the points of the above-ground objects such as trees, buildings, bridges, etc. This is not an easy task in many cases, which is why a large number of point cloud filtering strategies have been proposed so far. However, due to the irregularities in the topography of the Earth’s surface, all point cloud filtering approaches employ several user-defined parameters, which makes point cloud filtering dependent on the parameter values defined. As observed easily, the topography of the surface of the Earth is mostly complex, which makes it hard to define the most appropriate parameter values for optimal point cloud filtering performance. In such cases, the analysts have to try different parameter values to find the best filtering result [11], which is not practical and takes a long time [12]. Hence, an automated process is needed to minimize the filtering errors caused as a result of incorrect parameter definition. This study aims to automate a Simple Morphology-Based (SMRF) [13] point cloud filtering algorithm by estimating its parameters through the metaheuristic Whale Optimization Algorithm (WOA) [14].

2 Material and Methods

2.1 Test Site and Data Used

The proposed point cloud filtering methodology was applied in a test site located in the Fatih Egitim Faculty campus of Trabzon University, Trabzon, Turkey. The point cloud of the study area was produced from 261 aerial photos taken by a RICOH GR DIGITAL 4 (6 mm) digital camera mounted on a Gatewing \times 100 UAS. The aerial photos were acquired within a flight conducted at an altitude of 160 m along fifteen flight lines. Both the forward and sideways overlap was set to 80% during the flight. A point cloud with a point density of 9 points/m² was produced through the Structure from Motion (SfM) algorithm. The test site is shown in Fig. 1. The test site includes different complex-shaped buildings surrounded by trees, which can be seen in the figure.

2.2 Proposed Point Cloud Filtering Approach

The proposed approach automates the SMRF algorithm using the metaheuristic WOA algorithm. The SMRF algorithm is based on the application of successive morphological opening operations against a DSM. The SMRF algorithm divides the point cloud into grids. Then, the points with minimum elevation are used to generate an initial minimum surface. The SMRF algorithm uses five parameters as; c , which is the cell size of the gridded surface; s , which refers to the maximum slope of the ground surface; t , which specifies the height threshold that refers to the maximum vertical distance a point can be above the possible ground surface once the opening process is completed; e , which defines the elevation scaling factor that scales the elevation considering the slope of the possible DSM generated after all non-ground points on the minimum surface are identified; and w , which defines the size of the window that applies opening operation [13, 15].

The parameters of the SMRF algorithm were optimized with the WOA algorithm, which is a population-based optimization algorithm that simulates the hunting behavior of humpback whales [14]. Like many other population-based algorithms, the WOA algorithm starts with a set of random solutions for the problem at hand. These solutions are improved until a stopping criterion is achieved [16]. Let \vec{X}_b be the best candidate solution in the current iteration (i.e. generation), the WOA algorithm updates and improves the solutions by considering three rules [14, 17]:

- Encircling the prey

The position of a candidate solution $\vec{X}(t + 1)$ is updated as [14]:

$$\vec{D} = \left| \vec{C} \cdot \vec{X}_b - \vec{X}(t) \right| \quad (1)$$

Fig. 1 Test site



$$\vec{X}(t + 1) = \left| \vec{X}_b(t) - \vec{A} \cdot \vec{D} \right| \tag{2}$$

where, $p \in [0, 1]$. \vec{A} and \vec{C} are computed as;

$$\vec{A} = \left| 2\vec{a} \cdot \vec{r} - \vec{a} \right| \tag{3}$$

$$\vec{C} = \left| 2 \cdot \vec{r} \right| \tag{4}$$

where, \vec{r} is a random vector whose elements vary between 0 and 1; and \vec{a} linearly decreases from 2 to 0 [17].

- Spiral updating position

The position of a candidate solution $\vec{X}(t+1)$ is updated as [14]:

$$\vec{X}(t+1) = \vec{D}' \cdot e^{bl} \cdot \cos(2\pi l) + \vec{X}_b(t) \quad (5)$$

where, $\vec{D}' = |\vec{X}_b(t) - \vec{X}(t)|$ refers to the distance between the prey and i th prey, b is a constant defining the logarithmic spiral shape and l defines a random number between -1 and 1 [18].

- Search for prey

The position of a candidate solution $\vec{X}(t+1)$ is updated as [14, 18]:

$$\vec{D} = |\vec{C} \cdot \vec{X}_{rand} - \vec{X}| \quad (6)$$

$$\vec{X}(t+1) = \vec{X}_{rand} - \vec{A} \cdot \vec{D} \quad (7)$$

where, \vec{X}_{rand} is a random whale position vector [14, 18].

The WOA iterates until a stopping criterion is reached. This study used the Total Error (E_T) metric [19] to minimize the filtering errors within each iteration. In other words, the proposed methodology aimed to find the best parameter values that ensured the minimum E_T in each iteration. The total error metric was given in [12, 19, 20];

$$E_T = (E_O + E_C)/(P_G + P_{NG}) \quad (8)$$

where, E_O refers to the omission error that defines the number of misclassified reference ground points, E_C refers to the commission error that defines the number of misclassified reference non-ground points. P_G and P_{NG} denote the number of reference ground and non-ground points, respectively [12]. This study used a total of 10,000 reference points selected from the point cloud to find the optimal parameter values. Note that 5000 of them were for the ground points, whereas 5000 of them were for the non-ground points. All reference points were randomly selected through the polygons that were manually digitized over the orthophoto image of the test site. Table 1 shows the optimum parameter values that achieved the minimum E_T . The table also shows the upper and lower bounds defined for these parameters.

3 Results

The performance of the proposed filtering methodology was compared not only against that of the standard SMRF algorithm but also against those of popular filtering algorithms Cloth Simulation Filtering (CSF) [21] and Progressive TIN Densification

Table 1 Parameter values

Parameter	Lower bound	Upper bound	Optimum
c	0.1	3	2.9
s	0.05	0.3	0.05
t	0.25	2	1.9
e	0.05	2.5	2.4
w	2	48	16

Table 2 Computed metric values

Method	E_O	E_C	E_{T1}	E_{T2}	E_T
SMRF	125	1626	0.025	0.325	0.175
PTIN	891	330	0.178	0.066	0.122
CSF	526	214	0.105	0.043	0.074
Proposed	269	447	0.054	0.089	0.072

(PTIN) [22]. Table 2 provides the E_O , E_C , , Type I Error (E_{T1}), Type II Error (E_{T2}) and E_T values computed from the filtering results. Note that the E_{T1} is calculated by the ratio between the number of misclassified reference ground points and the number of all reference ground points; whereas the E_{T2} is computed as the ratio between the number of misclassified reference non-ground points and the number of all reference non-ground points [12, 19, 20]. The metric values given in Table 2 were computed using 10,000 reference points (5000 for ground and 5000 for non-ground features) that were different than those used to optimize the parameter values. Note also that the best values for each metric were shown in boldface in the table. As seen in Table 2, the point cloud obtained from the proposed method achieved the best E_T value of 0.072. The CSF result got the second best E_T value of 0.074. The SMRF result yielded the greatest E_T value of 0.175.

Figure 2 shows the original DSM and DTMs produced from the filtered point clouds. As seen in the figure, the SMRF algorithm kept a considerable amount of the non-ground points, which is justified by the metric values given in Table 2. As also seen in the figure, the proposed method and CSF algorithm presented a very similar performance as it is very hard to notice the difference between the DTMs produced from these methods.

4 Conclusion

The variations in the topography of the surface of the Earth make point cloud filtering a challenging task. In many cases, the analysts have to try different parameter values to get the best filtering performance from point cloud filtering algorithms, which is

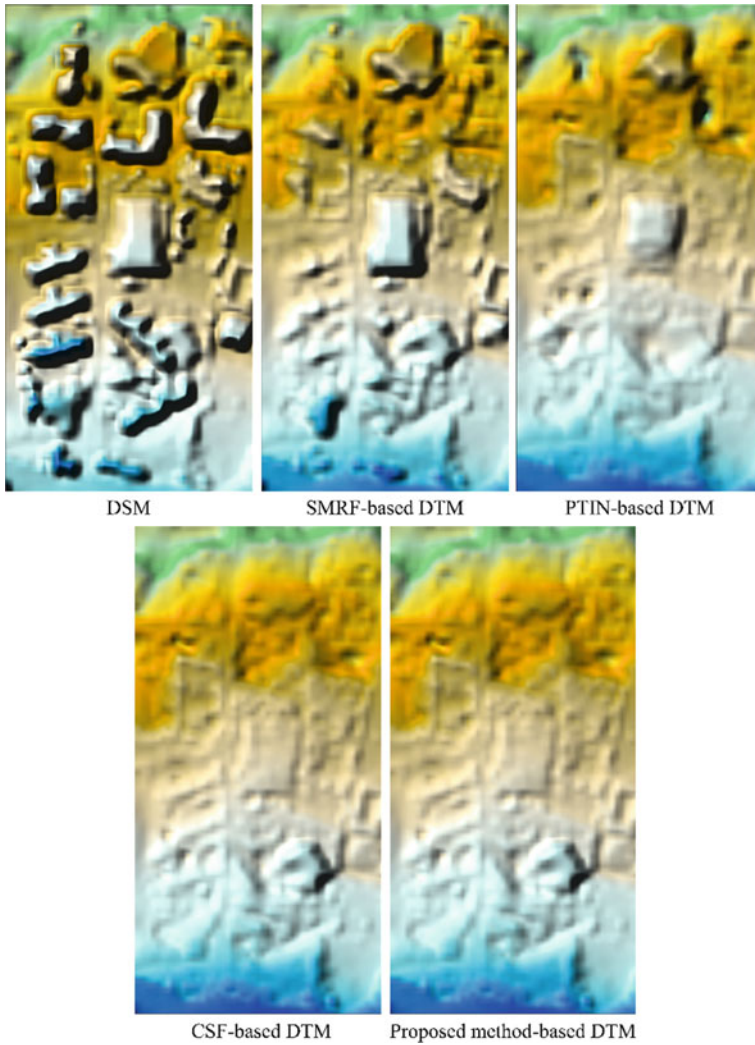


Fig. 2 Produced DTMs

another factor that makes the point cloud filtering process a challenging and time-consuming task. On the other hand, unsuitable parameter values lead to greater filtering errors. Hence, this study aimed to automate a morphology-based filtering algorithm SMRF through the use of a metaheuristic algorithm WOA to avoid user intervention to minimize user-related filtering errors. The proposed method was found to be successful in estimating the optimal parameter values to achieve the optimal filtering performance. It can also be concluded that the proposed method can be effectively used for UAS-based point clouds.

Acknowledgements I would like to thank the Department of Geomatics Engineering of Karadeniz Technical University for providing aerial photos of the test site.

References

1. International Organization for Standardization (ISO). <https://www.iso.org/obp/ui/#iso:std:iso:tr:19122:ed-1:v1:en>. Last Accessed 19 March 2021
2. Birdal AC, Avdan U, Türk T (2017) Estimating tree heights with images from an unmanned aerial vehicle. *Geomat Nat Haz Risk* 8(2):1144–1156
3. Chou TY, Yeh ML, Chen YC, Chen YH (2010) Disaster monitoring and management by the unmanned aerial vehicle technology. In: ISPRS TC VII symposium—100 years ISPRS, Vienna, Austria
4. Dubbini M, Curzio LI, Campedelli A (2016) Digital elevation models from unmanned aerial vehicle surveys for archaeological interpretation of terrain anomalies: case study of the Roman castrum of Burnum (Croatia). *J Archaeol Sci Rep* 8:121–134
5. Eker R, Aydın A, Hübl J (2018) Unmanned aerial vehicle (UAV)-based monitoring of a landslide: Gallenzerkogel landslide (Ybbs-Lower Austria) case study. *Environ Monit Assess* 190(1):28
6. Kachamba DJ, Ørka HO, Gobakken T, Eid T, Mwase W (2016) Biomass estimation using 3D data from unmanned aerial vehicle imagery in a tropical woodland. *Remote Sens* 8(11):968
7. Mohan M, Silva CA, Klauber G, Jat P, Catts G, Cardil A, Hudak AT, Dia M (2017) Individual tree detection from unmanned aerial vehicle (UAV) derived canopy height model in an open canopy mixed conifer forest. *Forests* 8(9):340
8. Iglesias L, Santos-Berbel D, Pascual V, Castro M (2019) Using small unmanned aerial vehicle in 3D modeling of highways with tree-covered roadsides to estimate sight distance. *Remote Sens* 11(22):2625
9. Yilmaz V, Güngör O (2019) Estimating crown diameters in urban forests with unmanned aerial system-based photogrammetric point clouds. *Int J Remote Sens* 40(2):468–505
10. Yücel MA, Şanlıyüksel Yücel D, Yalçiner CÇ, Yılmaz D (2018) 3D modelling of historical remains using unmanned aerial vehicle, a case study: Gallipoli Peninsula. In: XXVIII international symposium on modern technologies, education and professional practice in geodesy and related fields, pp.101–107, Sofia, Bulgaria
11. Serifoglu Yilmaz C, Yilmaz V, Güngör O (2018) Investigating the performances of commercial and non-commercial software for ground filtering of UAV-based point clouds. *Int J Remote Sens* 39(15–16):5016–5042
12. Yilmaz V (2021) Automated ground filtering of LiDAR and UAS point clouds with metaheuristics. *Opt Laser Technol* 138:106890
13. Pingel TJ, Clarke KC, McBride WA (2013) An improved simple morphological filter for the terrain classification of airborne LIDAR data. *ISPRS J Photogramm Remote Sens* 77:21–30
14. Mirjalili S, Lewis A (2016) The whale optimization algorithm. *Adv Eng Softw* 95:51–67
15. Graham A, Coops NC, Wilcox M, Plowright A (2019) Evaluation of ground surface models derived from unmanned aerial systems with digital aerial photogrammetry in a disturbed conifer forest. *Remote Sens* 11(1):84
16. Aljarah I, Faris H, Mirjalili S (2018) Optimizing connection weights in neural networks using the whale optimization algorithm. *Soft Comput* 22(1):1–15
17. Mostafa Bozorgi S, Yazdani S (2019) IWOA: An improved whale optimization algorithm for optimization problems. *J Comput Design Eng* 6(3):243–259
18. Gharehchopogh FS, Gholizadeh H (2019) A comprehensive survey: whale optimization algorithm and its applications. *Swarm Evol Comput* 48:1–24

19. Sithole G, Vosselman G (2004) Experimental comparison of filter algorithms for bare-Earth extraction from airborne laser scanning point clouds. *ISPRS J Photogramm Remote Sens* 59(1–2):85–101
20. Montealegre AL, Lamelas MT, De La Riva J (2015) A comparison of open-source LiDAR filtering algorithms in a Mediterranean forest environment. *IEEE J Select Topics Appl Earth Obs Remote Sens* 8(8):4072–4085
21. Zhang W, Qi J, Wan P, Wang H, Xie D, Wang X, Yan G (2016) An easy-to-use airborne LiDAR data filtering method based on cloth simulation. *Remote Sens* 8(6):501
22. Axelsson P (2000) DEM generation from laser scanner data using adaptive TIN models. *Int Archiv Photogramm Remote Sens* 33(4):110–117

Some Enhancement of Aerial and Terrestrial Photo for 3D Modeling of Texture-Less Object Surface



Catur Aries Rokhmana and Hanif Muhammad Fauzi

Abstract Today, the combination of Aerial and Terrestrial photos has been more implemented for 3D modelling purposes. This 3D modelling technique getting popular because it is supporting with photogrammetry structure from motion algorithm (SFM). The SFM algorithm makes automation in the processing step. One of the main problems that will occur in the automation of 3D modelling objects with the SFM algorithm is whether objects have texture-less surfaces. The purpose of this research is to evaluate some enhancement processes that were applied before running the SFM algorithm for 3D modelling. Some pre-processing enhancements are a combination Contrast-Limited Adaptive Histogram Equalization (CLAHE) from Fiji-ImageJ and JPEG to RAW Ai artefact algorithm from Topaz Labs. Two sample objects are tested which are a heritage object that has a texture-less wall surface object and a paddy field that has a similar object pattern. Some aerial and terrestrial photos have been enhanced before processing in 3D modelling. The result shows that applying preprocessing enhancement can improve the completeness of the object, especially in texture-less wall surface area. Pre-processing enhancement improves the geometric accuracy and number of vertex and surfaces also. In the future, the combination of the Jpeg to Raw Ai and the CLAHE enhancement should be explored for the best 3D model solution.

Keywords 3D modeling · Texture-less objects · JPD to RAW enhancement · CLAHE

1 Background

In the last 5 years, the platform technology for visualizing a 3D virtual reality or digital twin world has increased. As a consequence, the demand for a 3D model of the object has also increased. Many 3D modelling instrumentations have already on

C. A. Rokhmana (✉) · H. M. Fauzi
Department of Geodetic Engineering, Gadjah Mada University, Yogyakarta, Indonesia
e-mail: caris@ugm.ac.id

© The Author(s), under exclusive license to Springer Nature Switzerland AG 2023
K. Jain et al. (eds.), *Proceedings of UASG 2021: Wings 4 Sustainability*,
Lecture Notes in Civil Engineering 304,
https://doi.org/10.1007/978-3-031-19309-5_21

289

the market and it is smaller and more portable. In general, there are two popular technologies for doing 3D modelling which is based on an optical camera (passive sensor) with structure from motion-photogrammetry and lidar scanning (active sensor). This paper is focused on utilizing a camera sensor for 3D modelling. Some dominant factors are working with the camera for the automatic 3D modelling, such as (1) lens quality; (2) pixel spatial resolution; (3) base/high ratio; (4) ground control accuracy; and (5) object condition or texture. Only the object condition and image quality factors that dealt with in this paper.

This study has chosen “Panggung Krapyak” a heritage object [1] and the Paddy field area. The object represents two challenging conditions, which are (1) the object is large; and (2) it has a dominantly similar pattern or texture-less wall skin. Due to the large size of the object, so the combination of the aerial photograph and terrestrial photograph should be implemented in this case study. Today, the combination of aerial and terrestrial photos has been more implemented for 3D modelling purposes. Meanwhile, the texture-less object skin will make it difficult for doing automation in processing. Working with scale-invariant feature transform (SIFT) in the alignment process will provide difficulties if the object texture is homogeneous. This texture-less object skin makes potentially reduce accuracy and reduce the number of the right point matching result. The purpose of pre-processing image enhancement is to improve photo orientation accuracy and minimize errors in dense matching using an algorithm such as scale-invariant feature transform (SIFT) during processing alignment [2].

Working with an optical technique for 3D modelling has two main challenges due to its environments, which are (1) homogenous lighting direction issues, and (2) texture of the object skin issue. The purpose of this study is to evaluate and implement some image enhancement for reducing those two issues. Other’s problems that can occur in photo quality i.e., motion blur, noise sensor, jpeg artefacts, and depth of field errors [2] are not detailed and discussed in this paper. Several methods can be used for processing image enhancement. This paper utilizes (1) contrast limited adaptive histogram equalization (CLAHE) and (2) restore photo quality from jpeg format to raw format (Jpeg to Raw). Contrast limited adaptive histogram equalization (CLAHE) is an enhancement method for contrast value in certain areas of a photo [3]. Changing the photo format from jpeg to raw is a method for improving dynamic range, colour space, white balance, and image quality restoration [4]. This image enhancement process has been implemented before 3D modelling processing with the structure from motion (SFM) algorithm.

1.1 Conceptual Background

The Contrast Limited Adaptive Histogram Equalization (CLAHE) is one of the contrast enhancement techniques for an image. The Fiji-ImageJ software with CLAHE-Plugin is used as a script tool for implementing CLAHE [5]. This is a point operator that does not change the image geometry. It only deals with the digital

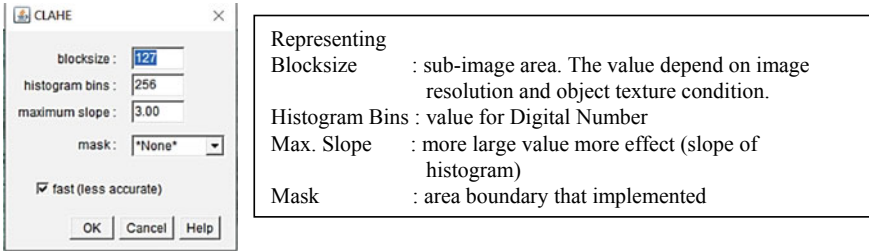


Fig. 1 Interface CLAHE operator in Fiji-ImageJ software

number value of the pixel. CLAHE is a derivative of the Adaptive Histogram Equalization (AHE) method in terms of restrictions contrast value. In the CLAHE method, an image will be divided into several processing areas called sub-image, tiles, or blocks. There are two main parameters in CLAHE processing, namely, block size (BS) and clip limit (CL). These two parameters control the quality improvement in the sub-image. The results of photo processing will have a higher brightness level when the clip limit value increases. The higher the clip limit value, the photo will have lower intensity and the histogram will be sloping. If the block size value becomes larger, the dynamic range becomes wider, and the contrast of the image increases [3]. CLAHE method is an application of the histogram equalization to the specified sub-image. The original image histogram will be cropped and distributed over each gray value of the pixel. The distribution of the histogram is different from the adaptive histogram equalization method because the intensity of each pixel has been limited based on the maximum value. However, the enhanced image and the original image have the same minimum and maximum gray values [3]. According to Fiji-ImageJ software, three parameters determine the result (see Fig. 1).

The JPEG to RAW operator is a method in image enhancement, which is to change the image quality due to the effect of image compression in JPEG format. The JPEG format has a smaller size in storage because it reduces the decrease in quality to speed up the photo processing. In general, the JPEG image has more visual artifact effect imagery. So, this JPEG to RAW operation will change or remove the artifact image geometry but not on the edge of the object in the image. This operator is implemented by Jpeg to RAW Ai Topaz Labs software [6]. The algorithm was used to improve the quality of the image format, namely Dejpeg-m-spline. The effect of this operator can be seen as removing artifacts in the image. So, the image will look more emphasize the features. According to Jpeg to Raw Ai Topaz-Labs. software, two dominant parameters control the result (see Fig. 2).

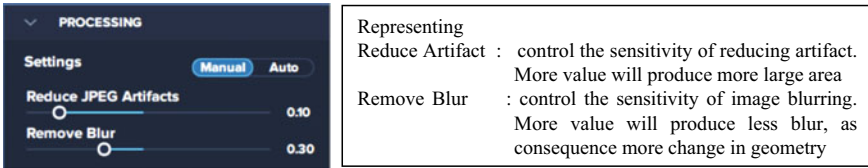


Fig. 2 Interface JPEG to RAW AI operator in Topaz Labs. software

2 Data and Methodology

The Panggung Krapyak Data. This research was conducted for the building called the “Panggung Krapyak” which is located in D. I. Yogyakarta (see Fig. 3). The “Panggung Krapyak” is a heritage building that has built in the Mataram Kingdom era that was built during the time of Sultan Hamengkubuwono I. The function of this building was for hunting and the place of defense of the Yogyakarta Palace from protecting enemies coming from the south. This building is located to the south of the “Keraton” and forms a straight line with the “Tugu” object. So, the “Panggung Krapyak” is part of the axis imaginary or philosophical axis of Yogyakarta (Balai Pelestarian Cagar Budaya DIY, 2019). The “panggung krapyak” is one of the buildings that can be used as a test because it has a cube model with a texture-less white color wall of the building.

Figure 4 shows the methodology for this case study. As a quality control, several ground control points have been used as independent checkpoints and some shape-dimensional measurements also. The control point has to measure by GNSS RTK (Realtime Kinematic) survey technology for 2 mm accuracy. While the dimensioning check has measured by tape with 2 mm accuracy also.

The aerial photo data acquisition has taken by the DJI drone platform Mavic Pro with an image size 12Mpix. The flight path design is done manually because there are many obstacles around the object. The shooting distance varies considerably between 5 to 10 m. This recording produces a GSD value of 1.6 cm to 3.3 cm.

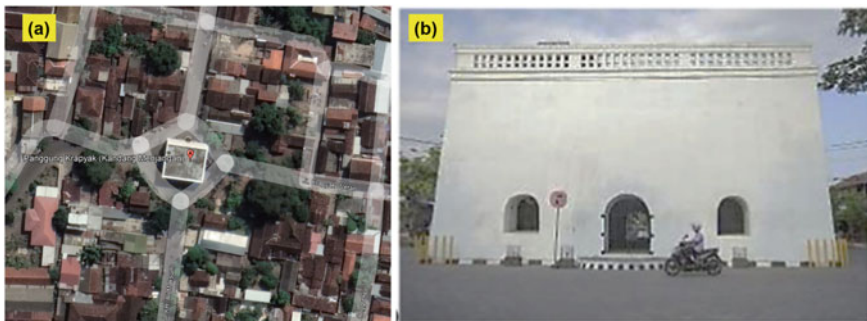


Fig. 3 Heritage object “Panggung Krapyak” a google maps and b photos

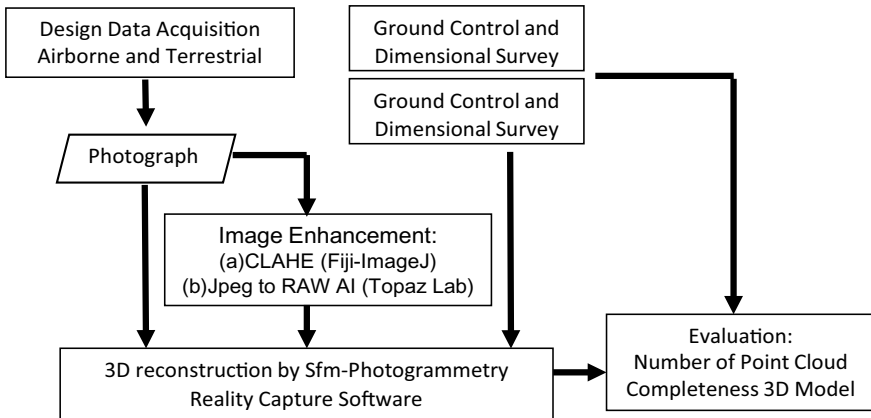


Fig. 4 Methodology in this study

The resulting overlap amount ranges from 80% up to 85%. The amount of side lap generated ranges from 70% up to 80%. Meanwhile, the terrestrial photo was also taken with the same camera as the aerial photo. Figure 5 shows the camera exposure position and ground control point, which is a combination of aerial and terrestrial positions.

The number of all photos used is 1409 which are 787 terrestrial and 622 elevated or aerial images. To get the same lighting condition and remove the shadow effect, the photo should be taken in a certain sun direction. The acquisition began at 2:42 p.m. to take a southern side. The acquisition began at 3:35 p.m. to take a western-eastern side. The acquisition started at 12:13 p.m. to take the top and surrounding area. This will reduce the shadow effect on each side of the building.

The Paddy Field Data. The research is located in the paddy fields of Desa Pendoworejo, Girimulyo District, Kulon Progo Regency, Special Region, Yogyakarta, Indonesia. There are 5 Ground Control Points (GCP) used with the placement of each point >200 m between the GCP point. All of the GCP have been

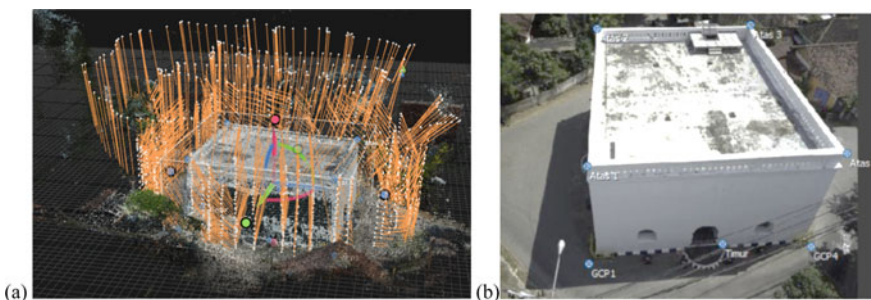


Fig. 5 a Camera exposure position and b GCP distribution



Fig. 6 Sample aerial photo of paddy field (a) Raw in JPG format (b) after CLAHE enhancement

surveyed with the GNSS Static Survey technique to achieve 5 mm positional accuracy. Aerial photo data was acquired using the DJI Mavic Pro UAV drone. The aerial photo data acquisition was carried out within 1 (one) day of implementation on March 20, 2021. The data acquisition in Pendoworejo Village used 1 flight path with an area of 18 hectares using 3 batteries in the measurement due to the relatively short battery life.








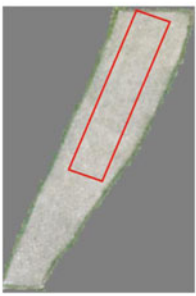

The acquisition of aerial photos has sidelap and overlap percentages respectively 60% and 80% with a flying height of 75 m and a flight speed of 6 m/s. The takeoff and landing location of the flight path is at the GCP 1 point which is north of Jl. Raya Kaligesing because the location is an open area and includes a shooting area, it is more efficient in terms of time and energy from the tool when taking off, landing, and aerial shooting. The aerial photo has a Ground Sampling Distance (GSD) of less than 3 cm (see Fig. 6). A bund or boundary in the paddy field after CLAHE image enhancement is easier to see. The Jpeg to Raw enhancement is not implemented in these aerial photos, because in general the aerial photo always has texture or heterogeneous objects.

3 Results and Discussion

3.1 The Visual Comparison

Table 1 shows some samples for visual comparison before and after the image enhancement process. The dominant differences can be seen in the wall and other texture-less objects. The CLAHE result looks more textured image which is good for SIFT point detection. Unfortunately, this CLAHE operator also emphasizes the noise or artifact in the original jpeg image. This can be a problem because the noise artifact is a random pattern and does not represent the original objects. Meanwhile,

Table 1 Visual comparison: original Jpeg, CLAHE, and Jpeg to Raw AI

Original JPEG	CLAHE	Jpeg to RAW AI
		
		<p data-bbox="753 601 871 624">Not Implemented</p>
		<p data-bbox="753 830 871 853">Not Implemented</p>
		<p data-bbox="753 1125 871 1148">Not Implemented</p>
<ul data-bbox="259 1301 479 1448" style="list-style-type: none"> • Some artifacts in the homogenous object do not represent the actual object's skin • Minim texture skin that makes it difficult for image matching • Edges between objects are not so clean 	<ul data-bbox="503 1301 686 1499" style="list-style-type: none"> • Some artifacts in the homogenous object more emphasized • More texture skin, but some of the texture is emphasized of an artifact also. So it does not represent the actual skin • Edges between objects are more emphasized 	<ul data-bbox="710 1301 918 1465" style="list-style-type: none"> • Some artifacts in homogenous objects are removed and look more clear and close to the actual object's skin • Less texture skin makes it difficult for image matching • The edge between the objects is cleaner

the Jpeg to Raw results makes the wall looks like a clean wall. This reduces the artifact noise in the original Jpeg image. Unfortunately, this operator makes the wall looks more texture-less, which is not good for future image matching process.

The best parameter setting for CLAHE and Jpeg to Raw AI can be concluded. This setting parameter is always a try-and-error process due to the variation in Sunlight direction and atmosphere condition. Some patterns can be concluded which are:

1. In CLAHE enhancement parameter setup: the smaller object size that should be detected in the image, then, the small number in block size should be set. In general, the block size number 50–100 is enough for all kind of photos that has a GSD of less than 5 cm.
2. The CLAHE enhancement also emphasizes the artifact noise. So, it is recommended not to use an image with as much artifact due to jpeg compression. Using Tiff image format that has a minor artifact effect would be better.
3. In Jpeg to Raw Ai enhancement parameter: the blurring parameter should be set between 0.7 and 0.9 for reducing the artifact, while at the same time getting a sharp edge of objects.
4. The combination of both enhancements should be the best choice. First, using the Jpeg to Raw Ai enhancement for removing the artifact effect in jpeg compression. Then, implement CLAHE enhancement to emphasize texture in the object's skin.

3.2 The 3D Reconstruction Results

The final 3D reconstruction has been processed three times which the same parameter setting. Each of the processing options uses different data inputs which are (1) original jpeg image; (2) CLAHE enhancement; and (3) Jpeg to Raw AI enhancement. The parameter for evaluating the 3D model quality can be classified in geometric aspect and semantic completeness of the object. Table 2 shows the comparison of the geometric aspect of the 3D reconstruction Results. The best empirical geometric accuracy can be shown from the dimensioning error and checkpoint error. The best geometric accuracy is data with CLAHE enhancement then followed by Jpeg to Raw AI enhancement. The improvement of geometric quality is more than 35% relative to the original result. This is because the enhancement process improves the texture and reduces the artifact also. The best image should be more texture and minimize artifact noise. The combination of booth enhancement can be used for that purpose. The Jpeg to Raw Ai enhancement can be used for removing artifact noise. Then, the CLAHE enhancement processing can be used to emphasize the texture objects. The CLAHE enhancement process can also improve the time processing in alignment adjustment by more than 35%.

Table 3 shows the comparison of the 3D model completeness. The Jpeg to Raw Ai enhancement gives the best for overall 3D model completeness. Then, followed by CLAHE enhancement, while the original Jpeg has failed 3D model in some texture-less surface. The CLAHE effect makes the photo over-textured and also enhanced

Table 2 Geometric comparison for Panggung Krapyak data: original Jpeg, CLAHE, and Jpeg to Raw AI

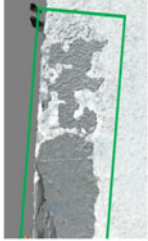




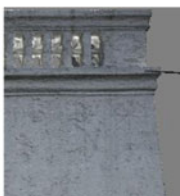
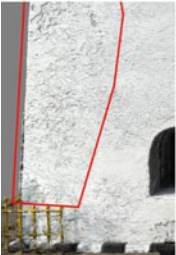


Parameter	Original JPEG	CLAHE	Jpeg to RAW AI
The bundle adjustment and dimension check			
Number of image-oriented/total image	1408/1409	1408/1409	1408/1409
Number of tie point	2.054.757	1.433.118	1.678.294
Max Residual Error (pix)	16.26	3.84	4.72
Mean Residual Error (pix)	0.89	0.64	0.66
Alignment time process	00:26:15	00:11:53	00:28:07
Dimensioning length error 8 Length objects	0.460 m	0.035 m	0.063 m
GCP checkpoint Ave. from 4 checkpoints	X: -0.372 m Y: -4.232 m Z: -16.536 m	X: 0.004 m Y: 0.001 m Z: 0.001 m	X: 0.006 m Y: 0.001 m Z: 0.002 m

the artifact noise. So that the artifact makes the model error in planar or texture-less skin. Meanwhile, the Jpeg to Raw Ai enhancement gives the best 3D model in planar or texture-less skin due to it can remove the artifact noise. The number of vertices represents the result from the dense point matching operation but does not always represent the completeness of the 3D model. This is because not all the point matching is representing the right point in the 3D model. Some of the points may be an error point matching. The CLAHE enhancement gives the densest point number. The CLAHE enhancement has a minor change in color from the original image. This makes the 3D model texture from the enhancement process darker than the original color. The overall 3D model completeness by implementing image enhancement has 30% more complete than its original picture. The processing time for building 3D has significantly reduced when using an image from Jpeg to Raw Ai enhancement. This is because the image from Jpeg to Raw Ai gives the less vertex number.

Table 4 shows the comparison of the distance test between points. It shows that CLAHE image enhancement can improve distance measurement accuracy. This shows the original photo data before pre-processing has an RMSE value of 386,911 mm, while data after pre-processing image enhancement using CLAHE has an RMSE value of 100,995 mm. There are some notes regarding the dimensioning test as follows:

1. Pre-processing with CLAHE image enhancement makes the boundary paddy field easier to identify the objects. This makes measurement more reliable.
2. This enhancement makes the edge object more reliable also. The CLAHE operator is a point operator that only changes the digital number. So, it does not change the object's geometry.




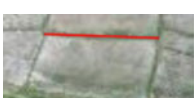
Table 3 The 3D model completeness comparison for Panggung Krapyak data: original Jpeg, CLAHE, and Jpeg to Raw Ai

Parameter	Original JPEG	CLAHE	Jpeg to RAW AI
The Completeness			
Number vertex points	22.421.846	22.978.198	22.222.719
Triangle mesh	44.728.214	45.840.430	44.351.390
Overall process	07:44:34	07:33:55	05:53:32
Samples image			
			
			

4 Conclusion

This paper shows the effect of the image enhancement process in the final 3D reconstruction model. There are two pre-processing for image enhancement which is (1) CLAHE, and (2) Jpeg to Raw Ai algorithm. Each enhancement gives a different result. The CLAHE enhancement is superior for emphasizing the texture-less object. Meanwhile, the Jpeg to Raw Ai enhancement fit for reducing the artifact noise due to the image compression effect. All of the image enhancement processes will be improving the geometric accuracy and the completeness of the 3D model. It also improves the processing time, even if it is not significant. Implementing the enhancement process will change a color that makes it darker than the original color. In the future, the combination of both enhancements should be explored. The enhancement process to make the image more texture but free from artifact noise also. So, the

Table 4 The distance test comparison for paddy field data: original Jpeg and CLAHE

Objects distance	Original JPEG	CLAHE	Field measurement
	11,700 mm	11,500 mm	11,440 mm
	12,100 mm	11,950 mm	11,900 mm
	10,600 mm	10,500 mm	10,460 mm
	17,800 mm	17,600 mm	17,650 mm
Average differences	386.911 mm	100.995 mm	

first process of implementing the Jpeg to Raw Ai enhancement is for removing the artifact noise. Then, the following implemented CLAHE enhancement to emphasize the texture object’s skin.

References

1. Anonim (2019) “Panggung Krapyak”, Direktorat Jendral Kebudayaan, Kementerian Pendidikan dan Kebudayaan, 30 Oktober. <https://kebudayaan.kemdikbud.go.id/bpcebyogyakarta/panggung-krapyak-bantul/>. Accessed 14 June 2020
2. Ballabeni A, Apollonio FI, Gaiani M, Remondino F (2015) Advances in image pre-processing to improve automated 3d reconstruction. *Int Arch Photogramm, Remote Sens Spat Inf Sci—ISPRS Arch* 40(5W4):315–323
3. Ma J, Fan X, Yang SX, Zhang X, Zhu X (2017) Contrast limited adaptive histogram equalization based fusion for underwater image enhancement. *March*, 1–27
4. Nguyen RMH, Brown MS (2018) RAW image reconstruction using a self-contained sRGB–JPEG image with small memory overhead. *Int J Comput Vision* 126(6):637–650
5. Zuiderveld K (1994) Contrast limited adaptive histogram equalization. Academic Press Professional Inc., *Graphics gems IV*, pp 474–485
6. TopazLabs (2020) JPEG to RAW AI. <https://topazlabs.com/jpeg-to-raw-ai/>. Diakses tanggal 10 Desember 2020

Role of Drone Technology in Sustainable Rural Development: Opportunities and Challenges



Venkata Ravibabu Mandla, Nagaveni Chokkavarapu,
and Veerendra Satya Sylesh Peddinti

Abstract Climate change and local weather conditions have caused several issues in the farming sector. The rapidly expanding global population is an issue that must be addressed to secure food and water supplies through the use of information technology in precision agriculture and smart farming. These technical advances in precision agriculture are represented by unmanned aerial vehicles (UAVs). UAVs or DRONES help in agriculture by counting the number of plants, visual inspection of the crop field, water management, erosion analysis, plant counting, soil moisture analysis, crop health assessment, irrigation scheduling, analyzing plant physiology, and yield forecasting. Drones can be used to facilitate development by reporting and collecting data in rural development in terms of agriculture land boundaries, water resources and their surface area, village boundaries, monitoring forest area, observation of hilly and tall plant regions, and soil condition in terms of water content, moisture, electrical conductivity, pH, and temperature. Repetitive collection of image and video data helps to analyze changes in rural development. Rural development aims to improve rural communities' physical infrastructure and basic services. Delay in detecting problems associated with rural development may further deteriorate soil and water resources making them more vulnerable. This paper focuses on various opportunities and challenges in sustainable rural development and the application of UAVs in almost every aspect of human life, allowing people to make significant advances in human life support.

V. R. Mandla (✉)

CGARD, National Institute of Rural Development and Panchayati Raj (NIRDPR), Rajendranagar,
Hyderabad, India

e-mail: mvravibabu.nird@gov.in

N. Chokkavarapu

Center for Environment, Jawaharlal Nehru Technological University, Hyderabad, Telangana, India

V. S. S. Peddinti

Department of Civil Engineering, National Institute of Technology (NIT) Warangal, Warangal,
Telangana, India

e-mail: pveerendrasatyasylesh@student.nitw.ac.in

© The Author(s), under exclusive license to Springer Nature Switzerland AG 2023

301

K. Jain et al. (eds.), *Proceedings of UASG 2021: Wings 4 Sustainability*,

Lecture Notes in Civil Engineering 304,

https://doi.org/10.1007/978-3-031-19309-5_22

Keywords Rural development · UAV · Drone · Agriculture · Water · Land · Sustainable development

1 Introduction

Unmanned Aerial Vehicles (UAVs), commonly known as drones, have been a game changer in the agriculture sector since 2011 because they are more inexpensive and easier to operate [1]. They fix vision issues caused by cloudy weather or inaccessibility to a tall crop area. In contrast to satellite and airborne cameras, they have a major advantage in terms of image resolution, avoid missing data due to clouds, can be operated at any time unlike satellites passing at a fixed time, have greater detail and lesser error, and to avoid repetitive flying drone data can be blended with satellite data to increase the accuracy of satellite data.

UAVs or DRONES help in agriculture by counting the number of plants, visual inspection of a crop field, water management, erosion analysis, plant counting, soil moisture analysis, crop health assessment [2], irrigation scheduling, and analyzing plant physiology, and yield forecasting. Drones use a variety of sensors depending on their intended use [3, 4]. Drones can be used to facilitate development by reporting and collecting data in rural development in terms of agriculture land boundaries [5], water resources and their surface area, village boundaries [6], monitoring forest area, observation of hilly and tall plant regions, soil condition [7] in terms of water content, moisture, electrical conductivity, pH, and temperature.

Drones are also commonly used for a variety of other uses, including surveillance, traffic monitoring and weather, fire suppression, irrigation, personal use, shooting, land surveying, and inspecting oil pipelines, power lines and other remote infrastructure [8]. By training unemployed youngsters, drone technology in rural may give complete growth and employment possibilities. This system and Artificial Intelligence can forecast future infrastructure possibilities. In agriculture, drone-attached sprayers may be used to spray insecticides and provide fertilizer as required. Crop insurance may be offered to farmers by determining the quantity and quality of seed per acre. Grain purchase and storage facilities can be established up to two to four weeks in advance. The grain name, as well as its quality and price, may be supplied to purchasers via the mobile application. Drones will contribute to the restoration of ecology and the sustainable environment by identifying open places for afforestation and planting on inaccessible locations using seed bombs. Detecting fires and spraying extinguishers decrease damage in the early stages of a fire. The movement of forest officials and animals in the surrounding areas can be followed, and food, water, and medications may be sent to locations where human transit is impossible.

Payload, cameras, trained personnel, experience with the software applications, environmental, wind and cloud, and price are all main impediments to drone use. However, continuous photographs aid in resource conservation and timely decision-making [9]. Employability can be generated based on pesticide and fertilizer spraying, reducing farmer illness and death. Lowering the dose of effective sprinkling

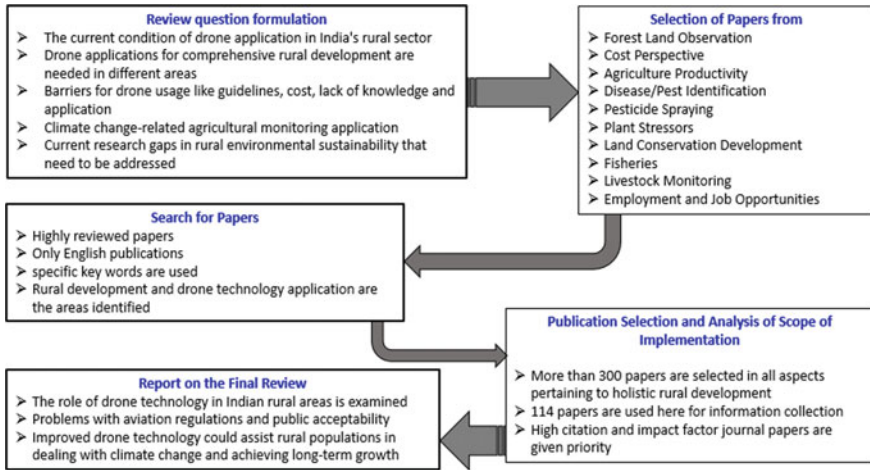


Fig. 1 Shows the current review process on literature collection for applications

technologies reduces the number of toxins left in the soil and plants that aren't being used. UAVs assess village sustainability by defining villages with adequate growth in terms of infrastructure and physical condition to increase villagers' quality of life. Furthermore, this mechanism aids resource distribution decision-making by locating villages in need of assistance in supplying municipal services, roads, and amenities in a priority-based manner. The process of review was done based on the details in Fig. 1 as the flowchart.

2 Applications for Forest Land Observation

Drones are used to carry seeds to places that are inaccessible to improve afforestation [10]. Forest tracking in the light of ecological balance by aerial maps helps to detect illegal logging/cutting for wood/commercial purposes and also in the context of the counting and illegal hunting and poaching of particularly endangered wildlife species [11]. Drones are found useful when observing large areas on the ground with tall and large canopy plants in forests. Thermal cameras mostly penetrate the canopy, and the rate of identification of poachers during the night was high due to the difference between the temperatures of the human body and the background [12]. The UAV speed should be high and the noise should be low so that hunters do not quickly flee from there and the response time is short. Choosing quieter propulsion systems or operating at higher altitudes would accomplish the requisite reduction, and higher altitudes would also cover a large strip of ground. Research is underway on the automatic classification of UAV images for wildlife monitoring [13]. Automatic object detection techniques [14] and thermal imagery [15] are now being used day

and night to observe the difference between animal and non-animal subjects. Other essential concerns are UAV policies, operating costs, and public discernment [16], amid increasing efforts [17] in this region.

3 Cost Effective

The spatial resolution of UAVs changes with flying height, thus it would be easy to correctly map small fields. Marginal farmers with holdings of less than one hectare own up to 67% of India's cropland [18]. The irrigated area maps generated from satellite images and the UAV map do not align [19]. To estimate the irrigation development, small field area mapping [20] and precise predictions are required.

Small farmers cannot bear the cost of drones [21] and one of the reasons that discourage them is a low literacy rate among them. Drones will help larger farms because each bit is constantly monitored and analyzed [22]. In this case, the manual cost of testing would be both costs efficient and time intensive. However, few studies suggest that there is no association between farm size [23] and the ability to adopt a drone [24]. Farmers should be trained in drone activity and encouraged to form community enterprises and their drones, as has traditionally been done with the farm equipment scheme. The creation of large-scale topographic maps for landscape and environmental management would allow for the provision of comprehensive and detailed information. Geotagging all of these assets would provide a clear picture of sustainable practice management [25].

A public-private partnership (PPP) strategy can be used to support agricultural drones for rural India's social and economic growth to integrate capacity, flexibility, performance, long-term vision, social interest and accountability. Soil data, hydrology and weather data can be provided by the government and commercial cloud services under this policy. This approach will help private sector investments and new entrepreneurs gain support and increase farmers' incomes agro-ecologically. Another potential use for community mapping is aimed at rural village boundary mapping along with agriculture land boundary mapping of owners [26].

4 Applications for Agriculture Productivity

UAV use in agriculture is a significant change in crop cycles and changes in response to climate change. Climate change is a change that is happening more in less time. UAVs help diagnose the effects on plants early and in a short time. Vegetation states like plant pigment concentration, and biomass can be evaluated [27] and quantified through different vegetation indices [28] from images acquired in the visible, red edge, and near-infrared spectral bands. Vegetation indices may be customized to specific applications, systems, and platforms, broadening the scope of the study. These new trends are readily applicable to UAV and drone platforms, which will

boost aerospace remote sensing shortly [29]. The Internet of Things and unmanned aerial vehicles (UAVs) have the potential to transform traditional agriculture into precision farming [30]. Ground-based soil sampling takes time and provides data only at the point of sample collection. Uniform nutrient distribution in the soil is impossible. Fertilizer application should be based on canopy density and health [31]. Such a method is known as variable application rate (VAR). Drone imagery can be used to produce VRA maps. These maps help to decrease soil pollution while reducing expenses [32].

5 Application for Disease/Pest Identification and Monitoring

Recent analysis indicates that this spectral evidence can be found in crops that are affected by floating pesticides, as well as in weeds that thrive in crops [33] and are resistant to herbicides. Disease-affected plant parts can be recognised with NDVI [34] using reflected infra-red light from green plants. Because of the significant shift in leaf reflectance behaviour, vegetation indices can identify morphological changes. UAV efficiency will be improved by creating digital archives of diseased images for public use [35]. In a few instances, pathogens travel in the form of spores through the wind from a diseased crop by a few kilometres or more distance. Drones may also detect diseases on a wider scale, allowing farmers to brace for the epidemic. Air sampling can help to detect pathogens in the air, making it possible to protect crops by taking precautions [36]. Traditional manual field surveys to detect pest infestations take a long time and require a lot of labour. Human detection errors are often found with these mechanisms. Drones and sensors, on the other hand, use reflected light energy and algorithms [37]. Detection of pest outbreaks is important to maintain crop health. Different infestations exhibit the same symptoms, making it difficult to determine the particular type of disease [38]. During pest outbreaks drones help to identify pest hotspots thus enabling us to use biological control organisms and pesticide spraying. Such an approach is multi-disciplinary where the integration of knowledge from engineers, ecologists and agronomists and software developers has the huge potential [39].

5.1 Pesticide Spraying

Crop spraying is much safer and more cost-effective by its autonomous and pre-programmed run on specific schedules and routes. Drones are also programmed to self-adjust their altitude and speed using ultrasonic echoing, TOF lasers and GNSS signals to achieve a uniform and optimum spraying results across varying topography. Usage of quadcopters because of their overall efficiency would minimize the number

of chemical pesticides and fertilizers to be applied in agricultural fields and also track the crop and yield [40]. When pesticide spraying is planned, a weather sensor device placed in the target region will assist the UAV in considering wind speed and direction [41]. This data is sent to the UAV to make the correct decision regarding the height and speed of the UAV. Wind speed and direction are taken into account to limit pollution load into the environment, cover all areas without leaving any patches, and avoid overlapping regions [42]. Due to limited battery support, cropping areas spread over a vast area cannot be covered by a single UAV [43]. In those cases, the area is split into small blocks based on the number of UAVs. Each UAV will be configured with a path planning algorithm [44].

Excessive use of chemical pesticides destroys soil composition because a vast amount of these pesticides drift outside the target area. According to [45], using 3 million metric tons of agrochemicals destroys 40% of the crops. Although terrestrial spraying is effective, it has the potential to cause cancer and neurological disorders. These issues have resulted in the use of unmanned aerial vehicles (UAVs) in precision agriculture [46] to monitor crops and spray pesticides. Future research developments include UAV connectivity with ground-based weather stations located in a specific region, as well as multi-UAVs with internet connectivity that are controlled by a single control system [47].

5.2 *Plant Stressors*

Plant stressors usually induce physiological changes in plants, thereby rendering their ability to do photosynthesis. Such changes in plant reflectance are detected by sensors in different spectral ranges. Remote sensing offers an easy and immediate solution for the identification of stress like drought [48], pathogens, nutritional deficiencies [49] and weeds [50]. Finding out water stress in plants with the help of a micro-hyperspectral green field imager and thermal camera [51] fixed to a UAV will provide complete details [52]. Management of plant water stress is important not only for the early detection of stress but also for the precise use of water [53] with the use of sprinklers and drip irrigation methods [54]. Soil moisture is regulated using the above-said methods would allow the fruit trees to attain good size and yield with improved quality parameters [55]. Farmers of Dahanu-Palghar tribal villages in Maharashtra, India have learned to use drones for organic farming, fish farming, crop rotation, bio-control, hydroponics, and bio-waste management, besides also using drone-based technologies on their orchards and farms. The use of different types of agricultural drones includes the creation of electronic maps of fields, operational monitoring of crop conditions [56] evaluation of germination, predicting crop yields [57], checking the quality of ploughing, and maintaining environmental monitoring of agricultural land, etc. [58].

6 Land Conservation Development

Both land conservation and land development programs should be designed to conserve natural resources and increase employment. It will also generate employment opportunities in the rural sector which may address social balance. Village modernization and urbanization should promote comprehensive land conservation measures and improve people's livelihoods [59]. Development authorities should ensure their efficiency by solving various issues which are arising from the beginning to the end of the project. Creative and critical thinking helps to derive the best possible sustainable solution to maintain the existing ecological balance with minimal disturbance to natural resources and biotic composition. The project must be constantly monitored and control measures are taken to achieve the desired result. Drones and UAVs can be used to make comprehensive reports in a short time, to easily understand the situation, and to make changes to tasks promptly. Completing the goal on time and completing it within the intended budget will save money and also make environmental balance possible [60]. Currently, the Maharashtra state government signed a partnership with the World Economic Forum (WEF) Centre for the Fourth Industrial Revolution exploring the use of drones to improve irrigation systems in the agricultural field by estimating soil conditions, crop yield prediction, crop disease, pest management, unpredictable seasonal variations etc.

A vigilant, prudence and gradual use of drones by rural indigenous people will help them get their land boundaries with the highest accuracy further bringing social and environmental justice [61]. UAV technology may be a suitable option for updating databases with accurate high-resolution geospatial information at a reasonable price [62]. Various developmental projects, industries, mining activities etc. in rural areas need land from local people and the government. They need land for establishing processing units, energy supply and water resources. Many times nearby lands are being encroached on even though they are having official land documents [63]. The same is applicable for commercial cropping by private organisations as they supply grains, fruits and agricultural commodities to manufacturing companies as the ready-packed food has increased tremendously in the world market [64].

Drones with high-resolution imagery help to produce real evidence to fight legal battles and also to monitor and document illegal activities. An example of indigenous communities in Indonesia has shown how drone imagery can be used in court to revoke operating licenses of mining companies after demonstrating illegal land trespassing beyond their concessions [26]. Social forestry aims to raise plantations with the local indigenous people's support to meet the requirement of timber, fuel wood, fodder etc. to reduce the pressure on the natural forest area. These forests are best monitored by small drones due to their capability to fly at higher altitudes with cameras that can penetrate through the canopy [65]. India has a coastline that stretches for about 7000 kms. Continuous monitoring of topographic changes is required for land management [66] and erosion control [67].

7 Fisheries

Major forms of employment in rural areas are agriculture, livestock and fisheries. Drones help to identify and delineate fish habitats and also the occurrence of species [68]. They can fly over freshwater bodies like rivers, streams and ponds, and lakes to identify the critical habitat, inlet topography, channel morphology and river bathymetry. [69] Explained the identification of freshwater fish speciation, their size, rate of detection and accuracy are the few census data collection process that can be conducted with an aerial survey using drones. Rapid characterization of hydro morphology along the river using UAV with high-resolution RGB imagery and a novel classification tool based on Artificial Neural Networks (ANN) will increase river water quality and ecosystem protection. These techniques leverage the use of unmanned aerial vehicles (UAVs) for environmental policy implementation as well as high-accuracy river monitoring and management [70].

8 Livestock Monitoring

Farmers in countries like Australia and Israel have embraced UAV technology to radically transform how they take care of their livestock. From the comfort of their homes, farmers can now use aerial surveillance, high-definition cameras and state-of-the-art sensors to keep a close eye on the location, health and general well-being of their cattle [71]. UAVs can count and monitor cattle, as well as detect abnormal animal behaviour that may signify disease. Drones may also be deployed for security purposes, sending alerts in the event of trespassing [72]. The expansion of agriculture near the forest area forces wild animals to move into villages, farms and cattle sheds in search of food. Elephants, lions, tigers, wolves, bears etc. enter during the night time causing damage to crops and animals by crossing boundaries of farmland. UAV offers a wide range of benefits when integrated into the plan and process to scare predators. A smart security system is a real-time working system that uses an algorithm to identify predator animals' faces and eyes [73]. Livestock detection and classification using artificial intelligence image processing for aerial surveys in large and inaccessible rugged terrain has given 96% accuracy for livestock detection and 92% for livestock counting [74]. Smart pasture is becoming increasingly important in the development of precision agriculture, particularly in agriculture-developed countries such as Australia and New Zealand, which are sparsely populated and have enormous rangelands but are developing intensive and large-scale farms [75]. The use of drones for livestock tracking aids in balancing the number of animals grazing in grassland with the carrying capacity of pastures [76]. To control soil erosion, the grazing capacity of pastures can be evaluated using aerial multispectral [77] and hyperspectral [78] imagery in all seasons in combination with land cover mapping.

9 Challenges Posed by Regulations for the Use of Drones in Agriculture

Different countries have enacted and enforced strict regulations regarding the loss of property, life and privacy using UAV data [79]. These regulations mainly focus on limits on altitudes and flight permissions, data collection and security systems. Despite the evident conveniences, expanded drone flights have increased public questions about safety and privacy [80]. Drones are a new type of small flying aircraft. Using them could endanger other aerospace users as well as those on Earth. Falling on the ground can be life-threatening [81]. The balance should be ensured between new technology on one side and safety, security and fundamental rights on the other hand. The effectiveness of UAVs in agriculture relies on their configuration, weight, payload, and price, with an emphasis on environmental sustainability. Recently, UAV autonomy has been eased to boost utilization in India's metropolitan areas [82].

10 Employment and Job Opportunities

The growing use of drones for various applications such as infrastructure, agriculture, and transportation is driving the potential market value of a business worth several billion dollars [83]. The innovative UAV platform for farming may attract rural youth due to its attractive and comfortable working conditions.

Drones also entice trained young people to start agricultural service companies, creating jobs and growing farmers' profitability [84]. The agricultural labour shortage amid the COVID19 pandemic, which has necessitated the implementation of physical distancing steps, has created many opportunities for the use of drones in agriculture. Labour shortage has become a major obstacle in India due to the migration of villagers in search of job opportunities and education purposes. Countries like India, where 55% population still depend on agriculture as basic employment, need large numbers of labour in all stages of agriculture. Such conditions lay new pathways for drones for different purposes without compromising basic needs.

The cost of drones, operational strategy, and the scarcity of technically qualified pilots are all major roadblocks to the growth of India's drone industry. In comparison to satellite images, UAVs have better and more affordable methods for monitoring and analyzing ecological phenomena at higher spatial and temporal resolutions [85]. Farmers who have already introduced precision farming practices to their crops, as well as those who are young and male, are more likely to respond. Such research would assist manufacturers and providers in selling to those farmers [86].

The Director of India Flying Lads (i.e., part of We Robotics) provides training to the tribal people of the Dahanu-Palghar belt of Maharashtra on crop rotation, aquaponics, hydroponics, fish farming, bio-waste management, organic farming, bio-based crop protection using Drone. Agriculture Insurance Company (AIC), India along with Skynet has carried out a few pilot investigations in Gujrat and Rajasthan to

evaluate UAV viability for agricultural surveying, and crop disease mapping for crop insurance claim settlement [87]. Drone data could also be used to detect and predict insect infestations, which insurance companies could then share with farmers. Drone data may be used to detect insurance fraud, preventing individuals from insuring the same plot of land several times. Because the majority of farmers in developing countries, such as India, are inexperienced with technology, a user-friendly UAV is required to perform agricultural operations by common people. A better user interface based on a human-centred approach will be more efficient [88].

By 2050, the world's population will reach 9 billion, necessitating a 70% increase in agricultural productivity. Drone technology with artificial intelligence (AI), machine learning (ML) [89], and remote sensing capabilities are becoming more popular due to its benefits. With its online 'Digital Sky Platform,' the central government has recognized the importance of unmanned aerial vehicles (UAVs), machine learning, and artificial intelligence [90] (www.equinoxsdrones.com).

10.1 Innovative Approaches in Agriculture Sector

New sophisticated automation technology that identifies its position and impediments while doing a task without the assistance of a trainer has moved UAVs closer to smart agricultural capabilities that can be readily adopted by anyone [91]. Insects play a vital role in pollination, and robot pollinators can replace dwindling honeybee populations. A synthetic pollinator made of animal hair covered with gel (direct touch) [92] or wind power generated by a UAV has aided pollen dispersion asymmetrically [93].

Agricultural field 2D and 3D [94] maps serve in evaluating crop health and growth [95], soil conditions, leaf area index, size, and so on with greater efficiency [96], and high-resolution maps allow for the demarcation of identical zones and nutritional quality areas [97]. Few applications of UAVs are given in Table 1.

11 Conclusions

The growing global population will also increase the food needs of the world population by 2050. More crops and increased cultivable areas are needed to meet growing food requirements. The 2030 Agenda for Sustainable Development contains land-related targets and indicators under SDGs 1, 2, 5, 11 and 15 [108]. Plants that are adaptable to evolving climate conditions and that produce more with less water are most valuable. Augmenting agricultural land while utilizing the natural resources available for comprehensive rural development will not only meet future needs but also conserve the ecosystem. An integrated geographic information system would help accomplish successful land administration and management in terms of land title, cost of land, land utilization, and development of land [109]. Climate change is happening rapidly under the current circumstances. Spatial technologies and drones

Table 1 Literature on UAV applications in various sectors in rural areas

S.no.	Literature work	Objective	Task	Title
1.	Ju and Son [98]	Multi-UAV system for agriculture using the distributed swarm control algorithm to evaluate the performance of the system	Total time, setup time, flight time, battery consumption, inaccuracy of land, haptic control effort, and coverage ratio	Multiple UAV systems for agricultural applications: control, implementation, and evaluation
2.	Sundar and Rathinam [99]	To find an optimal path for each vehicle starting and ending at its respective depot	Each target is visited at least once by some vehicle, the vehicle-target constraints are satisfied, and the sum of the length of the paths for all the vehicles is minimized	Algorithms for heterogeneous, multiple depots, multiple unmanned vehicle path planning problems
3.	Mersheeva and Friedrich [100]	To develop a system employing a team of micro UAVs for aerial sensing in disaster situations	Considering the problem of UAVs routing for obtaining these overview images	Routing for continuous monitoring by multiple micro AVs in disaster scenarios
4.	Manfreda et al. [101]	To provide an overview of the existing research and applications of UAS in natural and agricultural ecosystem monitoring to identify future directions, applications, developments, and challenges	To show recent advances in UAV platforms and potential limitations like sensing technologies, measurement protocols, and post-processing techniques	On the use of unmanned aerial systems for environmental monitoring
5.	Geipel et al. [102]	To capture standard RGB imagery datasets for corn grain yield prediction at three early- to mid-season growth stages	Combined spectral and spatial modelling, based on aerial images and Crop Surface Models for crop yield prediction	Combined spectral and spatial modelling of corn yield based on aerial images and crop surface models acquired with an unmanned aircraft system
6.	Uto et al. [103]	The high-accuracy estimation of the chlorophyll densities is confirmed by the chlorophyll indices based on the red-edge (RE) and near-infrared (NIR) spectral ranges, even under unstable illumination conditions	Acquiring aerial hyperspectral data from an altitude of 10 m using low-cost, small, light-weight UAVs	Development of a UAV-mounted miniature hyperspectral sensor system for agricultural monitoring

(continued)

Table 1 (continued)

S.no.	Literature work	Objective	Task	Title
7.	Zheng et al. [104]	To assess the data quality of one hyperspectral frame camera and evaluate the ability of rice nitrogen status monitoring	To lay a foundation for the promising application of UAV-based hyperspectral remote sensing in precision agriculture	Evaluation of a UAV-based hyperspectral frame camera for monitoring the leaf nitrogen concentration in rice
8	Shao et al. [105]	Cattle detection and counting system based on Convolutional Neural Networks (CNNs) using aerial images taken by an Unmanned Aerial Vehicle (UAV)	To avoid repetition of counting in images that have large overlaps to adjacent ones and to obtain the accurate number of cattle in an entire area	Cattle Detection and Counting in UAV Images Based on Convolutional Neural Networks
9.	Maluleke [106]	To explore the use of drones in policing stock theft by rural South African livestock farmers as an uncodded criminological technological edge	To combat stock theft cases which cause long-term pain and suffering to the rural livestock farmers	The use of drones in policing stock theft by the selected rural South African livestock farmers
10.	Michels et al. [107]	This paper contributes to the literature by identifying key determinants of smartphone adoption in agriculture	The findings are of interest to policymakers, researchers in the field of precision agriculture technologies as well as developers and providers of farm equipment and precision agriculture technologies that integrate with smartphones	Smartphone adoption and use in agriculture: empirical evidence from Germany

can be very useful for the analysis and protection from these changes. The influence of climate change, temperature [110], nitrogen [111], and timely fertilizer input [112] on grain protein content could be assessed using UAVs to ensure product quality [113]. The increasing nutritional grade is viewed as a method to increase farmer revenue. The use of information technology for specific local needs, as well as the introduction of emerging technologies, will be vital to its overall growth. The major future needs identified in rural development are policies and programs for input support, technology development, verification, and adoption.

Area and technology-specific policy and program-level interventions for profitable farming are the present need. The future generation is dependent on drones and they will create a new market. Further research into the adoption of drones should concentrate on data protection and confidence in the context of drone use. The role of extension services and drone providers in the adoption process should be recognized more in-depth as their expertise could compensate for farmers' possible lack of knowledge and skills concerning drones. Integration of Artificial intelligence with drone technology will enable the drone to take decisions [114] and be independent of human controllers. The next agricultural revolution will be data-driven, resulting in increased livelihoods for agricultural communities and increased agricultural production with minimal environmental impact. Supporting ecosystems would facilitate the growth of many innovative start-ups providing agricultural intelligence using drones and other emerging technologies as a service to rural communities. The knowledge gap among rural communities would be resolved by the emergence of a new breed of professionals and agricultural infomediaries, as well as the combination of various data sources and analytics.

References

1. Frankelius P, Norman C, Johansen K (2019) Agricultural innovation and the role of institutions: lessons from the game of drones. *J Agric Environ Ethics* 32(5):681–707
2. Kopačková-Strnadová V, Koucká L, Jelének J, Lhotáková Z, Oulehle F (2021) Canopy top, height and photosynthetic pigment estimation using Parrot Sequoia multispectral imagery and the Unmanned Aerial Vehicle (UAV). *Remote Sens* 13(4):705
3. Klein Hentz ÂM, Corte APD, Péllico Netto S, Strager MP, Schoeninger ER (2018) Tree detection: automatic tree detection using UAV-based data. *Floresta* 48:393
4. Lin Y, Jiang M, Yao Y, Zhang L, Lin J (2015) Use of UAV Oblique imaging for the detection of individual trees in residential environments. *Urban Forest Urban Greening* 14:404–412
5. Flores CC, Tan E, Crompvoets J (2021) Governance assessment of UAV implementation in Kenyan land administration system. *Technol Soc* 66:101664
6. Ramadhani SA, Bennett RM, Nex FC (2018) Exploring UAV in Indonesian cadastral boundary data acquisition. *Earth Sci Inf* 11(1):129–146
7. Hunt ER, Horneck DA, Spinelli CB, Turner RW, Bruce AE, Gadler DJ, Brungardt JJ, Hamm PB (2018) Monitoring nitrogen status of potatoes using small unmanned aerial vehicles. *Precis Agric* 19(2):314–333
8. Finn RL, Wright D (2012) Unmanned aircraft systems: surveillance, ethics and privacy in civil applications. *Comput Law Secur Rev* 28(2):184–194
9. Amaral LRD, Zerbato C, Freitas RGD, Barbosa Júnior MR, Simões IOPDS (2021) UAV applications in Agriculture 4.0. *Revista Ciência Agronômica* 51

10. Krupnick GA (2013) Conservation of tropical plant biodiversity: what have we done, where are we going? *Biotropica* 45(6):693–708
11. Schiffman R (2014) Drones flying high as a new tool for field biologists. *Science* 344:459
12. Silverberg, L.M. Vanvuuren, M. Vanvuuren, R. and Lutz, G. On the effectiveness of UAS for anti-poaching in the African arid savanna. *BioRxiv*, 660126 (2019).
13. Gonzalez LF, Montes GA, Puig E, Johnson S, Mengersen K, Gaston KJ (2019) Unmanned aerial vehicles (UAVs) and artificial intelligence revolutionizing wildlife monitoring and conservation. *Sensors* 16(1):97
14. Van Gemert JC, Verschoor CR, Mettes P, Epema K, Koh LP, Wich SA (2015) Nature conservation drones for automatic localization and counting of animals. In: Agapito L, Bronstein MM, Rother C (eds) *Computer vision—ECCV 2014 workshops, Part I*. Springer, Cham, Switzerland, pp 255–270
15. Christiansen P, Steen KA, Jørgensen RN, Karstoft H (2014) Automated detection and recognition of wildlife using thermal cameras. *Sensors* 14:13778–13793
16. Vincent JB, Werden LK, Ditmer MA (2015) Barriers to adding UAVs to the ecologist's toolbox. *Front Ecol Environ* 13:74–75
17. Cork L, Clothier R, Gonzalez LF, Walker R (2007) The future of UAS: standards, regulations, and operational experiences [workshop report]. *IEEE Aerosp Electron Syst Manag* 22:29–44
18. https://www.business-standard.com/article/news-ians/nearly-70-percent-of-indian-farms-are-very-small-census-shows-115120901080_1.html. Last accessed 2021/08/30
19. www.iwmi.cgiar.org/2018/06/irrigated-area-mapping-asia-and-africa/. Last accessed 2021/07/21
20. Mogili UR, Deepak B (2018) Review on the application of drone systems in precision agriculture. *Proc Comp Sci* 133:502–509
21. Paustain M, Theuvsen L (2017) Adoption of precision agriculture technologies by German crop farmers. *Precision Agric* 18:701–716
22. European Commission: Drones in Agriculture. Brussels, Belgium. https://ec.europa.eu/growth/tools-atabases/dem/monitor/sites/default/files/Drones_vf.pdf (2018). Last Accessed 2021/09/02
23. Nhamo L, Magidi J, Nyamugama A, Clulow AD, Sibanda M, Chimonyo VG, Mabhaudhi T (2020) Prospects of improving agricultural and water productivity through unmanned aerial vehicles. *Agriculture* 10(7):256
24. Zheng S, Wang Z, Wachenheim CJ (2019) Technology adoption among farmers in Jilin Province, China: the case of aerial pesticide application. *China Agric Econ Rev* 11:206–216
25. Pijl A, Bailly JS, Feurer DE, Maaoui MA, Boussema MR, Tarolli P (2020) TERRA: Terrain extraction from elevation rasters through repetitive anisotropic filtering. *Int J Appl Earth Obs Geoinf* 84:101977
26. Radjawali I, Pye O (2017) Drones for justice: inclusive technology and river-related action research along the Kapuas. *Geogr Helv* 72(1):17–27
27. García-Martínez H, Flores-Magdaleno H, Ascencio-Hernández R, Khalil-Gardezi A, Tijerina-Chávez L, Mancilla-Villa OR, Vázquez-Peña MA (2020) Corn grain yield estimation from vegetation indices, canopy cover, plant density, and a neural network using multispectral and RGB images acquired with unmanned aerial vehicles. *Agriculture* 10(7):277
28. Khan Z, Rahimi-Eichi V, Haeefele S, Garnett T, Miklavcic SJ (2018) Estimation of vegetation indices for high-throughput phenotyping of wheat using aerial imaging. *Plant Methods* 14(1):20
29. Xue J, Su B (2017) Significant remote sensing vegetation indices: a review of developments and applications. *J Sens* 1–17
30. Boursianis AD, Papadopoulou MS, Diamantoulakis P, Liopa-Tsakalidi A, Barouchas P, Salahas G, Karagiannidis G, Wan S, Goudos SK (2020) Internet of things (IoT) and agricultural unmanned aerial vehicles (UAVs) in smart farming: a comprehensive review. *Internet Things* 100187
31. Modica G, Messina G, De Luca G, Fiozzo V, Praticò S (2020) Monitoring the vegetation vigor in heterogeneous citrus and olive orchards. A multiscale object-based approach to extract trees' crowns from UAV multispectral imagery. *Comput Electron Agric* 175:105500

32. Veroustraete F (2015) The rise of the drones in agriculture. *Agriculture Editorial*, Ecronicon September 16
33. Barrero O, Perdomo SA (2018) RGB and multispectral UAV image fusion for Gramineae weed detection in rice fields. *Precision Agric* 19(5):809–822
34. Su J, Liu C, Hu X, Xu X, Guo L, Chen WH (2019) Spatio-temporal monitoring of wheat yellow rust using UAV multispectral imagery. *Comput Electron Agric* 167:105035
35. Xiao D, Feng J, Lin T, Pang C, Ye Y (2018) Classification and recognition scheme for vegetable pests based on the BOF-SVM model. *Int J Agric Biol Eng* 11(3):190–196
36. Ren Q, Zhang R, Cai W, Sun X, Cao L (2020) Application and development of new drones in agriculture. In: IOP conference series: earth and environmental science, vol 440, no 5. IOP Publishing, p 052041
37. Dara SK (2019) The new integrated pest management paradigm for the modern age. *J Integr Pest Manag* 10(1):12
38. Huang H, Deng J, Lan Y, Yang A, Zhang L, Wen S, Zhang H, Zhang Y, Deng Y (2019) Detection of helminthosporium leaf blotch disease based on UAV imagery. *Appl Sci* 9(3):558
39. Iost Filho FH, Heldens WB, Kong Z, de Lange ES (2020) Drones: innovative technology for use in precision pest management. *J Econ Entomol* 113(1):1–25
40. Gayathri Devi K, Sowmiya N, Yasoda RK, Muthulakshmi DK, Kishore B (2020) Review on the application of drones for crop health monitoring and spraying pesticides and fertilizer. *J Crit Rev* 7(6):667–672
41. Faial BS, Pessin G, Filho GPR, Carvalho ACPLF, Furquim G, Ueyama J (2014) Fine-tuning of UAV control rules for spraying pesticides on crop fields. In: 2014 IEEE 26th international conference on tools with artificial intelligence, pp 527–533
42. Faical BS, Freitas H, Gomes PH, Mano LY, de Pessin G, Carvalho AC, Krishnamachari B, Ueyama J (2017) An adaptive approach for UAV-based pesticide spraying in dynamic environments. *Comput Electron Agric* 138:210–223
43. Franchi A, Giordano PR, Secchi C, Son HI, Bülthoff HH (2011) A passivity-based decentralized approach for the bilateral teleoperation of a group of UAVs with switching topology. In: 2011 IEEE international conference on robotics and automation, pp 898–905
44. Li X, Zhao Y, Zhang J, Dong Y (2016) A hybrid PSO algorithm based flight path optimization for multiple agricultural UAVs. In: 2016 IEEE 28th international conference on tools with artificial intelligence (ICTAI). IEEE, pp 691–697
45. Pimentel D (1995) Amounts of pesticides reaching target pests: environmental impacts and ethics. *J Agric Environ Ethics* 8(1):17–29
46. Islam N, Rashid MM, Pasandideh F, Ray B, Moore S, Kadel R (2021) A review of applications and communication technologies for Internet of Things (IoT) and Unmanned Aerial Vehicle (UAV) based sustainable smart farming. *Sustainability* 13(4):1821
47. Radoglou-Grammatikis P, Sarianniadis P, Lagkas T, Moscholios I (2020) A compilation of UAV applications for precision agriculture. *Comput Netw* 172:p107-148
48. Jorge J, Vallbé M, Soler JA (2019) Detection of irrigation inhomogeneities in an olive grove using the NDRE vegetation index obtained from UAV images. *Eur J Remote Sens* 52(1):169–177
49. Quemada M, Gabriel J, Zarco-Tejada P (2014) Airborne hyperspectral images and ground-level optical sensors as assessment tools for maize nitrogen fertilization. *Remote Sens* 6:2940–2962
50. Peña JM, Torres-Sánchez J, Serrano-Pérez A, de Castro AI, LópezGranados F (2015) Quantifying efficacy and limits of unmanned aerial vehicle (UAV) technology for weed seedling detection as affected by sensor resolution. *Sensors* 15:5609–5626
51. King BA, Tarkalson DD, Sharma V, Bjorneberg DL (2021) Thermal crop water stress index baseline temperatures for sugarbeet in arid western US. *Agric Water Manag* 243:106459
52. Zarco-Tejada PJ, González-Dugo V, Berni JA (2012) Fluorescence, temperature and narrow-band indices acquired from a UAV platform for water stress detection using a micro-hyperspectral imager and a thermal camera. *Remote Sens Environ* 117:322–337

53. Gago J, Douthe C, Coopman R, Gallego P, Ribas-Carbo M, Flexas J, Escalona J, Medrano H (2015) UAVs challenge to assess water stress for sustainable agriculture. *Agric Water Manag* 153:9–19
54. Girona J (2002) Regulated deficit irrigation in peach. A global analysis. *Acta Hort* 592:335–342
55. Fereres E, Soriano M (2007) Deficit irrigation for reducing agricultural water use. *J Exp Bot* 58:147–159
56. Popescu D, Stoican F, Stamatescu G, Ichim L, Dragana C (2020) Advanced UAV–WSN system for intelligent monitoring in precision agriculture. *Sensors* 20:817
57. Guo Y, Wang H, Wu Z, Wang S, Sun H, Senthilnath J, Wang J, Robin Bryant C, Fu Y (2020) Modified red blue vegetation index for chlorophyll estimation and yield prediction of maize from visible images captured by UAV. *Sensors* 20:5055
58. Pathak H, Kumar GAK, Mohapatra SD, Gaikwad BB, Rane J (2020) Use of drones in agriculture: potentials, problems and policy needs. *ICAR-NIASM* 300:13+iv
59. Yunus AM, Azmi FAM (2020) Drone technology as a modern tool in monitoring the rural-urban development. In: *IOP conference series: earth and environmental science*, vol 540. IOP Publishing, pp 012076
60. Memon ZA, Majid MZA, Mustaffar M (2006) A systematic approach for monitoring and evaluating the construction project progress. *J Inst Eng* 67(3):26–32
61. Paneque-Gálvez J, Vargas-Ramírez N, Napoletano BM, Cummings A (2017) Grassroots innovation using drones for indigenous mapping and monitoring. *Land* 6(4):86
62. Koeva M, Muneza M, Gevaert C, Gerke M, Nex F (2018) Using UAVs for map creation and updating. A case study in Rwanda. *Surv Rev* 50(361):312–325
63. Reyes-García V, Ledezma JC, Paneque-Gálvez J, Orta M, Gueze M, Lobo A, Guinart D, Luz AC (2012) Presence and purpose of nonindigenous peoples on indigenous lands: a descriptive account from the Bolivian lowlands. *Soc Nat Resour* 25:270–284
64. Montefrio MJF, Sonnenfeld DA (2013) Global–local tensions in contract farming of biofuel crops involving indigenous communities in the Philippines. *Soc Nat Resour* 26:239–253
65. Cummings AR, Cummings GR, Hamer E, Moses P, Norman Z, Captain V, Bento R, Butler K (2017) Developing a UAV-based monitoring program with indigenous peoples. *J Unmanned Veh Syst* 5:115–125
66. Adade R, Aibinu AM, Ekumah B, Asaana J (2021) Unmanned Aerial Vehicle (UAV) applications in coastal zone management—a review. *Environ Monit Assess* 193(3):1–12
67. Casella E, Rovere A, Pedroncini A, Stark CP, Casella M, Ferrari M, Firpo M (2016) Drones as tools for monitoring beach topography changes in the Ligurian Sea (NW Mediterranean). *Geo-Mar Lett* 36(2):151–163
68. Kopaska J (2014) Drones—a fisheries assessment tool. *Fisheries* 39:319–319
69. Tyler S, Jensen OP, Hogan Z, Chandra S, Galland LM, Simmons J (2018) Perspectives on the application of unmanned aircraft for freshwater fisheries census. *Fisheries* 43:510–516
70. Casado MR, Gonzalez RB, Kriechbaumer T, Veal A (2015) Automated identification of river hydromorphological features using UAV high-resolution aerial imagery. *Sensors* 15(11):27969–27989
71. <https://dairynow.ca/two-farmers-using-drones-to-simplify-work/>. Last accessed on 2021/06/16
72. Al-Thani N, Albuaïnain A, Alnaimi F, Zorba N (2020) Drones for sheep livestock monitoring. In: *IEEE 20th mediterranean electrotechnical conference (MELECON)*, pp 672–676
73. Karl Y, Kim HK, Lee JH (2020) A smart security drones for farms using software architecture. *Int J Softw Innov (IJSI)* 8(4):40–49
74. Xu B, Wang W, Falzon G, Kwan P, Guo L, Sun Z, Li C (2020) Livestock classification and counting in quadcopter aerial images using Mask R-CNN. *Int J Remote Sens* 41(21):8121–8142
75. O’Grady MJ, Hare GMPO (2017) Modelling the smart farm. *Inf Process Agric* 4:179–187
76. Pádua L, Vanko J, Hruška J, Adão T, Sousa JJ, Peres E, Morais R (2017) UAS, sensors, and data processing in agroforestry: a review towards practical applications. *Int J Remote Sens* 38(8–10):2349–2391

77. de Jesús Marcial-Pablo M, Gonzalez-Sanchez A, Jimenez-Jimenez SI, Ontiveros-Capurata RE, Ojeda-Bustamante W (2019) Estimation of vegetation fraction using RGB and multi-spectral images from UAV. *Int J Remote Sens* 40(2):420–438
78. Pi W, Du J, Bi Y, Gao X, Zhu X (2021) 3D-CNN based UAV hyperspectral imagery for grassland degradation indicator ground object classification research. *Eco Inform* 62:101278
79. Tobór D, Barcik J, Czech P (2017) Legal aspects of air transport safety and the use of drones. *Zeszyty Naukowe. Transport/Politechnika Śląska* 97:167–179
80. Luppicini R, So A (2016) A technological review of commercial drone use in the context of governance, ethics, and privacy. *Technol Soc* 46:109–119
81. Stöcker C, Bennett R, Nex F, Gerke M, Zevenbergen J (2017) Review of the current state of UAV regulations. *Remote Sens* 9:459
82. Marinello F, Pezzuolo A, Chiumenti A, Sartori L (2016) Technical analysis of unmanned aerial vehicles (drones) for agricultural applications. *Eng Rural Dev* 15:870
83. Mazur M, Wisniewski A, McMillan J (2016) Clarity from above: PwC global report on the commercial applications of drone technology. Drone Powered Solutions, PriceWater house Coopers, Warsaw
84. Sylvester G (ed) (2018) E-agriculture in action: drones for agriculture. Food and Agriculture Organization of the United Nations and International Telecommunication Union
85. Harris JM, Nelson JA, Rieucan G, Broussard WP III (2019) Use of drones in fishery science. *Trans Am Fish Soc* 148(4):687–697
86. Michels M, Fecke W, Feil J-H, Mubhoff O, Pigisch J, Krone S (2020) Smartphone adoption and use in agriculture: empirical evidence from Germany. *Precision Agric* 21:403–425
87. Sinha JP, Kushwaha HL, Kushwaha D, Singh N, Purushottam M (2016) Prospect of Unmanned Aerial Vehicle (UAV) technology for agricultural production management. In: International conference on emerging technologies in agricultural and food engineering agricultural and food engineering department. IIT Kharagpur, pp 53–66
88. Hong A, Lee DG, Bühlhoff HH, Son HI (2017) Multimodal feedback for teleoperation of multiple mobile robots in an outdoor environment. *J Multimodal User Interfaces* 11(1):67–80
89. Singhal G, Bansod B, Mathew L, Goswami J, Choudhury BU, Raju PLN (2019) Chlorophyll estimation using a multi-spectral unmanned aerial system based on machine learning techniques. *Remote Sens Appl Soc Environ* 15:100235
90. <https://www.equinoxdrones.com/blog/importance-of-drone-technology-in-indian-agriculture-farming>. Last accessed on 2021/07/16
91. Sofonia JJ, Phinn S, Roelfsema C, Kendoul F, Rist Y (2019) Modelling the effects of fundamental UAV flight parameters on LiDAR point clouds to facilitate objectives-based planning. *ISPRS J Photogram Remote Sens* 149:105–118
92. Jiyu L, Lan Y, Jianwei W, Shengde C, Cong H, Qi L, Qiuping L (2017) Distribution law of rice pollen in the wind field of small UAV. *Int J Agric Biol Eng* 10(4):32–40
93. Chechetka SA, Yu Y, Tange M, Miyako E (2017) Materially engineered artificial pollinators. *Chem* 2(2):224–239
94. Hovhannisyann T, Efendyan P, Vardanyan M (2018) Creation of a digital model of fields with the application of DJI phantom 3 drone and the opportunities of its utilization in agriculture. *Ann Agrarian Sci* 16(2):177–180
95. Chebrolu N, Läbe T, Stachniss C (2018) Robust long-term registration of UAV images of crop fields for precision agriculture. *IEEE Robot Autom Lett* 3:3097–3104
96. Guillén-Climent ML, Zarco-Tejada PJ, Berni JA, North PR, Villalobos FJ (2012) Mapping radiation interception in row-structured orchards using 3D simulation and high-resolution airborne imagery acquired from a UAV. *Precision Agric* 13(4):473–500
97. Torres-Sánchez J, de Pena JM, Castro AI, López-Granados F (2014) Multi-temporal mapping of the vegetation fraction in early-season wheat fields using images from UAV. *Comput Electron Agric* 103:104–113
98. Ju C, Son HI (2018) Multiple UAV systems for agricultural applications: control, implementation, and evaluation. *Electronics* 7(9):162

99. Sundar K, Rathinam S (2017) Algorithms for heterogeneous, multiple depot, multiple unmanned vehicle path planning problems. *J Intell Rob Syst* 88(2):513–526
100. Mersheeva V, Friedrich G (2012) Routing for continuous monitoring by multiple micro AVs in disaster scenarios. In: ECAI. IOS Press, pp 588–593
101. Manfreda S, McCabe MF, Miller PE, Lucas R, Pajuelo Madrigal V, Mallinis G, Ben Dor E, Helman D, Estes L, Ciraolo G, Müllerová J (2018) On the use of unmanned aerial systems for environmental monitoring. *Remote Sens* 10(4):641
102. Geipel J, Link J, Claupein W (2014) Combined spectral and spatial modelling of corn yield based on aerial images and crop surface models acquired with an unmanned aircraft system. *Remote Sens* 6(11):10335–10355
103. Uto K, Seki H, Saito G, Kosugi Y (2013) Development of UAV-mounted miniature hyperspectral sensor system for agricultural monitoring. In: 2013 IEEE international geoscience and remote sensing symposium-IGARSS 2013, pp 4415–441
104. Zheng H, Zhou X, Cheng T, Yao X, Tian Y, Cao W, Zhu Y (2016) Evaluation of a UAV-based hyperspectral frame camera for monitoring the leaf nitrogen concentration in rice. In: 2016 IEEE international geoscience and remote sensing symposium (IGARSS), pp 7350–7353
105. Shao W, Kawakami R, Yoshihashi R, You S, Kawase H, Naemura T (2020) Cattle detection and counting in UAV images based on convolutional neural networks. *Int J Remote Sens* 41(1):31–52
106. Maluleke W (2020) The use of drones in policing stock theft by the selected rural South African livestock farmers. *J Soc Sci* 48(4):1–20
107. Michels M, Fecke W, Feil JH, Musshoff O, Pigisch J, Krone S (2020) Smartphone adoption and use in agriculture: empirical evidence from Germany. *Precision Agric* 21(2):403–425
108. Land Portal, Land and the Sustainable Development Goals (SDGs) (2021). <https://landportal.org/node/52263>
109. Expert group on land administration and management, framework for effective land administration a reference for developing, reforming, renewing, strengthening or modernizing land administration and management systems (2019). https://ggim.un.org/documents/FELA_Consultation_Draft.pdf
110. Raja L, Vyas S (2019) The study of technological development in the field of smart farming. In: Smart farming technologies for sustainable agricultural development. IGI Global, Hershey, PA, USA, pp 1–24. <https://www.igi-global.com/chapter/the-study-of-technological-development-in-the-field-of-smart-farming/209543>
111. Ohdaira Y, Sasaki R, Takeda H (2013) Analysis of factors affecting seed protein compositions and protein contents in rice of seed-protein mutant cultivars under different cropping seasons. *Jpn J Crop Sci* 82:18–27
112. Sakaiya E, Inoue Y (2012) Investigating error sources in remote sensing of protein content of brown rice towards operational applications on a regional scale. *Jpn J Crop Sci* 81:317–331
113. Hama A, Tanaka K, Mochizuki A, Tsuruoka Y, Kondoh A (2020) Estimating the protein concentration in rice grain using UAV imagery together with agroclimatic data. *Agronomy* 10(3):431
114. Rupnik R, Kukar M, Vračar P, Košir D, Pevc D, Bosnić Z (2018) AgroDSS: A decision support system for agriculture and farming. *Comput Electron Agric* 1–12. <https://doi.org/10.1016/j.compag.2018.04.001>

Disaster Risk Mapping from Aerial Imagery Using Deep Learning Techniques



Amit Kumar Jena, Sai Sudhamsa Potru, Deepak Raghavan Balaji, Abhinayana Madu, and Kuldeep Chaurasia

Abstract In regions prone to natural disasters, the buildings must follow specific construction standards to avoid demolition. One of the factors that predict the risk of damage is the roof material. This paper investigates the performance of various deep convolutional neural network architectures to classify buildings based on roof material from aerial drone imagery. We also propose a method that is an ensemble of ResNet, ResNeXt, and EfficientNet variants of convolutional neural networks, which performed the best in our experiments. We obtained a log loss value as low as 0.4373 using the proposed method. Therefore, the proposed method can be used to perform an accurate classification of roof material using aerial drone imagery.

Keywords Deep learning · Remote sensing · Ensemble learning · Disaster-risk-management · Transfer learning

1 Introduction

In areas like the Caribbean with a high risk of natural disasters like earthquakes, floods, and hurricanes, there is a risk of immense damage to life and property if the buildings do not follow modern construction standards. While the buildings can be retrofit to follow these standards, officers must inspect them manually, which is a time-consuming, labour-intensive, and expensive process. Roof material is a particularly relevant characteristic that determines risk, and it is also a predictor of

A. K. Jena (✉)
IIT ISM Dhanbad, Dhanbad, India
e-mail: amitjena40@gmail.com

S. S. Potru · K. Chaurasia
Bennett University, Greater Noida, India

D. R. Balaji
Rajalakshmi Engineering College, Chennai, India

A. Madu
SRK Institute of Technology, Vijayawada, India

other risk factors like building materials. Modern developments in computer vision and machine learning can enable us to classify buildings according to their roof material accurately. Hence, these techniques can be beneficial to building inspectors to make inspections faster and cheaper, and target resources where they create the most impact. We obtained a set of high-resolution aerial drone images of a few regions in the Caribbean, trained several deep convolutional neural networks, and compared their results to this dataset [1].

We experimented with several Convolutional Neural Network (CNN) architectures for image classification. Some of the models we used were ResNet, Inception, ResNeXt, and EfficientNet. All these models were pre-trained on the ImageNet dataset. We used transfer learning to fine-tune these models on our dataset. We made the final predictions using an Ensemble of the four most accurate models, which had the lowest log loss scores.

2 Related Work

Deep learning was explicitly proposed in 2006 by Hinton et al. [2]. The primary motivation of deep learning is to have neural networks with many layers to model the learning process similar to that of the human brain. In recent years Convolutional Neural Networks have been used extensively in the field of Computer Vision. Computer vision exploded in recent years when Alexnet [3] won the ImageNet Competition in 2012. Since then, there have been several models that made object detection, classification, and other applications of Computer Vision more accurate.

Several papers have been written on building identification and rooftop extraction from high-resolution aerial imagery, which is the first task in our work. Guo [4] proposed a very efficient method using CNNs to identify buildings from Google Earth images. The authors of this paper also experimented with another supervised machine learning method called adaptive boosting (AdaBoost), which lost to CNN by a small margin. Li [5] suggested a novel method to extract rooftops from remote sensing imagery using higher-order conditional random fields (HCRF). They have combined the high-level information obtained by unsupervised image pre-segmentation and low-level pixel information.

Many researchers have worked previously on geospatial data classification, although few have aimed toward classifying buildings for disaster risk prediction. One of the pieces of literature in this domain by Luus [6] outlined the segregation of land into 21 predefined classes based on their usage. In this paper, a multiview deep learning approach was proposed. Fu [7] used a multiscale Fully Convolutional neural network for land classification from remote sensing imagery. They introduced Atrous convolution to increase the density of the output class maps. Their methods were performed on datasets with insufficient labelling, which is a common drawback in remote sensing datasets. Despite this drawback, an efficient classification method was proposed by Scott [8]. They used data augmentation specifically tailored for remote sensing images and Transfer Learning with CaffeNet, GoogleNet,

and ResNet. They used the UC Merced dataset to train the proposed models. Narloch [9] used a deep convolutional neural network (DCNN) to predict the compressive strength of cement stabilized rammed earth (CSRE), trained and tested on SEM (scanning electron microscope) image database. This is similar to the problem the current paper is addressing, which is to predict the demolition risk using rooftop images.

3 Study Area and Data Resources

3.1 Maps

The dataset consists of high-resolution aerial drone images of 7 different regions (Borde rural, Borde Soacha, Mixco 1 and Ebenezer, Mixco 3, Castries, Dennery, and Gros Islet) across three different countries (Colombia, Guatemala, St. Lucia). Table 1 shows the geographical coordinates of each region.

Due to the high level of resolution covering a large area mass, the images' size is rather humongous. The smallest image out of the seven, that of mixco 3, is of size 1.6 Gigabytes and the rest scales up to 10 Gigabytes in size. The resolution, pixel dimension, and size of each image are shown in Table 2.

3.2 Other Data Resources

There is a folder for each country and a sub-folder for each region. These sub-folders contain the tiff image of that region along with a thumbnail of the map, one imagery JSON file, one train GEOJSON file, and one test GEOJSON file. The thumbnail provides an overview of the actual map with much less resolution to help visualize

Table 1 Location of the study area

Country	Site name	Central scene coordinates
Columbia	Borde rural	4.54758°N, 74.16113°W
	Borde soacha	4.56878°N, 74.16776°W
Guatemala	Mixco 1 and Ebenezer	14.62212°N, 90.58445°W
	Mixco 3	14.61027°N, 90.57494°W
St.Lucia	Dennery	13.91171°N, 60.89208°W

Table 2 Details of the dataset

Region	Spatial resolution (cm)	Pixel dimension	Size (GB)
Borde Rural	3.94	5318 * 31,315	4.5
Borde Soacha	4.25	40,159 * 45,650	4.5
Mixco 1 and Ebenezer	4.31	27,604 * 26,641	2.0
Mixco 3	3.78	26,066 * 19,271	1.6
Dennery	4.16	21,184 * 41,534	2.5

the image on a computer screen since a default image viewer cannot load the TIFF images due to their large size and resolution. There is an imagery data file containing the coordinates for the town's outline in the tiff image. The training GEOJSON file contains the unique building ID, building footprint (Geospatial coordinates of each building in the training set), roof material, and verified field. The test GEOJSON file contains the unique building id and building footprint (Geo-spatial coordinates of each building in the test set).

4 Methodology

Figure 1 shows an outline of the methodology followed in this research work. After analysing the dataset, we divide the dataset into training and cross-validation sets, to ensure they have the same image distribution. Then we performed data augmentation techniques to increase the no. of training samples. We train three deep learning models on the training set separately and performed hyperparameter tuning on them to ensure their best performances. The models were: ResNet, EfficientNet and ResNeXt. We perform test time augmentation on the test set and finally combine the predictions from the variants of these three models.

4.1 Data Preprocessing

Data Extraction

Images of building rooftops were extracted from each town's high-resolution aerial image using the geojson file provided alongside it. The file consists of the building footprint in polygonal coordinates, which were parsed using geopandas python package [10] and the exact rooftop image was extracted from the big .tiff image using Rasterio python package.

Cross-Validation

The test data needs to be classified into five different classes of roof material. The training data is imbalanced because in the real world not all categories are equally

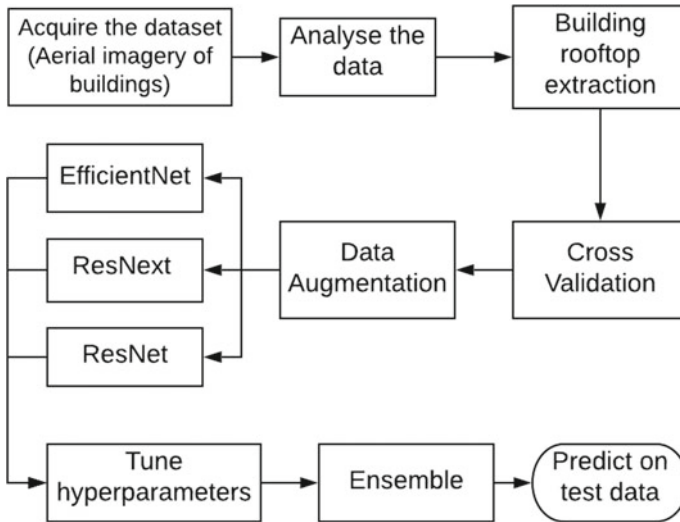


Fig. 1 Methodology

found. In our dataset, there are many more data entries for *healthy metal* than there are for *other*. The distribution of the training data into different categories is shown in Table 3.

As is evident from Table 3, there is an imbalance in the training data. This can cause the model to overrepresent some classes and underrepresent others. Also, the cost of misclassifying an abnormal class as normal is very high. For example, it is very important to not classify *incomplete* as *healthy metal*, even though there is more training data available for *healthy metal*. For this reason, we made a stratified cross-validation set of the data, which has the same proportions of class labels as the input dataset. This set is used to check the trained model’s performance before making predictions on test data and to tune the hyperparameters of the model for best performance.

Data Augmentation

Data Augmentation is an efficient technique for improving training data diversity by performing transformations on the images. Data Augmentation techniques include cropping, padding, flipping, zooming, etc. For the rooftop images, the transformations performed were vertical flip, zoom, and increasing the brightness of the image. The Fastai library was used to perform data augmentation and training pre-trained CNN models on our data [11]. The performance of the model improved by a significant degree by using data augmentation. A regularization technique called Mixup, proposed by Zhang [12], was also used in this research work. In this technique, instead of providing raw images, we take a linear combination of two images and pass it as input to the model. The accuracy of the model was improved by using this technique.

Table 3 Distribution of the training data

Category	Sample_image	Count	Description
Concrete_cement		1518	Roofs are made of concrete or cement
Healthy_metal		14,817	Includes corrugated metal, galvanized sheeting, and other metal materials
Incomplete		669	Under construction, extremely haphazard, or damaged
Irregular_metal		5241	Includes metal roofing with rusting, patching, or some damage. These roofs carry a higher risk
Other		308	Includes shingles, tiles, red-painted, or other material

4.2 Deep Learning Methodology

Convolutional Neural Networks have shown relatively good results for Image classification and other computer vision tasks without much feature engineering in various research works. The use of transfer learning removed the dependence on large datasets to train accurate deep learning models, by using pre-trained models and then fine-tuning them on the target dataset. Many such pre-trained CNN architectures were used for experiments in our research and their performances were compared. The most accurate models were chosen to make a final ensemble to get the best results. All the models were trained using a mixed-precision training technique [13].

Hyperparameters

To find optimal learning rates to train each of our models, we used the cyclical learning rate method suggested by Smith [14]. For most of the models that we used for experiments, the optimal maximum learning rate was of the order of $1e-5$. The momentum and weight decay were set to 0.9 and 0.01, respectively, for all the models. The batch size was 32 during the training process of the models.

Progressive Resizing

We used the progressive resizing technique to improve our models' generalization capability, which eventually gave us better scores. The models were initially trained using smaller images and later trained on larger images. Training with smaller images made the training process fast and training with larger images later improved the accuracy of the models. In our experiments, the images were first resized to 128×128 and trained for 10 epochs. Then the images were resized to 256×256 and trained for 15 epochs. Finally, we unfreeze all the pre-trained model layers and train them for 10 more epochs on the dataset.

Residual Neural Networks (ResNet)

To get an accurate prediction of the roof material, the CNN must consist of many layers. The depth of neural networks has proved to be a crucial factor for achieving better performance in classification tasks. But learning better networks is not as easy as stacking more layers. Stacking more layers provides us with the vanishing/exploding gradients issue [15]. This problem has been addressed through the normalized initialization and intermediate normalization layers, which enable deeper networks to start converging to the Stochastic Gradient descent using back-propagation. But this method exposes the *degradation* problem where, as the network depth increases, accuracy gets saturated and decreases rapidly. He [16] addressed this problem by using deep residual neural networks (ResNet), where skip connections are established, enabling us to make more layers, thereby increasing the accuracy of the model. In ResNet, we can go up to 200 layers before which the accuracy gets saturated. The best ResNet model for our purpose was the pre-trained ResNet-152 model from the Fastai python library.

ResNeXt

Xie [17] proposed an improvisation of the ResNet models. Their models, called ResNeXt, have shown better results for image classification as compared to ResNet models. They introduce a new dimension to the neural network called *cardinality*, in addition to depth and width. In neural networks, linear transformations are performed on the current layer to obtain each neuron in the next layer. This paper proposes aggregating a set of transformations with the same topology instead of performing linear transformations only. The size of this set of transformations is called *cardinality*. We have used the pre-trained model ResNeXt-101 64×4 , a 101-layer deep model with cardinality 64 [18] in our experiments.

EfficientNet

Tan and Le [19] introduced a new CNN architecture called EfficientNet. The paper demonstrates a method of scaling the three dimensions of a CNN, namely, depth, width, and height. It is found that scaling any one dimension does not improve the accuracy linearly. Instead, the accuracy quickly saturates. Although ResNets allows us to go deeper than normal, going deeper than 200 layers does not improve CNN's efficiency. The solution to this problem lies in scaling multiple dimensions together. But scaling multiple dimensions arbitrarily results in sub-optimal accuracy and efficiency. The proposed scaling technique as discussed above is the basis for EfficientNet architectures. Scaling does not change the layer operations of a network. So an optimal base network is chosen on top of which optimal scaling parameters (α , β , γ , ϕ) are searched. Setting the value of $\alpha = 1.2$, $\beta = 1.1$, and $\gamma = 1.15$ and experimenting with the values of ϕ gives EfficientNet b1-b7.

For the roof material classification task mentioned in this paper, pre-trained models of EfficientNet implemented here [20] were used using the Fastai library. EfficientNet b5, b6, and b7 variants were used in our experiments.

4.3 Ensemble Modelling

In addition to augmenting training data, we have performed test time augmentation on the test data and aggregated the prediction probabilities to get a more accurate prediction [21]. Ensembling is a method of classifying new data points by taking a set of classifiers and combining them in some aggregate function. The weighted average was used in the present classification task as an aggregate. The ensemble was performed on the outputs obtained from ResNet-152, ResNeXt-101 64×4 , EfficientNet b6, and EfficientNet b7.

5 Results

The performance metric that we use to evaluate the models’ accuracy is the **log loss** function. It is an error metric, hence, a lower value is better (as opposed to an accuracy metric, where a higher value is better). The log loss can be calculated through Eq. (1).

$$\text{loss} = \frac{-1}{N} \sum_{i=1}^N \sum_{j=1}^M y_{ij} \log p_{ij} \tag{1}$$

Some sample test images along with their predicted results are shown in Fig. 2. The performances of the individual pre-trained models on the validation set and the test set after training them using the above said approaches are shown in Table 4.

The least log loss of **0.4373** was obtained from the ensemble of ResNet-152, ResNeXt-101 64×4, EfficientNet b6 and EfficientNet b7.



Image	Results
	<p>Concrete Cement: 0.00196</p> <p>Healthy Metal: 0.99082</p> <p>Incomplete: 0.00059</p> <p>Irregular Metal: 0.00600</p> <p>Other: 0.0063</p>
	<p>Concrete Cement: 0.650338</p> <p>Healthy Metal: 0.18774</p> <p>Incomplete: 0.109148</p> <p>Irregular Metal: 0.030715</p> <p>Other: 0.004717</p>

Fig. 2 Predictions on some test images

Table 4 Performance of individual models

Model	Training loss	Validation loss	Error rate	Testing loss
ResNet-152	0.465180	0.475009	0.182246	0.4723
ResNeXt-101 64×4	0.591409	0.378783	0.139543	0.4898
EfficientNet b6	0.527126	0.520498	0.191325	0.4610
EfficientNet b7	0.584133	0.396385	0.147613	0.4526

6 Conclusion

Image Classification using deep learning techniques is a powerful alternative to manual inspection in Disaster Risk Management. We obtained a log loss value of 0.4373 on the test dataset. This suggests that we can make good predictions about the strength of the buildings using this model. The methods employed in this research work are based on the latest developments in image classification. The model can be improved with future developments in the field to make the predictions more accurate. Since modern neural networks tend to be overconfident about their predictions, better calibration techniques can be explored further to reduce the overall log loss. Training the model with Label Smoothing loss or using temperature scaling as proposed by Guo [22] may improve the model's capability to predict more accurate probability values for each class.

Acknowledgements This research work was supported by LeadingIndiaAI, an AI and deep learning Skilling and Research institution. We want to thank our program coordinator Dr. Madhushi Verma, director of LeadingIndiaAI, Dr. Deepak Garg, Dr. Vipul Mishra, and Dr. Tapas Badal, for providing us with the opportunity to work on a machine learning project and guiding us through the process. The data was prepared by WeRobotics and World Bank Global Program for Resilient Housing. We would also like to thank Bennett University for conducting this research work.

References

1. WeRobotics (2019) Open AI Caribbean challenge: mapping disaster risk from aerial imagery. WeRobotics Blog, viewed 11 December 2021. <https://blog.werobotics.org/2019/10/08/open-ai-caribbean-challenge-mapping-disaster-risk-from-aerial-imagery/>
2. Hinton G, Osindero S, Welling M, Teh YW (2006) Unsupervised discovery of nonlinear structure using contrastive backpropagation. *Cogn Sci* 30(4):725–731
3. Alom MZ, Taha TM, Yakopcic C, Westberg S, Sidike P, Nasrin MS, Van Esesn BC, Awwal AAS, Asari VK (2018) The history began from alexnet: a comprehensive survey on deep learning approaches. [arXiv:1803.01164](https://arxiv.org/abs/1803.01164)
4. Guo Z, Shao X, Xu Y, Miyazaki H, Ohira W, Shibasaki R (2016) Identification of village building via Google Earth images and supervised machine learning methods. *Remote Sens* 8(4):271
5. Li E, Femiani J, Xu S, Zhang X, Wonka P (2015) Robust rooftop extraction from visible band images using higher-order CRF. *IEEE Trans Geosci Remote Sens* 53(8):4483–4495

6. Luus FP, Salmon BP, Van den Bergh F, Maharaj BTJ (2015) Multiview deep learning for land-use classification. *IEEE Geosci Remote Sens Lett* 12(12):2448–2452
7. Fu G, Liu C, Zhou R, Sun T, Zhang Q (2017) Classification for high-resolution remote sensing imagery using a fully convolutional network. *Remote Sens* 9(5):498
8. Scott GJ, England MR, Starns WA, Marcum RA, Davis CH (2017) Training deep convolutional neural networks for land–cover classification of high-resolution imagery. *IEEE Geosci Remote Sens Lett* 14(4):549–553
9. Narloch P, Hassanat A, Tarawneh AS, Anysz H, Kotowski J, Almohammadi K (2019) Predicting compressive strength of cement-stabilized rammed earth based on SEM images using computer vision and deep learning. *Appl Sci* 9(23):5131
10. Geopandas (2019) Making work with geospatial data easier, viewed 24 December 2019. <http://geopandas.org/>
11. Howard J, Gugger S (2020) Fastai: a layered API for deep learning. *Information* 11(2):108
12. Zhang H, Cisse M, Dauphin YN, Lopez-Paz D (2017) Mixup: beyond empirical risk minimization. [arXiv:1710.09412](https://arxiv.org/abs/1710.09412)
13. He T, Zhang Z, Zhang H, Zhang Z, Xie J, Li M (2019) Bag of tricks for image classification with convolutional neural networks. In: *Proceedings of the IEEE/CVF conference on computer vision and pattern recognition*, pp 558–567
14. Smith LN (2018) A disciplined approach to neural network hyper-parameters: Part 1—learning rate, batch size, momentum, and weight decay. [arXiv:1803.09820](https://arxiv.org/abs/1803.09820)
15. Glorot X, Bengio Y (2010) Understanding the difficulty of training deep feedforward neural networks. In: *Proceedings of the thirteenth international conference on artificial intelligence and statistics. JMLR workshop and conference proceedings*, pp 249–256
16. He K, Zhang X, Ren S, Sun J (2016) Deep residual learning for image recognition. In: *Proceedings of the IEEE conference on computer vision and pattern recognition*, pp 770–778
17. Xie S, Girshick R, Dollár P, Tu Z, He K (2017) Aggregated residual transformations for deep neural networks. In: *Proceedings of the IEEE conference on computer vision and pattern recognition*, pp 1492–1500
18. ResNext WSL, PyTorch, viewed 13 December 2021. https://pytorch.org/hub/facebookresearch_WSL-Images_resnext/
19. Tan M, Le Q (2019) Efficientnet: rethinking model scaling for convolutional neural networks. In: *International conference on machine learning*. PMLR, pp 6105–6114
20. lukemelas/EfficientNet-PyTorch, Github, viewed 14 December 2021. <https://github.com/lukemelas/EfficientNet-PyTorch>
21. He K, Zhang X, Ren S, Sun J (2015) Delving deep into rectifiers: surpassing human-level performance on imagenet classification. In: *Proceedings of the IEEE international conference on computer vision*, pp 1026–1034
22. Guo C, Pleiss G, Sun Y, Weinberger KQ (2017) On the calibration of modern neural networks. In: *International conference on machine learning*. PMLR, pp 1321–1330

High-Resolution Mapping of Forest Canopy Cover Using UAV and Sentinel-2



Charanjeet Singh Nijjar, Sachchidanand Singh, Tanisha Jaiswal,
and Shivani Kalra

Abstract Remote sensing plays an important role in characterizing the land surface by extensively concerning its spatial resolution. Most of the time, spectral and temporal resolution becomes a limitation, which now can be overcome via unmanned aerial vehicle (UAV) as a remote sensing platform. The study utilizes the Google Earth engine cloud-based platform to prepare the classified maps from Sentinel 2 and UAV datasets using the Random Forest algorithm. The canopy cover was estimated using UAV data and divided into 4 classes: very dense forest, moderately dense forest, open forest and scrub forest. The majority (39%) areas were under scrub forest. Furthermore, the land use land cover was prepared using UAV data and showed superior results with 95.5% overall accuracy compared with 86.5% of Sentinel 2. Lastly, the tree count of the area was estimated using high-resolution data. The predicted number of trees was 3052, with an accuracy of 82%. The tree count algorithm works better in plantation and even canopy-size trees. Thus, this methodology ultimately helps to achieve the sustainable use of resources concerning their availability, demand and exploitation in the study area. The estimated results can help policymakers, government officials, and local people halt desertification and better sustainable forest management.

Keywords Forest management practice · Forest canopy cover · Sustainable development · UAV

C. S. Nijjar (✉)

North-Eastern Space Application Centre (NESAC), Umiam, India

e-mail: nijjarcharanjeet.iirs@gmail.com

S. Singh

Indian Institute of Technology Roorkee, Roorkee, India

e-mail: ssingh1@wr.iitr.ac.in

T. Jaiswal

Delhi Technological University (DTU), Delhi, India

S. Kalra

Indian Institute of Remote Sensing, Indian Space Research Organization (IIRS-ISRO), Dehradun, India

© The Author(s), under exclusive license to Springer Nature Switzerland AG 2023

K. Jain et al. (eds.), *Proceedings of UASG 2021: Wings 4 Sustainability*,

Lecture Notes in Civil Engineering 304,

https://doi.org/10.1007/978-3-031-19309-5_24

1 Introduction

Forest management and research require accurate tree species characterization and distribution in a forested area. It helps manage vegetation, breaching invasive species, habitat mapping, and ultimately sustainable management and development [1–3]. For better practices, remote sensing and Geographic Information System (GIS) has played a crucial part as it helps in mapping forest spatially over a large area [4]. Various studies have shown its importance in forest mapping [5–7] and ecological research [8, 9].

The Earth-observing satellite missions, the Landsat series, have been widely used for research because of cost efficiency and global coverage [10]. LANDSAT allows the mapping of forests, but the type of tree species cannot be identified due to its 30 m resolution [11, 12]. Also, in terms of free optical data, Sentinel 2 has the best spatial resolution of only 10 m in Red, Blue, Green and Near-infrared (NIR) bands and global coverage of 5 days with the Sentinel 2 constellation. Hence, very high-resolution satellites like Quick Bird and World-View 2 are used to monitor the forest [13–16]. Advancements in technologies introduced hyperspectral, LiDAR sensors that helped to identify tree species with higher accuracy [17, 18]. Hyperspectral sensors were used based on the narrow bandwidth spectra characteristics of different tree species [19, 20] and plant-related disease estimation [21]. Some studies address the problems related to background noise and spectral characteristics of hyperspectral [22, 23]. Unlike other sensors, LiDAR senses the vertical height of the trees, helping in studies related to tree height, volumetric estimation, identification of species, elevation and intensity channels [24–29]. Though these methods have high performance, they are proven very expensive in their apparatus, flight and processing [30].

As per the difficulties mentioned above with different satellites and sensors, unmanned aerial vehicles (UAV) are now more frequently used in forestry applications [31–34]. It overcomes the problem of processing, costing and poor spatial resolution with spectral mixing. Simple red, green and blue bands have facilitated broad application potential [35]. UAVs can quickly generate land use maps because of their ability to capture the best imageries of land use and land cover [36]. Image classification is the most commonly applied method for land use/cover maps generation [37–40]. It is a process of labelling the pixels belonging to spectral data [41]. Generally, the salt-pepper effect is observed and reduces accuracy [42]. Consequently, object-based classification is now being used more frequently. Several researchers have confirmed that UAV-based object classification has produced very high accuracy [43–48]. Lots incorporate machine learning to deal with classification problems [49].

This study uses UAV-generated imageries in the Nayla area, Rajasthan. The land use land cover (LULC) maps are generated in the cloud-based google earth engine platform. Forest canopy density mapping is analyzed using object-based classification using a random-forest algorithm. The proposed methodology allows better tree characterization and accurate tree counting.

2 Material and methods

2.1 Study Area

Nayla is in Jaipur district, Rajasthan, India, and has a total geographical area of 671 hectares with 4665 people, according to the census 2011. The surveyed area occupies around 868304.9 m². It has a semi-arid climate with three seasons: winter, summer and monsoon. Temperature ranges from as cool as 5 °C in winters and as high as 48 °C in summers. The monsoon months range from June to September, with an average rainfall of 942.3 mm in Jaipur districts. The average elevation is 360 m from sea level. The area is covered with highly undulating hills of Jamwa Ramgarh, Viratnagar and Shahpur. The area is covered with younger and older alluvium, sand and clay [50]. Forest near Nayla is stretched on Aravalli hills. Forest of Tropical Dry Deciduous Forest is majorly present near the study area. Some are *Anogeissus pendula*, *Anogeissus latifolia*, *Acacia catechu*, *Terminalia tomentosa*, *Terminalia balerica*, *Terminalia arjuna*, *Boswellia serrata*, *Dendrocalamus strictus*, and *Lanea grandis* (Fig. 1).

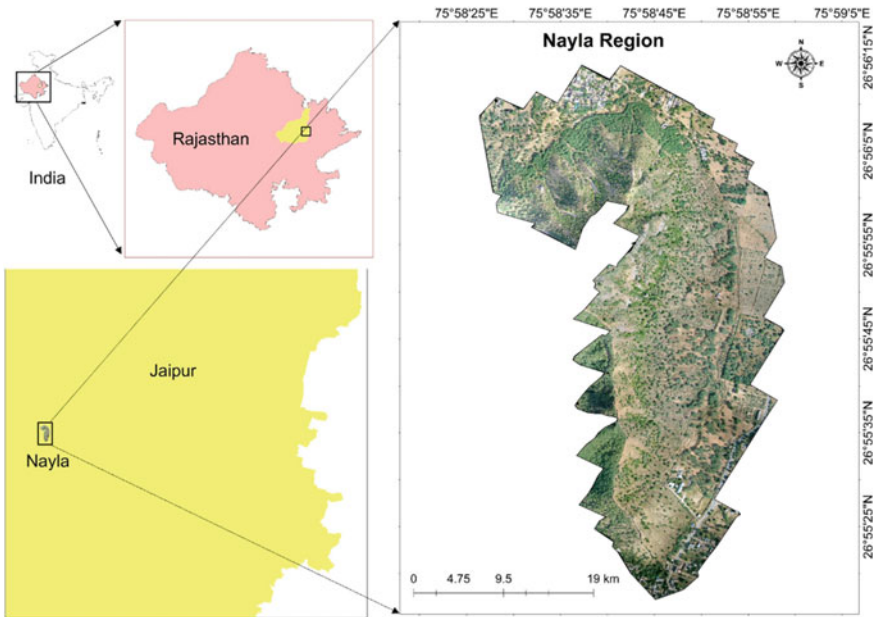


Fig. 1 The study area map of the Nayla region (Area = 868,304 m²)

2.2 Datasets and Tools Used

Google earth engine (GEE) [51, 52], a web-based platform for processing satellite imageries, was incorporated to prepare the land use land cover maps of the Nayla region. The datasets used in this study are Sentinel 2 MSI Level 1-C imagery at 10 m spatial resolution, obtained for November 2020 using a JavaScript algorithm. The Nayla region's high-resolution UAV ortho imagery (0.1 m) was obtained from a field survey in November 2020.

2.3 Methodology

The following steps were performed to prepare the land use land cover maps.

1. High-resolution UAV imagery of Nayla was ingested in the GEE asset manager.
2. Sentinel 2 MSI Level 1C imagery was filtered for November.
3. Training datasets, namely Barren, Trees, Rocks, Urban and Shadow, were created.
4. Around 590 points and 173 points were selected for preparing total training datasets for UAV and Sentinel 2, respectively.
5. Out of which, 70% were kept for training, and 30% were kept for testing.
6. A random forest classifier with 50 decision trees was used to classify the UAV and Sentinel 2 datasets.
7. The accuracy assessment was performed using the remaining 30% testing dataset.
8. The overall methodology is shown in Fig. 2.

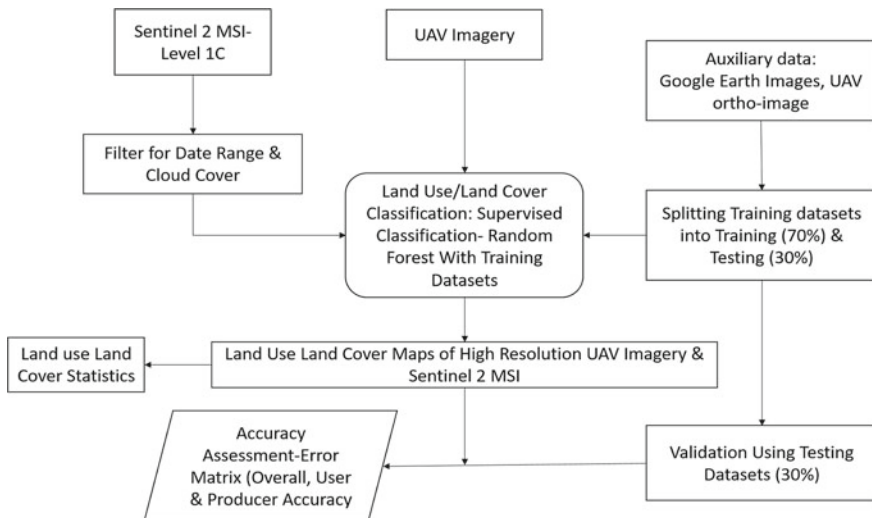


Fig. 2 Overall methodology used in the study

The following steps were performed to prepare the Forest Canopy Density maps and Tree Count Map using UAV data.

1. The object-based classification was performed in eCognition software.
2. Reclassification was done to make 5 classes.
3. For tree count sample data set of tree canopy was given as sample set.
4. Prediction for tree count was done.

3 Results and Discussion

3.1 LULC Comparison of Sentinel-2 (S2) and UAV (0.04 m Spatial Resolution Data)

The high-resolution satellite data proves good for monitoring, managing and making policies for a sustainable future. The LULC for the Nayla region was prepared using both UAV and Sentinel 2. The study further tries to differentiate the classifications performed on high-resolution UAV datasets and mid-range resolution Sentinel 2 datasets. Figure 3 shows the classified image of the Nayla region into 5 classes, namely, Barren, Tree, Shadow, Rocks and Urban, which comprises 868304.9 m² in total. Barren and tree class has been overestimated in Sentinel 2 data compared to the UAV dataset. The area distribution of each class is shown in Table 3. The estimation using Sentinel 2 for Barren class is almost 40,000 m² (5%) more than UAV, and in Trees class is 1,68,000 m² (20%) more than UAV. Whereas, as per Table 1, Shadow, Rocks and Urban class have been underestimated in Sentinel 2 data by 15%, 1%, and 6%, respectively. For any department's management and policy purposes, especially for urban management, agroforestry or plantation purposes, the difference is significant, particularly in the tree and shadow class. All the classification and Forest working plans and sustainable yields are monitored and managed with the help of mid-range spatial resolution like sentinel 2. Thus, a 15% to 20% difference from the actual case in these important classes would lead to an undervaluation of the sustainable management schemes (Figs. 3, 4 and Table 2).

Accuracy Assessment

The error matrix was prepared for both UAV (Table 1) and Sentinel 2 (Table 2) datasets. The overall accuracy and kappa coefficient for UAV are estimated to be 95.48% and 0.92, respectively and that for Sentinel 2 is estimated to be 86.54% and 0.82, respectively.

Table 1 Accuracy assessment for UAV dataset

	Class	Reference test information					Row total	User accuracy
		Barren	Tree	Shadow	Rocks	Urban		
Remote sensing classification	Barren	100	0	0	0	0	100	100.00
	Tree	0	49	4	0	0	53	92.45
	Shadow	0	1	5	0	0	6	83.33
	Rocks	0	0	0	2	0	2	100.00
	Urban	1	1	0	1	13	16	81.25
Column Total		101	51	9	3	13	177	
Producer Accuracy		99.01	96.08	55.56	66.67	100.00		

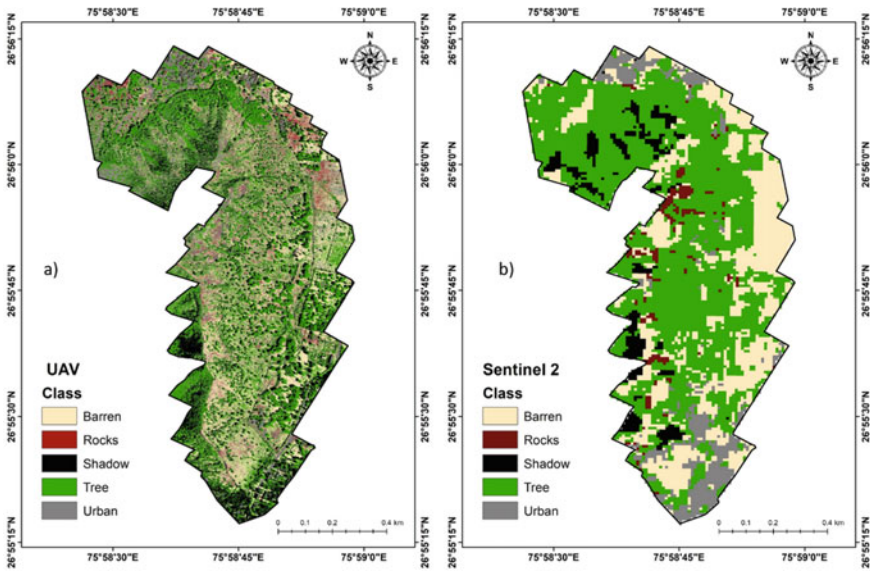


Fig. 3 Land use land cover map of Nayla region using **a** UAV and **b** Sentinel 2 dataset

3.2 Forest Canopy Density (FCD) Mapping Using UAV (0.04 m Spatial Resolution) Data

FCD is another important parameter to be kept in the account concerning forests. The canopy cover was estimated using UAV data and divided into 4 classes (Fig. 4b): very dense forest (FCD > 70%), moderately dense forest (FCD 40–70%), open forest (FCD 10–40%) and scrub forest (FCD < 10%). It is estimated that the majority (39%) of the region falls in scrub forest, followed by open forest, moderately dense forest and very

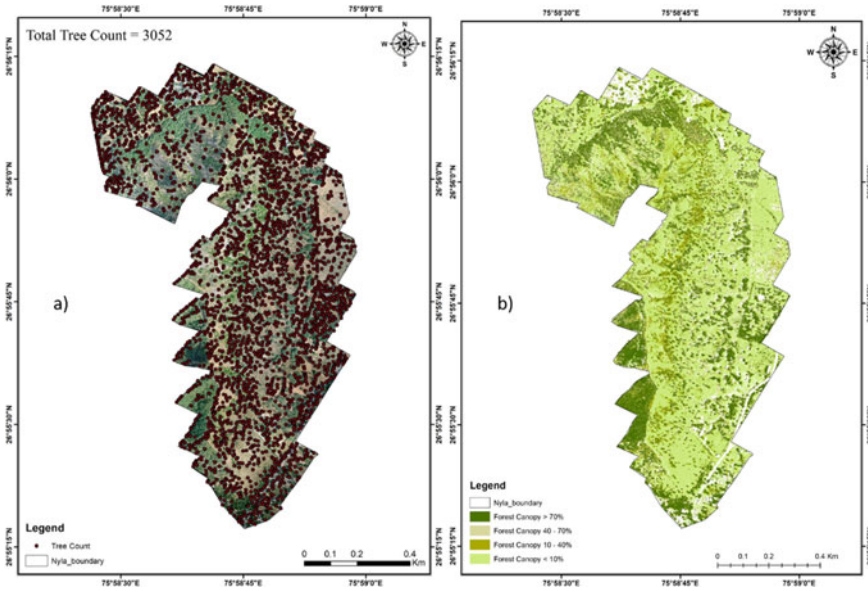


Fig. 4 Nayla area with a tree count map and b forest canopy density map

Table 2 Accuracy estimation for Sentinel 2 datasets

	Class	Reference test information					Row total	User accuracy
		Barren	Tree	Shadow	Rocks	Urban		
Remote sensing classification	Barren	11	2	0	0	1	14	78.57
	Tree	1	13	0	0	0	14	92.86
	Shadow	0	1	5	0	0	6	83.33
	Rocks	0	0	0	5	0	5	100.00
	Urban	2	0	0	0	11	13	84.62
	Column Total	14	16	5	5	12	52	
	Producer Accuracy	78.57	81.25	100.00	100.00	91.67		

dense forest, having area coverage of 13%, 11% and 4%, respectively, as shown in Table 4. This implies that sparse vegetation is predominant in the region. Furthermore, the remaining (33%) region is covered by built-up areas and settlements.

Table 3 Area distribution of Nayla region using UAV and Sentinel-2 data

Class	Area (m ²) covered as per UAV	Percentage	Area (m ²) covered as per Sentinel-2	Percentage
Barren	196,338	22.61	236,221	27.17
Tree	322,401	37.12	490,981	56.46
Shadow	181,318	20.88	49,107.1	5.65
Rocks	33,293.9	3.84	21,343.1	2.46
Urban	134,954	15.55	71,806.7	8.26
Total	868,304.9		868,304.9	

Table 4 Canopy Class distribution of Nayla region using UAV data

Class	Area (m ²)	Percentage
Forest canopy density > 70%	29448.07	3.4
Forest canopy density 40–70	93469.82	10.76
Forest canopy density 10–40%	115054.06	13.25
Forest canopy density < 10%	337200	38.84
Other (roads, settlements, etc.)	293132.96	33.75
Total area	868304.9	

3.3 Tree Count Mapping using UAV Data

Tree count is the unique approach to High-resolution data, a future technology that helps estimate the count of planted trees and track them over the years. In the study, the predicted tree count (Fig. 4a) is estimated to be 3052, with an overall accuracy of 82%. The reason for this accuracy is the different sizes of tree canopy diameter and, the merging of the canopies, less spacing between trees. This algorithm works best for planted trees like orchids and plantations. Therefore, accuracy can be further enhanced if the canopy is of equal size, meaning the forest is almost the same age.

4 Conclusion

The study proposes using a random-forest algorithm to perform a high-resolution classification of forest canopy cover from UAV and Sentinel-2 datasets in a Google Earth Engine cloud-based platform. The resulting image was classified into 5 land cover classes. The overall accuracy for the UAV and Sentinel 2 datasets was obtained as 95.5% and 86.5%, respectively. Furthermore, the estimation of the tree counts revealed that the region contains around 3052 trees in an overall area of 0.86 km². It is also estimated that the majority (39%) of the region has a canopy density of less than 10%, indicating scrub vegetation. These findings would help the policymakers,

government officials, and local people to stop desertification and advance better sustainable forest management in the forest areas.

References

1. Shang X, Chisholm LA (2013) Classification of Australian native forest species using hyperspectral remote sensing and machine-learning classification algorithms. *IEEE J Sel Top Appl Earth Obs Remote Sens* 7(6):2481–2489
2. Boschetti M, Boschetti L, Oliveri S, Casati L, Canova I (2007) Tree species mapping with Airborne hyper-spectral MIVIS data: the Ticino Park study case. *Int J Remote Sens* 28(6):1251–1261
3. Jansson G, Angelstam P (1999) Threshold levels of habitat composition for the presence of the long-tailed tit (*Aegithalos caudatus*) in a boreal landscape. *Landsc Ecol* 14(3):283–290
4. Fassnacht FE et al (2016) Review of studies on tree species classification from remotely sensed data. *Remote Sens Environ* 186:64–87
5. Gemmill FM (1995) Effects of forest cover, terrain, and scale on timber volume estimation with Thematic Mapper data in a Rocky Mountain site. *Remote Sens Environ* 51(2):291–305
6. Congalton RG, Green K, Tepley J (1993) Mapping old growth forests on national forest and park lands in the Pacific Northwest from remotely sensed data. *Photogramm Eng Remote Sens* 59(4):529–535
7. Pax-Lenney M, Woodcock CE, Macomber SA, Gopal S, Song C (2001) Forest mapping with a generalized classifier and Landsat TM data. *Remote Sens Environ* 77(3):241–250
8. Ekstrand S (1996) Landsat TM-based forest damage assessment: correction for topographic effects. *Photogramm Eng Remote Sens* 62(2):151–162
9. He HS, Mladenoff DJ, Radeloff VC, Crow TR (1998) Integration of GIS data and classified satellite imagery for regional forest assessment. *Ecol Appl* 8(4):1072–1083
10. Salovaara KJ, Theessler S, Malik RN, Tuomisto H (2005) Classification of Amazonian primary rain forest vegetation using Landsat ETM+ satellite imagery. *Remote Sens Environ* 97(1):39–51
11. Itten KI, Meyer P (1993) Geometric and radiometric correction of TM data of mountainous, forested areas. *IEEE Trans Geosci Remote Sens* 31(4):764–770
12. Frank TD (1988) Mapping dominant vegetation communities in the Colorado Rocky Mountain Front Range with Landsat Thematic Mapper and digital terrain data
13. Waser LT, Küchler M, Jütte K, Stampfer T (2014) Evaluating the potential of WorldView-2 data to classify tree species and different levels of ash mortality. *Remote Sens* 6(5):4515–4545
14. Immitzer M, Atzberger C, Koukal T (2012) Tree species classification with random forest using very high spatial resolution 8-band WorldView-2 satellite data. *Remote Sens* 4(9):2661–2693
15. van Lier OR, Fournier RA, Bradley RL, Thiffault N (2009) A multi-resolution satellite imagery approach for large area mapping of ericaceous shrubs in Northern Quebec, Canada. *Int J Appl Earth Obs Geoinf* 11(5):334–343
16. Wang L, Sousa WP, Gong P, Biging GS (2004) Comparison of IKONOS and QuickBird images for mapping mangrove species on the Caribbean coast of Panama. *Remote Sens Environ* 91(3–4):432–440
17. Shen X, Cao L (2017) Tree-species classification in subtropical forests using airborne hyperspectral and LiDAR data. *Remote Sens* 9(11)
18. Dalponte M, Bruzzone L, Gianelle D (2012) Tree species classification in the Southern Alps based on the fusion of very high geometrical resolution multispectral/hyperspectral images and LiDAR data. *Remote Sens Environ* 123:258–270
19. Vyas D, Krishnayya NSR, Manjunath KR, Ray SS, Panigrahy S (2011) Evaluation of classifiers for processing Hyperion (EO-1) data of tropical vegetation. *Int J Appl Earth Obs Geoinf* 13(2):228–235

20. Becker BL, Lusch DP, Qi J (2007) A classification-based assessment of the optimal spectral and spatial resolutions for Great Lakes coastal wetland imagery. *Remote Sens Environ* 108(1):111–120
21. Wu C, Niu Z, Tang Q, Huang W (2008) Estimating chlorophyll content from hyperspectral vegetation indices: Modeling and validation. *Agric For Meteorol* 148(8–9):1230–1241
22. Treuhaft RN, Asner GP, Law BE, Van Tuyl S (2002) Forest leaf area density profiles from the quantitative fusion of radar and hyperspectral data. *J Geophys Res Atmos* 107(D21):ACL-7
23. Dalponte M, Bruzzone L, Vescovo L, Gianelle D (2009) The role of spectral resolution and classifier complexity in the analysis of hyperspectral images of forest areas. *Remote Sens Environ* 113(11):2345–2355
24. Nilsson M (1996) Estimation of tree heights and stand volume using an airborne lidar system. *Remote Sens Environ* 56(1):1–7
25. Ørka HO, Næsset E, Bollandsås OM (2010) Effects of different sensors and leaf-on and leaf-off canopy conditions on echo distributions and individual tree properties derived from airborne laser scanning. *Remote Sens Environ* 114(7):1445–1461
26. Ørka HO, Næsset E, Bollandsås OM (2009) Classifying species of individual trees by intensity and structure features derived from airborne laser scanner data. *Remote Sens Environ* 113(6):1163–1174
27. Magnussen S, Næsset E, Gobakken T (2010) Reliability of LiDAR derived predictors of forest inventory attributes: a case study with Norway spruce. *Remote Sens Environ* 114(4):700–712
28. Naesset E (1997) Estimating timber volume of forest stands using airborne laser scanner data. *Remote Sens Environ* 61(2):246–253
29. Naesset E (1997) Determination of mean tree height of forest stands using airborne laser scanner data. *ISPRS J Photogramm Remote Sens* 52(2):49–56
30. Mitchard ETA et al (2012) Mapping tropical forest biomass with radar and spaceborne LiDAR in Lopé National Park, Gabon: overcoming problems of high biomass and persistent cloud. *Biogeosciences* 9(1):179–191
31. Mlambo R, Woodhouse IH, Gerard F, Anderson K (2017) Structure from motion (SfM) photogrammetry with drone data: a low cost method for monitoring greenhouse gas emissions from forests in developing countries. *Forests* 8(3):68
32. Goodbody TRH, Coops NC, Marshall PL, Tompalski P, Crawford P (2017) Unmanned aerial systems for precision forest inventory purposes: a review and case study. *For Chron* 93(1):71–81
33. Tang L, Shao G (2015) Drone remote sensing for forestry research and practices. *J For Res* 26(4):791–797
34. Paneque-Gálvez J, McCall MK, Napoletano BM, Wich SA, Koh LP (2014) Small drones for community-based forest monitoring: an assessment of their feasibility and potential in tropical areas. *Forests* 5(6):1481–1507
35. Onishi M, Ise T (2021) Explainable identification and mapping of trees using UAV RGB image and deep learning. *Sci Rep* 11(1):1–15
36. Akar Ö (2018) The Rotation Forest algorithm and object-based classification method for land use mapping through UAV images. *Geocarto Int* 33(5):538–553
37. Liu T, Yang X (2015) Monitoring land changes in an urban area using satellite imagery, GIS and landscape metrics. *Appl Geogr* 56:42–54
38. Jebur MN, Mohd Shafri HZ, Pradhan B, Tehrany MS (2014) Per-pixel and object-oriented classification methods for mapping urban land cover extraction using SPOT 5 imagery. *Geocarto Int* 29(7):792–806
39. Agarwal S, Vailshery LS, Jaganmohan M, Nagendra H (2013) Mapping urban tree species using very high resolution satellite imagery: comparing pixel-based and object-based approaches. *ISPRS Int J Geo-Inf* 2(1):220–236
40. Foody GM (2004) Thematic map comparison. *Photogramm Eng Remote Sens* 70(5):627–633
41. Richards JA, Jia X (2006) Feature reduction. *Remote sensing digital image analysis: an introduction*, pp 267–294
42. Sun W, Heidt V, Gong P, Xu G (2003) Information fusion for rural land-use classification with high-resolution satellite imagery. *IEEE Trans Geosci Remote Sens* 41(4):883–890

43. Hussain E, Shan J (2016) Object-based urban land cover classification using rule inheritance over very high-resolution multisensor and multitemporal data. *GISci Remote Sens* 53(2):164–182
44. Colkesen I, Kavzoglu T (2017) The use of logistic model tree (LMT) for pixel-and object-based classifications using high-resolution WorldView-2 imagery. *Geocarto Int* 32(1):71–86
45. Goodin DG, Anibas KL, Bezymennyi M (2015) Mapping land cover and land use from object-based classification: an example from a complex agricultural landscape. *Int J Remote Sens* 36(18):4702–4723
46. Tehrani MS, Pradhan B, Jebuv MN (2014) A comparative assessment between object and pixel-based classification approaches for land use/land cover mapping using SPOT 5 imagery. *Geocarto Int* 29(4):351–369
47. Johnson BA (2013) High-resolution urban land-cover classification using a competitive multi-scale object-based approach. *Remote Sens Lett* 4(2):131–140
48. de Pinho CMD, Fonseca LMG, Korting TS, de Almeida CM, Kux HJH (2012) Land-cover classification of an intra-urban environment using high-resolution images and object-based image analysis. *Int J Remote Sens* 33(19):5973–5995
49. Franklin SE, Ahmed OS (2018) Deciduous tree species classification using object-based analysis and machine learning with unmanned aerial vehicle multispectral data. *Int J Remote Sens* 39(15–16):5236–5245
50. Bagrana B et al (1872) Forest blocks Jaipur, no 92
51. Gorelick N, Hancher M, Dixon M, Ilyushchenko S, Thau D, Moore R (2017) Google earth engine: planetary-scale geospatial analysis for everyone. *Remote Sens Environ*
52. Singh S, Dhasmana MK, Shrivastava V, Sharma V, Pokhriyal N (2018) Estimation of revised capacity in Govind Sagar reservoir using google earth engine and GIS, no May

Design and Method of an Agricultural Drone System Using Biomass Vegetation Indices and Multispectral Images



S. Meivel , S. Maheswari , and D. Faridha Banu 

Abstract Manual power is not sufficient to solve agricultural tasks. Heavy tasks are creating problems of soil contamination and seed contamination. It affected the plant after the locust and plant diseases spread. Drone mapping technology and the classification of DSM ortho mosaic image techniques provided the solutions to the problems. Vegetation indices helped with the identification of plant growth with the help of a drone. Drone mapping and surveys capture hyperspectral images. The images can be calculated using pix4Dmapper. The process is based on initial processing in stage 1, point clouding, meshes generation in stage 2, generation of the index, and DSM and ortho mosaic images in stage 3. We converted 1200 multispectral images and calculated vegetation index values. We measured plant height, plant temperature, the distance between plants, growth vegetation, the soil index of the agricultural land, the water index of the agricultural land, the disease index of the agricultural land, and the vegetation index of the agricultural land. This research proposed identifying the vegetation index on a single agricultural land using an NDVI multispectral image and a hyperspectral image (Geli et al. [1]). We utilized some vegetation indices using drone mapping. The research work started with multispectral image analysis. We collected over 1200 multispectral images in Tif format. It includes NIR band images, Red_edge band images, Green band images, Blue band images, and Red band images. All images are analyzed and tested for calculating vegetation indices of different agricultural land. We have extracted and classified remote sensing images of the agricultural land in a different direction [2]. In the future, we can find the vegetation value of agricultural land and plants using multispectral thermal images

S. Meivel (✉)

Department of Electronics and Communication Engineering, M. Kumarasamy College of Engineering, Thalavapalayam, Karur, Tamil Nadu 639113, India
e-mail: meivels.ece@mkce.ac.in

S. Maheswari

Department of Electrical and Electronics Engineering, Kongu Engineering College, Thoppupalayam, Perundurai, Tamilnadu 638060, India

D. Faridha Banu

Department of Electronics and Communication Engineering, Sri Eshwar College of Engineering, Coimbatore, Tamilnadu 641202, India

for deciding on water irrigation for agricultural places. Our outcome results are displayed as the following: plant growth areas, diseased plant areas, locust damaged plant areas, water detection areas, and soil quality index using the Vegetation index.

Keywords Drone mapping · Remote sensing · Vegetation indices · Spraying automation · Pix4D mapper

1 Introduction

Nowadays, smart cameras are involved in agricultural systems for controlling processes, GPS mapping [3], image processing, and precision farming with automation of fertilizer and pesticide services. We can reduce fuel and electricity usage whenever we use smart agricultural systems to apply NDVI and NIR image processing. NDVI image quality is established by combining the red and NIR channel pixel combinations [4]. This research focused on reducing CO₂, the environmental impact [5], and the cost of the agricultural system [6]. Various databases and precision working are integrated into this system. It can monitor plant height, number, vegetation coverage levels, and biomass levels. The system can control plant disease using biosensors and an online field sprayer. Multispectral cameras used in drone surveys monitor soil and vegetation indexes. NDVI can separate the plant pixel and the soil pixel. Plant growth (from 620 to 660 nm) and low values for soil index are mostly reflected in NIR reflection [7]. Plant light absorption was supported by the chlorophyll activity for the NIR transition (from 660 to 740 nm). Reflection wavelengths of plants are 740 nm higher than soil, and NIR and NDVI = 780 nm are used. The optical path of the image is determined by pixel adjustment. Rabatal et al. described the NDVI + BPF filter combination principle for RED + NIR band mixing. The NDVI camera is needed for plant detection using a difference index with a red threshold of DIRT. Plant Forward Looking Infrared (FLIR) thermal cameras and NDVI cameras use low-cost agricultural systems to modify algorithms [8].

The wavelength of agricultural land changes every day when atmospheric conditions and environmental pollution change [9]. The Multispectral camera automatically adjusted the NIR image and NDVI images using the brightness and contrast of sunlight illumination [10]. All multispectral wavelengths of light images are varied and tabulated in Excel format using the SDCARD setup of the NDVI camera. We need to increase production by maintaining cultivation and controlling irrigation systems using a Drone automation system [11]. The field is monitored using various image sensors (NDVI and NIR) in all atmospheric situations. The NDVI sensor captured the irrigation area and Disease areas for solving the agricultural problem without manpower. The system is supported for predicting the damage of plants, sprayer control, and saving the data in the daily database. We utilized vegetation indices [12] like NDVI—Normalized difference vegetation

index, RVI—ratio vegetation index, MSR—Modified simple ratio, TVI—Transformed Vegetation Index, MTVI—Modified Triangular Vegetation Index 1 and 2, GNDVI—Green Normalized Difference Vegetation Index, EVI—Enhanced Vegetation Index, SAVI—Soil Adjusted Vegetation Index, LCI—Leaf Chlorophyll Index, LAI—Leaf Area Index, TSAVI—Transformed Soil Adjusted Vegetation Index, WdVI—Weighted difference vegetation index, NDWI—Normalized Difference Water Index, MNDWI—Modified Normalized Difference Water Index, WRI—Water Ration Index, SWI—Soil Water Index, AWDI—Alternate Wet and Dry Irrigation index, and NDMI—Normalized Difference Moisture Index [13].

2 Literature Survey

In Wu et al.'s paper [14], they described remote sensing-based agricultural crop monitoring. This research is used for determining key food production systems. The paper described the crop watch structure and methodology, preprocessing, and crop condition monitoring. NDVI, VHI, VCI, and TCI vegetation indices were simulated and estimated as crop averages. The paper explained the estimation of crop yield and production for food availability. Cropping intensity is estimated and monitored for the food supply. Cropping information is calibrated and validated using data management.

Giordan et al. [15] published a paper on the investigation of landslides using low-cost remote sensing for high-resolution using UAV. The paper described drone path planning and data processing. Case study of the San Germano rockslide and the PIAN DELLA MUSSA landslide described in this paper. The paper analyzed rockslide vegetation and the methodology of UAV camera view [1]. On March 7, 2014, all data were mapped into a 3D model. Landslide measurements and rockslide measurements are analyzed using drone mapping. The geomorphological map of the Pian Della Mussa landslide aided in the detection of rock cracking and plant lines using drones.

Joyce et al. [16] described LiDAR mapping and RADAR image data technologies. Drone LIDAR technology in RADAR technology is used for Drone mapping and automation of airborne landing and takeoff positions. The paper explained geological hazard assessment with landslides and erosion. It gave details about synthetic aperture radar and seismic and tectonic hazards. It mentioned LIDAR usage from 2004 to 2012. It determines floods and tsunamis in target areas. It compared LIDAR's working functions for checking flooded areas using the synthetic aperture of RADAR.

Mendes et al. [17] described photogrammetry with UAV surface models. It described the survey camera, the Canon IXUS 127, for UAV path planning. It described field tests, image acquisition, and its processing. The paper displayed the ortho mosaic generated by Micmac, PS, pix4D, and Agisoft. It mentioned point cloud places using all software. It identified plastic plates using a derivation of the

Root Mean Square. The results show a survey of plastic places using ortho mosaic and point clouds.

The reference paper [18] described the use of unmanned aerial vehicles (UAVs) for landslide mapping and deformation analysis. It described a digital elevation model (DEM) for detecting high-resolution UAV images. The paper provided a case study about data acquisition from an experimental view. The UAV mapping was captured by a Nikon 800 camera on an LTBT aircraft. The paper described a method of object-oriented analysis of landslide OOA and semi-automatic detection. It explained digital image correlation methods for displacement using NCC calculation. All the results are displayed by using landslide recognition with the classification and deformation computations using UAV images.

The Landslide ArcGIS Toolbox with a landslide zone called Model Builder as described in the [19] paper. The paper produced an area of the result. The paper elaborated on the geological setting of the study area. An extract of the geological map depicts the region between the Germanasca Valley, the Piedmont Region, and Northwest Italy. The methodology for the mapping of morphometric factors was introduced in those study places. Using the statistical analysis, the author received the index for the landslide susceptibility map. The Landslide Susceptibility Map was validated and tested using Matlab, and the result plotted the affected area by a landslide.

The Vasuki et al. [20] paper described semi-automatic mapping of geological structures using UAV images. The paper analyses the rock surface images with high resolution. This topic covered data acquisition using UAV images and analyzed the photogrammetry data. The paper explained fault map generation using feature extraction and first, second, and third stage segment linking. The methods compared the semiautomatic fault map with the manual interpretation of the mapping. It described automated 3D structure analysis. It compared orientation data and field measurements of 3D analysis.

Westoby et al. [21] paper described “Structure-from-Motion” photogrammetry. It provided an outline of a low-cost photogrammetric technique for obtaining datasets of high resolutions termed “structure from motion” [SfM]. The paper described all photogrammetric survey methods with SfM methods. Image acquisition and keypoint extraction are implemented in the SfM workflow. The paper compared terrestrial laser scanning using acquisition, processing, and results. The paper’s author identified water content in rock. A practical application involves the SfM output for a particular time and the establishment of a GCP network to facilitate the transformation to the extraction of metric data and the hypothesized effectiveness of an aerial for the terrestrial data collection method.

The paper described (2019) by Song et al. a remote sensing-based method [22] for drought monitoring using eigenvectors. The paper described the land surface temperature (LST) index [23], the temperature condition index (TCI), and the temperature-vegetation water stress index (T-VWSI). The paper compared the normalized difference vegetation index (NDVI) and the T-VWSI indices. The remote sensing data

and preprocessing using MODIS datasets were analyzed using LST with enhanced vegetation index (EVI) values. Agricultural meteorological methods describe and evaluate the drought eigenvectors. The construction of drought indices and optimal remote sensing drought index verified the DI values. T-VWSI results were used to build the best RSM-(T-VWSI) fitting model, which was then compared to R2 and error measures in months [24]. The paper analyzed NDVI mapping, T-VWSI mapping, and EVI for vegetation growth.

The Willem et al. [3] described multi-sensor NDVI data continuity for vegetation monitoring. AVHRR, MODIS, and VIIRS satellite images are described by NDVI indices. Atmospherically corrected MODIS data sets show the NDVI value as a constant [14]. Canopy reflectance and NDVI are simulated using AVHRR, MODIS, and VIIRS satellite images. Atmosphere radiative transfer simulations and cross-sensor surface NDVI translation are calculated and simulated in this paper. Multi-sensor NDVI values are correlated and scattered on multisensory NDVI. NDVI_Rayleigh, NDVI_Aerosol, and NDVI_H2O values and cross-sensor NDVI uncertainties are compared for AVHRR, MODIS, and VIIRS satellite images.

Li et al. [25] described that The Ground Reference Data method is used for climate and vegetation checking. Sample plots are compared in pixel number and some kilometers for land cover. The author analyzed statistical Analysis values of Landsat-7 ETM + and Landsat-8 OLI Spectral Band and The paper evaluated the Correlation Analysis of Vegetation Indices Derived from ETM + and OLI that is based on the LSWI, NBR, and NDVI values.

Taniguchi et al. [1] described Inter-sensor NDVI relationships for Soil ISO lines. The paper compared Soil ISO lines in different NDVI vegetation indices. The leaf area index (LAI) is equated to Soil ISO lines. The paper derived some steps of the inter-NDVI relationship. The author simulated the GEOSAIL and PROSPECT of Relative transfer models RTM. Soil parameters were checked and simulated using NDVI vegetation indices. The author compared NDVI derivation relationships in NDVI differences between the two sensors ($vB - vA$).

Teillet et al. [26] described radiometric processing Considerations using NDVI VIs. The results are computed using NDVI and plotted in the graph for FWHM of Generic sensor cases and FWHM of different sensor cases.

The paper described a comparison of other vegetation indices SAVI, MSAVI, RVI, and DVI. Miura et al. [10] described equations of spectral vegetation index and Translation formulas and Theorems. Solved Biomass indices theorems using Fourier series with DFT image algorithms.

Myneni et al. [27] described "FAPAR and NDVI". It prescribed NDVI statistical value and FAPAR Technical work. It displayed NDVI analysis and statistical rate of vegetation.

Pinto et al. [28] described the NDVI theorems and solved the biomass transfer theorems. The paper described the correlation analysis and RBSE percentage values of the NDVI vegetation indices.

Rahman et al. [29] used NDVI of agricultural land views to describe atmospheric conditions and weather location. It analyzed the solar spectrum values and remote sensing of drones.

3 Design of an Agricultural Drone

The proposed Drone design is having fertilizer and seed sowing method of mechanism. It has 6 wings and a single tank to spray fertilizer or pesticides when predicting vegetation indices using target images [25]. BLDC motors are balanced to drive the drone system with a tank. The stand of Taking off and land-on position is based on auto rotatable and fixed [30]. The eight nozzles are used for spraying pesticides and fertilizing the through the nozzles. The Seed sowing options are provided in the middle of the drone system and the system is automated with an IoT controller [31]. Mobile operated the drone to direct left movement, right movement, top movement, and land-on movement [32]. When detection of dry areas, auto adjusted type setup mechanism comes initial position and opened the drive to seeds sowing to the agricultural land. The drone setup was utilized and designed for seed sowing and fertilizing using vegetation calculation with multispectral images [33].

Methodology

Drone survey-based biomass vegetation indices are shown in Fig. 1. The following steps are provided the classified results after classified images and outcome results occurred.

1. Collected 1200 multispectral images from Drone
2. Analyze the Drone mapping
3. Extract the Ray Cloud
4. Processing
5. Feature Extraction of Vegetation Indices
6. Classification of the indices
7. Outcome result displayed.

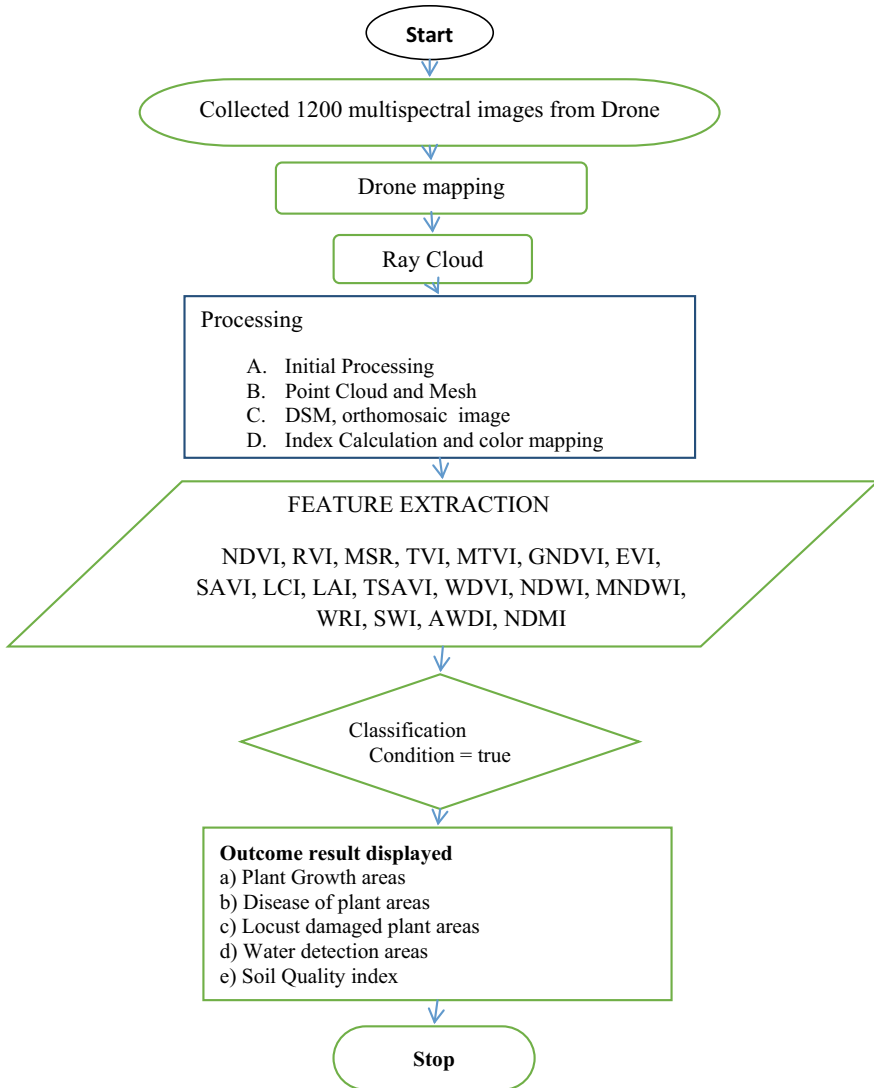


Fig. 1 Drone survey-based biomass vegetation indices

3.1 Drone Mapping



The drone mapping set depends upon no of Drone survey images from starting stage to the finishing stage. In Fig. 2, these mapping images have 915 images including the NIR band, Green band, Red band, and red_edge band. We can view every pointed image data using pix4dmapper [34]. This mapping technique merged all bands of image wavelengths in nm using the generation of reflectance mapping. The four bands Tif file have data like the wavelength of images, the reflectance of images, moisture in coloring, Temperature in coloring, water content level in coloring, plant vegetation in coloring, plant disease in coloring, and soil quality in coloring [35].

Starting images to ending images must be aligned with the same pixel due to maintaining equal pixel reading when activation of drone mapping [36]. All bands' wavelengths are in nm and mentioned minimum pixel value per band, maximum pixel value per band, average pixel value per band, Standard deviation of pixel per band, and variance of pixel per band after generated reflectance map. Here green band in 550 nm, NIR band in 790 nm, Red band in 660 nm, and red_edge in 735 nm [37]. Region views are shown from the index value, then select and draw in the target land.

3.2 Ray Cloud

The Ray cloud is the next step and is used for collecting tie points, point clouds, and point groups. In point groups, we can select unclassified images, ground images, road surface images [26], high vegetation images, building images if it is a building, and

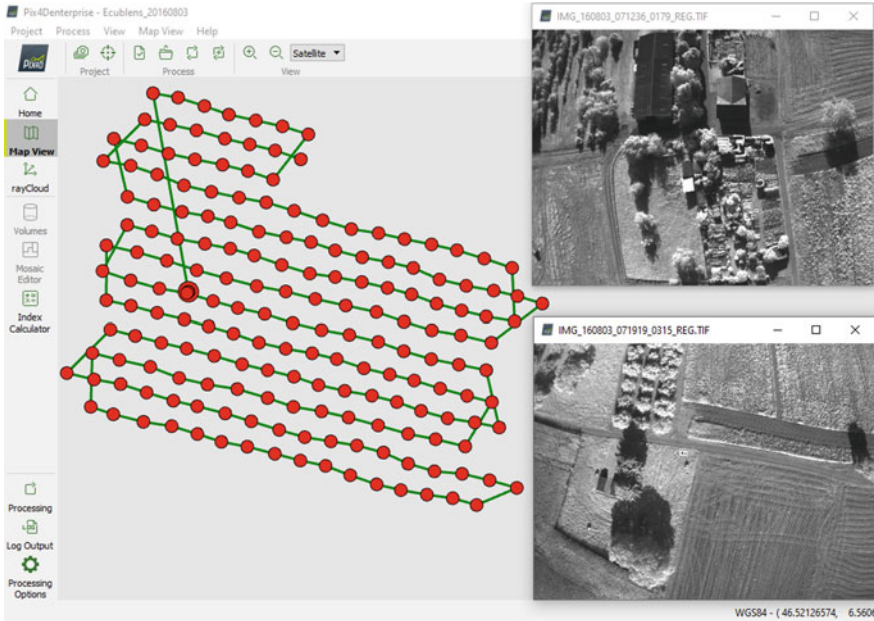


Fig. 2 Drone mapping

human-made objects. The Ray clouds images are shown in Fig. 3. Grass images are easily detected in this method [4]. This graph mapping shows a fully green color in 0–100% vegetation and blue color in dry soil. The grey color is shown in 3D for rotation of the 3D reflectance mapping. 915 image values are stored in single ray clouds and 3D mapping [38]. We can collect the source details like that the used camera type is Sequoia_4.0_1280×960 (NIR), and the Number of Automatic Tie Points is 1230. Initial Position [m]: 312144.16, 5154825.52, 553.87, Computed Position [m]: 312145.12, 5154825.27, 554.18, Initial Orientation (Omega, Phi, Kappa) [degree]: 2.03, 3.00. Initial Accuracy (Horizontal, Vertical) [m]: 2.03, 3.00 [39].

All the 1200 images are in the TIF file as NIR, Green, Red, and Red Edge. The images are calibrated using pix4dmapper and tested along the mapping route [40]. We can run 374,406 classification images in pix4dmapper. Drone mapping classifies point clouds. We can navigate and clip the target image location using pix4dmapper. After calibration, we can take the new images. The clouds of images are collected with multispectral data in single images and drone mapping with GPS location for doing analysis [41]. A single point is linked to several images, and all points are linked to some cloud cells. Ray Cloud mapping points were connected, calibrated, and tested in all 1200 images for merging NIR, Green, Red, and Red_edge [42]. The Mapping point of Ray Clouds in all 1200 images is shown in Fig. 4.

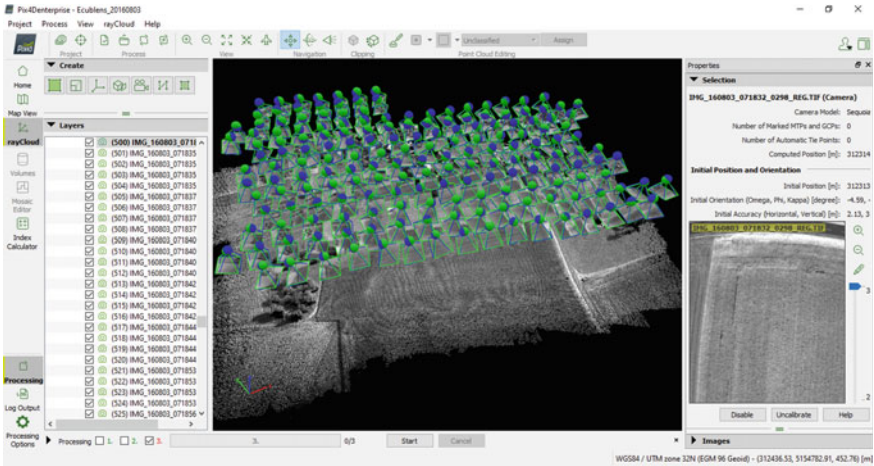


Fig. 3 Ray Clouds of 915 images

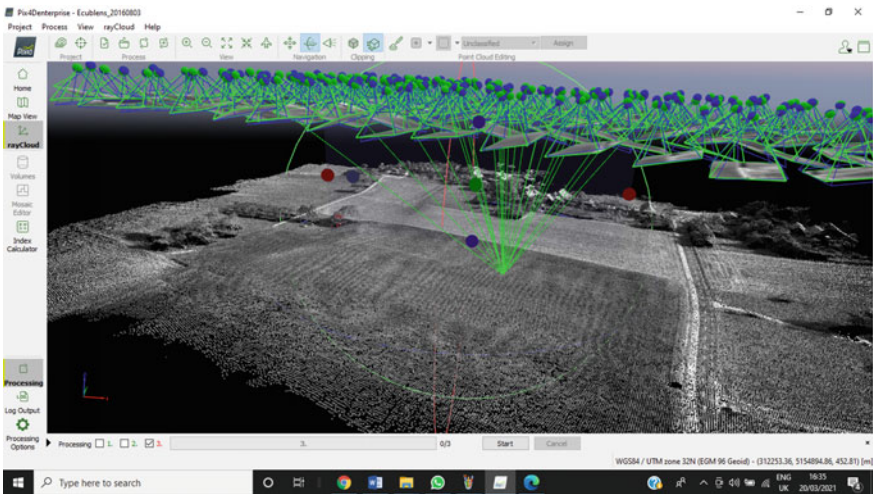


Fig. 4 Mapping point of ray clouds in all 1200 images

3.3 Processing

3.3.1 Initial Processing

When processing is started, the initial processing sets the full Key points image scale, matching aerial grid, and automated calibration [43].

3.3.2 Point Cloud and Mesh

This process sets classifying points for classification. We can generate a 3D textured mesh. The processing areas are calibrated [44].

3.3.3 DSM, Ortho Mosaic Image

We can set automatic GSD at 10.687 cm/pixel. The DSM ortho mosaic image is used to calibrate all index values [45].

3.3.4 Index Calculation

The NDVI of the Ortho mosaic image is shown in Fig. 5. The vegetation indices are calculated using the following equation.

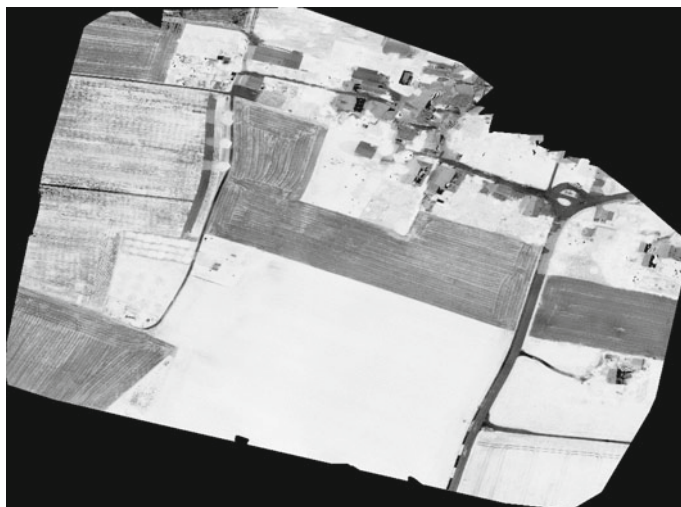


Fig. 5 NDVI of orthomosaic image

(a)	Normalized difference vegetation index (NDVI)	=	$(nir - red)/(nir + red)$
(b)	Ratio vegetation index (RVI)	=	nir/red
(c)	Modified simple ratio index (MSR)	=	$(nir - 445)/(red - 445)$
(d)	Triangular vegetation index (TVI)	=	$(0.5 * (120 * (nir - green) - 200 * (red - green)))$
(e)	Modified triangular vegetation index (MTVI)	=	$0.5 * (120 * (nir - green) - 200 * (red_edge - green))$
(f)	Green normalized difference vegetation index (GNDVI)	=	$(nir - green)/(nir + green)$
(g)	Enhanced vegetation index (EVI)	=	$2.5 * (nir - red)/((nir + 6 * red - 7.5 * 0.5) + 1)$
(h)	Soil adjusted vegetation index (SAVI)	=	$((nir - red)/(nir + red + 0.5)) * (1 + 0.5)$
(i)	Leaf chlorophyll index (LCI)	=	$(850 - red_edge)/(850 + 680)$
(j)	Leaf area index (LAI)	=	$((0.69 - ((nir - red)/(nir + red + 0.5)) * (1 + 0.5)))/0.59 * 1.5/0.91$
(k)	Transformed soil adjusted vegetation index (TSAVI)	=	$0.08 * (nir - 0.08 * red - 0.08)/((red + 0.08 * nir - 0.08) + 0.1 * 1 + 0.08^2)$
(l)	Weighted (near-infrared-red) difference vegetation index (WDVI)	=	$nir - (0.9034 * red)$
(m)	Normalized difference water index (NDWI)	=	$(nir + 70 - 1240)/(860 + 1240)$
(n)	Modification of normalized difference water index (MNDWI)	=	$(green - 1.55)/(green + 1.55)$
(o)	Water ratio index (WRI)	=	$(green + red)/(nir + 0.5)$
(p)	Standardized water-level index (SWI)	=	$(nir - 0.100)/0.14$
(q)	Automated water extraction index (AWEI)	=	$4 * (green - 2.20) - (0.25 * nir + 2.75 * 1.60)$
(r)	Normalized difference moisture (Water) index (NDMI)	=	$(nir - 1600)/(nir + 1600)$

3.3.5 Color Mapping

This is classified into three types. They are equal areas. Equal spacing and Jenks. We can assign several classes, say $32 > 32$ classes is not possible in the application of `pix4dmapper` [46]. Color mapping classes are based on red, yellow, and green color mapping areas and atmospheres. The vegetation indices NDVI, RVI, MSR, TVI, MTVI, GNDVI, EVI, SAVI, LCI, LAI, TSAVI, WDVI, NDWI, MNDWI, WRI, SWI, AWDI, NDMI are classified using color mapping and After color mapping imaging of NDVI, RVI, MSR, TVI, MTVI, GNDVI, EVI, SAVI, LCI, LAI, TSAVI, WDVI, NDWI, MNDWI, WRI, SWI, AWDI, NDMI, we can get feature extraction

of the 915 images in a single clouding image [2]. All feature-extracted images [1] are displayed in Figures 6, 7, 8, 9, 10, 11, 12, 13, 14, 15, 16, 17, 18, 19, 20, 21, 22 and 23.



Fig. 6 Benchmarking of normalized difference vegetation index (NDVI): 2020

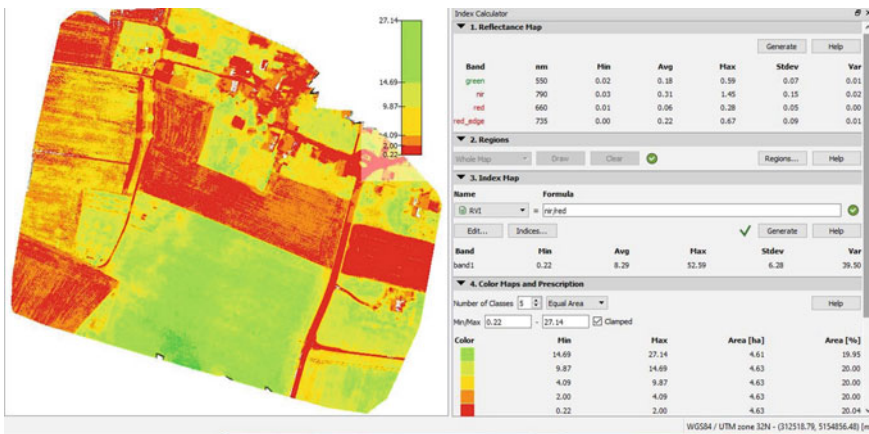


Fig. 7 Benchmarking of ratio vegetation index (RVI)

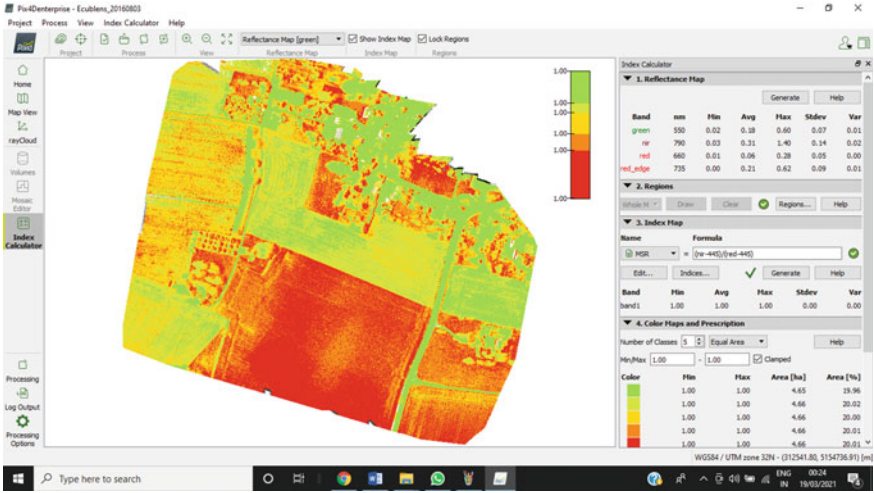


Fig. 8 Benchmarking of modified simple ratio index (MSR)

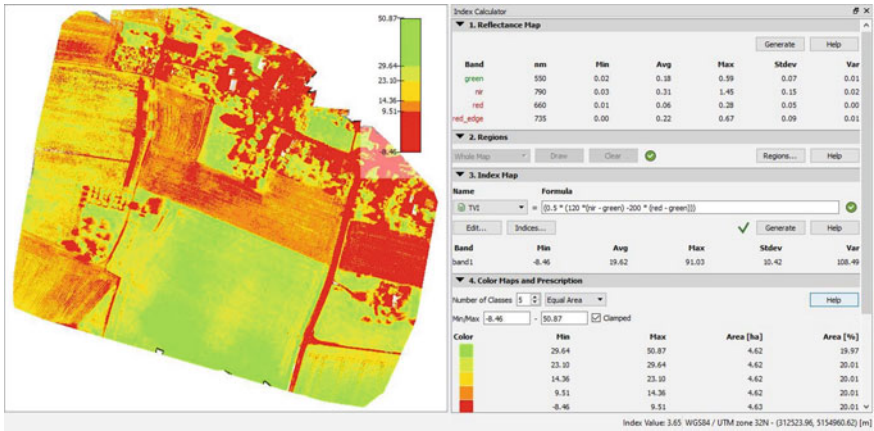


Fig. 9 Benchmarking of triangular vegetation index (TVI)

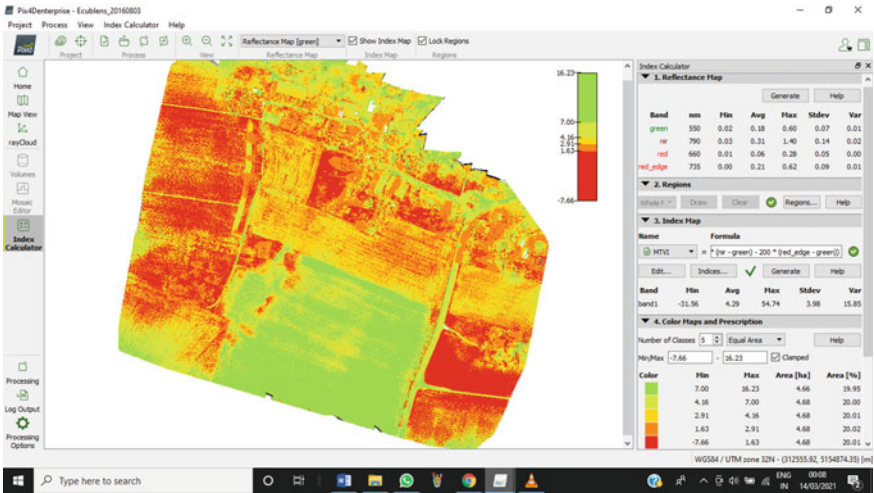


Fig. 10 Benchmarking of modified triangular vegetation index (MTVI)

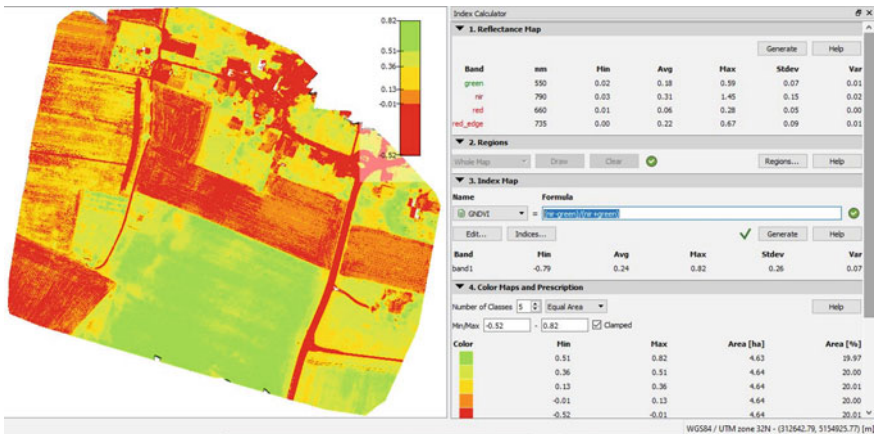


Fig. 11 Benchmarking of green normalized difference vegetation index (GNDVI)

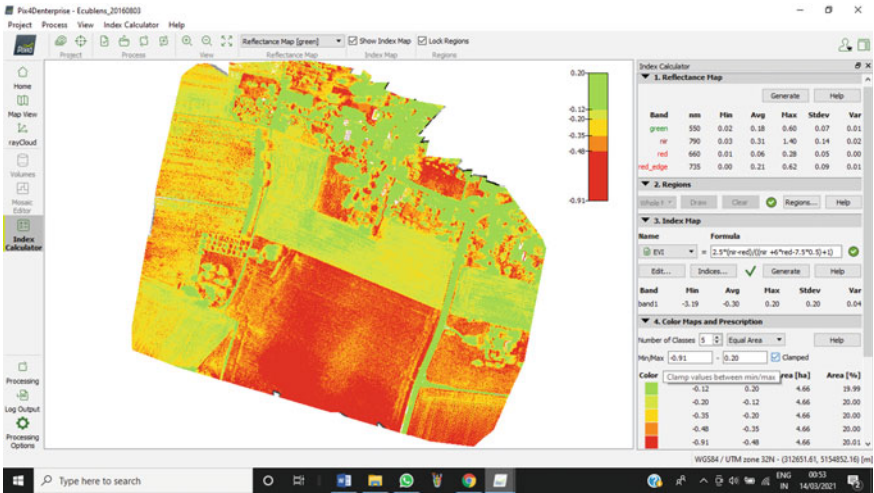


Fig. 12 Benchmarking of enhanced vegetation index (EVI)

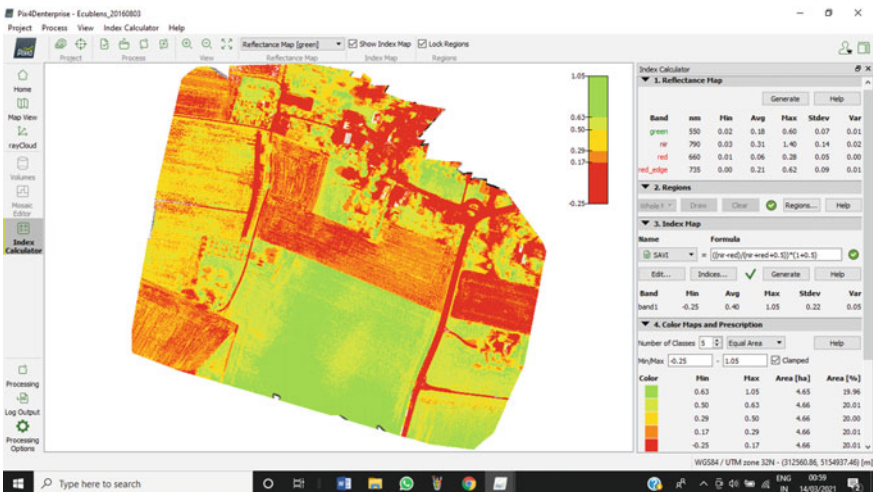


Fig. 13 Benchmarking of soil adjusted vegetation index (SAVI)

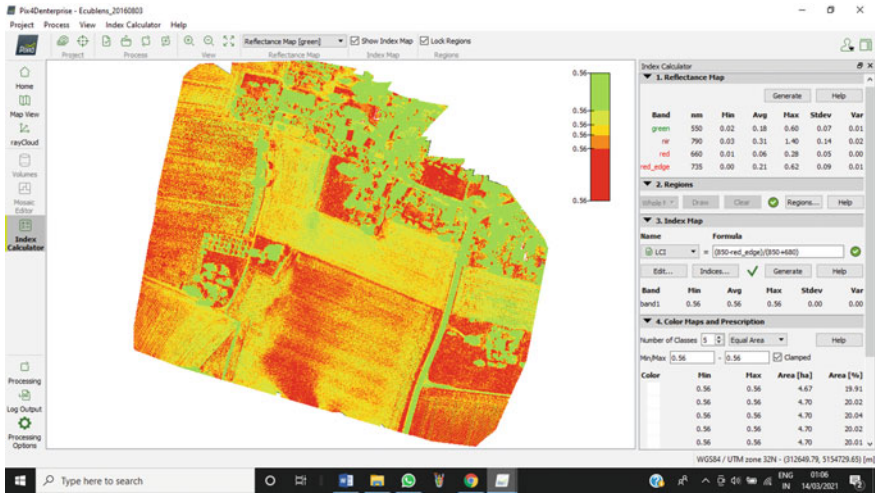


Fig. 14 Benchmarking of leaf chlorophyll index (LCI)

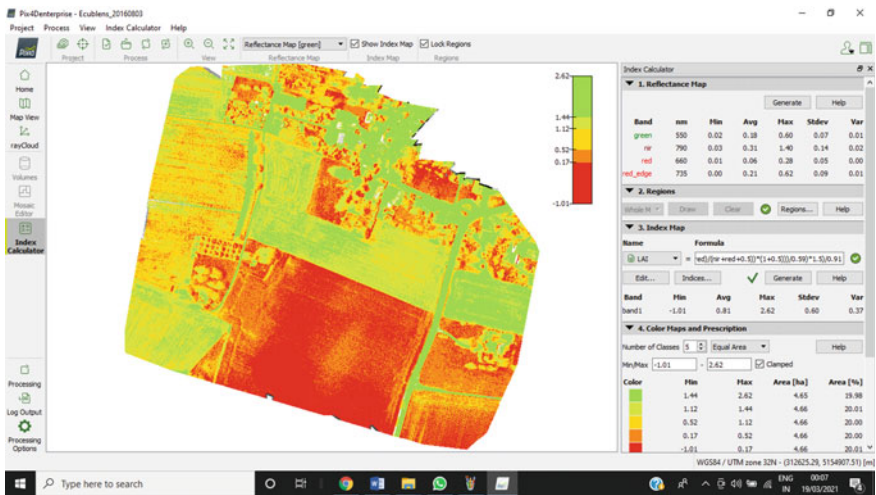


Fig. 15 Benchmarking of leaf area index (LAI)

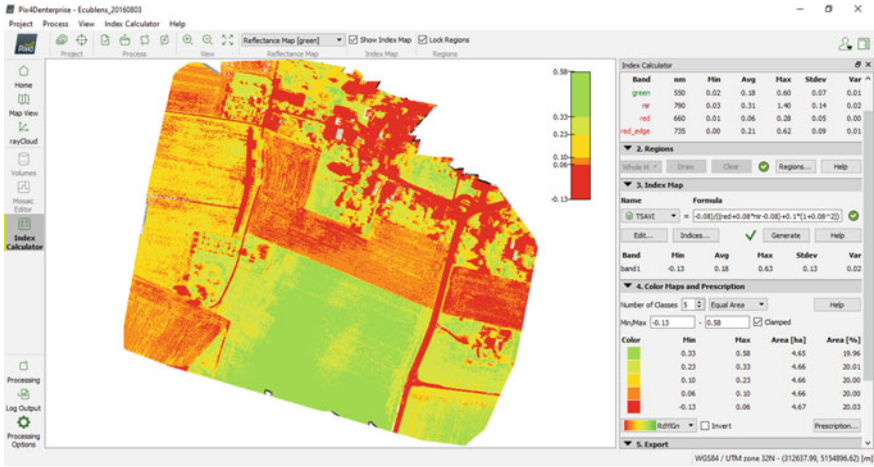


Fig. 16 Benchmarking of transformed soil adjusted vegetation index (TSAVI)

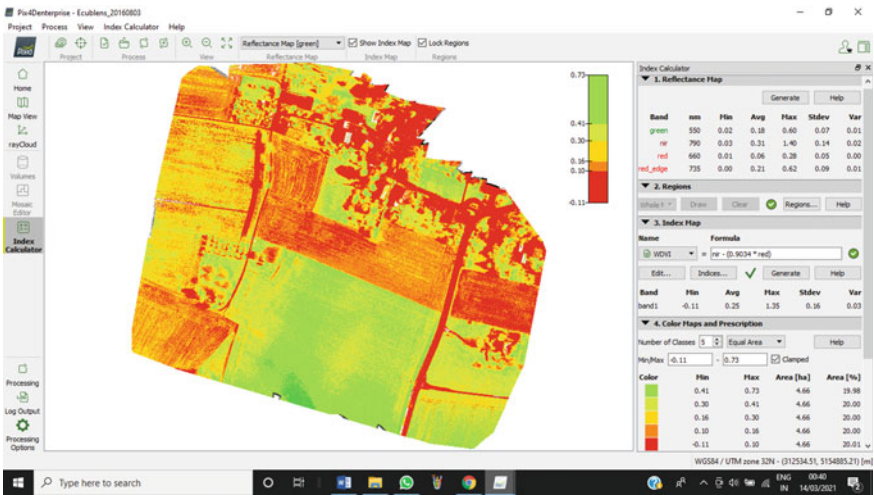


Fig. 17 Benchmarking of weighted (near-infrared-red) difference vegetation index (WDI)

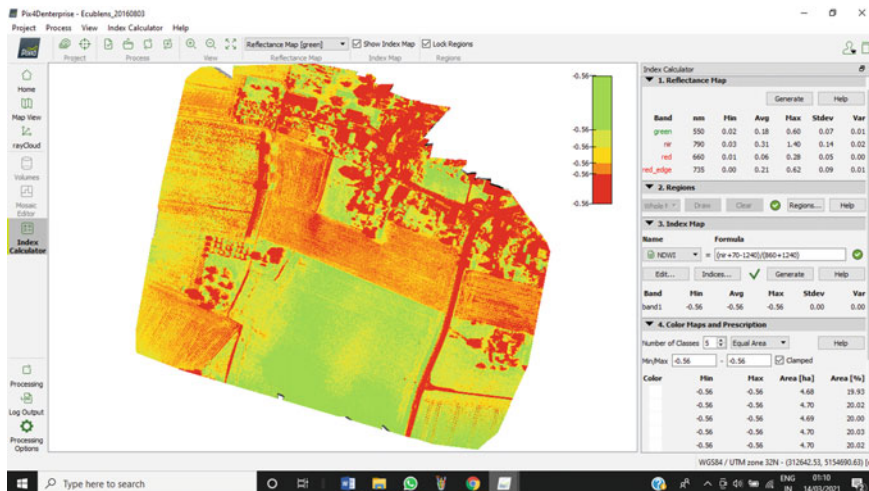


Fig. 18 Benchmarking of normalized difference water index (NDWI)

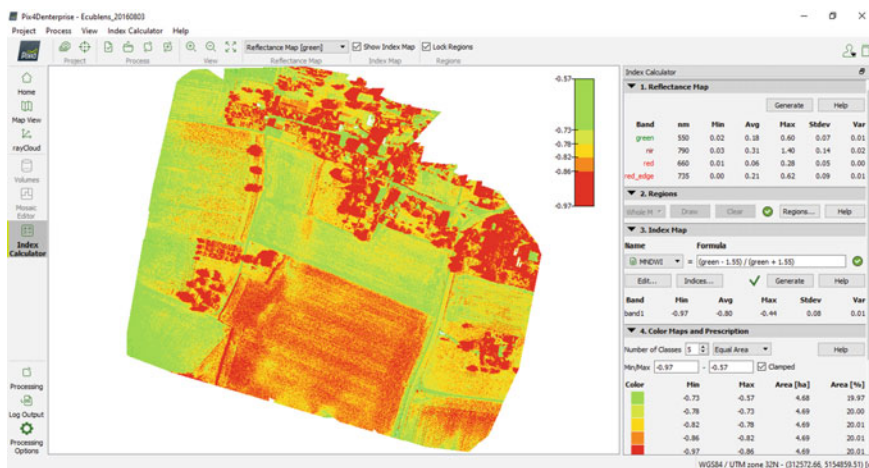


Fig. 19 Benchmarking of modification of normalized difference water index (MNDWI)

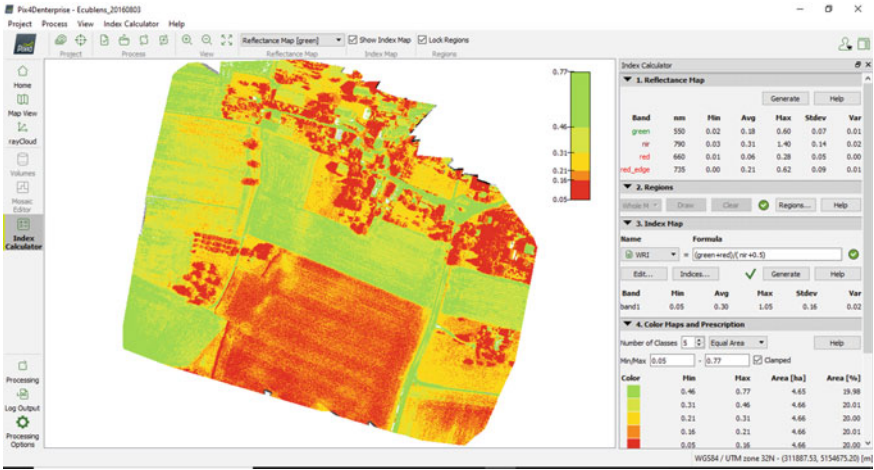


Fig. 20 Benchmarking of water ratio index (WRI)

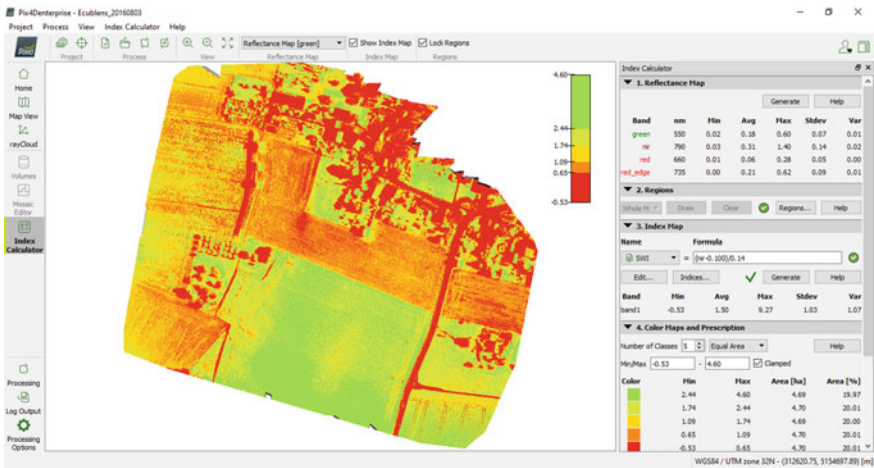


Fig. 21 Benchmarking of standardized water-level index (SWI)

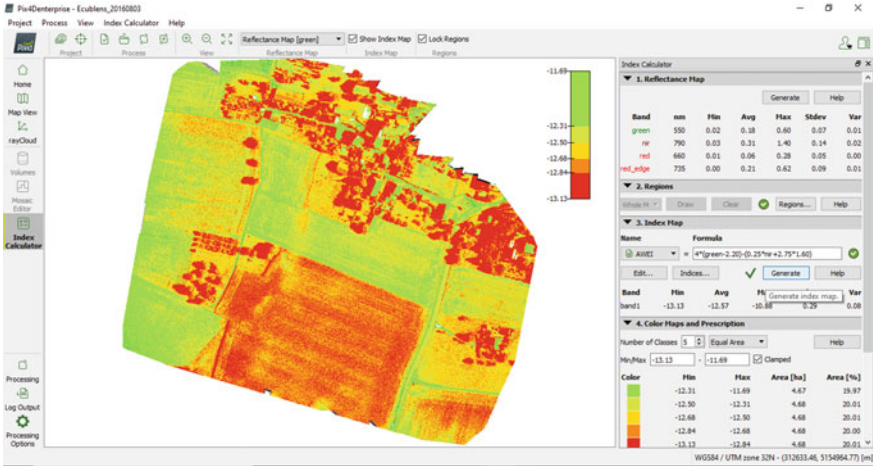


Fig. 22 Benchmarking of automated water extraction index (AWEI)

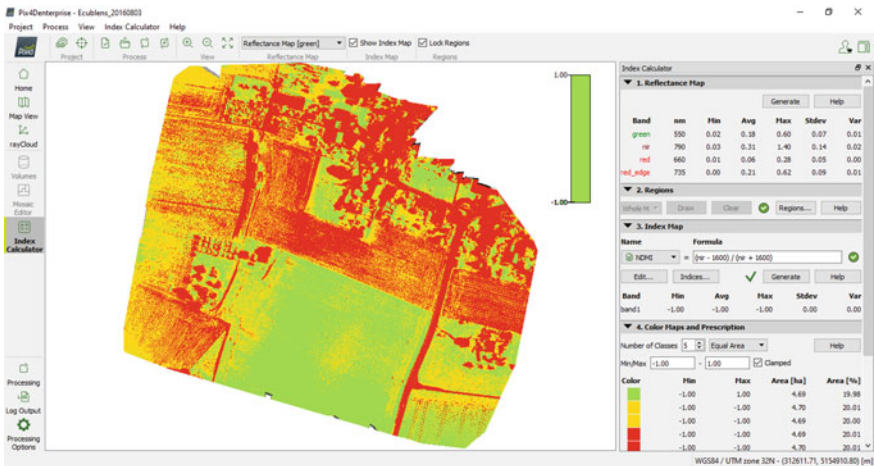


Fig. 23 Benchmarking of normalized difference moisture (water) index (NDMI)

3.4 Feature Extraction

3.4.1 Compared Plant Health Value Between in (20.07.2016 and 03.08.2016)

The Plant health value calculated in two days on 2016, See Figs. 24 and 25.

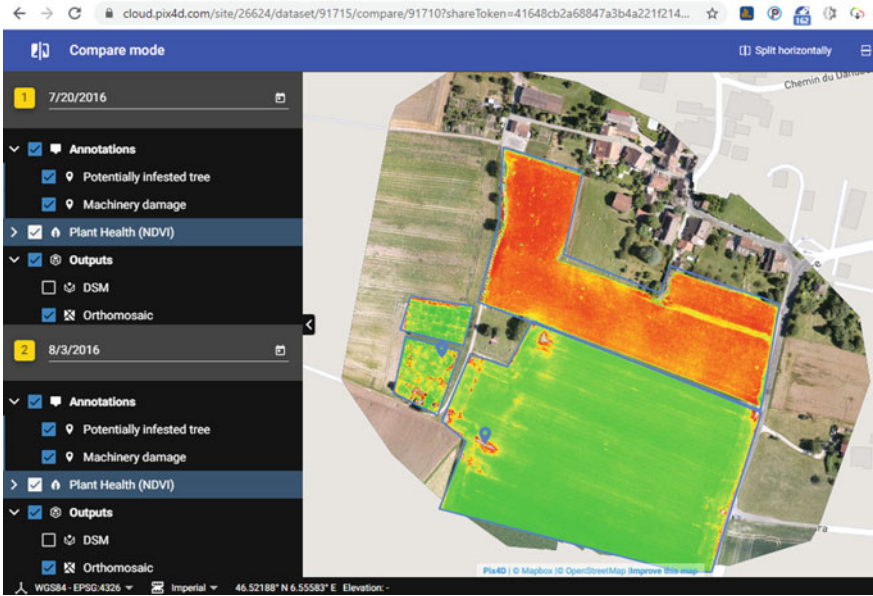


Fig. 24 Plant health value on 20.07.2016

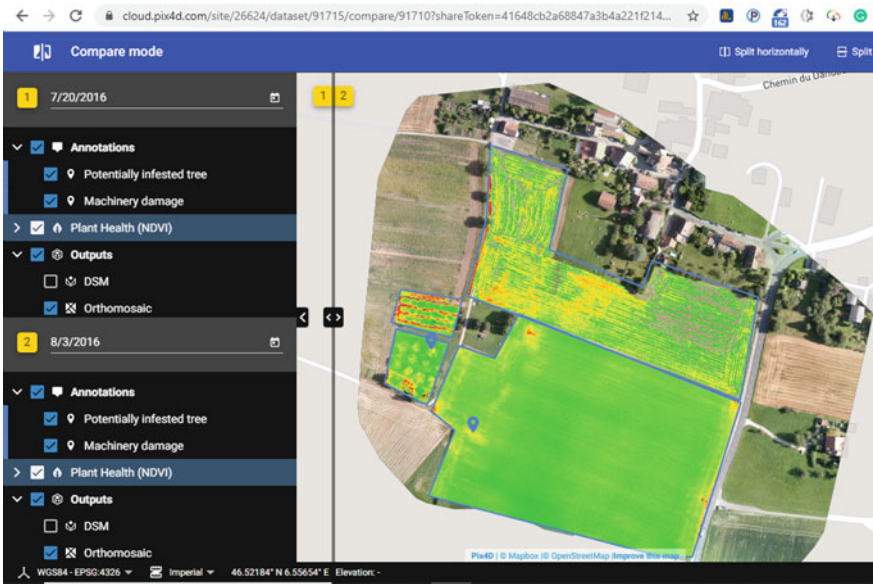


Fig. 25 Plant health value on 03.08.2016

3.5 Classifications of Vegetation Indices

Table 1 showed the value of Plant Growth Vegetation indices. Table 2 showed the Disease indices of the land. Table 3 showed the Locust damaged plant indices of the land. Table 4 showed the Soil quality indices of the land. Table 5 showed Water detection indices in surface of the land. The Classification of VIs value compared with decision value. This showed in Table 6.

Table 1 Plant growth vegetation indices [30]

S. no	VIs	Band	Min	Avg	Max	StdDev	Var
1.	NDVI	1	-0.64	0.63	0.96	0.26	0.07
2.	RVI	1	0.22	0.29	52.59	6.28	39.50
3.	MSR	1	1.00	1.00	1.00	1.00	0.00
4.	TVI	1	-8.46	19.62	91.03	10.42	108.49
5.	MTVI	1	-31.56	4.29	54.74	3.98	15.85

Table 2 Disease indices

S. no	VIs	Band	Min	Avg	Max	StdDev	Var
1.	NDVI	1	-0.64	0.63	0.96	0.26	0.07
2.	GNDVI	1	-0.79	0.24	0.82	0.26	0.07
3.	EVI	1	-3.19	-0.30	0.20	0.20	0.07
4.	SAVI	1	-0.25	0.40	1.05	0.22	0.05
5.	REDEGE	1	0.00	0.21	0.62	0.09	0.01
6.	LCI	1	0.56	0.56	0.56	0.00	0.00

Table 3 Locust damaged plant indices

S. no	VIs	Band	Min	Avg	Max	StdDev	Var
1.	NDVI	1	-0.64	0.63	0.96	0.26	0.07
2.	LAI	1	-1.01	0.81	2.62	0.60	0.37
3.	RVI	1	0.22	0.29	52.59	6.28	39.50
4.	GNDVI	1	-0.79	0.24	0.82	0.26	0.07
5.	SAVI	1	-0.25	0.40	1.05	0.22	0.05

Table 4 Soil quality indices

S. no	VIs	Band	Min	Avg	Max	StdDev	Var
1.	SQI	1	0.49	0.49	0.49	0.49	0.02
2.	SAVI	1	-0.25	0.40	1.05	0.22	0.05
3.	TSAVI	1	-0.13	0.18	0.63	0.13	0.02
4.	EVI	1	-3.19	-0.30	0.20	0.20	0.07
5.	WDVI	1	-0.11	0.25	1.35	0.16	0.03

Table 5 Water detection indices on surface [13]

S.no	VIs	Band	Min	Avg	Max	StdDev	Var
1.	NDVI	1	-0.64	0.63	0.96	0.26	0.07
2.	NDWI	1	-0.56	-0.56	-0.56	0.00	0.00
3.	MNDWI	1	-0.97	-0.80	-0.44	0.08	0.01
4.	WRI	1	0.05	0.30	1.05	0.16	0.02
5.	SWI	1	-0.53	1.50	9.27	1.03	1.07
6.	AWEI	1	-13.13	-12.57	-10.88	0.29	0.08
7.	NDMI	1	-1.00	-1.00	-1.00	0.00	0.00

3.5.1 Classification of VIs with decision value

See Table 6.

Table 6 Classification of VIs with decision value

Vegetation indices [4]	Decision value	Identification
Normalized difference vegetation index (NDVI)	1 to 0 -0.1 to 0.1 0.2 to 0.5 0.6 to 1.0	Water bodies Rocks, sand, or snow Shrubs and grasslands or senescing crops Dense vegetation or tropical rainforest
Standardized water-level index (SWI)	SWI > 2.0 SWI > 1.5 SWI > 1.0 SWI > 0.0 SWI < 0.0	Extreme drought Severe drought Moderate drought Mild drought Non drought
Soil quality index	SQI < 1.13 SQI = 1.1 to 1.45 SQI > 1.46	High-quality soil Moderate quality soil Low-quality soil
Ratio vegetation index (RVI)	<1 >1	Vegetation Non-vegetation

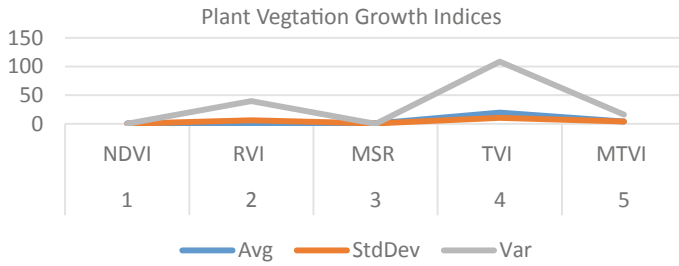
(continued)

Table 6 (continued)

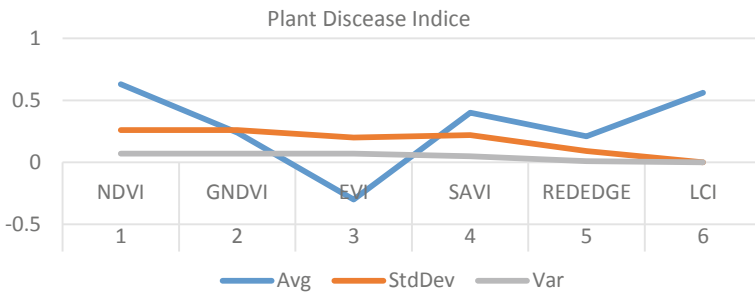
Vegetation indices [4]	Decision value	Identification
Modified simple ratio index (MSR)	0.0 to 0.5 0.5 to 1.20	40% vegetation 60% vegetation
Triangular vegetation index (TVI)	0–10 10–20	30 ⁰ triangular vegetation 80% triangular vegetation
Modified triangular vegetation index (MTVI)	1–3 3–8 8–10	Lower growth Higher growth Yield cultivation stage
Green normalized difference vegetation index (GNDVI)	–0.1 to 0.1 0.2 to 0.5 0.6 to 1.0	Depressed and aged vegetation Moderate vegetation Higher green vegetation
Enhanced vegetation index (EVI)	–1 to 0 0 to 1	Low vegetation quality Higher vegetation quality
Soil adjusted vegetation index (SAVI)	L = 0 L = 0.5 L = 1	High green vegetation Default—moderate green vegetation No green vegetation
Leaf chlorophyll index (LCI)	LCI = –0.5 to 0.5 LCI = 0.5 to 1.0	Found locust damaged areas No locust damaged areas
Leaf area index (LAI)	LAI < 4 LAI > 4	A good estimation of VI No estimation of VI
Transformed soil adjusted vegetation index (TSAVI)	0.1 – 0.5 0.6 – 1.0	Transformed soil No transformed soil
Weighted difference vegetation index (WDVI)	0.1 – 0.5 0.5 – 1.0	Found 50% LAI of green vegetation Found 100% LAI of green vegetation
Normalized difference water index (NDWI)	–0.0 to –0.6 0.6 to 1.0	Found 10% water index Found 60–100% water index
Modification of normalized difference water index (MNDWI)	Positive value Negative value	Water molecule here No water molecule here
Water ratio index (WRI)	>1 <1	Water content available No water content available
Automated water extraction index (AWEI)	Positive value Negative value	Water content is 100% Water content 5%
Normalized difference moisture (water) index (NDMI)	–2 to 0 0 to 1	No moisture content in the land Moisture content is available

4 Graph for Vegetation, Plant Disease, Locust Damage, Soil Quality, and Water Detection

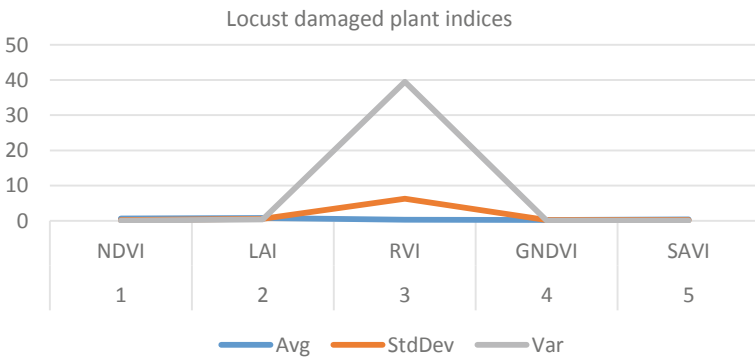
(a) Graph of Plant Vegetation indices



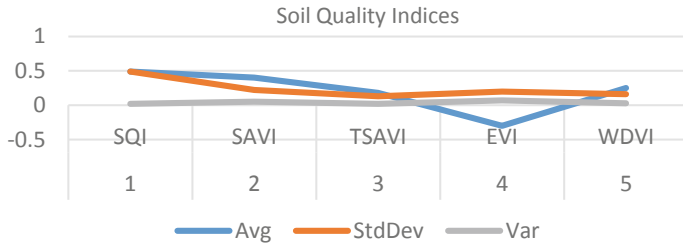
(b) Graph of Disease Indices



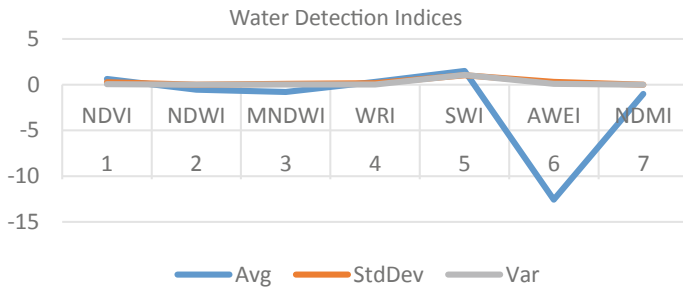
(c) Graph of locust damaged plant indices



(d) Graph of soil quality indices



(e) Graph of Water detection Indices



5 Final Result

The final result of proposed agricultural images are detected after feature extraction. The final results are shown in Figs. 26 and 27.

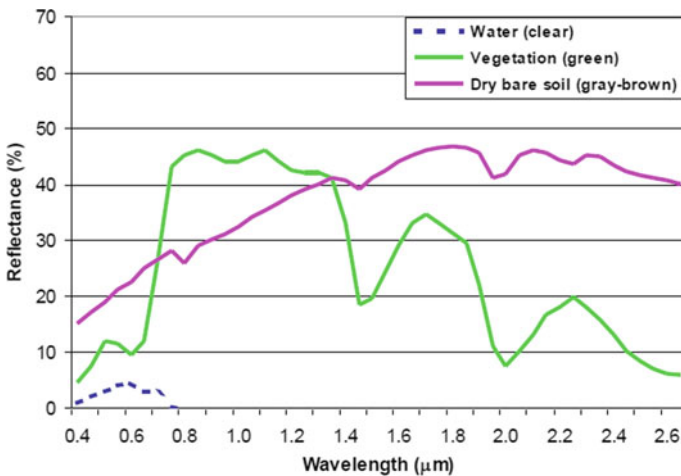


Fig. 26 Reflectance versus wavelength

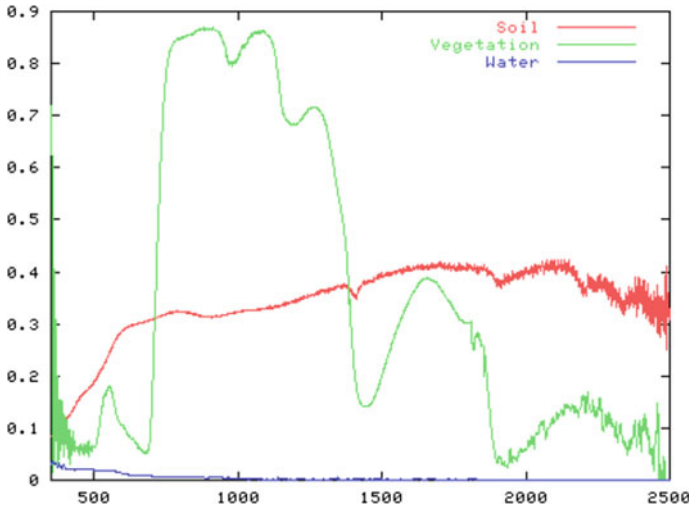


Fig. 27 Vegetation versus water versus soil

6 Future Work

This research work proposed the identification of vegetation index in different agricultural lands using NDVI multispectral cameras, hyperspectral cameras, and thermal cameras [47]. The multispectral camera for image collection has four frequency bands: green, red, red edge, and near-infrared (NIR).

- NDVI, RVI, MSR, TVI, and MTVI vegetation indices can detect the growth and vegetation of an agricultural plant with a minimum of 10 km.
- The NDVI, GNDVI, EVI, SAVI, Red_edge, and LCI vegetation indices measured the disease of agricultural plants with coverage spreading a minimum of 10 km.
- The NDVI, LAI, RVI, GNDVI, and SAVI vegetation indices can detect the spread and vegetation growth of an agricultural plant in an area of a minimum of 10 km.
- The SQI, SAVI, TSAVI, EVI, and WDVI soil quality indices can detect soil moisture and soil quality of an agricultural plant with a minimum of 10 km.
- The NDVI, NDWI, MNDWI, WRI, and SWI water detection indices can detect the water percentage and dry percentage of an agricultural plant with a minimum coverage of 10 km.

7 Conclusion

The outcome results are displayed as the Plant Growth Areas, Disease of Plant Areas, Locust Damaged Plant Areas, Water Detection Areas, and Soil Quality Index using the Vegetation Index. Reflectance vs. vegetation is 47% (approximate), reflectance

vs. soil quality is 48% (approximate) in 18 um wavelength, and reflectance vs. water is 4% (approximate) in 0.6um wavelength. Content is 4% with moisture in the agricultural land and it has dry bare soil. NDVI, RVI, MSR, TVI, and MTVI vegetation indices showed 90% (approximate) plant growth detection. NDVI, GNDVI, EVI, SAVI, Red_edge, and LCI were measured and showed an indication of 1% (approximate) plant diseases. NDVI, LAI, RVI, GNDVI, and SAVI were measured and showed an indication of no locust spreading. Soil quality indices measured and showing higher soil quality content include SQI, SAVI, TSAVI, EVI, and WDVI. NDVI, NDWI, MNDWI, WRI, and SWI indices are measured and shown at 4% water spread content.

References

1. Geli HME, González-Piqueras J, Neale CMU, Balbontín C, Campos I, Calera A (2020) Effects of surface heterogeneity due to drip irrigation on scintillometer estimates of sensible, latent heat fluxes and evapotranspiration over vineyards. *Water* 12:81
2. Loayza H, Silva L, Palacios S, Balcazar M, Cheruiyot E, Quiroz R (2017b) Dataset for low-cost UAV-based agricultural remote sensing platform (UAV-ARSP) for surveying crop statistics in sampling areas. <https://doi.org/10.21223/P3/J2QZCH>
3. Joyce KE, Samsonov SV, Levick SR, Engelbrecht J, Belliss S (2014) Mapping and monitoring geological hazards using optical, LiDAR, and synthetic aperture RADAR image data. *Nat Hazards* 73(2):137–163. <https://doi.org/10.1007/s11069-014-1122-7>
4. Garrido-Rubio J, González-Piqueras J, Campos I, Osann A, González-Gómez L, Calera A (2020) Remote sensing-based soil water balance for irrigation water accounting at plot and water user association management scale. *Agric Water Manag* 238:106236
5. Zaitunah A, Samsuri, Ahmad AG, Safitri RA, et al (2018) Normalized difference vegetation index (NDVI) analysis for land cover types using Landsat 8 oli in besitang watershed, Indonesia. In: *IOP conference series: earth and environmental science*, vol 126, pp 012112. <https://doi.org/10.1088/1755-1315/126/1/012112>
6. Mazzia V, Comba L, Khaliq A, Chiaberge M, Gay P (2020) UAV and machine learning based refinement of a satellite-driven vegetation index for precision agriculture. *Sensors* 20:2530
7. Ballesteros R, Intrigliolo DS, Ortega JF, Ramírez-Cuesta JM, Buesa I, Moreno MA (2020) Vineyard yield estimation by combining remote sensing, computer vision, and artificial neural network techniques. *Precis Agric* 21:1242–1262
8. Pádua L, Adão T, Sousa A, Peres E, Sousa JJ (2020) Individual grapevine analysis in a multi-temporal context using UAV-based multi-sensor imagery. *Remote Sens* 12:139
9. James H (2018) Ethical tensions from new technology: the case of agricultural biotechnology (CABI 2018); Laliberte AS, Rango A (2009) *IEEE Trans Geosci Remote Sens* 47:761. <https://doi.org/10.1109/TGRS.2008.2009355>
10. Miura T, Yoshioka H, Suzuki T (2008) Evaluation of spectral vegetation index translation equations for the development of long-term data records. In: *IEEE international conference on geoscience and remote sensing symposium*, III–712, vol 3. IEEE, Boston, MA
11. Helman D, Bahat I, Netzer Y, Ben-Gal A, Alchanatis V, Peeters A, Cohen Y (2018) Using time series of high-resolution planet satellite images to monitor grapevine stem water potential in commercial vineyards. *Remote Sens* 10:1615
12. Sari F, Kandemir I, Ceylan DA, et al (2020) Integration of NDVI imagery and crop coverage registration system for apiary schedule. *J Apic Sci* 64(1). <https://doi.org/10.2478/JAS-2020-0011>

13. Kandykakis Z, Falagas A, Karakizi C, Karantzalos K (2020) Water stress estimation in vineyards from aerial SWIR and multispectral UAV data. *Remote Sens* 12:2499
14. Ahmad F (2013) Phonologically tuned MODIS NDVI-based time series (2000–2012) for monitoring of vegetation and climate change in northeastern Punjab, Pakistan. *Glob J Hum Soc Sci* 12(13-B):37–54
15. Cui C, Zhang W, Hong Z, Meng L (2020) Forecasting NDVI in multiple complex areas using neural network techniques combined with feature engineering. *Int J Digital Earth* 1–17. <https://doi.org/10.1080/17538947.2020.1808718>
16. Dadhwal V, Singh R, Dutta S, Parihar J (2002) *Tropic Ecol* 43(1):107; Ferro CJS, Warner TA (2002) *ASPRS American society for photogrammetry and remote sensing* 68:51; Ge S, Carruthers R, Gong P, Herrera A (2006) *Environ Monit Assess* 114:65. <https://doi.org/10.1007/s10661-006-1071-z>
17. Dong J, Nai-bin W, Xiao-huan Y, Ji-hua W (2003) Study on the interaction between NDVI profile and the growing status of crops 13(1):62–65. <https://doi.org/10.1007/s11769-003-0086-4>
18. Fan X, Liu Y (2016) A global study of NDVI difference among moderate-resolution satellite sensors. *ISPRS J Photogramm Remote Sens* 121:177–191. <https://doi.org/10.1016/j.isprsjprs.2016.09.008>
19. Fan X, Liu Y (2017) A generalized model for inter-sensor NDVI calibration and its comparison with regression approaches. *IEEE Trans Geosci Remote Sens* 55(3):1842–1852. <https://doi.org/10.1109/TGRS.2016.2635802>
20. Franke J, Heinzl V, Menz G (2006) Assessment of NDVI-differences caused by sensor specific relative spectral response functions. In: *IEEE international conference on geoscience and remote sensing symposium*. IEEE, Denver, CO, pp 1138–1141
21. Giordan D, Manconi A, Tannant DD, Allasia P (2015) UAV: low-cost remote sensing for high-resolution investigation of landslides. In: *2015 IEEE international geoscience and remote sensing symposium (IGARSS)*. <https://doi.org/10.1109/igarss.2015.7327042>
22. Hanuschak G, Delince J, Unit A (2004) In: *Proceedings of the third world conference on agricultural and environmental statistical application*. Cancun, Mexico, pp 2–4
23. Guha S, Govil H (2020) An assessment on the relationship between land surface temperature and normalized difference vegetation index. *Environ Dev Sustain*. <https://doi.org/10.1007/s10668-020-00657-6>
24. Xue J, Su B (2017) Significant remote sensing vegetation indices: a review of developments and applications. *J Sens* 2017, Article ID 1353691, 17p. <https://doi.org/10.1155/2017/1353691>
25. Le Moigne J, Zavorin L, Stone H (2011) *Image registration for remote sensing*, vol 40. Cambridge University Press, Cambridge; Lebourgeois V, Dupuy S, Vintrou E, Ameline M, Butler S, Begue A (2017) *Remote Sens* 9. <https://doi.org/10.3390/rs9030259>
26. Miura T, Yoshioka H, Fujiwara K, Yamamoto H (2008) Inter-comparison of ASTER and MODIS surface reflectance and vegetation index products for synergistic applications to natural resource monitoring. *Sensors* 8(4):2480–2499. <https://doi.org/10.3390/s8042480>
27. Myneni RB, Williams DL (1994) On the relationship between FAPAR and NDVI. *Remote Sens Environ* 49(3):200–211. [https://doi.org/10.1016/0034-4257\(94\)90016-7](https://doi.org/10.1016/0034-4257(94)90016-7)
28. Pinto LS, Ray A, Reddy MU, Perumal P, Aishwarya P (2016) *Proceedings of the IEEE international conference on recent trends in electronics, information & communication technology (RTEICT)*, pp 825–828. <https://doi.org/10.1109/RTEICT.2016.7807942>
29. Rahman H, Dedieu G (1994) SMAC: a simplified method for the atmospheric correction of satellite measurements in the solar spectrum. *Int J Remote Sens* 15(1):123–143. <https://doi.org/10.1080/01431169408954055>
30. Gong C, Buddenbaum H, Retzlaff R, Udelhoven T (2019) An empirical assessment of angular dependency for Red_edge-M in sloped terrain viticulture. *Remote Sens* 11:2561
31. Le Moigne J, Campbell WJ, Cromp RF (2002) An automated parallel image registration technique based on the correlation of wavelet features. *IEEE Trans Geosci Remote Sens* 40(8):1849–1864. <https://doi.org/10.1109/tgrs.2002.802501>

32. Giovos R, Tassopoulos D, Kalivas D, Lougkos N, Priovolou A (2021) Remote sensing vegetation indices in viticulture: a critical review. *Agriculture*. <https://doi.org/10.3390/agriculture11050457>
33. Cogato A, Meggio F, Collins C, Marinello F (1896) Medium-resolution multispectral data from Sentinel-2 to assess the damage and the recovery time of late frost on vineyards. *Remote Sens* 2020:12
34. Ferrer M, Echeverría G, Pereyra G, Gonzalez-Neves G, Pan D, Manuel Mirás-Avalos J (2020) Mapping vineyard vigor using airborne remote sensing: relations with yield, berry composition and sanitary status under humid climate conditions. *Precis Agric* 21:178–197
35. Xie C, Yang C (2020) A review on plant high-throughput phenotyping traits using UAV-based sensors. *Comput Electron Agric* 178:105731
36. Adamides G (2020) A review of climate-smart agriculture applications in cyprus. *Atmosphere* 11:898 [CrossRef]
37. Sozzi M, Kayad A, Marinello F, Taylor AJ, Tisseyre B (2020) Comparing vineyard imagery acquired from Sentinel-2 and Unmanned Aerial Vehicle (UAV) platform. *OENO One* 189–197
38. Di Gennaro SF, Dainelli R, Palliotti A, Toscano P, Matese A (2019) Sentinel-2 validation for spatial variability assessment in overhead trellis system viticulture versus UAV and agronomic data. *Remote Sens* 11:2573
39. Brook A, de Micco V, Battipaglia G, Erbaggio A, Ludeno G, Catapano I, Bonfante A (2020) A smart multiple spatial and temporal resolution system to support precision agriculture from satellite images: proof of concept on Aglianico vineyard. *Remote Sens Environ* 240:111679
40. Ronchetti G, Mayer A, Facchi A, Ortuani B, Sona G (1967) Crop row detection through uav surveys to optimize on-farm irrigation management. *Remote Sens* 2020:12
41. Vallentin C, Dobers ES, Itzerott S, Kleinschmit B, Spengler D (2020) Delineation of management zones with spatial data fusion and belief theory. *Precis Agric* 21:802–830
42. Hadizadeh M, Rahnama M, Poor HA, Hesari B, Kazemi M (2020) The comparison between remotely-sensed vegetation indices of Meteosat second-generation satellite and temperature-based agrometeorological indices for monitoring of main crops in the northeast of Iran. *Arab J Geosci* 13:509. [CrossRef]
43. Devaux N, Crestey T, Leroux C, Bruno T (2019) Potential of Sentinel-2 satellite images to monitor vine fields grown at a territorial scale. *OENO One* 1:51–58
44. Vélez S, Barajas E, Rubio JA, Vacas R, Poblete-Echeverría C (2020) Effect of missing vines on total leaf area determined by NDVI calculated from sentinel satellite data: progressive vine removal experiments. *Appl Sci* 10:3612
45. Meyers JM, Dokoozlian N, Ryan C, Bioni C, Heuvel JEV (2020) A new, satellite NDVI-based sampling protocol for grape maturation monitoring. *Remote Sens* 12:1159
46. Khaliq A, Comba L, Biglia A, Aimonino DR, Chiaberge M, Gay P (2019) Comparison of satellite and UAV-based multispectral imagery for vineyard variability assessment. *Remote Sens* 11:436
47. Kerkech M, Hafiane A, Canals R (2020) VddNet: vine disease detection network based on multispectral images and depth map. *Remote Sens* 12:3305

UAV-LiDAR and Terrestrial Laser Scanning for Automatic Extraction of Forest Inventory Parameters



Khadija Meghraoui, Hamza Lfalah, Imane Sebari, Souhail Kellouch, Sanaa Fadil, Kenza Ait El Kadi, and Saloua Bensiali

Abstract The determination of the Dendrometric parameters of forest stands has a silvicultural and ecological interest for the forester, in particular for the evaluation of the dynamics of growth and productivity, and the evaluation of indicators of good ecological status. Currently, UAV-LiDAR (Unmanned Aerial Vehicle-Light Detection and Ranging) has become the new trend for measurement professionals, offering very high-resolution data collection at considerably lower survey costs. In addition, this technology has started to prove its utility in forest inventory applications namely to extract dendrometric parameters, where direct and conventional measurements are sometimes difficult. As for the TLS (Terrestrial Laser Scanning) technology, it has made it possible to obtain several abundant and refined structural information under the forest canopy. In the context of extraction of forest inventory parameters, the precision of extracting tree height for example using TLS alone, is insufficient. Hence

K. Meghraoui · I. Sebari (✉) · K. Ait El Kadi

Research Unit of Geospatial Technologies for A Smart Decision, Hassan II Institute of Agronomy and Veterinary Medicine, Rabat, Morocco

e-mail: i.sebari@iav.ac.ma

K. Meghraoui

e-mail: k.meghraoui@iav.ac.ma

K. Ait El Kadi

e-mail: k.aitelkadi@iav.ac.ma

H. Lfalah · I. Sebari · K. Ait El Kadi

Cartography–Photogrammetry Department, School of Geomatics and Surveying Engineering, Hassan II Institute of Agronomy and Veterinary Medicine, Rabat, Morocco

S. Kellouch

AXIGEO, 4040 Marrakech, Morocco

S. Fadil

Department of Water and Forests, Rabat, Morocco

S. Bensiali

Department of Applied Statistics and Computer Science, Hassan II Institute of Agronomy and Veterinary Medicine, Rabat, Morocco

e-mail: s.bensiali@iav.ac.ma

© The Author(s), under exclusive license to Springer Nature Switzerland AG 2023

375

K. Jain et al. (eds.), *Proceedings of UASG 2021: Wings 4 Sustainability*,

Lecture Notes in Civil Engineering 304,

https://doi.org/10.1007/978-3-031-19309-5_26

the contribution of the combination of ALS (Aerial Laser Scanning) with TLS data to fill any information gaps that may exist. The main goal of this study is to present an approach to the automatic extraction of dendrometric parameters from UAV-LiDAR and TLS data. The proposed methodology is based on performing a TLS survey at a plot level and an ALS scan of the entire area. Our methodology is essentially made up of two steps: automatic crown delineation and automatic extraction of dendrometric parameters (position, Diameter at breast height, height, stem curve, concave and convex hull). For the first step, we compared the segmentation of the point cloud by the Watershed algorithm and by the SEGMA pipeline. Whereas the extraction of the dendrometric parameters was carried out using a set of algorithms namely RHT (Random Hough Transform) and LSR (Least Square Regression). The study focused on UAV-ALS and TLS datasets from different regions and with different densities (the Mediterranean, tropical, and coniferous forest). The validation was done using measurements carried out manually on the datasets. The results show that delineation by SEGMA gave a percentage of crown detection varying from 98 to 113% (over-segmentation) with diameters having a coefficient of determination varying from 56 to 90% depending on the area while the Watershed algorithm presented an over-segmentation of the actual crowns. Whereas the results for the DBH determination, the RHT and LSR algorithms both displayed almost 1–4 cm deviations from the reference while the height was extracted with 1–8 mm deviations.

Keywords Crown delineation · Dendrometric parameters · Forest inventory · LSR · Point cloud · RHT · SEGMA · TLS · Tree segmentation · UAV-LiDAR · Watershed

1 Introduction

1.1 Background

The sustainable management of forests requires a preliminary estimation of the attributes of the forests. Unmanned Aerial Vehicle (UAV)-based remote sensing techniques have proved their usefulness in forest inventory applications as well as for ecological purposes [1]. In this context, the UAV-LiDAR system has become a promising technology and is starting to be used often for forest management, due to its ability to provide very accurate estimates of the three-dimensional structure of the forest.

The Drone based LiDAR has become the essential solution for professional measurements. This solution is used to generate high-resolution DTMs for terrain analysis. Nowadays, this technology is very efficient and precise. Indeed, a detailed planning flight makes it possible to obtain results during data acquisition, and therefore to derive very high-resolution DEM. The advantage of drone platforms is that they are flexible and adaptable in various contexts and accept access to remote and dangerous areas without risk for operators.

Recently, the development of technological solutions has enabled the use of drones as a novel remote sensing alternative offering very high-resolution data collection at a considerably lower survey cost. Current research into the use of drones as a tool for 3D data collection includes a variety of studies including forestry. These studies often use image matching techniques. The downside of the point clouds generated by this approach is that few points will be measured within the canopy and the underlying surface in areas of dense vegetation. LiDAR systems have evolved and sensors collect data from ground systems, and airborne systems, including unmanned aerial vehicles (UAV).

In forestry, LiDAR data is used for monitoring changes in vegetation and developing inventories, assessing the risk of disasters caused by wind or fire, and mapping ecosystems and forest habitats. Different parameters characterizing forest stands can be estimated from LiDAR data, and this by using one of the two major approaches: in particular an approach based on the area, known as the zonal approach (using the average height and density of the stands) or an approach based on a single tree (detection and measurement of individual trees). If the objective is to predict forest attributes at the plot and stand level over large areas, then the area approach is used. Using LiDAR data, it was possible to estimate tree height at stand level as well as individual stem volumes and other dendrometric parameters. More recently, some studies have demonstrated the possibility of differentiating tree species through the three-dimensional description offered by point clouds [2]. In addition, previous studies have proven that information from LiDAR data can be used to obtain precise estimates of tree height and, therefore, stand volume and biomass, as well as to extract high-precision digital models.

The terrestrial laser scanning technology has made it possible to obtain several abundant and refined structural information under the forest canopy [3]. The detailed stem measurements offered by a terrestrial scan provide a means of better understanding the relationships that involve tree growth, allometry, stem mechanisms, and canopy structure [4]. This information is provided by forest inventories and it begins with the determination of diameter at breast height (DBH), tree height (h), tree species, and basal area which are all essential for some forestry studies such as the evaluation of the potential of forest fires or aboveground biomass among others.

On one hand, TLS does not offer much in terms of time and efficiency, but because of its accuracy and stability, it is widely used in forest resource surveys. What's more, TLS does not require other special equipment, and it is relatively simple to use. It captures the vertical structure of the forest, especially the lower canopy, which offers unique advantages in the acquisition of a high-precision DEM. However, due to the topography variations and limited field of view of the scanners in vertical directions, as well as the shadow effects of other objects, it is often difficult for TLS to capture data of the upper canopy. Therefore, the precision of tree height extraction using TLS alone is insufficient [5]. On the other hand, UAV LiDAR offers advantages over TLS in acquiring a relatively complete forest canopy and retrieving relevant structural parameters at a larger scale and in less time.

1.2 Forest Inventory Parameters

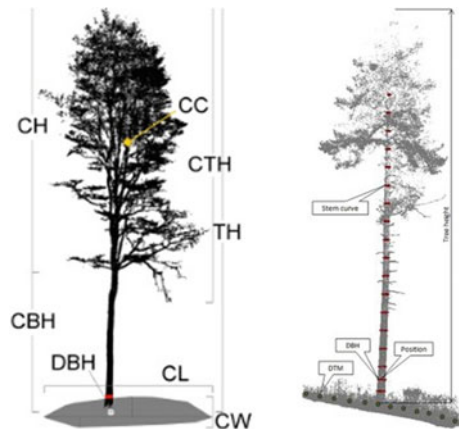
The main pillars of forest management are the assessment of the resources of stands, and their desired states. They are based on the measurement of the characteristics of trees and stands. The main attributes of trees are Diameter, Height, Shape, Volume, or information on Biomass and Crown. The diameter, measured as the length of the straight line passing through the center of the tree, is measured by accepting that the cross-section of the tree is circular. It is widely used to calculate the volume of trees. Tree height is the vertical distance from a point of interest on the tree to the surface of the ground (Fig. 1).

The tree’s position: The position is generally understood as the position of the center of the base of the trees. among the methods of determination that exist there is one that uses all the points up to a height specified by the user (for example 60 cm) above the lowest point of the tree and calculates the median coordinates of X and Y. The Z coordinate is defined as the median Z value of n points closest to the terrain at that X, Y position [6]. Another method uses an approach that relies on a Random Hough Transform (RHT) for the detection of circles on tree points 1.3 m and 0.65 m above the lowest point of the cloud. Finally, the position of the tree is defined as the intersection of the vector formed by the centers of the two estimated circles with the surface of the DTM [6].

The Diameter at Breast Height (DBH): To determine this parameter, two methods are usually used, a Random Hough Transformation (RHT) for circle detection with an adjustable number of circle estimation iterations: The process of extracting DBH is illustrated in Fig. 2. For sliced point cloud data, the RHT method is used to sequentially perform the circular detection from multiple sub-regions in each layer respectively until the extraction of all the sliced point clouds is complete [8].

A Least Square Regression (LSR), this algorithm employs an algebraic estimation of the circle and a geometric reduction of the distances.

Fig. 1 (Right) Example of forest inventory parameters: CBH: Crown Base Height, CH: Crown Height, CTH: Crown Total Height, CL: Crown Length, CW: Crown Width, CC: Crown Centroid, DBH: Diameter at Breast Height [6]. (Left) Illustration of basic tree parameters [7]



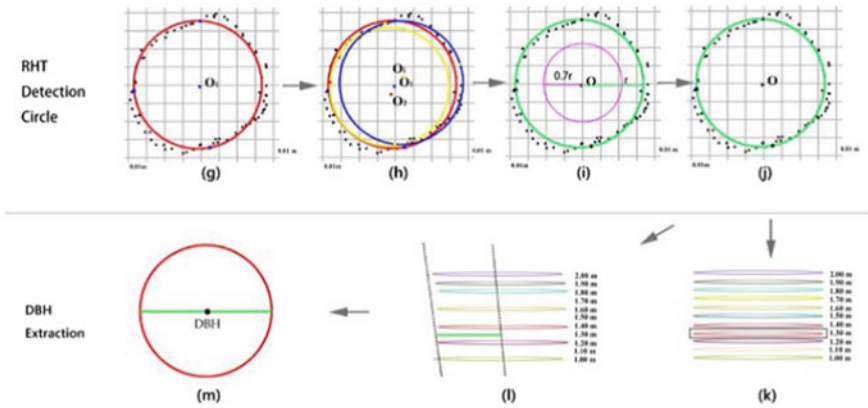


Fig. 2 Principle of the RHT algorithm [8]

The previous two methods use a subset of the tree point cloud—a horizontal slice 1.25 to 1.35 m above the calculated tree position. To successfully fit the circle, at least 4 points in this slice are needed [6]. Five factors likely affect correct estimates of DBH: the diameter of the stem, a missing part of the DBH ring, the percentage of noise points, and the number of points creating the ‘DBH ring’.

Height measurement: Using the locations of the extracted trees, the point clouds are clipped at an interval of 1.00 m [6]. The RHT method is used to obtain the diameter of multilayer trunks and the centers of the circles, and the multilayer centers of the circles are used to fit a straight line in space, which is the direction of growth of the tree. Using that straight line, the height is calculated.

Stem curve: For the analysis of the stem curve and shape, there is an approach that exploits the position of stem centers and stem diameters calculated at different heights above the position of the tree base. Starting at 0.65 m and followed by 1.3 m, 2 m, and then every meter above the ground. The circles (defining the center and the local stem diameter) are fitted by the RHT algorithm to horizontal slices of the tree point cloud cut at appropriate heights. The determination stops when the estimated diameter is twice as large as in the previous two circles, indicating the expansion of the tree cloud in the crown [6]. The result of the algorithm is a list of diameters at different heights of the stem.

Planar tree projection: The planar tree projection areas are calculated using a 2D convex/concave hull (envelope) of the tree point cloud projected orthogonally on the horizontal plane at the height of the base position of the tree. The convex hull is calculated using the “Gift wrapping” algorithm, then the area of the resulting polygon is calculated. Since convex shapes do not match the actual shape of many irregular trees well, there is a concave plane projection [6]. The concave projection extends the convex shell algorithm by using the “Divide and conquer” algorithm to divide the sides of the polygon based on the maximum length given to the side of the polygon.

1.3 Objectives

This paper aims to present an innovative methodology to use both UAV-LiDAR and terrestrial Laser scanning to perform automatic extraction of a set of forest inventory parameters.

To process the collected data, we went through two essential stages each using specific algorithms: segmentation of the point cloud followed by automatic extraction of the desired parameters.

This study also attempts to examine the efficiency of determining dendrometric parameters from UAV-LiDAR and TLS data.

2 Materials and Methods

2.1 Study Area

The study area for the UAV-based LiDAR was conducted in three different regions, a Mediterranean forest in Morocco, located at the forest of Maamora which represents the largest lowland sub-region in the world. It covers an area of 133,000 ha, of which 60,000 ha is pure cork oak. The part studied is home to the cork oak (*Quercus Suber*) which is an evergreen tree exploited for its bark which provides the cork. This species is native to southwestern Europe and northwestern Africa as shown in the photo below (Fig. 3).

The second and the third points clouds represent a coniferous forest in California, this area is characterized by a predominance of trees with needle-like perennial leaves. As opposed to deciduous trees, coniferous forests are accompanied by a uniform layer of small shrubs and grasses.

The last ALS point cloud represents a tropical forest in Congo, this forest which covers nearly three million km² and is shared between six countries. The TLS data

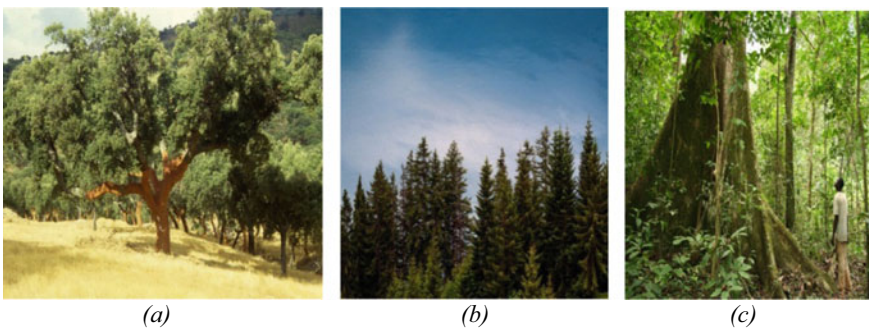


Fig. 3 a Maamora forest, b Coniferous forest, c Tropical forest

which is a plot used to examine our methodology consisted of a set of deciduous trees.

2.2 UAV-LiDAR Data

The first UAV-LiDAR data was obtained in July 2017 with the Unmanned Aerial Vehicle Matrice 600 pro equipped with the Velodyne VLP-16 LiDAR sensor. This sensor has a range of 100 m, a point accuracy of up to 3 cm, and a frequency of 72 kHz. The height of flight was 40 m with a speed of 3 m/s, and the georeferencing was done by the Comnav T300 GNSS receiver. The second was acquired by Can drone (June 2020), and the last one from YellowScan (February 2020) (Fig. 4 and Table 1).



Fig. 4 a DJI M600 pro drone used for the first point cloud. b Photo of the first mission

Table 1 Characteristics of the ALS point cloud used

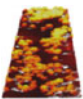


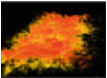

Data set	Density (points/m ²)	Number of points (million points)	Area (m ²)	Volume (Mb)	Source
	562	11.13	19 802	976.8	DJI M600 pro + Velodyne VLP-16
	312	2.95	9479	236.7	Can drone (June 2020)
	299	3.14	10,496	251.3	Can drone (June 2020)
	49	6.62	134,123	580.5	YellowScan (February 2020)

Table 2 Characteristics of the TLS point cloud used

Data set	Density	Number of points	Area	Volume	Source
	5199 points/m ²	723,000 points	139 m ²	55.2 Mb	www.computree.onf

2.3 TLS Data

The TLS data representing a plot with deciduous trees were downloaded from the site of the Computree platform, showing a density of 5199 points/m² and an area of 139 m² (Available for download at www.computree.onf) (Table 2).

2.4 Methodology

In this paper, we suggest a methodology based on a first segmentation of the ALS point cloud, followed by a second segmentation of TLS point clouds on the plot level. The first segmentation will provide a delineation of individual tree crowns for which we extracted some attributes. Whilst the second segmentation aims to delineate individual trees, from which other dendrometric parameters are to be automatically extracted in the final step using specific algorithms (Fig. 5).

Segmentation algorithms for ALS

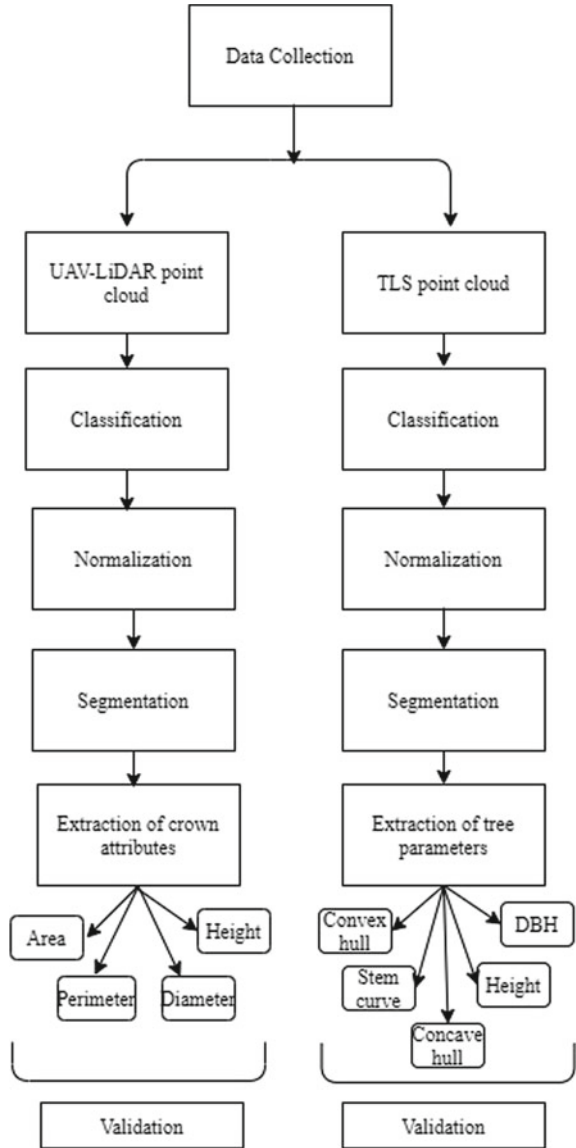
SEGMA. This method is based on detecting and filtering maxima to identify peaks. The crowns are then delimited using the Watershed algorithm and corrected according to geometric criteria. The method is based on the version initially developed by St Onge and implemented in the Computree platform. The steps for detecting the maxima are as follows: (i) Creation of the CHM from a normalized point cloud (ii) Filling of the holes (iii) Smoothing of the CHM by a Gaussian filter (iv) detection of the maxima.

Watershed. This is a simple method that can be explained by the movement of water through a landscape, Rainwater falls everywhere and the water moves in the direction of the steepest slopes. For tree crown segmentation, the movement is rather upward to local maxima, which we assume are treetops. A start point is placed in each raster cell above a height threshold. A path is placed from each starting point by iteratively moving to the neighboring raster cell with the highest value until a local maximum is reached. The starting points that reach the same local maximum define a segment.

Segmentation algorithms for TLS

Automatic voxel-based approach. This automatic approach is based on the distance between points and the minimum number of points forming trees, with a specification

Fig. 5 Workflow chart depicting the steps performed in this study



of the size of the voxel that includes the points. In the first step of segmentation, all the vegetation is divided into slices. Within these slices, clusters with a minimum number of points N defined by the user and a maximum distance S between the two closest points are built. The next step is to rebuild the bases of the trees. For each cluster whose centroid height is less than 1.3 m above the ground, we find the 10 neighboring clusters (closest) up to the distance $2S$. We assume that these clusters come from the same tree base. All these clusters are merged into segments. These

segments are tested to check if they are formed of at least five clusters and if the maximum dimension of the segment is at least 1 m to be identified as a tree.

Semi-automatic voxel-based approach. This method makes it possible to isolate the trees to obtain a point cloud per tree from a terrestrial point cloud. This segmentation is said to be semi-automatic since it contains a manual editing phase to improve the results of the automatic part. We have chosen to implement it on the Compu-tree platform. This method is a pipeline (a processing chain) applied to the cloud to be processed, passing through the various stages that follow: (i) Classification and generation of the DTM. (ii) Creation of a slice parallel to the DTM. This slice will then make it possible to detect starting points for each tree (seeds). (iii) Creation of a voxel grid, where each box references the list of points it contains in 3D. This will then make it possible to establish neighborhood relations between boxes. (iv) Segmentation of the voxel grid of points already created, from 3D seeds. The principle is to create a topological neighborhood relationship between the boxes containing points, to “contaminate” the whole tree from the seeds, first upwards, then downwards.



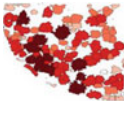





3 Results

In this section, we will present the results obtained after applying the algorithms proposed in our methodology to the different clouds available to us. For the California point cloud, it was found that it presents several quadrants of different density, we, therefore, proceeded to a division of the latter to treat every two quadrants of different densities to assess the robustness of the proposed algorithms (Table 3).

The different algorithms and automatic extraction methods explained in the methodology were tested on the TLS point cloud used, and the segmentation results were (Fig. 6).

Different other dendrometric parameters to explore from the TLS point cloud are in particular:

Table 3 ALS point cloud segmentation results

Forest Type	Mediterranean forest (Maamora, Morocco)	Coniferous forest (California, less dense quadrant)	Coniferous forest (California, denser quadrant)	Tropical forest (Congo)
SEGMA				
Watershed				

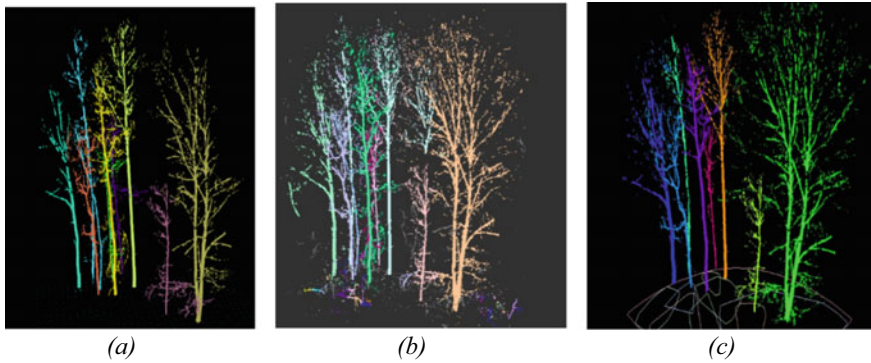


Fig. 6 **a** Segmentation of the TLS point cloud by the automatic approach, **b** Segmentation of the TLS point cloud using the semi-automatic approach, **c** Segmented and manually edited TLS point cloud

Tree position: This parameter is very necessary because it is from the planimetric position of the tree that all the dendrometric parameters will be measured (The position of the tree is mentioned by the gray sphere (Fig. 7) and its coordinates can be exported with other attributes).

DBH: Measurement of DBH by RHT and LSR gave the following result (measurement in cm).

Height: The height of this same tree was determined (in m).

Stem curve: The stem curve, which is one of the most interesting parameters that can be extracted from a TLS cloud, was determined for the same tree above.

The exported results are in the form of a list of diameters corresponding to each height of the curve.

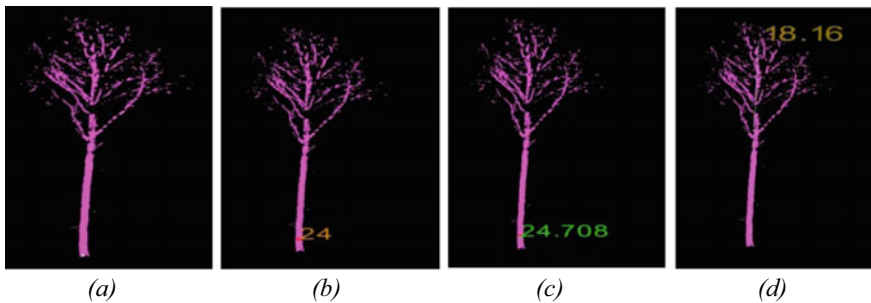


Fig. 7 **a** Example of determining a tree position after segmentation. **b** DBH measurement by the RHT algorithm. **c** DBH measurement by the LSR algorithm

Convex and concave hull

These two dendrometric parameters were calculated for the tree shown in Fig. 7 (Figs. 8, 9 and Table 4).

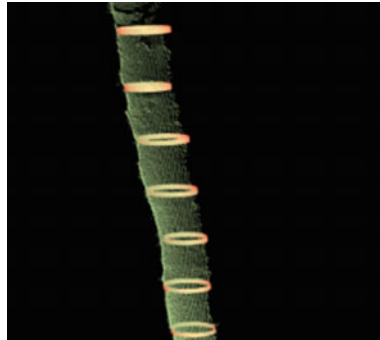


Fig. 8 Stem curve illustration

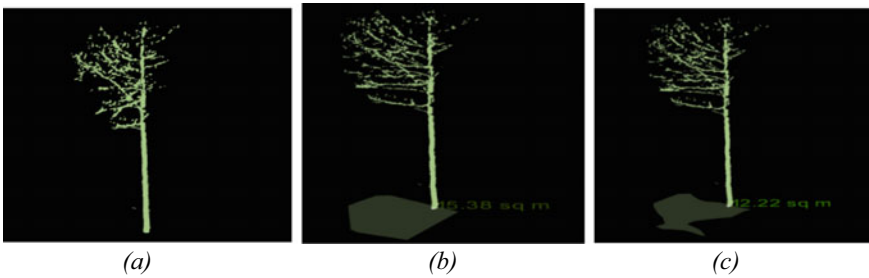


Fig. 9 **a** Individual tree used for the determination of hull, **b** Example of concave hull measurement, **c** Example of convex hull measurement

Table 4 Diameters corresponding to the different sections of the curve

Height (m)	Diameter (cm)
0.65	25.4
1.30	24
2.00	25.8
3.00	24.4
4.00	22.6

4 Validation

To validate the results of the ALS point clouds results, we established the manual extraction of certain crowns on the CHM, so that they can be compared with the crowns obtained from the segmentation algorithms. For each data set, a validation of the number of crowns detected, the area of the canopy, the diameter, the perimeter, and the height was carried out by calculating the percentages of detection, RMSE, R^2 , and adjusted R^2 . Below are the validation crowns extracted manually and comparative tables (Fig. 10 and Tables 5, 6 and 7).

For the Congo Forest point cloud, the comparison was done using a set of reference crowns that mainly contain high canopy trees, with manually segmented crowns preferably being selected from the larger ones as they must be visible from the

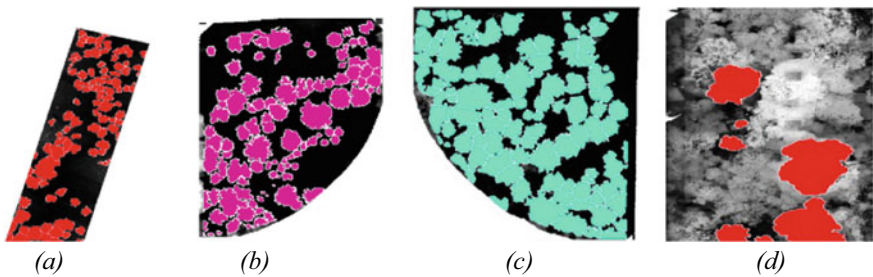


Fig. 10 **a** Validation crown for the Mediterranean forest, **b** Validation crown for the less dense quadrant of the coniferous forest, **c** Validation crown for the denser quadrant of the coniferous forest, **d** Validation crown for the tropical forest

Table 5 Number of crowns detected (Mediterranean forest)

Number of crowns	Reference	SEGMA	Watershed (implemented on R)
		123	139
Pourcentage	–	113%	135%

Table 6 Number of crowns detected (First Coniferous forest)

Number of crowns	Reference	SEGMA	Watershed (implemented on R)
		104	102
Pourcentage	–	98%	143%

Table 7 Number of crowns detected (Second coniferous forest)

Number of crowns	Reference	SEGMA	Watershed (implemented on R)
		106	117
Pourcentage	–	110%	191%

Table 8 Statistics of crown attributes delimited by Watershed and SEGMA for the Mediterranean forest

	Diameter		Perimeter		Height	
	Watershed	SEGMA	Watershed	SEGMA	Watershed	SEGMA
RMSE (DL = 13)	0.94	0.60	5.90	3.14	0.43	0
R ²	0.70	0.88	0.67	0.86	0.91	1
Adjusted R ²	0.68	0.87	0.64	0.85	0.90	1

outside. Otherwise, algorithms tend to create erroneous segments that cannot be validated (Tables 8, 9, 10 and 11).

The validation of the TLS results was made by the manual extraction of two parameters only, namely the height and the DBH for two individuals since these two parameters are the most important and the others which remain are determined by the same principle with some small differences. The manual measurements made are as follows:

Table 9 Statistics of crown attributes delimited by Watershed and SEGMA for the less dense quadrant of the coniferous forest

	Diameter		Perimeter		Height	
	Watershed	SEGMA	Watershed	SEGMA	Watershed	SEGMA
RMSE (DL = 13)	1.84	1.63	11.83	9.78	2.10	3.48
R ²	0.66	0.56	0.62	0.65	0.95	0.86
Adjusted R ²	0.64	0.53	0.59	0.63	0.94	0.85

Table 10 Statistics of crown attributes delimited by Watershed and SEGMA for the denser quadrant of the coniferous forest

	Diameter		Perimeter		Height	
	Watershed	SEGMA	Watershed	SEGMA	Watershed	SEGMA
RMSE (DL = 13)	1.73	0.86	11.23	5.84	0.19	0.05
R ²	0.52	0.8	0.47	0.82	0.99	1
Adjusted R ²	0.49	0.78	0.43	0.81	0.99	1

Table 11 Statistics of crown attributes delimited by Watershed and SEGMA for the tropical forest

	Diameter		Perimeter		Height	
	Watershed	SEGMA	Watershed	SEGMA	Watershed	SEGMA
RMSE (DL = 13)	5.02	3.81	48.79	31.76	0.003	0.004
R ²	0.89	0.90	0.66	0.76	1	1
Adjusted R ²	0.87	0.88	0.61	0.72	1	1

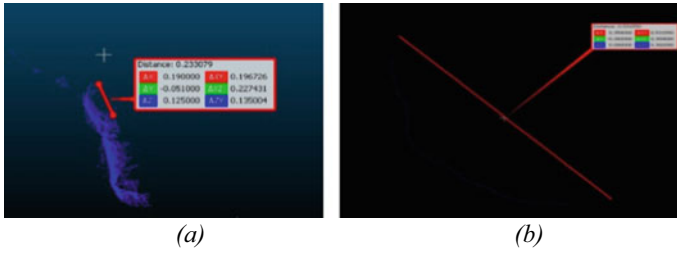


Fig. 11 a DBH measurement for tree N°1, b DBH measurement for tree N° 2

DBH: the cloud was cut at the level of 1.30 m and the diameter was measured at this height (Figs. 11).

Height: we used the Z dimension of the bounding box (Fig. 12 and Tables 12 and 13).

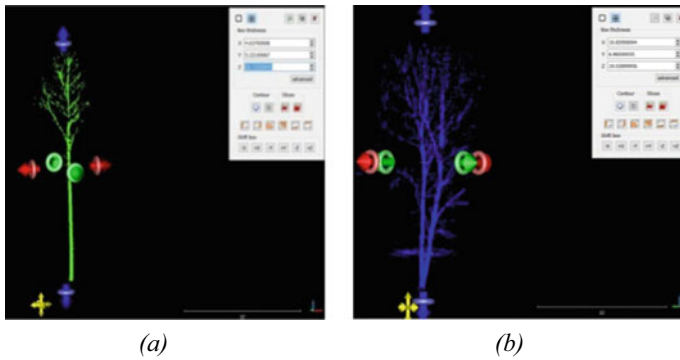


Fig. 12 a Tree height measurement N° 1, b Tree height measurement N° 2

Table 12 Comparative table of the parameters extracted manually and those determined by the algorithms

N° tree	DBH (cm)			Height (m)	
	Reference	RHT	LSR	Reference	Automatic extraction
1.	23.308	24	24.708	18.152	18.16
2.	53.155	56.4	56.8	19.039	19.04

Table 13 Differences between manually extracted measurements and algorithm measurements

N° Tree	DBH difference (cm)		Height difference (cm)
	RHT	LSR	
1.	0.7	1.4	0.8
2.	3.2	3.6	0.1

5 Discussions

Our study focuses mainly on the introduction of a new methodology combining terrestrial LiDAR data with those of the UAV-LiDAR to carry out an improved forest inventory. The integration of the data acquired by the two platforms consists of the fusion of the cloud of TLS points at each plot with the corresponding part of the drone ALS point cloud. The idea is to provide an alternative that can allow the forest manager to easily, automatically, and more accurately measure the attributes of the trees in a forest stand. These attributes are of visceral importance as they form the basis of any forest study.

Our results concerning the ALS data confirm that the different segmentation methods lead to very different results. In general, the performance of the methods used is better in the coniferous forest and the forest of Maamora, characterized by an average density of trees, than in dense forest stands like that of the Congo. At the very level of the Maamora cloud and everywhere else, it has been found that where there is a high density leading to the overlapping of the crowns of the trees, the algorithms have difficulty distinguishing one from the other. This point made the difference between the SEGMA algorithm and the Watershed algorithm that we implemented on R. Indeed, the latter was able, visibly, to segment the overlapping crowns where SEGMA was unable to delimit the individual crowns. The same remark was raised at the level of the Congo Forest in which the density of the canopy, its heterogeneity, and the presence of different stages of tree growth limited our segmentation approach. However, we tried to act on the configuration of the algorithms to bring out only the most imposing specimens in terms of the height and size of the crowns. SEGMA method gave better results in terms of crown attributes which is hardly enough to judge its performance as Watershed identified contours much more accurately and visually realistically. However, the validation carried out could be biased as long as the crowns extracted manually do not necessarily correspond to the reality on the ground. The only conclusion that we can then draw is that a tropical forest characterized by a high density, a heterogeneous vertical and horizontal structure, and a difference in terms of growth stages would be difficult to segment and the results obtained would not correspond at all to reality.

Our study identified the developed SEGMA method as the best method to segment crowns. It identifies the closest number of crowns corresponding to reality, but also the lowest RMSEs when comparing the segmented crowns with the reference data set. Indeed, even if the SEGMA method is significantly more efficient at segmenting separate crowns, the Watershed method also works well in areas where the crowns overlap as long as it has succeeded in detecting the boundaries of each crown that remains to be seen by field data.

For the TLS part of our methodology, we used an existing dataset comprising a plot with a few trees. It measured the DBH, the Height, the Stem curve, and the concave and convex envelopes. The validation was done by measuring the DBH and the Height manually on the point cloud corresponding to two different trees. A

validation by field data would have been, without doubt, better except that we did not have the conventional measurements of the trees present on the cloud used.

The approach proposed in our methodology provides for a better description at the level of the individual tree. Indeed, the dendrometric parameters extracted are all the more important as they will assist the forester to manage and develop forest areas. The improvement over conventional methods is the automation of the measurement process and the possibility of extrapolation to the entire stand.

The measurement of the dendrometric parameters in itself is only an intermediate step to assist any study that has an appeal to the forest in its many aspects. The next studies should deal much more in-depth with the area of space technologies as well as the algorithms for segmentation and automatic extraction of dendrometric parameters to revolutionize forest measurement, which remains an essential tool for the preservation of the natural ecological spaces of our territory.

6 Conclusion and Future Work

The detailed description of a forest stand is a crucial step in understanding it, apprehending it, and above all managing it to exploit or preserve it in the most optimal way possible. This description is the affair of a branch of forestry which is none other than the forest inventory. The latter has always been carried out conventionally and several experiments have been carried out in the direction of the exploitation of the potential offered by geospatial technologies and more precisely UAV-LiDAR and terrestrial LiDAR which offer a multitude of advantages and make it possible to drastically optimize the inventory process.

This research project falls within this perspective and has as its main objective the exploitation of UAV-LiDAR and TLS data for the extraction of dendrometric parameters of a forest stand.

To meet the objectives set, the development of an appropriate methodology is an essential step. Much of the implementation of the latter involves the use and comparison of different algorithms for segmentation and automatic extraction of the desired parameters. Each algorithm has its characteristics and specificities, we were able, thanks to the different datasets, to explore and analyze the results of these methods to finally assess the effectiveness of each of them.

The results obtained demonstrated the effectiveness of the algorithms in segmenting ALS clouds, with some differences depending on the characteristics of each type of forest. Our study especially underlines the particularity of forest stands and the need to choose segmentation methods adapted for each type. A method developed for a given case would not be completely transferable to others. As for the dendrometric parameters from the TLS data, the proposed approach demonstrates certain ease of determination, the precision of the measurement, and the possibility of improving the results of the forest inventory by adding parameters previously not exploited.

In addition, this study is an outline that prepares the ground for integrating LiDAR technology into forest inventory operations given the undeniable advantages it presents in terms of cost and time reduction.

To conclude our research project, we would like to offer the following recommendations for future studies:

- Apply the proposed methodology using data from a TLS and ALS mission in the same area with the collection of field data for validation.
- Adapt the segmentation algorithms to the nature of the forest studied and propose appropriate algorithms for dense forests.
- Integrate spectral information or intensity of LiDAR returns or both to potentially improve segmentation results.
- Evaluate the performance of algorithms for the automatic extraction of dendrometric parameters under different conditions of density, tree species, and survey season.

Acknowledgements We would like to thank the company AXIGEO which provided us with its expertise in the use of UAV-LiDAR as well as all the necessary equipment for the accomplishment of the mission held in Morocco.

We also extend our sincere thanks to YellowScan, developer of UAV-LiDAR systems, who provided us with one of the LiDAR points cloud that we used in our study.

We also acknowledge the tremendous help of Mr. HESHI Jacky, CANDRONE Solutions Specialist, in his availability to respond to us at any time and his test data provided to us.

We also thank Mr. VANDENDAELE Bastien, doctoral researcher at the University of Sherbrooke, for his availability and his help, and his recommendation to use Computree as well as his various advices in the use of LiDAR data.

Finally, a special acknowledgement is addressed to the teaching staff of the Geomatic Sciences and Topographic Engineering School at the Hassan II Agronomic and Veterinary Institute for all the efforts made, in particular in terms of Lasergrammetry and Photogrammetry.

References

1. Picos J, Bastos G, Míguez D, Alonso L, Armesto J (2020) Individual tree detection in a eucalyptus plantation using unmanned aerial vehicle (UAV)-LiDAR. *Remote Sens* 12(5):885
2. Apostol B, Lorent A, Petrila M, Gancz V, Badea O (2016) Height extraction and stand volume estimation based on fusion airborne LiDAR data and terrestrial measurements for a Norway spruce [*Picea abies* (L.) Karst.] test site in Romania. *Notulae Botanicae Horti Agrobotanici Cluj-Napoca* 44(1):313–323
3. White JC, Coops NC, Wulder MA, Vastaranta M, Hilker T, Tompalski P (2016) Remote sensing technologies for enhancing forest inventories: a review. *Can J Remote Sens* 42(5):619–641
4. Moskal LM, Zheng G (2012) Retrieving forest inventory variables with terrestrial laser scanning (TLS) in urban heterogeneous forest. *Remote Sens* 4(1):1–20
5. Tian J, Dai T, Li H, Liao C, Teng W, Hu Q, Xu Y, et al (2019) A novel tree height extraction approach for individual trees by combining TLS and UAV image-based point cloud integration. *Forests* 10(7):537
6. Trochta J, Krůček M, Vrška T, Král K (2017) 3D Forest: an application for descriptions of three-dimensional forest structures using terrestrial LiDAR. *PLoS ONE* 12(5):e0176871

7. gim-international Homepage. <https://www.gim-international.com/content/article/terrestrial-laser-scanning-in-forest-inventories>. Last accessed 18/12/2017
8. Liu G, Wang J, Dong P, Chen Y, Liu Z (2018) Estimating individual tree height and diameter at breast height (DBH) from terrestrial laser scanning (TLS) data at plot level. *Forests* 9(7):398

A UAS-Based Approach for Orchard Geo-Information Management System



Abhishek Adhikari , Minakshi Kumar, and Shefali Agrawal

Abstract The orchard management has improved by adequately utilizing the Remote Sensing (RS) and Geo-Information System (GIS). With the expansion of orchards in recent years, the sector has been facing a lack of skilled workers and specialists for optimal irrigation utilities, nutrient intake, canopy pruning, pest prevention, disease detection, and orchard quality management name a few. Sustainable orchard management will get a potential boost if the orchard database is well documented with standardized remote observation. Also, the observations recorded have optimal spectral, spatial, and temporal parameters to estimate overall changes in the orchard health. The Unmanned Aerial System (UAS)-based RS and GIS provide an approach that allows users to collect data efficiently and orderly. The following case study focuses on mapping a mango orchard by utilizing the derived product of the UAV remote sensing, an RGB ortho-imageries for analysis and generation of the orchard geo-management system.

The geo analysis of the orchard is broadly subdivided into two major categories: spatial and spectral properties of the canopies and surroundings. First, the canopies' precise position was determined. Next, the tree height is estimated using the shadow's length, location, and time when the image was captured. From the classified image, individual canopies are labeled, and their top crown size is compared between manually drawn, semi-automatically generated, and field calculated values. It was observed that even though the area difference between these methods was only 1.08 m² on average, the difference in perimeter was 8.2 m on average. The automated process can precisely map borders to the pixel level. Simultaneously, the manual method is limited to human perception of boundaries and will vary from user to user. The canopies' spectral response provides insight and permits the interpretation of their physical properties like health, fruit maturity, and diseases. Furthermore, manual and semi-automatic generated canopies were compared concerning object-based averaged spectra. It was observed that the canopies' histogram was bimodal in the green

A. Adhikari (✉)

Civil Engineering Department (IITR), Roorkee 247667, India
e-mail: abhishek_a@ce.iitr.ac.in

M. Kumar · S. Agrawal

Indian Institute of Remote Sensing (ISRO), Dehradun 248001, India

band in both cases. This can be attributed to the two-year cycle of *Mangifera indica*. Hence some trees were bearing abundant fruits while other canopies bore lesser fruits. Further analysis by estimating canopies center, their accurate position is mapped which is very useful for logistics and management like planning for minimal distance to cover every tree for plucking fruits, visiting, or pruning, simulation of the spread of canopies, simulation of infectious disease, inter canopy gaps (between canopies or ground where sunlight illumination is available) to name a few. Finally, the orchard features such as ‘Canopy Positional Proximity Value’ (CPPV), a positional parameter of an individual tree concerning other trees in the orchard, are defined, which is further used to determine the ‘Orchard Compactness Factor’ (OCF) as an indicator of how densely the trees are packed in an orchard. OCF and CPPV provides information on orchard density as well as shape-size factor for the orchard geo-management. Hence, UAS-RS and GIS are potential tools that can mitigate many problems associated with orchard geo-management, which may further enhance the overall orchard productivity and sustainability.

Keywords Tree canopy · Arboriculture · OBIA · Orchard geo-information system (OGIS) · Unmanned aerial system (UAS)

1 Introduction

Orchards have been part of human civilizations since ancient times. The orchards provide aesthetic values and supply staple food, lumber, and medicinal products. The orchards are the artificial construction of a single or group of tree species generally arranged in a pattern along with anthropogenic utilities, grown mainly for harvesting fruits, nuts, vegetables, spices, and flowers over a small region. The orchard may have different types of trees and arrangements in various patterns. The canopy is which most visible part of the tree and bears fruits and flowers. Thus, canopy observation is one of the necessary factors for knowing the orchard’s health. Also, for extensive orchards, the manual examination is time-consuming and costly. Despite being the source of beneficial products, the orchard’s arboriculture research needs much progress to build a productive and sustainable orchard system. With the rise of modern technology, tracking canopies is done by terrestrial, aerial, and satellite platforms, which are laced with state-of-the-art remote sensing sensors and geolocation. Amongst these, terrestrial sensors provide details of individual trees. Still, the data generated are costlier (and field intensive) to build and maintain. At the same time, most freely available satellite-based sensors are coarse (up to 10 m) in resolution and have fixed revisit time limitations. The best approach for orchard monitoring is currently the UAS and UGV (Unmanned Ground Vehicle) based remote sensing approach to examine the canopies. The UAV-RS (Remote Sensing) provides a multi-dimensional view of the orchard perceived from different viewpoints. They also cover large distances in a short time and supply ultra-high-resolution imagery of the orchard.

The UAV is growing as one of the most versatile machines for surveying. They are being used in space explorations to deep-cave missions. In global research and surveys, drones are used for various applications [6, 7, 9, 11, 14, 28]. In recent years there have also been studies related to forest and tree canopies using UAV remote sensing [5, 8, 12, 15, 17, 18, 21, 24, 25, 29]. Similarly, few studies are focused on using UAV-RS orchard surveys, which will be discussed below. The following paper does not dwell on specific orchard management issues like evapotranspiration, yield estimation, or pest detection. It explores the fundamental ontological aspect of using the commercial off-the-shelf DSLR on a UAV for remote orchard properties extraction. It also compares similarities and differences between the manual and automated approaches to canopy feature extraction. This paper is organized as follows in six sections, as discussed below.

2 Literature Review

The orchards are cultivated throughout various terrain, from semi-arid to high-altitude geographies. There are age-old practices for orchard cultivation. With changing times and rising resource demands, there have been many innovations in orchard management. The UAV-RS-based surveying methods for orchards, plantations, and agroforestry are gaining quite popularity [26, 30]. The UAV-RS-based analysis, a recent method, is still growing, and as it gets more refined, more opportunities are on the rise. The orchard-based RS studies lie between crops and forest remote sensing, except they are smaller in size and are artificially generated resources. There are also not many research papers specific to UAV-RS orchard management, although similar work exists in forest and agricultural RS specialization.

Few papers deal with individual tree delineation [17], which provides high accuracy in tree canopy extraction. Also, few studies on spatial feature extraction of individual trees [13, 18, 20] like height and crown diameter. These papers expressed using SfM (structure from motion) and DSM to extract these features. Even though the results were quite acceptable, the quality of 3D and DSM (Digital surface model) of vegetation is still challenging due to lack of the tie points. Still, the papers cover the basics of orchard and canopies parameters extraction. There are few papers specific to orchard study of evapotranspiration [10, 22], health observation [16], disease detection [1] and yield estimation [4, 21]. There are many products for UAV-based agriculture and forest for sustainable management; not many tools are available for UAV-RS orchard management. Sun et al. [27] used UAV visual imaging for 3D morphological remote canopy evaluations to facilitate the orchard canopy management and control of modern standard orchards. When utilized together, the spectral and spatial properties provide a deeper insight into the industry's challenges. The study bridges the conventional orchard resources management and UAV-RS technology to provide a better resource management paradigm.

3 Material Used

3.1 Study Area

The study area is located near Nahar, Post Koti, Tehsil Vikasnagar, in Dehradun. It is approximately 16 km Northwest of Dehradun city-center. Its (UTM zone 43 N) central point is longitude; its latitude is 782051.684 E and 3371015.043 N Meters. The average elevation is about 648 m above sea level. The study area is an orchard that contains young mango, *Mangifera indica*, and trees owned by the locals. The mango orchard provides healthy fruits and many raw materials used in carpentry, ceremonies, and medicines [23]. The flowers bloom in March end, and by the last of June, the fruits are ready to be plucked. Figure 1 represents the study area map (inside the red box). The reference data are manually collected sample tree data from the field. The instrument used was a densitometer, “Leica Disto D8”. The ten sample canopies were randomly chosen from the dataset, and their canopy height and width along NS and EW directions were recorded from the site.

3.2 Dataset and Tools Used

The dataset used is provided by the PRSD department IIRS-ISRO, Dehradun. The camera used was a Commercially off-the-shelf (COTS) DSLR from SONY, Model: NEX-5 T, without a lens. The UAV model used for surveying was UX5. The UX5

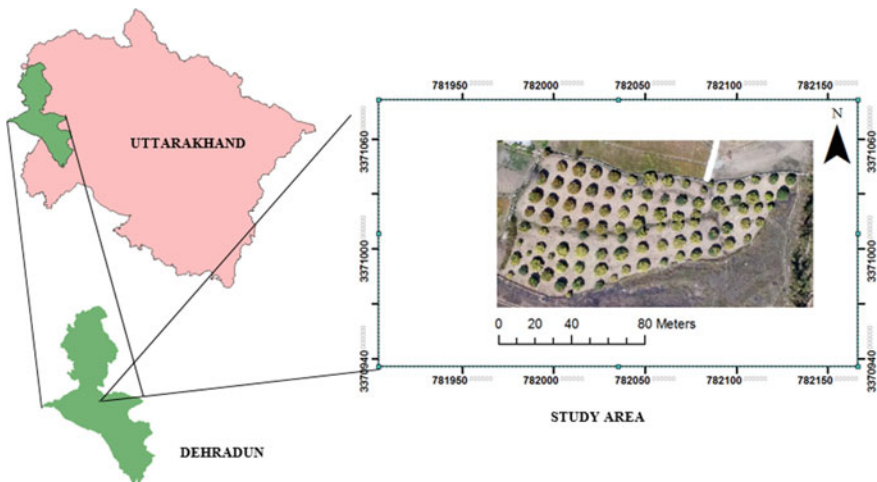


Fig. 1 Study area map

Table 1 Dataset properties

S. no	Characteristics	Values
1.	Size of image	3274 × 4267 Pixels
2.	Date of acquisition	21/march/2016
3.	Time of acquisition	13:32 IST
4.	GSD (Ground sample distance)	13 cm/pixel

is a fixed-wing micro-MS-UAV with a weight of 1 kg and a wingspan of 1 m. The additional details of the dataset are shown in Table 1.

Most programming for processing and analytics was done in R and python. Other tools and software used to assist in completion are Erdas Imagine, ArcGIS, and ENVI, which were for map-making, image processing, and visualization.

4 Methodology

In the following study, the orchard data collection and data processing was conducted as per previous work [3], as shown in Fig. 2. The ultra-high-resolution RGB images using a camera over a UAV platform were collected along with field samples. Then the individual pictures were processed and combined to form the georeferenced ortho-image. The object-based classification provided a better solution for the canopy classification than the pixel approach. Thus the ortho-image was segmented using Simple linear iterative clustering zero (SLICO) [2] with a superpixel of size 451 pixels (approx.). Also, Grey Level Correlation Matrix (GLCM) based textural raster was also used. Finally, a Random Forest (RF) classification was implemented for pixel-based, without textures and variable textural bin sizes. In a recent paper by Adhikari et al. [3], it was observed that for current study area classifier with the input of three bands and Shape Index (SI) (RGB + SI) (model name “OBIA-RF type-2”) gave the best results amongst all models. The complex canopy objects (merged canopies) are manually delineated and saved as shapefile.

In the current study, a few data analysis parameters for orchards are extracted and analyzed. Three significant analyses are based on Spatial, Spectral, and overall orchard-influenced features. The objective is to provide ontologically better insight using currently available knowledge from literature. The tree height is estimated from the shadows cast in the first spatial section. This approach has used shades from raw data and has checked how good they are at estimating the tree height. It is measured using the manually masked image of the tree canopy and its shadows. The model based on Bretagne’s VSOP 87 theory [19] is used to calculate the solar azimuth and elevation angle. The rough height is estimated from the shadow using the calculated shadow length, elevation angle, and center of the tree.

The other spatial properties, the center point positional value of canopy, perimeter, Shape Index (SI), and area, are also investigated. The position, perimeter, and

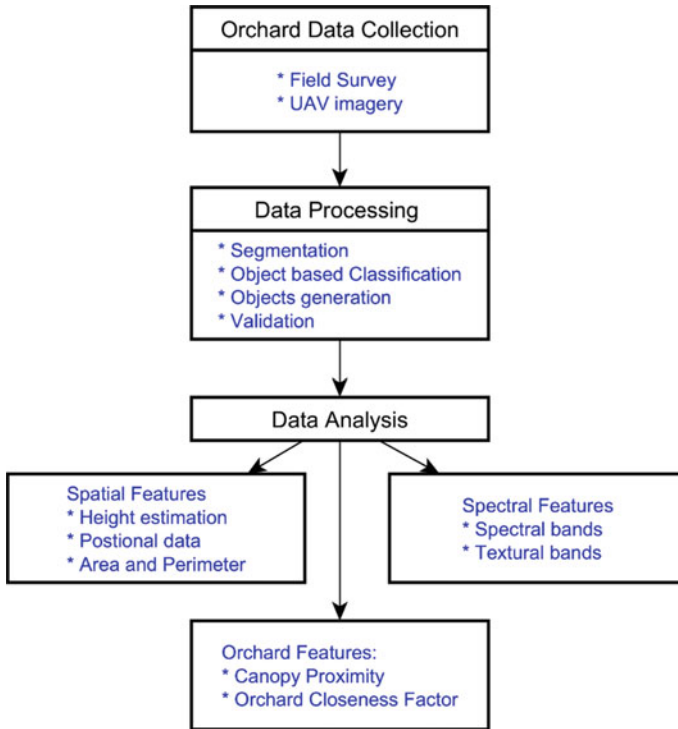


Fig. 2 Methodology flowchart

canopies area were calculated for the manually generated and semi-OBIA-RF type-2 model using the ArcMap measure tool. This data was used to compare the area between field, manual, and model-generated canopies to validate the image's recordings. All three values are statistically plotted for further analysis. The difference in canopy centers was compared between type-2 and manual-generated canopies. This was then used to find the nearest neighbors of an individual tree canopy object. This parameter was further used to rank the average proximity of the canopy concerning the cluster. The average proximity of each tree, when presented as an integrated sum along with normalized by total trees, gives a rough estimate of how closely each tree is packed concerning the whole cluster. It depends on cluster size and canopy centroid closeness to the orchard center. It is termed the "orchard compactness factor for n trees," which tells a rough estimate of how closely the " N " (total) trees are packed in a cluster. Tree canopy height, length, and width samples were measured on the field for area validation. The field data were collected using a measuring tape and diameter from North–South and East–West; the average was taken.

Tree canopy spectral and textural information is essential to understanding the canopy properties related to its species, health, and growth. The spectral canopy feature is visible, but the variation amongst individual canopies in the orchard gives

a general idea of the behavior of canopies. The type-2 canopy objects have also been compared with manually generated canopy using the histogram overlaying. Furthermore, the parameters were observed using a scatterplot to analyze patterns and how closely one parameter is linked to another in both extracted canopy types. The details of the descriptive analysis and findings are presented in the next section.

5 Results and Discussion

This study section focuses on the descriptive analysis of the input parameters extracted from the results. For the tree height estimation, the Solar altitude angle was 56.10°, and azimuth was 210.93°, derived from location and time data. The latitude and longitude information and date and time were taken from the image’s metadata to calculate the angles. The regression plot was used to find the relation between field and extracted values of tree height. In Fig. 3, the link between field and image data for tree height estimation was linear, positive, and strong. The regression estimation (the red dotted trend-line) of the tree height was the factor of 1.1625 (trend-line) with a standard error of 0.0124 units overall. This slight deviation can be due to the error generated while recording field data. Most of the trees were young, and shadows provide a rough estimation of tree heights.

The next step was estimating individual tree canopy size (area) and comparing the values from different approaches. In this, the data (area) from the field and image were compared. The field measurement included measuring the width of the canopy east–west and north–south, finally taking the average to get the diameter, and calculating the radial area of the canopy. The canopies were numbered, as shown in Fig. 4. From Fig. 5, it was observed that manual, type-2, and field-collected samples produced a similar result. Due to the property of SLIC of high boundary adherence

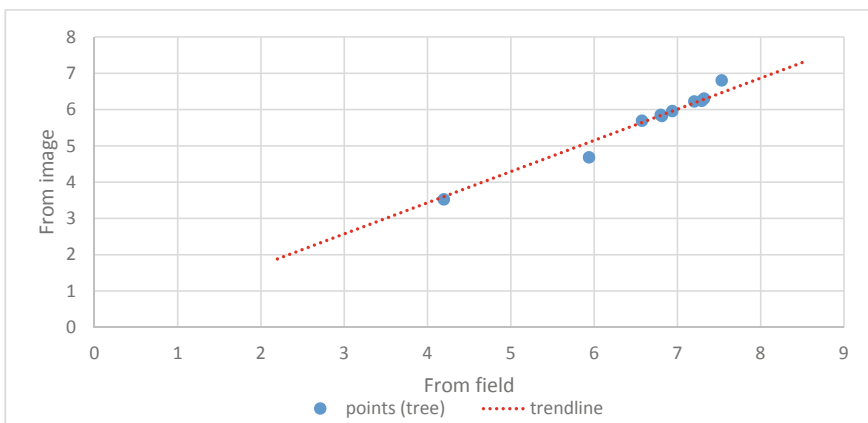


Fig. 3 Regression plot between field-measured and image-derived height



Fig. 4 Labelled canopies of the orchard

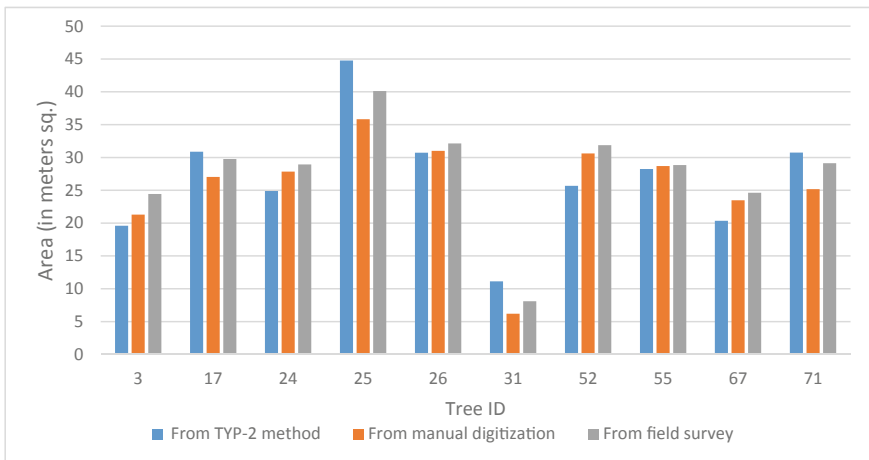
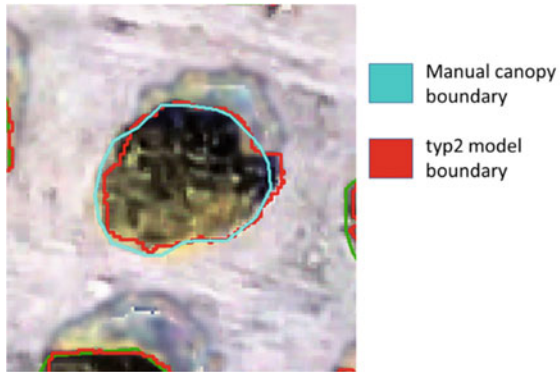


Fig. 5 Comparison of difference areas between manual, automated (type-2), and field canopy area data

but at high-resolution proper boundary adherence is not achieved with the manual approach might be the reason for subtle differences. The field data gives the radial area of the tree. Hence it might contain non-canopy regions. Some error exists at a few locations due to improper delineation due to shadows and ground vegetation. The area overall is over-estimated in automatic methods compared to manual methods by a factor of 1.08 m² on average.

The Difference in Perimeter varies significantly with the automated process over-estimating by the factor of 8.162 m per canopy. It can be attributed to the fact that the manual method tends to generalize the borders. In contrast, due to high boundary

Fig. 6 Tree ID 55 boundary sketch



adherence, the automatic process tends to take minor border details into account. Hence current automatic method tends to give a higher perimeter value in the canopy perimeter. A comparison using the manual and automated method for aerial calculation varies from the individual delineation approach. Furthermore, small holes or extensions can be neglected from manual drawing to generalize the area. The latitude and longitude are defined for the centroid of tree canopies. The geometric centroid varies up to 0.266 m with a standard deviation of 0.144 when manual and type-2 methods are compared. The shape index is also changing, and the average difference is 0.355 per canopy. It was observed that most of the SI of manually extracted canopies are below one, while the shape index of the tree-top from the type-2 model is above one. Figure 6 represents one example of tree ID 55 (notice delineation behavior of manual and automated approach).

It was observed that there was not much difference between manually extracted canopies and OBIA-RF type-2 canopies when band 1 to band 10 (Red (B1), Green (B2), Blue (B3), Mean (B4), variance (B5), homogeneity (B6), contrast (B7), dissimilarity (B8), entropy (B9), and second moment (B)), as shown in Fig. 7. The tree canopy spectral behavior is almost the same for both canopy objects. The mean feature values of object type-2 are slightly lower than the mean of manually generated objects.

In Fig. 8, the relative Kernel Density Estimations (KDE) over normalized (norm) values of the histograms reveal that both canopies are similar in spectral properties but vary in spatial properties like SI and perimeter. There is a minor sub-class (the green band has bimodal histograms) within the canopy. The dual peaks are visible because mangoes are in their blooming cycle, and new leaves and flowers are dominant in many trees. But few trees are not budding in this season, leading to a double hunchback in the histogram of the green (B2) band. The perimeter is more prominent in the type-2 canopies due to better boundary adherence. Overall manual canopies have slightly higher spectral property values while type-2 objects have higher values of perimeter and SI.

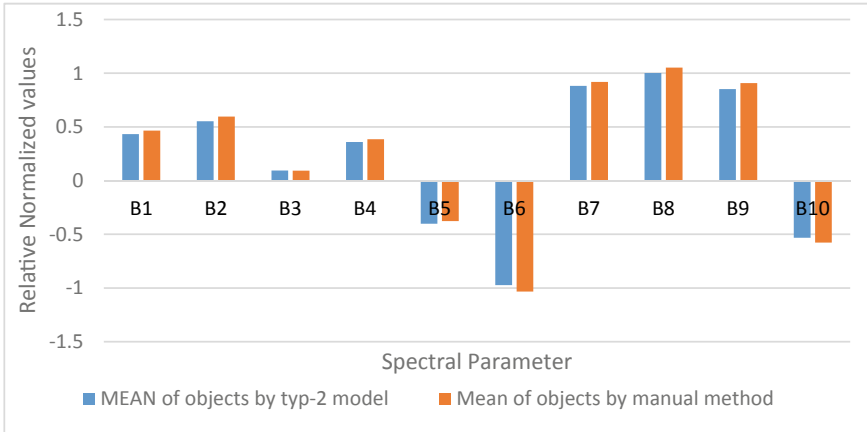


Fig. 7 Comparison of spectral properties

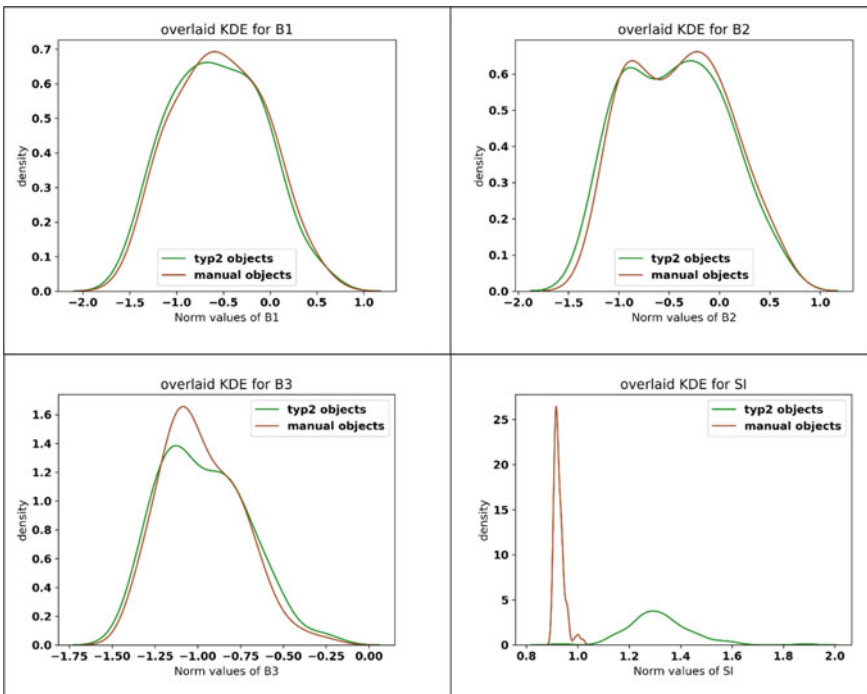


Fig. 8 KDE plots for three spectral bands and shape index (SI)



Fig. 9 Canopy proximity ranking based on proximity distances

The total sum of canopies area off all trees in the orchard using the type-2 model was 2432.3 m², while the manual method estimates 2325.3 m². Two new parameters were also defined and investigated to determine orchard-feature concerning tree canopy positions. An individual tree’s proximity percentage (Canopy Positional Proximity Value (CPPV)) is defined as the canopy’s closeness to the other trees. The larger the value more distant it is from the other trees. It is calculated by averaging the distance from other trees to a particular tree (as shown in Eq. 1). It is given rank in the ascending order called proximity ranking—the ranking from center-most (minimal CPP value) to the corner-most canopy (maximum CPP value). Thus, Tree number 1 denotes the centermost tree in the cluster, while 99 represents the group’s corner-most tree, as shown in Fig. 9. It can be further analyzed to assess the chances of disease spread for a particular canopy.

$$Canopy\ Positional\ Proximity\ Value_i = \frac{\sum_1^N Distance\ from\ tree_n}{N} \quad (1)$$

Furthermore, overall, the canopy density can also be described as the sum of the relative proximity of tree canopy concerning each other (Canopy Positional Proximity Value, as retrieved from Eq. 1) by the total number of trees and termed as Orchard Compactness Factor (OCF) as shown in Eq. 2. It explains how close the canopies are packed in a particular orchard or within a well defined boundary.

$$OCF = \frac{\sum_1^N (Canopy\ Positional\ Proximity\ Value_i)}{N} \quad (2)$$

For the current study area, the calculated *OCF* was observed to be 55.447 m/tree for the type-2 model and 55.478 m/tree for manual canopies, which is quite similar. The orchard tree density is approximately 119.3 trees/hectare. The *OCF* considers positional arrangement (proximity) of each tree with respect to other trees and is easily defined for unconventional-shaped orchards, thus providing information on the tree density as well as shape-size parameter of an orchard.

6 Conclusion

The study investigates UAV-RS derived RGB orthoimage for orchard and canopy image-based definitions and various properties comparison between manual and automated generated canopy objects (type-2 model). The tree's height is one of the essential characteristics collected by conventional field surveys. It was observed that shadow height was overestimated by the factor of 1.1625 (trend-line) with a standard error of 0.0124 units. The linear regression model was quite accurately able to predict size but still had minor errors. It is attributed to multiple sources of error like model-fitting, field measurement, and human-based errors.

A sample of ten trees was selected randomly from a population for area comparison. Data from the field, type-2 model, and polygon (manually generated) were compared. It was observed that the area estimates were quite close, while the field value was much higher than in most of the cases. The area of canopies is one of the primary data gathered in the conventional vegetation surveys. The other spatial factors like perimeter and shape index were also compared between manual and type-2 models. Due to good boundary adherence, the type-2 canopies had a relatively larger perimeter than the manual canopies. The *SI* indicates objects' complexity (compactness); most manual-generated canopies have *SI* lower than one, while type-2 was more spread *SI* and most of it more significant than 1. Hence the type-2 objects are more complex than manual ones as they represent the canopies in their proper shape. The previous known spectral parameters are analyzed and showed highly similar behavior in both models. In B2 (green), there was a bimodal distribution indicating two sub-class within. Due to the budding of mango trees, few were not budding then and had a darker complexion leading to a slightly bi-modal density histogram of the green band. It may further assist in production estimation and Spatio-temporal variation in vegetation health assessment.

The centroid of canopies was quite close in both type-2 and manual models. The centroids were used for nearest neighbor detection and proximity analysis. The proximity analysis covers two crucial features of vegetation survey, frequency, and density of canopies. The canopies were relatively ranked from the centermost to the corner-most tree using proximity percentage within the cluster. The overall orchard compactness of the tree canopy was calculated and found to be 55.447 m/tree for the type-2 model and 55.478 m/tree for the manual approach. It is the mean of the distance of all the trees from one another. The smaller the orchard compactness factor more densely the canopies are packed. Thus, the UAS-based automated delineation

is similar to manually extracted objects alongside a few irregularities. Furthermore, using canopy positional proximity values provide a better way to analyze and categorize the tree canopies than the conventional method. Also, the Orchard compactness factor for a small orchard, which uses the shape and position of individual canopies, provides a better understanding than the orchard density factor, another factor to relate orchard overall density and shape. Through combining the spatial, spectral, and emergent orchard properties, overall orchard canopies were geo-cataloged and are easily used for further analysis and management.

This study used a three visible band (RGB) COTS camera dataset from a single UAS flight for developing an Orchard GIS (OGIS). The following case study highlights the potential of UAS-RS and promotes further investigation of different orchards and sensors with UAS-RS and GIS. The above research likewise highlights the possibility of using modern technology for orchard's tree height, position, canopy area, shape, spectra, and derived features for better OGIS than conventional techniques. Furthermore, this study may be stretched to study different fields like forestry, agriculture, and plantations with UAS-RS with GIS, so they will benefit from implementing automated feature extraction and geo-management.

References

1. Abdulridha J, Batuman O, Ampatzidis Y (2019) UAV-based remote sensing technique to detect citrus canker disease utilizing hyperspectral imaging and machine learning. *Remote Sens* 11(11):1373. <https://doi.org/10.3390/rs11111373>
2. Achanta R, Shaji A, Smith K, Lucchi A, Fua P, Süsstrunk S (2012) SLIC superpixels compared to state-of-the-art superpixel methods. *IEEE Trans Pattern Anal Mach Intell* 34(11):2274–2281. <https://doi.org/10.1109/TPAMI.2012.120>
3. Adhikari A, Kumar M, Agrawal S, Raghavendra S.(2020) An integrated object and machine learning approach for tree canopy extraction from UAV datasets. *J Indian Soc Remote Sens* 1–8. <https://doi.org/10.1007/s12524-020-01240-2>
4. Apolo-Apolo OE, Pérez-Ruiz M, Martínez-Guanter J, Valente J (2020) A cloud-based environment for generating yield estimation maps from apple orchards using UAV imagery and a deep learning technique. *Front Plant Sci* 11. <https://doi.org/10.3389/fpls.2020.01086>
5. Bagaram MB, Giuliarelli D, Chirici G, Giannetti F, Barbati A (2018) UAV remote sensing for biodiversity monitoring: are forest canopy gaps good covariates? *Remote Sens* 10(9):1–28. <https://doi.org/10.3390/rs10091397>
6. Baranwal E, Seth P, Pande H, Raghavendra S, Kushwaha SKP (2020) Application of unmanned aerial vehicle (UAV) for damage assessment of a cultural heritage monument. In: *Lecture notes in civil engineering*, vol 51. Springer, pp 123–131. https://doi.org/10.1007/978-3-030-37393-1_13
7. Crommelinck S, Bennett R, Gerke M, Nex F, Yang MY, Vosselman G (2016) Review of automatic feature extraction from high-resolution optical sensor data for UAV-based cadastral mapping. *Remote Sens* 8(8):689. <https://doi.org/10.3390/rs8080689>
8. Fernandez-Gallego JA, Kefauver SC, Kerfal S, Araus JL (2018) Comparative canopy cover estimation using RGB images from UAV and ground. In: Neale CM, Maltese A (eds) *Remote sensing for agriculture, ecosystems, and hydrology XX*, vol 10783. SPIE, p 20. <https://doi.org/10.1117/12.2501531>
9. Franke J, Becker M, Menz G, Misana S, Mwita E, Nienkemper P (2009) Aerial imagery for monitoring land use in East African wetland ecosystems. In: 2009 IEEE international

- geoscience and remote sensing symposium, V-288-V-291. <https://doi.org/10.1109/IGARSS.2009.5417676>
10. Gonzalez-Dugo V, Zarco-Tejada P, Nicolás E, Nortes PA, Alarcón JJ, Intrigliolo DS, Fereres E (2013) Using high resolution UAV thermal imagery to assess the variability in the water status of five fruit tree species within a commercial orchard. *Precision Agric* 14(6):660–678. <https://doi.org/10.1007/s11119-013-9322-9>
 11. Honkavaara E, Arbiol R, Markelin L, Martinez L, Cramer M, Bovet S, Chandelier L, Ilves R, Klonus S, Marshal P, Schlöpfer D, Tabor M, Thom C, Veje N (2009) Digital airborne photogrammetry—a new tool for quantitative remote sensing?—a state-of-the-art review on radiometric aspects of digital photogrammetric images. *Remote Sens* 1(3):577–605. <https://doi.org/10.3390/rs1030577>
 12. Huang H, Li X, Chen C (2018) Individual tree crown detection and delineation from very-high-resolution UAV images based on bias field and marker-controlled watershed segmentation algorithms. *IEEE J Sel Top Appl Earth Obs Remote Sens* 11(7):2253–2262. <https://doi.org/10.1109/JSTARS.2018.2830410>
 13. Iizuka K, Yonehara T, Itoh M, Kosugi Y, Iizuka K, Yonehara T, Itoh M, Kosugi Y (2017) Estimating tree height and diameter at breast height (DBH) from digital surface models and orthophotos obtained with an unmanned aerial system for a Japanese Cypress (*Chamaecyparis obtusa*) forest. *Remote Sens* 10(2):13. <https://doi.org/10.3390/rs10010013>
 14. Lv Z, Zhang P, Benediktsson JA (2017) Automatic object-oriented, spectral-spatial feature extraction driven by Tobler's first law of geography for very high-resolution aerial imagery classification. *Remote Sens* 9(3). <https://doi.org/10.3390/rs9030285>
 15. Mohan M, Silva CA, Klauber C, Jat P, Catts G, Cardil A, Hudak AT, Dia M (2017) Individual tree detection from unmanned aerial vehicle (UAV) derived canopy height model in an open canopy mixed conifer forest. *Forests* 8(9):1–17. <https://doi.org/10.3390/f8090340>
 16. Naveed Tahir M, Zaigham Abbas Naqvi S, Lan Y, Zhang Y, Wang Y, Afzal M, Jehanzeb Masud Cheema M, Amir S (2018) Real-time estimation of chlorophyll content based on vegetation indices derived from multispectral UAV in the kinnow orchard. *Int J Precis Agric Aviat* 1(1):24–31. <https://doi.org/10.33440/j.ijpaa.20180101.0001>
 17. Nevalainen O, Honkavaara E, Tuominen S, Viljanen N, Hakala T, Yu X, Hyypä J, Saari H, Pölonen I, Imai NN, Tommaselli AMG (2017) Individual tree detection and classification with UAV-based photogrammetric point clouds and hyperspectral imaging. *Remote Sens* 9(3). <https://doi.org/10.3390/rs9030185>
 18. Panagiotidis D, Abdollahnejad A, Surov P, Chiteculo V (2017) Determining tree height and crown diameter from high-resolution UAV imagery. *Int J Remote Sens* 38(8–10):2392–2410. <https://doi.org/10.1080/01431161.2016.1264028>
 19. Reda I, Andreas A (2004) Solar position algorithm for solar radiation applications. *Sol Energy* 76(5):577–589. <https://doi.org/10.1016/J.SOLENER.2003.12.003>
 20. Salami E, Barrado C, Pastor E (2014) UAV flight experiments applied to the remote sensing of vegetated areas. *Remote Sens* 6(11):11051–11081. Multidisciplinary Digital Publishing Institute. <https://doi.org/10.3390/rs6111051>
 21. Sarron J, Malézieux É, Sané C, Faye É (2018) Mango yield mapping at the orchard scale based on tree structure and land cover assessed by UAV. *Remote Sens* 10(12):1900. <https://doi.org/10.3390/rs10121900>
 22. Sepulcre-Cantó G, Zarco-Tejada PJ, Jiménez-Muñoz JC, Sobrino JA, Miguel ED, Villalobos FJ (2006) Detection of water stress in an olive orchard with thermal remote sensing imagery. *Agric For Meteorol* 136(1–2):31–44. <https://doi.org/10.1016/j.agrformet.2006.01.008>
 23. Shah K, Patel M, Patel R, Parmar P (2010) *Mangifera Indica* (Mango). *Pharmaco Rev* 4(7):42–48. Wolters Kluwer -- Medknow Publications. <https://doi.org/10.4103/0973-7847.65325>
 24. Shin P, Sankey T, Moore MM, Thode AE (2018) Evaluating unmanned aerial vehicle images for estimating forest canopy fuels in a ponderosa pine stand. *Remote Sens* 10(8):1266. <https://doi.org/10.3390/rs10081266>
 25. Singh A, Kushwaha SKP (2020) Forest degradation assessment using UAV optical photogrammetry and SAR data. *J Indian Soc Remote Sens* 1–9. <https://doi.org/10.1007/s12524-020-01232-2>

26. Stefas N, Bayram H, Isler V (2019) Vision-based monitoring of orchards with UAVs. *Comput Electron Agric* 163:104814. <https://doi.org/10.1016/j.compag.2019.05.023>
27. Sun G, Wang X, Ding Y, Lu W, Sun Y (2019) Remote measurement of apple orchard canopy information using unmanned aerial vehicle photogrammetry. *Agronomy* 9(11):774. <https://doi.org/10.3390/agronomy9110774>
28. Tiwari A, Sharma SK, Dixit A, Mishra V (2021) UAV remote sensing for campus monitoring: a comparative evaluation of nearest neighbor and rule-based classification. *J Indian Soc Remote Sens* 49(3):527–539. <https://doi.org/10.1007/s12524-020-01268-4>
29. Zhang K, Robinson J, Jing L, Science A (2016) Canopy vertical parameters estimation using unmanned aerial vehicle (UAV) imagery. In: 2016 IEEE international geoscience and remote sensing symposium (IGARSS), pp 2276–2279. <https://doi.org/10.1109/IGARSS.2016.7729588>
30. Zhang C, Valente J, Kooistra L, Guo L, Wang W (2019) Opportunities of UAVs in orchard management. *Int Arch Photogram Remote Sens Spat Inf Sci - ISPRS Arch* 42(2/W13):673–680. <https://doi.org/10.5194/isprs-archives-XLII-2-W13-673-2019>

High-Speed Wi-Fi Systems for Long Range FANETS: Real Problems, Experiments, and Lessons Learnt



Utkarsh Ahuja

Abstract With the combinational use of geospatial and UAV technology, people have shown that much clearer and more precise surface features of the area under consideration can be extracted. Usually, for this, a good quality camera with limited memory is used. Although there are advancements in battery technology, the amount of time required in extracting data, analyze it and then rescheduling another flight is still a challenge. With advancements in Wi-Fi chips, which are light, reliable, and also cost reasonably less, one can set up a system for the swarm of UAVs to collect geospatial imagery data and simultaneously send that data over to the ground for real-time analysis. This will not only save the time for gathering data but will also provide newer opportunities for research. Also as the overall integrated systems are costly, this technology can be used for smaller missions and tinkered UAV projects. This paper discusses vastly experiments that were done for high-speed data transfer rates, the problem one faces during the design of such systems, and lessons learned for further research. FANETS—Flying Ad-Hoc NETWORKS are being widely studied. These days much of the discussions are limited to radio connectivity, which is dependent on heavy equipment loaded on large UAVs. The scope of this study is limited to more affordable, medium to small UAVs that are widely used in geospatial technology as they are agile and small in size. This paper also gives a brief about probabilistic aspects of regular practice that leads to a successful connection. Where there is a large number of nodes, how can hopping help, is also briefly discussed along with its further scopes of research?

Keywords FANET · UAV · Wi-Fi · Ad-Hoc

U. Ahuja (✉)
I-188, Phase 1, Ashok Vihar, Delhi 110052, India
e-mail: utkarshessence.ahuja@gmail.com

© The Author(s), under exclusive license to Springer Nature Switzerland AG 2023
K. Jain et al. (eds.), *Proceedings of UASG 2021: Wings 4 Sustainability*,
Lecture Notes in Civil Engineering 304,
https://doi.org/10.1007/978-3-031-19309-5_28

411

1 Introduction

In the 21st century, data and data delivery became the workhorse of modern industries. Autonomy in businesses, hardware, travel, and ways of living has shown massive productivity in our lives. With the increase in data delivery rates per second, entertainment industries got a sharp boom in the market as high-quality video streaming became easy and handy. With the incoming of Artificial Intelligence data understanding and deciding, results became much faster but presenting them across multiple computers required increasing the speed of the internet. On wireless communication, this required an increase in frequency. Increasing frequency reduces the wireless range of connectivity. But if lesser data speeds that will imply lesser data delivery. UAVs, these days require faster data speeds for quicker results, along with a good reasonable wireless range. Thus, we need to find a solution for both longer ranges as well as reliable and faster data speeds. The networking should be robust and intelligent. Autonomy must be part of the system and decisions must be taken quickly without human intervention.

2 Limiting the Scope

With the limited apparatus, the scope of experiments and conclusions are limited. Thus for connectivity small Wi-Fi modules were used that worked on 2.4 GHz, small System On Chip (SOC) Computers that had 5 GHz Wi-Fi Technology, a quality long-range powerful router with both 2.4G and 5G channel frequency, a long-range powerful repeater, and some lab equipment to put all of them together. The apparatus is an implementation of FANET [1–3]. The repeater and router became part of the ground control station while the Wi-Fi modules and SOC computers became part of FANETs. The path was given, waypoints were decided and geo-fencing algorithms were implemented on the flying UAVs. This information was known to all other UAVs that were part of the experiment. The prominent spatial information of all UAVs is shared in the entire network.

3 Setting Up the Apparatus

The Router was configured such that it serves both 2.4G and 5G frequencies simultaneously. This was done so that the communication to the ground has a completely different spectrum than that of the data delivery. Thus, keeping both the data delivery and communication differences one can have better reliability of the system.

The Flight Controller was already coded with the software that had waypoints and pathways that UAV had to follow. It could be controlled from the ground using the Wi-Fi module. With advancements in a tracking system, adaptive flight control and

decision-making using SOC Computer, instructions to the flight controller could be given from the SOC in the future. The source of power for the flight controller was the same as that for the whole system. The controller had hard wire connections with a Wi-Fi module, with SOC Computer, with GPS receiver, and a battery for operation. All the outputs from the Flight Controller were limited to information signals only, since the power for the Wi-Fi module, SOC Computer was provided from the battery directly, implying that there is no power loss from the flight controller to any electronics attached to it. The flight controller can be instructed from the ground by both the Wi-Fi module as well as by onboard SOCC. This redundancy was made to be sure of optimum communication.

The Wi-Fi Module was well suited for the long-range purpose, as it didn't require great power, was comparable to the costs of connecting wires and solder, and had a quick response and less boot-up time to get connected. The overall module is a microcontroller in itself in which one could burn small scripts for routing the information received from the ground. It works on IEEE 802.11 b/g modes so it has great transferable speeds for instructive data packets coming from the ground. These systems also come with an additional antenna that could be strapped to the airframe such that to receive the maximum signal from the ground. Some researchers have shown much better ways to pick up signals from the ground by making specific hardware that rotates and moves the antenna around the airframe eventually getting maximum signal power reception [4]. The Wi-Fi module had its own power source that could sustain for about 16 h. Voltage regulator modules were placed between the wiring from Flight Controller to Wi-Fi Module as well as between the battery and Wi-Fi module. This was done to ensure a steady current flow across this module as there are spikes of current output from the Flight Controller, whenever the power intake of the power distribution board connected to the Flight Controller increases. These overshoot signals were quite common during the system design and its testing. Thus keeping the Wi-Fi module protected and healthy, only then we can have reliable connectivity across the swarm. The other hardwired connection was between this system as well as SOC Computer. Over the air (OTA) programming was enabled. In this configuration, the module can be programmed while in the air. The only operational part could be programmed. Some modules come with additional memory chips as well that could be only modified by wiring them up. So basic Read Only Code for communication could be done on the ground while the operational part could be modified with ease while the system is airborne. This ensures permanent system security with system accessibility.

The SOC Computer (SOCC) had a running script for data delivery. Since it is an onboard computer it can make decisions based on the algorithm that was running over it. Also giving autonomy to the system can only be done through this hardware. There are two ways to communicate with the SOCC. One was from the SOCC itself and the other was from the Wi-Fi module. The basic instruction code for safe landing and Return to Home (RTH) was burnt in all three devices namely the SOCC, Wi-Fi module, and the flight controller. The action could be called from either of the communication channels. The SOCC further can perform other tasks

such as tracking, following, giving coordinates for pattern formation, etc. to the Flight Controller autonomously.

The GPS Receiver was attached to both Flight Controller and to SOCC. The idea behind this is again the redundancy as discussed earlier. Also if the swarm is made for Remote Sensing then pictures need to be aligned precisely with the earth coordinates for an accurate result. Also, this gives the idea about the position when high-speed data transmission is in trouble. The power for the receiver was given from the power source of the Wi-Fi module with voltage and current regulators between the connection ensuring durability and reliability of the system.

The Data Delivery system is basically a software implementation of networking protocols. There are many APIs and different classes in computer languages that already serve this purpose. Thus the system can be developed based on any relevant and needed routing schemes [1]. The data stack that is supposed to be sent is decided. The stack includes the data along with its GPS coordinates along with a time stamp that should be the same as both the collected image/data and GPS coordinates. Although all the flight data is stored in the flight controller which is also shared via Wi-Fi module to the ground. Another copy of that data is made and stored on the SOCC as well. This data is shared among UAVs when one of them stops listening on the 5G Network. This redundancy helps in retrieving information about the UAV and answering the question that what was UAV doing at what location and what did it capture before it went disconnected. The data is saved on Secure Digital (SD) card and is easily accessible.

Positioning all the hardware onto the UAV is really important. If the UAV is large then the flight controller is placed in the center of the surface plate with no high current wires around it. This is to ensure that magnetic effects due to the high current drawn by motors shouldn't affect the magnetic sensor readings. The Global Positioning System (GPS) Receiver module could be placed near the flight controller. The SOCC can also be placed near the Flight Controller with power input to the opposite side of the Flight Controller to ensure no current problems. The battery is at the center but below the surface plate. This is because all the electronics need to be at the top to receive signals. Although the antenna, if present for the Wi-Fi module is at the center perpendicular to the plane of the battery, hangs vertical pointing to the ground. Since the antenna is usually long, minor eddy currents due to battery drain will not hamper what the antenna will receive. In some situations, people have placed a polystyrene slab and then fixed the antenna in between to have more distance from the battery and to avoid vibrations from the airframe. The former makes more sense than the latter. Also keeping the shape aerodynamic is another problem. The antenna mustn't receive vortex or turbulence from the propellers and wings. This will add a lot of noise to the signal received. In the absence of the antenna, the Wi-Fi module can be placed on one of the legs of the UAV and the same weight can be towed to the other leg for much greater stability. A few grams of extra weight will not affect much of the battery performance as compared to the few processing power used for stability

will. This is done to avoid any electronic interferences from the equipment that might be lying in the vicinity of the antenna.

The area for testing was an open grass field. The field had been mowed properly and then watered. This was done to avoid any flying dust and husk that could collide with the propellers. Also, the particle size is comparable to the wavelengths used, thus to avoid Mie scattering watering was important.

The Waypoints were already decided on the ground and all nodes are aware of the path that is planned for the UAVs. The person on the ground can perform multiple operations for the path planning that could be done for the UAVs in real-time.

For every experiment **Wind and Weather Conditions** were noted. Although in gusts of wind only a communication system was tested and UAVs weren't flown.

The Long Range Wi-Fi Repeater worked on a 2.4G frequency. In normal weather conditions (no precipitation and winds speed <5kmph) the range can reach up to 7 kilometers. Thus for the system for long-range Wi-Fi connectivity, this was the best choice.

Possible Scenarios

For the systems to be durable one needs to understand what sorts of situations UAVs might be used. There are five main elements, air, water, earth, fire, and space. Space will remain out of our scope.

Earth: Remote Sensing; **Water:** Flying in situations while raining, fog, or snowfall; **Air:** Dusty Winds; **Fire:** domestic and forest.

We can think of all other possibilities and can create situations to test the system's performance. Based on the conditions then bring improvements to the system. With the addition of Artificial Intelligence (AI), the system can self-regulate under different conditions. This concept is also known as situational awareness. Thus, the research is limited to gathering active concepts and parameters that will allow the system to respond autonomously in different situations.

4 System Design Proposal

Network hopping as described in [5] appears easy but apparently is more difficult to implement. This idea can be taken and further recommendations could be made. As discussed earlier, all three major systems namely the Flight Controller, SOCC, and Wi-Fi module can be controlled from the ground. Also, Flight Controller can be controlled from both SOCC and Wi-Fi Module. There is another interdependency, the Wi-Fi Module can control SOCC when the module is reprogrammed from the ground. The control is limited to rule out major risks, thus it can just request the SOCC to change its mode from client to an access point (turning on hotspot). In this case, the more reliable network from the Wi-Fi module can still remain in contact with the ground while nodes that have lost connection totally from the ground can

connect to this access point to transfer their data to the ground. The limitation is that the bandwidth is less and only required important data (totally dependent on situations) is sent back to the ground.

Firstly the major question that arises is that when multiple nodes are connected to the access point and there is no connection from the ground how will data reach the ground? In this case, quick switching is done. The moment the farthest node loses connection since its last location is known, the node next to the farthest visible node in the same direction is requested to give an access point. Now the moment this step is taken the nodes within its near range switch their connection to a new access point. The names and addresses of these access points are pre-decided so the lost node tries to connect all the nodes which were in its near region through AP. Also, the lost node has lost communication over 5G, and 2.4G is still connected. Since the range of both nodes (lost and AP) overlap, this new access point is discovered and quickly connected. The data transmission then is such that the incoming data is chunked and sent to all other discoverable nodes with a tag 'for ground'. Then these nodes send this data via a 2.4G network to the ground. In this case, the performance of the system falls but reliability is still maintained. Also, there is a memory limit on all of these nodes, thus, the data they are collecting themselves has to be sent to the ground.

In continuation of this process, after a while when data limits are approachable the system that being is the host, requests the ground that limit is being reached, and the ground requests the other node to be an access point. The other node first sends all its data via the 5G network after switching, then it becomes an access point. During data relieving all other nodes also do the same, but not the earlier node serving as the access point. The farthest node records the data but doesn't share it. The earlier access point node relieves the data and flags, 'not to be served for AP' or access point and moves away from the local network formed over the air. The new node is now discoverable by the lost node. The process repeats as earlier. In this case, the ground decides which node is to be the access point. Although there are proposals for this system to be automated as well, just on one condition that the edge node should never be an access point. Figure 1 explains well.

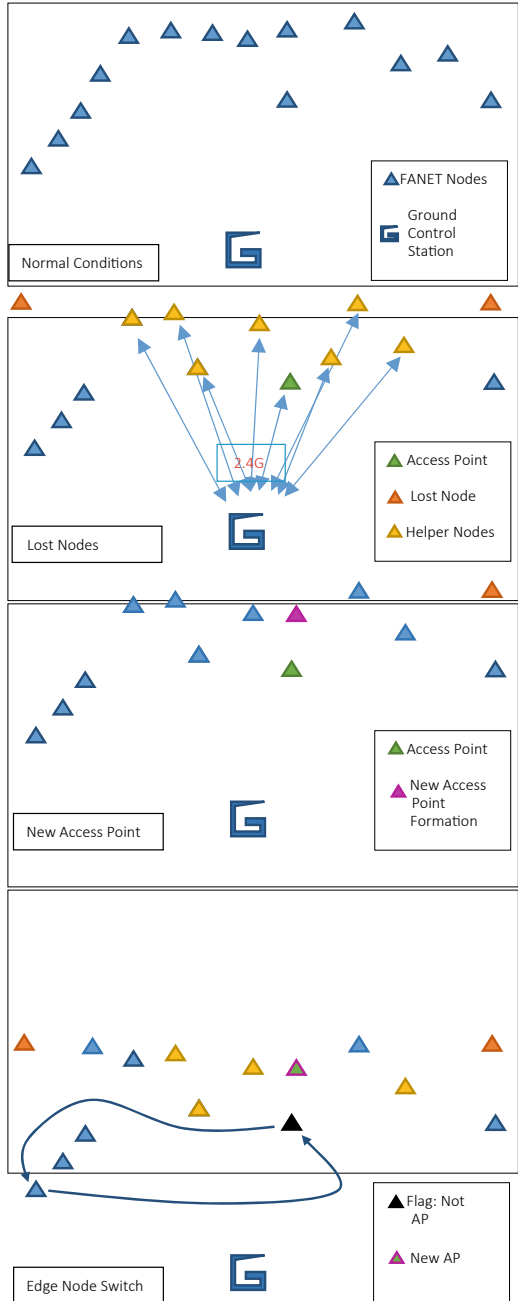
4.1 Common Situations and Practices

Situation: What if the node serving as Access Point fails?

Practice: OTA network is sharing information directly to the ground using a 2.4G network. If any case ground doesn't receive any reply from the access point serving node, then it checks the data coming from all other nodes. In this case, all other nodes have a flag enabled that contains information about the access point and if it is active or not. The ground checks for that flag.

In the case where the ground is receiving a connection, and the 5G connection fails, the other nodes will not have the flag and then the ground will request a new node to serve as an access point. This failed node will return home.

Fig. 1 Communication process in proposed FANET



Situation: Flying the FANETs in open fields for research and testing.

Practice: Antenna Configuration: Never point all the antennas in one direction. In the case where the router at the ground has four antennas, point three of them inclined with the three axes (XYZ) and the last one inclined forty-five degrees to all of them for maximum reception. Some researchers have shown antenna arrays to be promising [6]. Field: Watering the field is important for avoiding any dust and husk particles that could harm the propeller and hamper the strength of the signal due to Mie scattering. Ground Control Fencing: Usually people tend to protect their area with metallic fencing or nets that have thin metallic wires winded into ropes. The fencing will interfere with the signals. Never let anything or anyone stay in between the line of sight of the communication system [7]. Always keep your Personal Computer systems away from multiple electronic devices during the test as they too interfere with the signals. Flying the UAVs in such that they are collinear with the router is not recommended, this causes interference in communication. Although choosing different channels using MIMO (Multiple Input and Output) Antennas can help lower down the effect, provided that the frequency the channel exploits aren't overlapping. But remember that the nodes flying farther use channels with lesser frequency.

Probabilistic View: Given the surrounding and weather conditions in the case of the 2.4G network, consider the probability of successful connection between a single FANET node to the Ground node as 'p'. And of failure as $1 - p$. Let 'X' be our random variable.

So $P(X = \text{successful connection}) = p$

$P(X = \text{unsuccessful connection}) = 1 - p$

Also, let 'q' define the probability of successful connection of lost node to Access Point Node on 5G network. Then that of failure is $1 - q$.

Since both events are independent thus, expectation E for successful connection during a lost node is 'PQ' and for unsuccessful is $(1 - p) * (1 - q)$. Also, the joint distribution of both events will also be the same since both events are independent. Since:

$$p, q < 1$$

Thus, P^{kQ^t} , where both $k, t > 1$, which implies multiple hops, the expectation of the event involving multiple hops will always be less than 'PQ'

Naturally $p^k q^t < PQ$. Thus more hopping implies a lesser probability of successful connection.

In the next section let us see how different scenarios affect these variables.

5 Experiments and Solutions

Fire: In all sorts of fire, domestic, commercial, and forest, soot particles whose size is comparable to the frequencies used in this system (Mie Scattering), along with ionized air will interfere with the frequencies. Thus if the probability of success drops

by some amount 't', then: Expectation will be as $(p - t) * (q - t)$, which is quadratic with 't'. If there is another hop then Expectation drops as $(p - t) * (q - t)^2$. This implies the expectation of successful connection drops exponentially with more hops of the data packet sent from the lost node to the ground. Now let us understand how does 't' change with different types of fires. For domestic fires, many researchers have shown how UAVs help in extinguishing fires, by spraying water through the windows. In this case 't' is negligibly small. Thus this scenario is similar to Open Field.

Now consider a large commercial fire, in this case, large UAVs with water pockets for spraying will have to enter the arena of fire. The communication pathway will look like the Fig. 2.

Hopping is a requirement, because if communication is done in the line of sight, then the path from ground to UAV will be close enough to fire and soot, thus making values of 't' larger.

In case of forest fires hopping will have to be increased. The approach toward the fire must be from the direction of the wind. This is to avoid drag and smoking (Fig. 3).

In this case, the middle UAV will serve as Access Point for the 5G network. The node connected directly to the ground shall communicate over 2.4G. The last node (rightmost), as we call it 'explorer node' will not be able to connect over a 2.4G network, it will use only 5G to connect to the middle node.

Fig. 2 FANET Schematic in case of Commercial Fire

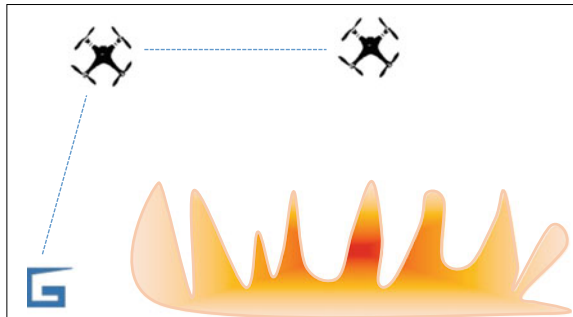


Fig. 3 FANET Schematic in case of Forest Fire

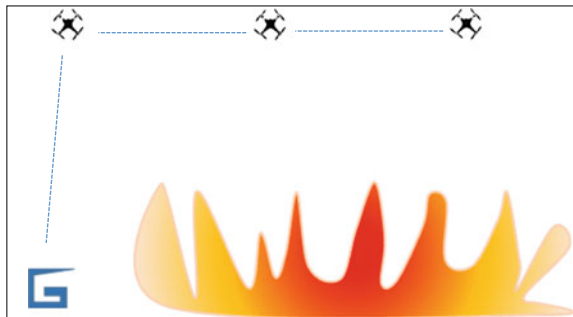
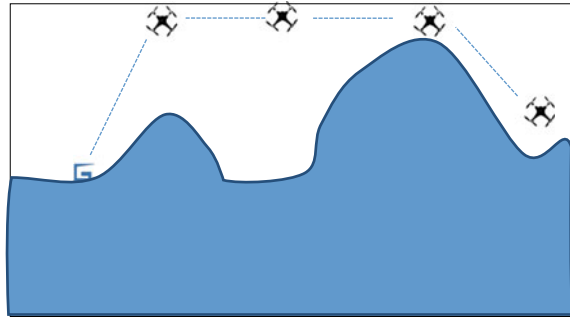


Fig. 4 FANET Schematic in case of Remote Sensing in mountainous regions



Earth: Consider remote sensing in mountainous regions. The first preference must be that the ground station should be at a greater or comparable height as compared to the sensing area. Greater height will give an advantage, lesser hopping will be required. Figure 4 depicts it well.

In this case, switching is required to be done. The right-most node is the explorer node, and adjacent to it is the switching node. Since this node is also not visible this will act as virtual ground (VG) for the explorer node. The virtual ground will be geofenced and if it crosses that region farther from the ground, it will autonomously come near to the ground to get connected, while the explorer will either hover or land. The second node from the left will act as AP. The way this works is as:

Step 1: Only the explorer node can wander, the rest of the nodes are geofenced and can be treated as static nodes [3].

Step 2: The node adjacent to the explorer node will become VG. This node will receive data from a wanderer, the wanderer knows the data holding capacity of this node, thus after a certain amount of data is sent, it will stop sending data over a 5G network. Although it will send location and other high priority (example: system information) data via 2.4G to VG.

Step 3: Data held by VG has to be relieved, thus VG's 5G network switches to the client, while 2.4G is still an AP. In this configuration, the last node explorer node is still connected over to the ground. The VG, which is a client on 5G now will connect to the node serving AP. It will deliver data to it.

Step 4: Once all data is relieved, it will switch back to VG continuing the same process as before. This sort of hopping or relaying, though is not that efficient in data delivery, but is reliable and can serve exploring areas under threat or not easy to reach.

Problems faced: Such tests are carried out at higher altitudes, thus fog, clouds, and high-speed winds must be avoided. For such situations, directional antennas could be used [8].

Similar strategies could be used in urban areas with taller buildings around. This will help to analyze areas around the building. This system gives an opportunity

in civil engineering to remotely sense and create models for larger structures of buildings. There are studies and results that depict about the scattering of signals by the walls and materials in it. The power consumption is also calculated [9].

Water: In the case of rainfall, and snowfall, Mie Scattering effect is prevalent. Also while propagating through water, light bends, some part of it is reflected and the light that emerges is not intended to follow the path towards which it was sent to. In cases like these, a hefty amount of noise is added. Also, the same signal will be received multiple times. This is because a ray of light that passes through more drops will be received a little time after than the ones that traveled a lesser number of drops. Thus during rainfall, this system will have a very short range.

6 Lessons Learnt

Results from an experiment like these vary a lot due to so many natural random effects. Thus results will never be consistent. Although the conclusion will always be so.

For all situations, research and development are majorly focused on the variable 't'. The idea is how should we reduce 't' based on different scenarios. The practices that we have discussed help in the propagation of the signal with minimum interference. Experiments, if carried out in different environments will give different results, thus discussing the practices and lessons learned to become more relevant.

The major factors that relate to the value of 't' directly are, **transmission power, Antenna directionality, radiation pattern, and medium of travel**. These factors are prevalent, however, custom designing of communication systems and many other factors will involve. But presently that research and its result are out of our scope. Smart antennas could be a better solution in open fields as they can form beams in the direction of the receiver [10]. Such systems can be used on grounds because the antennas are larger in size. For medium, to large UAVs, these systems can be helpful.

In open spaces, one should always take care of the weather conditions, antenna configuration, large metallic structures, dust, line of sight and fog conditions

In closed testing areas, one should see that large safety nets aren't in the pathway of the signal along with the factors discussed above.

7 Conclusions

Table 1 concludes with possible factors that affect the signal strength. While designing this phenomenon must be taken into consideration.

Table 1 Major phenomenon adding to loss of signal strength thereby increasing values of ‘t’

Medium of travel	Dispersion, scattering, diffraction
Antenna	Orientation and inclination, low transmission power, ineffective beamforming, and directionality
Weather	Dusty winds, fog, and mist
Pathway	Larger objects and interfering blockages
Computational power	The weak processing power of router, inefficient processing of SOCC
Architectural and civil	design of the ground station, light echo
Electronics	Interfering electronics

References

1. Khan MF, Yau K-LA, Noor RM, Imran MA (2020) Routing schemes in FANETs: a survey. *Sensors* 20:38
2. Singh K, Verma AK (2015) Experimental analysis of AODV, DSDV and OLSR routing protocol for flying adhoc networks (FANETs). In: 2015 IEEE international conference on electrical, computer and communication technologies (ICECCT), Coimbatore, India, pp 1–4. <https://doi.org/10.1109/ICECCT.2015.7226085>
3. D. Dugaev, S. Zinov, E. Siemens and V. Shuvalov, "A survey and performance evaluation of ad-hoc multi-hop routing protocols for static outdoor networks," 2015 International Siberian Conference on Control and Communications (SIBCON), Omsk, Russia, 2015, pp. 1–11, DOI: <https://doi.org/10.1109/SIBCON.2015.7147048>.
4. Xie J, AI-Emrani F, Gu Y, Wan Y, Fu S (2016) UAV-carried long-distance Wi-Fi communication infrastructure. In: AIAA 2016-0747. AIAA Infotech @ Aerospace
5. Purta R, Nagrecha S, Madey G (2013) Multi-hop communications in a swarm of UAVs. *Simul Ser* 45
6. Breheny SH, D’Andrea R, Miller JC (2003) Using airborne vehicle-based antenna arrays to improve communications with UAV clusters. In: 42nd IEEE international conference on decision and control (IEEE Cat. No. 03CH37475), Maui, HI, USA, vol 4, pp 4158–4162. <https://doi.org/10.1109/CDC.2003.1271801>
7. Betzalel N, Ben Ishai P, Feldman Y (2018) The human skin as a sub-THz receiver—does 5G pose a danger to it or not? *Environ Res* 163:208–216. <https://doi.org/10.1016/j.envres.2018.01.032>. Epub 2018 Feb 22 PMID: 29459303
8. Etinger A, Golovachev Y, Shoshanim O, Pinhasi GA, Pinhasi Y (2020) Experimental study of fog and suspended water effects on the 5G millimeter wave communication channel. *Electronics* 9:720. <https://doi.org/10.3390/electronics9050720>
9. Duong D, Xu Y, David K (2018) Comparing the performance of Wi-Fi fingerprinting using the 2.4 GHz and 5 GHz signals. In: 2018 IEEE 87th vehicular technology conference (VTC Spring), Porto, Portugal
10. Porcello JC (2013) Designing and implementing multibeam smart antennas for high bandwidth UAV communications using FPGAs. In: 2013 IEEE aerospace conference, Big Sky, MT, USA, pp 1–12. <https://doi.org/10.1109/AERO.2013.6496887>

Algal Bloom Detection Using UAV Imagery: A Case Study on Waddepally Lake, Warangal



Allu Ayyappa Reddy, M. Shashi, and Kumarapu Kumar

Abstract Algal blooms are commonly grown in the aquatic environment due to the excessive nutrients (nitrogen and phosphorous) present in ponds and reservoirs. Harmful algal blooms can produce toxic compounds that can contaminate the water and cause serious and harmful effects on aquatic life. Along with algal blooms the presence of other organic matter also makes huge gallons of water unfit for consumption. Remote Sensing is one of the efficient and well-established technologies that is used for the detection of phytoplankton present in the water. Monitoring the rapid growth of algal blooms continuously requires high-resolution spatial and temporal satellite data sets that are costly and hard to get. The images acquired through Unmanned Air Vehicle (UAV) produce high spatial resolution information to continuously monitor the algal bloom growth variation cost-effectively. In this proposed work, the algal bloom presented in the Waddepally Lake (Warangal, India) was captured by using a multispectral sensor mounted in DJI Phantom 4 Pro V2.0. RGB images were acquired and pre-processed in Pix4D Mapper Pro to develop the orthomosaic image. NGRDI, NGBDI, GNDVI, and ExGI indices are used in this proposed work to extract the algal bloom matter present in the lake and the data is compared with the Sentinel-2A images for validation purposes. UAV plays an important role in continuously monitoring the algae biomass and developing the precautionary warning system accurately.

Keywords Algal bloom · Indices · Orthomosaic · Remote sensing · Unmanned air vehicle

A. Ayyappa Reddy (✉) · M. Shashi · K. Kumar
Department of Civil Engineering, NIT Warangal, Warangal, India
e-mail: aa721015@student.nitw.ac.in

M. Shashi
e-mail: mshashi@nitw.ac.in

K. Kumar
e-mail: kkumar@student.nitw.ac.in

1 Introduction

Algal blooms are naturally occurring phenomena in marine and freshwater ecology. The study of environmental factors such as nutrient and light availability, water pH, wind speed, and water temperatures. Toxic and non-toxic algal species can clog fish gills, deplete oxygen levels in the water, release toxins and kill fish and other organisms. Dinoflagellates, diatoms, and cyanobacteria are the main causes of harmful algal blooms (HABs). Toxins produced by each of these phytoplankton groups may be harmful to aquatic and terrestrial organisms. So many methods are used to detect and estimation of algae present in the water. In that, the Remote Sensing technique is used to detect the phytoplankton (algae) presence based on the spectral reflectance of the surface features but the accuracy is low because the spatial resolution of the satellite imagery is at meter level [1, 2]. High spatial resolution (in centimeter-level) imagery will be helpful to identify the macrophytes and phytoplankton presented in water but it is cost-effective and the revisit period is more [3, 4].

UAVs are flying at the terrestrial level and the images have a high spatial resolution (in centimeters) but the spectral bands are limited. UAVs are generally having RGB bands, which are used to identify the surface features but their internal structures will not be captured [2]. The spectral reflectance of algae blooms is sensitive to red and green bands, and a regular RGB digital camera sensor can be used to estimate the coverage of algae on the water surface. Combinations of RGB bands from a RGB camera, including NGRDI (Normalized Green Red Difference Index), NGBDI (Normalized Green Blue Difference Index), GNDVI (Green Normalized Difference Vegetation Index), and ExGI (Excess Green Index) were used to distinguish offshore floating green tide [3, 5–7]. A supervised, pixel-based Random Trees classifier was utilized as a detection mechanism to estimate the percent cover of submerged filamentous algae and rooted macrophytes from aerial photos. Multi-spectral and hyperspectral bands are used to classify the different features based on their spectral reflectance of the features on a particular band.

In the present study, RGB bands are used for capturing the algal parameters present in the water body. Algal bloom images are easy to mosaicking by the generation of ground control points (GCPs) based on the tone and texture parameters but water is difficult to image because of wave interference, sunlight reflection, shadows, water turbidity, and the absence of ground control points or unique landscape features in a continuous body of water [3, 6, 8]. Fluid-lensing techniques and structure-from-motion photogrammetry algorithms are being developed in response to ripple distortion to enhance the clarity and dimensions of water imagery [6]. To improve the chances of smooth mosaicking in water, UAV pilots can fly with a fraction of land, coast, or a specific object in the photos but for a large area of water bodies, it is difficult to maintain. The coverage area of the phytoplankton presence in the water is to be measured from the orthorectified image product mosaicked from a picture assortment, wherever the geometric distortion has been corrected and therefore the imagination has been color balanced to supply a seamless mosaic dataset. The amount

of coverage area can be determined using several mechanisms, with supervised pixel-based random classifiers and maximum likelihood algorithms being particularly useful for detecting submerged filamentous algae and rooted macrophytes from a UAV orthomosaic image [8].

The main objective of the present study is the detection and classification of algal blooms from RGB images of UAV imagery using indices and classification algorithms and validation with the classified images from Sentinel—2A images.

2 Study Area

For the tri-cities of Warangal urban, drinking water is supplied from the Waddepally Lake and Bhadrakali Lake, which was located in Warangal, Telangana, India (see Fig. 1). In those two, the Kakatiya Rajulakam digs Waddepally Lake and it is not only used for drinking purposes but also irrigating the surrounding lands. Waddepally Lake covered an area of 272.45 ha and the perimeter is 26.35 km in the position of 17.983° N and 79.511° E. It has a storage reservoir to sustain the needs of drinking water in summer and the storage capacity is 0.8 TMC (Thousand Million Cubic Feet). A railway track has divided the lake into a lake and storage part. In this study area, excessive nutrients passed from the surrounding crops and rainwater to the storage point of the lake, and a huge volume of macrophytes and floating algae were found which was identified by using the UAV images.

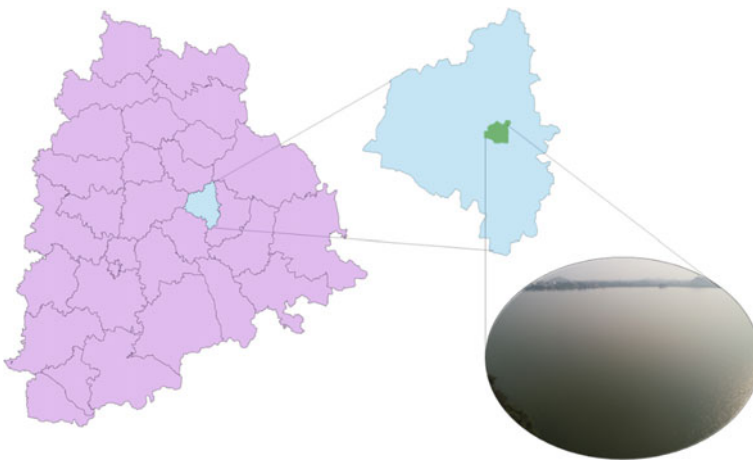


Fig. 1 Waddepally Lake location in Telangana

3 Methodology

The methodology of detection and validation of algal bloom present in the lake from the UAV imagery and satellite imagery are shown in Fig. 2.

3.1 Data Collection

UAV:

Aerial images were acquired using a DJI Phantom 4 Pro V2.0 Quadcopter attached with a 20-megapixel camera which is moving at speed of 10 m/s to detect the phytoplankton and macrophytes presence in the water. CMOS sensor was attached to the camera to capture the RGB images using the wavelengths of 660 nm (Red), 550 nm (Green), and 470 nm (Blue). This camera has an 8.8 mm focal length and the resolution is 5472×3648 pixels. Flights were conducted to acquire the images of the lake at a height of 100 m with 70% overlapping, face toward the center and the camera angle is 90° . The flight path of the UAV is designed in the Pix4Dcapture application along with the supporting application of Ctrl + DJI. DJI Phantom 4 Pro V2.0 Quadcopter rotorcraft is capable to perform a survey on the field for a period of 20–30 min with one battery. For acquiring the total images of the lake, 7 flights were performed.

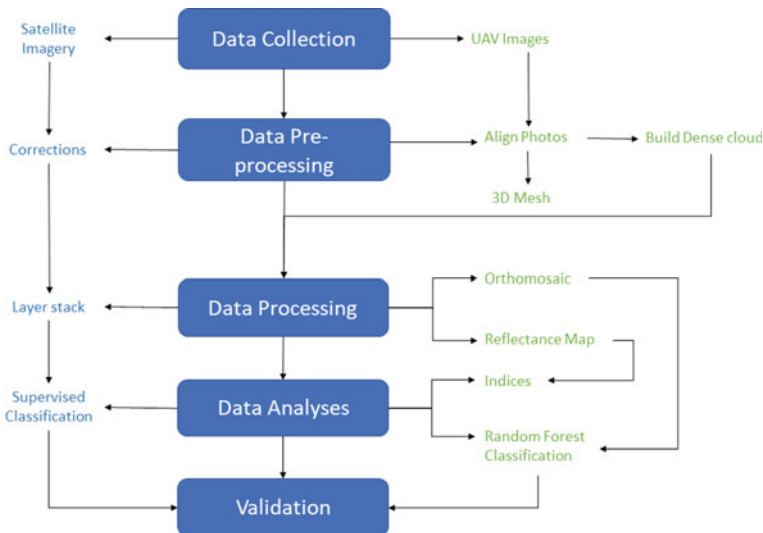


Fig. 2 Methodology flowchart of the algal detection using UAV imagery

Satellite Imagery:

Sentinel—2 images were collected to validate the analysis of UAV imagery. A 10 m spatial resolution and multispectral bands of Sentinel—2A L1C products are collected on the date of 12th February 2021 from USGS GloVis website. Layer stacks Band—2, 3, 4, and 8 (Blue, Green, Red, and NIR) were used to perform the classification of the land cover features present in the lake.

3.2 Data Preprocessing

The ground control points (GCP) of UAV images are collected automatically by using the inbuilt GPS (Global Positioning System) and IMU (Inertial Measurement Unit) in a quadcopter. These GCPs help locate the camera positions and the roll, yaw, and pitch movement of the quadcopter collected by using the Ctrl + DJI application. Based on the inertial measurements and GCP's Pix 4Denterprice software aligning the photos automatically. After aligning the photos, tie points are generated from the key points of the cameras to calibrate the images. A Dense point cloud is prepared from the automatic tie points of the calibrated images to reconstruct the model and it stores the location (latitude, longitude, and altitude) and color information of each point, which provides accurate measurements. This point cloud data is useful for generating the orthomosaic, DSM (Digital Surface Model), and Reflectance maps. 3D mesh is created to visualize the shape of the model from the projected images and it is decreasing the complexity of the model but it is not useful for performing the measurements.

Sentinel—2A L1C products are ortho-rectified and spatially registered and also radiometrically and geometrically corrected products. While preprocessing, atmospheric corrections are performed to the image to remove the atmospheric effects from images.

3.3 Data Processing

A Point Cloud is a collection of data points, which are generated from the preprocessing of UAV imagery, and these are used to develop the orthomosaic, reflectance maps, and 3D meshes. The orthomosaic generation is dependent on orthorectification and it eliminates the perspective distortions from the images using the DSM (Digital Surface Model). The orthomosaic image is used to perform the measurements and classification of the objects using algorithms. The Orthomosaic image of the study area is represented in Fig. 3.

Reflectance maps are generated from the surface reflectance of the objects on a particular wavelength and the pixel value is computed based on the weighted average of all the pixels. Reflectance maps have the radiometric information, which

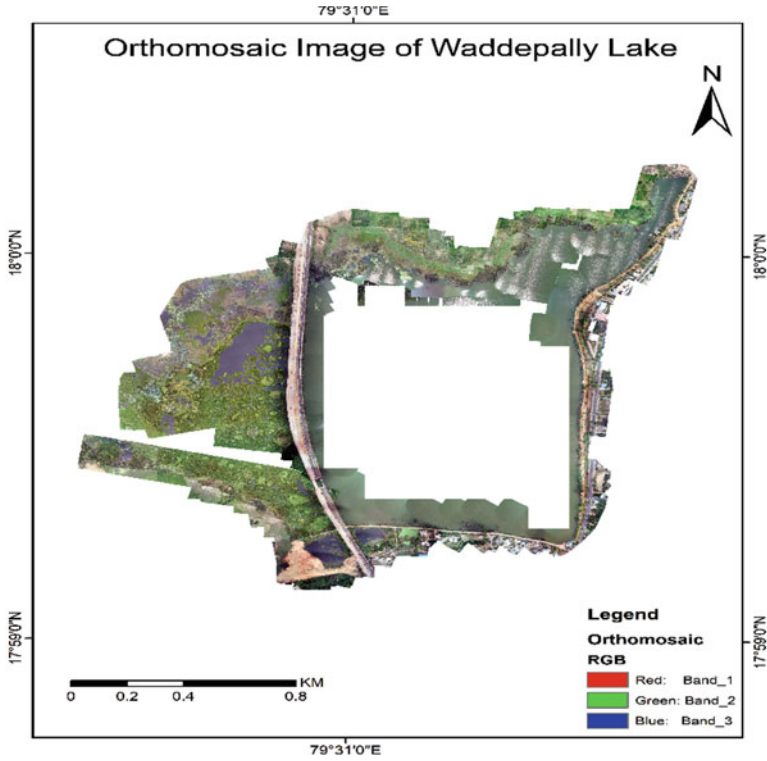


Fig. 3 Orthomosaic image of Waddepalli Lake from UAV imagery

is combined to generate the index maps for detecting the features, based on the indices values. Reflectance maps of red, green, and blue bands of UAV imagery showed in Fig. 4.

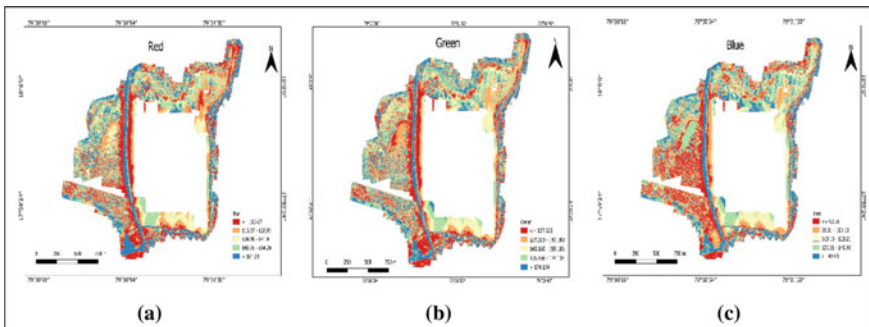


Fig. 4 Reflectance maps of red (a), green (b), and blue (c) bands of UAV imagery

The corrected products of the Sentinel—2A imagery are layer stacked into a single image for classifying the land cover features.

3.4 Data Analysis

Indices:

Reflectance maps of R, G, and B bands are used to develop the NGRDI, NGBDI, GNDVI, and ExGI indices for the identification of phytoplankton present in the water. The equations of the indices are listed below:

$$NGRDI = \frac{Green - Red}{Green + Red} \quad (1)$$

$$NGBDI = \frac{Green - Blue}{Green + Blue} \quad (2)$$

$$GNDVI = \frac{2 \times Green - Red - Blue}{2 \times Green + Red + Blue} \quad (3)$$

$$ExGI = 2 \times Green - Red - Blue \quad (4)$$

Classification:

QGIS software was used to train the samples and apply a pixel-dependent supervised classifier based on Random Trees to the UAV orthomosaic image. To train the dataset, nearly 20 training sites were chosen per each class (algae, water body, and road network) and used in the Random Forest (RF) algorithm to classify land cover features.

Layer stack of Sentinel—2A image is classified by using the supervised classification method in ERDAS Imagine software. A Maximum likelihood (ML) algorithm was performed to classify the image from the signatures of each class and is prepared by training the datasets from the layer-stacked image.

3.5 Validation

Accuracy of the indices, classified orthomosaic image of UAV, and Sentinel—2A image are assessed by comparing the coverage area of the algae and performing the accuracy assessment tool using the field data and ground truth data. Accuracy assessment tool performed for the land cover classification in Semi Classification Plugin (SCP) in QGIS, for that 20 random samples of each class have been taken and assign the original class value to each sample.

4 Results and Discussion

Observation from the ortomosaic image of UAV imagery (Fig. 3), there is a loss of water body in the image because the calibration of the image is not performed due to the lack of GCPs in ripple distortion and level surface of a water body but the remaining portion of the lake images are produced the centimeter level (2.91 cm ground sample distance) information. NGRDI, NGBDI, GNDVI, and ExGI indices are used to identify the phytoplankton from the water and soil parameters and also to monitor the intensity of vegetation growth from RGB images.

NGRDI of UAV imagery is used to monitor the intensity of vegetation growth and it is shown in Fig. 5. NGRDI values generally vary from -1 to 1 the low value indicates the built-up and barren and the higher value represents the vegetation which includes algae and macrophytes. Understanding from the Fig. 5 is less than 0.021 is built-up, 0.021 to 0.062 represents water, and more than 0.062 indicates the presence of vegetation and phytoplankton.

NGBDI of UAV imagery represents the activity of vegetation and the value varies from -1 to 1.0 as shown in Fig. 6. The lower value (less than 0.091) of NGBDI represents the built-up and mud water (high reflectance features), and the high value (more than 0.145) represents the phytoplankton.

GNDVI and ExGI indices are used to represent the photosynthetic activity of vegetation and distinguish the vegetation from soil and it is shown in Figs. 7 and

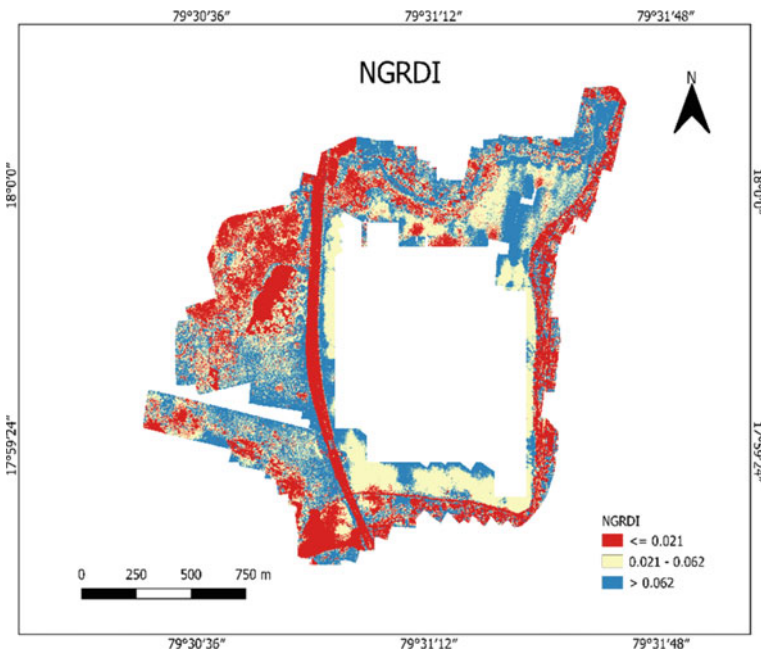


Fig. 5 Normalized Green Red Difference Index (NGRDI) of UAV imagery

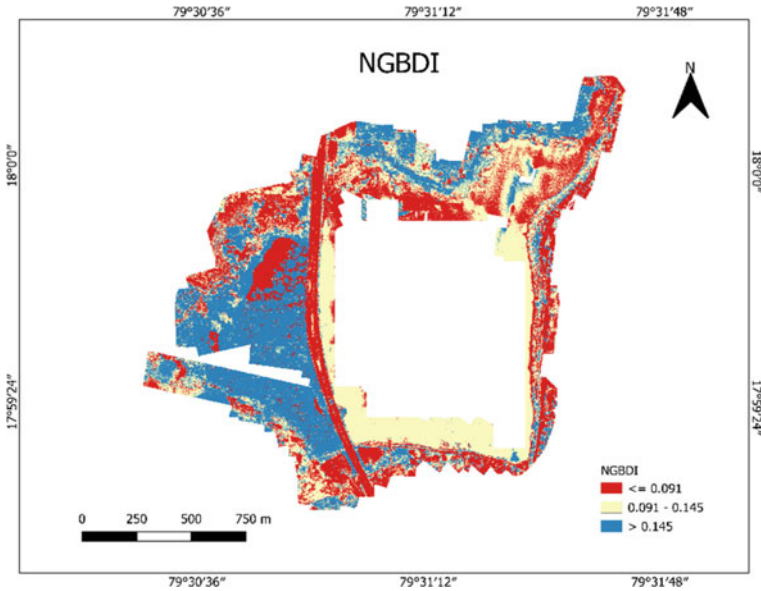


Fig. 6 Normalized Green Blue Difference Index (NGBDI) of UAV imagery

8 respectively. Like the NGRDI and NGBDI, low values of the GNDVI and ExGI represent the high reflectance parameters such as buildup, soil, etc. and the high value indicates the vegetation parameters such as Algae, macrophytes, trees, etc.

These four indices are producing the information on algae and macrophytes' presence in the total area and are validated by using the land cover classification of UAV imagery and sentinel—2A imagery. Land cover classification of UAV imagery using the Random forest classification algorithm and Sentinel—2A imagery using the Maximum likelihood algorithm is shown in Figs. 9 and 10 respectively.

In this study, RGB images of UAVs are identifying the surface level parameters and it is unable to detect the depth of the microphytes below the surface level of the water bodies with visible spectral bands.

The coverage area of algae and the percentage of the accuracy compare the accuracy of the indices and classification maps and it is represented in Table 1.

The coverage area of the algae from the indices is nearly equal to each other, and the classified UAV imagery is nearly equal to each other. As compared to classified Sentinel—2A imagery, classified UAV imagery has a higher percentage of correctness and a higher Kappa coefficient.

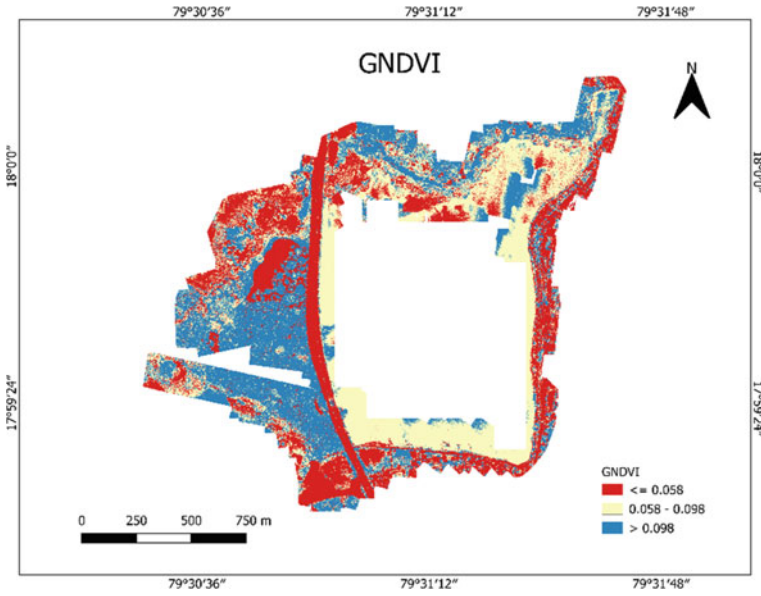


Fig. 7 Green Normalized Difference Vegetation Index (GNDVI) of UAV imagery

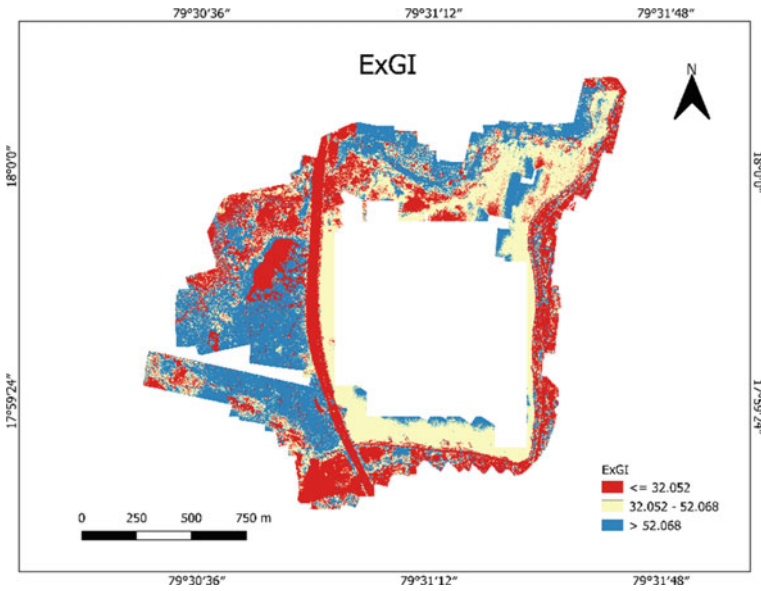


Fig. 8 Excess Green Index (ExGI) of UAV imagery

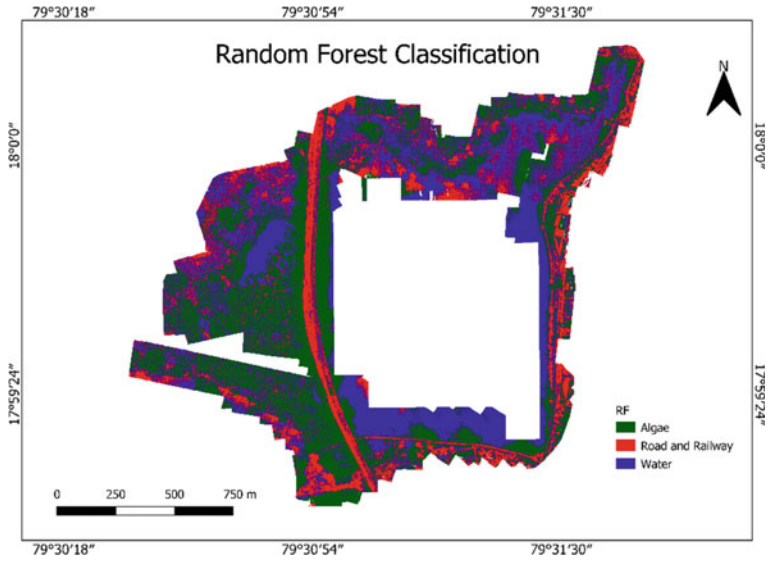


Fig. 9 Land cover classification of UAV imagery using random forest algorithm

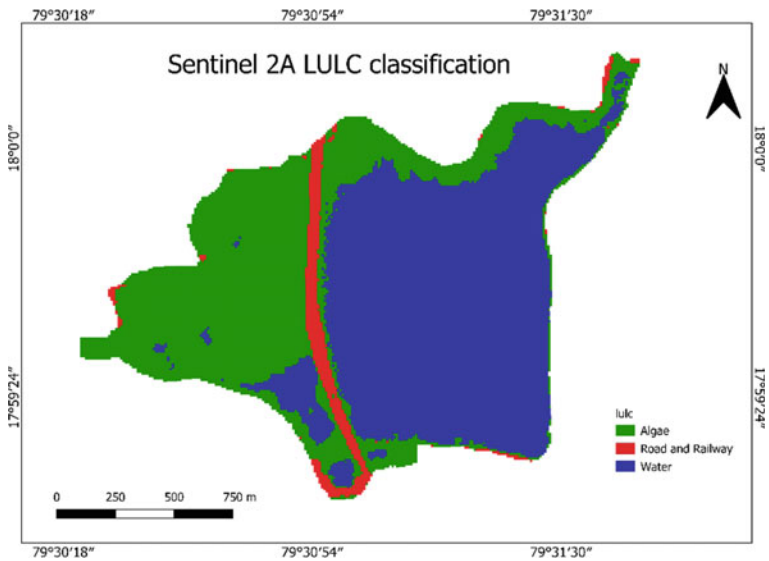


Fig. 10 Land cover classification of Sentinel—2A image using maximum likelihood algorithm

Table 1 Accuracy and coverage area of the algae from the indices and land cover classification

Indices/classification	The coverage area of algae (hectares)	% of correctness	Kappa
NGRDI	60.12	–	–
NGBDI	64.89	–	–
GNDVI	66.78	–	–
ExGI	65.24	–	–
UAV imagery (RF classification)	68.91	96.04	0.9327
Sentinel—2A (ML algorithm)	93.52	89.29	0.8571

5 Conclusion

Algal bloom detection using UAV images is more accurate compared to satellite imagery but it is unable to detect the macrophyte's depth below the water table using RGB images. Using the RGB images detection and measurement of the surface area of the algae can only perform but the type of algae and volume of the algae is not possible to measure. Multispectral and hyperspectral data may provide much information like the type, and nature of algae and for measuring the depth of algae bathymetry analysis has to be performed.

References

1. Kim H-M et al (2016) Application of unmanned aerial vehicle imagery for algal bloom monitoring in river basin. *Int J Control Autom* 9(12):203–220. <https://doi.org/10.14257/ijca.2016.9.12.18>
2. Kimura F et al (2019) Early detection system of harmful algal bloom using drones and water sample image recognition. *Sens Mater* 31(12):4155–4171. <https://doi.org/10.18494/SAM.2019.2417>
3. Wu D, Li R, Zhang F, Liu J (2019) A review on drone-based harmful algae blooms monitoring. *Environ Monit Assess* 191(4). <https://doi.org/10.1007/s10661-019-7365-8>
4. Taddia Y, Russo P, Lovo S, Pellegrinelli A (2020) Multispectral UAV monitoring of submerged seaweed in shallow water. *Appl Geomat* 12:19–34. <https://doi.org/10.1007/s12518-019-00270-x>
5. Park CW, Jeon JJ, Moon YH, Eom IK (2019) Single image based algal bloom detection using water body extraction and probabilistic algae indices. *IEEE Access* 7:84468–84478. <https://doi.org/10.1109/ACCESS.2019.2924660>
6. Kislik C, Dronova I, Kelly M (2018) UAVs in support of algal bloom research: a review of current applications and future opportunities. *Drones* 2(4):1–14. <https://doi.org/10.3390/drones2040035>
7. Tait L, Bind J, Charan-Dixon H, Hawes I, Pirker J, Schiel D (2019) Unmanned aerial vehicles (UAVs) for monitoring macroalgal biodiversity: comparison of RGB and multispectral imaging sensors for biodiversity assessments. *Remote Sens* 11(19). <https://doi.org/10.3390/rs11192332>
8. Kislik C, Genzoli L, Lyons A, Kelly M (2020) Application of UAV imagery to detect and quantify submerged filamentous algae and rooted macrophytes in a non-wadeable river. *Remote Sens* 12(20):1–24. <https://doi.org/10.3390/rs12203332>

Ballistics Algorithm for Airborne Remote Sensor Position in Catastrophe Zones



Vipinkumar R. Pawar, Sudhakar Mande, and Imdad Rizvi

Abstract The configuration of the camera and Field Of View (FOV) in a closed range photogrammetry are the most important parameters to obtain images of the field in quality. UAVs are central Wide Range photogrammetry tools, with cameras for large field items, for obtaining the optimal standard of photos by offering different usable algorithms of flight planning geographic location. This paper suggests an algorithm to find the exact Geo-Coordinates for the location detection of the UAV flight planning algorithm for the application of Closed Range Photogrammetry to the Battle field Susceptibility Zone analysis. Terrain Slope and Aspect have been considered in order to maintain the measured angle of view, field of vision, and land surface image quality. Identifying the pitch and aspect terrain (Azimuth) using the Digital Elevation Model (DEM) ISRO CartoSat Remote sensing info. In order to improve three-dimensional landscape pictures for 3d modelling, Battle Field Analysis, this algorithm should maximize the functionality of the numerous usable UAV airplane planners.

Keywords ISRO · DEM · LISS III · LSI · SI · LRI · OSM · NDVI · VI

1 Introduction

1.1 Close Range Photogrammetry in Field Assessment

Closed range photogrammetry concept was proposed by Aime Laussedat deputed in in the French Army Corps of Engineers as a colonel in year 1840. Closed Range Photogrammetry is a most popular technique to collect the information about specific

V. R. Pawar (✉)
Mumbai University, Mumbai, India
e-mail: vipinkumar.research@gmail.com

S. Mande
Don Bosco Institute of Technology, Mumbai University, Mumbai, India

I. Rizvi
Higher Institute of Technology, Sharjah, United Arab Emirates

terrain profile in multidirectional angle of vision. Due to multidirectional graphical visualization, analysis of any terrain profile becomes easier [1]. Generally Aerial photography is most popular concept to collect data for photogrammetry. For Aerial photography, generally Planes, gliders, drones and quadcopters are used to collect photographs of specific terrain. Now a days using UAV technology, applications of photogrammetry increased rapidly [2].

1.2 UAV Role in Closed Range Photogrammetry for Field Assessment

Natural Fields are non-ignoring tragedies, which cannot control by human activities and cannot predict. But in some extent, we can predict the pre-activities of Battle fields by monitoring the preened symptoms to reduce the human loss. In this paper, we have concentrated on Battle field Susceptibility Zones as a study area.

Analysis of battle field hazard and victim analysis, it is necessary to deploy automated UAVs to take real-time photographs of disaster-prone areas [3, 4].

Due to large geological structure just like rock, terrain slopes, conventional methods for surveying is time-intense and the results are unverifiable, which can misjudge the constancy of geological surfaces. The most common techniques are digital photogrammetry (DP) practices in the field of natural slopes.

An IoT enabled unmanned aerial vehicles (UAVs) structure connected through Mobile network can identify and verify the strength of disaster [5–7].

Real world Calamity management applications of UAVs deviate according to their role during several phases of disaster management and can generally be categorized as shown in the Fig. 1.

Also, implementation of discharge navigation support system by factor-dependent inter-UAVs for disaster risk reduction is realistic possibilities. Generally speaking, the software factor produces UAV discharge guidance plans and selects the safest plan as the discharge navigation route, taking into account situations of calamity and territorial parameters etc. Alternatively, UAVs engage in efficient navigation by discharge [7].

By considering the role of UAVs in the field of Closed Range Photogrammetry for the assessment and analysis of Battle field susceptibility Zone in Battle field, it is necessary to optimize the performance of UAV flight planning by providing precised Geo-Location in the form of WGS84 coordinate systems as Longitude, Latitude and Altitude of Snapping point (Fig. 2).

In this paper, Sect. 2 explained the exact problem statement identified by considering the decreased quality of images obtained by UAVs only because of unguided field of view.

In Sect. 3, Exact methodology has been proposed with the help of remote sensing data collected from Satellite image (ISRO-CARTOSAT and NASA:USGS-ASTER DEM) to identify the exact coordinates of UAV position for perfect adjustment of



Fig. 1 Categorisation of applications of UAVs-based IoT platform in disaster management [5]

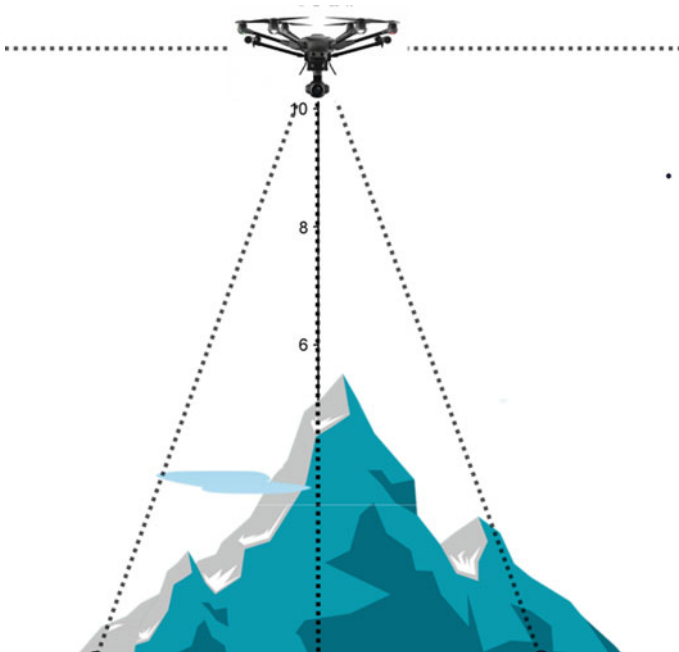


Fig. 2 Current image acquisition method by UAVs

camera field of view. Digital Elevation model is used to identify the terrain slope to predict the Battle field Susceptibility Zone stated in Sect. 3.1.

In Sect. 3.1.3 gives the Battle field Prone area which generally mapped in red zone shown in Fig. 18 having heavy risk of battle field. This mapped zone is the exact location, where UAV images need to be taken.

In Sect. 3.2 direction of the slope direction is calculated in the form of aspect, which is most effective parameter while identifying position of UAV. Sections 3.1 and 3.2 combined provides the exact battle field susceptibility area where pre-disaster monitoring using UAV is required. This area has been consider as a field of view for UAV camera.

In Sect. 4, results shows the comparative table of center of image and the perpendicular axis of field of view so that, we can identify the practical location of UAV in three dimension parameter.

2 Problem Statement

In close range photogrammetry, 3D images need to be developed to enhance the 3D model of disaster-prone area. Angle of vision of camera must be set in such a way that, centroid of image area must be in a line of sight [8]. The angle of vision is the degree of the observable object that is perceived at any moment. In the case of optical payload, it is a solid angle concluded which a gauge is sensitive to electromagnetic radiation. Otherwise image formation may stretch the exact content [8, 9] (Fig. 3).

Unmanned Aerial Vehicles (UAVs) arise as perfect vision product in the form of photography acquisition technology due to having high mobility in complex and

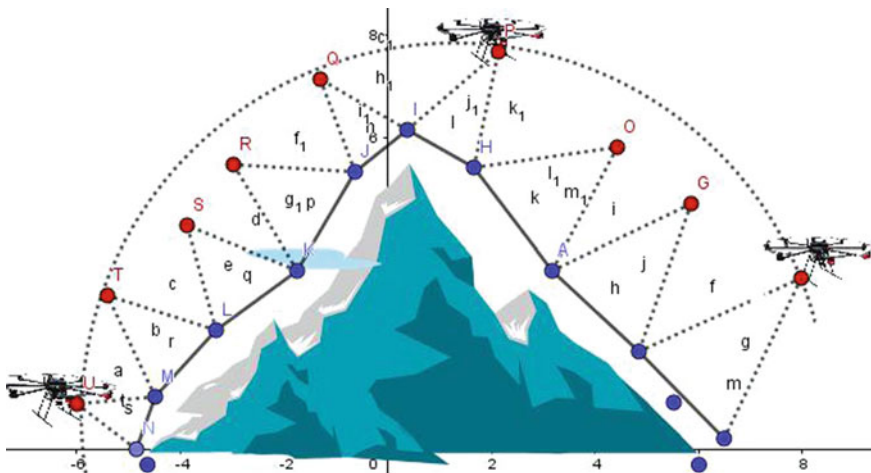


Fig. 3 Current image acquisition method by UAVs

heavily built terrain. The non-heritable images can be used to create 3D model victimization of traditional multi-angle view approaches to photography in high definition. Nonetheless, the quality parameters of the resulting 3D model are extremely predictable in the anticipatory flight navigation plan requiring skilled human intervention, especially in complicated and uneven urban and hazardous environments [10].

While taking a photograph to associate as many coded citation point markers as possible diffuse over the whole thing, it is important to achieve a high measure quality [11].

The actual problem statement is found that, in processing a high functioning and authentic multiple-spectral 3D photograph capture equip, milestones are primarily traced from the following parameters: best sensor payload placement and location and FOV (Field of View) as shown in Fig. 4 design, rich and semirigid structural, authentic and exact photograph capture and precise multiple-sensor data combination [6].

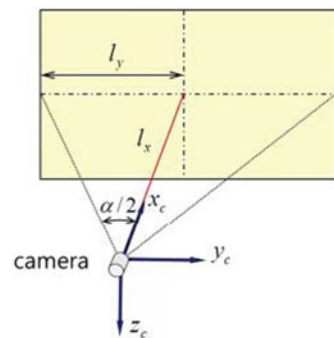
As shown in Fig. 4, the field of view (FOV) of each photographic unit should be chosen appropriately to deal with the estimated location. In this case, certain methods should be used to modify the mechanical instrumentation to make better adjustment of the payloads during assembly and inspection phases. Typically most units of data capture should have some tolerance angle for tilting or spinning. If one machine is installed, the position of each unit marked should be repositioned tightly so that the reassembly and reassembly of the unit can be positioned in exactly the same position [10].

UAVs can be positioned at varying altitudes depending on weather status and user requirements. However, by modifying the altitude of the UAVs, the coverage area also varies [3].

UAV's 3D placement of the blended integer additive programming problem was investigated in order to obtain the best location in the form of latitude and longitude, altitude, and users in inclined directions according to WGS84 (Global Geographical Coordinate System Standard) [12].

Using best track change and facility position issues as a method to detect better 3D positioning utilizing several UAVs.

Fig. 4 Layout of FOV and camera position



Currently, positioning algorithm is previously developed by Lin et al. [14], in which 2D plane surface is used estimate the location of UAV for taking the photographs.

The positioning association between the UAV and the area of interest on the 2D aircraft is shown in Fig. 5.

$$x = \frac{h}{Z_b} X_b; y = \frac{h}{Z_b} Y_b; z = 0 \tag{1}$$

In Ref. [15], 3D Placement of UAV in 3 axis coordinate system is proposed (Fig. 6).

As shown in above figure, location $(x^0; y_0^0; z_{min})$ is expected flight location of UAV unfortunately, while dealing with external environment, UAV must have to navigate through $(X, Y, Z) = (\text{Longitude, Latitude, Altitude})$ navigation coordinates systems. In Ref. [15], respective algorithm fails to predict the geocoordinate location identification.

To find out exact and precised geographical location and elevation of UAV for Battle field analysis using Closed Range Photogrammetry, Algorithm stated in this paper is the final and finest solution to find exact geocoordinates of UAV in 3 axis, means in the form of (Longitude, Latitude, Altitude).

Fig. 5 The position relationship between the UAV and the target location

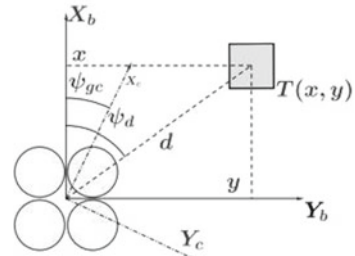


Fig. 6 3D placement of UAV in 3 axis coordinate system [15]

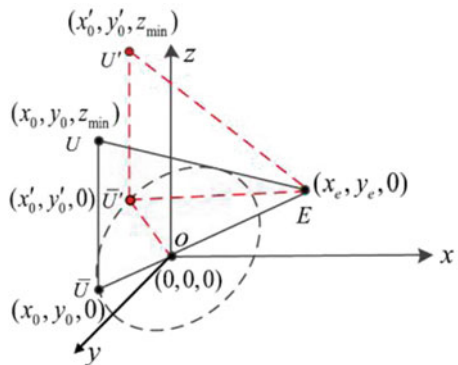
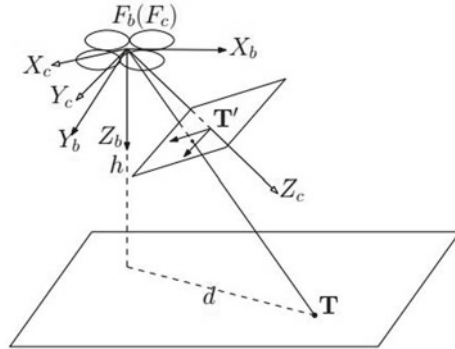


Fig. 7 The relationship between UAV camera and the target object



In this algorithm, after identification of target object, we can get the exact geo-coordinates of snapping point of UAV in the form of Longitude, Latitude and Elevation as shown in Fig. 3.

3 Methodology

3.1 Identification of WSN Cluster for Battle Field Prone Area (Fig. 7)

The location of the target point $P = [x, y, z]$ can be determined using the traditional pinhole imaging method [14].

3.1.1 Battle Field Index (LI)

Battle field Index is slope elevation index range from 0 to 1 where 0 means at surface and 1 means extremely heavy gradient. It is formulated as,

$$\text{SlopeIndex (SI)} = \frac{\text{Slop}}{90} \tag{2}$$

Slope is maximum rate of change in pixel of DEM with respect to its neighbor. Slope is measured in units of degrees as below (Figs. 8 and 9),

$$\text{Slope} = \tan^s \left(\frac{dz}{dx} \right)^2 \times \left(\frac{dz}{dy} \right)^2 \frac{180}{\text{---}} \tag{3}$$

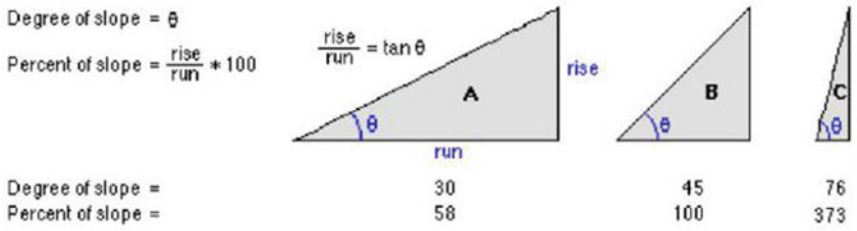


Fig. 8 Comparing values for slope in degrees versus percent

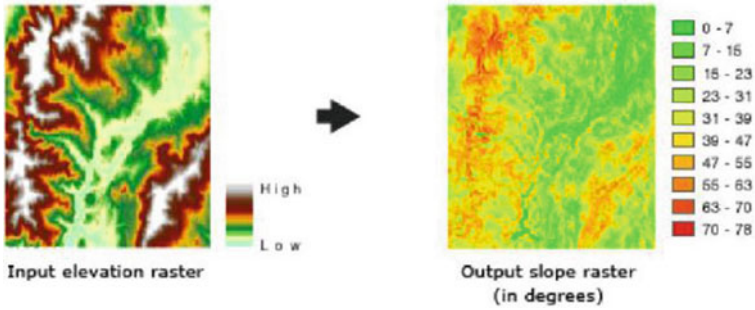


Fig. 9 Comparing values for slope mapping

While using above formula, we have to take care the following things, consider 3×3 matrix is used to calculate slope from 'e',

$$\frac{dz}{dx} = \frac{((i + 2f + c)(g + 2d + a))}{8 \cdot YCellsize} \tag{4}$$

The rate of change in the direction of x for cell e is determined as (Fig. 10),

$$\frac{dz}{dy} = \frac{((i + 2h + g)(c + 2b + a))}{8 \cdot XCellsize} \tag{5}$$

Fig. 10 3×3 matrix from DEM

a	b	c
d	e	f
g	h	i

3.1.2 Battle Field Slope Index (LSI)

Battle field Index is slope elevation index range from 0 to 1 where 0 means at surface and 1 means extremely heavy gradient. It is formulated as,

$$0 < \text{Battle field Slope Index (LSI)} < 1 \quad (6)$$

Battle field Slope Index indicated in Fig. 13, the maximum slope with reference to color indicated in red, yellow and green. Where red indicates heavy slope, yellow indicates moderate slope and green indicate very low slope profile. LSI ranges from 0.3 to 1, because normally 30° or more slope profile will be responsible for battle field.

3.1.3 Battle Field Prone Area

Battle field prone area is defined as, the exact populated area where battle field may damage the living things as well as infrastructure. It means that battle field normally occurred anywhere heavy terrain profile is available with low vegetation. But not all battle fields made affect on human life. Only those battle fields affect the living thing, which are occurred either at city area or road area. So, identification of such areas called Battle field prone area (LPA). Exact analysis of road and city area, OpenStreetMap (OSM) provides vector data of road, highways in form line and city area in the form of polygon. Such an area identified as a intersection of Battle field Risk Index and vectored area of road and urban zone.

$$\text{LPA} = (\text{LRI} \setminus \text{Road}(\text{vectored})) + (\text{LRI} \setminus \text{Urban}(\text{vectored})) \quad (7)$$

Intersection of battle field risk index and road and urban area to identify exact battle field susceptible zone where actual sensor network need to deploy.

3.2 Battle Field Wireless Sensor Network Cluster Zone

Normally battle fields occurred at any heavy terrain profile area, but all are not responsible for human or living loss. Battle field Prone area is Intersection of Battle field sensitive area with civilization, normally road and Urban areas consisting human movement continuously. so, the battle field area which is nearer to road and urban area must be consider as Battle field Prone area which may responsible for heavy life loss.

$$\text{Battle field Slope Index (LSI)} = \frac{\text{Slope}}{90} > 30^\circ \quad (8)$$

Slope is maximum rate of change in pixel of DEM with respect to its neighbor

$$LCZ = LRI + LPA \tag{9}$$

from equation LRI and LSI, LCZ can be calculated as below,

$$LCZ = LRI + \left[\frac{LRI}{\text{Road}_{\text{vectored}}} + \frac{LRI}{\text{City}_{\text{vectored}}} \right] \tag{10}$$

3.3 DEM Aspect

While dealing with terrain slope, the direction of slope also makes more impact in disaster prone area prediction as flood direction and debris flow direction is related to slope direction of any mountain.

Aspect term is used to provide slope direction from 0 to 360°.

As shown in above figure, 0° means north direction, 90° represents east direction, 180° indicates south direction and 270° shows west direction respectively as shown in Fig. 11. And related ASPECT image shown in Fig. 12.

Taking into account the rate of change in both the x and y directions for cell e, the dimension is measured using:

$$\text{Aspect} = \text{atan2}\left(\frac{dz}{dy}; \frac{dz}{dx}\right) \times 57 : 29 : 578 \tag{11}$$

The aspect elements is then transformed to compass focal point values (0–360°), according to the following rule: if aspect < 0 cell = 90:0 aspect else if aspect > 90:0 cell = 360:0 aspect + 90:0 else cell = 90:0 { aspect.

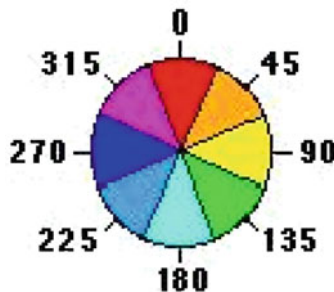


Fig. 11 Aspect colour code

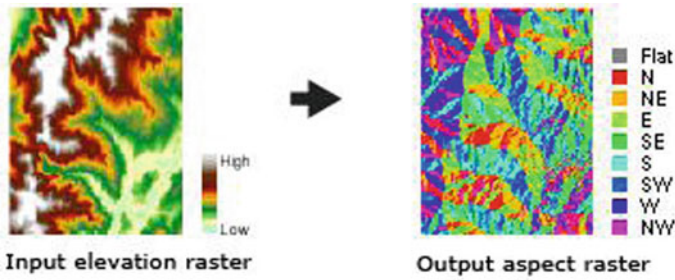


Fig. 12 Aspect representation on Map

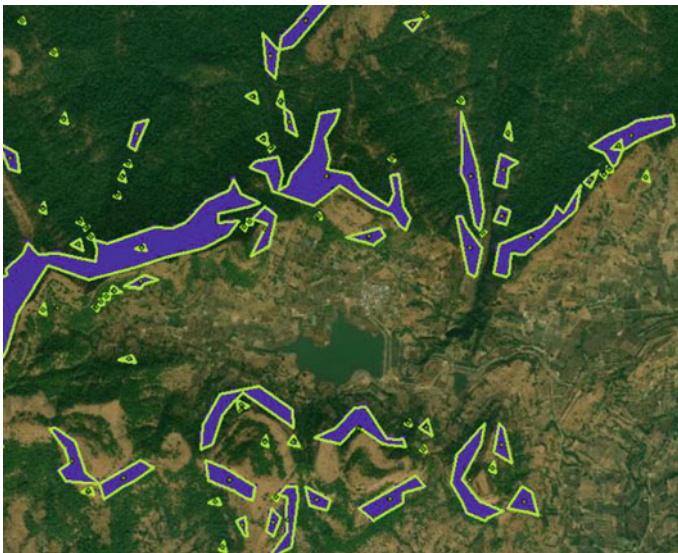


Fig. 13 Battelr field risk zone (Map view)

3.4 Identify Risk Zones

Centroid of all battle field risk zones are the center of angle of vision for UAV imagery. But, for identification of exact geographical location and height of UAV for taking proper image with perpendicular of surface, Optimized Geo-positioning algorithm for UAV need to be used as derived and justified in this paper. In Fig. 13, it is observed that, image has been taken having size $B_i \times B_i$. And camera payload installed on the drone having focal angle. It is considered as, image taken from the surface is completely flat with no slope, respectively having no aspect also (Fig. 14).

As per the following geometry, consider point A is a drone camera payload having focal angle. Image need to be taken having width W i.e. Length BC. Center of image is point D which is the center of image as C_i shown in above figure (Fig. 15).

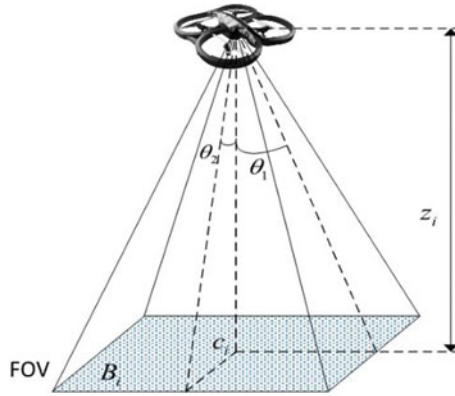


Fig. 14 Battle field risk zone (Graphical / Graphical view)

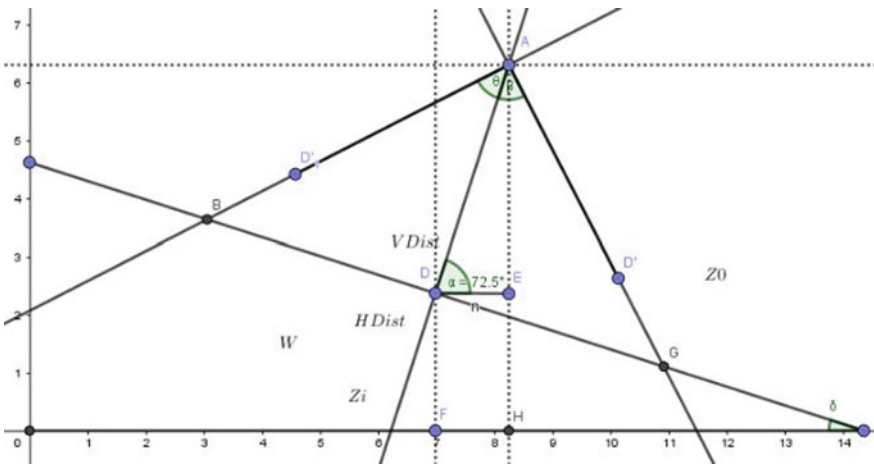


Fig. 15 Geometry of angle of vision

Terrain Slope is indicating by. Aspect of terrain slope is indicated by. While dealing with geocoordinate latitude and longitude are considered as x–y coordinates in cartesian coordinate system to find the exact location of drone in geographical area.

Z value always indicated the height of object with reference to sea surface. Z values always recorded in meters. And Geocoordinates are recorded in WGS84 system. While finding the specific distance with specific direction using Latitude and Longitude, geocoordinate constant is to be consider, here geocoordinate constant is given as (Fig. 16),

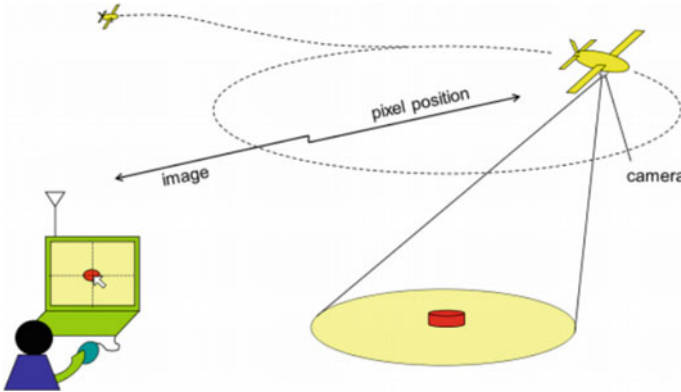


Fig. 16 Experimental setup for vision-based UAV position

$$f(x) = \frac{W}{2} \begin{bmatrix} \cos \theta \\ \sin \theta \end{bmatrix} \cos \alpha * k \tag{12}$$

where, 1 m = 0.00000625 map units. It has deriving the latitude by considering slope and aspect, and = 90

$$\text{Latitude}_{\text{Drone Position}} = [f(x) \cos] + \text{Latitude}_{\text{Centroid}} \tag{13}$$

Also can be deriving longitude of drone position as,

$$\text{Longitude}_{\text{Drone Position}} = [f(x) \sin] + \text{Longitude}_{\text{Centroid}} \tag{14}$$

To find the expected height of UAV payload with reference to sea surface, We can state that with the reference to above image,

$$\text{DistanceAE} = \frac{W}{2} \left[\frac{\cos \theta \cos \alpha}{\sin \theta} \right] \frac{\sin \alpha}{\cos \alpha} \tag{15}$$

Modification of above equation will cancel cos

$$\text{DistanceAE} = \frac{W}{2} \left[\frac{\cos \theta \sin \alpha}{\sin \theta} \right] \tag{16}$$

So final equation of drone height will be,

$$\text{DistanceAE} = \frac{W}{2} \left[\frac{\sin \alpha}{\tan \theta} \right] \tag{17}$$

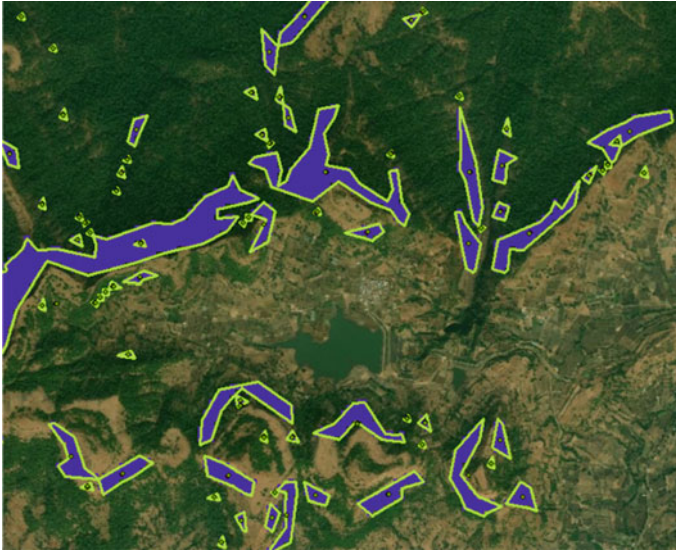


Fig. 17 Battle field risk zones with flag point i.e. centroid

But Distance AE is height difference between Centroid of Image and expected UAV height, to find the exact elevation above sea level, it is necessary to add elevation of centroid of image taken from DEM imagery.

So, exact height of UAV from above sea surface is noted as Z_0 (Fig. 17),

$$\text{DistanceAE} = \frac{W}{2} \frac{\sin \alpha}{[\tan \theta] + Z_i} \quad (18)$$

4 Results

Battle field prediction analysis has various parameters like, rainfall, slope, vegetation density and water catchment and much more. But fundamental parameters are slope index, in which surface slope makes more impact on battle field prediction analysis. So, by considering importance and fundamental aspect of battle field, slope index has been consider for Battle field Susceptibility area identification. Using slope index having above 0.3 rating gives following result.

Where Z_i is the height of centroid of image from sea surface collected from DEM imagery (Fig. 18).

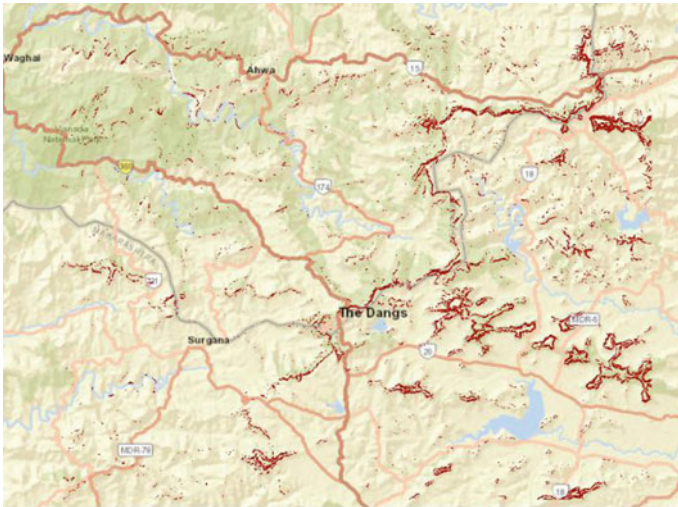


Fig. 18 High risk zone in red color

Area of interest is taken from Saputara hill station, Gujarat which is situated near border of Maharashtra-Gujarat territory, in India. This area is surrounded by heavy sloped hills and mountains. And lots of terrain variations also available. This area is coming under heavy rainfall zone. These battle field susceptibility zones are identified by Battle field Slope Index.

$$\text{Battle field Slope Index(LSI)} = \frac{\text{Slope}}{90} > 30^\circ \tag{19}$$

All Battle field susceptibility zones are considered as single image of interest for UAV image acquisition. So, centroid of the individual battle field susceptibility zone is considered as a center of image which is indicated as shown in Fig. 11 (Fig. 19).

Individual flag is representing the individual image center. By applying Optimized Geo-positioning algorithm for UAV, we will get exact X-Y coordinates of Drone positioning in WGS84 coordinate system (Fig. 20).

$$\text{Latitude}_{\text{Drone Position}} = [f(x) \cos] + \text{Latitude}_{\text{Centroid}} \tag{20}$$

where,

$$\text{Latitude}_{\text{Centroid}} = \text{Latitude of Individual flags in LSI}$$

and

$$\text{Longitude}_{\text{Drone Position}} = [f(x) \sin] + \text{Longitude}_{\text{Centroid}} \tag{21}$$

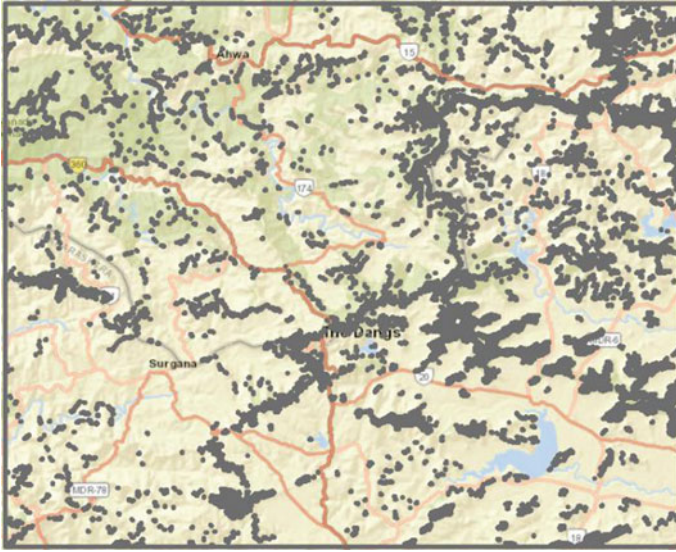


Fig. 19 Mapped high risk zone

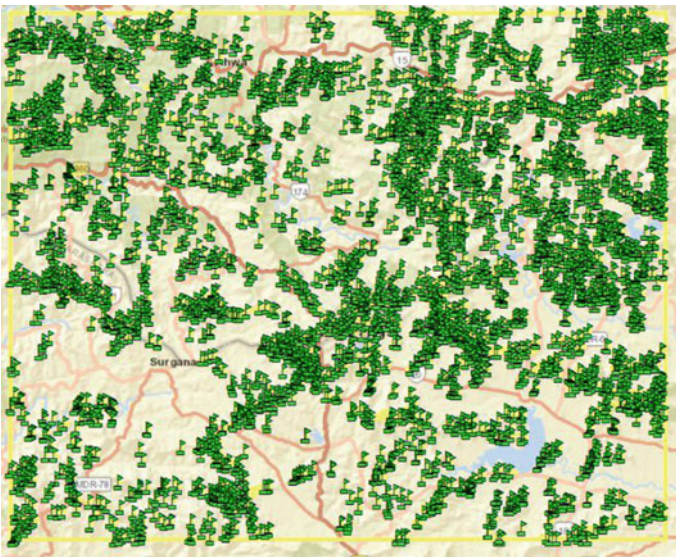


Fig. 20 Targeted flag point for payload penetration

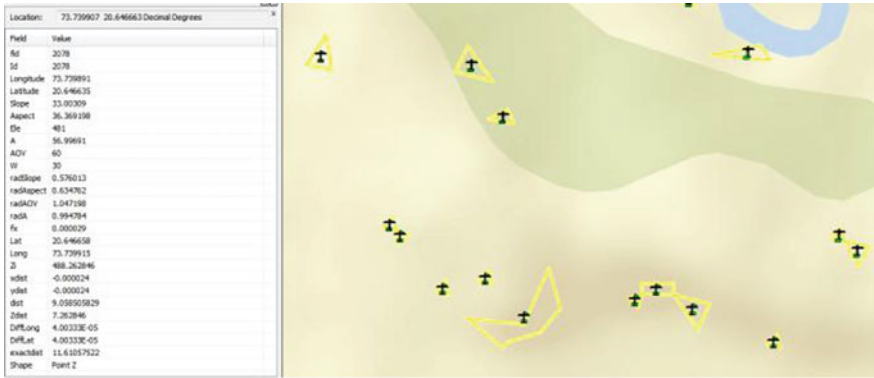


Fig. 21 Flag point of battle filed for target

where,

$$\text{Longitude}_{\text{Centroid}} = \text{Longitude of Individual flags in LSI}$$

and

To find the expected altitude for UAV for individual flag point,

$$Z_0 = \frac{W}{2} \left[\frac{\sin}{\tan} \right] + Z_i \tag{22}$$

where, Z_i represents elevation of individual flag point units in meters taken from DEM imagery. $\text{And} = 90 \text{ slope}()$ in degree.

Figure 21 represents the flag point of Battle field Susceptibility Index (LSI) and Optimized Geo-positioning algorithm for UAV based actual positioning. Magnifying individual LSI zone is shown as in Fig. 22.

Here, flag point representing the centroid of Battle field Susceptibility Zone and Flight point representing the actual optimized position of Point of view or also called as cam-era position. In this case, flag point is located at location 72.739914:20.646661 at elevation 481 m from sea surface. But by considering the slope index as, 33.00309° with aspect 36.369198°, perpendicular line of sight for Focal length of camera payload gives the optimized location 11.61057522 m away from flag point with elevation at 488.262846 m from sea surface.

In another case, flag point is located at location 72.740731:20.645318 at elevation 512 m from sea surface (Figs. 23 and 24).

But by considering the slope index as, 33.073549° with aspect 33.578812°, perpendicular line of sight for Focal length of camera payload gives the optimized location 11.90099797 m away from flag point with elevation at 519.494435 m from sea surface (Tables 1 and 2).

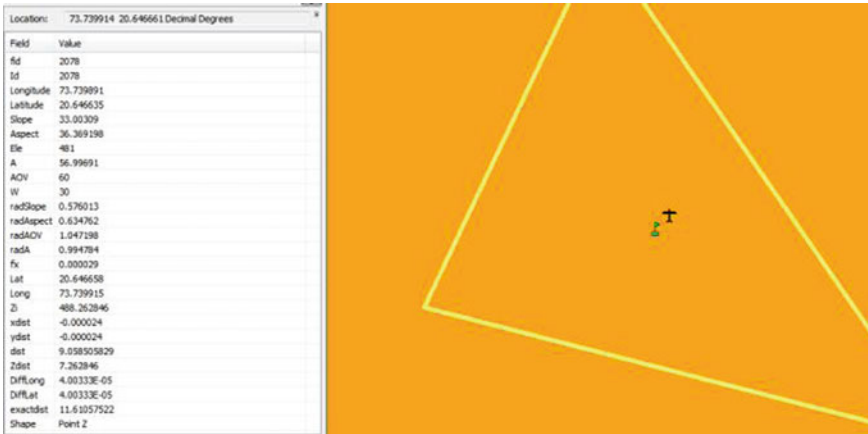


Fig. 22 Flag point of battle filed for target (Zoomed)

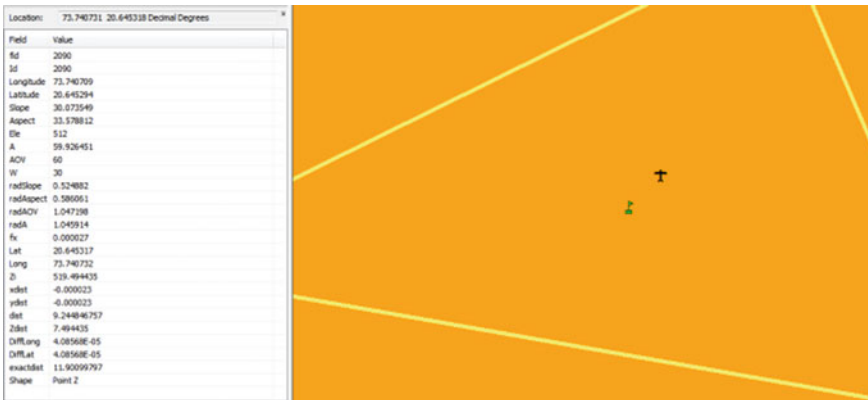


Fig. 23 Flag point representing the centroid of battle field susceptibility zone and flight point representing the actual optimized position of point of view

5 Conclusion

In this article, some flight planning algorithms are tested with detailed information regarding their flaws pertaining to the imaging process. An algorithm to provide accurate snapping position to obtain high quality images without altering the aspect ratio of the image is then introduced and implemented successfully by defining exact Goe-Coordinates with parameters of camera latitude, duration and altitude.

Implementation of the suggested algorithm reveals a minimum and maximum distance correction vector away from the flag point to be 6.1138 and 292.942613 m. The results show that previous algorithms concentrate on only the height profile but have taken care of the slopes during the production of algorithms for flight planning.

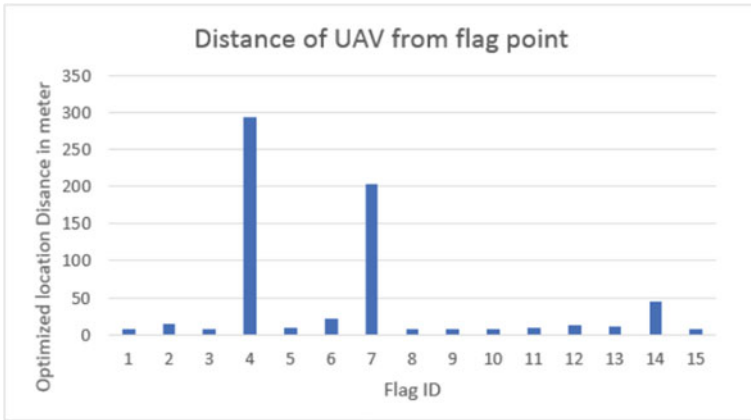


Fig. 24 Graph: flag ID versus distance in meters

Table 1 Test area

Id	Longitude (flag point)	Latitude (flag point)	Elevation (in meter)
1	73.55777778	20.7950203	228
2	73.80916667	20.7950203	446
3	73.81847222	20.7950097	470
4	73.87154231	20.79473843	535
5	73.93138889	20.79492367	941
6	73.95844944	20.79494142	828
7	73.96166667	20.79486111	812
8	73.81751621	20.7945688	495
9	73.90860541	20.79445014	546
10	73.96304986	20.79445014	810
11	73.81722222	20.79416667	499
12	73.8729312	20.79418287	538
13	73.9260509	20.7944582	752
14	73.94890208	20.79440642	861
15	73.55804986	20.79389459	219

In order to produce optimal pictures from the open environment of focus areas, Algorithms boost the course and trajectory of camera angles of Phantom models I, II, III and DJI drones.

After analysis of total 4340 flag points near Saputara territory, it is observed that, optimized location is average 44 m away from flag point.

Table 2 Location optimization data

Optimized latitude	Optimized longitude	Zi (in meter)	Zdist (height from flag point)	Distance of UAV from flag point in meter
20.795018	73.557775	235.3376	7.33761175	7.361405371
20.795045	73.809191	453.4073	7.407331947	14.07267037
20.794999	73.818462	477.2545	7.254548744	7.701821813
20.794766	73.871569	542.4919	7.491853811	292.9426126
20.794905	73.93137	948.4163	7.416343889	9.317594166
20.794908	73.958416	834.5514	6.551378754	22.6180366
20.794832	73.961638	819.3316	7.331645475	202.2138202
20.794558	73.817505	502.344	7.344026554	

References

- Gomez C, Purdie H (2016) UAV-based photogrammetry and geocomputing for hazards and disaster risk monitoring – a review. *Geoenviron Disasters* 3(1). <https://doi.org/10.1186/s40677-016-0060-y>
- Katayama K, Takahashi H, Yokota N, Sugiyasu K, Kitagata G, Kinoshita T An effective multi-UAVs-based evacuation guidance support for disaster risk reduction. *IEEE*. 978-1-5386-7789-6/19/2019
- Shakoor S, Kaleem Z, Baig MI, Chughtai O, Duong, TQ, Nguyen LD (2019) Role of UAVs in public safety communications: energy efficiency perspective. *IEEE Access* 7:140665. <https://doi.org/10.1109/access.2019.2942206>
- Russo M, Carnevali L, Russo V, Savastano D, Taddia Y (2018) Modeling and deterioration mapping of façades in historical urban context by close-range ultra-lightweight UAVs photogrammetry. *Int J Arch Herit* 1–20. <https://doi.org/10.1080/15583058.2018.1440030>
- Ejaz W, Azam MA, Saadat S, Iqbal F, Hanan A (2019) Un-manned aerial vehicles enabled IoT platform for disaster management. *Energies* 12(14):2706. <https://doi.org/10.3390/en12142706>
- Meyers G, Zhu C, Mayfield M, Tingley DD, Willmott J, Coca D (2019) Designing a vehicle mounted high resolution multi-spectral 3D scanner: concept design. In: *Proceedings of the 2nd workshop on data acquisition to analysis*. ACM, pp 16–21
- Liu C, Liu X, Peng X, Wang E, Wang S (2019) Application of 3D-DDA integrated with unmanned aerial vehicle–laser scanner (UAV-LS) photogrammetry for stability analysis of a blocky rock mass slope. *Battle Fields*. <https://doi.org/10.1007/s10346-019-01196-6>
- Jiang R, Jauregui DV, White KR (2008) Close-range photo-grammetry applications in bridge measurement: literature review. *Measurement* 41(8):823–834. <https://doi.org/10.1016/j.measurement.2007.12.005>
- Ur Rahman S, Kim G-H, Cho Y-Z, Khan A (2018) Positioning of UAVs for throughput maximization in software-defined disaster area UAV communication networks. *J Commun Netw* 20(5):452–463. <https://doi.org/10.1109/jcn.2018.000070>
- Koch T, Körner M, Fraundorfer F (2019) Automatic and semantically-aware 3D UAV flight planning for image-based 3D reconstruction. *Remote Sens* 11(13):1550. <https://doi.org/10.3390/rs11131550>
- Goda I, L’Hostis G, Guerlain P (2019) In-situ non-contact 3D optical deformation measurement of large capacity composite tank based on close-range photogrammetry. *Opt Lasers Eng* 119:37–55. <https://doi.org/10.1016/j.optlaseng.2019.02.006>

12. Bor-Yaliniz RI, El-Keyi A, Yanikomeroglu H (2016) Efficient 3-D placement of an aerial base station in next generation cellular networks. In: Proceedings of the IEEE International Conference on Communications (ICC), Kuala Lumpur, Malaysia, May 2016, pp 1–5
13. Park S, Jung D (2019) Vision-based tracking of a ground-moving target with UAV. *Int J Aeronaut Space Sci*. <https://doi.org/10.1007/s42405-019-00142-z>
14. Lin L, Yang Y, Cheng H, Chen X (2019) Autonomous vision-based aerial grasping for rotorcraft unmanned aerial vehicles. *Sensors* 19(15):3410. <https://doi.org/10.3390/s19153410>
15. Wang D, Bai B, Zhang G, Han Z (2019) Optimal placement of low-altitude aerial base station for securing communications. *IEEE Wirel Commun Lett* 8:869–872. <https://doi.org/10.1109/lwc.2019.2897774>

Practical Applications for UAS Designed to Assist Climatologists in Studying Toxic Gas Emissions Relative to Climate Change



Ian Godfrey and José Pablo Sibaja Brenes

Abstract The rapid advancement of the Unmanned Aerial Systems (UAS) technology and applications provide a unique opportunity to assist the United Nations with their 17 Sustainable Development Goals (SDG's). Further enhancement of the UAS sector has brought forward tangible applications that illustrate how this technology can assist in improving community health, collective education and stimulate economic growth. There are numerous practical examples of how UAS contribute to the SDG's of climatologists today. Outlined in this paper are some of the most prominent UAS applications and their resulting benefits to society. The development and global roll out of the UAS has created significant opportunity for climate scientists studying toxic gas emissions and the chemistry of Earth's atmosphere. UAS make emission monitoring more accurate, contribute to gas leak detection at industrial facilities and greatly assist plant efficiency and optimization. UAS help simplify the data collection process by allowing remote pilots to quickly survey industrial plants and allow them to carry payloads of scientific equipment such as spectrometers which can be used for Differential Optical Absorbance Spectroscopy (DOAS) or thermal cameras designed to detect thermal anomalies. The research illustrated here shows real-world practical examples of using UAS technology on natural emissions at the active crater of the Poás Volcano in Costa Rica and the Industrial power plant of Tampa Electric (TECO) in Tampa, Florida.

Keywords Sustainable Development Goals SDG's · Climate change · Preservation · Natural resources · Oceans · Forests · Energy · Water · Urbanization · Technology · Transportation · Ecosystems · Pollution · Atmospheric chemistry · Acid rain · Sustainability

I. Godfrey (✉)
Tampa, FL, USA
e-mail: Igodfrey@mail.usf.edu

J. P. S. Brenes
Heredia, Costa Rica
e-mail: jose.sibaja.brenes@una.cr

1 Introduction to UAS

Unmanned Aerial Systems (UAS) and their applications have grown exponentially for the past decade and the technology has shown promising advancements in many sectors, especially environmental and vegetation mapping and monitoring. Certain applications in Earth science and environmental studies have gained significant attention from professional researchers [1, 2]. Research institutions and universities like the Laboratory of Atmospheric Chemistry of the National University (LAQAT) of Costa Rica continue to adapt and implement new technological advancements such as using UAS and their associated payloads. Scientists stated that drones have the potential to revolutionize capabilities for field investigators [3].

Various instruments are now being remotely operated especially drones, remote control watercraft, and multibeam sonar, all of which are now assisting climatologists studying climate change to better understand how CO₂ emissions correlate to the melting ice sheets like the front of a calving glacier in Antarctica [4]. Additionally; Due to high maneuverability, compactness, ease of use, various applications continued to be discovered especially in the field of Earth science; where drones can be used to study aspects of climate change, glacier dynamics, spring erosion, landslides, and volcanic activity or they can be used for atmospheric sampling [1, 5]. It's not just natural resource applications for UAS developing rapidly, others such as disaster management, special habitat monitoring, search and rescue, endanger species documenting and tracking, cultural heritage management and traffic monitoring all serve as lucrative UAS applications [2].

2 Equipment Used

Parrot Drones Anafi Thermal—which has a folded size of 218 × 69 × 64 mm, its unfolded size is 242 × 315 × 64 mm and fits tightly in a compact carrying case. The UAS has a total weight of 315 g. The maximum transmission distance for the Anafi Thermal is 4 km or 2.4 miles, 4,000 m, or 13,123 ft, making it ideal for long-distance UAS missions. The Parrot Skycontroller 3 allows for maximum transmission and minimal interference. The maximum flight time is 26 min. The UAS has a maximum horizontal speed of 34 mph a maximum vertical speed of 4 m or 13.1 ft/s. Maximum wind resistance is 31 mph, and the maximum working altitude is 4,500 m, 14,763 ft above sea level. The DJI Phantom 3 and 4 along with a DJI Matrice-200, Matrice-600 Pro and Mavic Mini were also used in the data collection process.

3 Imaging

UASs have successfully been deployed to map fine-scale vegetation and land areas used for agriculture, Antarctic ice sheet melting and glacial cracking, soil conditions, and to take atmospheric samples. The advantages of UAS are their ability to collect images, video and associated data at more economical prices and with lower risk. Advancements in payloads have resulted in higher resolution imaging abilities at more useful vantage points than ground surveys or satellite platforms [6]. “Images taken by small UAS are becoming an alternative to high-resolution satellite images, which are much more expensive, to study variations in crop and soil conditions. Finding an adequate approach for industrial or rural areas remains a pending task” [3]. Therefore by implementing UAS technology many of these SDG’s can be achieved. Thermal imaging cameras onboard UAS are excellent tool for forest fire management [2]. Adding thermal imaging to your inspection allows you to see thermal anomalies and cold spots along areas of sensitive and expensive industrial equipment such power lines, solar cells, hot springs and volcanic craters. Thermal imaging cameras highlight where anomalies may be present and the images and data can be built into existing data bases and used for future investigations.

The Earth science and climatologists studying the atmosphere have begun utilizing various payload packages and software programs. Imaging is important in the data collection process for 3D Digital Surface Models DSM and sensors or samplers in several unique and innovative applications are taking this even further by allowing researchers to plot pollutants and create AERMOD plots. The development of new UAS with new imaging capabilities is revolutionizing the potential uses for more than just Earth surface imagers. For example, Short Wavelength Infrared or SWIR cameras are now being implemented into strategies for UAS solar cell inspections. SWIR cameras have the ability to capture pictures through smog, clouds, smoke and haze. SWIR cameras are the only wavelength technology that can capture images through cloud coverage and have a clear resolution image. This opens a world of possibilities for both industrial and Earth science researchers [5].

4 Payloads

Since 2020 there have been several companies making progress with miniaturized hardware and advanced software in gas detection applications via UAS for both sampling and imaging. For example, three innovative and useful payloads for mapping pollutants are: First the Sniffer 4D by Soarability a company in Shenzhen China has a software package that can accurately map detailed gas pollution analysis data for simple visualization. Second, the FLIR Systems in the USA has also been developing products related to pollution distribution. The FLIR Systems MUVE C360 has been frequently used in North America for industrial plant gas leak inspections. Third the AILF U10 Laser by Coptrz is a methane leak detection device which

enables rapid identification of methane from up to 100 m away. The device is powered by DJI SkyPort, the U10 is seamlessly integrated with DJI Matrice 200 V1/or V2 platforms. Many other beneficial payloads such as compact light weight spectrometers, thermal imaging cameras and other specialized equipment are also contributing to the rapid advancement of UAS capabilities. With proper software, to facilitate the data collection process associated with these payloads UAS can fly a specified preprogrammed grid pattern which can be flown multiple times per day [7].

5 Topography

For topography mapping photogrammetry technique is frequently used by remote pilots. The strategy is known as structure from motion SfM, where 2-D images are transformed into 3-D topographic surfaces. Structures from Motion techniques were successfully implemented to produce high resolution digital elevation models over the lower reaches of a glacier in 2015. By using UAS scientists used the models to identify areas of interest for further observation and analysis. Many of these areas of interest were not otherwise observable without the use of UAS [5]. UAS can be ideal for mapping nutrient blooms, red tide outbreaks, sediment plumes and floods, UAS were successfully deployed to identify an intermittent stream network in the St. Denis National Wildlife Area in Saskatchewan, Canada [5]. It was also determined that UAS imagery could be an improvement to Global Positioning System GPS acquired ground-truth points for classifying an intermittent stream network across the same large-scale satellite image [6]. UAS have become a crucial component in precision agriculture especially for specialty crops, forest resource management, vegetation monitoring and spring monitoring [2].

6 UAS Software

Software for UAS is advancing simultaneously with the hardware systems. As market maturity approaches more emphasis will be placed on software development for detect and avoid situations, more precise autonomous flight abilities and enhanced data collection capabilities. The development of these technologies will benefit the United Nations with their Sustainable Development Goals by utilizing autonomous surveillance of industrial infrastructure such as oil and gas pipelines, solar farms, mines, and other development projects. This technology is also positioned to assist with the surveillance of volcanic terrains, glacial ice sheets, and can benefit natural disaster response and relief programs. UAS delivery services are expected to be implemented in the US over the next five to ten years and UAS software companies are working to secure their space in this market [8]. With so many technical applications for UAS, the software associated with advanced UAS applications may have

the most potential. According to the UAV software company Measure, by implementing UAS power companies, oil refineries and other industrial plants can avoid hazardous man-hours, save costs, and minimize downtime for inspections without sacrificing data quality. For example, in the research paper titled *Drones for Power Plants*, the researchers explain that: “Large structures are particularly well suited for drone inspections. A drone can conduct a visual inspection in a fraction of the time and a fraction of the cost of other method, while typically providing data that is more comprehensive and more detailed. Operators keep their boots on the ground while getting a thorough look at the tops of stacks, tanks, or other large structures. With professional-level manual flight skills and a high-quality camera payload, knowledgeable pilots can scan surfaces to identify damage and capture images for further analysis and classification” [7].

According to a research paper titled *Drones for Power Plants* the software company Measure explains; “Mapping using digital terrain model (DTM), digital surface model (DSM) and contour maps. Data is typically captured using entry-level commercial drone equipment such as a DJI P4P or Mavic. Data is then transferred to a third party or uploaded to an automated software system for processing into a final data product. The energy industry has always been a leader in utilizing Geographic Information Systems (GIS) and remote sensing data to monitor infrastructure and make decisions. From maps of critical infrastructure to inspections of power production assets, energy companies have built expensive data bases of information. One of the best ways to maximize the return on your drone program is to integrate drone data into existing workflow” [7].

3D modeling and mapping using UAS has become strategically important for climatologists monitoring glacial ice sheets, fresh water spring erosion and water levels, volcanic emissions and monitoring agricultural land use [5]. The software package Pix4D specialized in photogrammetry the process of measuring from images and is frequently used by geologists mapping difficult to reach landscapes. Pix4D also utilized data from lasers which are one of the most precise ways to measure distances. Pix4D can incorporate data from LiDAR which is being used by UAS professionals for various applications. For example ICE the state owned electricity and telecommunications company in Costa Rica used LiDAR for mapping electrical infrastructure all around the country. Pix4D’s technology is about measuring from images, but LiDAR can also be incorporated into the workflow. UAS photogrammetric are being successfully used to generate DSM illustrating forest canopy metrics relative to logging, forest fires, urban development, and landslide results and now an enhanced understanding of forest processes can be studied. Complications and challenges continue to exist such as rural unstable terrain and heavy cloud coverage due to high elevations often seen by researchers in Costa Rica, therefore good penetration capabilities are essential for mapping regions such as tropical forests [9]. For example, on the northern flanks of the Irazú volcano there is a nature refuge that can be observed and documented more accurately than with ground methods by using UAS to generate DSMs.

7 Costa Rican Institute of Electricity ICE LiDAR Application

By implementing LiDAR technology ICE scanned the 767 km or 476 miles of transmission lines for analysis. ICE needed to complete the topographic survey of the 2,440 km or 1516 miles of transmission lines of the National Electrical System (SEN). This allowed the company to observe objects close to lines, towers and substations and make wise decisions that ensured the safety of the transfer of electricity from generation plants to distribution centers for a 24/7 supply. Recording data from above is much more accurate for complicated topography, such as rivers, mountains, and canyons. LiDAR helps these types of institutions determine the minimum distances between the conductors and the ground along each line, so that the maximum transmission capacity is defined. This strategy increased the power capacity that lines can transfer and optimized their use and helped ICE plan their expansion. LiDAR also assisted ICE with the collection of high-precision data to address emergencies, such as in the replacement of the transmission line after earthquakes for example, identify areas with invasion of wooded areas where trees exist that could fall on drivers. LiDAR was also used by ICE to document road junctions to coordinate the location of services. LiDAR is also being used for wildlife reserves and facilitating the management of natural resources by gathering data sets used to predict canopy cover, biomass estimation, health of the forest and growth rate [2]. Therefore using LiDAR can also be a beneficial tool for monitoring deforestation which is an important subject to the United Nations.

8 Volcanic Applications

1. Natural resource management has become one of the most significant applications for UAS in developing nations [2]. For example researchers from the LAQAT used a Phantom 3 to monitor the Poás volcano in Costa Rica and to collect a water sample from an active volcanic crater lake over 9,000 ft above sea level. Professors from LAQAT have seen possible changes and morphology of the Botos Lagoon the dormant crater of the Poás volcano. There is something that could be emitting gas at the bottom of the lagoon and that could lead to a low pH level. UAS have helped visualize the Crater Lake via images and video and also provided a way to take deep water samples. Images obtained by using UAS to monitor the Poás volcano have helped investigators locate structures on the floor of the Botos Lagoon which may be prehistoric volcanic vents. These structures were first identified by using UAS which is a good example of the potential for UAS in Earth and environmental sciences. Research like the water sampling from the crater lake of the Poás volcano illustrate the immense potential for UAS which have exponential potential for monitoring environmental disasters such as oil spills and water sampling of remote or hazardous locations [5,

10]. The slopes of many volcanoes serve as fertile agricultural regions essential to the food supply of the region and are therefore important to monitor for crop optimization. Using UAS for checking the health of a crop is a popular application in UAS for precision agriculture [2]. By implementing UAS technology in the field professors from LAQAT were able to accurately measure the height and direction of the volcanic gas plume. Aerial images showed tropical trees of various colors fill the forest surrounding the Botos Lagoon and some dead trees have fallen into the lake. During periods of increased activity, this UAS observation method is used before researchers move closer to the active crater for further measurement. The measurements at the Poás volcano with UAS have helped to search for rivers around the crater and to gather data to that side of the volcano where accessibility is much more difficult.

2. UAS have also assisted the National Commission of Emergency (CNE) in Costa Rica by assisting their analysis of the direct impact zone and dead forest to the west of the Turrialba volcano. On March 12, 2015 three eruptions of large proportion of ash were reported to the CNE, which forced the closure of Juan Santamaria International Airport in the capital city San Jose. Due to the expulsion of large amounts of gases and ash containing juvenile material, and the output of magma, authorities acknowledged that the Turrialba volcano had moved to

Fig. 1 The Poás Volcano

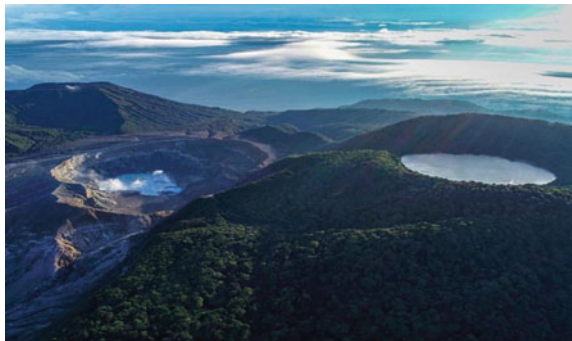


Fig. 2 Phantom 3 over the Botos Lagoon



Fig. 3 Images of volcanic plume height



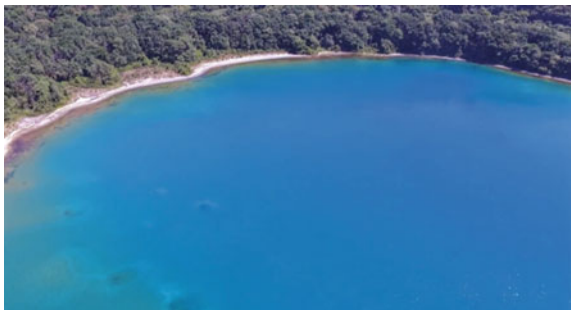
Fig. 4 Landslide below observation platform



Fig. 5 Large structure on the crater lake floor



Fig. 6 Small structures on the crater lake floor



a new much more dangerous activity stage. During October 2015, the volcano entered into a period of shorter eruptions, but with a higher level of explosiveness. During this time period UAS were essential for the observation and correlated safety recommendation for communities surrounding the Turrialba volcano. This eruption in 2015 produced a lot of ash dispersion through the Central Valley. During the day many people had respiratory and visibility problems which lasted for at least three days. The local hospitals in the Central Valley, especially in Coronado, were crowded, with people experiencing complications with asthma, allergies and eye irritation. The plume rose more than 5 km or 3.1 miles above the Turrialba volcano summit.

These flights circled the active Turrialba crater and then extend outward for about 1.3 miles or 2.2 km from the volcano and then returning to the park ranger station called La Central. Depending on the findings from the drone flights, there were follow up studies to expand on previous research. Since the Turrialba emissions have had such a wide range of effects on the entire surrounding region the CNE continued using UAS by lining consistent observation flights of the area called La Silva which is within the restriction ring around the active crater of the Turrialba volcano. These UAS flights provided essential observation of some of the most affected areas concerning toxic SO₂ emissions, ash fall and burnt up volcanic debris that potentially blends with a river or creek. Photographs taken by a drone 984 ft or 300 m above the Turrialba volcano summit directly over the active crater of the volcano, allowed volcanologists for the first time look inside the depths of the active crater unexposed to any risk [10].

Researchers studying the Turrialba Volcano believe there are also small magma batches close to the surface here in the active crater of the Turrialba volcano. During the time of the fly over the inner crater measured 620 ft or 189 m wide. By using drone technology and the digital elevation model or DEM

Fig. 7 AERMOD plots of May 15, 2015, Turrialba volcano eruption



Fig. 8 AERMOD plots of May 15, 2015, Turrialba volcano eruption



Fig. 9 Phantom 4 drone flight path

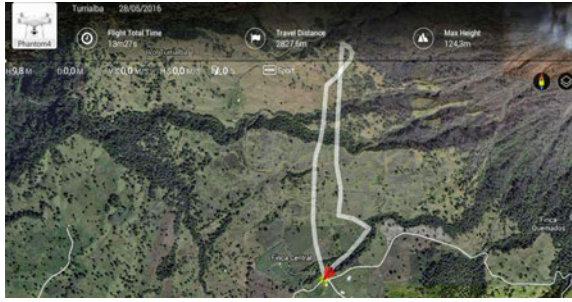


Fig. 10 Turrialba volcano direct impact zone



Fig. 11 Summit of the Turrialba volcano



Fig. 12 Geological survey images from Phantom 4



generated from images taken by the drone, geologists and volcanologists collaborated to monitor the Turrialba volcano. By using UAS and DEM software these scientists were able to calculate the volume of material that would fit in that hole which was 81.2 ft^3 or 2.3 million m^3 . What was discovered from the drone flight images is that the active crater's inner walls exhibit slopes that exceed 55° of inclination and the mouth of the volcano is 413 ft of 126 m deep. The crater measured $742,000 \text{ ft}^2$ or $69,000 \text{ m}^2$ during March of 2016. Images taken by the UAS also contributed new data to other areas of interest such as the volcanic vent where volcanic gases and other materials like ash get ejected from [10].

To create a successful flight plan for an aerial observation with a drone close to an active volcano there are several major factors that all have to be met. Weather variables such as rain and wind conditions are usually looked at first, if all is well then any potential earthquakes in the area much be taken into consideration, and also if there is an eruption column releasing gases and ash it's important to monitor the altitude of the eruption column relative to the wind direction and speed relative to height of the drones flight plan [10]. The images taken by the drone were processed at the National Laboratory of Materials and Structural Models at the University of Costa Rica using the Agisoft 3D modeling and mapping software. The digital elevation model or DEM generated from images taken by the drone were very useful in understanding how volcanic craters form and evolve during periods of increased volcanic activity. This UAS evaluation of the Turrialba volcano was conducted in March of 2016, right after there were several significant eruptions which would inevitably change the geology of the crater [10].

3. UAS keep researchers and professor away from harm, with the drone we can observe up close the intensity of the volcanic fumarole. UAS provide a way to take measurements of gas and the temperature of the emissions. UAS were also used for a complex volcanic degassing study that investigated the Turrialba volcano in Costa Rica and the Masaya volcano in Nicaragua where a low resolution < 1 ultraviolet (UV) spectrometer was carried by a DJI Matrice 2 in a circular flight path around and then threw the volcanic gas plumes to quantify the SO_2 flux of both the Turrialba and Masaya Volcanoes which at the time in 2018 were the two most active volcanoes in Central America [10, 11].

The Matrice 2 was capable of carrying payloads of scientific equipment such as the Flame spectrometer which was used for the volcanic degassing research and Differential Optical Absorbance Spectroscopy (DOAS) at the Turrialba and Masaya Volcanoes [11]. Drones are capable of accurately monitoring SO_2 emissions coming from both volcanoes and power plants making them very beneficial to climatologists measuring the effects of climate change [3]. LAQAT is now using UAS to help students make thesis papers on subjects ranging from industrial chemistry, environmental management, and other important topics for volcanic studies. Thesis papers and associated projects lead to published papers. In the end, the University is giving information to different institutions and local governments for control, risk management and sustainable development of the natural resources of the nation and UAS are assisting these efforts.

Implementing an accurate and consistent volcanic gases monitoring program in countries of high levels of volcanic activity serves the United Nations sustainable development goals and serves as a great eruption forecasting method. The dangerous complication arises when volcanologists are tasked with collecting gas samples which requires they to enter regions of significant volcanic hazards. UAS are providing a safe and effective alternative for volcanologists studying volcanic gas plumes [12]. UAS are allowing park rangers and volcanologists to observe these danger zones with accuracy and precision, they can share the data and compile data bases of information which facilitate the eruption forecasting methods of the volcanologists.

Measuring volcanic gases is an essential eruption forecasting method used today because any change in the ratios of certain gases can indicate an imminent eruption. The concentrations of carbon dioxide CO_2 , sulfur dioxide SO_2 , and hydrogen sulfide H_2S can be measured by flying UAS right through the eruption column [11, 12]. “The total amount of gas being emitted can be used to calculate the exchange of volatiles between the deep Earth and the atmosphere. Researchers need to know which reactive species are coming out of the volcano so that the interactions between volcanoes, climate, and ozone can be better understood. These compounds contain such halogens as chlorine and bromine, and a drone

Fig. 13 LAQAT team UAS control point



Fig. 14 Active crater of the Turrialba volcano



Fig. 15
Telecommunications towers

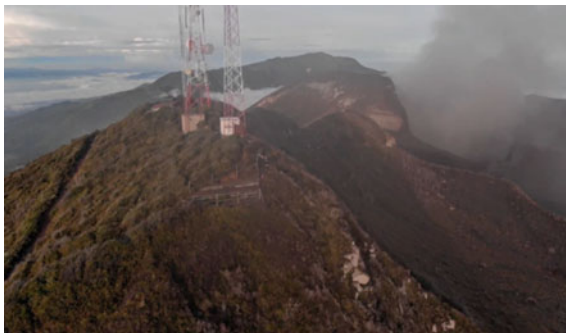


Fig. 16 Turrialba summit

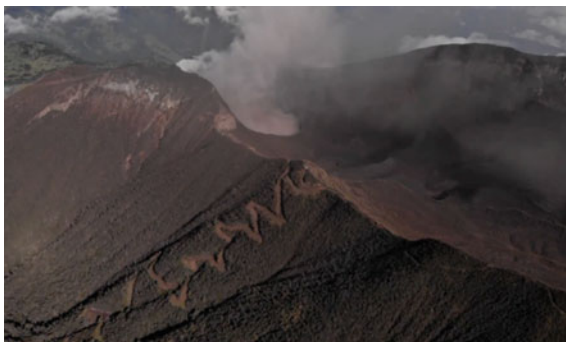
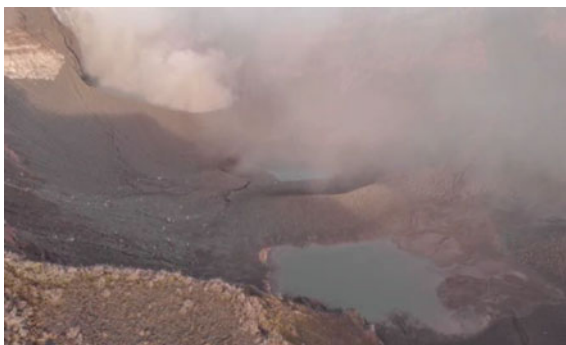


Fig. 17 Turrialba volcano
summit



hovering directly in the gas at varying distances from the source can help scientists determine how the compounds change as the plume ages” [12].

The total amount of gas being released from a volcano can be calculated to understand the inner working of the Earth. UAS are now assisting these research efforts investigating the exchanges of volatiles between the deep Earth and the atmosphere. The volcanic emission and atmospheric chemistry of surrounding areas can also be used to monitor the volcanic activity and contribute to collective

Fig. 18 Fumarole at Turrialba volcano



Fig. 19 Active west crater of the Turrialba volcano



Fig. 20 Fumarole releasing volcanic gases



knowledge associated with the effects of climate change. This was accomplished at the Turrialba volcano by flying transects underneath the entire width of the gas plume to measure the total output, or flux, of SO_2 [11, 12].

One of the most problematic sites of the country was the Irazú volcano National Park to the west of Turrialba. This region received a major amount of ash from Turrialba because it is a volcanic building higher than the Turrialba

volcano; the wind direction carried the ash to the Irazú volcano where it actually shielded the Central Valley from some ash from the Turrialba volcano eruption.

4. January 2020 investigators working on a specialized project at the Irazú Volcano flew a Mavic Mini into the active crater to make internal observations of the crater lake and the crater walls. The study focus was to document the geological morphology of the active crater. The images taken by the drone showed close up views or sections that cannot be observed from ground observations along the crater rim. Photographs showed sections of the southeast wall had large vertical cracks developing from increased rain in the region [10]. Due to several earthquakes with an epicenter that intersects the fault of the Irazú volcano located below the active crater in early 2020 the cracking crater wall was an important area requiring an investigation. UAS provided a quick safe and efficient method to document these cracks and forward the information to research team in real time.

Fig. 21 UAS image main crater of the Irazú volcano



Fig. 22 UAS image crater lake Irazú volcano



Fig. 23 Erosion on the South-East crater wall



Fig. 24 Cracking on the South-East crater wall

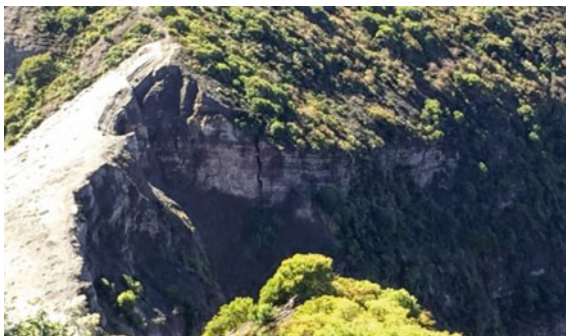


Fig. 25 Rockslides on the East crater wall



Fig. 26 Plant growth on the North crater wall



Fig. 27 Plant growth on the West crater wall



Fig. 28 Rockslide on East crater wall



Fig. 29 Mavic Mini at Irazú summit



Fig. 30 UAS image Diego de la Haya crater



9 Industrial Applications

UAS are revolutionizing how industrial companies manage data sets. For example a construction technology firm named Veerum implemented a UAS for 3D imaging tasks to build (Digital Twins) of work in process buildings. This created a new validation mechanism for management at Veerum which facilitated overall company optimization. Startup firms in the US have raised \$3billion to develop certain civil UAS applications [8]. In fact using UAS for atmospheric sampling has become such a popular application large Fortune 500 and publically traded companies are beginning to leverage UAV technologies into their new projects. The DOW Chemical Company has begun developing a drone fleet and associated program to measure emissions. Further enhancement of the UAS sector has brought forward tangible applications that illustrate how this technology can assist in improving community health, collective education and stimulate economic growth such as using UAS to measure harmful pollutants like Nitrogen dioxide or NO_2 , Nitrogen oxide or NO or a combination of the two chemical species referred to as NO_x . Both of these pollutants contribute to the formation of acid rain and the deterioration of the ozone [10]. Therefore any technology to help monitor and these toxic emissions will serve the United Nations and their SDG's.

Atmospheric sampling using UAS has been recognized by several advanced corporations. During October of 2020, the DOW Chemical Company collaborated with Montrose Environmental to test certain UAS for measuring emissions from industrial power plants. Dr. Patrick Clark explained that; in order to minimize the hazard to employees the Dow Chemical Company collaborated with Montrose Air Quality Services LLC from California. Together they evaluated the use of UAS for the measuring source emissions from Dow chemical manufacturing facilities. A proof of concept test was first conducted at the Dow Chemical Company facility located in St. Charles, Louisiana. The Dow Chemical Company flew the DJI Matrice 600 UAS equipped with EPA's Kolibri sensor/sampler attached to the undercarriage. Pollution sampling was implemented by flying the UAS downwind to the plume. The Dow Chemical Company was measuring for nitrogen oxide NO and nitrogen dioxide NO_2

carbon as carbon dioxide or CO_2 and carbon monoxide CO . UAS emission factor calculations using the carbon balance method proved accurate. “Emission factors were calculated for the nitrogen species emissions NO and NO_2 . The results determined by the UAS were compared to EPA Reference Methods conducted at the same time and also compared to the facility’s Continuous Emissions Monitoring System (CEMS) results” [13].

10 TECO Tampa Electric Company

The Tampa Electric Company (TECO) has been using UAS and has been considering hiring a UAS company for more advanced inspection applications. For sophisticated UAS projects, service contracts can be easier than starting an employee training program from the ground up.

Fig. 31 TECO Big Bend Power Plant Tampa, Florida



Fig. 32 UAS Thermal image of discharge water

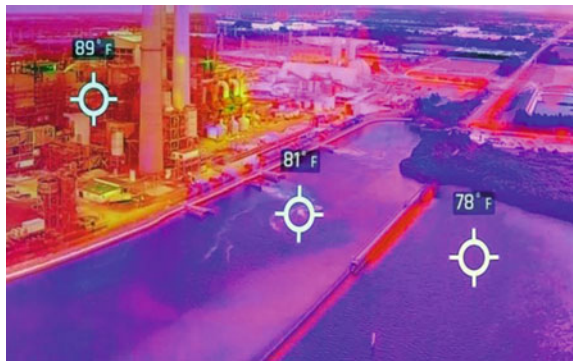


Fig. 33 1 h CO₂ dispersion from the TECO Big Bend power plant in Tampa Florida

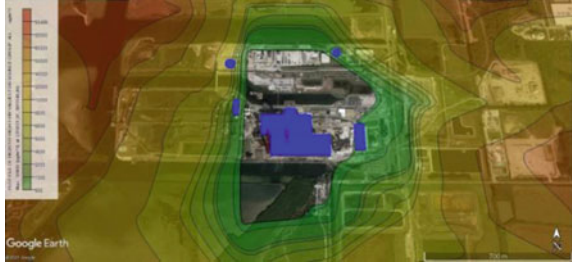


Fig. 34 1 h CO₂ dispersion from the TECO Big Bend power plant in Tampa Florida



Fig. 35 24 h CO₂ dispersion from the TECO Big Bend power plant in Tampa Florida

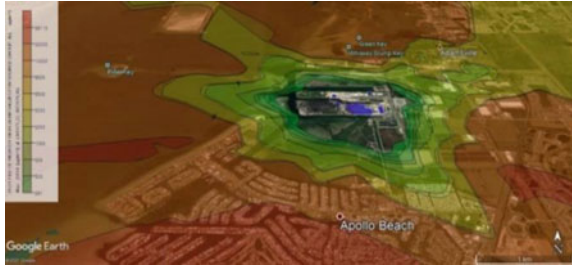


Fig. 36 24 h CO₂ dispersion from the TECO Big Bend power plant in Tampa Florida



Fig. 37 1 h NO_x dispersion from the TECO Big Bend power plant in Tampa Florida



Fig. 38 1 h NO_x dispersion from the TECO Big Bend power plant in Tampa Florida



Fig. 39 24 h NO_x dispersion from the TECO Big Bend power plant in Tampa Florida



Fig. 40 24 h NO_x dispersion from the TECO Big Bend power plant in Tampa Florida

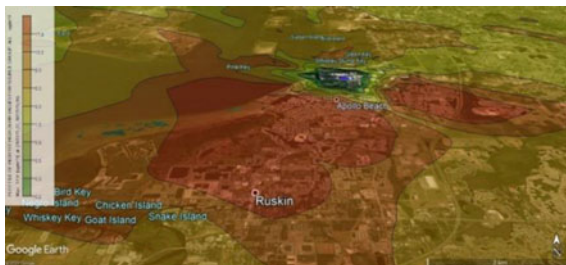


Fig. 41 1 h SO₂ dispersion from the TECO Big Bend power plant in Tampa Florida

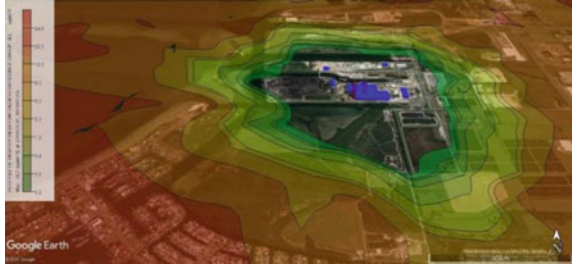


Fig. 42 1 h SO₂ dispersion from the TECO Big Bend power plant in Tampa Florida



Fig. 43 24 h SO₂ dispersion from the TECO Big Bend power plant in Tampa Florida

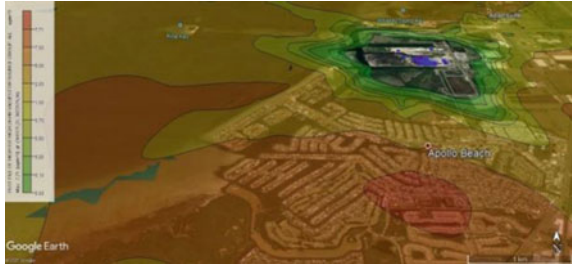


Fig. 44 24 h SO₂ dispersion from the TECO Big Bend power plant in Tampa Florida



11 UAS Solar Farm Application

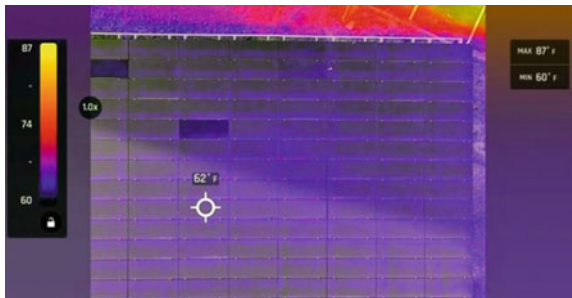
Solar farms that adopt new technologies that best serve their owners and their efforts will improve overall performance. For example; “DECOM has been an early adopter of drone technology to reduce time that managers and crew members are spending in the field, improve overall asset and plant performance, and reduce hazardous and unsafe tasks for crew members. DECOM turned to a drone service provider to perform scheduled inspections via aerial thermal imaging, which has helped to reduce the amount of time personnel spend on a single inspection and away from other duties. The drone inspections reduce the costly consequences of shutting plants down when an isolated issue occurs. Incidents such as blown overhead fuses in a transformer line can be inspected by drones while keeping the plant running. In the case of an annual substation inspection, the drone is able to perform the inspection without the need to shut it down” [14].

UAS software companies like Measure have designed sophisticated software to assist inspections of industrial infrastructure. Research has shown many benefits to using this type of software for advanced UAS applications and that the software increases accuracy of image processing. For example; “Thermal images are compiled

Fig. 45 Tampa electric Big Bend Solar Farm



Fig. 46 UAS thermal image of Solar Farm



into orthomosaics that remove damage artifacts such as solar flares prior to final analysis. By mitigating for the potential false positive identification via extensive thermal data capture, aerial thermography results have previously been validated by DECOM to result in a >98% reporting accuracy” [14].

12 UAS for Sustaining Populations of Endangered Species

There are numerous practical examples of how UAS contribute to the SDG’s of climatologists today. For example, in the state of Florida in the United States specifically the Tampa Bay region, UAS systems are being used by United States Geological Survey (USGS) and Environmental Service Departments to monitor and track manatee populations around the waters surrounding the powerplants. As endangered species the Florida Manatee is closely watched and protected by international institutions like the UN and is incorporated into the SDG’s of the organization.

Warm discharge water and surrounding areas become a winter sanctuary for the Florida Manatee because when cold fronts decrease the water temperatures in Florida, the warmer waters surrounding the powerplants become areas where these creatures can avoid heat stress. By implementing UAV technology the staff at Tampa Electric was able to count daily the manatee population in the waters surrounding the plant. Taged manatee under observation for rehabilitation purposes are more easily identifiable once released back into the bay. For the 2020–2021 season in the water surrounding the TECO Big Bend power station there was a daily low count of 57 manatees and a high count of 568 manatees bringing the daily average to 261 manatees. Florida Manatee (*Trichechus manatee latirostris*) which is a sub specie of the West Indian Manatee is protected by both state and federal laws because sustaining the population of these creatures is important to both the state and country. These regulations are aligned with those of the United Nations Environmental Plan for the Caribbean Environment. In the United States; “The manatee are protected under federal law by the Marine Mammal Protection Act of 1972 and by the Endangered Species Act of 1973, which makes it illegal to harass, hunt, capture or kill any marine mammal. The manatee is also protected by the Florida Manatee Sanctuary Act of 1978, which states: “It is unlawful for any person, at any time, intentionally or negligently, to annoy, molest, harass, or disturb any manatee.” UAS provide a unique opportunity for safely monitoring endangered and rare animal species, not just the manatee. Research using UAS to track endangered species in real time has proven to be more economical concerning the logistics of resources required for such projects. UAS are able to cover vast amounts of wildlife reserve where ground based methods would otherwise not be possible” [2].

Fig. 47 Powerplant discharge water



Fig. 48 Resting manatees



13 Results

UAS and the various applications for the management of natural resources offer many advantages to alternative methods. UAS provide better study design flexibility efficiency data collection ability with better resolution at a more economical price point compared to high resolution satellite data. Advancements in the UAS sector have opened the door to new possibilities for monitor the climate and the environment, and is therefore of great interest to the United Nations and their Sustainable Development Goals [2]. UAS are helping the government of Costa Rica by assisting with the generation of terrain maps for hydro-electric projects and assisting with aerial watch for any changes in forest density. UAS help professors working for the National University by mapping the dangerous volcanic regions with low risk to researchers; UAS are providing a way for fast remote measurements with less risk. UAS are helping climatologists visualize changes in volcanic lagoons. UAS are also extremely beneficial devices for monitoring landslides during the rainy season and documenting changes in the volume of the land that has slid from the higher elevations. UAS are affective at enhanced pollution detecting and monitoring from both industrial sources such as power plants and natural sources like volcanoes. UAS provide opportunity to gather complex and sophisticated data sets and they're associated platforms allow users to share valuable information with a multitude

of collaborators simultaneously providing required data points in decreased time frames.

By implementing UAS technologies several elements of society such as industrial complexes, environmental service providers and conservationists all benefit from more precise and accurate information available obtained through deploying UAS. Technological advancements in the UAS sector has also greatly contributed to the reduction of costs and manpower requirements associated with accomplishing these SDG's. UAS applications continue to grow exponentially with drone delivery, LiDAR mapping and industrial plant inspection at the forefront of the industry. The AERMOD plots shows that, depending on the wind pattern in the Tampa area, dispersion occurs in all directions around the TECO plant, with a major component to the southwest of the power generation plant. In the surroundings of the TECO Company 328 ft or 100 m the influence of CO₂, NO_x and SO₂ is low, for the 1-h or 24 h plots. The dispersion has a greater influence towards the area of Apollo Beach and Ruskin, where there are areas of accumulation and dilution of pollutants. The levels calculated according to the AERMOD program specify that the CO₂, NO_x and SO₂ values are below the levels recommended by the US-EPA. The height ratio of the chimneys/buildings is adequate to have a good dispersion.

14 Conclusion and Forecasts

Toxic gas emissions such as Sulfur dioxide or SO₂ which are the direct result of burning fossil fuels contribute to climate change and acid rain in the region. UAS capabilities can now greatly assist climate scientists by providing an aerial observation perspective which allows for increased data collection with improved safety. UAS are now investigating the geothermal energy potential in the northern volcanic region of Costa Rica. Helping ICE monitor and maintain the National System of Electricity via LiDAR, along with optimizing their solar fields and energy plants [10]. UAS are assisting the SINAC with search and rescue, monitoring dangerous areas like active craters and to keep an eye on rural areas of the National Parks that could otherwise take days to hike out too. UAVs can help boarder protection and security to help prevent illegal immigration. UAS also reduce the costs of industrial inspections associated with oil, gas and energy production. This research outlines practical applications and practices designed to counter the present-day challenges deriving from atmospheric pollution and climate change, an essential area of the United Nations SDG's and a crucial component for global sustainability. UAS are beginning to transform working strategies and work flow tasks in many industries. For example UAS are being used after natural disasters like hurricanes to monitor and document asset damage by insurance companies. The UAS market has a forecasted annual impact of \$31 billion to \$46 billion on the GDP of the United States by 2026. UAS hardware manufacturing in the US is forecasted to reach \$20 billion by 2026. When the global growing commercial market is considered especially in developed nations such as India, China, United Arab Emirates, European Union and

Japan the potential is enormous. Studies are being conducted into the feasibility of drone delivery services with certain companies like Alphabet (Google), United Postal Service (UPS), Amazon and Walmart already beginning investing [8]. Flytrex a startup raised \$7.5million in 2019 and now Flyrex and the North Carolina DOT are authorized by the Federal Aviation Administration (FAA) to test drone delivery operations by flying directly over people and moving vehicles, they can fly at night using a lighting system onboard the UAS, and they have been authorized to fly beyond visual line of sight BVLOS in certain airspaces [15]. The lifespan of lithium-ion batteries is expected to double by 2025 making UAS delivery a much more feasible and profitable enterprise moving forward [8].

Acknowledgements Both of the first and second authors acknowledge that there was no financial assistance received for this research and publication, nor any competing financial interests. The first author recognizes that all AERMOD plots were created by the second author via data provided by the Environmental Service Department of Tampa Electric an Emera Company.

References

1. Using UAV-based systems to monitor air pollution in areas with poor accessibility. *Hindawi J Adv Transp* 2017:8204353. <https://doi.org/10.1155/2017/8204353>
2. Mishra PK, Rai A Role of unmanned aerial systems for natural resource management. *J Indian Soc Remote Sens.* <https://doi.org/10.1007/s12524-020-01230-4>
3. Mayer H (1999) Air pollution in cities. *Atmos Environ* 33(24–25):4029–4037
4. Wendel J (2017) Science at the border between ice and ocean. *Eos* 98. <https://doi.org/10.1029/2017EO088187>
5. Kelleher C, Scholz CA, Condon L, Reardon M (2018) Drones in geoscience research: the sky is the only limit. *Eos* 99. <https://doi.org/10.1029/2018EO092269>
6. Shanafield M, Bourke SA, Zimmer MA, Costigan KH (2021) An overview of the hydrology of non-perennial rivers and streams. *WIREs Water* 8(2). <https://doi.org/10.1002/wat2.1504>
7. Drones for power plants: use cases and best practices for drones at coal and gas power plants
8. Cohn P, Green A, Langstaff M, Roller M (2017) Commercial drones are here: the future of unmanned aerial systems. Capital Projects & Infrastructure, McKinsey & Company
9. Singh A, Kushwaha SKP Forest degradation assessment using UAV optical photogrammetry and SAR data. *J Indian Soc Remote Sens.* <https://doi.org/10.1007/s12524-020-01232-2>
10. Godfrey I Investigating the volcanoes of Costa Rica
11. *J Geophys Res: Solid Earth* 123(8)
12. D'Arcy F, Stix J, de Moor JM, Rüdiger J, Diaz JA, Alan A, Corrales E (2018) Drones swoop in to measure gas belched from volcanoes. *Eos* 99. <https://doi.org/10.1029/2018EO102329>
13. Patrick Clark PE, Richardson J (2020) Using unmanned aerial systems (UAS – drones) to measure NO_x emissions from stationary sources. Montrose Environmental & Dow Chemical Company
14. DEPCOM CASE STUDY Solar EPC/O&M provider improves site performance with advanced drone technologies
15. Lee I (2019) Drone delivery startup Flytrex raises \$7.5 million in Series B funding | SMBs keep pace with eCommerce giants on the drone delivery front. <https://www.uavcoach.com>
16. Drones for wind turbine inspections: how to use drones to reduce hazardous man-hours and optimize energy production

17. Adam-Poupart A, Brand A, Fournier M, Jerrett M, Smargiassi A (2014) Spatiotemporal modeling of ozone levels in Quebec (Canada): a comparison of kriging, land-use-regression (LUR), and combined Bayesian maximum entropy-LUR approaches. *Environ Health Perspect* 122(9):970–976
18. Pujadas M, Plaza J, Terés J, Artíñano B, Millán M (2000) Passive remote sensing on nitrogen dioxide as a tool for tracking air pollution in urban áreas: the Madrid urban plume, a case study. *Atmos Environ* 34(19):3041–3056
19. Alvear O, Calafate CT, Hernández E, Cano JC, Manzoni P (2015) Mobile pollution data sensing using UAVs. In: Proceedings of the 13th international conference on advances in mobile computing and multimedia, MoMM 2015, pp 393–397
20. Stolaroff JK, Samaras C, O'Neill ER, Lubers A, Mitchell AS, Ceperley D Energy use and life cycle greenhouse gas emissions of drones for commercial package delivery. *Nat Commun*. <https://doi.org/10.1038/s41467-017-02411-5>
21. McKinsey analysis; Teal Group (2017) 2017 World civil unmanned aerial systems market profile & forecast
22. The improvement in GDP will be generated by UAS manufacturing, associated services, and drone-enabled productivity improvements, such as more efficient inspection of remote pipelines
23. Includes venture capital (72.0 percent), private equity (16.5 percent), private “angel” investors (5.0 percent), among other sources
24. (2016) Public perception of drone delivery in the United States. USPS Office of the Inspector General, United States Postal Service. <https://www.uspsog.gov>
25. Zu C-X, Li H (2011) Thermodynamic analysis on energy densities of batteries. *Energy Environ Sci* 4:2614–2624
26. McFarlane DA, Lundberg J, van Rentergem G, Ramírez CJ (2017) An autonomous boat to investigate acidic crater lakes. *Eos* 98. <https://doi.org/10.1029/2017EO073409>
27. Branscombe A (2017) Can volcanic gas levels predict an eruption? *Eos* 98. <https://doi.org/10.1029/2017EO074949>

Review of Uncrewed Aerial Vehicle Swarm System Coordination and Communication



Chandra Has Singh, Vishal Mishra, and Kamal Jain

Abstract In this modern era, uncrewed aerial vehicles (UAVs) have effectively changed and transformed the aeronautical industry in an effective way. A specific technique created to increase this disintegration is the UAV swarm system. The UAV swarm has the ability to deliver missions effectively and self-coordinate the operations of multiple UAVs with no remote operator intervening. This paper comprehensively surveys the literature about various UAV swarm functioning. It proposes a swarm architecture considering the high parameters that allow wireless radio communication infrastructure for a high degree of swarm system reliability and autonomy. This review paper chronicle did preliminary test development to carry out this proposed swarm wireless radio communication system architecture. UAV's gradual integrated development of UAV swarms with UAV communications Autonomous self-coordination and organizing capability are central to advancing the utility of UAV swarm systems. Several limiting factors hamper the usability of UAVs and reduce performance, including communication, various networking challenges, size-load, and proper power considerations. In addition, the wireless radio system takes advantage of a highly reliable and robust infrastructure for wireless radio communications with secure one machine to another machine.

Keywords UAV swarm system · Hybrid swarm · Swarm communication · UAV ad-hoc network · Flying ad hoc networks

C. H. Singh · V. Mishra (✉) · K. Jain
Department of Civil Engineering, Indian Institute of Technology, Roorkee, India
e-mail: vmishra1@ce.iitr.ac.in

C. H. Singh
e-mail: chandrasah@ce.iitr.ac.in

K. Jain
e-mail: kjainfce@iitr.ac.in

1 Introduction

In its first stages of development, unmanned aerial vehicles (UAVs) were used for various military surveillance, and their applications mainly included search and rescue (SAR) and missions destroying any desired targets [1], and vigilant supervision of the border. For real-time activity change detection [2], strategic reconnaissance missions, and close support in combat missions [3].

Besides military and tactical applications, UAVs also play a vital role in various commercial and civilian work, such as post-disaster help and relief [4], cooperative forest fire prevention and surveillance [5, 6], and remote real-time wind turbine blades. Inspection [7], civil security operations [8], remote sensing and precision agriculture [9], structure inspection [10], track monitoring and management [11], UAVs for communication relay systems [12], and aerial and 3D mapping UAVs are being used in abundance for this [13]. For example, UAVs in globally very heart-breaking and known disasters such as the Kedarnath disaster 2013, the Tapovan area in Chamoli district of Uttarakhand, Garhwal Himalaya, the earthquake of Lahore, and disaster relief and management in Katrina, Tohok earthquake, Typhoon Morkot. The technique has been used. Haiti has played a vital role in the earthquake and the Amfan cyclone.

The research and development of UAVs have been growing at an unprecedented pace in the past few years, owing to its many advantages which cannot cater broad need and applicability. More and more UAVs appear to operate in groups or swarms of UAVs. Considering the nature of future modern warfare, where machines will be more beneficial than humans, in 2015, the United States launched a variety of UAV swarm research projects, such as the “Elves” project, which is a defense advanced research project. The project is part of the agency’s low-cost UAV Swarm technology. Compared to a single-UAV system, there are clear advantages of performing the task by forming swarms or formations by multi-UAVs, giving the technology a bright future. UAVs have become essential carrier vehicles for multifunctional functions in modern times, capable of carrying various payloads without human interaction. Therefore, considering the potential of UAVs, the use of military security, and civilian applications makes the concept of an attractive proposition. Aircraft flying with human pilot controls always have the potential to cause a pilot accident or severe damage to the aeroplane, which can be avoided in the case of UAVs.

With autonomous aircraft systems, these concerns are mitigated; additionally, manned aviation is expensive to operate. Human-crewed aircraft are costly to buy by any individual, and one has to undergo the process of training and to license to work, which makes its use by the individual prohibitive. In addition, a pilot would have to pay a lot to fly the aircraft. The high cost of fuel in use and multifunctional maintenance are additional prohibitive expenses for general aviation use for all types of civil and commercial applications. For these reasons, the role of UAVs has emerged as an attractive alternative in many ways.

Additionally, military applications have many multifaceted advantages for unmanned aircraft, although this paper has focused chiefly on protecting humans in war zones and various applications of UAVs in commercial applications.

- **Mission Stability:** In a single-UAV system, if a single UAV is shot down during a mission, it is considered a failure of the entire mission, and the task is terminated at that point. In the case of a single UAV, the mission ends if the UAV is shot down during the mission; however in case of an accident with a UAV in the system of UAV swarm, the mission is completed by another UAV and the mission continues to operate successfully [14].
- **Extensibility:** A single UAV has a fixed range of communication during the mission, which is a dedicated communication medium between the flying UAV and the central control station, whose coverage capability is limited to a limited area, ending after a certain point, the coverage area. The range depends on the environmental conditions around the mission area. Let's talk about multiple UAV systems than during the mission. The coverage area is extensive, which makes the task easy to operate, and its effect increases in many ways [15].
- **Mission Speed:** Research shows that when a UAV swarm is used to perform missions, missions can be completed faster and reduce time consumption. This is very useful and true, especially for search operations, as multi-UAV systems can operate and monitor search operations entirely and save time by completing tasks quickly and using resources completely [16].
- **Autopilot:** When a single UAV is used during a mission, it is entirely controlled by the pilot, direct control of all aircraft systems at the control station on the ground, which directly contains the entire mission of the aircraft. In most UAV swarm systems, the airborne onboard autopilot ensures controlled flight of the mission. It performs the mission in accordance with task and flight plans and other mission instructions received from the central control station. To carry out any assignment in the UAV Swarm system, all UAVs can adopt the approach while being self-sufficient or adopt the master and follower method in the multilayer communication system, thereby conducting the mission more smoothly [17].
- **Cost:** Various research suggests that by using multi-UAV systems, missions can be completed at a lower price. Resource mobilization at one time is more likely to occur. Still, it is rarely done when looking at the multifaceted benefits of UAV swarming in work operations and outcomes [18].
- **Communication Range:** A single UAV system requires direct communication between the UAV and ground pilots at all times or to maintain direct contact with central control stations. In contrast, a UAV swarm system divides communication into multiple stages with a specific UAV we call a master UAV that represents the entire group and controls the group by establishing contact with the ground in a way that Sends formation and action messages to other UAVs. It acts as a transceiver, expanding the range of our communication and combat capability, and can carry missions over great distances [19].
- **Radar Signature:** UAVs in swarm systems for military reconnaissance and target-oriented missions produce much smaller radar cross-sections than human-crewed

military aircraft. The radar of an enemy country does not readily catch that, increasing the security of military operations by leaps and bounds [20].

- **Field Coverage:** Aerial mapping and implementation of the collective behavior of UAVs for precision agriculture, which considers all types of onboard processes, including intelligent machine vision and avoidance of obstacles on the way. After evaluating the efficiency of the proposed system after considering such functions, we find that when we perform UAVs in a swarm system, we can execute the task with much less time and much greater efficiency and can cover many areas [21].

2 Current Development Direction in the UAV Swarm Industry

In today's era, the utility of UAVs is increasing in every field, and its industry has also increased in the same proportion. Developing a UAV swarm is a complicated development process. There are several limitations to the operation of UAVs, as they are smaller in size and have different payloads that control flight endurance. The flight control of the UAV is done through a remote controller operated by the pilot's hands or through software or apps installed on a computer and mobile.

Flight controls are operated via software that requires appropriate control parameters to be uploaded to the autopilot. The utility of a swarm created by a multiple UAV system becomes very attractive as it greatly enhances the functionality and frees it from the shackles of various limitations of a single UAV.

Usually, a UAV swarm is defined as a group or swarm that demonstrates the ability of multiple UAVs to work together to accomplish an important task and the ability to achieve a mission by coordinating with each other [22]. There are many examples of the swarm to be seen in nature itself. Bees live in their herds, coordinating with each other or in groups to perform their essential tasks. Migratory birds follow a specific flight pattern in coordination to move from one country to another and carry out the migration. Similarly, many UAVs direct and control the swarm's flight through interconnected communication devices and different sensor data. The mission is accomplished, which completely vanishes all the limitations of a single UAV [23].

The specific architectures of the tasks performed by the UAV swarm are shown in Fig. 1, showing the functioning of the UAV swarm through two distinct mechanisms that can be widely used in military and civil applications.

3 UAV Swarm Communication Implementation

Since the purpose of this paper is to review the arrangement of the UAV swarm radio communication system, the communication system of the UAV swarm is established on the one hand by one UAV with the other UAV as well as the connection of the

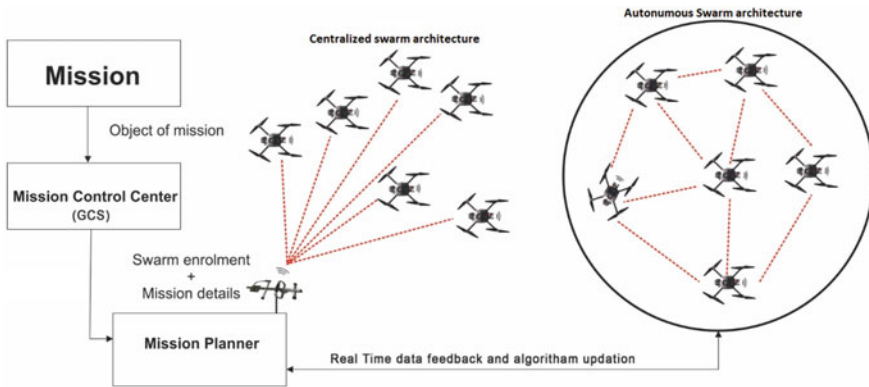


Fig. 1 UAV swarm flow architecture

UAV swarm to the central ground control station installed on the ground. So that the entire activity of the mission can be fully controlled when required.

- **Semi-autonomous—(Communication of UAV swarm through central control station):** The UAVs establish direct communication with the Central Control Center installed on the ground to receive real-time mission information and formation changes. Communication in this type of UAV swarm formation clearly establishes direct transmission of all members of the UAV swarm with the control station on the ground [24].
- **Fully autonomous—(Mutual communication of one UAV with another UAV without direct interference from the ground control station):** In this type of swarm’s communication system, all UAVs act like a node, which establishes communication among themselves when needed each node acts as both transmitter and receiver, increasing the UAV swarm manifold’s range of transmission [25].

UTU (UAV to UAV) communication and UTC (UAV to control station) communication are combined through various layers of wireless communication architecture. In other words, the UAV swarm communication architecture defines the mutual communication and information exchange between UAVs and communication systems and information between central ground control stations. In addition, keeping in mind the mutual communication of UAVs, the radio communication architecture system ensures the most critical and reliable transmission from sender to receiver [25].

In this review article, various UAV swarm radio communications architecture systems are presented and reviewed from the perspectives of both emerging academic research and engineering areas. The radio communication architecture compares the advantages and disadvantages of different systems considering all the technical aspects. Based on this, the real-time environment of the mission scenarios is discussed.

The authors hope that the comparative analysis reviewed through the special notes made in this paper can be helpful for using effective radio communication architecture and reliable radio communication systems for UAV swarms. The remainder of this review article is adjusted as follows, presenting a systematic, preliminary, and step-by-step comparison of the UAV swarm communication architecture that provides a comprehensive comparative overview of the existing architecture according to a readily accepted classification system [26].

4 UAV Swarm Architectures

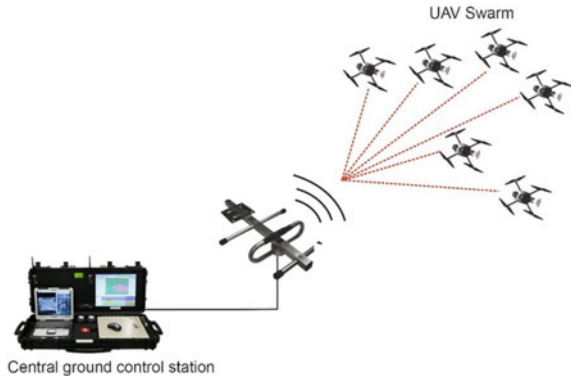
The radio communication network system plays a vital role in UAV swarm intelligence missions to enable fully controlled and complete mission implementation autonomously. In the early stages of UAV swarm implementation and development, a central control station has been established for control and instructions capable and powerful for range and multipoint communication in terms of sharing information with every UAV of the entire swarm.

Therefore, the centralized communication approach was extended from the traditional UAV control system to the multi-UAV control or swarm communication control architecture. As the UAV swarm systems grow in size and towards executing multiple missions simultaneously, a decentralized approach is apparently proposed. Envisioning and implementing radio communication from a decentralized approach introduces a complex architecture. Still, this multiple-stage communication system reduces the dependency of UAV swarms on central control stations for any mission-related implementation.

Many modern-day researchers and UAV experts from different fields have devoted themselves entirely to the research of UAV swarm communication architecture. In this section, we conduct a multidisciplinary review of these researches and present them systematically by adjusting the available general and systematic communication architectures for UAV swarm systems. In addition, we also make an economical analysis of the pros and cons of these communication architectures [27].

First, since wireless transmission time is primarily controlled and related to radio antenna array gain, the Yagi Uda antenna is used to transmit in a specific direction, significantly increasing the transmission range. In addition, the transmission efficiency can be multiplied by adapting the frequency band as per the requirement in the mechanism designed for multiple UAVs. The flight control time is optimized by dynamically controlling the UAV velocity dynamically according to the design of the UAV trajectory and the value of the optimal value of locations. In these iterations, optimization theory can be used to obtain optimal solutions. Even then, it can be challenging to guarantee the convergence of the original optimal problem [28].

Fig. 2 UAV swarm system with a centralized ground control station



4.1 Centralized Ground Control Communication Architecture

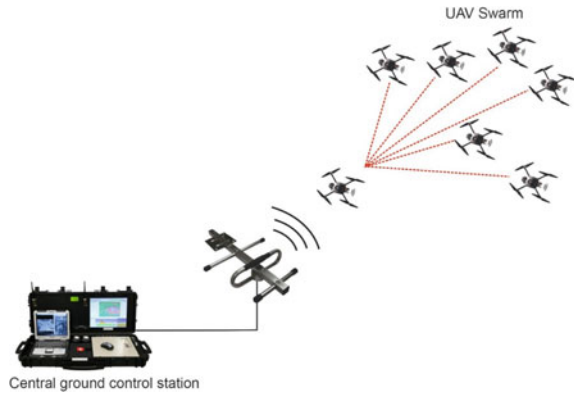
The centralized communications architecture evolved from the development of single-UAV systems and was later applied to the creation of UAV swarm technology. As shown in Fig. 2, it primarily consists of a central point to which all UAVs in the UAV swarm are effectively connected and responsible for exchanging information.

In this type of architecture, each UAV directly connects with the GCS (Ground Control Station) and receives control commands directly from the central control station, as shown in Fig. 2. In this type of system, the transmitter and receiver of the ground control station must be abundantly very powerful. So that the maximum energy consumption can be done at the central control station, and the UAV flying in the air can maximize the flight time to the safe limit by expanding its energy consumption to the minimum. This centralized communication architecture is relatively simple and stable, adopts a simple radio mesh algorithm, and is used for small-scale tasks. This type of central system is more suitable when the UAV swarm's size and mission coverage area are small and the mission complexity is relatively low. Among the applications of centralized radio communication systems, they are mainly used to simultaneously monitor a specific area from a central room and identify particular objects. This centralized system is a data-oriented wireless radio communication architecture designed for effective crowd monitoring and detecting suspect poachers in a forest [28].

4.2 Decentralized UAV Swarm Communication Architecture

However, UAVs generally fly at very high speeds and can increase the range of mission operations. UAVs keep connecting and moving with their radio mesh

Fig. 3 Decentralized communication architecture



network, so the radio mesh network stands out as the best option in the communication of the UAV swarm. This advantage would have been that each UAV swarm would be self-sufficient and have both communication roles, such as sending information and receiving sensor data from other UAVs in the network (Fig. 3).

Under the system of decentralized communication architecture, the UAV operates and performs the interactive communication system in real-time in an ad-hoc manner as per the requirement of the mission, eliminating the dependency of the central control station and all restrictions on the communication system [29].

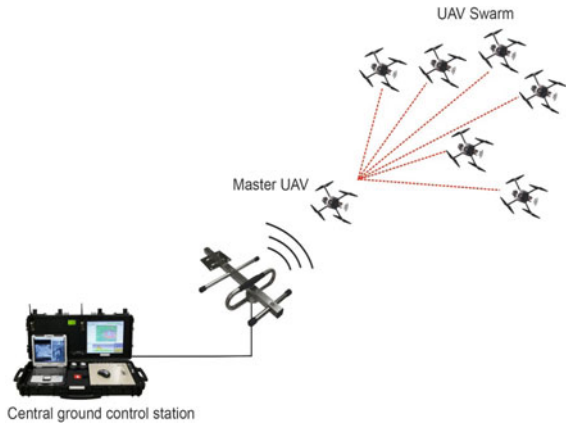
4.2.1 Single Group Swarm Radio Network

In the “Single group swarm Radio Network” shown in Fig. 4, mutual communication between swarm UAVs does not depend on the ground control station. Communication between the swarm and the ground control station relies on the functioning of a fast-processing UAV to process data from a sensor called a master UAV. In this single-layer radio communication system, the master UAV acts as a transceiver for data communication within the group, which is responsible for effectively functioning the mission by the UAV swarm and is a crucial component of communication.

UAVs in swarm share position and sensor information in real-time to optimize control and improve efficiency over their partners, using the adaptability and efficiency of this method. This enables the master UAV to send and receive swarm structural information, including mutual communication between the UAV and the central control station and critical command and instructional information.

Regarding master UAVs, two additional types of transceivers are required for data transfer: one for a group of UAVs to consume less energy and power for short-distance communication with another UAV and another for transceiver master UAVs. High power radio communicates long-term instructions with a centralized ground control station with the master UAV. Other UAVs only need to carry lightweight short-range transceivers at low energy cost and weight. This increases the communication range

Fig. 4 Single-group swarm radio network



of the network manifold for the coverage requirements of larger missions and makes the payload of smaller UAVs more efficient and more useful for tasks with smaller UAVs in size. However, to guarantee continuous connectivity of the swarm, the “Single group Swarm radio Network” architecture requires that the flight speed and flight pattern (heading orientation) of all UAVs in the swarm must be the same. This is important for the UAV swarm’s operation, and effectively controlled is necessary. Therefore, a group of smaller UAVs is always suitable for scenarios that use a single-layer radio communication network architecture. A real-time practical application of a “single-group swarm radio network” can be done for public safety environments where we have to simultaneously monitor security for a small area or security cover for a particular object [29].

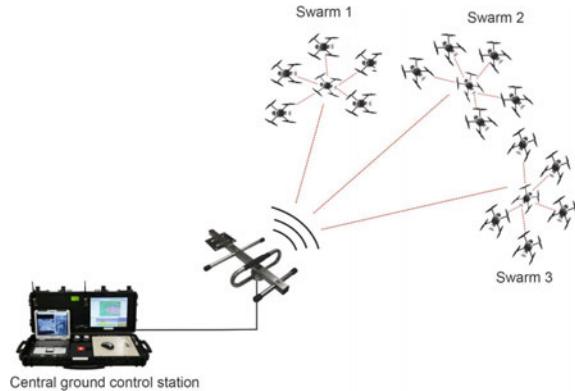
On the other hand, individual operation diversifications on the structure of UAVs in a UAV system have resulted in significant demand. We commonly encounter the need for a swarm of small, medium, and large UAVs whenever we implement real-world applications.

As a result, the “single-group swarm radio network” architecture described above falls short of achieving these objectives. While comparable UAVs commonly fly close together, various UAVs may be far apart. As an outcome, the swarm’s UAVs are split into groups depending on their mission objectives, with the identical UAVs operating in close vicinity. As described below, these architectures are characterized as “multiple group swarm radio networks” and “multilayer swarm radio communications networks”.

4.2.2 Multiple Group Swarm Radio Mesh Networks

The “multi-group swarm radio network” presents a viable solution to the problem since it eliminates all of the shortcomings of the single-group swarm radio mesh network. It has a centralized network design and a single-group swarm radio network.

Fig. 5 Multiple group swarm radio communication mesh networks architecture



Depending on the mission objectives, various kinds of groups have different applications. Intra-group UAVs interact in a radio mesh network, but inter-group UAVs do not (Fig. 5).

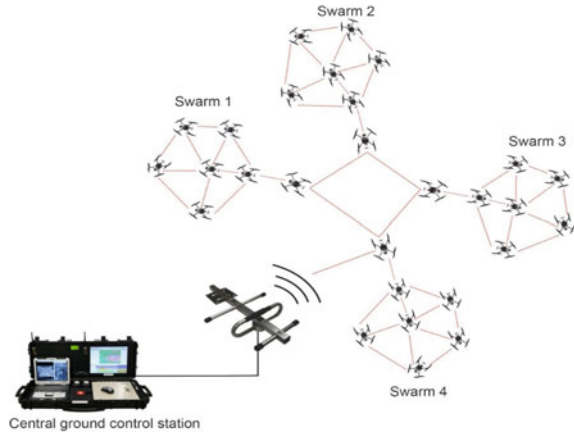
Intra-swarm communication systems are comparable to intra-group communication structures. Inter-group communication, also referred to as group-to-group (GTG) communication, is conducted by the central control station, which indicates master UAVs are still in charge of it. A multiple group swarm mesh network topology could be used if several types of UAVs are required for mission scenarios.

However, because the multiple group swarm radio mesh network design is semi-centralized, it is essential to emphasize the robustness of this architecture. At the same time, for G-T-G communication between the two UAVs in separate groups, the “multi-group swarm network” design suffers from a range of high latency issues. The efficient execution of multi-theater joint operations in various disciplines for military operations is a demonstration of how multi-group architecture is used. The central command station establishes a connection with multiple swarm groups simultaneously through different master UAVs, and the swarm’s groups perform operations in diverse locations of the mission area according to the central command station instructions [30].

4.2.3 Multilayer or Hybrid Swarm Radio Mesh Network

Another type of architecture considered suitable for any broad and diversified UAV mission deployment is the “multilayer swarm radio mesh network” architecture. In many respects, as presented in Fig. 6, this architecture departs from the multiple group swarm radio mesh network architecture. During the flight, a group of adjacent UAVs creates a mesh network, which is incorporated as the first layer of the communication architecture. In Sect. 4.2.2, the architecture of intra-group communication is detailed. In GTG communication, the various types of UAV groups, along with the second layer, rely primarily on master UAVs.

Fig. 6 Multi-layer swarm radio mesh network architecture



Various sorts of UAV groups use master UAVs to perform G-T-G communication, with the second layer serving an incredibly significant and active role. The nearest operational UAV interacts with the central control station, which is integrated as a third layer of the architecture during the flight. Each adjacent UAV can communicate effectively in the “multilayer swarm radio mesh network” architecture. The demand for a central control station relay is not required. At the first level, UAVs in the same group must interact about unlimited flights at different levels. Various groups of UAVs communicate with each other through master UAVs. The first and second levels, in turn, pass sensor data packets. As an outcome, all UAVs with multilayer swarms are self-sufficient and will establish ad-hoc basis communications with their nearby networks if mutual communication is not feasible. If mutual communication is not possible, it will establish contact with the next available neighbouring UAV. This architecture is resilient and secure since failure is not confined to a single spot. In a mission, when the number of UAVs changes, “the multilayer swarm radio mesh network architecture compensates for the increase or decrease of UAV nodes and quickly executes the mission by implementing network construction.” Therefore, multilayer swarm radio mesh network architecture best suits mission environments that change frequently.

Due to the complexity of UAV swarm operations, many network architectures are continuously changing, and communication between UAV nodes occurs on a massive scale. With the progress of research and communication technologies, UAV highlights the need for a future enhancement in this type of Swarm networking. The number of layers necessary to build a Swarm Radio Mesh Network Architecture with more UAVs is included.

As a result, the challenge of multi-UAV deployment to significantly decrease the overall cost of all scheduled users emerges, resulting in a more excellent workspace coverage and a much more sustainable and stable network setup. In this scenario, the iteration algorithm may be used as a realistic technique to decrease the aware applications by adjusting the transmission and flight control times suitably.

Because UAV wireless transmission primarily depends on antenna array gain or array manifolds formed by many UAVs, transmission time may be significantly decreased by effectively managing UAV spacing and location. Then, multi-UAV flight control time is optimized by dynamically managing the UAV velocity according to the effectiveness and optimum positions of the UAV trajectory design. These iterations allow us to utilize optimization theory to find a practical solution. However, confirming that the original ideal issue is fixed is challenging [31].

5 Conclusions and Discussions

This paper presents a concept-level proposal for using wireless radio networks as a communication central control station for various types of UAV swarm systems, as well as a comprehensive and in-depth review of the early stages of development phases and research. It comprehensively overviews the UAV swarm industry's development activities, extending beyond UAV swarm and in-house applications. Reviews developmentally tested paperwork and provide direction for different future capabilities work about the UAV swarm.

The specific development and coordination capabilities of autonomous communication with UAV-to-UAV communication are in a central role in advancing the utility of the UAV swarm system. Although swarm technology is not yet practically used in commercial applications, it is a rapidly growing field of potential, with the possibility of landing under the UAV industry in the future.

Using wireless radio frameworks with low power consumption and long distances available in the current era reduces the limiting factors for traditional UAV swarm communication approaches. The use of wireless radio networks for the UAV swarm will in many cases, promote greater efficiency and revolutionize commercial usability, especially with the increase of UAV-to-UAV communication capabilities in the presence of radio mesh networks with the capabilities of UAV swarm systems. Diffusion can be extended to various applications by leaps and bounds.

With the development of UAV technology and network communication, the mode of application of UAVs has also continued to evolve in parallel. The UAV swarm is a swarm intelligence-based solution proposed to extend the UAV application function and multi-UAV practical cooperative operations. UAV swarm has been used in many scenarios, such as wildfire monitoring, range monitoring, and disaster management. Therefore, to carry out research on UAV swarm technology is of great practical importance.

UAV swarm missions are highly mobile in operation, and the architecture of their mutual radio communications frequently changes, requiring communication networks with low latency and high reliability. Therefore, it is necessary to design radio communication architecture and mesh protocol with good applicability, high flow, and stability for continuous UAV function communication.

Although existing and consistent theoretical research and experiments in this direction have mainly solved some technical problems in UAV swarm communication architectures and radio mesh networks, many interesting, important, and yet challenging open issues are still worthy of further investigation. The solution which will bring revolutionary changes in the direction of the UAV swarm some of can be summarized as follows:

- Multilayer architecture may be better suited to the characteristics of communication and security in the needs of better-performing UAV swarm missions but simultaneously brings new challenges. Due to the importance of master UAVs in swarm communication, master UAVs during the task require a lot of ability to detect the failure and overcome it in a timely manner. Also, if a malfunction occurs again, it is imperative to have a very reliable and working algorithm to select the next UAV to act as a master UAV in such a situation at the same time as soon as possible. The data stored in the master UAVs must be synchronized with standby to execute the mission accurately and efficiently.
- Swarm communication can be intermittently associated with the increasing feature of UAVs in various critical areas and with the continuous change in mesh network architecture. Setting up mesh networks correctly and maintaining their protocols has always been a critical problem. Therefore, the solution of intermittent connectivity in UAV mesh network communication will remain a significant area for future research.
- Most of the researchers currently involved in the research focus more on the proposed Mesh Network Routing Protocol performance improvement. At the same time, UAV's mission implementation has far more important aspects to consider. However, security is an essential core material that any Also UAV swarm cannot be ignored in communication networks. Therefore, it is necessary to propose a solution to this problem by including new mesh networks and security components.
- Energy shortages in UAV networks with an energy crisis play an important role in limiting the efficiency of mission operations. All concerns about battery savings in UAV swarm mesh networks lie in the distance between them with the radio network and the wireless sensor network. Several energy-saving radio mesh protocols for UAV swarm radio networks have been tried to develop and implement but the applicability of these protocols in various UAV swarm radio network scenarios has not yet been proven as far as it is expected. Energy and radio mesh network protocols need to be tested in different mission scenarios.

References

1. George J, Sujit PB, Sousa JB (2011) Search strategies for multiple UAV search and destroy missions. *J Intell Rob Syst* 61(1):355–367
2. Coulter L, Lippitt C, Stow D, McCreight R (2011) Near real-time change detection for border monitoring. In: Proceedings from the ASPRS annual conference, pp 1–5
3. Eggers JW, Draper MH (2006) Multi-UAV control for tactical reconnaissance and close air support missions: operator perspectives and design challenges. In: Proceedings of NATO RTO human factors and medicine symposium, HFM-135. NATO TRO, Neuilly-sur-Seine, CEDEX, Biarritz, France, p 2011-06
4. Tang C, Zhu C, Wei X, Peng H, Wang Y (2019) Integration of UAV and fog-enabled vehicle: application in post-disaster relief. In: 2019 IEEE 25th international conference on parallel and distributed systems (ICPADS). IEEE, pp 548–555
5. Yuan C, Liu Z, Zhang Y (2017) Fire detection using infrared images for UAV-based forest fire surveillance. In: 2017 international conference on unmanned aircraft systems (ICUAS). IEEE, pp 567–572
6. Jiao Z, Zhang Y, Xin J, Mu L, Yi Y, Liu H, Liu D (2019) A deep learning based forest fire detection approach using UAV and YOLOv3. In: 2019 1st international conference on industrial artificial intelligence (IAI). IEEE, pp 1–5
7. Zhang D, Burnham K, McDonald L, Macleod C, Dobie G, Summan R, Pierce G (2017) Remote inspection of wind turbine blades using UAV with photogrammetry payload. In: 56th annual british conference of non-destructive testing-NDT 2017
8. Alsalam BHY, Morton K, Campbell D, Gonzalez F (2017) Autonomous UAV with vision based onboard decision making for remote sensing and precision agriculture. In: 2017 IEEE aerospace conference. IEEE, pp. 1–12
9. Guerrero JA, Bestaoui Y (2013) UAV path planning for structure inspection in windy environments. *J Intell Rob Syst* 69(1):297–311
10. Banić M, Miltenović A, Pavlović M, Ćirić I (2019) Intelligent machine vision based railway infrastructure inspection and monitoring using UAV. *Facta Univ, Ser: Mech Eng* 17(3):357–364
11. Mohajerin N, Histon J, Dizaji R, Waslander SL (2014) Feature extraction and radar track classification for detecting UAVs in civilian airspace. In: 2014 IEEE radar conference. IEEE, pp 0674–0679
12. Li B, Jiang Y, Sun J, Cai L, Wen CY (2016) Development and testing of a two-UAV communication relay system. *Sensors* 16(10):1696
13. Samad AM, Kamarulzaman N, Hamdani MA, Mastor TA, Hashim KA (2013) The potential of unmanned aerial vehicle (UAV) for civilian and mapping application. In: 2013 IEEE 3rd international conference on system engineering and technology. IEEE, pp 313–318
14. Cummings ML, Bruni S, Mercier S, Mitchell PJ (2007) Automation architecture for single operator, multiple UAV command and control. Massachusetts Inst of Tech Cambridge
15. Wang Q, Gao A, Hu Y (2021) Joint power and QoE optimization scheme for multi-UAV assisted offloading in mobile computing. *IEEE Access* 9:21206–21217
16. Xia Q, Liu S, Guo M, Wang H, Zhou Q, Zhang X (2021) Multi-UAV trajectory planning using gradient-based sequence minimal optimization. *Robot Auton Syst* 137:103728
17. Fabra F, Zamora W, Reyes P, Calafate CT, Cano JC, Manzoni P, Hernandez-Orallo E (2019) An UAV swarm coordination protocol supporting planned missions. In: 2019 28th international conference on computer communication and networks (ICCCN). IEEE, pp 1–9
18. Singh C, Mishra V, Harshit H, Jain K, Mokros M (2022) Application of UAV swarm semi-autonomous system for the linear photogrammetric survey. *Int Arch Photogramm, Remote Sens Spat Inf Sci* 43:407–413
19. Sivakumar A, Tan CKY (2010) UAV swarm coordination using cooperative control for establishing a wireless communications backbone. In: Proceedings of the 9th international conference on autonomous agents and multiagent systems, vol 3, pp 1157–1164
20. Klare J, Biallawons O, Cerutti-Maori D (2017) UAV detection with MIMO radar. In: 2017 18th international radar symposium (IRS). IEEE, pp 1–8

21. Albani D, Manoni T, Arik A, Nardi D, Trianni V (2019) Field coverage for weed mapping: toward experiments with a UAV swarm. In: International conference on bio-inspired information and communication. Springer, Cham, pp 132–146
22. Champion M, Ranganathan P, Faruque S (2018) A review and future directions of UAV swarm communication architectures. In: EIT, pp 903–908
23. Sampedro C, Bavle H, Sanchez-Lopez JL, Fernández RAS, Rodríguez-Ramos A, Molina M, Campoy P (2016) A flexible and dynamic mission planning architecture for uav swarm coordination. In: 2016 international conference on unmanned aircraft systems (ICUAS). IEEE, pp 355–363
24. Cesare K, Skeeel R, Yoo SH, Zhang Y, Hollinger G (2015) Multi-UAV exploration with limited communication and battery. In: 2015 IEEE international conference on robotics and automation (ICRA). IEEE, pp 2230–2235
25. Chen X, Tang J, Lao S (2020) Review of unmanned aerial vehicle swarm communication architectures and routing protocols. *Appl Sci* 10(10):3661
26. Sohail MF, Leow CY, Won S (2019) Energy-efficient non-orthogonal multiple access for UAV communication system. *IEEE Trans Veh Technol* 68(11):10834–10845
27. Yuan Z, Huang X, Sun L, Jin J (2016) Software defined mobile sensor network for micro UAV swarm. In: 2016 IEEE international conference on control and robotics engineering (ICCRE). IEEE, pp 1–4
28. Zhao J, Gao F, Ding G, Zhang T, Jia W, Nallanathan A (2018) Integrating communications and control for UAV systems: opportunities and challenges. *IEEE Access* 6:67519–67527
29. Liu Z, Wang X, Shen L, Zhao S, Cong Y, Li J, Xiang X et al (2020) Mission-oriented miniature fixed-wing UAV swarms: a multilayered and distributed architecture. *IEEE Trans Syst, Man, Cybern: Syst*
30. Shao J, Li M, Yang K (2020) Multilayer modeling for capability generation of UAV swarm system. In: 2020 IEEE 15th international conference of system of systems engineering (SoSE). IEEE, pp 000181–000186
31. Li J, Zhou Y, Lamont L (2013) Communication architectures and protocols for networking unmanned aerial vehicles. In: 2013 IEEE Globecom workshops (GC wkshps). IEEE, pp 1415–1420

Simulation of Clustering Protocol and Mobility Model for UAV Networks



Abhishek Joshi, Sarang Dhongdi, and K. R. Anupama

Abstract The network of autonomous Unmanned Aerial Vehicles (UAVs) is a powerful system that can assess the severity of damages during disaster events and support search and rescue missions. UAVs can carry payloads such as cameras, sensors, and a built-in navigation system and can be readily deployed in the surveillance region with limited or no infrastructure support. This work assumes that UAVs can be randomly deployed in the affected area for surveillance. The network is then arranged in the form of clusters of UAV nodes to create a hierarchy and aid in the collection and routing of sensed data. Metrics of residual energy and connectivity have been used to select a Cluster-Head (CH) node iteratively. This proposed clustering algorithm has been detailed in this paper. For the implementation of this protocol, an integrated platform of ROS and NS3 has been utilized to provide a more realistic deployment scenario. The proposed clustering protocol has been compared with prominent clustering protocols of Wireless Sensor Networks (WSNs) such as Hybrid Energy-Efficient Distributed (HEED) and Low-Energy Adaptive Clustering Hierarchy (LEACH) for analysis of parameters such as the lifetime of the network and clustering overhead. The mobility model achieved from the robot simulator has been compared against probabilistic mobility models available in the network simulator. The proposed deterministic clustering protocol outperforms in terms of network lifetime against prominent clustering protocols. Upon stimulation, it has also been observed that the realistic mobility model obtained from the robot simulator is more suited for real-world applications.

Keywords Clustering · Disaster monitoring · Mobility model · UAV network

A. Joshi (✉) · S. Dhongdi · K. R. Anupama
EEE Department, BITS Pilani—K. K. Birla Goa Campus, Sancoale, Goa, India
e-mail: p20130410@goa.bits-pilani.ac.in

S. Dhongdi
e-mail: sarang@goa.bits-pilani.ac.in

K. R. Anupama
e-mail: anupkr@goa.bits-pilani.ac.in

1 Introduction

Unmanned Aerial Vehicles (UAVs) have been proposed to be used as mobile, adaptive communication backbones for ground-based sensor networks. These UAVs and the sensor nodes collaboratively form a 3D airborne sensor network called Unmanned Aerial Network (UAN) to support civil and military applications. UAN can be unused for applications like surveillance, reconnaissance, remote sensing, search and rescue, aerial photography, crop surveys, on-demand emergency communications, traffic control, monitoring natural resources like oil or gas exploration and so on. The UAVs can also provide communication connectivity to sensors that cannot communicate because of terrain, distance, or other geographical constraints. Moreover, the UAVs themselves can have capabilities in terms of sensing and forming a network that can use existing infrastructure. UAVs can also form an ad-hoc network to forward network sensed data to the Ground Control Center (GCC) or Base Station (BS) in case of unavailability of infrastructure. The ad-hoc network formed by UAVs within the network has been termed as Flying Ad-Hoc Network (FANET). FANETs can be considered to be the subset of Mobile Ad-Hoc Networks (MANETs). In addition to this, FANETs can also be classified as a subset of Vehicular Ad-Hoc Networks (VANETs), which can be considered to be a subgroup of MANETs. As an emerging area of research, FANETs share common characteristics with these networks, and it also has several unique design challenges. Table 1 details FANET design challenges that distinguish them from MANETs and VANETs.

Major application categories of FANETs include search and rescue operations, traffic and urban monitoring, surveillance and patrolling, agricultural management, environmental sensing, event detection and monitoring and so on. In this paper, a FANET has been deployed to monitor a disaster-affected region. FANET deployment has been depicted in Fig. 1, which considers a single disaster event where UAVs have been randomly deployed. The UAVs have been assumed to be equipped

Table 1 FANET design challenges

Parameter	MANET	VANET	FANET
Node mobility	Low	High	Very high
Mobility model	Random	Regular	Regular for pre-defined paths but undefined for autonomous systems
Node density	Low	High	Very low
Radio propagation model	Close to ground	Close to ground	UAV to UAV, UAV to ground
Energy efficiency of protocols	Energy efficient	Not essential requirement	Energy-efficient protocols for the mini-UAVs but not an essential requirement for small-UAVs
Computation power	Limited	High	High

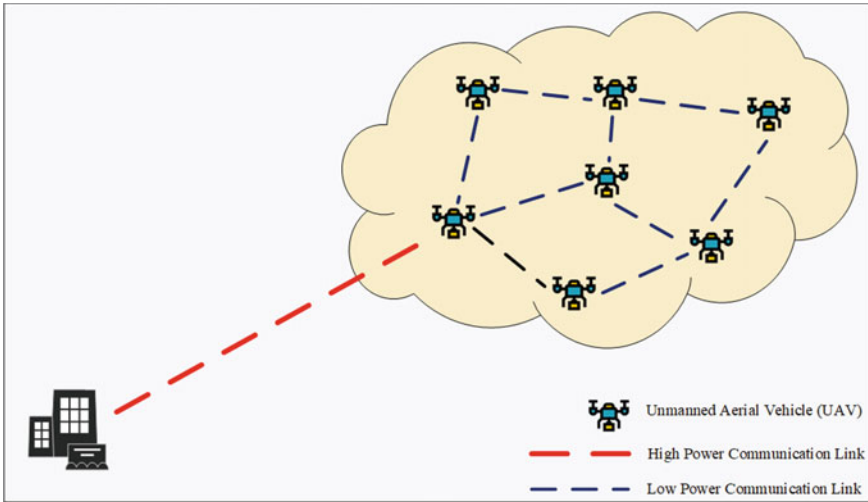


Fig. 1 FANET deployment for disaster monitoring application

with the appropriate set of sensors and camera modules to monitor the disaster event. The UAVs have also been considered to be equipped with Global Positioning System (GPS) and Inertial Measurement Unit (IMU) to fetch absolute geographical coordinates and timing values throughout their flight time. The UAVs within the network execute a deterministic clustering protocol proposed in this paper to elect a Cluster-Head (CH) UAV. The elected CH UAV collects the sensed data from the entire cluster and forwards the network data to the nearest BS.

The proposed clustering protocol has been simulated on a realistic co-simulator platform. The co-simulator platform includes Network Simulator-3 (NS-3) and Gazebo with Robot Operating System (ROS) as middleware. NS-3 has been selected as the preferred network simulator to simulate realistic message exchange within the network. Gazebo has been chosen to be the UAV simulator to simulate the physical parameters of UAV along with mobility in a realistic manner. The proposed clustering protocol has been thoroughly simulated against prominent clustering protocols like LEACH and HEED with varying UAV mobility. The mobility model achieved from the robot simulator has been compared against probabilistic mobility models available in the network simulator.

The organization of this paper is as follows: In Sect. 2, the literature survey of existing clustering protocols along with simulation platforms has been detailed. In Sect. 3, details about the proposed deterministic clustering protocol for FANET have been provided. Section 4, implementation of realistic simulation platform, has been provided. Results obtained for the proposed clustering protocol along with a comparative study of mobility models have been discussed in Sect. 5. Conclusions of this research have been provided in Sect. 6.

2 Literature Survey

Flying Ad-hoc Networks (FANETs) have been considered to be the emerging category of mobile Wireless Sensor Networks (WSNs) [1, 2]. In recent times, FANETs have demonstrated their ability in real-world applications such as search and rescue operations [3], forest fire monitoring [4], air pollution monitoring [5], flood monitoring [6], earthquake monitoring [7], remote sensing [8], precision agriculture [9], pipeline inspection [10] and so on.

Since FANETs are considered to be a subset of WSNs, they inherit identical challenges faced by WSNs. Additional constraints, such as rapid node movement and sparse deployment, need to be considered during the deployment and networking phases of FANETs. Such networking issues for UAVs have been taken into account in [11]. The work in [11] has been considered to be one of the initial works to explore networking problems and communication requirements for FANET applications. Unique challenges of UAV ad-hoc networks to conventional ad-hoc networks, which include rapid mobility of UAV nodes, frequent topology changes and link updates within the network, have been detailed in [12].

The clustering protocol in FANETs is based upon the formation of clusters where a CH node supervises each cluster. It results in the reduction of packets transferred to the BS node while reducing the energy consumption of UAV nodes. As a drawback, clustering protocols suffer from increased complexity in forming clusters. Prominent WSN clustering protocols, including LEACH and HEED, have been adopted for FANETs [13]. CA (Clustering Algorithm) [14] is a clustering-based routing protocol which supports real-time missions in FANET. MPCA (Mobility Prediction Clustering Algorithm for UAV Networking) [15] is a hierarchical routing protocol which predicts UAV movements while electing CH node within a cluster. DTM (Disruption Tolerant Mechanism) [16] is a clustering protocol adopted for FANETs which makes use of reactive routing protocol [17] to forward cluster data.

To develop reliable UAV-based networks, it is crucial to simulate UAV operations realistically. For FANETs, network simulators have been developed, such as NS-2 [18], NS-3 [19], QualNet [20] and OMNet [21]. These simulators make use of probabilistic mobility models such as Gauss Markov [22] or they can be specified in trace files created by other software tools like SUMO [23]. Although this software can produce realistic motion patterns of nodes, a few limitations can only make these patterns a priori, not on the fly. Also, the mobility model of network simulators is based on statistical probability, which implies that previous movements of nodes influence the next movement decision in the model; therefore, it has fundamental limitations to simulate realistic UAV motions for disaster operations.

On the other hand, robot simulators like Gazebo [24] can control the physical movement of UAVs. Gazebo is a tool widely used for the development of UAVs with various physical characteristics. It can incorporate multiple sensor modules for these UAVs. These sensor modules can provide realistic data which can be used for applications like UAV navigation. But robot simulators lack networking capabilities which prevent them from message exchanges within the network. Overall, solely

using the existing network simulators or robot simulators, we can only test either network performance or robot motion operations, not both of them together. To handle this issue, a co-simulator platform has been utilized, which combines the network simulator (NS-3) and the robot simulator (Gazebo) with the help of the Robot Operating System (ROS).

3 Clustering Protocol for UAV Networks

During the initial phase of the proposed clustering protocol, an individual UAV retrieves its respective ID, residual energy and position. From retrieved parameters, the UAV generates *Neighbour_Discovery_Message*. The *Neighbour_Discovery_Message* has been broadcast thrice at different random intervals, which has been the primary function of UAV ID (ID_i). Concurrently, the UAV also keeps listening for received broadcast messages from other UAVs. After receiving the broadcast, the UAV extracts the ID, residual energy and position and stores those received parameters into the neighbour table entry for a particular received UAV ID.

After completing a pre-defined time interval, an individual UAV within the cluster generates its respective neighbour table. The neighbour table consists of IDs of neighbouring UAVs along with their respective coordinates and residual energy values. Analyzing the neighbour table, individual UAV can calculate Connectivity Value (C_i). The connectivity Value (C_i) of the UAV represents the number of UAVs from which the particular UAV received the broadcast message. Based upon Connectivity Value (C_i) and Residual Energy (R_i) of the UAV, the UAV categorizes itself into one out of the nine sub-phases described in Table 2.

As represented in Table 2, essential criteria for sub-phase selection have been Residual Energy (R_i) and Connectivity Value (C_i) of the UAV. These parameters have been considered to be non-probabilistic parameters that have been an integral part of the Cluster-Head (CH) election process. Also, as interpreted from Table 2, the

Table 2 Sub-phase categorization

Sub-phase	Residual energy (R _i) (%)	Connectivity value (C _i) (%)
Sub-phase 1	>90	>90
Sub-phase 2		90–80
Sub-phase 3		80–70
Sub-phase 4	90–80	>90
Sub-phase 5		90–80
Sub-phase 6		80–70
Sub-phase 7	80–70	>90
Sub-phase 8		90–80
Sub-phase 9		80–70

Residual Energy (R_i) of the UAV has been given higher priority over the Connectivity Value (C_i) of the UAV to improve the energy efficiency of the network.

The flowchart of the sub-phase selection process of the UAV has been represented in Fig. 2. Initially, the UAV retrieves its current Residual Energy (R_i) and Connectivity Value (C_i). Then, it compares the present Residual Energy (R_i) against the maximum value of Residual Energy ($R_{\max(i)}$), which has been assigned to the UAV at the beginning of network operation. If the Residual Energy (R_i) is greater than 90% of the maximum value of Residual Energy ($R_{\max(i)}$) of the UAV, the UAV broadly categorizes itself within Sub-Phase-1 to Sub-Phase-3. If the Residual Energy (R_i) lies between 90 and 80% of the maximum value of Residual Energy ($R_{\max(i)}$) of the UAV, then the UAV broadly categorizes itself within Sub-Phase-4 to Sub-Phase-6. Suppose the Residual Energy (R_i) of the UAV lies between 80 and 70% of the maximum value of Residual Energy ($R_{\max(i)}$) of the UAV. In that case, the UAV broadly categorizes itself from Sub-Phase-7 to Sub-Phase-9.

After broadly categorizing the UAV based upon Residual Energy ($R_{\max(i)}$), the table takes into account the Connectivity Value (C_i) of the UAV. If Residual Energy (R_i) is greater than 90% of the maximum value of Residual Energy ($R_{\max(i)}$) and if the Connectivity Value (C_i) of the UAV is greater than 90% of the maximum value of Connectivity Value ($C_{\max(i)}$), the UAV categorizes itself into Sub-Phase-1. Suppose the Residual Energy (R_i) is greater than 90% of the maximum value of the Residual Energy ($R_{\max(i)}$) and the Connectivity Value (C_i) of the UAV lies between 90 and 80% of the Connectivity Value ($C_{\max(i)}$). In that case, the UAV categorizes itself into Sub-Phase-2. If the Residual Energy (R_i) is greater than 90% of the maximum value of Residual Energy ($R_{\max(i)}$) and Connectivity Value (C_i) of the UAV lies between 80 and 70% of the Connectivity Value ($C_{\max(i)}$), the UAV categorizes itself into Sub-Phase-3.

Suppose the Residual Energy (R_i) lies between 90 and 80% of the maximum value of Residual Energy ($R_{\max(i)}$), and the Connectivity Value (C_i) of the UAV is greater than 90% of the Connectivity Value ($C_{\max(i)}$). In that case, the UAV categorizes itself into Sub-Phase-4. Suppose the Residual Energy (R_i) lies between 90 and 80% of the maximum value of Residual Energy ($R_{\max(i)}$) and the Connectivity Value (C_i) lies between 90 and 80% of the maximum value of the Connectivity Value ($C_{\max(i)}$). In that case, the UAV categorizes itself into Sub-Phase-5.

Suppose the Residual Energy (R_i) lies between 90 and 80% of the maximum value of Residual Energy ($R_{\max(i)}$) and the Connectivity Value (C_i) of the UAV lies between 80 and 70% of maximum value of the Connectivity Value ($C_{\max(i)}$). In that case, the UAV categorizes itself into Sub-Phase-6.

If the Residual Energy (R_i) lies between 80 and 70% of the maximum value of Residual Energy ($R_{\max(i)}$) and Connectivity Value (C_i) of the UAV is greater than 90% of the maximum value of the Connectivity Value ($C_{\max(i)}$), the UAV categorizes itself into Sub-Phase-7. Suppose the Residual Energy (R_i) lies between 80 and 70% of the maximum value of the Residual Energy ($R_{\max(i)}$), and the Connectivity Value (C_i) lies between 90 and 80% of the maximum value of Connectivity Value ($C_{\max(i)}$). In that case, the UAV categorizes itself into Sub-Phase-8. Suppose the Residual Energy (R_i) lies between 80 and 70% of the maximum value of the Residual Energy

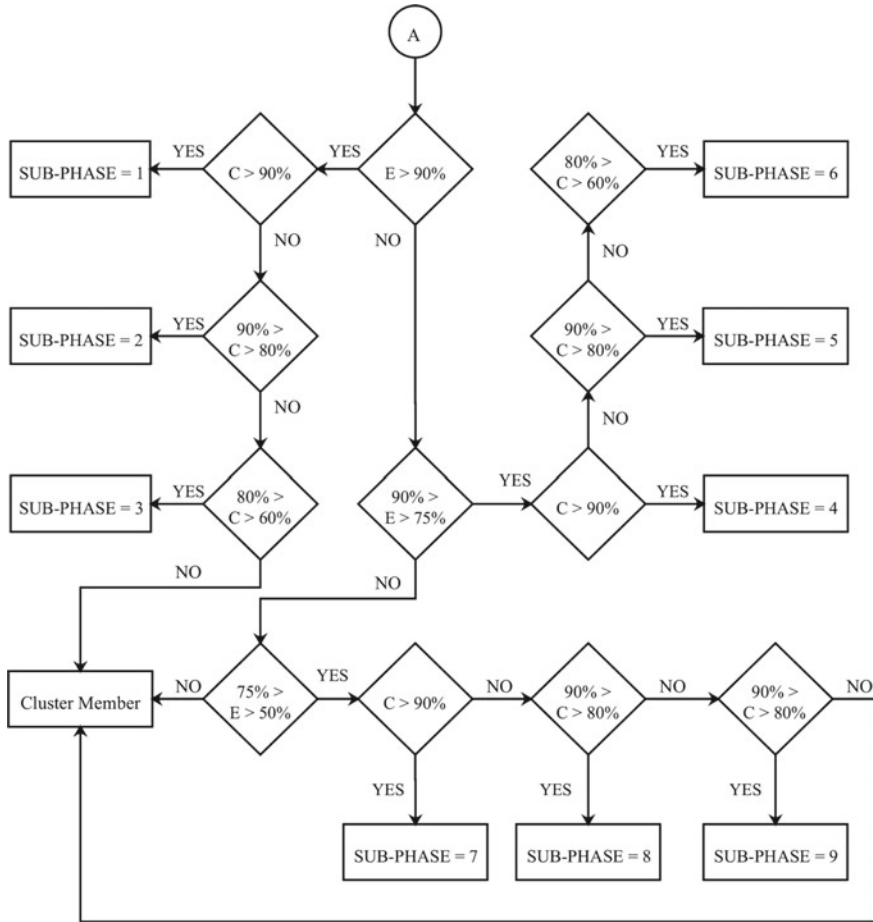


Fig. 2 Flowchart for sub-phase categorization

($R_{max}(i)$) and the Connectivity Value (C_i) lies between 80 and 70% of maximum value of Connectivity Value ($C_{max}(i)$). In that case, the UAV categorizes itself into Sub-Phase-9. Suppose the Residual Energy (R_i) of the UAV is less than 70% of maximum value of the Residual Energy ($R_{max}(i)$). In that case, the UAV cannot be chosen for Cluster-Head (CH) election policy, and it acts as Cluster-Member (CM) UAV.

After an individual UAV in the cluster identifies its sub-phase, the next phase of the clustering protocol begins. In this phase, an individual sub-phase has been allotted a specific time slot. During this time slot, the UAVs which are eligible from that particular sub-phase contend to become Cluster-Head (CH) UAVs. UAVs which result in the sub-phase with the lowest phase ID (i.e., P1) have been considered to be the most eligible candidates for Cluster-Head (CH) UAV because of the highest value

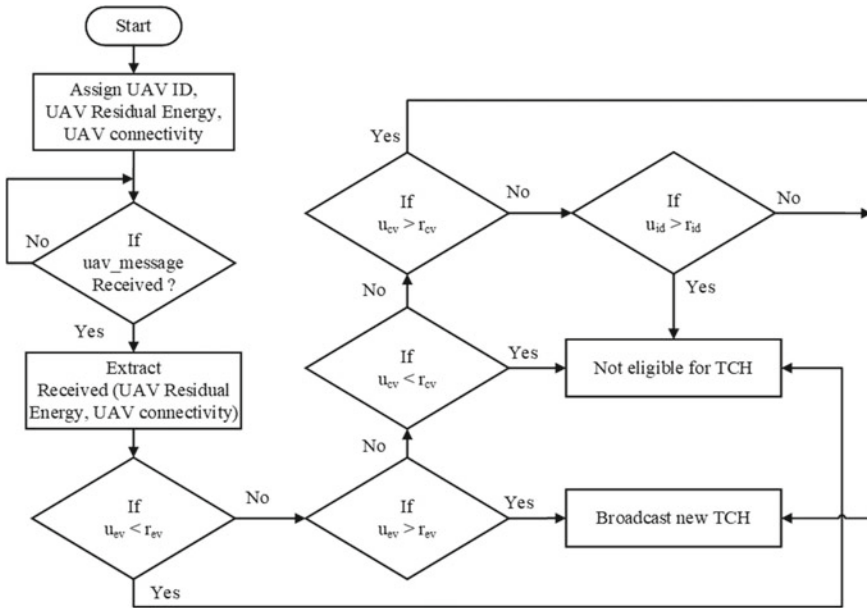


Fig. 3 Flowchart for Cluster-Head (CH) election

of the Residual Energy (R_i) along with the highest Connectivity Value (C_i). Thus, P1 sub-phase has been given the initial time slot to elect Cluster-Head UAV. UAVs that fall under P1 sub-phase broadcast Temporary Cluster-Head (TCH) message. In TCH message, the UAV mentions its ID, (ID_i) along with the sub-phase ID. The UAV broadcasts TCH messages within the defined phase at a random time interval.

Upon receiving the broadcast of TCH message, UAVs within individual isolated clusters execute the algorithm visualized in Fig. 3 to select the most eligible Cluster-Head (CH), which results in Final Cluster-Head (FCH). Terminologies used in the algorithm have been elaborated below:

- $u(cv)$ —UAV’s own connectivity value
- $r(cv)$ —UAV’s received connectivity value
- $u(ev)$ —UAV’s remaining energy value
- $r(ev)$ —UAV’s received remaining energy value
- $u(id)$ —UAV’s ID
- $r(id)$ —UAV’s received ID

During the preliminary stage of algorithm execution, the connectivity value of the UAV is used as the primary metric for Cluster-Head (CH) election. Upon receiving the TCH message, recipient UAV compares its own connectivity value ($u(cv)$) with received connectivity value ($r(cv)$). If received connectivity value ($r(cv)$) is lower than its own connectivity value ($u(cv)$), the UAV further compares residual energy values. Suppose the residual value of the UAV ($u(ev)$) is higher than the received

residual value of energy ($r(ev)$). In that case, the UAV concludes itself as the possible contender for the Cluster-Head election process and broadcasts the TCH message. If residual energy values of both UAVs result same, then UAV with higher ID has been given precedence. After executing the algorithm, the UAV concludes whether it is eligible to contend for Cluster-Head (CH) election process.

At the end of the individual phase, the UAV which makes the final broadcast of the TCH message broadcasts another message termed as Final Cluster-Head (FCH) message. The rest of the UAVs within that cluster receive this message. Upon receiving the FCH message, the rest of the UAVs which have been contending to get elected as Cluster-Head (CH) UAV consider themselves as Cluster-Member (CM) UAVs.

4 Implementation

Simulation of FANETs should imitate real-world scenarios along with their constraints as closely as possible. It helps in understanding network performance and the limitations in a real-world situation and helps in accelerating hardware deployment. FANET simulators have been broadly categorized into UAV simulators and network simulators. UAV simulators are essential in simulating realistic UAV mobility and pattern. One of the significant drawbacks of UAV simulators is the lack of message exchange capability. The lack of message exchange prevents networking protocols from being simulated using UAV simulators. Network simulators support message exchange among multiple nodes in the network. They also support physical communication and channel interfaces to simulate FANET operation realistically. One of the significant drawbacks of network simulators is the mobility models used in those simulators. Conventionally, network simulators use probabilistic mobility models of Gauss-Markov mobility models. These mobility models do not represent real-world UAV mobility in the realistic model.

A realistic simulation platform has been utilized in this research to overcome issues imposed by UAV simulators and network simulators. The preferred UAV simulator has been selected as Gazebo, and the preferred network simulator platform has been chosen as Network Simulator-3 (NS-3). Robot Operating System (ROS) acts as the middleware to integrate Gazebo and ROS. Details about the simulation platform have been provided in Fig. 4. The major building blocks of Fig. 4 include NS-3, Gazebo and ROS. The simulation platform uses the publisher-subscriber model to exchange data between these simulators. Gazebo fetches real UAV positions and velocity parameters and publishes them to the ROS node. ROS node subscribes to the UAV data and further publishes them to the corresponding UAV node in NS-3. UAV node in NS-3 executes network protocols and communicates with neighbouring UAV nodes while simulating realistic channel conditions. The neighbouring UAV node receives the updated position and velocity parameters and publishes them to the ROS node. The ROS node subscribes to the updated UAV parameters and further publishes them to the corresponding UAV node in the UAV simulator. The UAV

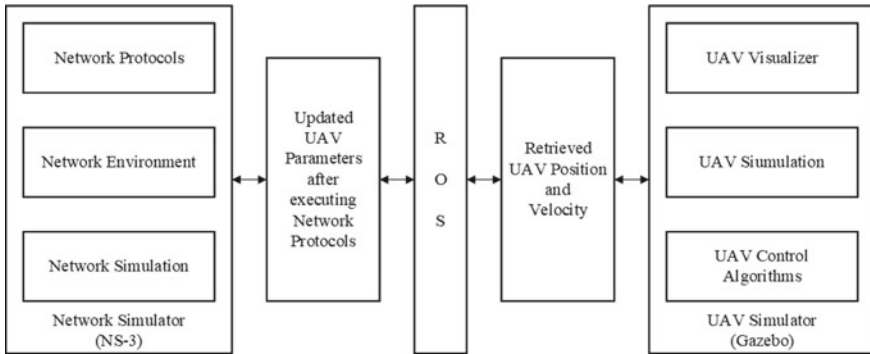


Fig. 4 Realistic FANET simulator connecting NS-3 and Gazebo using ROS

node in the UAV simulator subscribes to the updated UAV parameters and takes the UAV to the received position with received velocity while executing topology control algorithms and collision avoidance algorithms.

The proposed clustering protocol has been thoroughly simulated with varying UAV velocity. Also, the FANET has been simulated against standalone probabilistic models available in the network simulator. Details about the simulation and the discussion have been provided in the following section.

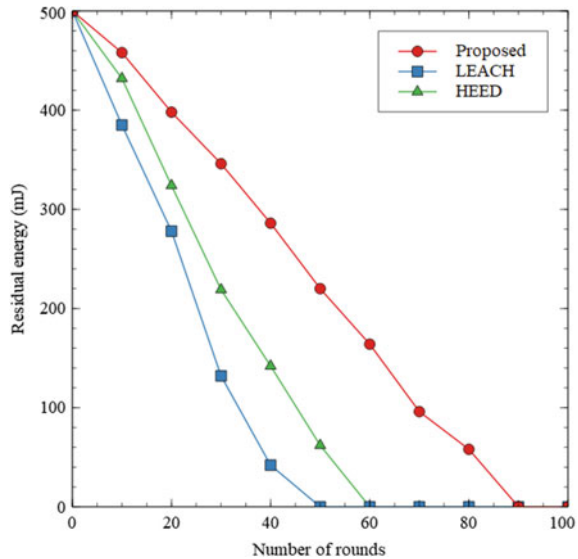
5 Results and Discussions

The proposed deterministic clustering protocol has been simulated on the network simulator against network lifetime parameters with varying UAV mobility. Network parameters considered for simulation have been tabulated in Table 3.

Table 3 Network simulation parameters

Network parameter	Value
Number of UAVs	5–30
Speed	0–30 m/s
Mobility model	Realistic Gazebo mobility model
Communication channel	802.11 ad-hoc mode
Bandwidth	11 Mbps
Simulation area	2 km × 2 km × 100 m
Low power range for UAV	150 m
High power range for UAV	1850 m
Initial energy of UAV	500 mJ

Fig. 5 Comparison of network lifetime between clustering protocols



The FANET has been thoroughly simulated for 100 runs to compare the proposed deterministic clustering protocol's performance against prominent clustering protocols available in the literature. Initially, UAV nodes within the clusters have been assumed to be hovering within the cluster, which implies no mobility parameter involved while simulating the network. Results obtained for stationary FANET have been visualized in Fig. 5.

Low-Energy Adaptive Clustering Hierarchy (LEACH) is considered to be a probabilistic clustering protocol in which the CH election policy for UAVs within the cluster is defined by random probabilities. LEACH does not regard UAV's remaining energy when electing CH, resulting in the network's remaining energy being exhausted in the fewest number of rounds possible. Hybrid Energy-Efficient Distributed (HEED) is a hybrid protocol that selects CH based on probabilistic and remaining energy parameters. In terms of the number of rounds needed to deplete the network's capacity, it outperforms LEACH. The clustering protocol proposed is fully deterministic. In the proposed clustering protocol, the CH election scheme is not dependent on probability. The remaining energy of the UAV is given primary selection criteria to elect CH UAV which results in optimum network lifetime in terms of the number of rounds for the network to exhaust the remaining energy.

The proposed deterministic clustering protocol has been compared against prominent clustering protocols like Low-Energy Adaptive Clustering Hierarchy (LEACH) and Hybrid Energy-Efficient Distributed (HEED). Due to the deterministic nature of its implementation, the proposed clustering protocol outperforms the in terms of network lifetime. Further, the FANET has also been simulated with varying UAV mobility. Initially, the FANET has been simulated with realistic mobility obtained from Gazebo. Later the FANET has been simulated with mobility models available

in NS-3. Results obtained from different mobility models have been visualized in Figs. 6, 7, 8, and 9. The proposed realistic mobility model outperforms the rest of the mobility models in terms of network lifetime.

The realistic mobility model's performance is better than other group mobility models like Reference Point Group Mobility (RPGM) because of the actual exchange of position and velocity parameters between network simulator and UAV simulator

Fig. 6 Residual energy of network with proposed mobility

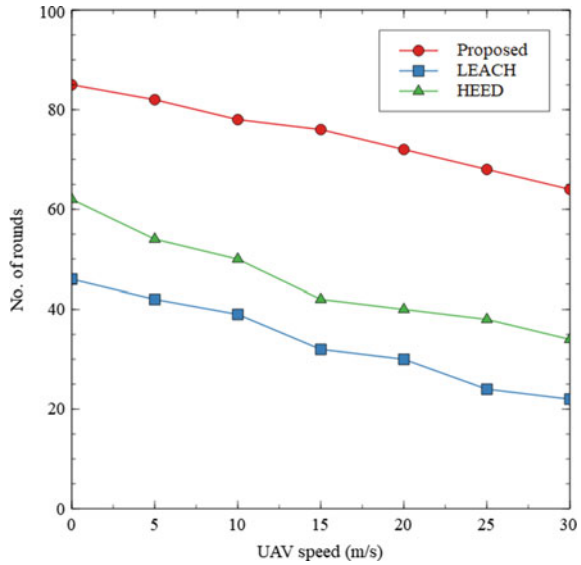


Fig. 7 Residual energy of network with Random Point Group Mobility (RPGM)

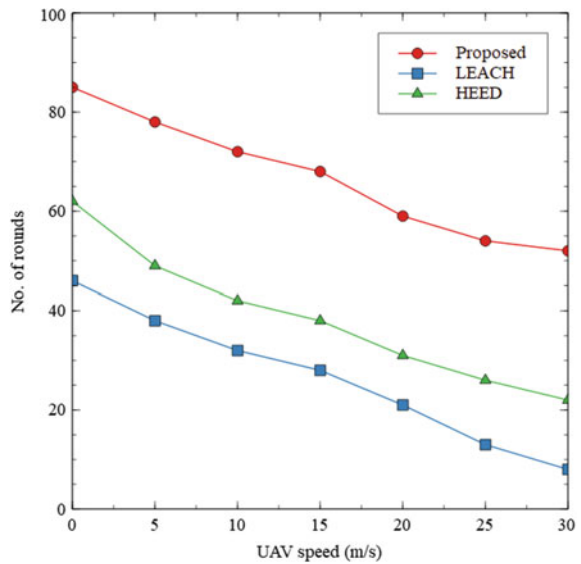


Fig. 8 Residual energy of network with Gauss Markov (GM) mobility

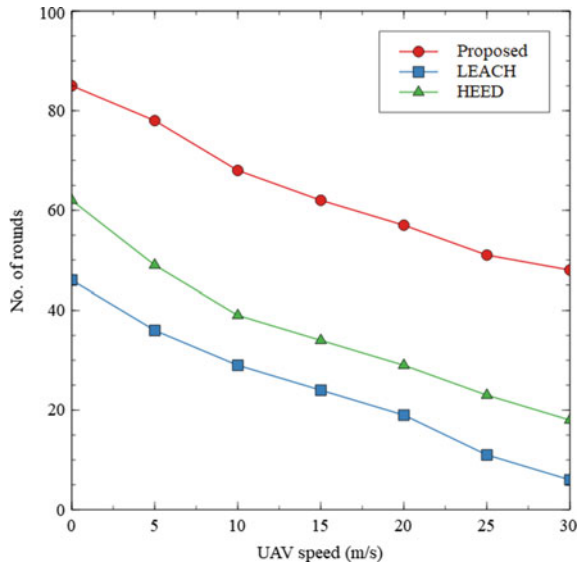
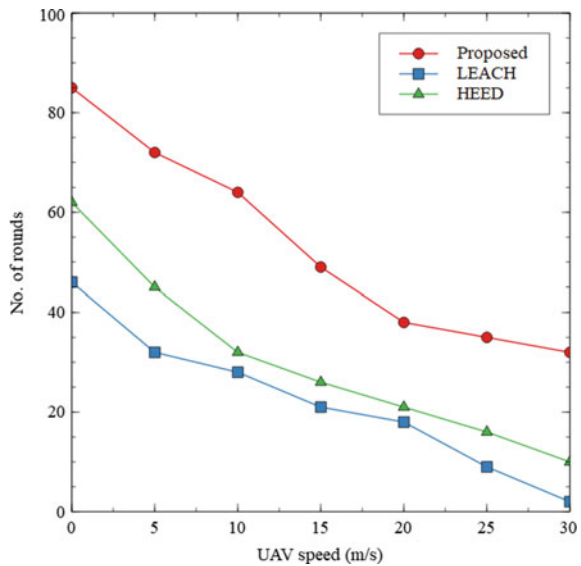


Fig. 9 Residual energy of network with Random Waypoint (RWP) mobility



rather than conventional mobility models probabilistic approach is taken into account while calculating mobility of group. At a higher speed, the performance of individual mobility models like Random Way-point Mobility (RWP) and Gauss-Markov Mobility Model (GM) deteriorates to group mobility models. Group mobility models are designed to consider changes in direction and speed; hence, they perform better than individual node mobility models. Thus, GM’s performance deteriorates at higher

speeds due to frequent link breaks, which translates into a reduction in terms of network lifetime.

6 Conclusion

In this paper, a FANET has been deployed in the disaster-affected area for surveillance. The deployment of UAVs within the network has been considered to be random. A deterministic clustering protocol has been proposed in this paper. The proposed protocol takes the residual energy of the UAV node and its connectivity value to elect CH within the network. The proposed deterministic protocol has been compared against prominent clustering protocols in the literature like LEACH and HEED. The clustering protocols have been thoroughly simulated against network lifetime parameters. The proposed deterministic clustering protocol outperforms LEACH and HEED in terms of the lifetime of the network.

The proposed deterministic clustering protocol has also been tested with varying UAV mobility within the network. A realistic simulation platform has been utilized to simulate UAV mobility. The realistic simulation platform includes a network simulator (NS-3), a UAV simulator (Gazebo) and ROS. The realistic mobility obtained from the UAV simulator has been compared against probabilistic mobility models available in the network simulator like RPGM, GM and RWP. The realistic mobility model available from the UAV simulator outperforms the network simulator's probabilistic models in terms of network lifetime when incorporated with the proposed deterministic clustering protocol.

References

1. Mukherjee A, Keshary V, Pandya K, Dey N, Satapathy SC (2018) Flying ad hoc networks: a comprehensive survey. In: Information and decision sciences, pp 569–580
2. Chriki A, Touati H, Snoussi H, Kamoun F (2019) FANET: communication, mobility models and security issues. *Comput Netw* 163–176
3. Korneev DA, Leonov AV, Litvinov GA (2018) Estimation of mini-UAVs network parameters for search and rescue operation scenario with Gauss-Markov mobility model. In: Systems of signal synchronization, generating and processing in telecommunications, pp 1–7
4. Sherstjuk V, Zharikova M, Sokol I (2018) Forest fire-fighting monitoring system based on UAV team and remote sensing. In: 38th international conference on electronics and nanotechnology (ELNANO)
5. Villa TF, Salimi F, Morton K, Morawska L, Gonzalez F (2016) Development and validation of a UAV based system for air pollution measurements. *Sensors* 2202
6. Perks MT, Russell AJ, Large AR (2016) Advances in flash flood monitoring using unmanned aerial vehicles (UAVs). *Hydrol Earth Syst Sci* 4005–4015
7. Zhu M, Du X, Zhang X, Luo H, Wang G (2019) Multi-UAV rapid-assessment task-assignment problem in a post-earthquake scenario. *IEEE Access* 74542–74557
8. Cho DH, Jang DS, Choi HL (2018) Heterogeneous, multiple depot multi-UAV path planning for remote sensing tasks. In: AIAA information systems

9. Vu Q, Raković M, Delic V, Ronzhin A (2018) Trends in development of UAV-UGV cooperation approaches in precision agriculture. In: International conference on interactive collaborative robotics
10. Kochetkova LI (2018) Pipeline monitoring with unmanned aerial vehicles. *J Phys* 042021
11. Frew EW, Brown TX (2009) Networking issues for small unmanned aircraft systems. *J Intell Robot Syst* 21–37
12. Song L, Huang TL (2010) A summary of key technologies of ad hoc networks with UAV node. In: International conference on intelligent computing and integrated systems. IEEE
13. Arafat MY, Moh S (2018) A survey on cluster-based routing protocols for unmanned aerial vehicle networks. *IEEE Access* 498–516
14. Liu K, Zhang J, Zhang T (2008) The clustering algorithm of UAV networking in near-space. In: 8th international symposium on antennas. IEEE
15. Zang C, Zang S (2011) Mobility prediction clustering algorithm for UAV networking. In: IEEE GLOBECOM workshops (GC wkshps)
16. Fu B, DaSilva LA (2007) A mesh in the sky: a routing protocol for airborne networks. In: IEEE military communications conference
17. Perkins C, Belding-Royer E, Das S (1999) Ad hoc on-demand distance vector (AODV) routing. In: Second IEEE workshop on mobile computing systems and applications
18. Issariyakul T, Hossain E (2009) Introduction to network simulator 2 (NS2). Springer, Boston
19. Carneiro G (2010) NS-3: network simulator 3. In: UTM Lab meeting
20. Devaraju JT (2011) A performance study of proactive, reactive and hybrid routing protocols using Qualnet simulator. *Int J Comput Appl* 8887
21. Varga A, Hornig R (2008) An overview of the OMNeT++ simulation environment. In: Proceedings of the 1st international conference on simulation tools and techniques for communications, networks and systems & workshops, pp 1–10
22. Broyles D, Jabbar A, Sterbenz JP (2010) Design and analysis of a 3-D Gauss-Markov mobility model for highly-dynamic airborne networks. In: Proceedings of the international telemetering conference
23. Krajzewicz D, Erdmann J, Behrisch M, Bieker L (2012) Recent development and applications of SUMO-simulation of urban mobility. *Int J Adv Syst Meas*
24. Koenig N, Howard A (2004) Design and use paradigms for Gazebo, an open-source multi-robot simulator. In: International conference on intelligent robots and systems

Obstacle Avoidance for Quadcopters in Formation Flying Based on A* Algorithm



Kumud Ranjan Roy 

Abstract Quadcopters take precedence over fixed-wing aircraft within the UAV family, owing to their distinctive characteristics such as vertical take-off and landing, reduced size and weight, high maneuverability, and more. With recent technological advancements, UAVs have become viable for a wide range of applications ranging from military to civilian, including traffic monitoring, aerial photography, surveillance, payload carrying search and rescue, and much more, especially for tedious, filthy, and dangerous jobs that endanger people, such as building fires and observatories in the woods, military purposes. To complete some of these missions, a swarm of Quadcopters must work together. Determining how a Quadcopter can autonomously achieve its goal position despite obstacles in its path is a complex issue. This paper uses the A* (A-star) algorithm to model path planning, trajectory generation, and autonomous control of a quadcopter. Path planning was thoroughly examined using various scenarios with various obstacle positions, and the dimensions of obstacles are much greater than the dimensions of the Quadcopter over the map. It was also observed whether the swarm (3 Quadcopters in “vee” formation) maintains the necessary formation throughout the created path.

Keywords A* (A-star) algorithm · Path planning · Trajectory generation · Autonomous control · Artificial intelligence

1 Introduction

An unmanned aerial vehicle is known as a quadcopter. UAVs are helpful in areas where humans cannot reach or perform in a timely and effective manner. Increasing work efficiency and productivity, reducing workload and production costs, fine-tuning services and domain expertise, and addressing security issues on a large scale are just a few of the many benefits that UAVs provide to industries worldwide.

K. R. Roy (✉)

Department of Instrumentation Engineering, SGGS Institute of Engineering and Technology, Nanded, Maharashtra, India

e-mail: kumudr91@gmail.com

© The Author(s), under exclusive license to Springer Nature Switzerland AG 2023

517

K. Jain et al. (eds.), *Proceedings of UASG 2021: Wings 4 Sustainability*,

Lecture Notes in Civil Engineering 304,

https://doi.org/10.1007/978-3-031-19309-5_34

The Newton–Euler technique helps to formulate a detailed mathematical nonlinear dynamic model of the Quadcopter derived [1]. A traditional Proportional Integral Derivative (PID) and Fuzzy-PID controllers on a circular trajectory to present data analysis of Quadcopter dynamic attitude on a circular trajectory. The Simulink toolbox from Matlab was used to simulate attitude stability with both control systems. As a result, each control system's identification is easily visible. Each control system algorithm that affects the horizontal movement on a circular trajectory, such as roll and pitch angles, is thoroughly explained [1, 2]. Sliding mode control (SMC) for trajectory tracking and control formation of various unmanned aerial vehicles, based on the leader–follower concept (UAV). Sliding mode control is a reliable method for controlling nonlinear systems while keeping them impervious to external perturbations. Essentially, it uses the sliding mode control method to track the quad rotor-leader trajectory. A Sliding mode control algorithm is then used to control the formation during flight. All of the methodology in this paper is implemented with the Robot Operating System, and the findings show that the proposed control strategy is effective in [3–6]. An environment modeling technique for unmanned aerial vehicle (UAV) route planning is presented in this paper, along with height dimension reduction. According to the classical grid method, this method considers a vertical plane to the yz-plane and includes the start and endpoints. The environment model could be created by re-dividing the plane by the grid method and comparing its height and obstacles. The above concept condenses the three-dimensional environment model's dimensions and ignores obstacles that are lower than the UAV's flying height. As a result, the proposed environment model method's accuracy could be improved, and the path planning algorithm's efficiency could be improved even more [7, 8]. Using the A-star algorithm for route planning, a simulation experiment demonstrates this environment modeling method's efficacy [8, 9]. For both methods, this study conducts a comprehensive and comparative study of existing UAV path planning algorithms (Heuristic and non-heuristic or exact techniques are the two solution methodologies that categorize path-planning algorithms). Each algorithm is put to the test in three different obstacle scenarios. Each algorithm was tested with variations in global and local obstacle information availability, and the results were compared for computational time and solution optimality [7, 8, 10–12]. In a leader–follower configuration [13, 14], this paper presents a control algorithm for solving multiple quadrotor formation problems. For trajectory tracking control of a single robot, a combination of Sliding Mode Control (SMC) and linear quadratic regulator (LQR) is used. Position control, which serves as the outer loop, is governed by a linear quadratic regulator, which provides the inner loop with reference attitude angles. The inner loop, responsible for attitude angles, is stabilized and converged using Sliding Mode Control [13]. The controllers for a multi-quad system that flies in a tight, rigid formation are proposed in this paper. The model of the aerial truck under consideration is highly nonlinear. As a result, a control strategy for avoiding collisions between adjacent vehicles is proposed. The collision avoidance strategy is used in particular for the considered system's flatness property. The simulation results show how effective the controller is being submitted [10, 15]. A group of quadcopters wanted to run in a formation [3, 11, 13–16]. A PID controller is used to

control each Quadcopter, and a sliding mode controller is used to solve the formation flying problem, which uses a leader–follower structure. Running the Matlab/Simulink environments can be used to assess the performance of the control laws [13, 14]. It proposes model predictive control (MPC) based formation strategies for quadrotors and explains distributed consensus control. First, the problem of formation control is split into horizontal and vertical motions. The follower’s horizontal formation control uses distributed consensus control and an MPC-based formation approach. In horizontal motion, the leader uses the MPC to track the given waypoints and produces the desired formation trajectory for each follower based on the follower’s flight information, expected trajectory, and given formation pattern [16].

This paper proposed a method centered on the discussion mentioned above, the use of Quadcopters for applications such as network establishment and airborne mapping has increased dramatically. Hence the need to provide the collective efforts of a swarm of Quadcopters flying close nearby and these applications will bring challenges to automatic flight control systems (FCS) (which produce the necessary maneuvering commands to keep the path and formation in place), trajectory planning (which defines the path between the given initial and target positions that is optimized and free of obstacles) and obstacle avoidance. This paper aims to guide a swarm of Quadcopters from point A to point B while avoiding obstacles and finding an optimized path that is both efficient and effective.

The following is the layout of this paper: Sect. 2 provides a short overview of the quadrotor system’s nonlinear mathematical model and flight control systems, as well as problem statements. Section 3 describes the path planning and formation flying of a swarm of Quadcopters. Section 4 presents the numerical simulation results and discussions. Finally, in Sect. 5, the conclusion is reached.

2 Mathematical Modeling

Four identical, evenly spaced rotors make up a quadrotor UAV. Changes in rotor speed produce the quadrotor’s aerodynamic moments. Each rotor generates F_1 , F_2 , F_3 , and F_4 thrusts, while ϕ , θ , and ψ reflect roll, pitch, and yaw angles, respectively. The dynamics of quadrotors are modeled in both a body frame and an inertial frame [17–20]. The quadrotor model’s linear and angular positions can be characterized using translational and rotational coordinates, respectively as shown in Fig. 1. Before the Quadcopters dynamic model is derived, the following assumptions are made.

Assumptions

- (a) The Quadcopter is a rigid body with symmetrical mass distribution.
- (b) Propellers have a rigid design.
- (c) The origin of the body’s fixed frame and the center of gravity are the same.
- (d) The Earth’s gravitational field (g), the Quadcopter’s mass (m), and the Quadcopter’s body inertia matrix (j) are all constants.

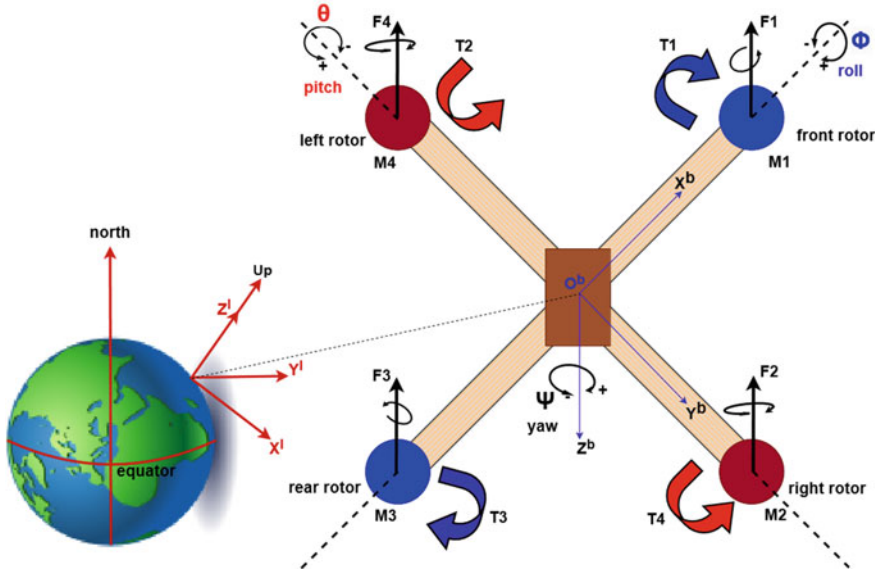


Fig. 1 Schematic of a quadcopter having body-fixed and inertial frame of reference

- (e) The thrust factor (kn) and torque factor (km) are constants.
- (f) The inertia of motors and rotors is not taken into account.

There are six degrees of freedom in a quadcopter: three for position and three for orientation. The kinematics of a quadcopter is determined using Newton–Euler angles rotation matrix R_i^b , where X^I, Y^I, Z^I represent the inertial frame and $X^b, Y^b,$ and Z^b represent the body-fixed reference frame as in the Fig. 1.

The quadrotor model can be described in translational and rotational coordinates that denote its linear and angular positions respectively

$$P_{NED} = (x, y, z) \in \mathbb{R}^3, O_B = (\phi, \theta, \psi) \in \mathbb{R}^3 \tag{1}$$

where $P_{NED}=(x, y, z)$, and $O_B = (\phi, \theta, \psi)$ gives the linear and angular orientation of the quadcopter in the inertial frame respectively.

The rotation matrix transforms the coordinates from the body frame to the inertial frame is R_i^b and it is known as a Direction Cosine Matrix (DCM) or Rotation Matrix (R_i^b) [21]:

$$\begin{bmatrix} X^b \\ Y^b \\ Z^b \end{bmatrix} = \begin{bmatrix} 1 & 0 & 0 \\ 0 & c_\phi & s_\phi \\ 0 & -s_\phi & c_\phi \end{bmatrix} \begin{bmatrix} c_\theta & 0 & -s_\theta \\ 0 & 1 & 0 \\ s_\theta & 0 & c_\theta \end{bmatrix} \begin{bmatrix} c_\psi & s_\psi & 0 \\ -s_\psi & c_\psi & 0 \\ 0 & 0 & 1 \end{bmatrix} \begin{bmatrix} X^I \\ Y^I \\ Z^I \end{bmatrix} \tag{2}$$

$$\begin{bmatrix} X^b \\ Y^b \\ Z^b \end{bmatrix} = \begin{bmatrix} c_\theta c_\psi & c_\theta s_\psi & -s_\theta \\ -c_\phi s_\psi + s_\phi s_\theta c_\psi & c_\phi c_\psi + s_\phi s_\theta s_\psi & s_\phi s_\theta \\ s_\phi s_\psi + c_\phi s_\theta c_\psi & -s_\phi c_\psi + c_\phi s_\theta s_\psi & c_\phi c_\theta \end{bmatrix} \begin{bmatrix} X^I \\ Y^I \\ Z^I \end{bmatrix} \quad (3)$$

$$\begin{bmatrix} X^b \\ Y^b \\ Z^b \end{bmatrix} = R_I^b \begin{bmatrix} X^I \\ Y^I \\ Z^I \end{bmatrix} \text{ and } \begin{bmatrix} X^I \\ Y^I \\ Z^I \end{bmatrix} = R_b^I \begin{bmatrix} X^b \\ Y^b \\ Z^b \end{bmatrix} \quad (4)$$

where $c(\cdot)$ and $s(\cdot)$ denote $\cos(\cdot)$ and $\sin(\cdot)$ respectively. When performing a rotation in the opposite direction, we must use the orthogonal property to compute the inverse of the matrix, i.e., the transpose of a rotation matrix equals the inverse.

The equation below shows the relationship between propeller thrust and angular velocity:

$$f_i = k_n \omega_i^2 [\text{N}] \quad (5)$$

The thrust and torque produced by the propellers have a relationship. Let T represent the torque generated by the I propeller. The propeller's torque is affirmed as follows:

$$T_i = k_m F_i [\text{N} \cdot \text{m}] \quad (6)$$

k_m is a constant in the equation that connects the thrust and torque produced by propellers. U_1 , U_2 , U_3 , and U_4 are the symbols for the four control inputs and are used to characterize control inputs:

$$\begin{aligned} U_1 &= F_1 + F_2 + F_3 + F_4 \\ U_2 &= F_4 - F_2 \\ U_3 &= F_3 - F_1 \\ U_4 &= T_2 + T_4 - T_1 - T_3 \end{aligned} \quad (7)$$

The quadrotor model can be presented in state space form as

$$\dot{X} = f(X, U) \quad (8)$$

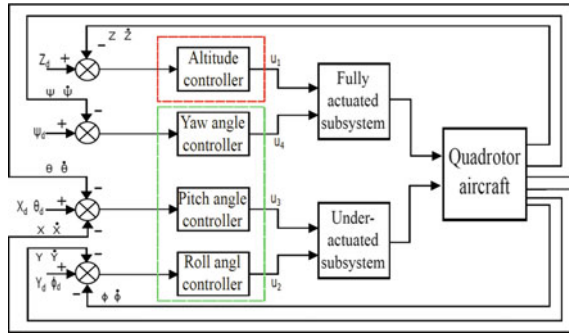
where X and U represent state vectors, and control inputs respectively.

The state vector and control input vector is given as follows in the equation as shown in Eqs. (10) and (11)

$$\begin{aligned} x_1 &= \phi, x_2 = \dot{\phi}, x_3 = \theta, x_4 = \dot{\theta}, x_5 = \psi, x_6 = \dot{\psi} \\ x_7 &= z, x_8 = \dot{z}, x_9 = x, x_{10} = \dot{x}, x_{11} = y, x_{12} = \dot{y} \end{aligned} \quad (9)$$

$$X = [x_1 \ x_2 \ x_3 \ x_4 \ x_5 \ x_6 \ x_7 \ x_8 \ x_9 \ x_{10} \ x_{11} \ x_{12}]^T \quad (10)$$

Fig. 2 The flight control architecture and functional block diagram of the controller



$$U = [U_1 \ U_2 \ U_3 \ U_4]^T \tag{11}$$

To simplify the control architecture as shown in Fig. 2, we consider attitude and altitude dynamics in this paper. Let the quadrotor model’s attitude and altitude subsystem be expressed as [5]

$$\begin{bmatrix} \dot{x}_1 \\ \dot{x}_2 \\ \dot{x}_3 \\ \dot{x}_4 \\ \dot{x}_5 \\ \dot{x}_6 \\ \dot{x}_7 \\ \dot{x}_8 \\ \dot{x}_9 \\ \dot{x}_{10} \\ \dot{x}_{11} \\ \dot{x}_{12} \end{bmatrix} = \begin{bmatrix} x_2 \\ a_1x_4x_6 + b_1u_{21} \\ x_4 \\ a_2x_2x_6 + b_2u_{22} \\ x_6 \\ a_3x_2x_4 + b_3u_{23} \\ x_8 \\ -g + b_4(\cos x_1 \cos x_3)u_1 \\ x_{10} \\ b_4(\cos x_5 \sin x_3 + \sin x_5 \cos x_3 \sin x_1)u_1 \\ x_{12} \\ b_4(\sin x_5 \sin x_3 - \cos x_5 \cos x_3 \sin x_1)u_1 \end{bmatrix} \tag{12}$$

where the following parameters are used:

$$a_1 = \frac{l_{yy} - l_{xx}}{l_{xx}}, a_2 = \frac{l_{zz} - l_{\infty}}{l_{yy}}, a_3 = \frac{l_{xx} - l_{yy}}{l_{zz}} b_1 = \frac{1}{l_{xx}}, b_2 = \frac{1}{l_{yy}} \text{ and } b_3 = \frac{1}{l_{zz}}$$

In Eq. (12), g stands for gravitational acceleration, m for vehicle mass, and $[I_{xx}, I_{yy}, I_{zz}]$ for the moment of inertia.

Stabilization is critical for fully actuated and underactuated devices like the Quadcopter in Fig. 2, which is inherently unstable because of its six degrees of freedom and four actuators. A control system for a quadcopter is modeled using SMC controllers having four sliding surfaces to regulate attitude (pitch, roll, and yaw) and altitude (Z

height). The Quadcopter's location (X and Y axes) is controlled by an inner feedback loop, and the output of these two controllers is fed into the pitch and roll controllers of the outer control loop as shown in Fig. 2.

The roll moment control variable has the equation as

$$U_2 = \frac{1}{b_1} [k_1 \text{sgn}(s) + k_2 s - a_1 \dot{\theta} \dot{\psi} + \ddot{\phi}_d + c_1 (\dot{\phi}_d - \dot{\phi})] \quad (13)$$

The pitch moment control variable U_3 has the equation as

$$U_3 = \frac{1}{b_2} [k_3 \text{sgn}(s) + k_4 s - a_2 \dot{\phi} \dot{\psi} + \ddot{\theta}_d + c_2 (\dot{\theta}_d - \dot{\theta})] \quad (14)$$

The yaw moment control variable U_4 has the equation as

$$U_4 = \frac{1}{b_3} [k_5 \text{sgn}(s) + k_6 s - a_3 \dot{\phi} \dot{\theta} + \ddot{\psi}_d + c_3 (\dot{\psi}_d - \dot{\psi})] \quad (15)$$

The altitude having thrust force regulation variable U_1 has the equation as

$$U_1 = \frac{m}{\cos\phi\cos\theta} [k_7 \text{sgn}(s) + k_8 s + g + \ddot{z}_d + c_4 (z_d - \dot{z})] \quad (16)$$

The x and y linear accelerations of a quadcopter can be condensed into

$$\begin{aligned} U_x &= \frac{m}{U_1} [k_9 \text{sgn}(s) + k_{10} s + \ddot{x}_d + c_5 (\dot{x}_d - \dot{x})] \\ U_y &= \frac{m}{U_1} [k_{11} \text{sgn}(s) + k_{12} s + \ddot{y}_d + c_6 (\dot{y}_d - \dot{y})] \end{aligned} \quad (17)$$

Now Eqs. (16) and (17) are put in matrix notation:

$$\begin{bmatrix} \ddot{x} \\ \ddot{y} \end{bmatrix} = \frac{u_1}{m} \begin{bmatrix} \sin\phi & \cos\phi \\ -\cos\phi & \sin\phi \end{bmatrix} \begin{bmatrix} \varnothing \\ \theta \end{bmatrix} \quad (18)$$

The desired pitch and roll:

$$\begin{bmatrix} \varnothing_d \\ \theta_d \end{bmatrix} = \frac{u_1}{m} \begin{bmatrix} -\sin\phi & -\cos\phi \\ \cos\phi & -\sin\phi \end{bmatrix}^{-1} \quad (19)$$

3 Flight Controller Design

The Flight Control System (FCS) referred to as Fig. 2 is critical in controlling the movement of a Quadcopter from one stage to another because it provides the necessary maneuvering commands during the journey of the Quadcopter.

This takes the desired location of the Quadcopter as an input and converts it into the desired U_1 , U_2 , U_3 , and U_4 values, which influence the rotation/rpm of the four motors. To perform the above-mentioned task, FCS needs a critical element known as a controller [17, 18, 22–24].

3.1 Path Planning

Path planning is computing a continuous path that will take the Quadcopter from its starting point to its final destination. As a result, a suitable path is described as a set of actions that guide the UAV from its initial configuration (state) through some intermediate configurations to its final destination configuration. The route planning algorithm can decide the next state and the action to be taken in the current state. From the set of all possible states that can be visited from the current state, the algorithm selects the next most suitable state. There are two types of route planning algorithms discussed [7, 8]:

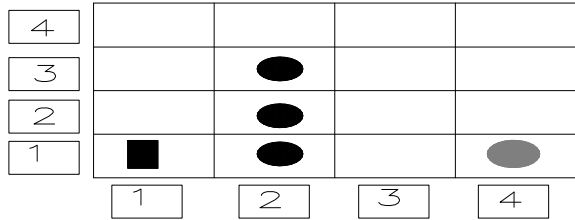
- The aim is Point-to-point problems aim to design a waypoint path through an obstacle field from one point to another.
- The goal is to design a way-point path that allows the UAV to cover the entire area in a given field.

Types of Path Planning algorithms are Potential Field, Floyd–Warshall, Genetic Algorithm, Dynamic Programming, Approximate RL (Reinforcement Learning), MILP (Mixed Integer Linear Programming), A* (A-STAR) algorithm, A* (A-STAR) algorithm is used in this paper to design a path that avoids obstacles.

3.2 A-Star Algorithm

A-Star Algorithm A*(A-star) is a heuristic function to estimate the path cost from the current vertex to the target vertex, focusing on the target, which can help to find the path much sooner. It utilizes the best-first search to discover the least expensive route from the original node to the target node. It is easy to understand from Fig. 3 that Quadcopter (Rectangle) has to traverse the terrain and reach the target (Oval). A* (A-star) algorithm uses the distance between the current location and the target and moves to the square that has the smallest distance [9].

Fig. 3 Representation of initial and target positions in a 4 × 4 map



$$\text{Total cost function : } f(n) = g(n) + h(n)$$

where: $h(n)$ = the distance(cost) to that node and $g(n)$ = the distance(cost) to get from that node to the target node.

And, the optimized path between the initial and target position as given in Fig. 4a will start like this.

The start position is (1, 1). The successive node (only one, in this case, is (1, 2). There is no ambiguity until the Quadcopter reaches nodes (2, 4). There are two nodes (3, 4) and (3, 3). The successor node can be determined by evaluating the cost to the target from both nodes. $f(n)$ for (3,3) is the smallest of the two, hence the successor node is $f(n)$. Quadcopter runs into a dead end it has to take alternate path to reach the target position. From Fig. 5 it has learnt so far that Node (2, 1) will be chosen as the successor node instead of Node (1, 2).

The Quadcopter will continue to traverse the route until it ends up at the block at Node (4, 1). And path traversal in the presence of a dead end and this is done by maintaining two lists open and closed. The list OPEN stores all successive paths that are yet to be explored The list CLOSED stores all paths that have been explored.

From Fig. 6, the start node has 2 successors (2, 1) and (1, 2). From the initial calculation (2, 1) is chosen and the robot travels along that node, how, ever once it

Fig. 4 Determining the optimized path between initial and target positions

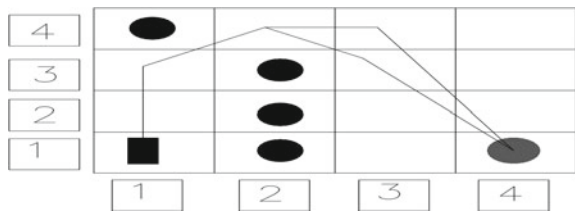


Fig. 5 Determining alternate path in the presence of dead end

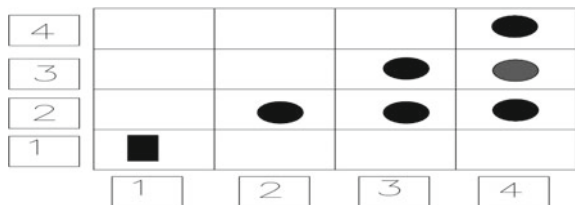


Fig. 6 Path traversal in the presence of dead end

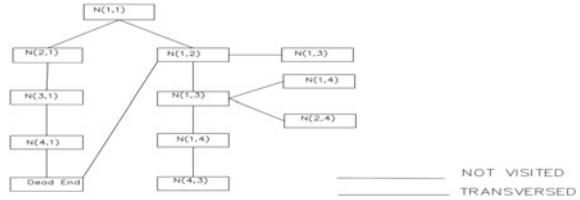
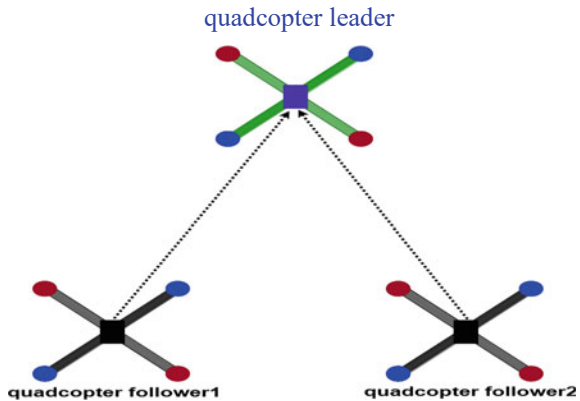


Fig. 7 Formation of quadcopters in a leader–follower scheme



reaches the dead end, it discards the node (2, 1) and takes the second successor (1, 2), and explores that route.

3.3 Formation Flying

Formation Flying comprises two or more Quadcopters flying closed together in an organized manner. One of the Quadcopters is designated as the leader, and the others are called followers as shown in Fig. 7.

In the leader–follower formation configuration, the leader quadcopter is controlled to follow an optimized path, while the followers are controlled to synchronize their motion with the leader even in the presence of disturbances or obstacles [15].

4 Simulation Results

Simulink is a multi-domain simulation and Model-Based Concept block diagram environment. It helps with embedded device architecture, simulation, automated code creation, and continuous testing and verification. Simulink is a tool for modeling and simulating dynamic systems that includes a graphical editor, customizable block

Table 1 Simulation parameter

Symbol	Value	Description
m	0.75 kg	The total mass of the quadcopter
L	0.25 m	Distance from centre of quadcopter to the motor
I	0.019688×10^{-3}	Quadcopter moment of inertia around X-axes
I_{yy}	0.019688×10^{-3}	Quadcopter moment of inertia around Y axes
I_{zz}	0.039380×10^{-2}	Quadcopter moment of inertia around Z axes
b	7.66×10^{-5}	Thrust coefficient
d	5.63×10^{-6}	Drag coefficient

libraries, and solvers. Model-based design is a method for developing complex structures, such as control systems, signal processing systems, and communications systems, quickly and affordably.

In Simulink, design a Quadcopter with its FCS. Some physical parameters are needed to create a Simulink model of the quadcopter [25]. In the given Table 1, those parameters are mentioned.

A map is created with predefined obstacles, as well as the starting and ending positions. The optimized path from initial to goal is created using the A* algorithm, which avoids obstacles. The size of the obstacle must be much larger than the Quadcopters' size when using the A* algorithm to generate an optimal course.

Scenario 1:

The Fig. 8 depicts the A*-optimized route for the specified obstacle pattern, complete with initial and target location fixes. The “*” (stars) denotes a group of obstacles, and the line denotes the A* algorithm’s optimized course.

Scenario 2:

The terrain map obtained from the obstacles pattern defined in Fig. 8 is depicted in Fig. 9.

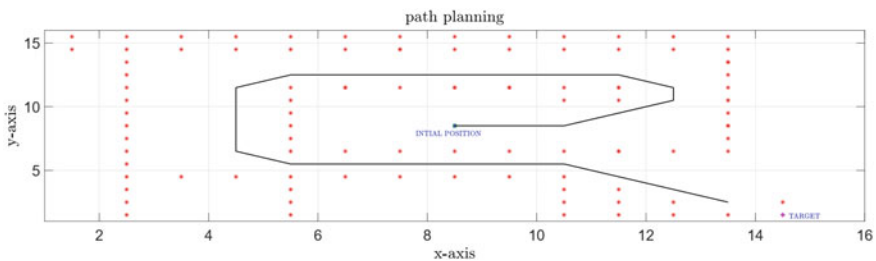


Fig. 8 Path generated by A* algorithm for given obstacle pattern

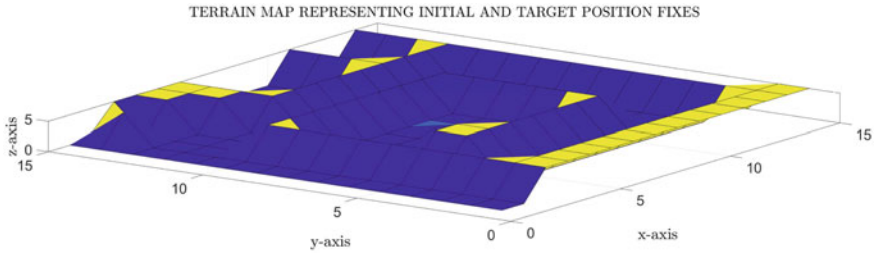


Fig. 9 Terrain map representing initial and target position fixes

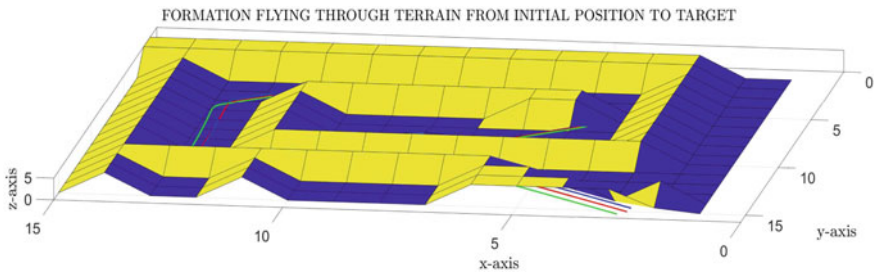


Fig. 10 Quadcopter flying through terrain from initial position to target

Scenario 3:

The terrain map obtained from the obstacles pattern is shown in Fig. 8 and the optimized path that the Quadcopter takes through the terrain from its initial location to the target position, is shown in Fig. 10.

Scenario 4:

The terrain map obtained from the obstacles pattern and the optimized route that a swarm of Quadcopters takes through the terrain from their initial position to their target position in a formation as defined in Fig. 8 are depicted in Fig. 11.

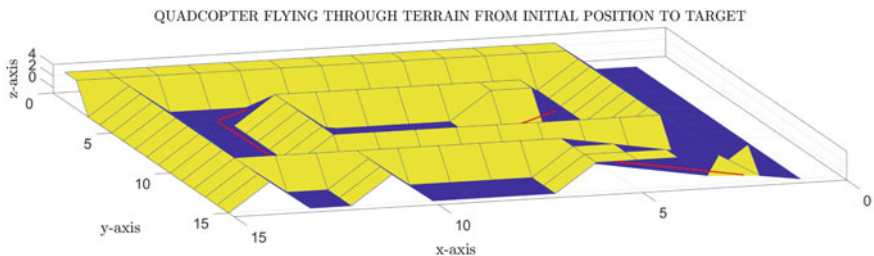


Fig. 11 Formation flying through terrain from initial position to target

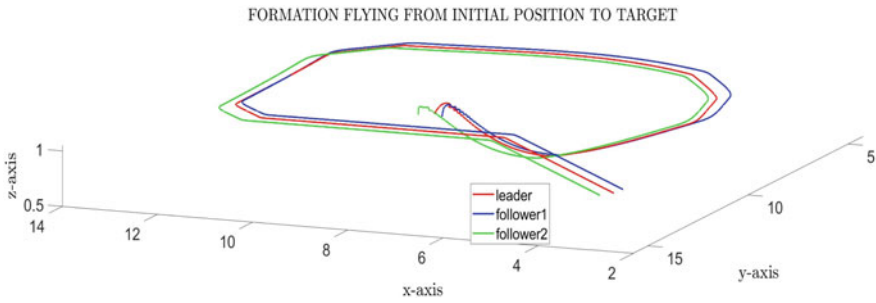


Fig. 12 Representing a swarm of quadcopters in (vee) formation

Scenario 5:

Figure 12 represents the swarm of Quadcopters moving from the initial position to the target position in a formation as specified in Fig. 9.

A much more complex trajectory is achieved by planning the obstacle pattern with narrow spaces in between obstacles.

5 Conclusion

The method for achieving optimal path in different scenarios using the A* algorithm is given along with a comprehensive explanation of Quadcopter dynamics, mathematical model of Quadcopter, and flight control system architecture. Following a thorough examination, it was discovered that the stated swarm of Quadcopters (3 vee formation) is intact while traveling through the created road, which is free of obstacles. The path following the algorithm described above is used in a variety of 3D terrain models. The detailed simulation results show that a swarm of Quadcopters successfully avoided obstacles when in formation. The entire work is based on the assumption that the obstacles are huge compared to the Quadcopter, limiting the Quadcopter’s freedom of motion in one direction. The scope of this work can be increased in two ways by taking into account the fact that obstacles will change (i.e., providing position and velocity profile to the obstacles), and to obtain 3D route planning, the obstacles’ dimensions can be scaled down to the Quadcopter level.

References

1. Abbas NH, Sami AR (2017) Tuning of PID controllers for quadcopter system using hybrid memory based gravitational search algorithm–particle swarm optimization. *Int J Comput Appl* 172(04):9–18
2. Kuantama E, Vesselenyi T, Dzitac S, Tarca R (2017) PID and fuzzy-PID control model for quadcopter attitude with disturbance parameter. *Int J Comput Commun Control* 12(4):519–532
3. Redrovan DV, Kim D (2018) Multiple quadrotors flight formation control based on sliding mode control and trajectory tracking. In: 2018 international conference on electronics, information, and communication (ICEIC). IEEE, pp 1–6
4. Zheng E-H, Xiong J-J, Luo J-L (2014) Second order sliding mode control for a quadrotor UAV. *ISA Trans* 53(4):1350–1356
5. Tripathi VK, Behera L, Verma N (2015) Design of sliding mode and backstepping controllers for a quadcopter. In: 2015 39th national systems conference (NSC). IEEE, pp 1–6
6. Maqsood H, Qu Y (2020) Nonlinear disturbance observer based sliding mode control of quadrotor helicopter. *J Electr Eng Technol* 15(3):1453–1461
7. He Z, Zhao L (2017) The comparison of four UAV path planning algorithms based on the geometry search algorithm. In: 2017 9th international conference on intelligent human-machine systems and cybernetics (IHMSC), vol 2. IEEE, pp 33–36
8. Lv Z, Yang L, He Y, Liu Z, Han Z (2017) 3D environment modeling with height dimension reduction and path planning for UAV. In: 2017 9th international conference on modelling, identification, and control (ICMIC). IEEE, pp 734–739
9. Feng Q, Gao J, Deng X (2016) Path planner for UAVs navigation based on A* algorithm incorporating intersection. In: 2016 IEEE Chinese guidance, navigation and control conference (CGNCC). IEEE, pp 2275–2279
10. Radmanesh M, Kumar M, Guentert PH, Sarim M (2018) Overview of path-planning and obstacle avoidance algorithms for UAVs: a comparative study. *Unmanned Syst* 6(02):95–118
11. Alonso-Mora J, Montijano E, Schwager M, Rus D (2016) Distributed multi-robot formation control among obstacles: a geometric and optimization approach with consensus. In: 2016 IEEE international conference on robotics and automation (ICRA). IEEE, pp 5356–5363
12. Radmanesh M, Kumar M, Guentert PH, Sarim M (2018) Overview of path-planning and obstacle avoidance algorithms for UAVs: a comparative study. *Unmanned Syst* 06(02):95–118
13. Ghamry KA, Zhang Y (2015) Formation control of multiple quadrotors based on leader-follower method. In: 2015 international conference on unmanned aircraft systems (ICUAS). IEEE, pp 1037–1042
14. Wu F, Chen J, Liang Y (2017) Leader-follower formation control for quadrotors. In: IOP conference series: materials science and engineering, vol 187. IOP Publishing, p 012016
15. Arogeti S, Ailon A (2015) Collision avoidance strategies for quadrotors in tight formation flying. In: 2015 23rd Mediterranean conference on control and automation (MED). IEEE, pp 847–852
16. Chang C-W, Shiau J-K (2018) Quadrotor formation strategies based on distributed consensus and model predictive controls. *Appl Sci* 8(11):2246
17. Schmidt DK (2011) *Modern flight dynamics*. McGraw-Hill Education, Europe
18. Stengel RF (2015) *Flight dynamics*. Princeton University Press
19. Vachtsevanos KPVGJ (2015) *Handbook of unmanned aerial vehicle*. Springer Reference
20. McLain TW, Beard RW (2012) *Small unmanned aircraft theory and practice*. Princeton University Press, Princeton and Oxford
21. Dhadekar DD, Sanghani PD, Mangrulkar K, Talole S (2021) Robust control of a quadrotor using uncertainty and disturbance estimation. *J Intell Rob Syst* 101(3):1–21
22. Nelson RC (1989) *Flight stability and automatic control*, 2nd ed. WCB, McGraw-Hill
23. Sujit P, Ghose D (2004) Search using multiple UAVs with flight time constraints. *IEEE Trans Aerosp Electron Syst* 40(2):491–509
24. Stevens BL, Lewis FL (1992) *Aircraft control and simulation*. Wiley

25. Cooke A, Cowling I, Erbsloeh S, Whidborne J (2007) Low-cost system design and development towards an autonomous motor vehicle. In: 22nd international conference on unmanned air vehicle systems, p 28-1
26. Enomoto M, Yamamoto Y (2015) Modelling, simulation and navigation experiments of unmanned aerial vehicle. In: 2015 IEEE international conference on mechatronics and automation (ICMA). IEEE, pp 482–487
27. Kurak S, Hodzic M (2018) Control and estimation of a quadcopter dynamical model. *Period Eng Nat Sci* 6(1):63–75
28. Srigrarom S, Lin HX, Saw ZY, Zhang J, Lim CH (2015) Design and build of swarm quadrotor UAVs at UGS. In: 15th AIAA aviation technology, integration, and operations conference, p 3288
29. Ali Q, Montenegro S (2016) Explicit model following distributed control scheme for formation flying of mini UAVs. *IEEE Access* 4:397–406

Coverage Estimation Using Probabilistic Line-of-Sight Model for Unmanned Aerial Vehicle Communication



Ankita K. Patel and Radhika D. Joshi

Abstract Aerial platforms have recently gained significant popularity for the rapid development of relief networks in emergencies. These platforms are capable to deliver essential wireless communication for various applications such as public safety, natural disasters, or adding coverage to existing terrestrial networks. A reliable prediction of coverage resulting from an aerial base station is important to provide essential air-to-ground wireless services for disaster-affected areas. Line-of-sight (LoS) is an essential component of air-to-ground wireless channels, particularly useful for radio planning and coverage prediction. The performance of an air-to-ground link can be evaluated on three key parameters: elevation angle, communication range, and altitude between the aerial base station and ground receiver. In this paper, we proposed an elevation-dependent line-of-sight model to estimate the area coverage of an aerial base station. The proposed model is derived from statistical parameters of building distribution, defined by the International Telecommunication Union for four urban environments: urban, suburban, dense urban, and high-rise urban. Coverage of aerial base station is estimated from building blockage probability which is formulated as a weighted function of the developed LoS model. Estimated coverage is simulated for elevation angle and communication range between UAV and ground receiver for low altitudes up to 500 m. We restricted UAV altitude up to 500 m due to the limitation on flying altitude by regulating authorities. Our results contribute to identifying the optimum elevation angle and communication range between UAV and ground receiver for line-of-sight communication. Based on the results, we deduced that the optimum elevation angle to attain 100% coverage is between 60 and 80° for all urban environments. We observed a significant reduction in the communication range with declination in UAV altitude, to attain the same amount of coverage for urban, dense urban, and high-rise urban environments. For

A. K. Patel (✉)
Pune Institute of Computer Technology, Pune, India
e-mail: ankitaketan@gmail.com

R. D. Joshi
College of Engineering, Pune, India
e-mail: rdj.extc@coep.ac.in

suburban, altitude is not playing a significant role in the range of communication to achieve area coverage.

Keywords Aerial base station · Building blockage probability · Communication range · Coverage estimation · Line-of-sight probability · UAV

1 Introduction

In recent years Unmanned Aerial vehicles (UAV) discover many applications in surveillance and rescue, military, delivery of goods, telecommunication, precision farming, wildlife monitoring, and many more [1]. UAV can be used as a relay or an aerial base station (ABS) to support in realisation a wireless recovery network for a natural disaster where the existing network is destroyed. Homeland Security Bureau in the USA deployed this concept as a communication architecture for system recovery [2]. The ABSOLUTE [3] project is another example of emergency supplementary network deployment funded by the European Commission.

In an emergency condition, ABS can be deployed quickly, with the minimum manpower requirement. The important requirement for these applications is to provide adequate coverage over a known radius for emergency response. The most unique feature that distinguishes UAV communication from the conventional system is the likelihood of establishing a line-of-sight (LoS) link for air-to-ground communication. The availability of a line of sight has a large effect on wireless channel performance. It is particularly useful for radio network planning and area coverage. The line-of-sight probability is mainly dependent on UAV altitude, elevation angle, environment (urban or rural), and communication range with the ground user.

For an emergency, the number of deployed ABS could be limited. This fact mandates the full exploitation of the deployed ABS by estimating the performance of the radio channel. This leads us to develop an analytical model to estimate the area coverage for ABS that can be useful for low-altitude UAV communication. We developed an elevation-dependent low altitude probabilistic LoS model based on statistical parameters of urban scenarios defined by the International Telecommunication Union (ITU). This model will help in RF planning for an aerial network without having any site-specific information. In a disaster condition where infrastructure is destroyed, it is unlikely to avail city map. In this case, the proposed model can be used for RF planning of a city based on statistical parameters of the urban environment. The estimation of the area coverage for ABS was obtained from the blocking probability of LoS ray for various urban conditions. A simple algorithm is used to obtain blocking probability from the proposed LoS model. Performance of estimated area coverage is analyzed for elevation angle, UAV altitude, and coverage range.

The structure of the paper is as follows. In Sect. 2 we reviewed the techniques proposed in the literature for channel modelling and performance evaluation of links. Section 3 discusses the propagation modelling approach of line-of-sight probability

for urban environments. Section 4 is dedicated to area coverage estimation from the developed model. Simulation results of the area coverage are described in Sect. 5. Section 6 is for concluding remarks.

2 Related Work

For a UAV communication system, it is important to understand the communication channel thoroughly and to evaluate the QoS parameters for the same. This motivates us to develop a generalized channel model and estimate area coverage from the developed model. In literature, various studies are available either on channel modelling or evaluating the performance of the network. In this study, we have evaluated the performance of the channel based on the developed model.

There is a need for a generalized model which does not rely on sight-specific information to evaluate the performance of the channel. In literature, there is a lack of a generalized RF propagation model which can easily link with RF propagation conditions. Many studies are available on measurement-based channel models given in [4–6], these are site-specific and do not give a generalized approach for channel modelling. Cai et al. [4] modelled a suburban city of Madrid using USRP, whereas Khawaza et al. [5] performed ultrawideband (UWB) measurement using a P410 UWB kit to model the channel. Suburban and urban measurements for three cities are performed by Matolak [6] to model the channel. Geometry-based modelling approaches for line-of-sight modelling are available in [7, 8]. Feng et al. [7] proposed a theoretical modelling approach for the dense urban city. Statistical parameters like building height, building width, street width, street angle distribution, and building coverage are used for modelling. This approach is very specific to geometry considered by the author, not a generalized approach for city modelling. Al Hourani [8] developed the line-of-sight analytical model based on the geographic model of Melbourne city. A path loss model for line-of-sight, non-line of sight, and obstructed line of sight were developed by Feng et al. [9]. This model cannot be generalized as it was based on a single city. Holis and Pechac [10] deduced a generic statistical model for air-to-ground path loss, but this model was obtained for high-altitude platforms. Another generic statistical model approach is given by Al Hourani et al. [11], for low altitude platform above 500 m of the ground. In our study, we considered an altitude below 500 m due to limitations in the flying altitude of UAVs as per guidelines provided by the regulatory authority of India. The proposed work presents a generalized line-of-sight modelling approach for four different urban environments to evaluate the area coverage of aerial base stations.

Previous work has attempted to study the performance of coverage such as Zhao et al. [12] considered the relative distance between multiple UAVs to estimate area coverage for UAV mounted base station for sensor networks. Mozaffari et al. [13] studied the performance of air-to-ground channels based on a single UAV's altitude and coverage radius. On-demand user-based coverage is implemented by Hatiao et al. [14], where ABS can change its position as per the user's movement while

maintaining connectivity between UAVs. A 3D layout of ABS is considered by Kalantari et al. [15] to cover a maximum number of users with minimal transmission power. Al Hourani [16], estimated ABS coverage and information rate for air-to-ground links based on the altitude of the UAV. Maurila Matracia et al. [17] present a new stochastic framework for urban and rural areas.

The main contribution of our work is the modelling of line-of-sight probability and estimation of area coverage using ITU-R parameters. This allows rapid estimation of the link performance without relying on site-specific information. This study will help to optimize the key parameters for an aerial base station such as elevation angle, altitude, and communication range.

3 System Model

Aerial platforms deployed at low altitudes are quasi-stationary platforms such as quadcopters, balloons, and helicopters. These are easier to deploy and can go in line with the cellular concept, as low altitude combines superior coverage with a confined cell radius. These platforms are dependent on the end user's application.

3.1 Statistical Propagation Model

Developing an RF model requires an accurate study of the conditions and constraints of the environment. The layout and characteristics of the buildings are some of the most important conditions in an urban environment. The international telecommunication union (ITU) [18] has suggested statistical parameters α_s , β_s and γ_s , that describe the general statistics of a certain area. These parameters are explained below:

- α_s : the ratio of building area covered in a land to the total area of land (dimensionless)
- β_s : mean of the number of buildings per unit area in buildings/km²
- γ_s : a variable that describes the building height distribution as per Rayleigh probability distribution:

$$P(h) = \frac{h}{\gamma_s} e^{-\frac{h^2}{\gamma_s^2}} \quad (1)$$

where h is the height of the building in meters. By following the steps given in [18] Probability of Line of Sight can be obtained is

$$P(LoS) = \prod_{n=0}^m \left[1 - \exp \left\{ -\frac{(ht - \frac{(n+\frac{1}{2})(ht-hr)}{m+1})}{2\gamma_s^2} \right\} \right] \quad (2)$$

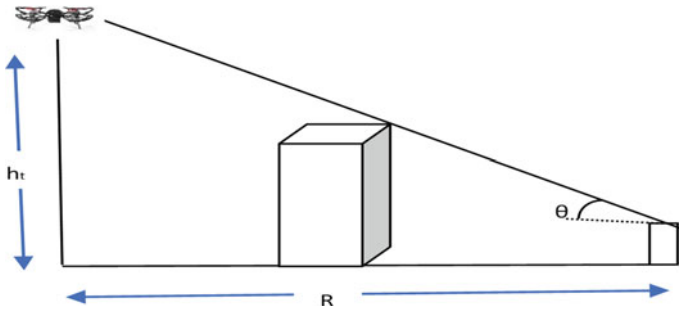


Fig. 1 The geometry of line-of-sight scenario for air to ground link

where $m = \text{floor}(R\sqrt{\alpha_s\beta_s} - 1)$ and R is the distance between transmitter and receiver as depicted in Fig. 1; h_t and h_r are transmitter and receiver heights, respectively. Receiver height h_r is much lower as compared to UAV altitude h_t and building heights; then the ground distance R can be written as $h_t/\tan(\theta)$; where θ is the elevation angle as shown in Fig. 1. The resulting plot of the $P(\text{LoS})$ series will be smooth for the large values of h_t and can be defined as a continuous function of θ . Four different environments; suburban, urban, dense urban, and high-rise urban are selected for simulation of $P(\text{LoS})$.

For simulation, buildings are randomly generated using statistical parameters, in a 1×1 km area with a resolution of 1 m. The statistical parameters; α_s is (0.1, 0.3, 0.5, 0.5), β_s is (750, 500, 300, 300) and γ_s is (8, 15, 20, 50) for suburban, urban, dense urban and high-rise urban environment, respectively. The entire area is divided into small grids. The calculations were made for azimuthal angles between 0 and 360° of altitude up to 500 m. The LoS probability for a specific elevation angle is calculated as a median of data obtained from an azimuthal angle. The simulation was performed for an entire range of elevation angles from 0 to 89° for four simulation environments.

3.2 Modeling Line of Sight Probability

The simulation results show the LoS probability between UAV and ground receiver. The elevation angle between 60 and 90° is more realistic for UAV applications for all the environments to ensure 100% line-of-sight communication. We observed that trend shown in Fig. 2 can be approximated as a simple S curve equation. The LoS probability is modelled as a simple S curve equation of the following form:

$$P_{LoS} = \frac{1}{a_3 + e^{-(-a_1+a_2(\theta-a_4))}} \tag{3}$$

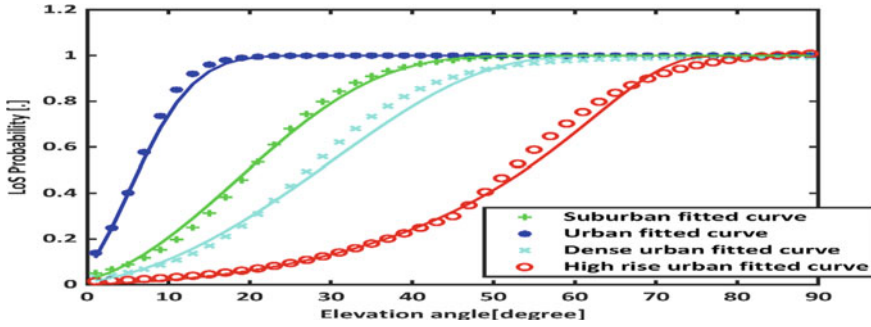


Fig. 2 Calculated line-of-sight probability, with their related curve fitting for suburban, urban, dense urban and high-rise urban environments

Table 1 Parameters of LoS probability calculation

Environment	a_1	a_2	a_3	a_4
Suburban	2.1778	0.3557	1	0
Urban	3.0734	0.1565	0.9989	0.158
Dense urban	3.4912	0.1304	1.007	0.3344
High-rise urban (0–45°)	4.2234	0.0815	1.5747	0.114
High-rise urban (45–90°)	4.7313	0.1209	0.9801	13.144

where $a_1, a_2, a_3,$ and a_4 the empirical parameters given in Table 1 are obtained from the least-square curve fitting method. These results are compared with the model given in [19], where a shadowing model of roadside buildings is explored. Link blockage probability is defined as a function of azimuthal and elevation angle. Several test cases use from both models and they give similar results. Figure 2 shows that our model follows the calculated LoS modelling for all four environments. For high-rise building distribution, parameters are calculated separately for angles below and above 45°.

4 Coverage Estimation

An accurate coverage estimation can be achieved by determining an optical line of sight in an area where a building and terrain database is available. Building blockage probability is the estimate to obtain an optical line of sight between the UAV transmitter (Tx) and receiver (Rx). Building blockage probability states that each building lying between UAV and receiver is below the line-of-sight ray as shown in Fig. 3. Coverage will depend on the distance between transmitter and receiver and buildings which do not obstruct LoS ray. Coverage can be estimated from building blockage probability using an algorithm as described in [18], which is based on parameters α_s

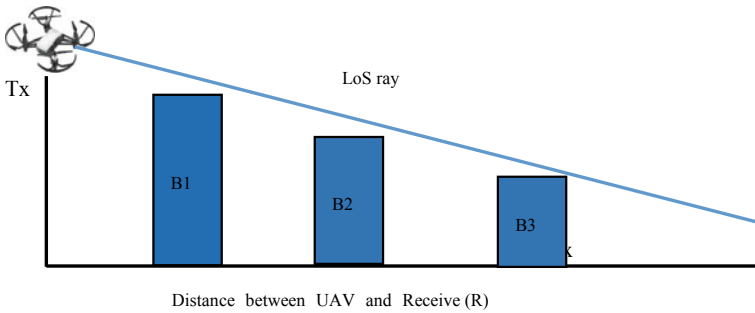


Fig. 3 Building geometry for LoS ray between transmitter and receiver

and β_s . The first step is to calculate the number of buildings between the UAV and ground receiver with the help of parameters α_s , β_s , and LoS probability defined in Sect. 3.

4.1 Steps to Estimate Coverage and Building Blockage Probability

Step 1: Calculate the number of buildings between UAV and receiver.

To obtain the number of buildings between transmitter and receiver, a ray will be pass-through $\sqrt{\beta_s}$ buildings, arranged in a rectangular grid. Only a fraction of α_s land will be covered. The expected number of building pass through per kilometre are:

$$b = \sqrt{\alpha_s \beta_s} \tag{4}$$

If R is the distance between transmitter and receiver then the number of the building between UAV and receiver are

$$B_{ur} = R\sqrt{\alpha_s \beta_s} \tag{5}$$

Step 2: Obtain the distance of each building from a transmitter.

All the buildings are evenly spaced between transmitter and receiver. The distance between two buildings is:

$$d_b = R/B_{ur} \tag{6}$$

The distance of each building from the transmitter is:

$$d_x = (x + 1)d_b \quad (7)$$

where x is the count of buildings between Tx and Rx and x is given by $\{0, 1, \dots, (B_{ur} - 1)\}$.

Step 3: Obtain building blockage probability which describes that LoS ray will be present at x th building is given by

$$P_b = \prod_0^{B_{ur}-1} P_{LoS} d_x \quad (8)$$

Step 4: Estimate area coverage from building blockage probability:

$$C = \frac{P_b}{B_{ur}^2} \quad (9)$$

Area coverage for a given scenario is estimated from an above-mentioned algorithm, LoS probability given in Eq. 3 and statistical parameters α_s , β_s . Estimated coverage is mainly dependent on three parameters UAV altitude, elevation angle, and communication range. Simulation is performed to evaluate the effect of these three parameters on estimated coverage.

5 Simulation and Results

Simulation is performed for four environments: suburban, urban, dense urban and high-rise urban. For a simulation area of 1×1 km is considered with randomly generated buildings as per statistical parameters defined in [18]. Table 2 shows the parameters considered for simulation.

The results presented in Figs. 4 and 5, were obtained for the estimation of the area coverage for elevation angle and communication range for four environments. From Fig. 4, it is observed that area coverage is linearly increasing with elevation angle and

Table 2 Simulation parameters

Parameters	Value
Area	1×1 km
UAV altitude	100–500 m
Elevation angle	$0-90^\circ$
Communication range	100 m–1 km
Distance between buildings	20 m

falls after attaining the maximum value. This trend is common in all environments. Based on experimental results, we identified the optimum elevation angle to achieve maximum coverage in the range of 60–80° for altitudes 200, 300, 400 and 500 m for all environments. For an altitude of 100 m, the optimum elevation angle lies between 35 and 65°. The high elevation angle is recorded for high altitude to attain the same amount of area coverage.

Figure 5 shows the estimation of area coverage with a communication range for different altitudes. The maximum altitude considered for the suburban area was 300 m, above this, there is no significant change was observed. This is due to less

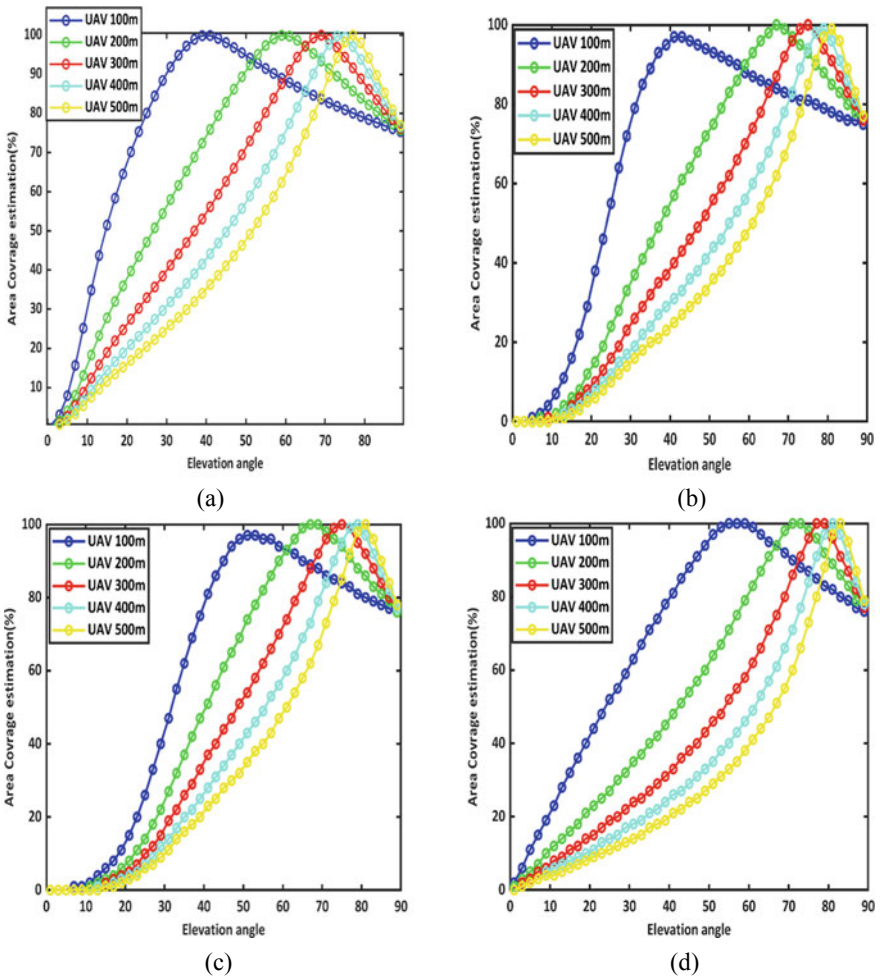


Fig. 4 Wireless communication coverage estimation with elevation angle between UAV and ground receiver: **a** suburban, **b** urban, **c** dense urban, and **d** high-rise urban

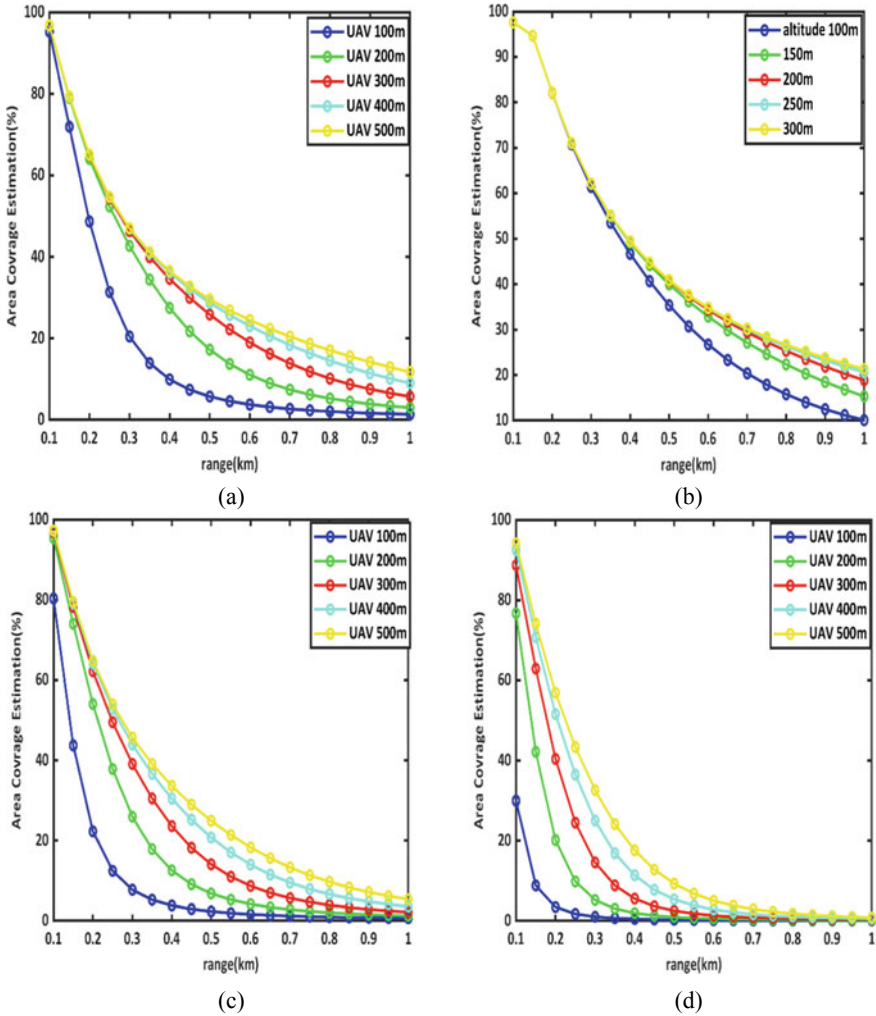


Fig. 5 Wireless communication coverage estimation with communication range: **a** suburban, **b** urban, **c** dense urban, and **d** high-rise urban

infrastructure density in the area. The higher the building density lower is the communication range. It is observed that maximum communication range can be achieved at higher altitudes. To cover at least 50% of the area, the distance between the UAV and ground receiver should be 500 m. For the suburban scenario, altitude is not having a greater impact on the communication range rather for other environments, altitude plays a significant role. For suburban areas, altitude does not play a significant role while calculating communication range for a certain value of area coverage. Our results help to evaluate the performance of the area coverage for an urban scenario

to elevation angle, altitude, and communication range. This can be utilized for the RF planning of disaster-affected areas without prior knowledge of the site.

6 Conclusion

This paper developed a generalized low altitude elevation-dependent LoS propagation model for four different urban environments; urban, suburban, dense urban, and high-rise urban. This model facilitates RF planning of airborne base stations to fulfil connectivity for the disaster-affected area. The proposed technique is based on simple statistical urban parameters, not dependent on the 3D model of the site. For the disaster-affected areas, the proposed model can be used for RF planning of a city, based on statistical parameters without any prior knowledge of the city map. This model showed that line-of-sight between UAV and ground receiver can be expressed as a function of elevation angle. An algorithm is defined to estimate area coverage from the developed model, as a function of building blockage probability. Performance of estimated coverage was evaluated for three important parameters of UAV propagation: elevation angle, communication range, and UAV altitude. A simulation was performed for a low altitude between 100 and 500 m. Results show the optimum elevation angle lies between the range of 60–80° for Low altitude LoS propagation. UAV altitude plays a significant role to evaluate an optimum communication range for more than 50% coverage except for the Suburban environment.

Future work will include the analysis of air-to-ground UAV channels for large-scale and small-scale fading effects at low altitudes and estimate performance parameters for the same.

References

1. Mozaffari M, Saad W, Bennis M, Nam Y, Debbah M (2019) A tutorial on UAVs for wireless networks: applications, challenges, and open problems. *IEEE Commun Surv Tutor* 21(3):2234–2360
2. FCC (2009) The role of deployable aerial communications architecture in emergency communications and recommended next steps. White Paper. <http://hraunfoss.fcc.gov/edocspublic/attachment/DOC309742A1.pdf>
3. ABSOLUTE (Aerial Base Station with Opportunities Links for Unexpected and Temporary Events). <http://www.absolute-project.eu/reports/publications>
4. Cai X, Plaza AG, Alonzo D, Zhang L, Rodriguez CB, Yuste AP, Yin X (2017) Low altitude UAV propagation channel modelling. In: *Proceeding 11th European conference antenna and propagation (EuCAP' 17)*, Paris, France, pp 1443–1447
5. Khawaja W, Guvenc I, Matolak D (2016) UWB channel sounding and modelling for UAV air-to-ground propagation channels. In: *Proceeding IEEE global communication conference (GLOBECOM' 16)*, Washington, USA, pp 1–7
6. Matolak D (2017) Air-ground channel characterization for unmanned aircraft systems—part III: the suburban and near-urban environments. *IEEE Trans Veh Technol* 66(8)

7. Feng Q, Tameh E, Nix A, McGeehan J (2006) Modeling the likelihood of line-of-sight for air-to-ground radio propagation in urban environments. In: IEEE GLOBECOM'06
8. Al Hourani A (2020) On the probability of line-of-sight in urban environments. *IEEE Wirel Commun Lett* 9(8)
9. Feng Q, McGeehan J, Tameh E, Nix A (2006) Path loss models for an air-to-ground radio channel in urban environments. In: 63rd IEEE vehicular technology conference, vol 6, pp 2901–2905
10. Holis J, Pechac P (2008) Elevation-dependent shadowing model for mobile communications via high altitude platforms in built-up areas. *IEEE Trans Antennas Propag* 56:1078–1084
11. Al Hourani A, Kandeepan S, Jamalipour A (2014) Modeling air-to-ground path loss for low altitude platforms in urban environments. In: Proceedings GLOBECOM symposium, selected areas communication satellites space and communication, Austin, TX, USA
12. Zhao T, Wang H, Ma Q (2020) The coverage method of unmanned aerial vehicle mounted base station sensor network based on relative distance. *Int J Distrib Sens Netw* 16(5)
13. Mozaffari M, Saad W, Bennis M (2016) Efficient deployment of multiple aerial vehicles for optimal wireless coverage. *IEEE Commun Lett* 20(8):1647–1650
14. Haitao Z, Haijun W, Weiyu W (2018) Deployment algorithms for UAV airborne networks towards on-demand coverage. *IEEE J Sel Area Commun* 18
15. Kalantari E, Yanikomeroglu H, Yongacoglu A (2016) On the number and 3D placement of drone base station in wireless cellular network. In: IEEE 84th vehicular technology conference (VTC_fall), Montreal, QC, Canada, 18–21 Sept 2016
16. Al Hourani A (2016) Coverage and rate analysis of aerial base station. *IEEE Trans Aero Space Electron Syst* 52(6)
17. Matracia M, Kishk MA, Alouini MS (2021) Coverage analysis for UAV-assisted cellular networks in rural areas. *IEEE Open J Vehic Tech* 2:194–206 9420290 [10.1109/OJVT.2021.3076814](https://doi.org/10.1109/OJVT.2021.3076814)
18. ITU-R (2005) Rec. P.1410-5 propagation data and prediction methods for the design of terrestrial broadband millimetric radio access systems. P Ser, Radio Wave Propag
19. ITU-R (2003) Rec. 681-3 propagation data required for the design of earth-space land mobile telecommunication system. P Ser Radio Wave Commun

Blockchain Technology Based Security for UAV IoT Environment



Renu Mishra and Sandeep Saxena

Abstract Recent emerging technologies are being utilized for the quench of connectivity in real time scenarios. A push is coming to make the information available to humans from the real-time environmental data collected through small sensing devices. Wireless ad-hoc network is a base architecture for Internet of Things (IoT), Unmanned Aerial Vehicle (UAV) and drones etc. In this series, IoDT (Internet of Drone Things) came as the future of drones backend via the Internet of Things, smart vision, cloud computing, enhanced communication, big data, and advanced security approaches. Rapid growth in sensing devices connected to the Internet with intelligence and capabilities also opens the door for attackers because more devices are connected means more chances of security vulnerabilities. Since data authentication is handled only by the central station, which may lead to the chances of device spoofing and false authentication brings less reliability after all. Blockchain (BC) technology is introduced to address such security concerns by eliminating the role of central authority. Blockchain Technology gives decentralized and non-tamperable solutions for the most demanding security service i.e. Authentication. This paper starts with unique characteristics and security challenges in such IOT environment and further covers the authentication process by blockchain with its potential benefits. The multilayer ecosystem is illustrated to fulfill the requirement of the UAV IoT environment, where multiple devices are equally working in a cooperative manner to perform an authorized action. The paper presented a complete study about the integration of blockchain in IoT enabled UAV.

Keywords Blockchain · UAV · IoT · Mutual authentication · Consensus mechanism · Internet of drones · Internet of things · Smart contract

S. Saxena
Galgotias College of Engineering and Technology, Greater Noida, India

R. Mishra (✉)
Dept. of CSE, SET, Sharda University, Greater Noida, India
e-mail: renutrivedi@galgotiacollege.edu

1 Introduction

These days, we understand the wide useful region caught by IoT pervasively like Unmanned Aerial Vehicle (UAV), natural engineering, surveillance, modern observing, agribusiness area, seismic location and development industry. The capsule of IoT Environment and BC has been gaining significant attention. Various more opportunities may lie in future applications if combined with emerging technologies [1]. Recently more and more new applications are being popular in the commercial sectors that are getting benefits from basic UAV-IoT but the overall prosperity depends on how it is integrated with the Internet and other advanced technologies [2]. The term “Internet of Drones” (IoD) refers to the networking and collaboration of intelligent Air vehicles and drones through the production, transfer, and analysis of data while enhancing traffic congestion, travel time, and security. This article is a thorough study of different security issues in UAV systems and summarizes the various characteristics of blockchain technology and its utility in UAV systems. The objective of this work is to give a broader outlook to the readers, on following points.

- How certain blockchain features can help to overcome the security breaches of UAV systems
- What will be the potential impact of combining blockchain and UAV technology on other emerging technologies
- How different issues can be addressed in the development of derived blockchain-based UAV systems
- How can someone explore potential research directions that can be beneficial for the development of blockchain-based UAV system.

In this article, we sum up that these Internet of Things (IoT) security issues can be reduced with the aid of potent distributed technology, like blockchain, to empower the UAVs and make them safer, more accurate, and simpler to control. The paper can demonstrate how the use of UAV and blockchain technology can advance a variety of industries. We also made an effort to suggest potential research avenues that could aid in the creation of a blockchain-based UAV system.

2 Security Issues and Goals in Internet of Drones (IoD) Environment

Unlike traditional networks, here networks related functions are done by the nodes themselves with equal functional responsibility[3]. The security mechanisms for any traditional networks, cannot be fully applied in IoT. The absence of centralized authority in ad hoc networks makes routing and key management activities very crucial because routing is cooperation based. Need has raised to plan a secure solution to facilitate the application user, who is having some sensitive information and hesitate to take advantage of IoT [4]. Nodes connected to a common link

should be able to identify the other node's identity and credentials. These identities and credentials must be mutually authenticated and also shielded to avoid future questions. The identification also leads to the privacy issue, so a good security solution must cover confidentiality, availability, and integrity of information carried in packets during routing because the information may be forwarded and misused by malicious node [5]. During routing an attacker may disturb the control information to make other entities benefits in unplanned ways [6]. To design an Integrated secure routing solution became essential for recent networking paradigms like Content-based Networking and Internet-of-Things (IoT) [7]. To welcome the advent of new ad-hoc networking paradigms, work can be started as an opportunity to propose a framework towards secure routing for possible attacks during the routing process. At the top level, Quality-of-Service will also be facilitated simultaneously by introducing security services [8]. Initially, UAV were developed for the military for a risky mission to save the life of the pilots and sometimes for providing essential supplies to soldiers in batter fields. Recently the researcher's focus has been shifted towards Internet of Drones (IoD) for non-military and commercial domains [2] due to efficient hardware which has become very small and powerful and involvement of computer software support to provide mobility and autonomous operation [3]. Unmanned Arial Vehicle (UAV) consists of Mobile flight nodes, which are more vulnerable to security threats with open broadcast it may require individual security solutions [9]. Some key security requirements in IoD networking include:

Availability: It ensures the accessibility of data and services to authorized parties at appropriate times.

Confidentiality: It safeguards the information not to be revealed to an unauthorized party, especially in strategic and military applications. Only the intended parties can use confidential information.

Data integrity: It gives the assurance of the accuracy and consistency of a message that is going toward the destination. Even in the presence of channel noise, data has not tampered over its entire communication cycle.

Authentication: It is about proving or showing something to be genuine. In the process of authentication system recognizes the identity of the peer node. Without associating an incoming request with a set of identifying credentials, an attacker could enter as a better node.

Non-repudiation: In terms of security, it is a way to get assurance that the parties cannot later deny having sent and received the message. It can help to detect and isolates any compromised and undesired function.

We might make out the details of the IoT security risks related to the UAV connection by paying serious attention. Blockchain technology can serve as the solution of authentication, authorization, data integrity and protection, confidentiality, access control, and cyber-attack. Additionally, it becomes crucial to create a suitable consensus mechanism for IoD and integrate performance enhancing strategies like caching into the ecosystem. This article concludes that these Io-UAV security concerns can be reduced with the aid of potent distributed technology, like as blockchain, to empower the UAVs and make them safer, more precise, and simpler

to handle. The article can demonstrate how the use of UAV and blockchain technologies can advance a variety of sectors. Additionally, we attempted to offer relevant research avenues that could aid in the creation of a blockchain-based UAV system.

3 Challenges and Opportunities Through Blockchain in IoDs

Despite its many benefits, FANET (Flying Adhoc Network) encountered several problems that are very typical.

- (a) Autonomous- In FANET we recall the need for self-organized security policies in the absence of centralized administration.
- (b) Changing topology- Mobile nodes are roaming very frequently and can be connected arbitrarily which pushes the security policy of routing protocols in the danger.
- (c) Route discovery-Since node movement has been very often, therefore dynamic update mechanism is required to assist automatic best route selection.
- (d) Bandwidth optimization- Wireless Routing protocol has to maintain the topological control information which requires extra overhead over bandwidth. Bandwidth should not be wasted and protocols should be bandwidth concentric too [12].
- (e) Constraint resources—Node lives on battery power, and also have the scarce storage capacity so designing of complex security algorithms is restricted.
- (f) Openness-Mobility of the nodes in FANET brings higher threats by allowing the access of network to both genuine users and attackers.

Blockchain is a specific kind of database where data is kept in blocks that are connected together. To achieve security and trust, each new piece of data is kept as a separate block and chained onto the previous block in a distributed way, which suggests that the information entered is irreversible. Blockchains cannot be changed unless a majority has agreed to do so since each block has its own unique mathematical hash. IOT, like any other communication technology, may have unique flaws or vulnerabilities that open doors for attackers [10]. A system becomes vulnerable when there is a flaw in the hardware or software, which makes it susceptible to exploitation. The attack might take the form of a channel weakness, which would allow for message manipulation and the introduction of bogus information [11]. IOTs require many degrees of security techniques because the environment can be accessed by both authorized users and adversaries. The only way to authenticate during data exchange is through the central authority. The security could be compromised via information tampering, device spoofing, and fake authentication when sharing data. Blockchain (BC) technology is presented as a component of IOT with the aim of eliminating a central server to address such security and privacy problems. Over the advantages of blockchain, we have to design an blockchain architectures to set the trade-off between power consumption, performance, and security.

4 Overview of the Previous Blockchain-Based Solutions on UAV IoT Environment

The majority of studies have attempted to use multilevel and multi-domain solutions to address security issues relating to data sharing in IoD networks, but none of these approaches are suitable due to intensive computations and limited battery capacity. The majority of the security issues with IoD can be resolved using Blockchain's appealing properties, such as decentralization, immutability, and tamperproof storage. Over the years, there has been a lot of research and development towards putting such a solution into practice.

Blockchain has been introduced as an alternate technique by a number of academics to maintain security and privacy in the IoD [12–14]. For the purpose of serving several UAV networks, a literature on the use of blockchain is presented where the authors classified various methodologies according to the UAV network applications [15, 16]. Without the need for centralized governance, Blockchain provides decentralized architecture with a distributed, shared, and immutable ledger, ensuring data security [17, 18]. Numerous efforts have been made in various dimensions to secure IoDs, but none of them can be directly applied to IoDs [19, 20]. With off-chain data storage to fit into the resource-constrained IoD landscape, derived blockchain architecture [21, 22] entered the picture to address the issues mentioned above. To separate the data into off-chain and on-chain data and preserve just the on-chain in the blockchain, decoupling of data is suggested in [23, 26]. The privacy preservation and protection difficulties and challenges, in particular authentication, are part of the IoD security. The use of a digital signature as an authentication method can help to prevent unauthorized changes to fields that can be changed. Digital signatures from all to the intermediate node are appended and verified by the next hop to check the misbehavior. Traditional methods for creating digital signature are very complex, and cannot be implemented in IoD due to the high computation overhead. Vehicle authentication based on Blockchain technologies has been presented with smart contracts to identify malicious vehicles. Before being added to the group more than 51% of the existed nodes accept the node's integration then only a new node can join. A distributed PKI system is utilized for trusted key distribution. For authentication, various Blockchain based Authentication and Access control mechanisms are also being proposed to maintain the privacy of the participating entities which also needs improvement as lightweight algorithm.

5 Ecosystem of Blockchain Based Secured UAV

Standard blockchain based proposals were wrapped in huge interactions that are again not suitable for such resource constraint environment. The conventional blockchain architectures suffers from below specific issues related to IoD.

- Mining processes for ensuring proof of work are very heavy and battery exhaustive even dedicated firms also.
- Consistent state in block chain is also comes after synchronization, which requires a huge communications overhead.
- Size of blockchain tends to grow as new blocks are added into so traversing transactions in the chain requires huge time.
- High mobility of IoD systems the network typologies tend to change.

Already a lot of work has been done in a different dimension for making the IoD secured, but none can be applied directly for IoDs. Blockchain-based access control for IoD must be developed in order to maintain a balance between transparency and privacy. To cover above challenges, we must understand the working of different phases in blockchain to fulfill the need of IoD as derived blockchain architecture with the help of below diagram

IoD has very much constraint environment which creates hurdles in adoption of blockchain as an unconventional security mechanism. Above diagram brings a lightweight general architecture for developing Blockchain in IoD. A multilayer Ecosystem of Blockchain based secured UAV is illustrated in Fig. 1, which can be add-up as security extension to revolutionize the existing system. Different aspects of UAV are addressed in different layers as,

Application plane: All the service providers in different application sectors of UAV are using this layer for intercommunications.

Control plane: Here, Blockchain can be utilized to decouple the data with the help of lightweight consensus protocol as proof of work (POF) and smart contract

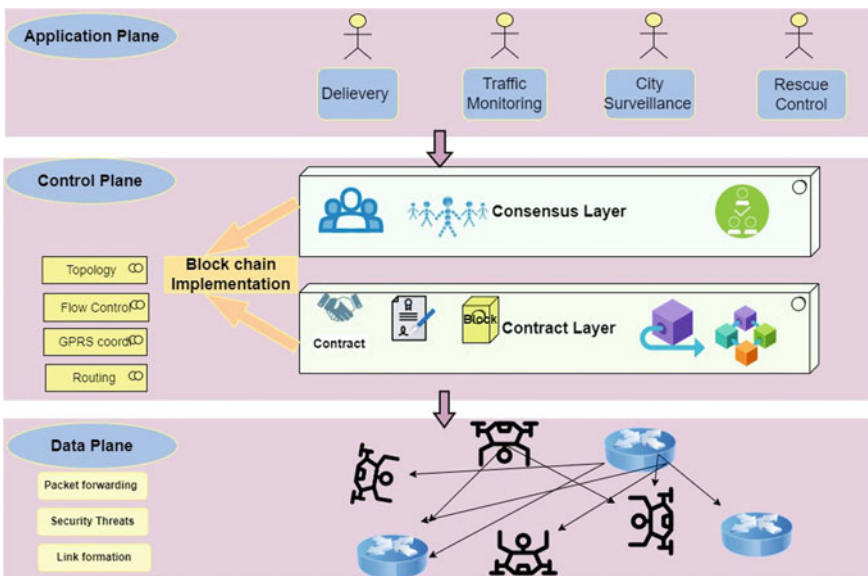


Fig. 1 Layered ecosystem of blockchain based secured UAV

formation with flow control policies, decision related to routing and topology change in UAV. A smart contract keeps track of IoT UAV and responds in accordance with the access control guidelines it contains. If any security policy is violated and, the system notifies based on the smart contract. The registration of a new drone is required for access control and traceability. Transactions which are simply the interactions are signed to ensure that each drone is in control of its block. The main issue of storage requirements must be addressed either by offchain data storage mechanism or data compression techniques.

Data Plane: Different UAVs are interconnected in I-planet which handles packet forwarding, security threats and link formation etc.

In this section, we explained the working flow of blockchain application prototype to get the authentication and other security services in UAV environment (Table 1).

These are crucial steps to implementing a general security framework in any existing constrained network. The proposed system model can be further utilized in supply chain management, home automation, the manufacturing industry, and many other useful scenarios.

Table1 Work flow of block chain prototype

<i>Phase 1: Transaction initiated</i>
<ul style="list-style-type: none"> • One UAV A passes certain information to another UAV B which is called the transaction
<i>Phase 2: Transaction is being encrypted and Signed</i>
<ul style="list-style-type: none"> • A encrypt the transaction with B's Public key and uses it's private key to sign the transaction
<i>Phase 3: Request for the storage on Block chain</i>
<ul style="list-style-type: none"> • UAV A transmits the transaction to a Peer to Peer (P2P) network where the blockchain protocols are implemented • The blockchain network stores the certain numbers of transactions in a Block and broadcast it throughout the network
<i>Phase 4: Transaction validation</i>
<ul style="list-style-type: none"> • All the participants UAVs allow to append the Block in the chain after achieving successful consensus in the form of POW • Consensus protocol confirms the block validation from the participants • The valid block is sent to the participants to permanently storage of in the current chain of block
<i>Phase 5: Data retrieval</i>
<ul style="list-style-type: none"> • UAV B can access the information from the confirmed Block using its private key

6 Future Research Directions

Researchers and manufacturers both are recommended to reimplement the current UAV network to take security advantage of the blockchain and smart contracts. However, the widespread use of private blockchains is creating redundant data, fragmentation, and also prompting criminal activity. Participating stakeholders of the area have raised the demand of interoperability to obtain portability and scalability among these isolated blockchains. Intercommunication among different blockchains can be guaranteed only if all the common issues are addressed in each of the UAV. In Fig. 2 we listed the common issues in UAVs connected through Internet to achieve global interoperability.

Interoperability between blockchains also aims to reduce the cost and volume of redundant transactions. Route deconfliction and planning must be in very much efficient way for such resource constraint UAV networks. This is possible by integrating a blockchain that links operators and UAVs with airspace authorities. On the other hand, geofencing is not explored yet, a blockchain-based solution would be a good fit for this application. This is possible by integrating a blockchain that links operators and UAVs with airspace authorities.

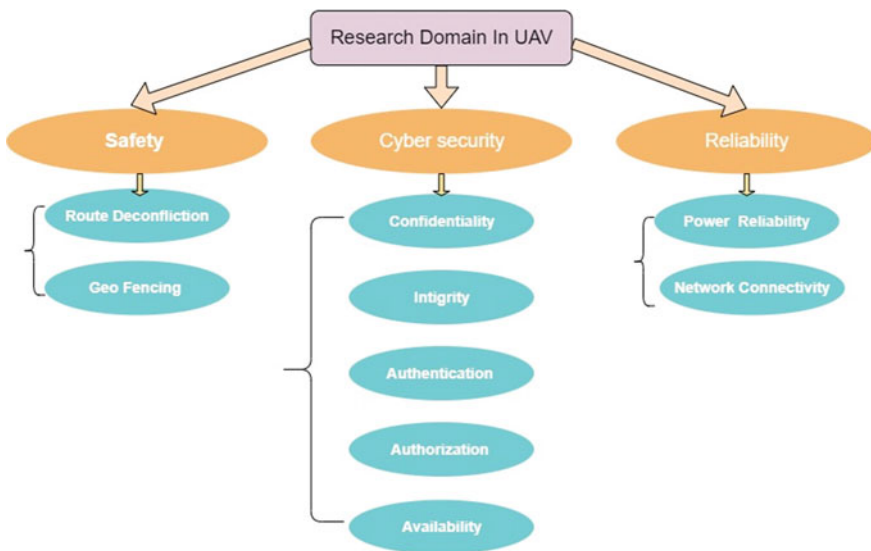


Fig. 2 Research domains in blockchain based UAV

7 Conclusion

Although UAVs have the potential to significantly improve driving experiences in the near future, security for both users and service providers still needs to be improved. In order to meet the IoV systems' security requirements, blockchain has evolved. Even so, Blockchain still needs to be customized to excel in such environments. We tried to summarize our best knowledge about different application of UAV, challenges pertaining to each scenario and also discuss the way to enhance the utility of UAV in other scenarios through blockchain. Now it has proved that blockchain is more suitable than any other conventional security approaches to open the door as security solutions in data sharing and/or storage still further, analysis and research attention is required for designing special real-time architectures of blockchain to offer better performance and throughput. According to the paper, these UAV security issues can be resolved with the aid of potent distributed technology, such as blockchain, empowering the UAVs and enhancing their safety, accuracy, and controllability. The work can demonstrate how the use of UAV and blockchain technology can advance a variety of industries. We also made an effort to suggest potential research avenues that could aid in the creation of a blockchain-based UAV system.

References

1. Kung Y-H, Hsiao H-C (2018) Groupit: lightweight group key management for dynamic IoT environments. In: ISLPED '18, Seattle, WA, USA
2. Gu H, Potkonjak M (2018) Efficient and secure group key management in IoT using multistage interconnected PUF. In: Conference: the international symposium
3. Sciancalepore S, Piro G, Boggia G, Bianchi G, Public key authentication and key agreement in IoT devices with minimal airtime consumption
4. Singh M, Aujsla GS, Bali RS (2022) Derived blockchain architecture for security-conscious data dissemination in edge-envisioned internet of drones ecosystem. *Cluster Comput* 25:2281–2302. <https://doi.org/10.1007/s10586-021-03497-9>
5. Touati L, Challal Y (2015) Efficient CP-ABE attribute/key management for IoT applications. In: IEEE international conference on computer and information technology, Liverpool, United Kingdom
6. SO-FPSO-KM: Self-Organized Fuzzy Particle Swarm Optimization based Key Management Algorithm in MANET. *J Adv Res Dyn Control Syst* 10(03)
7. Gu H, Xu T, Potkonjak M (2016) An energy-efficient puf design: computing while racing. In: Proceedings of the 2016 international symposium on low power electronics and design. ACM, pp 142–147
8. Kaur I, Rao AL (2013) Adaptive group key management in mobile ad-hoc networks (MANETs). *Int J Comput Appl* 70(11):0975–8887
9. Gu H, Potkonjak M (2018) Securing interconnected PUF network with reconfigurability. In: 2018 IEEE international symposium on hardware oriented security and trust (HOST). IEEE
10. Renu SS, Energy efficient integrated framework for secure routing and key management in mobile ad-hoc networks. *Int J Eng Adv Technol (IJEAT)*. ISSN: 2249-8958
11. Mishra R, Sharma S, Agrawal R (2010) Vulnerabilities and security for ad-hoc networks. In: Proceedings IEEE international conference on networking and information technology, pp 192–196

12. Mohanta B, Jena D, Satapathy U, Patnaik S (2020) Survey on IoT security: challenges and solution using machine learning, artificial intelligence and blockchain technology. *Internet Things* 11:100227
13. Garg S, Aujla GS, Erbad A, Rodrigues JJ, Chen M, Wang X (2021) Guest editorial: blockchain envisioned drones: realizing 5g-enabled flying automation. *IEEE Netw* 35(1):16–19
14. Aujla GS, Singh M, Bose A, Kumar N, Han G, Buyya R (2020) Blocksdn: Blockchain-as-a-service for software defined networking in smart city applications. *IEEE Netw* 34(2):83–91
15. Alladi T, Chamola V, Sahu N, Guizani M (2020) Applications of blockchain in unmanned aerial vehicles: a review. *Veh Commun* 23(100249)
16. Mehta P, Gupta R, Tanwar S (2020) Blockchain envisioned UAV networks: challenges, solutions, and comparisons. *Comput Commun* 151:518–538
17. Dorri A, Steger M, Kanhere SS, Jurdak R (2017) Blockchain: a distributed solution to automotive security and privacy. *IEEE Commun Mag* 55(12):119–125
18. Dorri A, Kanhere SS, Jurdak R, Gauravaram P (2019) Lsb: a lightweight scalable blockchain for IoT security and anonymity. *J Parallel Distrib Comput* 134:180–197
19. Aggarwal S, Chaudhary R, Aujla GS, Kumar N, Choo K-KR, Zomaya AY (2019) Blockchain for smart communities: applications, challenges and opportunities. *J Netw Comput Appl* 144:13
20. Jindal A, Aujla GS, Kumar N, Villari M (2019) Guardian: blockchain-based secure demand response management in smart grid system. *IEEE Trans Serv Comput* 13:613
21. Xu C, Wang K, Li P, Guo S, Luo J, Ye B, Guo M (2018) Making big data open in edges: a resource-efficient blockchain-based approach. *IEEE Trans Parallel Distrib Syst* 30:870
22. Feng C, Yu K, Bashir AK, Al-Otaibi YD, Lu Y, Chen S, Zhang D (2021) Efficient and secure data sharing for 5g flying drones: a blockchain-enabled approach. *IEEE Netw* 35(1):130–137
23. Michelin R, Dorri A, Steger M, Lunardi R, Kanhere S, Jurdak R, Zorzo A (2018) Speedychain: a framework for decoupling data from blockchain for smart cities, pp 145–154
24. Ge C, Ma X, Liu Z (2020) A semi-autonomous distributed blockchain-based framework for UAVs system. *J Syst Arch* 107:101728
25. Allouch A, Cheikhrouhou O, Koubâa A, Toumi K, Khalgui M, Nguyen Gia T (2021) UTM-chain: blockchain-based secure unmanned traffic management for internet of drones. *Sensors* 21(9):3049
26. Kang J, Xiong Z, Niyato D, Ye D, Kim DI, Zhao J (2019) Toward secure blockchain-enabled internet of vehicles: optimizing consensus management using reputation and contract theory. *IEEE Trans Veh Technol* 68(3):2906–2920

Power Management of Drones



D. S. Vohra, P. K. Garg, and S. K. Ghosh

Abstract The Drones are used for multifarious activities right from surveillance, express shipping, precision crop monitoring, geographic mapping of inescapable terrain and locations etc. To perform effectively in ibid actions, the drones must keep flying for adequate time in the air. Flying for a longer duration is a necessity for many applications, which is primarily dependent upon the batteries they are using. The batteries which are normally used now-a-days in drones are Lithium Polymer (LiPo) batteries. These batteries are rechargeable and are available in various forms as per the size and use of drones. The longer sustenance of LiPo batteries depends on Voltage level, Capacity, Discharge rate, Activation time, and Charging time. Continuous power to drones is generally maintained by charging aforesaid LiPo batteries whenever Drone returns to earth/site. However, there are other options also to recharge the LiPo batteries, which avoid drones returning to their base. It includes using Polls, Recharging Stations, Solar Voltaic Cells based Drones. Moreover, there is an advanced methodology through which Drones can be recharged using other Drones while in flight. Apropos, this Paper will elaborate upon how to choose an appropriate LiPo Battery Pack based upon various parameters for Drones, Basic principle of working of LiPo batteries (i.e., Intercalation and De-Intercalation), Various forms/Configurations of LiPo batteries and Cell sizes, Maintenance of LiPo batteries and alternates to LiPo batteries for drones which include Charging stations, Charging Drones while on Flight and Use of Solar voltaic cells.

Keywords LiPo battery · Power management · De-intercalation · Discharge rate · Charging time

D. S. Vohra (✉)

Research Scholar, Department of Civil Engineering, Indian Institute of Technology (IIT) Roorkee, Roorkee, India

e-mail: ds_vohra@ce.iitr.ac.in

P. K. Garg · S. K. Ghosh

Department of Civil Engineering, Indian Institute of Technology Roorkee, Roorkee, India

e-mail: p.garg@ce.iitr.ac.in

S. K. Ghosh

e-mail: sanjay.ghosh@ce.iitr.ac.in

© The Author(s), under exclusive license to Springer Nature Switzerland AG 2023

555

K. Jain et al. (eds.), *Proceedings of UASG 2021: Wings 4 Sustainability*,

Lecture Notes in Civil Engineering 304,

https://doi.org/10.1007/978-3-031-19309-5_37

1 Introduction

Drones are used for diverse activities right from surveillance, express shipping, precision crop monitoring, geographic mapping of inaccessible terrain and locations [2, 3]. To perform effectively in ibid actions, the drones must keep flying for some time in air. Remaining in air for a good duration is therefore a necessity for drones. Their stay in air is totally dependent upon the batteries which they use. The batteries which are normally used now-a-days in drones are Lithium Polymer Batteries, also called as LiPo batteries.

The above-mentioned batteries are rechargeable. The options are to recharge them once the drone comes back to earth/platform or to recharge them using Polls/Recharging Stations. In addition, there are methods through which they can be recharged using other drones also while in flight.

2 Importance of Power Management

Power management is very important and need to be well understood before moving on for making drones for any kind of activity. It is the power which drives a drone. The drones get this power from its batteries. A powerful battery ensures that the drone flies faster, higher and stays in air for longer amount of duration. Drones are required to be in air for longer duration for better photography results. However, the weight of the battery increases with more power as more cells are needed to make it more powerful. Hence, there is a balance that needed to be established between weight and the time for which we want drone to stay in the air. Power management therefore plays a pivotal role in increasing the time flight of a drone. The various civilian and military application where we require drone to sustain in air for longer duration is given in succeeding paragraphs.

3 Applications

3.1 Civil Applications

The various civil applications in which drones are expected to fly for longer duration are given below [4, 7, 10, 12, 20, 21]:

- Providing wireless coverage
- Inspection of power lines
- Counting wildlife
- Delivering medical supplies to inaccessible regions
- Forest fire detection and monitoring

- Humanitarian aid
- Landslide measurement
- Illegal landfill detection
- Construction
- Crowd monitoring
- Crop surveying
- Agriculture insurance
- Soil examination
- Irrigation monitoring
- Inspection of airports
- Urban planning
- Campus monitoring
- Contour detection
- Boundary extraction from images.

3.2 Military Applications

The various military applications (throughout the globe) in which drones are expected to fly for longer duration are given below [18]:

- Real-time monitoring
- Surveillance
- Patrolling
- Demining
- Natural disaster management including landslides
- Convoy protection
- Landslide investigation
- Search and rescue.

4 General Classification of Drone/UAVs

The general classification of drones based on different types, range and endurance is enunciated in Table 1.

5 Management of Power in Drone

The maximum power that is consumed in a quadcopter is by the propeller and the motors. The motors which are used in drones must be brushless motors so that the motors take less power. In addition, the propellers are to be designed in such a way, so that with less power more sustenance in the air is possible.

Table 1 Classification of drones [6]

Category	Type	Range (km)	Endurance	Usage
Group 1	Very close range	5	20–45 min	Reconnaissance
Group 2	Close range	50	1–6 h	Reconnaissance
Group 3	Short range	150	8–12 h	Reconnaissance & surveillance
Group 4	Mid-range	650	12–24 h	Reconnaissance & surveillance
Group 5	Endurance	>650	>24 h	Reconnaissance & surveillance

In addition, it is also important that the appropriate battery is used post calculating the entire power requirement by the drone and the weight it is going to lift. The users should not use a battery that is of higher amperage or less amperage. The flight controller also takes a good amount of current. So, if a drone is used for less work, least number of sensors are required and consequently, a specific flight controller, which is referred to as the brain of the drone, for fulfilling the sensor requirement to be used.

6 Choosing a Battery Pack for Drones

Choosing the correct battery is very important while provisioning for the power of drones. Presently the batteries which are used in Drones are LiPo batteries. The main parameters to check while identifying suitable LiPo batteries for Drones are given below.

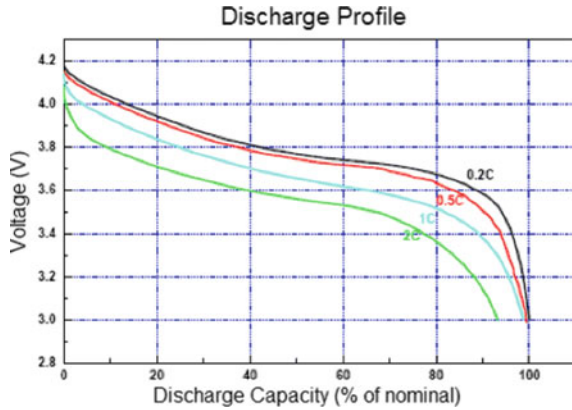
6.1 Voltage Level

The nominal voltage for LiPo battery is 3.7 V whereas maximum voltage, they can acquire is 4.2 V. However, their voltage can drop down to 3.0 V too, but that condition must be avoided each and every-time. The LiPo battery showing a nominal voltage is enunciated in Fig. 1.

Fig. 1 LiPo battery showing nominal voltage (3.7 V).
 Courtesy <https://learn.adafruit.com/assets/979>



Fig. 2 Discharge capacity versus voltage. *Courtesy* <https://learn.adafruit.com/assets/979>



For example, Fig. 2 shows how a voltage drops from maximum voltage to 3.0 V where the circuitry gets automatically cut off. At 3.4 V, the battery starts showing sign that it requires a recharge.

6.2 Capacity

It is measured in Mili Ampere Hour (mAh). It means how much current can be acquired from the battery at a fixed rate of some amperes in total one hour. For example, 1000 mAh is equivalent to 1 Amp Hour as shown in Eq. (1).

$$1000 \text{ mAh} = 1 \text{ Ah} \quad (1)$$

This also means how much time after we need to recharge the battery. The greater the capacity, the more time it will keep the equipment running. In the context of drones, 5000 mAh LiPo battery is generally used. There are companies who make batteries of larger size, but the grey area is, that the overall weight of the drone will increase. The lifting power of a drone will therefore get restricted if we use batteries of higher weight.

In addition, the temperature of the motor must be checked at regular intervals, otherwise, there are chances of the battery getting burnt and ultimately the machine which is running via such over exhausted LiPo batteries. Voltage is easy to measure in comparison of capacity. Voltage is always measured in Voltage and has a direct relation with other important parameters. Voltage is like a water in a transparent beaker which is easily measured. However, beaker, which is opaque in nature, refers to capacity. The only way to measure it to empty the beaker.

6.3 Discharge Rate

It is the rate of discharge of current from battery. The discharge rate is harder to understand in comparison of voltage and capacity. The discharge rating is also called a C rating. It is measure of what is the maximum rate in which a voltage can be discharged from the batteries without the batteries being damaged. It is also known as the safe current that can be drawn from a battery. C refers to discharge rate. The maximum safe current that can be drawn from a battery can be calculated from the Eqs. (2) and (3)

$$50C = 50 \times \text{Safe Current in Amperes or Capacity, C} \quad (2)$$

The C rating can be calculated as given in Eq. (3)

$$50 \times 5A \text{ (for battery of 5 A)} = 250A \quad (3)$$

Therefore, battery can sustain a maximum load of 250 A. A current higher than this will lead to damage of the battery. The battery can even burst into flames. The battery has two ratings; one is a continuous rating and the second is a burst rating. The burst rating is applicable in ten (10) second bursts and not continuously as in continuous rating. The burst rating will come in handy when we need to accelerate a vehicle. For normal working, we do not consider burst rating. The burst rating of a battery is always greater than the continuous rating. The battery discharge rate is always measured in terms of continuous rate and not burst rate. To come on to, which C rating is better, is a question that is very hard to answer. We should either consider the C-rating which is required or consider burst rating also. For example.

A user wants to purchase Slash VXL R/C truck. It works on a continuous current 65 A and a burst current of 100 A. Therefore, a 2S 5000mAh 20C LiPo will be adequate to meet the requirement. It has a maximum safe current discharge of $20 \times 5 \text{ A} (=5000 \text{ mA})$ i.e., 100 A which is higher than 65 A and equivalent to 100 A. The terrain in which the R/C truck must operate, and the speed in which it must operate also plays a pivotal role in deciding the battery. It is very much possible that the final requirement of current is higher than the requirement of the battery alone. So, a cushion is always required and need to be maintained for the exact magnitude of current that is required out of that battery. A battery of more than 200 C suits maximum applications. But if we are driving a heavy R/C truck, we must have a 400 C battery pack. In addition, there are other factors too that influence battery selection. Same are given in succeeding Paragraphs.

Actual ampere required by a drone is the summation of current required for propellers and motors, flight controller and other sensors if fixed over drone. For example, if a motor draws 9 A of current continuously at a rate of 65% of power, and as quadcopter has four brushless motors so 9 times 4 which is equal to 36. Hence, 36 A current is drawn from the battery. Moreover, $(36 * 1000)$ divided by 60 min = 600 mAh is consumed per minute by the quadcopter. If user buys a 9000 mAh battery

for the quadcopter, then $9000/600 = 15$ min of 65% continuous power usage will be provided by the battery to the drone. For information about safe ampere which can be drawn from the battery, refer to Eqs. (2) and (3).

6.4 Activation Time

Activation cycles to be strictly adhered to for recharging of batteries. The voltage of the battery should not go below 3.0 V in any case at any single instance. The battery behaves normally if the battery is always sustained at a voltage level of 3.0 V or above.

6.5 Charging Time

Battery capacity and charging capacity must be known if needed to calculate the charging time. If a battery is of 1500 mA_H and a 1 Amp Hour charger is available to charge the battery, then charging time can be calculated as in Eq. (4).

$$1.5\text{Ah}/1\text{Ah} = 1.5 \text{ h} \tag{4}$$

6.6 Lifespan

Life of a LiPo battery can be elongated if we adhere to the basics required for the smooth working of the ibid battery. The life of a LiPo battery generally comes out to be two years [13]. The following practices need to be adhered to if the battery's lifespan needs to be increased.

- Never discharge a battery below 3.0 V.
- Never overcharge above 4.2 V.
- Never discharge a battery a rate not specifically used for it.
- Never overheat batteries.
- Discharge LiPo battery in a LiPo Discharge Bags, as meant for them. Dispose them accordingly after full discharge.

6.7 Cost

The cost of a battery also plays a pivotal role for a user, as some batteries are of better quality, but their rates are very high. The cost of a LiPo battery ranges from Rs. 400 to Rs. 2500. These batteries can easily be ordered through Flipkart or Amazon in India.

7 Principle of Working of LiPo Battery

The LiPo batteries work on the concept of intercalation and de-intercalation. Lithium ions become a positive electrode material and a negative electrode material, The liquid electrolyte becomes the conductive medium in LiPo battery. A microporous separator lies between the electrodes, which makes ions migrate from each side. Electrolyte is a polymer and not a liquid electrolyte. Higher specific energy is being provided by these batteries [19]. The intercalation and deintercalation procedure are elucidated in succeeding Paragraphs.

7.1 Intercalation

The positive electrode turns into an anode, and the negative electrode turns into a cathode during charge. The lithium-oxide electrode becomes the positive electrode. During charge, oxidation at the anode produces positively charged and negatively charged electrons. The uncharged material, produced during oxidation, stays at the anode. Ions move through the electrolyte whereas the electrons move through the external circuit. Recombination occurs at the cathode during reduction half-reaction. Conductive media is provided by electrolyte and conducting media.

7.2 Deintercalation

The electrons flow from anode to cathode via an external circuit. It discharges the potential of the cell of the LiPo battery. During charge, electrons move from the cathode to the anode via an external circuit. This energy acquired from the charging cycle is transformed as chemical energy in the cell of LiPo battery. Cathode and anode allow the Li ions to move in and out through a process called insertion or intercalation and extraction or deintercalation respectively, as elucidated in Fig. 3. These batteries are also called “rocking-chair batteries” or “swing batteries as Lithium ions rock back and forth”.

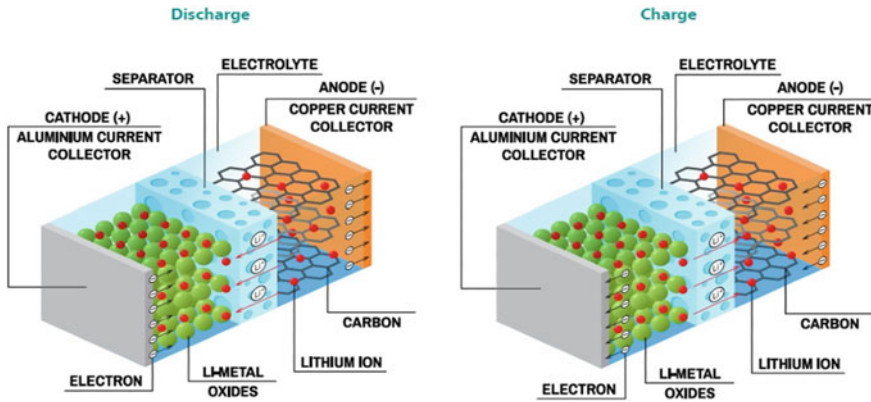


Fig. 3 Intercalation and de-intercalation [19]

In the discharge cycle, lithium ions carry the current within the battery from anode to cathode, through the electrolyte and microporous separator diaphragm. The loss of energy from contact resistance at interfaces of electrodes is equal to twenty percent of the total energy flow in batteries. The single Li Cell is charged in two stages viz., Constant current (CC) and Constant Voltage (CV) whereas as a Li-ion battery (a set of Li-ion cells in series) is charged in three stages as Constant Current, Balance and Constant voltage. In the CC phase, constant current is applied to the battery till the highest voltage per cell is reached. In the Balance Phase, the charging current is reduced. This stage can be skipped by some chargers also. In the CV phase, a voltage equal to the maximum cell voltage multiplied by the number of cells in series per battery is applied.

8 Various Forms/Configurations of LiPo Batteries and Cell Sizes

Battery consists of many rectangular cells where each cell holds a charge of 3.7 V. If the cells are connected in series, the voltage becomes double of 3.7 V i.e., 7.4 V, if two cells are connected. Whereas if the capacity of the battery needs to be increased, then the cells are to be connected in parallel. 3S2P means two cells in series and two cells in parallel in a battery. More voltage means higher power to drive the cells of a battery. For more power, the battery capacity needs to be increased.

8.1 Battery Voltage

One LiPo cell has a voltage of 3.7 V. 14.8 V battery means four cells are connected in series. A battery of 4S means there are 4 cells in series. So, a four-cell (4S) pack is 14.8 V, a three-cell (3S) pack is 11.1 V, and so on.

$$3.7 \text{ V battery equals One cell} \times 3.7 \text{ V} = 1\text{S battery} \quad (5)$$

$$7.4 \text{ V battery equals Two cells} \times 3.7 \text{ V} = 2\text{S battery} \quad (6)$$

$$11.1 \text{ V battery equals Three cells} \times 3.7 \text{ V} = 3\text{S battery} \quad (7)$$

$$14.8 \text{ V battery equals Four cells} \times 3.7 \text{ V} = 4\text{S battery} \quad (8)$$

$$18.5 \text{ V battery equals Five cells} \times 3.7 \text{ V} = 5\text{S battery} \quad (9)$$

$$22.2 \text{ V battery equals Six cells} \times 3.7 \text{ V} = 6\text{S battery} \quad (10)$$

$$29.6 \text{ V battery equals Eight cells} \times 3.7 \text{ V} = 8\text{S battery} \quad (11)$$

$$37.0 \text{ V battery equals Ten cells} \times 3.7 \text{ V} = 10\text{S battery} \quad (12)$$

$$44.4 \text{ V battery equals Twelve cells} \times 3.7 \text{ V} = 12\text{S battery} \quad (13)$$

The voltage determines the sustenance of drone in the air. It affects the RPM of the brushless motor. A brushless motor of 2,500 kV, that motor will spin 2,500 RPM for per volt application. More voltage means faster is the Drone [1]. While selecting the battery, the current requirement needs to be understood. Voltage affects the motor speed too. Voltage is directly proportional to the power of the motor as given in Eq. (14).

$$X = V * A \quad (14)$$

where X refers to power, V refers to voltage, A refers to current. So, in case of some hobbyists who are keen to run their machines with greater speed need to have higher voltage. The total current drawn can be calculated by the formula as given in Eq. (15).

$$\begin{aligned} \text{Max Current Drawn } (I) &= \text{Capacity (Amp hour)} \\ &\times \text{Rate of discharge } (C) \end{aligned} \quad (15)$$

For example, Max current is drawn for 4100 mAh three cell LiPo battery, 10 C rating can be calculated as $4.1 \times 10 = 41 \text{ A}$.

9 Maintenance of Lipo Battery

Maintenance of a battery, if properly done, gives us additional time for drones to fly in the air. Moreover, the same battery can be used multiple times. In respect of the same, certain precautionary measures to be adhered to are covered in succeeding paragraphs so that more are available from the same battery.

9.1 Charging

Precautions to be observed during charging of LiPo battery are elucidated below.

1. Never use Nickel Cadmium (NiCd) or Lead Acid Charger. Use LiPo charger only and select LiPo mode in that.
2. Charge the battery in an open area away from materials that can catch fire.
3. Batteries are not to be charged inside of the model.
4. Do not charge batteries below zero degrees i.e., freezing temperature.
5. Do not charge batteries, if cells are hot from inside.
6. Put the charger on proper cells count.

9.2 Discharging

Precautions to be observed during discharging of LiPo battery are elucidated below.

1. Do not discharge battery at higher discharge rates.
2. Temperature of battery should not increase by 140° .
3. Batteries should never be discharged below 3.0 V.
4. The recommended cut-off is 3.4 V
5. User should constantly monitor the discharging process.
6. In case of an untoward accident, remove the battery for one hour.
7. User must check the physical condition of the battery before discharging the battery.

10 Alternatives to Lipo Batteries

The LiPo batteries are those batteries that are used the most in all types of rotor Drones. This paper, therefore, focuses on LiPo batteries as the advantages of LiPo batteries on Lithium-Ion batteries and Nickel Cadmium batteries are much more. The alternatives of LiPo batteries are discussed in the succeeding paragraphs. The alternatives are those areas that are also being researched throughout the world. These methods have one great advantage over LiPo powered Drones as they can provide power for longer times and in some cases, Drone does not have to return to the ground for recharging itself.

10.1 Charging Stations

Drones, instead of coming back to start, they can also recharge through various charging stations which can come in their path. The Drones automatically land on these platforms, do recharging of the diffused battery, and again carry on with their tasks [16].

The charging station is a pole or a platform (Fig. 4) that is specifically made for providing power to Drones. It increases the sustenance of Drones in air as Drones do not have to come back to earth stations [11]. The charging station consists of the following elements broadly:

- A charging system for Drones has a base structure connected to a power grid.
- A connector extendable from the base structure.
- Charging interface compatible with a charging port of a Drone.
- A computerized controller at the base structure enabled to communicate with a Drone.
- To initiate, control and stop charging power.

There are problems associated with charging poles or platforms, in the form of installation, charging, security, ownership, battery allocation and online management [8]. There are other problems in relation with locating the ibid charging stations too, as the charging stations may have many drones or have less drones.

10.2 Charging While on Flight

Drones can be charged while on a flight using other drones. In such cases, a small drone carries a battery, and it lands over the bigger Drone which required power to remain afloat (Fig. 5) [5, 14]. Docking platform is attached to the main flyer drone. A flying Drone, smaller in stature will rest on this docking platform [9] (Fig. 6).

Fig. 4 Charging station (pole) [14]

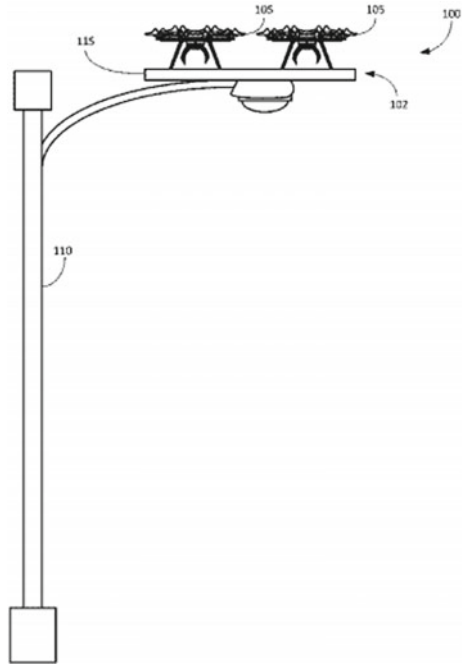


Fig. 5 Charging while on flight [8]



10.3 Solar Batteries

Solar batteries use sunlight to power the cells of the battery, which will help in providing continuous power supply to the drones. This will help the Drones in extended sustenance in air and the Drone will not have to return to the ground for recharging itself. As the solar power is easily available and is a renewable source of energy. Drones can easily use the sunlight. Solar voltaic cells are used in abundance in such scenario. Solar voltaic cells have power which is greater than 550 W/Kg

Fig. 6 Drones using solar batteries [16]



or 1.5 MJ/Kg if used in sunlight (full). The energy density of solar batteries is on a higher side in comparison to normal batteries. The problem comes as they never operate at their full efficiency [17].

11 Conclusion

The appropriate management of power in drones is the key towards longer sustenance of Drones in air for various applications. The LiPo batteries are the best batteries which provide power to the Drones in current scenario. It is therefore of paramount importance to understand the characteristics and proper use of these batteries. However, there are other alternatives to these LiPo batteries viz., Charging Stations (Poles), Solar Cells in Drones and Charging Drones while on flight, which can be used to keep Drones flying in air for longer durations. This will help in all civil and military applications (as covered above) where Drones are required to stay in air for longer duration. Based on literature review, being carried out and knowing the recent research in respect of power management of Drones, it can be concluded that either LiPo batteries need to be evolved or charging stations or charging the Drones while in flight need to be more researched. The ibid subject is still at nascent stage and lot of development for continuous power to Drones is still required to be done as Drones are the future technology and their demands in various civilian and military fields are increasing on an exponential scale [15].

References

1. Ali R, Mohammed R, Muhammad T, Kim SH (2018) Development of intelligent drone battery charging system based on wireless power transmission. MDPI J Appl Syst 1(44)
2. Bürkle A (2009) Collaborating miniature drones for surveillance and reconnaissance. In: Proceedings of the SPIE 7480, unmanned/unattended sensors and sensor networks VI, 74800H. <https://doi.org/10.1117/12.830408>

3. Cai G, Jorge D, Lakmal S (2014) A survey of small-scale unmanned aerial vehicles: recent advances and future development trends. *J Unmanned Syst* 2(2):175–199. <https://doi.org/10.1142/S2301385014300017>
4. Crommelinck S, Bennett R, Gerke M, Yang MY, Vosselman G (2017) Contour detection for UAV-based cadastral mapping. *J Indian Soc Remote Sens*
5. Fujii K, Higuchi K, Rekimoto J (2013) Endless flyer: a continuous flying drone with automatic battery replacement. In: *IEEE 10th international conference on ubiquitous intelligence & computing*
6. Hassanalian M, Abdelkefi A (2017) Classifications, applications, and design challenges of drones: a review. *Prog Aerosp Sci* 91:99–131. <https://doi.org/10.1016/j.paerosci.2017.04.003>
7. Hayat S, Yanmaz E, Muzaffar R (2016) Survey on unmanned aerial vehicle networks for civil applications. *IEEE Commun Surv Tutor* 18(4):2624–2661
8. Huang H, Savkin AV (2020) A method of optimized deployment of charging stations for drone delivery. *IEEE Trans Transp Electrif* 6(2)
9. Jain KP, Mueller MW (2020) Flying batteries: in-flight battery switching to increase multirotor flight time. In: *IEEE international conference on robotics and automation (ICRA)*
10. Jun N, Lili Y, Jingchao Z, Weixing C, Yan Z, Xiuxiang T (2017) Development of an unmanned aerial vehicle-borne crop-growth monitoring system. *Sensors* 17:502–525. <https://doi.org/10.3390%2Fs17030502>
11. Kemal N, Chowdhary G, How JP, Vavrina MA, Vian J (2015) An automated battery management system to enable persistent missions with multiple aerial vehicles. *IEEE Trans Mechatron* 20(1)
12. Khadanga G, Jain K (2021) Cadastral parcel boundary extraction from UAV images. *J Indian Soc Remote Sens* 49(3):593–599
13. Kumbhar A, Koohifar F, Guvenc I, Mueller B (2017) A survey on legacy and emerging technologies for public safety communications. *IEEE Commun Surv Tutor* 19:97–124
14. Lee D, Zhou J, Lin WT (2015) Automated battery swapping system for quadcopter. In: *IEEE international conference on unmanned aircraft systems (ICUAS)*
15. Motlagh NH, Taleb T, Arouk O (2016) Low-altitude unmanned aerial vehicles-based internet of things services: comprehensive survey and future perspectives. *IEEE Internet Things J* 3(6):899–922
16. Raciti A, Rizo SA, Susinni G (2018) Drone charging stations over the buildings based on a wireless power transfer system. In: *IEEE/IAS industrial and commercial power systems technical conference (ICPS)*
17. Ranquist EA, Steiner CM, Argrow B (2016) Exploring the range of weather impacts on UAS operations. *J Natl Center Atmosp Res (NCAR)* (Boulder, Colorado)
18. Scherer J, Yahyanejad S, Hayat S, Yanmaz E, Andre T, Khan A, Rinner B (2015) An autonomous multi-UAV system for search and rescue. In: *Proceedings of the first workshop on micro aerial vehicle networks, systems, and applications for civilian use*, pp 33–38
19. Shah FA, Sheikh SS, Mir UI, Akhtar S (2019) Battery health monitoring for lithium-ion batteries. In: *International conference on power generation systems renewable energy technologies (PGSRET)*
20. Shukla A, Jain K (2020) Automatic extraction of urban land information from unmanned aerial vehicle (UAV) data. *Earth Sci Inf* 13(4):1225–1236
21. Tiwari A, Sharma SK, Dixit A, Mishra V (2021) UAV remote sensing for campus monitoring: a comparative evaluation of nearest neighbor and rule-based classification. *J Indian Soc Remote Sens* 49(3):527–539

Technology for Power Supply to UAVs through Medium of Air



Devineni Pavan and Merugu Suresh

Abstract In recent years, as the usage of drones is increased, the batteries of the drones play a vital role in their function. At the same time, though the capacity of the drone battery has been increasing it is not sufficient for many multiple functioning of drones. Moreover, the current technology of drones is used for taking pictures. If there is sufficient energy for drones, they can be used for many multiple functions. In this paper, a new process has been introduced in which the drone batteries are charged through the waves transmitted by the device affixed to a tower, where the tower is used as a source of medium. The receiver chip is affixed to the battery of drones which receives the waves from farther distances and converts them to DC. In this process, series resonance is used in the transmitter device to get the waves and is amplified to get the desired output. The output is transmitted through directional antennas, for overall 36° . These transmitted waves will be received by the receiving chip by filtering the noise and converted to DC (Power supply for batteries of electronic gadgets). The result of this method is that it revolutionizes drone technology because if there are sufficient energy drones can be used for multiple functions.

Keywords Transmitter device · Receiving module · Printed circuit board · Drone · Antenna

D. Pavan (✉) · M. Suresh
Department of Electronics Communication Engineering, CMR College of Engineering & Technology, Hyderabad, Telangana, India

M. Suresh
e-mail: msuresh@cmrcet.org

© The Author(s), under exclusive license to Springer Nature Switzerland AG 2023
K. Jain et al. (eds.), *Proceedings of UASG 2021: Wings 4 Sustainability*,
Lecture Notes in Civil Engineering 304,
https://doi.org/10.1007/978-3-031-19309-5_38

571

1 Introduction

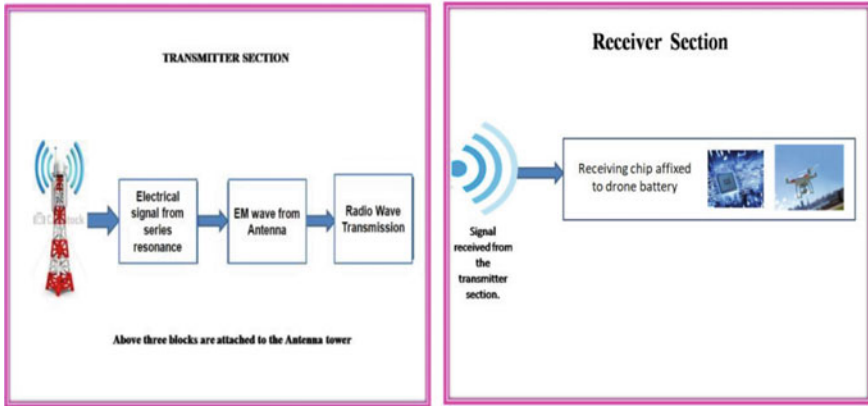
Drones are commonly known as Unmanned Aerial Vehicles (UAVs) used in the military. 90% of the drone applications are found in the military. With an increase in industrial growth, drones find their market in a wide variety of applications for monitoring gas and oil operators. UAVs are also used for monitoring natural calamities like volcanic [1], earthquakes, etc. UAVs are also used in the operation of surveillance, radio access, communications, and commercial purposes [2–6]. As applications of UAVs are increasing in many fields, there is a need to improve the battery lifetime of drones. However, battery capacity is severely restricted due to constraints on the size and weight of drones and also the battery can be easily drained due to more power consumption with increased applications. Drones can be operated for a long time by providing wireless charging technology. Wireless charging is a technology of transmitting power through an air gap to electrical devices for energy replenishment. It involves a power transmitting device and a receiver, sometimes in the form of a case attached to the drone or even built into the drone itself [7, 8].

Drones used in commercial applications operate for less than 20 min which deepens the need for wireless charging of drones to operate them continuously. Traditional charging methods require the drones to be placed at an exact location in the charging stations to get charged wirelessly. Therefore, a new wireless technique is needed to charge the drones irrespective of their position in the stations that provide charging and also to charge drones in a way that they are in the vicinity of stations to provide wireless charging.

This paper focuses on wireless power transfer using electromagnetic (EM) energy specifically Radio frequency (RF) waves. The radio wave is ubiquitous in our daily lives in form of signal transmission from TV, Radio, Wireless LAN, mobile phones, etc. [8]. This paper represents the system overview in Sect. 2 and series resonance in Sect. 3. The working process is represented in Sect. 4. Section 5 represents the overall output representing the distance of wireless power supply and rate of power received at the receiver part for electronic gadgets. Sections 6 and 7 represent the future and conclusion of the paper.

2 System Overview

Overview of System Design



The above block diagram represents the transmitter and receiver sections. The transmitter device generates the power in the form of electrical waves through a process known as series resonance. The electrical energy is converted to electromagnetic energy through transmit antenna and is transmitted as radio waves. At the receiver section, the waves generated from the transmitter section are received and then converted to electrical waves through the receiver antenna. The electrical waves are converted to DC providing a power supply to the battery of drones. The receiver chip is affixed within the drone, connected to its battery. The receiver chip consists of a GPS module that helps to trace the drone through the location of the tower, by which the drones are charged. Figure 1 represents the microstrip antenna which receives RF waves at the receiving end and converts them to electrical waves.

3 Series Resonance

Series resonance is a condition that usually occurs in series circuits, where the current becomes a maximum when the capacitor and inductor reactance are the same. In series resonance, maximum current is obtained at the resonant frequency. In a series RLC circuit, a frequency point occurs where the inductive reactance of the inductor becomes equal in value to the capacitive reactance of the capacitor. In other words, $X_L = X_C$. The frequency at which resonance occurs is called the Resonant Frequency (f_0) of the circuit, and as we are analyzing a series R-L-C circuit, a series resonance is produced at this resonance frequency. One of the most important circuits used in electrical and electronic circuits is Series Resonance circuits. These circuits can be

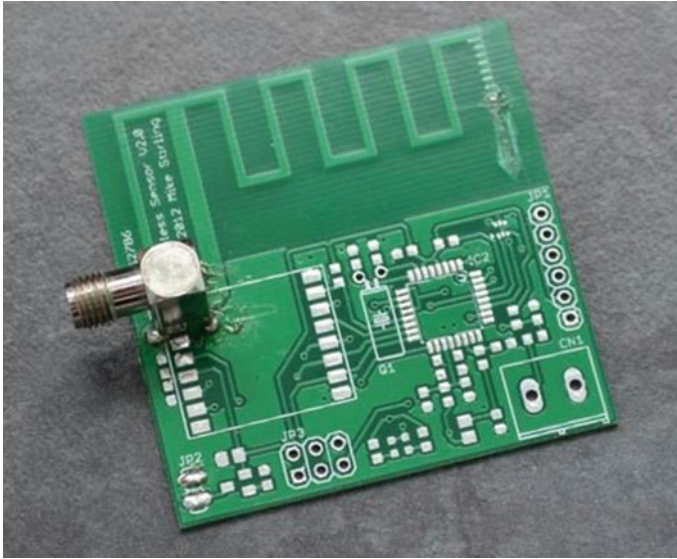


Fig. 1 Micro-strip antenna

found in various forms such as in noise filters, A.C mains filters in television and radio tuning circuits providing a selective tuning circuit for receiving channels with different frequencies.

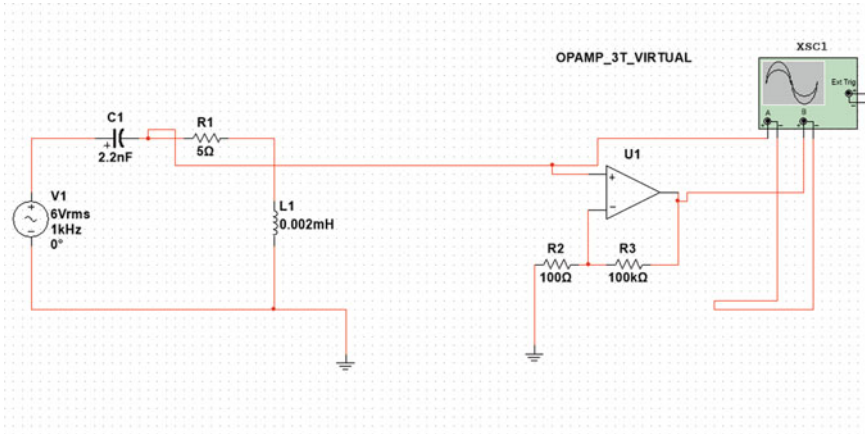
We know about R-L-C circuits: i. inductive reactance i.e. $X_L (X_L = \omega L = 2f\pi L)$.
ii. Capacitive Reactance i.e. $(X_C = 1/\omega C = 1/2f\pi C)$. The output is taken at the resistor from the circuit. The input given to the series resonance is from the transformer of six volts. The components required for a series resonance circuit are:

Capacitor: 2.2 nF

Resistor: 5 Ω Inductor: 0.002 mH

AC power supply of six volts.

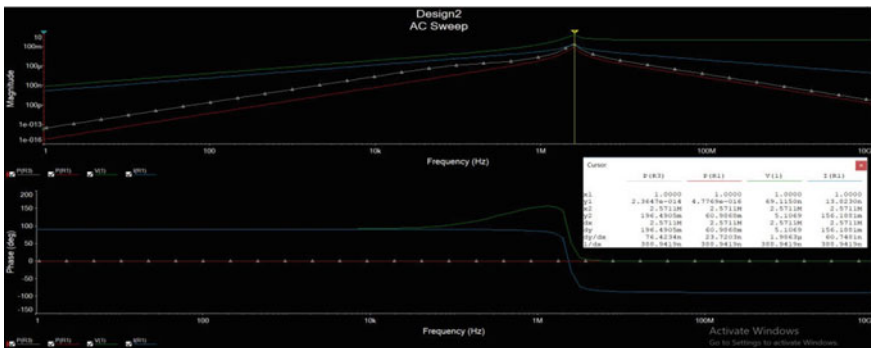
Op-amp feedback resistors: 100 Ω , 100 Ω .



The above figure represents the Series resonance circuit design that should be embedded into the transmitter device.

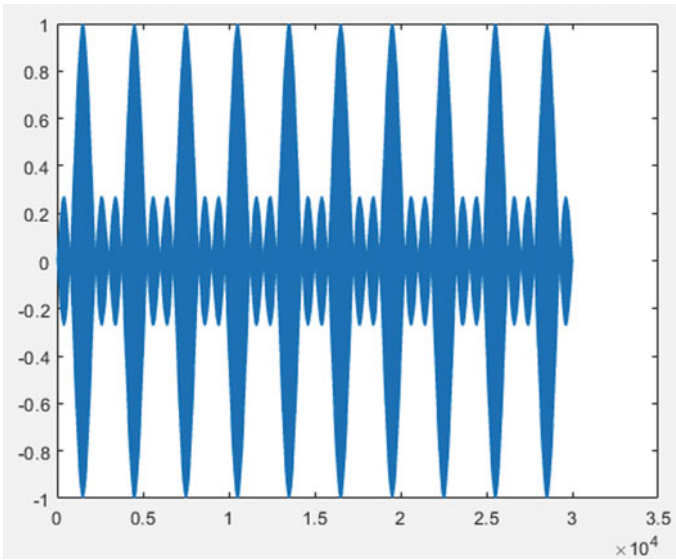
Related Work

The work includes the designing of the circuit and testing the output of series resonance i.e. voltage of series resonance. The time domain output radio wave of AM modulator from the transmit antenna and also which is mentioned in detail in the next pages. The below figure represents the output waveform of the series resonance from resistor output in MultiSim.



From the above simulation picture, it is shown that the output voltage of the series resonance is 5.10. As the frequency of the electrical wave obtained from the series resonance circuit is i.e. 1 kHz, we modulate the electrical wave by multiplying it with an oscillator with a carrier frequency of 2.5 MHz. The modulator allows the transmit antenna size to be less and transmission of signal with less interference. After modulation, the received signal frequency is reduced to a charging frequency (Range: 80–300 kHz) using a frequency divider and is received using a bandpass filter in the charging signal frequency range.

The below figure represents the time domain output radio wave of AM modulator from the transmit antenna in Matlab.



After modulation, the high-frequency components (3.001 and 2.999 MHz) received at the receiver antenna are converted to a charging frequency range using a frequency divider by 10, 16, etc. and then the wave is applied to a band pass filter and converted to DC.

4 Working Process

The process consists of a series resonance that transfers the output from the given input of six volts. After the functioning of the series resonance from the inputs as a resistor, capacitor and inductor the output frequency from the process is three MHz. The power at the resistor in the transmitter section is represented as P (T) i.e.

$$P (T) = 196.405 \text{ mW}$$

$$\text{Output Frequency} = 2.5 \text{ MHz.}$$

$$P(R) = P (T) * G (T) * G(R) * \lambda^2 / (4 * \pi * R)^2.$$

Where $\lambda = C/F$.

From the above equation P (T) represents the power at the transmitter section and G (T) & G(R) represent the gain at Transmitter and receiver. P(R) represents the received power.

$$P(R) = 196.405 \times 10^{-3} * 1.64^2 * 100^2 / (4 * 3.14 * 50)^2.$$

Where $\lambda = 3 \times 10^8 / 3 \times 10^6 = 100 \text{ m}$.

$$P(R) = 13.4 \text{ mW}.$$

From the above calculations the output from the transmitter section and the receiver section is solved. The waves are transmitted through directional antennas for 360° to the receiver. From the series resonance circuit, the output from the resistor is converted to waveforms and transferred wirelessly through an antenna and the receiver antenna receives the RF signal and converts it to the electricity required for the drones. Therefore the distance between the Transmitter and receiver is 50 m where the transmitted waves are received by the receiver which is affixed to the battery of drones.

5 Future Trends and Challenges

So far, this paper has addressed the wireless charging technologies, with an emphasis on those adopted by the WPC. Wireless charging for drones up to 5 W, which makes it a suitable technology to cover wireless charging for a wide range of low-power products such as mobile phones, iPods, Bluetooth earpieces, etc. It is envisaged that future standards will extend the power capability to 120 W so that more portable devices such as iPods and notebook computers can be covered. With the increasing amount of wireless power, several technical challenges will arise, namely thermal, electromagnetic compatibility (EMC), and electromagnetic field (EMF) problems etc. Further GPS will be affixed to the receiver of the drones to trace them, from the process as, the tower from which the drones are receiving charging, therefore from the location of the tower and from the location of the receiver which will be affixed to the battery of drones will be traced.

6 Conclusion

The commercialization of drones in the 1910s has clearly sped up the research and development activities in wireless charging systems. In this paper, the historical developments of wireless power transfer technologies for drones have been described. The power generated from the series resonance is addressed in terms of frequency. The circuit diagram and the simulation output of the series resonance are described. The conversion and transmission of the series resonance output frequency are shown and the receiving process of frequency and its conversion of electricity to the battery of drones is described. The calculations and waveforms for both transmission and receiver are shown. In theory, the evolution of wireless power supply systems and features of drones for the usage of their batteries was shown and wireless power supply can be incorporated into different drones. Therefore this revolutionizes the

present mode of charging and reduces the time spent on charging the drones and more wireless power systems and products are expected to enter the consumer markets soon.

Appendix

The code for AM modulation in Matlab is given by

```
fp = 10^3;           %low frequency electrical signal
fc = 3*10^6;        %Carrier signal
fs = 2*(fc+(2*fp)); %Sampling frequency
t = 0:1/fs: 0.005;
x = sin(2*pi*fp*t);
y = ammod(x,fc,fs); %AM Modulator
figure(1)
plot(y)
```

References

1. Lu M, Bagheri M, James AP, Phung T (2018) IEEE, wireless charging techniques for UAVs: a review, reconceptualization, and extension
2. Astuti G, Giudice G, Longo D, Melita CD, Muscato G, Orlando A (2009) An overview of the 'volcan project': an UAS for exploration of volcanic environments. *J Intell Robot Syst Theory Appl* 54(1-3):471-494
3. Waharte S, Trigoni N, Julier SJ (2009) Coordinated search with a swarm of UAVs. In: 2009 6th IEEE annual communications society conference on sensor, mesh and ad hoc communications and networks workshops, vol 0, no c, pp 1-3
4. Nikolic J, Burri M, Rehder J, Leutenegger S, Huerzeler C, Siegwart R (2013) A UAV system for inspection of industrial facilities. In: 2013 IEEE aerospace conference, pp 1-8
5. Ryan A, Zennaro M, Howell A, Sengupta R, Hedrick JK (2004) An overview of emerging results in cooperative UAV control. In: 2004 43rd IEEE conference on decision and control (CDC) (IEEE Cat. No.04CH37601), vol 1, pp 602-607
6. Wan S, Lu J, Fan P, Letaief KB (2017) To smart city: public safety network design for emergency. *IEEE Access*, 1-1
7. Sang-Won K, In-Kui C, Sung-Yong H (2017) Comparison of charging region differences according to receiver structure in drone wireless charging system. *IEEE*. 978-1-5090-4032-2
8. Lienhard JH (1983) Boss Ket's pilotless 'buzz-bomb'. *Automotive News*, GM 75th Anniversary Issue

An Efficient Application of Machine Learning for Assessment of Terrain 3D Information Using Drone Data



Ankush Agarwal, Aradhya Saini, Sandeep Kumar, and Dharmendra Singh

Abstract Plant height is beneficial in defence-related applications during the movement of troops as terrain information is required in advance. This terrain information is of utmost importance to obtain knowledge about possible paths especially in unexplored areas. This information facilitates safe movement of troops. While exploring an unexplored area, vegetation cover area need to be checked carefully, because of the tall and dense bushes. During vegetation monitoring various parameters like plant growth, soil moisture, water availability, the need for fertilizers, etc. are observed. All these parameters are necessarily checked to monitor the growth of the plant. The plant growth parameter is reflected from the plant height. In the modern era, smart farming and precision agriculture have been applied, in which monitoring of plant growth-related parameters are optimized and the necessity of any parameter is fulfilled as per the demand and position in the field. In the extension of smart agriculture, the need for the usage of drones arises while monitoring the fields. Drones provide good spatial resolution and can be flown according to the need and application. In this work, the objective is to calculate the plant height using a drone in order to ensure safe troops movement and on other side to monitor the healthy growth of the plant. The application can be helpful for defense as well as civilian purpose. For achieving this, a machine learning-based model has been proposed in which multiple ground control points (GCPs) of different heights have been used to train the model, which results in minimizing the output error. The challenge is to get drone data and manually recorded GCPs height correctly so that the training can be accomplished successfully for better results.

A. Agarwal (✉) · S. Kumar

Department of Computer Science and Engineering, Indian Institute of Technology Roorkee, Roorkee, Uttarakhand 247667, India

S. Kumar

e-mail: sgargfec@iitr.ac.in

A. Saini · D. Singh

Department of Electronics and Communication Engineering, Indian Institute of Technology Roorkee, Roorkee, Uttarakhand 247667, India

e-mail: dharm@ec.iitr.ac.in

© The Author(s), under exclusive license to Springer Nature Switzerland AG 2023

K. Jain et al. (eds.), *Proceedings of UASG 2021: Wings 4 Sustainability*,

Lecture Notes in Civil Engineering 304,

https://doi.org/10.1007/978-3-031-19309-5_39

Keywords Crop health · Crop height · Digital surface model · Drone · GCP based height calibration · Machine learning · Smart agriculture

1 Introduction

The process of obtaining information regarding the terrain of an area is of great importance in defence applications as it provides state-of-the-art terrain intelligence to armed forces. Terrain is militarily critical as it helps to determine the ability of armed forces to take and hold areas as well as move troops and material into and through areas. The terrain information comprises of the density of vegetation cover and the height of the plants present within the cover. This terrain information is of utmost importance pertaining to geographical areas that are unexplored as prior knowledge about the possible optimal paths (terrain) between source and destination in such areas can help the troops in movement [1]. This evaluation of terrain characteristics plays an essential role for defence purposes through derivation of military potential of various types of terrains for areas where availability of ground information is limited [2]. With reference to the terrain map objectives, constraints are dependent on time, avoidance of enemies, distance etc. The terrain may comprise of various species of plants such as vegetation, bushes and shrubs in rare or dense volume. It is quite important to obtain plant height to know the hideout locations, in conjunction with terrain information, as this is imperative for smooth mobility of troops from one place to another while assessing mobility potential of inaccessible areas. The calculation of plant height helps the troops to perform correct calculations regarding the area of movement and be well prepared in advance. This can also help them to understand where they have to be alert, as enemies may be hidden in the taller and dense bushes.

Anthesis or flowering is the point at which crop height is considered to be at its peak [3]. Crop height can be defined as the shortest distance considered between the upper bound of the plant's main photosynthetic tissues and the ground level [4]. It is most commonly observed that the plant height measurement is carried out using a measuring rule [5], which in its simple form is an inefficient, laborious, and a subjective method for data collection. Therefore, there is a need for precise, rapid, in-season data acquisition for monitoring the environmental influences throughout the development cycle of the crop. In addition, the method should be sufficiently able to meet the needs of the large number of crop trial measurements.

Alternative methods have been proposed such as Light detection And Ranging (LiDAR) or RGB high resolution UAV imagery in order to estimate plant height [5–7]. LiDAR is an efficient way of measuring large areas of trees quantitatively. However, application of LiDAR scanning performed (from the ground with a terrestrial laser scanner) to crops with quite limited vertical extent or a canopy volume densely populated by leaves and stems appears limited [5]. This is because the system demands to be moved over a high number of places and viewing biases

also get incorporated leading to impact in spatial resolution. Also; very dense vegetation may obstruct laser beams from reaching all the way to the bare earth [8]. RGB image-based retrieval of crop height has been widely used because of advantages such as high versatility, low cost and smaller-cheaper-lighter sensors [5].

Precision-agriculture management strategies are quite important for crop health improvement. The analysis of plant height, crop density and leaf-area cover are useful for increasing the crop yield and subsequently enhancing agricultural production. Imaging sensors such as thermal, RGB, multispectral in conjunction with Unmanned Aerial Vehicles (UAV) helps to build vegetation index [9, 10], which indicates canopy cover, Leaf Area Index (LAI), disease incidence etc. Hyperspectral imagery has been collected using UAVs for height estimation and is inclusive of vegetation monitoring [11]. Also, the utility of UAVs is well demonstrated through metrics such as thermal emittance, plant height which are essential in the field of vegetation monitoring environment [12, 13]. A number of UAV applications have been addressed like various classification techniques have been critically evaluated to classify remotely sensed data by using high-resolution drone imagery for class wise area estimation [14, 15]. A machine learning-based approach to calibrate sensor band values for computing optimal vegetation index with the drone data [16]. To correctly classify the terrain, a technique has been proposed to detect and remove the shadow from the high-resolution UAV imagery [17]. UAVs helps us by collecting multiple images of the same area, which is quite important while assessing the impact of the environmental conditions on the plant performance, along with stating it as an essential phenotype for the crop product optimization and improvement [18]. Height is a good indicator of the yield and carbohydrate storage capacity [19] while also being an important parameter for the site-specific agricultural management practices [20].

High resolution has always seen to improve the model accuracy of the plant-height but this approach requires more processing time, higher costs and more sensor angle variation [21]. A change detection approach for land terrain monitoring has been evaluated with Sentinel-2 and drone data by applying neural network [22]. Willkomm et al., [23] modelled plant height to be an average 10–20 cm shorter when compared with the ground truth estimates while generating a spatial resolution stated as 0.5 cm. However, it can be seen that UAV models have the tendency to underestimate heights as, this has been performed for rice plantation and also an adjustment of the density of plants also needs to be investigated. Malambo et al. [24] has used Digital Surface Model (DSM) and Terrestrial Laser Scanning (TLS) for maize and plant height detection. It has suggested the use of laborious height management. However, impact of changing canopy structure and wind needs to be observed.

A study for target detection using hyperspectral images for various applications has been demonstrated for both defence and civilian [25]. In a comparison of the statistical approaches, new technology such as synthetic aperture radar (SAR) data and neural network is used for the target detection [26]. A computer vision-based approach for extracting and monitoring rail track where UAV imagery has been used to calculate gauge and marked over and under measured gauge [27]. A computer vision-based approach for joggled fish plate detection has been performed using

UAV imagery [28]. Vision based correct localization of rail track in UAV imagery is proposed using single georeferenced image [29]. A leaf wetness in strawberry plant has been detected using the color and thermal imagery and it was found that color imaging yielded good classification results for differentiating between wet and dry leaf surfaces [30]. The work suggests neural networks and multisource data integration have great potential for analysing and interpreting targets. This work aims to provide solutions to the army officials for taking decisions regarding the movement of army troops in the real world terrain. The proposed tile-based A* approach is observed to have gained appreciation for optimal path finding. Also the halt schedule has been introduced in this work in order to avoid collision between troops [31]. A mathematical formulation for encoding of the transportation network between ground-troop movement in a dense and complex terrain has been proposed in which they have constructed a generic method for developing infinite number of graceful signed graphs for optimal encoding of the road network for planning possible automation of troop-movement strategies [32]. In this work employment of interoperability and armor protection concerning future of tracked personnel carrying vehicles lowers the possible losses. Also the maintenance and procurement costs are lowered for Armour Personnel Carriers (APCs) and Infantry Fighting Vehicles (IFVs) [33].

The main objective of this paper is to estimate terrain information in terms of the plant height from the drone data that will be beneficial for defence as well as civil application. Estimation of plant height is useful in various applications like for planning troop's movement in defence, terrain actual scenario estimation, plant growth and monitoring in precision agriculture etc. Using UAVs with HD camera for computing the plant height is less reported in the literatures, therefore in this paper, a machine learning-based approach has been proposed and explored to monitor terrain scenario by estimating plant height using drone data. Another advantage of using the machine learning is that it provides better efficiency and ease in automation.

Supplementary information from drones and GCPs is used in developing the model. The challenge here is a need for drone imagery to provide the precise level of terrain information and correctly recorded plant height of GCPs by which the model can be precisely trained.

2 Study Area and Data Description

The description of the study area and the dataset used in this study is given in the subsections.

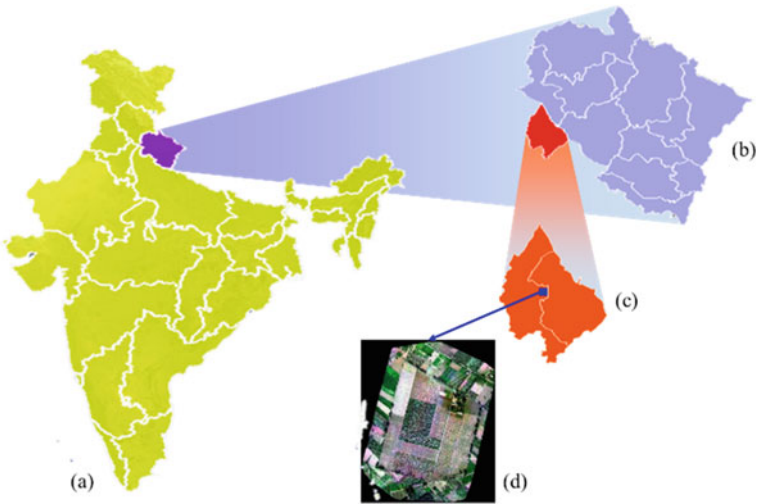


Fig. 1 The directed map to reach to the study area as **a** India political map, zoomed-in segments. **b** Uttarakhand state. **c** Haridwar district, and **d** data acquired by drone

2.1 Study Area

The study area chosen is located at Dhanori, a place nearby Roorkee which is a tehsil of Uttarakhand, a state lying in the northern part of India. It is an agriculture field having the central latitude and longitude as $29.930014^{\circ}\text{N}$ and $77.964504^{\circ}\text{E}$ respectively. The directed map of the study area is shown in Fig. 1.

2.2 Data Description

Drone data. The DJI Matrice 100 quadcopter has been used for data acquisition in this study which has Zenmuse X3 gimbal with a camera along with the attached GPS unit. The camera captures the 4 K RGB HD/FHD/UHD data in the form of images (4000×3000 at 12 M) and video ($4096 \times 2160\text{p}$ at 12 fps) [34]. The FOV (Field of View) of camera is 94° with an aperture of $f/2.8$ [35]. The drone is flown at an altitude of 120 m above the ground level to capture the images having a forward and side overlap of 75% and a spatial resolution of 0.05 m. The data is preprocessed with the help of a tool which results in the output datum having a map projection of UTM WGS-84N 43 zone. The specifications of drone used to capture the data and its sensor specifications are listed in Table 1a, b respectively.

In-situ data. Regular field visits were conducted to record the ground truth information and monitor the growth of various crops each of which were in a different stage. During the field visits, sugarcane and wheat are the major crops. The data was

recorded manually as well with the drone. While manually recording the data, in-situ plant height is measured using a measuring tape (in cm) along with the geotag information. For a plant of small height like wheat, rice, etc., measurements were taken from the ground and followed up to the height where most of the plant leaves occur and for taller plants like sugarcane, measurements were taken from the ground and followed up to the height where most of the leaves started bending. Table 2 shows the details of field visits conducted along with the data acquisition date and date ID (D_ID) that will be used as a nomenclature in the further sections. Growth stages of wheat crop (as sample) on different dates during in-situ data collection is shown in Fig. 2 and GCPs overlay on google earth imagery for the D_ID: D1 for the various measurements during in-site data collection is shown in the Fig. 3.

Table 1 a Specifications of the drone. b Specifications of the sensor

(a)	
Items	Specifications
Type	Quadcopter
Max takeoff weight	3600 g
Battery	6000 mAh LiPo 2S
Battery model	TB47D, TB48D
Flight planning software	DJI drone deploy
Endurance	20 min with each battery
Maximum speed	17 m/s
(b)	
Name	X3
Model	FC350
Number of pixels	12.4 M
Max image size	4000 × 3000
ISO	100–1600
Shutter	8–1/8000 s
FOV	94°
CMOS	Sony EXMOR 1/2.3"
Lens	20 mm, f/2.8

Table 2 Details of field visits conducted

SN	D_ID	Acquisition date
1	D1	09-Jan-2019
2	D2	30-Jan-2019
3	D3	08-Mar-2019
4	D4	27-Mar-2019

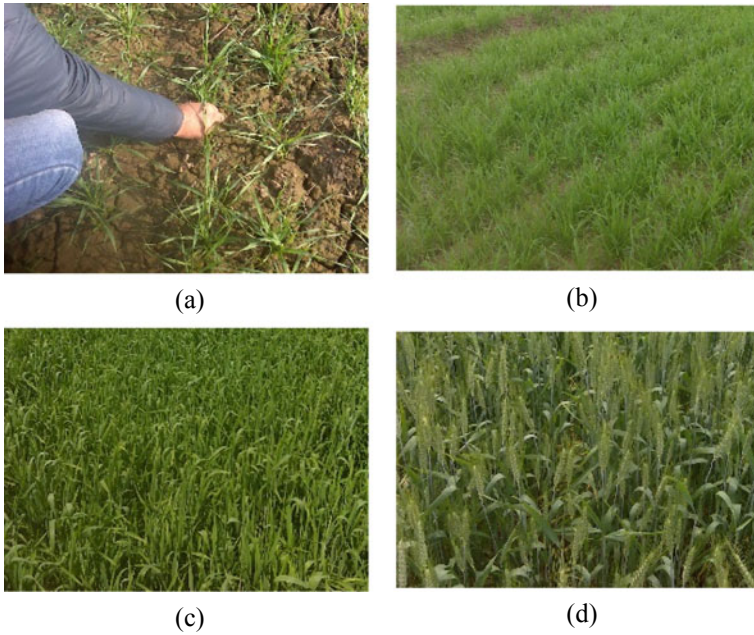
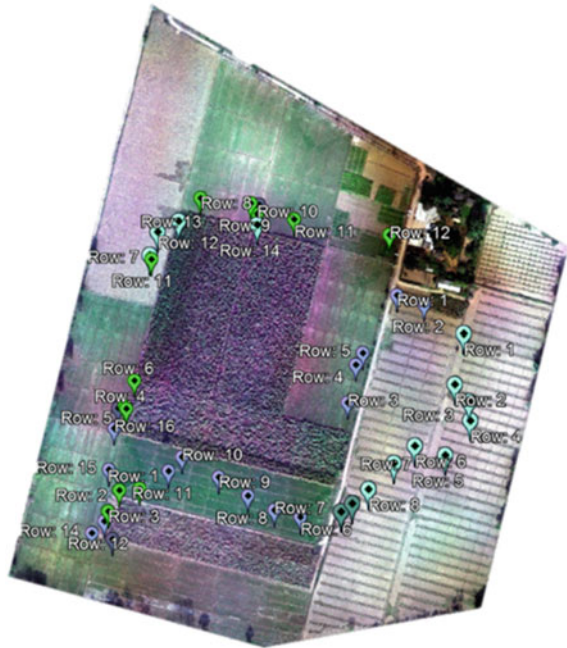


Fig. 2 Growth stages of wheat crop of D_ID, **a** D1, **b** D2, **c** D3, and **d** D4

Fig. 3 GCPs overlay on google earth imagery



3 Algorithm Development and Implementation

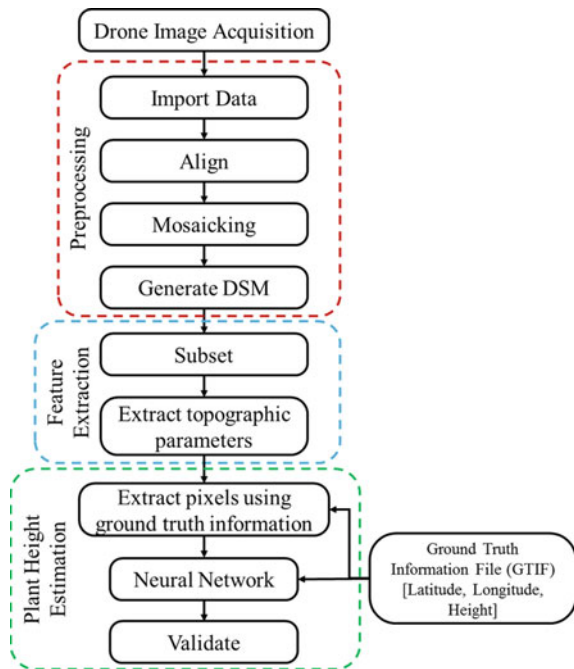
The objective of the field visit is to obtain plant height measurement for estimation of terrain. The height is recorded manually with their geotag information. Apart from this, the drone is used to capture the entire field, which is used for further analysis. The workflow of the proposed methodology is shown in Fig. 4. The detailed explanation of each step is given in the further section.

3.1 Preprocessing of Drone Data

Images collected by the drone during field visits were imported in Pix4D Mapper for further preprocessing [36]. The preprocessing steps include aligning of the images, building of dense point cloud, generation of orthomosaic and digital surface model. The stepwise explanation of each preprocessing step is given below.

Step 1—Aligning of the images: The first and preliminary step is the aligning of images, in which images are matched with each other to determine the camera position for each of the image and to calibrate the camera parameters. This process ends with the removal of those images that do not fit with the rest of the images and are known as distorted images.

Fig. 4 The workflow of the proposed methodology



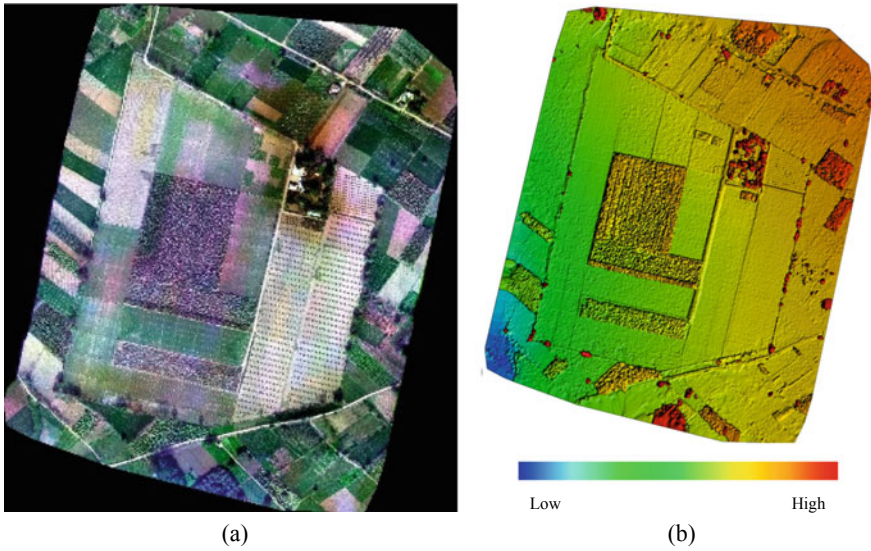


Fig. 5 Sample. **a** RGB orthomosaic, and **b** DSM (whereas blue color denotes less height and moving towards red denotes high height)

Step 2—Building of dense point cloud: After aligning of images, a dense point cloud is generated on the basis of estimated camera positions which ensures to provide the depth map information for each overlap area in images accurately by removing the outliers.

Step 3—Generation of Orthomosaic and DSM: After generation of dense cloud, the orthomosaic and DSM are created in which few parameters are considered with their values are alignment accuracy: high, dense cloud quality: medium, input image resolution: 0.05 m, generated DSM resolution 0.08 m (approx.), and coordinate system: WGS 84/UTM, Zone 43 N. The RGB orthomosaic and DSM are shown in Fig. 5a, b respectively.

3.2 Extraction of Topographic Parameters

The preprocessing steps include changing the map projection, taking the subset, and extracting topographic parameters. For this purpose, ENVI tool provided by Harris Geospatial Solutions is used [37, 38]. The stepwise explanation of each step is given below.

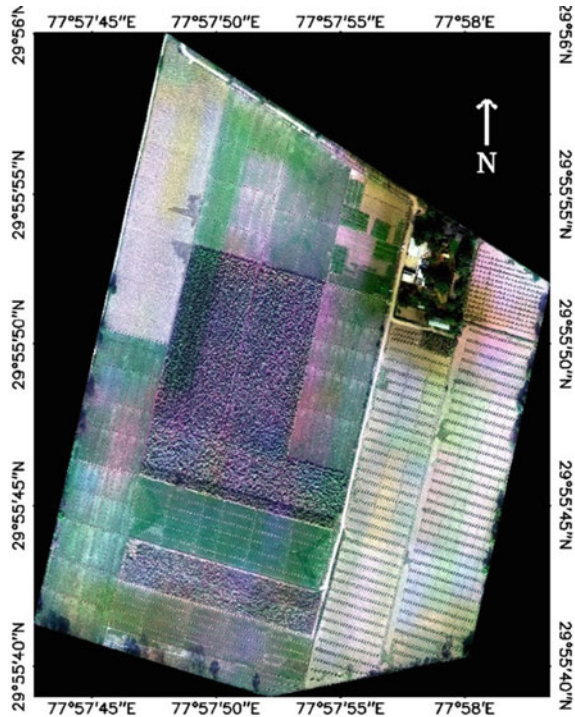
Step 1—Changing the map projection: In the first step, the map projection of the generated orthomosaic and DSM are converted from UTM WGS-84N 43 zone to

Geographic Lat/Long for further processing. The spatial resolution of both orthomosaic and DSM after changing the map projection is 0.092×0.082 m from west to east and north to south direction respectively.

Step 2—Subset: After changing the map projection, a subset of the study area is cropped from the orthomosaic drone imagery and DSM, which are bounded by same latitude-longitude pair of 29.933314° , 29.927528°N and 77.961844° , 77.967663°E . The region excluding the study area in the bounded latitude-longitude pair is masked with a value 0 and the total number of pixels are 7822×6062 . The sample subset RGB orthomosaic imagery of the study area for the D_ID: D1 is shown in the Fig. 6.

Step 3—Extracting topographic parameters: The subset received from DSM is used to extract the topographic parameters. These topographic parameters are then used to generate the relation for the calculation of plant height after getting trained with the ground truth height measurement. A total of 11 topographic parameters have been extracted out of which only 4 parameters (slope, aspect, shaded relief, and profile convexity) are selected for generating the relation for plant height estimation. These selected parameters are chosen because it is observed that these parameters are directly promotional to the height of the plant. The topographic parameters that are extracted from DSM are stored in a file with their geotag information. The parameters chosen for estimating the height is shown in the Fig. 7.

Fig. 6 RGB orthomosaic imagery of the study area



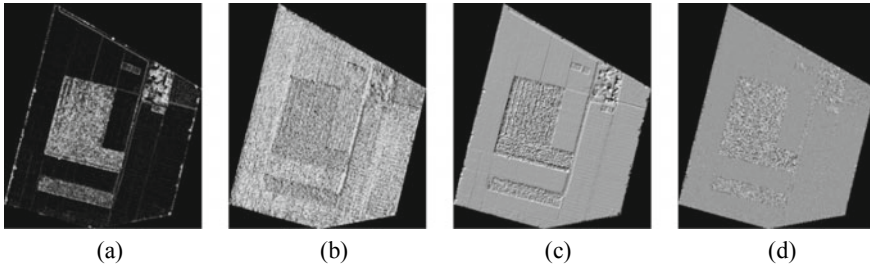


Fig. 7 Parameters chosen for estimating the height, **a** slope, **b** aspect, **c** shaded relief, and **d** profile convexity

3.3 Extraction of Topographic Values for Training

This step includes the extraction of topographic parameters values of GCPs for training purpose and the neural network part which is accomplished with MATLAB 2018b [39].

Step 1—Extraction of parameters values at GCPs: The step starts by loading a topographic parameter file which was saved in the previous step, along with a ground truth information file (GTIF) which was created during the time of field visit that contains latitude, longitude and height information of various GCPs position. The required bands are extracted from the topographic parameter file. Then the values from these parameters were extracted for the corresponding GCPs from the Fig. 7. A total of 150 GCP of different crops having different height and stages of different dates were taken, out of which 70, 15, and 15% of GCPs were used for training, testing and validation purpose by the neural network. Afterwards, these extracted band values of GCPs are given at the input of the neural network to generate the relation with the ground truth GCPs height as target.

Step 2—Training of network: The neural network is a feed-forward backpropagation which has 4 input nodes, 10 hidden neurons, and 1 target node. Several hidden nodes were experimented and it is found that 10 hidden neurons were given better results and thus 10 neurons were considered. At input, the extracted values of GCPs from the required bands of topographic parameters are provided and at output node, measured height of various GCPs during in-situ data collection are provided. This creates a network and generates a relation between topographic parameters and targeted height. The generated relation is then validated in the further section and the schematic diagram of the neural network which is shown in Fig. 8.

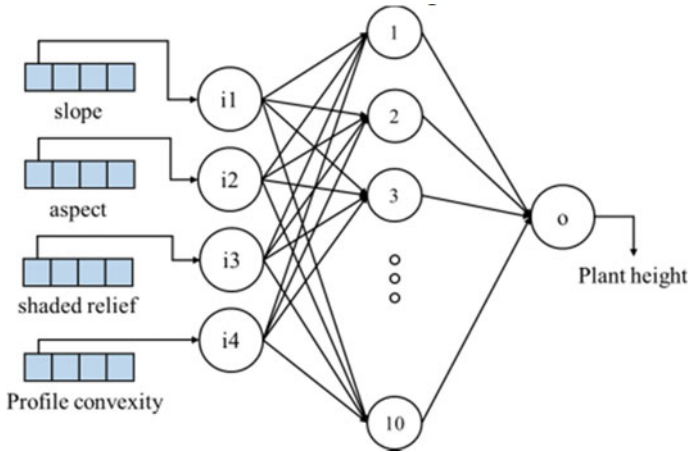


Fig. 8 The architecture of the neural network

4 Results and Discussions

During the field visits, measurement of plant height manually and capturing field data using drone are of main concerns. After processing, the result obtained from output of network is evaluated in time series for selected area as well as the whole image which are shown in the subsequent sections.

4.1 Height and Error Estimation

Height was estimated for different dates and it is observed that it is quite matching with the ground truth measurement. The generated result from the network is shown in Fig. 9. It has been inferred that the red line shows the height measured during field visits on D_ID: D2-D4 of various crops, green bars show the height estimated from the network, and black line shows the error between measured and estimated height that can be calculated with the help of Eq. (1). It is clearly seen that there are few outliers which may be because of few boundary GCPs position falls in other class and thus result in an error.

$$\text{Error} = \text{Actual Height} - \text{Estimated Height} \tag{1}$$

The same is plotted in the scatter plot and it is observed that there is a good agreement between actual and estimated plant height (in cm) as shown in Fig. 10, with the Root Mean Square Error (RMSE) of 20.978. On the horizontal axis, ground truth measured height is provided while on the vertical axis estimated height from the network is provided and red line is 1:1 slope line.

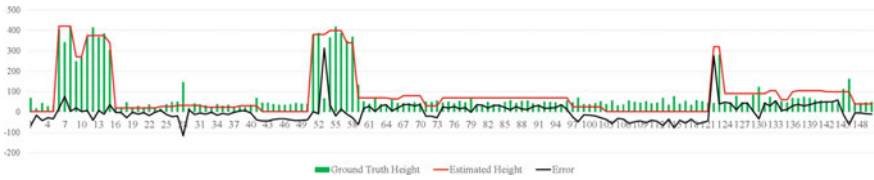
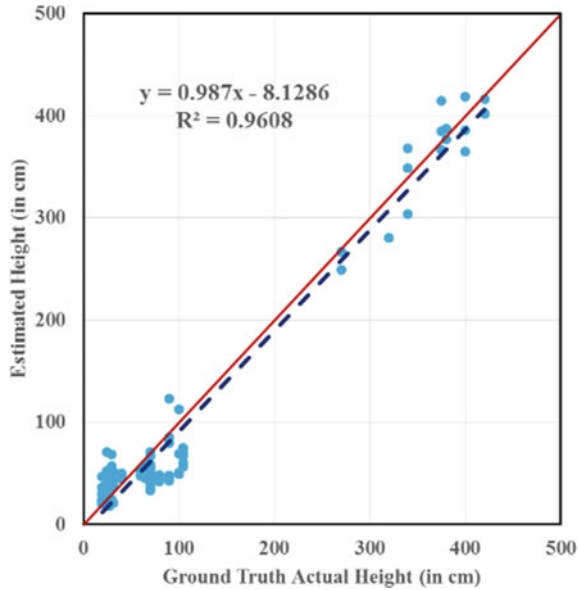


Fig. 9 Performance evaluation of network

Fig. 10 Scatter plot



4.2 Time Series Plot of Plant Height

Plant heights keep on changing during the growing season. As mentioned earlier, study area mainly consists of fallow land, wheat (which is sown on different dates at the sowing time), and sugarcane (which is at its peak stage and is harvested). Plant height measurement (in cm) of wheat crop varied significantly which is at different growth stages across the dates as shown in Fig. 2. Plant height estimates from the neural network and ground-truth measurement of the wheat crop for D_ID: D2–D4 are shown in Fig. 11 in which number of samples of the in-situ measured height for the D_ID: D2, D3, and D4 are 25, 43, and 27 respectively.

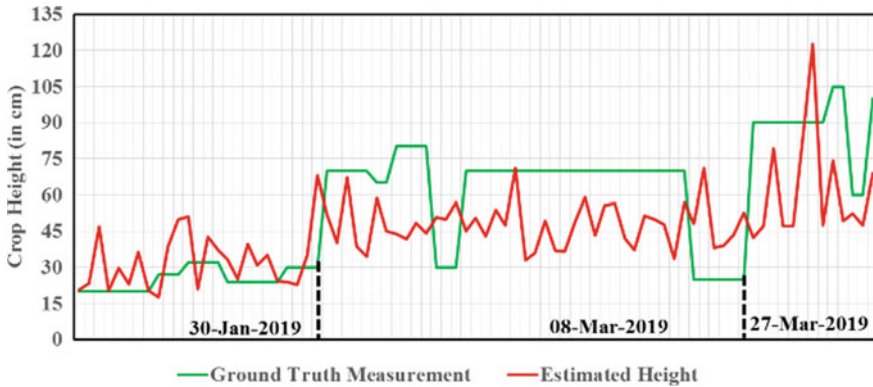


Fig. 11 Changes in the crop height trend of the wheat crop for D_ID: D2–D4

4.3 Evaluation for Whole Region

The generated network is applied to the whole study area for the D_ID: D1 having the dimension 7822×6062 , which results in a good output having a minimum and maximum values (in cm) of 2.6666 and 419.9983 while during ground truth measurement, the minimum and maximum values (in cm) are 5 and 420. The sample result for the D_ID: D1 is shown in Fig. 12 (a). Afterwards, to generate the 3-D plot, the drone imagery is up-scaled by a factor of 100 and resultant image has a dimension of 78×60 , which results in a minimum and maximum value (in cm) of 45.0511 and 320.3055. The up-scaled result in 2-D and 3-D is shown in Fig. 12b, c respectively. The same procedure is followed for rest of the D_IDs, whose 3-D results are shown in Fig. 12d–f.

To analyze the accuracy and robustness of this methodology, we have taken the subset from the study area and the result set of all the D_ID: D1–D4 is shown in the Fig. 13 with their respective zoomed-in segments.

4.4 Improvement in Plant Height Accuracy

A relation between the plant height of ground truth measurement and the height estimated from the network is generated in order to minimize the error and improve the accuracy of estimation. A relation in the form of $y = f(x)$ is generated, in which x is the height estimated from the network and y is the improved calibrated height. It is found that the trend line of the calibrated data is much closer to the 1:1 slope line than the trend line of before calibrated height. The RMSE values of before and after calibration are 20.978 and 13.171 respectively which shows that there is a significant improvement in the accuracy. The correlation between the before calibration and after calibration height data is shown in Fig. 14. On the horizontal axis,

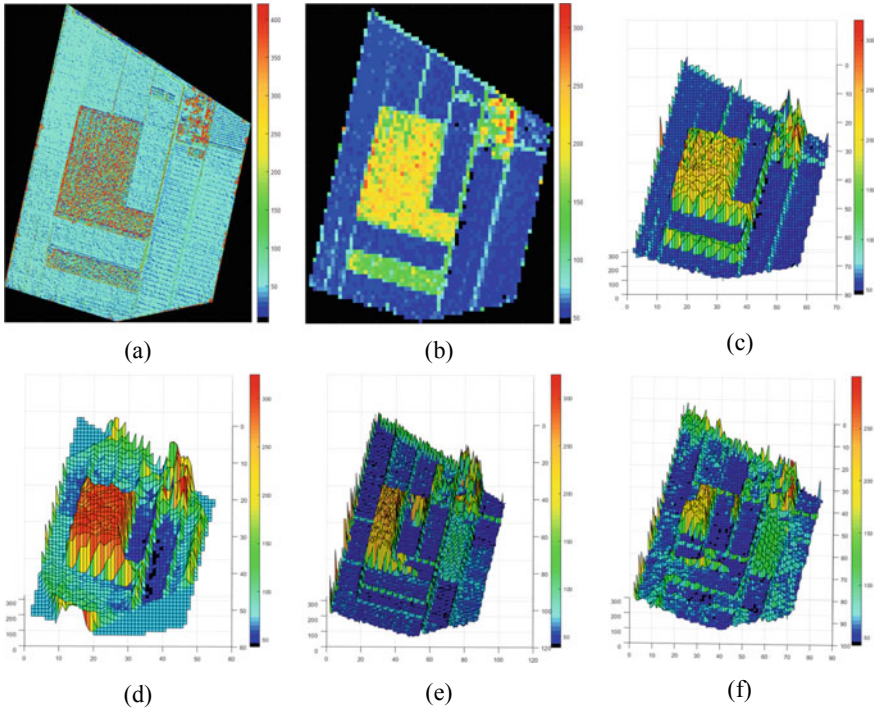


Fig. 12 Estimated height for D_ID: D1 on **a** drone imagery, up-scaled drone imagery **b** in 2-D, **c** 3-D, for rest of the D_IDs in 3-D for **d** D2, **e** D3, and **f** D4

ground truth measured height is provided while on vertical axis before calibration and after calibration heights are provided which are plotted with respect to ground truth measured height. The generated relation is shown in the Eq. (2).

$$y = 0.9014x + 10 \log(x) + \exp(\log(x)) \tag{2}$$

The relation is then applied to the same set of GCPs to test the performance of the calibration. It is noticed that the plant height estimated from the network is quite improved after applying the generated relation. It is fairly noticed from Fig. 15 that the error is minimized and accuracy is improved. The generated relation is found useful in the sense that it is capable of minimizing the error in the estimation of the plant height. The green bars represent the ground truth measured plant height, red line represents the plant height estimated from the network (before calibration), and black line represents the plant height by improving the relation (after calibration).

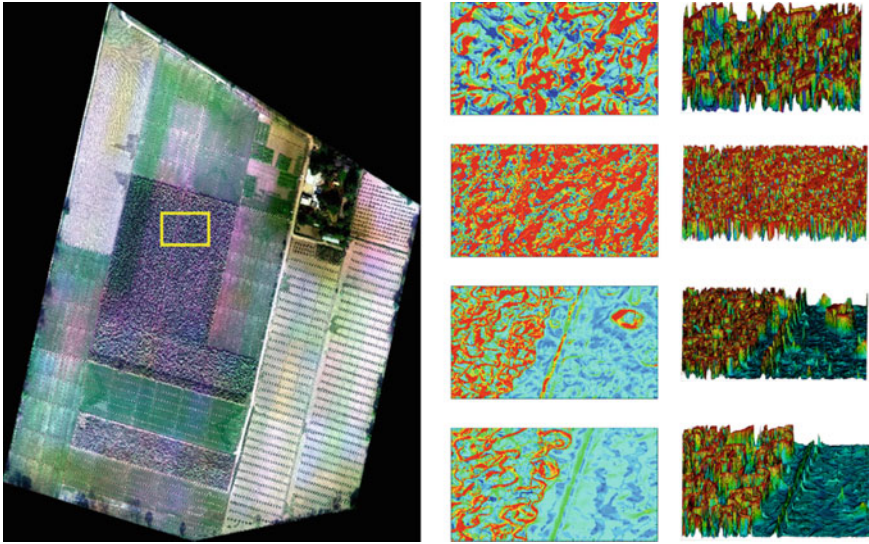


Fig. 13 A subset is in yellow box with zoomed-in segments in 2-D and 3-D of D_ID. **a** D1, **b** D2, **c** D3, and **d** D4

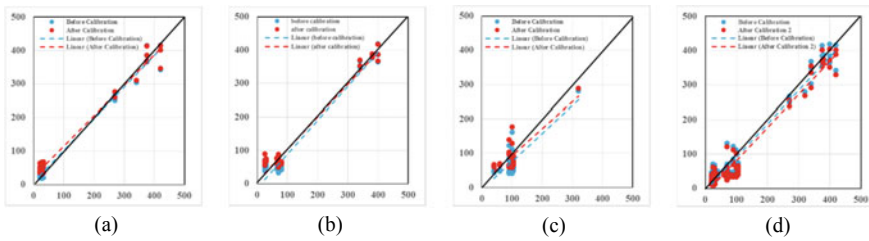


Fig. 14 Comparison of before and after calibration data for D_ID. **a** D2, **b** D3, **c** D4, and **d** D2–D4. The black line is 1:1 slope

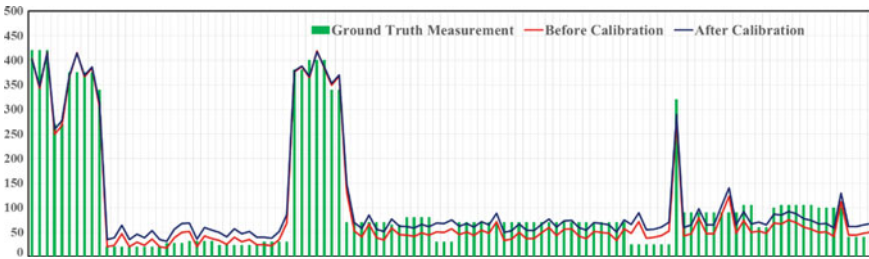


Fig. 15 Accuracy improvement in plant height

5 Conclusion

In this paper, a machine learning based novel approach has been explored in which a feed forward neural network is used to estimate the plant height by using drone data. The advantage of this method is that it is used to generate the relation between ground truth measured height and extracted topographic parameters. The relation is then optimized to minimize the error and it is found that a proposed method has good potential to estimate the plant height using the RGB drone camera.

Acknowledgements The author would like to extend appreciation to all the lab members who have always inspired and supported in the work. The author would also like to express thanks to RailTel Corporation of India Ltd., Delhi, India and Indo-French Centre for Applied Mathematics (IFCAM) for sponsoring this work. The author would also express sincere gratitude to Krishi Vigyan Kendra, Dhanori, Roorkee, Uttarakhand, India for providing a comfortable zone to record data for this research. Finally author would thank all the colleagues who helped during field visits.

References

1. Rishiwal V, Yadav M, Arya KV (2010) Finding optimal paths on terrain maps using ant colony algorithm. *Int J Comput Theory Eng* 2(3):416
2. Sabol DE, Minor TB, McDonald EV, Bacon SN (2016) Parent material mapping of geologic surfaces using ASTER in support of integrated terrain forecasting for military operations. In: *Military geosciences and desert warfare*, New York, NY, pp 311–337. https://doi.org/10.1007/978-1-4939-3429-4_20
3. Wheat growth guide | AHDB. <https://ahdb.org.uk/wheatgg>. Accessed 06 Aug 2019
4. Pérez-Harguindeguy N et al (2013) New handbook for stand-ardised measurement of plant functional traits worldwide. *Australian J Botany* 61:167–234
5. Madec S et al (2017) High-throughput phenotyping of plant height: comparing unmanned aerial vehicles and ground LiDAR estimates. *Front Plant Sci* 8:2002. <https://doi.org/10.3389/fpls.2017.02002>
6. Bareth G, Bendig J, Tilly N, Hoffmeister D, Aasen H, Bolten A (2016) A comparison of UAV- and TLS-derived plant height for crop monitoring: using polygon grids for the analysis of crop surface models (CSMs). *Photogramm Fernerkund Geoinf* 2016(2):85–94. <https://doi.org/10.1127/pfg/2016/0289>
7. Holman F, Riche A, Michalski A, Castle M, Wooster M, Hawkesford M (2016) High throughput field phenotyping of wheat plant height and growth rate in field plot trials using UAV based remote sensing. *Remote Sens* 8(12):1031. <https://doi.org/10.3390/rs8121031>
8. Risbøl O, Gustavsen L (2018) LiDAR from drones employed for mapping archaeology—Potential, benefits and challenges. *Archaeol Prospect* 25(4):329–338. <https://doi.org/10.1002/arp.1712>
9. Shi Y et al (2016) Unmanned aerial vehicles for high-throughput phenotyping and agronomic research. *PLoS ONE* 11(7):e0159781. <https://doi.org/10.1371/journal.pone.0159781>
10. Lan Y, Thomson SJ, Huang Y, Hoffmann WC, Zhang H (2010) Current status and future directions of precision aerial application for site-specific crop management in the USA. *Comput Electron Agric* 74(1):34–38. <https://doi.org/10.1016/j.compag.2010.07.001>
11. Aasen H, Burkart A, Bolten A, Bareth G (2015) Generating 3D hyperspectral information with lightweight UAV snapshot cameras for vegetation monitoring: From camera calibration to quality assurance. *ISPRS J Photogramm Remote Sens* 108:245–259. <https://doi.org/10.1016/j.isprsjprs.2015.08.002>

12. Efron S (2015) The use of unmanned aerial systems for agriculture in Africa. <https://doi.org/10.7249/RGSD359>
13. Xue X, Lan Y, Sun Z, Chang C, Hoffmann WC (2016) Develop an unmanned aerial vehicle based automatic aerial spraying system. *Comput Electron Agric* 128:58–66. <https://doi.org/10.1016/j.compag.2016.07.022>
14. Agarwal A, Singh AK, Kumar S, Singh D (2018) Critical analysis of classification techniques for precision agriculture monitoring using satellite and drone. In: 2018 IEEE 13th international conference on industrial and information systems (ICIIS), pp 83–88. <https://doi.org/10.1109/ICIINFS.2018.8721422>
15. Dwivedi AK, Roy S, Singh D (2020) An Adaptive neuro-fuzzy approach for decomposition of mixed pixels to improve crop area estimation using satellite images. In: IGARSS 2020–2020 IEEE international geoscience and remote sensing symposium, pp 4191–4194
16. Agarwal A, Kumar S, Singh D (2019) Development of machine learning based approach for computing optimal vegetation index with the use of sentinel-2 and drone data. <https://doi.org/10.1109/IGARSS.2019.8897896>
17. Agarwal A, Kumar S, Singh D (2020) An adaptive technique to detect and remove shadow from drone data. *J Indian Soc Remote Sens* 1–8
18. Chang A, Jung J, Maeda MM, Landivar J (2017) Crop height monitoring with digital imagery from unmanned aerial system (UAS). *Comput Electron Agric* 141:232–237. <https://doi.org/10.1016/j.compag.2017.07.008>
19. Chapman S et al (2014) Pheno-copter: a low-altitude, autonomous remote-sensing robotic helicopter for high-throughput field-based phenotyping. *Agronomy* 4(2):279–301. <https://doi.org/10.3390/agronomy4020279>
20. Lati RN, Filin S, Eizenberg H (2013) Estimating plant growth parameters using an energy minimization-based stereovision model. *Comput Electron Agric* 98:260–271. <https://doi.org/10.1016/j.compag.2013.07.012>
21. Fisher JR, Acosta EA, Dennedy-Frank PJ, Kroeger T, Boucher TM (2018) Impact of satellite imagery spatial resolution on land use classification accuracy and modeled water quality. *Remote Sens Ecol Conserv* 4(2):137–149. <https://doi.org/10.1002/rse2.61>
22. Agarwal A, Kumar S, Singh D (2019) Development of neural network based adaptive change detection technique for land terrain monitoring with satellite and drone images. *Def Sci J* 69(5):474. <https://doi.org/10.14429/dsj.69.14954>
23. Willkomm M, Bolten A, Bareth G (2016) Non-destructive monitoring of rice by hyperspectral in-field spectrometry and UAV-based remote sensing: case study of field-grown rice in north Rhine-Westphalia, Germany. *Int Arch Photogramm Remote Sens Spat Inf Sci* 41. <https://doi.org/10.5194/isprsarchives-XLI-B1-1071-2016>
24. Malambo L et al (2018) Multitemporal field-based plant height estimation using 3D point clouds generated from small unmanned aerial systems high-resolution imagery. *Int J Appl Earth Obs Geoinf* 64:31–42. <https://doi.org/10.1016/j.jag.2017.08.014>
25. Arora MK, Bansal S, Khare S, Chauhan K (2013) Comparative assessment of some target detection algorithms for hyperspectral images. *Def Sci J* 63(1):53–62. <https://doi.org/10.14429/dsj.63.3764>
26. Chaudhuri BB, Parui SK (1995) Target detection: remote sensing techniques for defense applications
27. Singh AK, Swarup A, Agarwal A, Singh D (2019) Vision based rail track extraction and monitoring through drone imagery. *ICT Express* 5(4):250–255. <https://doi.org/10.1016/j.ict.2017.11.010>
28. Saini A, Agarwal A, Singh D (2020) Feature-based template matching for joggled fishplate detection in railroad track with drone images. In: IGARSS 2020–2020 IEEE international geoscience and remote sensing symposium, pp 2237–2240
29. Singh AK, Swarup A, Phartiyal GS, Singh D (2020) Computational-vision based orthorectification and georeferencing for correct localization of railway track in UAV imagery. In: IGARSS 2020–2020 IEEE international geoscience and remote sensing symposium, pp 6475–6478

30. Swarup A, Lee WS, Peres N, Fraisse C (2020) Strawberry plant wetness detection using color and thermal imaging. *J Biosyst Eng* 45(4):409–421
31. Agrawal A, Joshi A, Radhakrishna M (2007) Move table: an intelligent software tool for optimal path finding and halt schedule generation. *Def Sci J* 57(5):721
32. Acharya M, Singh T (2006) Construction of graceful signed graphs. *Def Sci J. (New Delhi)* 56(5):801
33. Balos S, Grabulov V, Sidjanin L (2010) Future armoured troop carrying vehicles. *Def Sci J* 60(5)
34. DJI—The World Leader in Camera Drones/Quadcopters for Aerial Photography. DJI Official. <https://www.dji.com/matrice100/info>
35. M100_User_Manual_EN.pdf. Accessed 15 July 2019. https://dl.djicdn.com/downloads/m100/M100_User_Manual_EN.pdf
36. Professional photogrammetry and drone mapping software. *Pix4D*. <https://www.pix4d.com/>
37. Harris Geospatial. Wikipedia. Accessed 14 May 2019. https://en.wikipedia.org/w/index.php?title=Harris_Geospatial&oldid=896980003
38. ENVI®. Harris. Accessed 25 March 2016. <https://www.harris.com/solution/envi>
39. R2018b—MATLAB and Simulink product families. https://in.mathworks.com/products/new_products/release2018b.html